MTA Doktori Értekezés

(Rövid értekezés)

NYIRI GÁBOR

A MEMÓRIA AGYKÉREG ALATTI SZABÁLYOZÁSA

Kísérleti Orvostudományi Kutatóintézet

Budapest, 2020

Tartalomjegyzék

Előszó

Agyunk fontos képessége, hogy folyamatosan képes fejlődni és alkalmazkodni környezetéhez. Ennek egyik legfontosabb eszköze a tanulás és a memória. A tanulás képessége olyan sikeressé vált, hogy a mai ember nem csupán képes rá, de késztetést is érez annak gyakorlására, így a felfedezés és megismerés utáni vágy valamilyen formája minden ember életében fontos szerepet játszik. Ennek megfelelően, az emberi tanulás és a memória kutatása több oknál fogva rendkívül hasznos. Az emberi agy működésének megértése, részben a fent említett okok miatt, eredendő emberi kíváncsiságunk kielégítésére szolgál. Izgalmas felfedezni hogyan raktározódnak emlékeink, hisz ezek építik fel azt a történetet, ami alapján saját magunkat meghatározzuk és ami egyszer majd segíthet megérteni tudatunk működését is. Ugyanakkor a mindennapi élet szempontjából jelentős gyakorlati haszna is van ezeknek a kutatásoknak. Egyrészt lehetővé teszi, hogy az idegrendszeri eredetű megbetegedéseket célzottan gyógyítani tudjuk. Sajnos erre nagy szükség is van, mivel az idegrendszerrel kapcsolatos megbetegedések mára az egyik legnagyobb gazdasági és társadalmi terhet jelentik az emberiség számára. A központi idegrendszerrel kapcsolatos orvosi beavatkozások hatékonysága óriásit léphet előre, ha megismerjük az egyes agyterületek különböző sejttípusainak működését, ha felismerjük mely sejtek működésének változása vezet bizonyos megbetegedésekhez, és így specifikus módon képesek leszünk a személyre, sőt sejttípusra szabott orvosi eljárások kidolgozására. Optimális esetben ez nem csupán tüneti kezelést biztosíthat, hanem a betegek valódi gyógyulását is lehetővé teheti. Másrészt, az agy működésének megértése segíthet a mesterséges intelligenciák fejlesztésében is, amely a jövő társadalmát nagymértékben formáló technológiává válik majd. Mindezekhez elengedhetetlen az idegrendszer elemeinek, felépítésének és működésének pontos megértése, meg kell ismernünk az agy sejttípusait, azok kommunikációjának tulajdonságait, összeköttetéseik struktúráját és a működésük által irányított viselkedési és szabályozó folyamatokat.

A memóriát két főbb típusra szokás osztani, melyek tipikusan eltérő agyterületekhez kötődnek. Az implicit memória, jellemzően nem tudatos, ilyen például a finom mozgásokkal kapcsolatos motoros memória, aminek kézzel írás vagy hangszeres játék közben vesszük hasznát. A másik az explicit vagy deklaratív memória, ami tudatosan felidézhető emlékeket raktároz. A deklaratív memória, konkrét élethelyzetekhez, térbeli saját eseményekhez köthető típusát epizódikus memóriának nevezzük, melyek rövid időperiódusokat ölelnek fel és az eseményre vonatkozó specifikus kontextuális részleteket tartalmaznak. Ezek nyilvántartása a hippokampusz és a vele összekötött agyterületek feladata, amely az ún. kontextus függő emléknyomokat szervezi.

Agyunk felépítésének leegyszerűsített korábbi modellje szerint a különböző agyi folyamatok mint a szaglás, látás, tanulás, térbeli tájékozódás, beszéd, mind különböző agyterületek irányítása alatt áll. Bár ez a modell nem áll messze az igazságtól, a biológiai rendszereknél nem meglepő módon, a helyzet nem ilyen egyszerű. Jó példa erre az u.n. szomatoszenzoros, azaz érző agykérgi terület, melyről ma már ismert, hogy direkt mozgató

feladatokat is ellát (*1*), vagy a mozgató agykéreg, melyről ma már ismert, közvetlen érző feladatokat is ellát (*2*). A kontextuális emléknyomok raktározásában elsődlegesen felelősnek tartott hippokampális formációban a memória nyomok rögzítéséhez számos agyterület összehangolt működése szükséges, a környezeti ingerek előzetes szűrésétől kezdve, a hippokampusz működését koordináló ritmikus aktivitás szabályozásáig, melyeket mind jórészt a hippokampuszon kívüli, sokszor kéreg alatti agyterületek végeznek. Ugyanakkor meglepő módon számos főként kéreg alatti kontextuális memóriafolyamatokat irányító agyterületek sejtjei vagy azok jelátvivő rendszerei még mindig ismeretlenek.

Jelen értekezés, három tématerületet felölelő kutatásainkat mutatja be, melyekben a kontextuális memória hippokampuszon kívüli koordinálását végző új pályarendszereket vagy ismert pálya gyökeresen új tulajdonságát vizsgáltuk. Mindhárom kutatási téma eredményei segítenek új megvilágításba helyezni a kontextuális memória szabályozásáról alkotott korábbi elképzeléseinket, és általuk inspirálva a kutatások jelenleg is tartanak.

Rövid általános bevezetés után ismertetem e három tématerületen elért eredményeinket és a belőlük levonható tanulságokat. A témákhoz tartozó részletes kísérleti adatok, képek, illusztrációk, illetve további kiegészítő eredményeink a dolgozat mellékleteként csatolt eredeti közleményekben találhatók. Az értekezést rövid összefoglaló zárja.

Bevezetés

Az emlősállatok két előagyi területe a szeptum és a hippocampus alapvető fontosságú az éberségi, tanulási, memória, szorongásos, félelmi és emocionális folyamatokban, míg rendellenes működése szellemi hanyatláshoz vagy más kognitív rendellenességekhez vezethet. E területek beidegzést kapnak az agytörzsből, melynek fontos szerep jut alapvető szabályozó funkcióban, mint bizonyos típusú motoros és érzékelési folyamatok vagy az éberség és tudatosság koordinálása. Munkánkban ezeknek a területeknek a kapcsolatait vizsgáltuk.

A szeptum és a hippokampusz

A szeptum és a hippokampusz a limbikus rendszer részei. A hippokampusz alapvetően fontos a különböző típusú tanulási és memória folyamatokban (*3–6*), mint például az asszociatív (*7*), a térbeli (*8–11*), a deklaratív (*12*), a munkamemória (*11*, *13*), az epizodikus memória folyamatokban (*14*), a rövid és a hosszú távú memória nyomok rögzítésében és előhívásában (*9*, *15–17*), az éberségi és a figyelmi folyamatokban (*18*), a szorongás kialakulásában (*19*, *20*), az érzelmek feldolgozásában (*21*), a különböző érző és asszociációs kéreg területek felől érkező információk integrálásában (*22*), rövid távú memória nyomok tárolásában és előhívásában (*23*), miközben működésének zavara idő előtti kognitív problémákhoz vagy elbutuláshoz vezethet (*24*, *25*). A dorzális hippokampusznak elsősorban

a térbeli és kontextuális tanulási folyamatokban van szerepe, míg a ventrális hippokampusz inkább az érzelmi élet, félelem és szorongás szabályozásában játszik fontosabb szerepet (*26*).

Bazális előagy területén elhelyezkedő szeptális magok (mediális szeptum és Broca-féle diagonális köteg magvai) fontos átjátszó állomásai azon felszálló érző információknak (*27*), melyek a középagyat és agytörzset kötik össze az előagyi területekkel. A szeptális magoknak szintén alapvető funkciója van a tanulás és a memória folyamatokban (*28–30*), szabályozzák a térbeli memória folyamatokat (*31*), a munkamemóriát (*32*), a félelmet (*33*, *34*), a szorongást (*33*, *35*, *36*), az érzelmek és az agresszió folyamatait (*37*) és számos más érzelemmel összefüggő folyamatokat (*38*).

A szeptum és a hippokampusz erős anatómiailag és funkcionálisan kapcsolata

A memória folyamatokkal összefüggésben az egyik legfontosabb hippokampo-szeptális pálya a hippokampusz gátló GABAerg sejtjeinek egy típusától ered, míg a szepto-hippokampális pálya pedig több összetevőből áll így kolinerg, GABAerg és glutamaterg sejtek is vetítenek a szeptumból a hippokampuszba. Az emlős szepto-hippokampális rendszer egyik legjellemzőbb hálózati aktivitás mintázata az úgynevezett théta frekvencia sávban elhelyezkedő lassú hullámú oszcilláció, mely úgy tűnik a hippokampusz online aktív kódoló állapotát reprezentálja (*39–41*). Ez a hálózati oszcilláció fontos szerepet játszott a szepto-hippokampális rendszer működésének feltérképezésében. Számos kéreg alatti területről érkező pálya befolyásolja ennek a ritmusnak a kialakulását ideértve a mediális raphe régiót is, azonban továbbra is tisztázatlan, hogyan képes befolyásolni ezek a felszálló pályák a memória folyamatokat és azok honnan, hova és hogyan hordoznak érzelmi vagy motivációs információkat. Különösen nagy kihívás ezeknek a folyamatoknak a vizsgálata mivel (i) a kéreg alatti területről érkező felszálló pályák egy része még mindig ismeretlen. Például a szepto-hippokampális vetítéssel bíró, 2-es típusú vezikuláris glutamát transzporter pozitív (vGluT2) glutamaterg sejtek alapvető szerepét csak nemrégiben fedezték fel (*42*, *43*). Továbbá, ahogyan az épp saját munkáinkból is kitűnt, további pályák szintén felfedezésre vártak és bizonyára továbbiak is várnak még. Továbbá (ii) néhány felszállópálya esetében még a jelátvivő anyag tartalom természete is tisztázatlan (például nemrégiben tisztázódott hogy a medián raphéből érkező felszálló pálya távolról sem csak szerotonerg (*44*, *45*). Valamint (iii) a legtöbb tanulmány még mindig a jobban karakterizált és könnyebben vizsgálható agyterületekre fokuszál és elkerülte azokat a szepto-hippokampális rendszert beidegző nehezen jelölhető és manipulálható magokat, melyek megértése pedig fontos volna a rendszer működésének megértéséhez.

A mediális raphe régió

A mediális raphe régiónak (MRR) alapvető szerepe van mind az agykérgi mind pedig az agykéreg alatti hálózatok aktiválásának szabályozásában (*46*, *47*). A MRR-nak fontos szerep jut a félelmi viselkedés és az ehhez társuló bizonyos szorongásos

rendellenességekben. Bizonyos funkcionális rendellenességei akár skizofréniát vagy depressziót kiválthatnak (*48–54*). A MRR-t alapvetően egy szerotonerg magcsoportnak gondolták és a tudományos köztudatban még mindig ez az elképzelés uralkodik. Pedig régóta ismert,hogy bőséggel találhatók itt serkentő glutamaterg transzmisszióra képes a vezikuláris glutamát transzporter 3-as típusát (vGluT3) tartalmazó, valamint GABAerg azaz GABA (gamma-aminobutyric acid) transzmittert felszabadító sejtek is (*55–58*). A szerotonerg és a vGluT3 pozitív glutamaterg sejtek is sűrűn beidegzik az előagyi területeket (*45*, *47*, *59*), képesek a hippokampális aktivitás de-szinkronizálására és gátolják a szeptális idegsejtek ritmikus aktivitását, elnyomhatják a hippokampális éles hullám aktivitást és meggátolhatják a memória nyomok konszolidálódását, hálózati beépülését (*44*, *60*, *61*). Korábban sikerült azonosítanunk, hogy a vGluT3 pozitív glutamaterg sejtek képesek a szepto-hippokampális hálózat erős, gyors és pontos serkentésére (*44*, *45*). Meglepő módon azonban bármilyen sok információ gyűlt is össze az évek során a MRR működéséről és hatásáról, mégis ismeretlen volt annak pontos sejtösszetétele, azaz nem volt ismert, hogy hány féle sejttípus milyen ingerületátvivő anyagot használ a MRR-ban.

A nucleus incertus

A MRR GABAerg sejtjeinek vizsgálata közben észrevettük, hogy a MRR caudo-dorsalis határa mentén elhelyezkedő és nucleus incertus (NI) sejtjei jelentősen beidegzik a szepto-hippocampális rendszert. A NI-t korábban csupán egy peptiderg modulátoros magnak gondolták az itt található relaxin-3 peptid kifejeződése miatt. Összességében viszonylag kevés tudományos értekezés született a NI-szal kapcsolatban. Tudni lehetett, hogy legalább három különböző típusú sejt található itt: glutamaterg sejtek, valamint relaxin-3 neuropeptide- pozitív és negatív GABAergic sejtek (*62–65*). Bár a szakirodalomban található első eredmények azt sugallták, hogy a NI-nak fontos szerepe lehet a limbikus rendszer működésében, mégis célsejt szelektivitását és működését alig vizsgálták korábban. Meglepő módon az is kiderült, hogy a nucleus pontis oralis (nPO) limbikus rendszerre gyakorolt alapvető befolyását is a NI közvetíti, mivel a NI gátlása megszüntette az nPO serkentése által kiváltott hippokampális théta ritmus aktivitást. A relaxinerg NI rostok erősen vetítenek a limbikus területekre, mellyel a szeptális ritmusok és a hippokampusz függő tanulás és memóriát képes befolyásolni (*62–66*). Ennek megfelelően nem is meglepő, hogy fiziológiai adatok tanúsága szerint néhány NI sejt a hippokampális aktivitással fázis-kapcsoltan tüzel, miközben a relaxinerg jelátvitel mediális szeptumban történt gátlása, gátolja a térbeli munkamemória működését (*67*, *68*). Bár patkányban ismert volt, hogy néhány szeptális sejt rostokat küldd vissza a NI területére (*69*), mégis a NI efferens és afferens vetítési mintázata, cél-szelektivitása és különböző sejtjeinek viselkedésre gyakorolt hatása még mindig szinte teljesen ismeretlen volt.

Az acetilkolin-GABA kotranszmissziója és szerepe a memória szabályozásában

A tématerülethez tartozó mellékelt publikációk

V. T. Takács, T. F. Freund, G. Nyiri: Neuroligin 2 Is Expressed in Synapses Established by Cholinergic Cells in the Mouse Brain. *PLoS One.* 8 (2013).

V. T. Takács, C. Cserép, D. Schlingloff, B. Pósfai, A. Szőnyi, K. E. Sos, Z. Környei, Á. Dénes, A. I. Gulyás, T. F. Freund, G. Nyiri: Co-transmission of acetylcholine and GABA regulates hippocampal states. *Nature Communications*. 9 (2018)

Bevezetés

A hippokampusz sűrű beidegzést kap a bazális előagy szeptális területeiről eredő kolinerg sejtektől (*70*) és így ez központi szerepet játszik a szepto-hippokampális rendszer legtöbb bevezetőben említett funkciójában. A bazális előagyból felszálló kolinerg rendszer (*71*, *72*) alapvető szerepet játszik az agykérgi funkciók szabályozásában mint például a figyelem (*73*), a tanulás és memória (*74*), a szinaptikus plaszticitás (*75*), az alvás ébrenléti ciklusok szabályozása (*76*), és szerepe szintén jelentős bizonyos neurodegeneratív megbetegedésekben (*77*).

Bazális előagy kolinerg rendszerének korábbi modellje, a kolinerg rendszert célzó kezelések kifejlesztését célzó erőfeszítések és a kolinerg rendszer memóriafolyamatokban betöltött szerepe mind azon a feltételezésen alapultak, hogy a kolinerg rendszer sejtjei kizárólag egyetlen jelátvivő anyagot az acetilkolint szabadítják fel, főként nem-szinaptikus úgynevezett térfogati transzmisszióval (*78–83*). A kolinerg rostok által látszólag csak nagyon ritkán létesített szinapszisok is ezt a nem-szinaptikus jelátvitel koncepciót támogatták (*84*, *85*), mely szerint a szinaptikus vezikulákba csomagolt jelátvivő anyag azaz neurotranszmitter, az axon terminálisokból bármely irányban kiürülhet, majd az így ürült anyag az extracelluláris térben diffundálva jut el majdani szinapszisokon kívüli azaz extra-szinaptikus receptoraihoz melyeken keresztül végül hat majd a célsejtekre. Azonban olyan irodalmi adatok is születtek melyek a kolinerg jelátvitel rendkívül precíz időzítéséről szóltak büntetés és jutalmazás során (*86*), valamint több tanulmány az acetilkolin pontosan időzített ürülését támasztotta alá (*80*, *87*, *88*). Továbbá az, hogy a hippokampális szinaptikus plaszticitás függ a kolinerg hatás milliszekundumos pontosságú időzítésétől (*89*) szintén megdönteni látszott azt a tankönyvi adatot miszerint a kolinerg rendszer nem szinaptikusan jelátvitel segítségével működik, hisz az extra-szinaptikus felszabadulás és traszmitter diffúzió erre nem volna képes.

A bazális előagyi kolinerg sejtek alapvetően meghatározzák a hippokampusz ritmikus hálózati aktivitását (*90*, *91*), és a kolinerg rostok képesek gátolni a éles hullám (SWR) aktivitás kialakulását (*92*), ami a memória nyomok raktározását jelző egyik legjellemzőbb hálózati

tevékenység. Ha a kolinerg rostok ilyen jelentős mértékben befolyásolhatják a memória rögzítését is, különösen fontos ismerni, hogy ezt valóban nem-szinaptikus jelátvitellel és valóban csak acetilkolin segítségével teszik-e.

A bazális előagyból eredő kolinerg szinapszisok neuroligin 2 fehérjét tartalmaznak

Ezért megvizsgáltuk lehetséges-e, hogy a kolinerg rostok ugyanolyan szinapszisokat létesítenek mint más tipikus idegsejtek, még akkor is ha esetleg szinapszisaik kevésbé volnának felismerhetőek a klasszikus morfológiai feltételezések alapján. Ehhez először is megvizsgáltuk hogy megjelölhetőek-e a kolinerg szinapszisok egyéb más szinapszisokra jellemző fehérjék jelölésének segítségével. Ezekhez a vizsgálatokhoz részben olyan genetikailag módosított egereket használtunk, melyekben vírusok segítségével szelektíven megjelölhetőek a kolinerg sejtek.

Keresve azt a fehérjét, amely képes lehet megbízhatóan azonosítani a kolinerg szinapszisokat, megvizsgáltuk a neuroligin 2 (NL2) elhelyezkedését is a hippokampuszban (*93*). A NL2 szinaptikus sejtkapcsoló fehérjéknek tartott poszt-szinaptikus fehérje, amely kulcsszerepet játszik a GABAerg szinapszisok érésében és megfelelő működésében (*94*–*96*). Korábbi vizsgálatok bizonyították, hogy a NL2 kifejeződésének a gátlása gátolta a GABAerg szinaptikus jelátvitelt, míg túlzott kifejeződése növelte a GABAerg gátlást (*97*). Ezek az adatok azt sugallták, hogy a NL2 nem csupán egy sejt kapcsoló struktúra, hanem egy fontos szinaptikus funkcióval rendelkező fehérje is. Érdekes módon azonban az NL2 kifejeződésének genetikai módszerekkel történő fokozása növelte az egerek szorongási szintjét és olyan egyéb viselkedési változásokat okozott, melyek nem voltak könnyen magyarázhatóak egy máskülönben megerősödött GABAerg jelátvitel mellett (*97*, *98*). Ezért feltételezhető volt, hogy a NL2 nem csupán GABAerg szinapszisokban található és így nem csupán azok működését befolyásolja közvetlenül. Mi immunohisztokémiai és elektronmikroszkópos módszerekkel megvizsgáltuk a kolinerg szinapszisok NL2 tartalmát és azt találtuk, hogy azok szintén kifejezik az NL2-t több agyterületen is (*93*). A hippokampuszban a NL2 jelölés sűrűsége a kolinerg szinapszisokban hasonló volt a GABAerg szinapszisokban található NL2 jelölés sűrűségéhez. A NL2 jelölés új lehetőséget biztosított a kolinerg szinapszisok megjelölésére és így már megvizsgálhattuk, hogy a kolinerg rostok terminálisai milyen gyakorisággal létesítenek szinapszisokat.

Minden hippokampális kolinerg axon terminális létrehoz szinapszist

Korábbi tanulmányok ugyan arra a következtetésre jutottak, hogy csak kevés kolinerg terminális létesít szinapszist, feltételeztük, hogy ez esetleg csak szinapszisaik eltérő felépítéséből fakad és valójában az összes kolinerg terminális szinapszist képez. Hippokampális kolinerg rostokon, NL2 jelölés segítségével már képesek voltunk azonosítani a szinapszisokat. Mivel a NL2 tipikusan GABAerg szinapszisokban volt megtalálható, ahol a tipikus szinaptikus állványozó fehérje a gephyrin, megvizsgáltuk annak előfordulását is a

kolinerg szinapszisokban és azok szintén megtalálhatóak voltak bennük. Így azonosíthattuk a kolinerg szinapszisokat, és megvizsgálhattuk a szinapszisok előfordulását háromdimenziós elektronmikroszkópos rekonstrukciókkal (*93*). Virális pályakövetési módszerek és immunohisztokémiai módszerek segítségével megjelöltük a kolinerg rostokat a hippokampuszban. Hosszú kolinerg axonális szegmenseket rekonstruáltunk, majd azonosítottuk szinapszisaikat NL2 vagy a gephyrin immunogold jelölésével. A sejtkapcsolatok egy részét korábban nem tekintettük volna szinapszisnak, mert elektronmikroszkópos poszt-szinaptikus ozmium tetroxid festődésük szokatlanul gyenge volt, azonban a NL2 és a gephyrin jelölése egyértelműen azonosította az aktív zónáikat. Megállapítottuk, hogy gyakorlatilag az összes vizsgált hippokampális kolinerg terminális egy vagy akár több szinapszist is létrehoz. A hippokampusz CA1-ben azt találtuk, hogy az NL2 és a gephyrin pozitív kolinerg szinapszisok elsősorban piramissejt dendrit törzseket és tüske nyakakat céloznak, valamint néhány interneuron dendritet (*99*).

A kolinerg sejtek szinapszisai rendelkeznek a GABAerg jelátvitel molekuláival

Megvizsgáltuk, hogy e kolinerg szinapszisok NL2 és gephyrin tartalma valóban azt jelzi-e, hogy e szinapszisok képesek a GABAerg jelátvitelre is. Megállapítottuk, hogy legalább 80%-uk tartalmazott $GABA_A$ receptor gamma 2 alegység jelölést is, amelyet mind a dendriteken, mind a tüske szinapszisaikban kimutattunk. Ezután fluoreszcens fénymikroszkópos módszerrel lokalizáltuk a pre-szinaptikus GABAerg és kolinerg jelátvitel elemeit is és megállapítottuk, hogy minden szepto-hippokampális kolinerg sejt tartalmazza a GABA-t vezikulákba juttató vezikuláris GABA transzporter (vGAT) fehérjét, terminálisaik kifejezték a GABA-szintetizáló enzimét, a glutamát-dekarboxiláz 65-öt (GAD65) is és beágyazás utáni immunarany módszerrel megmutattuk, hogy a GABA maga is kimutatható a kolinerg terminálisokban (*99*).

A kolinerg sejtek összetett, GABAerg-kolinerg poszt-szinaptikus válaszokat váltanak ki

A kolinerg sejtek által kiváltott elektrofiziológiai válaszok tulajdonságait a hippokampusz CA1 interneuronjaiban vizsgáltuk, mivel ismert volt azok kolinerg beidegzése (*100*). Optogenetikai módszerek segítségével fénnyel aktiváltuk a hippokampusz kolinerg rostjait, ami összetett membránpotenciál válaszokat eredményezett: egy $GABA_A$-receptor függő hiperpolarizációt (csúcs: 13,8 ms), és egy kissé késleltetett (csúcs: 92 ms) acetilkolin receptor-függő depolarizációt. E válaszok szinaptikus jelátvitelről tanúskodnak, mivel mindkét válasz nagyon rövid kezdő késleltetéssel rendelkezett (2,8 és 7,4 ms), noha később ezek a szinaptikusan felszabadult neurotranszmitterek szintén hathatnak az extra-szinaptikus receptorokra. Mivel a tipikus extra-szinaptikus jelátvitel kiváltott válaszának kezdő késése kb. 60-160 ms (*101*), így a GABA és acetilkolin szinaptikus felszabadulása utáni válasz gyorsasága pontszerű, szinaptikus és/vagy közeli peri-szinaptikus receptorokon kell hasson (*99*).

Az acetilkolin és GABA tartalmú vezikulák is csak szinapszisokból ürülnek

Fiziológiai és anatómiai adataink azt mutatták, hogy a kolinerg terminálisok szinapszisokat létesítenek. A nem szinaptikus acetilkolin felszabadulása azonban továbbra is lehetséges lenne, ha a kolinerg vezikulák dokkolása és membránnal való fúziója a szinaptikus aktív zónákon kívül is megvalósulhatna. Ennek ellenőrzésére elektron tomográfia segítségével rekonstruáltunk hippokampális kolinerg rostokat, és 1 nm felbontással megvizsgáltuk a szinaptikus vezikuláik pontos térbeli elhelyezkedését a terminálisaiban a szinapszisaihoz viszonyítva. A háromdimenziós rekonstrukciókból szabad szemmel és statisztikai módszerekkel is kiderült, hogy a szinaptikus vezikulák kifejezetten az aktív zónák közelében csoportosulnak. Nem találtunk dokkolt vagy fúzionált (exocitotikus fúzión áteső) vezikulumokat szinapszisokon kívül, csak szinapszisokban (*99*). Ezek az eredmények cáfolták az acetilkolin nem-szinaptikus felszabadulását.

A vezikuláris térfogat korrelálhat a vezikula transzmitter tartalmával (*102*), így elektron tomográfia segítségével összehasonlítottuk a kolinerg és a GABAerg terminálisok vezikuláinak morfológiáját. A kolinerg terminálisok vezikulái szignifikánsan, körülbelül 60% -kal nagyobbak voltak, mint a szomszédos tisztán GABAerg terminálisok vezikulái és térfogatuk is szignifikánsan változékonyabb volt (*99*). A kolinerg terminálisok kicsi vezikulái pedig hasonlóak voltak a tisztán GABAerg terminálisok vezikuláihoz, ami arra utalhat, hogy a vezikulák két típusának mérete között még nagyobb különbség van.

Az acetilkolin és GABA tartalmú vezikulák ugyanabban a vezikula csoportban vannak

Annak további megerősítésére, hogy a két jelátvivő rendszer ugyanazt az aktív zónát használja, egér hippokampuszban, fluoreszcens mikroszkópiát használtunk. Megállapítottuk, hogy az acetilkolin tartalmú vezikulák is a kolinerg rostok GABAerg szinapszisaiban koncentrálódtak és a kolinerg valamint GABAerg szinaptikus vezikulák keverednek. Egér agykéregből izolált szinaptikus vezikulákon pedig kimutattuk, hogy az acetilkolin és a GABA különböző vezikulákba csomagolódik (*99*).

Kölcsönös auto-receptor moduláció szabályozza az acetilkolin és a GABA ürülését

Anatómiai adataink azt mutatták, hogy az acetilkolin és a GABA külön vezikulákban tárolódik, és vélhetően külön is szabadul fel. Először ezen vezikuláris felszabadulás pre-szinaptikus modulációját vizsgáltuk. Mivel korábban az acetilkolin receptorok (AChR) blokkolása megnövelte a GABAerg hiperpolarizáció amplitúdóját, feltettük, hogy ezért pre-szinaptikus muszkarin receptorok lehetnek felelősek (*100*). És valóban, glutamát receptorok blokkolása után, a muszkarinikus receptor blokkoló atropin szignifikánsan növelte mind a GABAerg gátló poszt-szinaptikus potenciálok (IPSP-k), mind a kolinerg serkentő poszt-szinaptikus potenciálok (EPSP-k) amplitúdóját. Az M2-típusú AChR-ek blokkolásával (*100*, *103*), reprodukálni tudtuk az atropin által kiváltott mindkét poszt-szinaptikus potenciál

növekedését, ami egyértelművé tette az M2 típusú AChR-ek szerepét, mind az acetilkolin, mind a GABA felszabadításának szabályozásában.

Korábban leírtuk a pre-szinaptikus $GABA_B$ auto-receptorok jelenlétét a szeptális kolinerg sejtekben (*104*), így kiderült, hogy a hippokampális kolinerg rostok terminálisai GABAerg moduláció alatt állnak. A szinaptikus átvitel szabályozásában játszott szerepük kipróbálásához blokkoltuk a $GABA_B$ receptorokat is. Ez is mind a GABAerg IPSP-k, mind a kolinerg EPSP-k amplitúdójának szignifikáns növekedéséhez vezetett.

Összességében ezek a kísérletek rávilágítottak, hogy a GABA és az acetilkolin összetett módon szabályozható pre-szinaptikusan, mind saját maguk, mind egymás jelpályáinak kölcsönös szabályozása által.

Különböző Ca-csatornák befolyásolják az acetilkolin és a GABA szinaptikus ürülését

A szinaptikus vezikulák felszabadulásának dinamikája főként a feszültség-függő kalcium-csatornák (VDCC) típusától függ, melyek a Ca^{2+} ionok által közvetített vezikula felszabadulását szabályozzák (*105*). Ugyanakkor egyazon sejtben a különféle vezikula típusokat akár különböző VDCC-k is szabályozhatják (*106*). És valóban, azt találtuk, hogy a P/Q típusú kalcium-csatornák szelektív blokkolása szignifikánsan csökkentette a GABAerg IPSP-ket, de nem okozott változást a kolinerg komponensekben. Ezzel szemben a kolinerg komponens erőteljesen csökkent az N-típusú kalcium-csatornák szelektív blokkolása után, míg a GABAerg IPSP-k nem mutattak szignifikáns változást. Amellett, hogy ez megerősítette, hogy a két jelátvivő anyag különböző vezikulákból ürül, igazolta azt is, hogy azokat különböző molekuláris útvonalak szabályozhatják.

Ugyanazon terminálisokban található különböző vezikula populációk, akár eltérő rövid távú plaszticitást lehetővé tevő, különböző vezikula felszabadulási mechanizmusokhoz is kapcsolódhatnak (*106*). És esetünkben is, míg a GABAerg transzmisszió mindig erős rövidtávú szinaptikus depressziót mutatott a kolinerg terminálisokban, addig a kolinerg komponens ezt nem mutatta.

A kolinerg sejtekből felszabaduló GABA a hippokampusz működési állapotát is meghatározza

A szeptális kolinerg sejtek alapvetően meghatározzák a hippokampusz ritmikus hálózati aktivitását (*90*, *91*), sőt korábban ismert volt, hogy —ellentmondásosnak tűnő módon— a kolinerg rostok képesek gátolni a éles hullám (SWR) aktivitás kialakulását (*92*). Ugyanakkor korábban ismeretlen volt a kolinerg rostokból felszabaduló GABA létezése és így annak hatása. Ennek vizsgálatára, optogenetikai kísérletekben, hippokampusz szeletekben, spontán SWR-t rögzítettünk és azt találtuk, hogy a kolinerg rostok optikai stimulálása valóban jelentősen csökkentette az SWR aktivitását. Amikor azonban a kolinerg transzmissziót blokkoltuk, ugyanaz az optikai stimuláció, ugyanúgy csökkenést okozott az SWR aktivitásában. Így bizonyítottuk, hogy a SWR aktivitás kolinerg sejtek általi gátlása, valójában a

szinapszisaikból felszabaduló GABA hatása. Mivel a SWR aktivitás éppen a memória nyomok raktározását mutató hálózati tevékenység, a kolinerg rostokból történő GABA-felszabadulás így képes a memórianyomok rögzítését közvetlenül befolyásolni.

A szepto-hippokampális kolinerg rostokból származó GABA felszabadulás szintén befolyásolhatja a hippokampusz epileptiform aktivitásának megjelenését is. Ezért megvizsgáltuk a kolinerg axonok GABA felszabadulásának hatását egy magas kálium koncentrációt használó, in vitro epilepszia modellben (*107*, *108*). Ezúttal is azt láttuk, hogy a kolinerg rostok optikai stimulálása csökkentette az epileptiform események számát, de a csökkenés akkor is jelen volt, ha a kolinerg receptorokat blokkoltuk. Ezek az eredmények azt mutatták, hogy a kolinerg rostokból a GABA szinaptikus transzmissziója önmagában is hatékonyan képes szabályozni a hippokampusz epileptiform aktivitását, aminek nagy jelentősége lehet az epilepsziás megbetegedések jövőbeli géntechnológiai kezelésében.

A kolinerg rostok GABAerg jelátvitelének jelentősége

A kolinerg rostok adják a hippokampusz egyik legsűrűbb és leghatékonyabb kéreg alól érkező pályarendszerét, ezért felfedezéseink alapvetően változtatják meg a hippokampális szabályozásról alkotott elképzeléseinket. Megállapítottuk, hogy az acetilkolin és a GABA az előagyi kolinerg sejtekből, a szinaptikus aktív zónában, külön vezikulákból, eltérő molekuláris szabályozás segítségével szabadul fel. Továbbá bizonyítottuk, hogy ez a GABA felszabadulás önmagában is hatékonyan képes befolyásolni a memóriafolyamatokban alapvető jelentőségű éles hullám aktivitást és önmagában is képes kordában tartani a hippokampusz esetleges epileptiform aktivitását.

A kolinerg kommunikáció domináns formájának évtizedekig a nem-szinaptikus felszabadulást tartották (*78–80*, *82*, *109*). Eredményeink bizonyították, hogy mind a GABA, mind az acetilkolin szinaptikusan ürül és szinaptikusan vagy a szinapszisok körül azaz peri-szinaptikusan vannak gyors receptoraik. Természetesen, önmagában a gyors szinaptikus válaszok nem zárják ki, hogy a felszabaduló transzmitterek további extra-szinaptikus receptorokon is hassanak. Így az általunk talált szinaptikus felszabadulás és a korábban elterjedt térfogati transzmisszió hipotézise közötti eltérés legvalószínűbb oka a szinapszisokból túlcsorduló jelátvivő anyag azaz az u.n. spill-over jelensége, amely lehetővé teszi a transzmitterek számára további extraszinaptikus receptorok elérését is.

Az előagyi kolinerg sejtek kulcsszerepet játszanak a hippokampusz aktivitási állapotának átalakításában (*90*). A magas kolinerg sejt aktivitás a théta oszcillációval és a külső információk gyors, mégis instabil tárolásával jár a hippokampuszban, míg az alacsony kolinerg aktivitást SWR aktivitás kíséri (*110*), ami fontosnak tűnik az instabil memória nyomok konszolidációja és a memória nyomok nagyagykéregben való raktározása szempontjából (*111*, *112*). A kolinerg moduláció klasszikus elméletei feltételezik, hogy a diffúz módon felszabaduló acetilkolin lassan áthangolná a kérgi hálózati aktivitást, különféle hálózati aktivitás mintázatok megjelenését téve ezzel lehetővé (*24*, *78*, *113*). És valóban, egy

nemrégiben végzett tanulmány kimutatta, hogy a mediális szeptum kolinerg sejtjei elnyomják az SWR aktivitást (*92*). A szerzők azt gyanították, hogy ez a GABAergic interneuronok M2 kolinerg receptorokon keresztüli gátlása miatt lehet. Mi ugyan megerősítettük, hogy a kolinerg rostok aktiválása valóban elnyomja az SWR-eket, de megmutattuk, hogy az a kolinerg rostokból ürülő GABA miatt valósul meg. Ez a gátlás csökkentheti az egyidejűleg aktív piramissejtek előfordulásának valószínűségét is, amely szükséges a SWR beindításához (*114*).

A kolinerg rendszer degenerációja az Alzheimer-kór patológiájának tipikus jellemzője (*77*), és ezeknek a betegeknek gyakran epilepsziás rohamaik is vannak (*115*). És valóban, a szeptális kolinerg pálya szelektív irtása növeli a rohamok előfordulását a hippokampuszban (*116–118*), míg a REM-alvás pedig, amely fokozott kolinerg sejt aktivitással jár (*119*), elnyomja az epilepsziás rohamokat (*120*, *121*). Korábban azonban nem értették, hogy akkor miért tapasztalták, hogy számos kolinerg agonista, éppen hogy kiváltotta az epilepsziás rohamokat (*122*). Ezért feltételezzük, hogy az előagyi kolinerg sejtek degenerációja elsősorban azért vezet epileptiform aktivitáshoz, mert az megfosztja a hippokampuszt egy jelentős GABAerg innervációtól is. Eredményeink valóban támogatták ezt az elképzelést, mivel a GABA felszabadulása az előagyi kolinerg rostokból önmagában elegendő volt az epileptiform aktivitás előfordulásának csökkentéséhez.

Eredményeink, amelyek egy szigorúan szabályozott, hatékony, szinaptikus GABA-jelátvitelt igazoltak a hippokampusz kolinerg rostjaiból, a korábbi modellek újraértelmezését kívánják, és akár alternatív megközelítések alapjául szolgálhatnak az Alzheimer-kórt érintő kolinerg beidegzés elvesztésének kezelésére.

A medián raphe szerepe a negatív élmények rögzítésében

A tématerülethez tartozó mellékelt publikációk

K. E. Sos, M. I. Mayer, C. Cserép, F. S. Takács, A. Szőnyi, T. F. Freund, G. Nyiri: Cellular architecture and transmitter phenotypes of neurons of the mouse median raphe region. Brain Structure and Function. 222, 287–299 (2017).

A. Szőnyi, K. Zichó, A. M. Barth, R. T. Gönczi, D. Schlingloff, B. Török, E. Sipos, A. Major, Z. Bardóczi, K. E. Sos, A. I. Gulyás, V. Varga, D. Zelena, T. F. Freund, G. Nyiri: Median raphe controls acquisition of negative experience in the mouse. Science (80). 366 (2019).

Bevezetés

Az állatok életének egyik fő mozgatórugója a pozitív tapasztalatok átélése iránti késztetés (mint például a táplálkozás, a társas kapcsolatok vagy a szaporodás), illetve a negatív élmények (mint pl. az éhezés, a veszélyek vagy a sérülések) elkerülése. Az állatok és így az ember túléléséhez is elengedhetetlen, hogy gyorsan fel tudja mérni az ártalmas helyzeteket, képes legyen azonnal válaszolni rájuk, emlékezzen a kiváltó körülményekre, és hogy képes legyen a hasonló negatív élményeket előre látni (*123–128*). Mind a pozitív élmények elérésére, mind pedig a negatívak elkerülésére számos agyterület összehangolt működésére van szükség. A negatív élmények elkerülésében központi szerepe van a laterális habenula (LHb) és a mediális ventrális tegmentum (mVTA) területeinek abban, hogy kiértékeljék a már kialakult helyzetet és megjósolják a jövőben esetleg előforduló negatív élményeket. Továbbá központi szerepe van a szepto-hippokampális rendszernek is, amely segít rögzíteni és visszahívni a negatív eseményekkel kapcsolatos emlékeket.

Jelentőségük ellenére még mindig nem jól ismert, hogy ezen agyközpontok hogyan koordinálják egymás aktivitását a negatív élmények során. Mivel az LHb közvetlenül nem vetít a szepto-hippokampális rendszerbe, feltételezték, hogy ezek összehangolását az agytörzs medián raphe régiója (MRR) végzi (*61*, *129–135*). Noha az MRR fontos szerepet játszik a hangulat, a félelem és a szorongás szabályozásában, a negatív tapasztalatok feldolgozásában betöltött szerepe továbbra is ismeretlen volt (*61*, *136*, *137*). A MRR szerotonint (5HT) és/vagy 3-as típusú vezikuláris glutamát transzportert (vGluT3) kifejező vetítő idegsejteket tartalmaz. Ám a több évtizedes vizsgálta ellenére ismeretlen maradt, hogy az MRR idegsejtek hogyan tudják támogatni ezeket a funkciókat (*45*, *58*, *138*). Bár a LHb, mVTA-ra, és a szeptális területek [a mediális szeptum (MS) és a Broca-féle diagonális köteg vertikális ága (VDB)] elengedhetetlenek a negatív élményekkel kapcsolatos viselkedések megértéséhez, mégis a koordinálásukban valamiképpen felelős kulcsfontosságú MRR neuronokat korábban nem sikerült azonosítani (*139*, *140*).

Az egér medián raphe régió idegsejt típusainak feltérképezése.

Az egér MRR-ban korábban négy különböző idegsejt típust azonosítottak a GABA pozitív gátló sejteket, illetve a szerotonin (5-HT) pozitív, a vGluT3 pozitív és az utóbbi kettőre egyaránt pozitív modulátoros sejteket. Azonban ismeretlen volt ezen sejttípusok aránya, illetve korábban nem vizsgálták meg szisztematikusan, hogy vannak-e a területen más idegsejtek is. Tekintettel arra, hogy az addig ezen a területen talált idegsejt populációk nem tudták teljesen megmagyarázni a MRR addig feltételezett szerepét, ezért pontos sztereológiai módszerrel megvizsgáltuk az itt található sejtek arányát és típusait (*141*). Azt találtuk, hagy a teljes MRR-ban a neuronok 2,1% -a volt 5-HT, 7% volt VGLUT3, 3,6% pedig 5-HT és vGluT3 kettős pozitív; míg a neuronok 61%-a volt GABAerg. Meglepő módon az idegsejtek több mint 25%-a mind a 4 sejtpopuláció jelölő anyagára negatív volt, és csak a NeuN idegsejteket jelölő fehérjére volt pozitívak.

A vGluT2-pozitív sejtek adják a MRR legjelentősebb vetítését

Tekintettel arra, hogy az agytörzsben nagyszámú vGluT2 pozitív idegsejt található megvizsgáltuk lehetséges-e, hogy a MRR sejtjeinek mintegy negyede vGluT2 pozitív (*142*). Ezekhez a vizsgálatokhoz olyan genetikailag módosított egereket használtunk melyekben vírusok segítségével szelektíven megjelölhetőek a vGluT2 pozitív sejtek. Ezután újabb teljes sztereológiai vizsgálatokkal kimutattuk, hogy a MRR neuronok legalább 20%-a vGluT2-pozitív. Ez magyarázatot adott arra a korábbi felfedezésünkre is miszerint a (korábban alapvetően szerotonergnek tartott) MRR vetítő rostjainak túlnyomó többsége glutamaterg serkentő jelátvitelt folytat előagyi célterületein (*44*). A MRR vGluT2-pozitív neuronok egyenletesen oszlottak el az MRR-ban. Fluoreszcens immunhisztokémiai módszerekkel azt is kimutattuk, hogy ez a sejtcsoport különálló, az itt korábban leírt egyéb idegsejt típusoktól különböző sejtpopulációt alkot, azokkal nem mutat átfedést.

Az MRR vGluT2-neuronok a negatív élményeket feldolgozó agyterületeket idegzik be

Virális pályajelölő, valamint immunohisztokémiai módszerek kombinálásával kimutattuk, hogy a vGluT2-neuronok erősen beidegzik a negatív élmények feldolgozásáért felelős LHb és mVTA sejtjeit, ugyanakkor elkerülik a pozitív élményekkel kapcsolatos laterális VTA dopaminerg sejtjeit.

Az averzióval azaz az elkerülő viselkedéssel összefüggő működést mutató dopaminerg sejtek mVTA-ból a mediális prefrontális kéregbe (mPFC) vetítenek (*143*, *144*). Retrográd pályajelölő anyagokat használva kimutattuk azt is, hogy a vGluT2-pozitív MRR sejtek éppen azokat a mVTA dopaminerg idegsejteket célozzák, amelyek a mPFC-be vetítenek megerősítve a feltételezést, hogy a vGluT2 sejtek feladata a negatív élményekkel és azok előrejelzésével kapcsolatos.

A glutamaterg LHb idegsejtek szintén beidegzik az MRR-t (*145*), de célsejtjeik ismeretlenek voltak. Kombinált pályajelölésekkel megállapítottuk, hogy közvetlen reciprok kapcsolat van az LHb-ba vetítő vGluT2-pozitív MRR idegsejtek és az MRR-ba vetítő vGluT2-pozitív LHb neuronok között. Ez a MRR és az LHb vGluT2-neuronjai közötti pozitív visszacsatolás fontos szerepet játszhat a negatív élményekre adott azonnali válaszban, hiszen ezek nem csak egymást idegzik be, hanem mindkét sejtpopuláció a negatív élményeket kódoló mVTA-t is célozza.

Az MRR vGluT2 neuronok beidegzése

Az MRR vGluT2-pozitív idegsejteket szinaptikusan célzó agyterületek azonosításához mono-transz-szinaptikus veszettség vírust használó sejttípus specifikus pályajelölő technológiát alkalmaztunk (*146*, *147*). Sikerült igazolnunk, hogy azok az agyterületek, amelyek alapvető szerepet játszanak a negatív tapasztalattal összefüggő viselkedésben, erősen konvergálnak a vGluT2-pozitív MRR sejtekre. Így a vGluT2-pozitív MRR-sejtek az egyik legerősebb szinaptikus bemenetüket pl. a LHb-ból kapják.

A MRR vGluT2-idegsejtek elősegítik az LHb sejtek depresszióval-összefüggő aktivitását

A negatív tapasztalatokkal összefüggő viselkedést és az azt követő depressziós tüneteket az LHb idegsejtek aktiválása nagymértékben elősegíti (*148–150*). Pásztázó elektronmikroszkópos vizsgálatok segítségével kimutattuk, hogy az MRR vGluT2-neuronok kiterjedt szinaptikus beidegzést adnak az LHb idegsejteken. Az LHb neuronokban az N-metil-D-aszpartát (NMDA) receptor-függő “burst”-aktivitás kulcsszerepet játszik a depresszió kialakulásában (*148*, *150*). Mi pedig megállapítottuk, hogy az MRR vGluT2-idegsejtek NMDA-receptort tartalmazó serkentő glutamaterg szinapszisokat hoznak létre az LHb-idegsejteken. Az LHb-ban az asztroglia sejtek erősen együttműködnek a depressziószerű tünetek kialakulásáért felelős sejtekkel (*148*). És valóban, elektronmikroszkópos eredményeink mutatták, hogy a LHb-ban, a MRR vGluT2 terminálisok szinapszisainak nagy részét asztroglia sejtek nyúlványai borították.

Ennek fiziológiai vizsgálatához szelektíven optogenetikai módszerekkel aktiváltuk az MRR vGluT2-pozitív rostokat a LHb-ban, ami ott megbízhatóan glutamáterg serkentő poszt-szinaptikus áramokat (EPSC-ket) váltott ki az LHb idegsejtjeiben, melyek gyakran az LHb sejtek „burst”-aktivitását is kiváltották. Ezek az EPSC-k, α-amino-3-hidroxi-5-metil-4-izoxazol-propionsav (AMPA) és NMDA-típusú serkentő glutamát-receptorok egyidejű blokádjaival megszüntethetőek voltak.

Az ártalmas ingerek szelektíven aktiválják a MRR vGluT2-idegsejteket.

Élő állatokban is megvizsgáltuk, hogy az azonosított MRR vGluT2-neuronok milyen fiziológiai válaszokat adnak pozitív és negatív ingerekre. Többcsatornás elvezetés és optogenetikai címkézés kombinációját használva, éber egerekben, elektródákkal megkerestük és azonosítottuk a vGluT2 sejteket. Ezt követően az állatokat vagy hirtelen adagolt levegő befújás segítségével megijesztettük, vagy pedig a szomjas állatoknak pozitív élményként jutalmazó vízcseppeket adtunk. Miközben az állatok számára erősen zavaró lég-befújás hatására az azonosított vGluT2-pozitív MRR idegsejtek nagy része erősen aktiválódott, addig a jutalom nem befolyásolta azok működését. Az enyhén zavaró LED fények villogása pedig csupán enyhe átmeneti aktivitást váltott ki a vGluT2-pozitív MRR neuronok egy kis alcsoportjában, melyek részben átfedésben voltak a levegő befújással aktivált sejt csoporttal.

Az MRR vGluT2-neuronok direkt aktiválása erősen negatív élményt okoz

Az, hogy a MRR vGluT2-neuronokat specifikusan az ártalmasnak vélt élmények aktiválják arra utal, hogy ezek kifejezetten a negatív tapasztalatokat dolgozzák fel. Ezért megvizsgáltuk azt is, hogy direkt optogenetikai aktiválásuk miként befolyásolja az állatok viselkedését. A kontroll egereket (CTRL egerek) kontroll vírussal injektáltuk. A kontrol vírusok mindig csupán fluoreszcens fehérjét fejeztek ki, de nem fejezett ki fényérzékeny csatornákat. Az állatok másik csoportjában (ChR2 egerek) pedig fénnyel aktiválhatóvá tettük a MRR vGluT2-neuronokat. Ezután minden állatba egy optikai szálat ültettünk az MRR fölé. Majd az egereket egy dobozba helyeztük, amely két látványra különböző, de egyforma méretű kamrát tartalmazott. Miközben az állatokat hozzászoktattuk a két kamrás dobozhoz, az egerek nem foglalkoztak a két kamra közötti különbséggel. Ezután 24 órával később az egereket ugyanabba a kamrába helyeztük és az MRR területét az állatokban megvilágítottuk, de csak az egyik kamrában. A ChR2 egerek azonnal megpróbálták elkerülni a kamrát, melyben a fény stimulálta a MRR vGluT2-neuronokat. Másnap a stimulált ChR2 egerek (szemben a CTRL egerekkel) erős kondicionált félelmet is mutattak a korábban a stimulációhoz kapcsolt kamrában.

Megvizsgáltuk azt is, hogy az MRR vGluT2-neuronok aktivitása elég erős-e ahhoz, hogy ellensúlyozza a motivált, élelmet kereső állat erősen pozitív elvárásait. Itt a fentebb említett ChR2 és CTRL egereket 10 nap alatt megtanítottuk arra, hogy orrukat jelző-lyukba dugva ételt kérhetnek. 24 órával később az egerek fény bevilágítást kaptak, amikor az orrukat a jelző-lyukba dugták. A ChR2-egerek, ezután szignifikánsan kevesebbet próbáltak egér tápot szerezni, ami egyértelműen jelezte, hogy a MRR vGluT2-neuronok aktivitása nem csupán kevéssé kívánatos, hanem mindenáron elkerülendő még akkor is ha az állat ösztöne szerint mindent megtenne hogy ételhez juthasson.

Az MRR vGluT2-neuronok aktiválása agressziót és depressziós tüneteket vált ki

Ismert volt, hogy a LHb aktivitása szerepet játszik az agresszív viselkedés kialakulásában (*151*). Ha az MRR vGluT2-neuronok aktivitása valóban a negatív élményeket közvetíti és az állatokat valóban annak aktív elkerülésére ösztönzi, akkor társas kontextusban az MRR vGluT2-neuronok aktivitása az egereket agresszív viselkedésre késztetheti. Ennek vizsgálatát ezúttal nem fénnyel, hanem egy speciális drog által aktiválható csatorna segítségével végeztük. Ezekben a vizsgálatokban DREADD-et (Designer Receptors Exclusively Activated by Designer Drugs) használtunk, amely tervezett felépítésű receptorok segítségével aktiválja a sejteket, amikor azok clozapin-N-oxidhoz (CNO) kötődnek. Az állatokat két csoportra osztottuk: az egyikben a MRR vGluT2 sejtek DREADD-et fejeztek ki ("hM3Dq-egerek") a másikban CNO-ra nem érzékeny kontrol vírust kifejező egerek voltak ("CTRL-egerek"). A kísérletek során intra-peritoneálisan injektáltuk a CNO-t és először két viselkedési tesztet végeztünk. A társas interakciós teszt során az egereket egy ismeretlen fajtárs egérrel új környezetbe helyeztük, és azt tapasztaltuk, hogy míg a kontroll egerek többnyire barátságosan szociális interakciót keresve viselkedtek, a hM3Dq-egerek rendkívül agresszívvé váltak a CNO hatására, ami csupán a MRR vGluT2-neuronok aktivitását fokozhatta. Öt nappal később megvizsgáltuk miként változtatja az állatok viselkedését egy kisebb méretű alárendelt idegen betolakodó egér, ha azt a vizsgált állat saját ketrecébe helyezzük. A betolakodó tesztekben a kontrol állatokkal összehasonlítva a hM3Dq-egerek ismét szignifikánsan agresszívebben viselkedtek a behatolóval szemben.

Egy külön kísérletben azt is megfigyeltük, hogy a MRR vGluT2-neuronok CNO-injekciókkal való kemogenetikus aktiválása fokozta a motoros aktivitást és az állatok viselkedése eleve agitáltabbá vált a kontrollerekhez képest.

A depressziós állapotot emberek esetében is gyakran kíséri agresszív (általában verbálisan agresszív) viselkedés (*152–154*), amelyet szintén elősegít az LHb idegsejtek krónikus túlzott aktiválása és burst-tüzelése (*148–151*, *155*). A fent említett CTRL- és hM3Dq-egerek segítségével megvizsgáltuk, hogy az MRR vGluT2-neuronok krónikus aktiválása elősegíti-e a depresszióhoz hasonló tüneteket. A kísérleti egerek hetente háromszor, három héten keresztül intra-peritoneálisan kaptak DREADD-agonista CNO-t. A 19. napon az egereket cukor preferencia teszttel vizsgáltuk, amely kimutatta, hogy MRR vGluT2-neuronok krónikus aktiválása az állatokban relatív érdektelenséget vált ki a kellemesebb cukoroldat iránt, ami a depresszió klasszikus tünetének tekintett anhedónia egyik tipikus jellemzője.

Továbbá a hM3Dq-egerek mellékveséinek tömege a post-mortem vizsgálat során is szignifikánsan magasabb volt a CTRL-egerekhez viszonyítva, ami igazolta ezen állatok megemelkedett stressz szintjét.

Az MRR vGluT2 idegsejtek aktiválják a memória rögzítését segítő MS/VDB idegsejteket

A negatív tapasztalatok gyors és hatékony feldolgozása és megjegyzése megköveteli a szepto-hippokampális rendszer gyors aktiválódását (*156*). Ennek egyik előfeltétele, hogy a MS/VDB területéről a hippokampuszba vetítő parvalbumin pozitív (PV) ritmuskeltő neuronok, a memória megszerzésében kulcs szerepet játszó hippokampális théta ritmus kialakulását elősegítsék (*157*, *158*). És valóban, a pályajelölési kísérletek tanulsága szerint a MRR vGluT2 neuronok nagyszámú rost segítségével idegzik be a MS/VDB területét. Az MRR vGluT2 idegsejtek szelektíven hoztak létre NMDA-receptort tartalmazó serkentő szinapszisokat a parvalbumin (PV) pozitív GABAerg sejteken az MS/VDB-ben. Retrográd pályakövetési módszerek segítségével az is látszott, hogy az MRR vGluT2 neuronok serkentésükkel közvetlenül a hippokampuszba vetítő PV sejteket célozzák az MS / VDB-ben.

Az LHb idegsejtek és a hippokampális hálózat théta-ritmus aktivitása fázis kapcsolt, összehangolt aktivitásuk pedig szükséges a megfelelő memória kialakulásához (*130*, *135*). Ezért megvizsgáltuk, hogy az MRR vGluT2-neuronok különböző axon ágai képesek-e mindkét terület egyidejű beidegzésére elágazó axon kollaterálisokkal. És valóban kettős retrográd nyomkövetés segítségével azt találtuk, hogy a vGluT2-pozitív MRR idegsejtek többsége mindkét agyterületre vetít különböző axon ágakkal.

Élő állatokban végzett optogenetikai kísérletek segítségével végül azt is kimutattuk, hogy a MRR vGluT2-neuronok 25 Hz-es fény-aktiválása, valóban, az emlékek kialakulását elősegítő théta oszcillációkat váltott ki a hippokampuszban.

Az MRR vGluT2-neuronok szükségesek a félelmi memória rögzítéséhez

Mivel a MRR vGluT2-sejteket kifejezetten a negatív tapasztalatok aktiválják, majd azok pedig erőteljesen a negatív élményekért, illetve azok megjegyzéséért felelős központokban vetítenek, így a MRR vGluT2-neuronok valószínűleg alapvető fontosságúak a félelmi memórianyomok rögzítéséhez. Ezért megvizsgáltuk, hogy a MRR vGluT2-neuronok szelektív gátlása képes-e a memórianyomok rögzítését gátolni. A korábbiakhoz hasonló optogenetikai kísérletekben ezúttal olyan receptor csatornákat kifejező vírusokat használtunk, amelyek fény segítségével nem serkentik, hanem gátolják a sejteket. Így kísérleti állataink MRR vGluT2-neuronjaiban Archaerhodopsin T-3 receptort fejeztettünk ki (ArchT-egerek), melyeket fényérzékeny receptort nem tartalmazó vírust kifejező kontroll állatokhoz hasonlítunk (CTRL-egerek). Az állatokat kézhez szoktatás után egy késleltetett kulcsingerhez kötött félelmi kondicionálás kísérletben vizsgáltuk. Az egereket először egy új „A" környezetbe helyeztük, ahol három hangjelzés után egy ijesztő elektromos láb ingerlést kaptak, miközben minden ijesztő ingerléssel egyszerre, egy időben tökéletesen összehangolt fény-bevilágítást is kaptak. A következő tesztekben az egerek nem kaptak több fényt. 24 órával később az egereket ugyanabba az „A" környezetbe helyeztük, hogy megvizsgáljuk az állatok félelmi emlékeit. Miközben a CTRL egerek erős kontextus függő félelmi viselkedés

mutattak addig a fény segítségével gátolt ArchT-egerek szinte semmilyen félelmi viselkedést nem mutattak. Azaz a MRR vGluT2-neuronok működése elengedhetetlen volt a félelmi élmények rögzítéséhez. A következő napon az egereket egy másik semleges környezetben is elhelyeztük („B" környezet), ahol az ArchT-egerek szignifikánsan alacsonyabb általános félelmet mutattak a CTRL egerekhez képest. Ezután ugyanabban a semleges környezetben újra megkapták a hangjelzéseket, amiket korábban már össze társítottak az ijedtséggel. A CTRL egerek nagyon magas félelmi szintet mutattak. Ezzel szemben a fénnyel gátolt ArchT-egerek szignifikánsan csökkentett félelmet mutattak, ami arra utal, hogy a kulcsingerhez kötött félelem emléke sem alakult ki. Végül tovább figyelve az állatokat az ArchT- és a CTRL-egerek félelem szintje közötti különbség még a kulcsinger befejezése után is szignifikáns maradt.

A MRR vGluT2 neuronok jelentőségének összefoglalása

Az állatoknak gyorsan fel kell mérniük a rájuk leselkedő veszélyeket, el kell dönteniük, hogy harcolniuk vagy menekülniük érdemes. Ezzel párhuzamosan hatékonyan fel kell fogniuk és meg kell tanulniuk, hogy mi vezetett a veszélyes helyzethez, hogy a jövőben azt elkerülhessék. Az LHb és az mVTA aktiválódnak a negatív tapasztalatok megszerzése során (*129*, *143*, *144*, *159*), amely elindítja a negatív élmények kódolását ezekben a magokban (*127*, *160*). Az mVTA dopaminerg neuronjainak aktiválása szintén negatív élményeket kódol (*143*, *161*), míg a lateral VTA neuronok aktivitása a pozitív megerősítésben játszik szerepet. Az LHb szinte kizárólag glutamaterg neuronokat tartalmaz, amelyek negatív élményt kódolnak és aktiválják az mVTA fent említett dopaminerg (DA) sejtjeit (*143–145*, *162*). Az LHb aktivitás közvetett módon gátolja a pozitív megerősítés kódolását is a laterális VTA-ban (*143*, *163*). Ezek a folyamatok fogják finom-hangolni a jövőbeli eseményekre adható stratégiákat (*127*, *160*, *164–167*), és a LHb és mVTA aktivitása megjósolhatóvá teszi a negatív élmények előfordulását (*125*, *161*, *168–172*). Mindehhez azonban az MS/VDB-hippocampális rendszert szintén a memória nyomok rögzítéséhez optimális állapotba kell kapcsolni, ami az emlékek alapján segíti a negatív élmények későbbi előrejelzését (*130*, *135*). Ugyanakkor, korábban nem volt ismert, hogy mely idegi kapcsolatok teszik lehetővé e rendszerek összehangolt aktiválását. Noha az MRR-ről ismert volt, hogy központi szerepet játszik a negatív tapasztalatok feldolgozásában (*61*, *136*), ismert sejttípusai nem vetítettek a LHb-ba, és az MRR-idegsejtek közel 25% -ának transzmitter fenotípusa és célsejtjei még szintén ismeretlenek voltak (*141*).

Felfedeztünk a MRR–ban egy korábban fel nem ismert vGluT2-pozitív idegsejt populációt, ami erősen beidegzi az LHb, mVTA és MS/VDB területeket. Ezek adják a MRR-ből vetítő neuronok legnagyobb populációját, glutamátergek és különálló sejtpopulációt alkotnak a MRR-ban. Számos környezeti tapasztalatszerzéssel kapcsolatos agyi központból kapnak monoszinaptikus bemeneteket (*129*, *159*, *173*). Az MRR vGluT2-idegsejtek túlnyomórészt az LHb mediális („limbikus") részét idegzik be, amely épp a MRR-ba és mVTA-ba vetít, de kerülik az LHb lateralis („pallidalis") részét, amely más jellegű információkat dolgoz fel (*145*, *170*, *174*,

175). Az MRR vGluT2-neuronok közvetlenül beidegzik az MRR-ba és mVTA-be vetítő LHb-sejteket, közvetlen visszacsatolást hozva ezzel létre MRR-LHb-mVTA tengelyen.

In vivo méréseink megerősítették az MRR vGluT2-neuronok központi és specifikus szerepét a negatív tapasztalatok kialakulásában. Az MRR vGluT2-idegsejteket erősen és specifikusan aktiválták az erős ártalmasnak vélt stimulusok, enyhén aktiválták a kevésbé zavaró stimulusok, míg a jutalmazó stimulusok nem befolyásolták aktivitásukat. Ez arra utal, hogy ezek az idegsejtek elsősorban a negatív tapasztalatok közvetítéséért felelősek. És valóban, ezen idegsejteknek épp a káros ingerek megélése pillanatában történő optogenetikai gátlása kiküszöbölte vagy jelentősen csökkentette a hippokampusz-függő kontextuális memórianyomok, és a hippokampusz-független kulcsingerhez kötött félelmi emlékek kialakulását. Tehát a MRR vGluT2-neuronok populációja egy olyan neuronhálózati központ amely elengedhetetlen a negatív tapasztalatok megfelelő feldolgozásához.

Az már korábban is ismert volt, hogy az LHb vagy a mVTA stimulálása hasonló hatásokkal jár (*143*, *165*, *176*, *177*), az MRR vGluT2 idegsejtek pedig mindkettőt erősen beidegzik, így nem volt meglepő, hogy optogenetikai aktiválásuk azonnali elkerülő, menekülő magatartást váltott ki, és az állat a rossz élmény kontextusát meg is jegyezte mivel másnap fényaktiválás nélkül is elkerülte az adott kontextust. További eredményeink is alátámasztották, hogy a MRR vGluT2 neuronok a negatív tapasztalatok aktív elkerülésében vesznek részt, azaz menekülést vagy agressziót váltanak ki.

Ismert, hogy a depresszió egy krónikusan fennálló negatív tapasztalatokon alapuló tanulási mechanizmus eredménye (*178*, *179*). A LHb neuronok előre válaszolnak a negatív eseményeket megelőző jelzésekre (*148*, *149*, *169*, *180*), így az állat negatív élménye a valódi negatív impulzusok nélkül is kialakulhat. Nem véletlen tehát, hogy a LHb krónikus serkentése depressziót okozhat a LHb idegsejtek burst-aktivitásának elősegítésével, amelyet a szomszédos gliasejtek is szabályoznak (*148–150*, *169*, *181*, *182*). Az MRR vGluT2 neuronok az LHb-sejtjeit erősen beidegzik NMDA-receptor-tartalmú serkentő szinapszisokkal, amelyeket LHb glia sejtjei vesznek körül. Ezek a MRR vGluT2 neuronok kiváltják LHb sejtek burst-aktivitását is. Ráadásul, serkentő visszacsatolás van az LHb és az MRR vGluT2-pozitív glutamáterg idegsejtjei között, ami támogathatja a szorongással és depresszióval összefüggő patológiás tanulást és így a LHb idegsejtek túlzott aktiválását, amennyiben a visszacsatolást nem sikerül hatékonyan szabályozni. És valóban, az általunk kemogenetikai módszerekkel krónikusan aktivált vGluT2-pozitív MRR idegsejtek anhedóniát okoztak a cukor-preferencia tesztben, ami a depresszió egyik tipikus tünete.

Az agresszió az egerekben és az emberekben is egyaránt ismert tünete a depressziónak (*152–154*) és ismert, hogy a LHb, valamint a MS/VDB szerepet játszik az agresszív viselkedés érzelmi feldolgozásában (*151*). És valóban, az általunk kemogenetikai módszerekkel krónikusan aktivált MRR vGluT2-neuronok szintén elősegítették az agresszív viselkedést. Az agressziót általában összekapcsolják az agitációval, amelynek jellemzői a nyugtalanság, és erősebb motoros tevékenységek. És valóban, az általunk kemogenetikai módszerekkel krónikusan aktivált MRR vGluT2 neuronok szintén elősegítették a megnövekedett mozgási

aktivitást. Mindez együttesen azt sugallja, hogy a vGluT2-pozitív MRR idegsejtek aktiválása elősegíti az agitációt és az aktív agresszív viselkedést.

Az MRR komplex hatással van az MS/VDB-hippokampális rendszer aktivitására és a kontextuális félelem-emlékek kialakulására, bár ennek mechanizmusát korábban kevéssé értették (*131*, *133*). A ritmus vezérlő PV-pozitív MS/VDB neuronok aktiválása elengedhetetlen a hippokampusz théta ritmusának kialakításához és a megfelelő epizodikus memória kialakulásához (*157*, *158*, *183*). A PV-pozitív MS/VDB idegsejteket az MRR glutamáterg sejtjei erősen beidegzik (*44*, *58*, *184*), de ezeknek a neuronoknak a identitása ismeretlen volt. Mi bemutattuk, hogy az MRR vGluT2 neuronok nem csak az LHb/mVTA tengely beidegzését végzik, hanem serkentő axonjaik nagy része elágazik és egyidejűleg beidegzi a PV-pozitív idegsejteket is a MS/VDB-ben. Eredményeink azt is mutatták, hogy a MRR vGluT2-neuronok azonnal és megbízhatóan elősegítik a memória rögzítéséhez szükséges hippokampális théta ritmus kialakulását és az állatok a stimulációt követő napon erős emlékeiket demonstrálva kerülték el az előző napi stimuláció helyszínét.

Eredményeink tehát igazolták, hogy a MRR vGluT2-pozitív neuron populációja egy az agy korábban fel nem ismert fontos központja, amely szükséges és elégséges is a negatív tapasztalatok megszerzéséhez. Az MRR vGluT2-idegsejtek az érzékszervi tapasztalatokkal kapcsolatos agyi területekről származó beidegzést kapnak, gátlásuk megzavarja a negatív emlékek kialakulását, aktivációja elősegíti az agitált viselkedést és károsnak tartott kontextus azonnali elkerülését idézi elő, még akkor is ha az állat egyébként rendkívül pozitív motivált állapotban volt éppen. Ha az elkerülés nem lehetséges pl. egy társas interakció során, akkor a sejtek aktiválása harcot és agressziót vált ki. A MRR vGluT2-pozitív sejtek aktiválása elősegíti a negatív tapasztalatokkal kapcsolatos hosszú távú memória kialakulását is, krónikus aktiválása depresszió-szerű viselkedést eredményez, valószínűleg az LHb idegsejtek hosszú távú burst-aktivitásának indukálásával (*148*, *150*), amit in vitro kísérleteinkben mi is kimutattunk.

Tehát a vGluT2-pozitív MRR idegsejtek azáltal szabályozzák a negatív tapasztalatok megszerzését, hogy egyidejűleg aktiválják mind az agy negatív élményfeldolgozó központjait, mind szepto-hippocampális rendszert az epizodikus memória nyomok kódolásának beindításához. A negatív tapasztalatok feldolgozása során bekövetkező hibás alkalmazkodási mechanizmusok számos hangulati rendellenesség alapját képezik, amelyek óriási társadalmi és gazdasági hatással vannak mind az egyénekre, mind a társadalomra, így e neuronális központ szelektív célzása új terápiás megoldások alapját képezheti.

A nucleus incertus szerepe a kontextuális emlékek rögzítésében

A tématerülethez tartozó mellékelt publikáció

A. Szőnyi, K. E. Sos, R. Nyilas, D. Schlingloff, A. Domonkos, V. T. Takács, B. Pósfai, P. Hegedüs, J. B. Priestley, A. L. Gundlach, A. I. Gulyás, V. Varga, A. Losonczy, T. F. Freund, G. Nyiri: Brainstem nucleus incertus controls contextual memory formation. *Science.* 364 (2019)

Bevezetés

A félelmi emlékek, melyek lehetővé teszik, hogy az állatok elkerüljék a számukra ártalmas helyzeteket, az ártalmas ingerek (feltétel nélküli inger) és az adott helyzet körülményeinek (a kontextus) társításával jön létre. Ezeket másként kontextuális memóriának is nevezzük. A dorzális hippokampusz alapvető szerepet játszik a kontextuális memória kódolásában, melynek CA1 piramissejtjei felelősek azért, hogy az emléknyomok kódolása után azok nagyagykéregbe juthassanak hosszú távú tárolás céljából (*185–187*). A CA1 piramissejtek az érzékszervi kontextuális információk egy egységes reprezentációját kapják proximális dendritjeiken, melyek a CA3 piramissejtjeitől érkeznek (*188*), míg az ártalmas inger sajátos tulajdonságai a CA1 piramissejtek disztális dendritjeire érkeznek közvetlenül az entorhinális kéregből (*189–191*). Sejt-szinten ezek a jelek asszociálódhatnak, azaz dendritikus kölcsönhatásaik hosszú távú szinaptikus plaszticitást eredményezhetnek a CA1 piramissejtekben (*192–194*). A CA1 piramissejtek néhány százaléka így u.n. memória engramot képezhet a kontextuális emlékek kódolására (*195*). A pontos epizodikus memória kialakulásához mind az érintetlen kontextuális információfeldolgozás, mind a közvetlen érzékszervi információkhoz kapcsolódó bemenetek szükségesek (*196–198*).

Az adott memória engram komponens kialakításában részt vevő piramissejtek számának finoman kiegyensúlyozottnak kell lennie (*199*). A piramis sejtek többségét gátolni kell, vagyis ki kell zárni a memória kódolásából a memória kialakulásának pillanatában, mert ha az ártalmas inger (azaz a feltétel nélküli inger) sajátos tulajdonságai túl sok piramis sejtben asszociálódnának a kontextussal, akkor az engram nem lenne elég specifikus, és így az emléknyom nem lenne felidézhető (*200*, *201*). A feltétel nélküli inger kizárása a hippokampusz CA1-ben szomatosztatint (SOM) kifejező u.n. oriens-lacunosum moleculare (OLM) gátló interneuronok révén érhető el (*200*). A OLM sejtek adják messze a legszerteágazóbb, legkiterjedtebb SOM-pozitív gátlósejt általi beidegzést a hippokampuszban (*200*, *202*). Az OLM sejtek szelektíven gátolják a piramissejtek disztális dendritjeit, amelyek az entorhinális kéregből érkező feltétel nélküli közvetlen érző bemenetet is kapják (*43*, *203–205*). És valóban, a dorzális CA1 SOM-pozitív neuronjainak ártalmas inger során történő mesterséges gátlása jelentősen megzavarja a félelmi tanulást (*200*, *201*). Ismert az is, hogy az OLM-sejtek aktivitását, az erősen figyelemfelkeltő pl. ártalmas ingerek, a bazális előagyi MS/VDB sejtjeinek aktivitásán keresztül fokozzák. Az itt található kolinerg sejtek megbízhatóan és

azonnal aktiválódnak fontos környezeti ingerek hatására (*86*, *200*) és erősen beidegzik a hippokampusz OLM-sejteket (*187*, *200*, *205*), míg az MS glutamaterg neuronjai az állat fontos ingerekre válaszul indított mozgásával korreláló aktivitás növekedést mutatnak, és szintén beidegzik a hippokampusz OLM sejtjeit (*43*, *206*).

Azonban, ha a bazális előagyi MS/VDB sejtjei túl sok a OLM sejtet aktiválnak és így azok túl sok piramissejtet gátolnak, akkor túl kevés piramissejt fog részt venni az engramok általi memórianyom kódolásában, ami pontatlan emlékhez, félelmi memória esetén generalizált félelemhez vezethet, mivel a félelem tárgyát nem sikerül pontosan rögzíteni (*207*). Így a hippokampális engramok megfelelő egyensúlyához az OLM-sejtek aktiválását megfelelően szabályozni kell. Az OLM idegsejtek gátló szabályozása ideális esetben egy hippokampuszon kívüli kéreg alatti területről kell származzon, amely már részben integrálta és feldolgozta a vonatkozó környezeti információkat, ám az OLM idegsejtekre érkező ilyen specifikus gátlás korábban nem volt ismert.

Az NI GABAerg neuronok szelektíven gátolják a hippokampusz SOM-pozitív interneuronjait

Virális sejt-specifikus pályajelölésekkel kimutattuk, hogy a nucleus incertus (NI) GABAerg sejtjei szelektíven idegzik be a hippokampusz stratum oriens és a gyrus dentatus hiláris rétegeit, éppen azon rétegeket, ahol a SOM idegsejtek találhatók (*208*). Kimutattuk azt is, hogy a NI-t körülvevő agytörzsi magok GABAerg sejtjei nem vetítenek a hippokampuszba, és az NI GABAergic neuronok nem használnak glutamátot, glicint, acetilkolint, szerotonint vagy más monoaminokat jelátvivő anyagként.

NI GABAerg idegvégződések hippokampális célsejt-szelektivitását számos különböző kombinált, sejttípus-specifikus, virális pályajelölés használatával vizsgáltuk. Ezek eredményei azt mutatták, hogy az NI rostok elsődleges célpontja a hippokampuszban a dendriteket célzó SOM-pozitív interneuronok, melyek lokális hatása elsősorban az OLM sejtektől származik (*200*, *202*, *209*).

Korrelált fény- és immuno-elektronmikroszkópos elemzéssel megállapítottuk, hogy a NI rostok hippokampális szinapszisai szimmetrikusak, poszt-szinaptikusan tartalmaznak $GABA_A$ receptor γ2 alegységeket és a GABAerg szinapszis specifikus gephyrin állványfehérjét.

A hippokampusz NI-ból érkező GABAerg rostjainak optogenetikai vizsgálata során, annak in vitro fény-stimulációja, megbízhatóan váltott ki gabazin (GABA antagonista)-érzékeny gátló poszt-szinaptikus válaszokat (IPSC-k) a CA1 stratum oriens interneuronokból, igazolva ezzel a $GABA_A$ receptor függő GABAerg jelátvitelt ezekben a szinapszisokban. Noha az NI GABAerg neuronok kifejezik a relaxin-3-at, a hippokampális SOM-sejtek pedig annak receptorát (*210*, *211*), mégis azt láttuk hogy ezen az időskálán a gabazin minden jelátvitelt blokkolni tudott. Összességében azt találtuk, hogy a NI rostok közvetlenül a SOM pozitív dendrit-célzó OLM interneuronokat célozzák a hippokampuszban hatékony GABAerg szinapszisokkal.

Az NI GABAerg neuronok gátolják az OLM sejteket serkentő MS neuronokat is.

A hippokampális SOM sejtek legfőbb extra-hippocampális serkentésüket MS glutamáterg és kolinerg idegsejtjeitől kapják (*43*, *200*, *205*). Feltételeztük, hogy az NI még hatékonyabban gátolhatja a hippokampális SOM-pozitív OLM sejteket, ha közvetett módon gátolja azok serkentését biztosító neuronokat is a MS-ben.

Ismét sejttípus specifikus virális pályajelöléseket használva kimutattuk, hogy a relaxin-3 pozitív NI GABAerg rostok erősen beidegzik az MS sejtjeit is, rajtuk is $GABA_A$ receptor γ2 alegység és gephyrin pozitív szimmetrikus szinapszisokat hoztak létre, miközben az NI-t körülvevő agytörzsi-területek nem vetítettek GABAerg rostokkal a MS-ba. Kimutattuk, hogy a NI relaxin-3 pozitív terminálisai gyakran adnak gephyrin pozitív szinapszisokat közvetlenül a MS glutamaterg és a kolinerg sejtjeire, ezzel gátolva a OLM sejtek hippokampuszon kívüli fő serkentő sejtjeit. Ezenkívül kettős retrográd pályakövetés segítségével megfigyeltük, hogy a hippokampuszt célzó egyes NI GABAerg neuronok jelentős része axon-kollaterálisokat küld a MS-ba is, biztosítva ezzel, hogy a NI GABAerg sejtek szinkron módon gátolhassák közvetlenül a hippokampális OLM sejteket és közvetetten azok serkentésének forrását a MS-ben.

A NI GABAerg rostjai fontos környezeti ingerek hatására azonnal aktiválódnak

Anatómiai és in vitro fiziológiai adataink mutatták, hogy az NI GABAerg neuronok ideálisak lennének az OLM sejtek MS-ból érkező aktiválásának ellensúlyozására, és így képesek lehetnek a piramissejtek memória kódolásának finomhangolására. Annak tesztelésére, hogy a NI GABAerg neuronok valóban reagálnak-e az érzékszervi ingerekre és a viselkedési állapotok változására, kalcium-csatorna aktiváción alapuló két foton mikroszkópos képalkotással vizsgáltunk éber egerek, NI-ból érkező hippokampális GABAerg rostjainak aktivitás változását, környezeti ingerekre (*200*, *212*). Az egerek különböző ingereket kaptak (zavaró levegő befújást, víz jutalmat, hangjeleket és fény felvillanásokat) véletlenszerűen, melyek mindegyikére egyértelmű aktivitás növekedést figyeltünk meg a NI GABAerg neuronok hippokampusz rostjaiban, és emellett láttuk, hogy az intenzívebb ingerek, mint például a zavaró levegő befújást vagy a víz jutalmazás, különösen erősen befolyásolták mind a NI GABAerg sejtek aktivitásának erősségét, mind pedig a hippokampuszban aktiválódott terminálisaik arányát.

Az NI GABAerg sejtek, környezeti ingereket feldolgozó agyterületekről kapnak szinapszisokat

A fent említett adatok azt mutatják, hogy az NI GABAerg neuronjai fontos környezeti ingereket továbbítanak az agytörzsből a hippokampuszba. Hogy megértsük, mely agyterületek információit összegzik a NI GABAerg neuronjai, speciálisan módosított veszettség vírussal mono-transz-szinaptikus pálya jelöléseket végeztünk (*147*). Azt találtuk, hogy a NI GABAerg sejtjei számos viselkedéssel és döntéshozatallal összefüggő agyterületről kapnak jeleket. Ezen agyterületek alapvető szerepet játszanak a mozgásban, az ártalmas vagy

jutalmazó ingerek feldolgozásában és a memória kódolásában. Nem találtunk jelölt idegsejteket a hippokampuszban, megerősítve, hogy valóban nincs közvetlen vetítés a hippokampuszból az NI-ba.

Az NI GABAerg sejtek képesek szabályozni a hippokampusz hálózati aktivitását

A hippokampusz théta ritmus aktivitás elengedhetetlen a kontextus függő memória kialakulásához (*207*, *213*) és tipikus miközben az állat felfedezi környezetét (*156*, *214*), ezért megvizsgáltuk a NI GABAerg neuronok hippokampális théta ritmus aktivitására gyakorolt hatását. Miközben optogenetikai kísérletek során fénnyel aktiváltuk a NI GABAerg sejtjeit, a dorzális hippokampuszba helyezett többcsatornás elvezetés segítségével vizsgáltuk meg a hippokampusz ritmikus aktivitását miközben az egerek szabadon viselkedhettek. Azt találtuk, hogy a NI GABAerg neuronok stimulálása csökkentette és átrendezte a hippokampusz théta aktivitását. A hatás a magas théta tartományban (8-12 Hz) erősebb, az alacsony théta tartományban (5-8 Hz) gyengébb volt. A többcsatornás elvezetésből származó áramforrás-sűrűség-elemzés kimutatta, hogy a változások alapvetően a piramissejtek disztális dendritjeinek elektromos aktivitás-változása miatt történtek. Épp ott ahol a piramissejteket az OLM sejtek gátolhatják. Ez megerősíti, hogy a NI hippokampális rostjai az OLM sejtek által beállított gátló egyensúly befolyásolásával képesek átrendezni a hippokampális théta ritmusú aktivitást.

Az NI GABAerg neuronok pontosan időzített serkentése gátolja félelmi memória kialakulását

A fenti eredményeink azt mutatták, hogy a NI GABAerg sejtjei, miután feldolgozták számos kulcsfontosságú viselkedés szabályozó agyterület jeleit, képesek közvetlen és közvetett módon is gátolni a hippokampális SOM-pozitív sejteket, méghozzá a fontos környezeti ingerek függvényében. Ezáltal a NI ideális lehet a hippokampális OLM sejtek segítségével a memória kialakulásában résztvevő hippokampális piramissejtek kiválasztásán keresztül a memória nyomok kódolását befolyásolni.

Ennek viselkedési tesztelését olyan optogenetikai kísérletekkel kezdtük, melyekben az állatok egy csoportjában, a NI GABAerg sejtjeiben vagy fénnyel aktiválható csatornákat kifejező vírus volt (ChR2 egerek) vagy fényre nem válaszoló kontrol vírus (CTRL egerek). Az egereket egy új környezetbe helyeztük („A” környezet), ahol négy ijesztő elektromos láb ingerlését és a NI sejtek fény megvilágítását alkalmaztuk, pontosan egyszerre időzítve. 24 órával később az egereket ugyanabba az „A” környezetbe helyeztük, ahol a CTRL egerek a várt erőteljes félelmi viselkedést mutatták, míg a ChR2 egerek szinte semmilyen félelmet nem mutattak. Az egy órával későbbi szorongás teszt pedig szignifikánsan alacsonyabb szorongási szintet mutatott ki a ChR2 egerekben, mint a CTRL egerekben. Egy további kontroll kísérletben egy héttel később megismételtük ezeket a kísérleteket egy másik környezetben, fény stimuláció nélkül, amikor viszont másnapra már mindkét csoport állat egyforma félelmet mutatott. Ezek az eredmények rámutattak arra, hogy a kontextuális félelmi memória

kialakulása blokkolható, ha az NI GABAergic neuronokat pontosan félelem pillanatában aktiváljuk.

Annak megerősítésére, hogy az NI GABAerg sejtek közvetlenül hatnak a hippokampusz SOM-pozitív sejtjeire, létrehoztunk egy második kísérleti csoportot ChR2 és CTRL egerekből, ismét a fent leírtak szerint. Itt azonban az optikai szálakat kétoldalt a dorzális hippokampuszba ültettük be. A fent ismertetetthez hasonló kontextuális félelmi kondicionálás kísérletekben a ChR2 egerek ismét szignifikánsan alacsonyabb félelmi szintet mutattak az „A" környezetben, ahol NI-ban fény stimulációt kaptak az ijesztő inger során, mint a „B" környezetben, ahol a NI-t nem stimuláltuk. Ez a hatás a CTRL egereknél nem volt kimutatható. Ezek az eredmények arra utalnak, hogy a NI GABAerg rostjai közvetlenül a dorzális hippokampuszban képesek gátolni a kontextuális memória kialakulását.

Az NI GABAerg neuronok pontatlan serkentése nem befolyásolja a félelmi memóriát

A kódolást végző hippokampális piramissejtek csoportjának a feltétlen inger (ijesztő elektromos inger) pillanatában kell kiválasztódnia és kell azonnal asszociálnia az ingert a kontextussal, amiben az állat épp tartózkodik. Az időzítés fontosságának tesztelésére minden kísérleti egerünk NI-ának GABAerg sejtjei fénnyel aktiválhatóak voltak. Az egereket két csoportra osztottuk, az egyik csoportban a NI GABAerg sejtek fény-stimulációja az ijesztő inger pillanatában történt, míg a másik csoportban a fény-stimuláció 15 másodperces eltolással érkezett. Azt találtuk, hogy pontos időzítés esetén, másnap az állatok ismét alig emlékeztek az ijesztő ingerre, azonban, ha a NI GABAerg sejtek fény-stimulációja késett az állatok emlékeit az már nem befolyásolta. Ez azt jelzi, hogy az NI GABAergic neuronok aktiválásának pontos időzítése nélkülözhetetlen annak megfelelő működéséhez, azaz a NI GABAerg rostok hatása pillanatszerű gátló hatásukon alapul és nem a hálózati ritmusok általános megzavarásán vagy egyéb lassú jelátvitel hatásán.

Az NI GABAerg neuronok pontosan időzített gátlása erősebb félelmi emléket alakít ki

Végül megvizsgáltuk, hogy az NI GABAerg neuronok gátlása a kontextuális félelemi kondicionálás során képes-e ellentétes hatást kiváltani, azaz vajon okozhat-e generalizált, erős félelmet. Optogenetika kísérleteink során ezúttal olyan (ArchaerhodopsinT-3 csatorna kifejező) vírusokat használtunk, melyek segítségével a NI GABAerg sejtjeit gátolni tudtuk (ArchT-egerek), míg a kontroll állatok ismét fényre érzéketlen vírust fejeztek ki (CTRL-egerek). Először az egereket az új „A" környezetbe helyeztük, ahol három hangjelzést kaptak, amelyek végén az egerek ismét ijesztő elektromos láb-ingerlést kaptak. A NI minden állatban folyamatos fény bevilágítást kapott a kísérletek során. 24 órával később az egereket visszahelyeztük az „A" környezetbe, ahol azt találtuk, hogy az ArchT-egerek szignifikánsan erősebb hippokampusz-függő kontextuális félelmet mutattak, mint a CTRL egerek. A kulcs ingerhez kötött félelmi emlékek (esetünkben a hangjelzéshez kötött félelem) alapvetően a hippokampusztól függetlenül jönnek létre (*215*). Hogy megvizsgáljuk befolyásolja-e

közvetlenül a kulcsingerhez kötött emléket a NI, másnap az egereket egy másik, semleges „B" környezetbe helyeztük és bemutattuk nekik a korábbi hangjelzéseket, de nem találtunk különbséget a két csoport között. Ez azt sugallja, hogy az NI GABAerg neuronoknak a kontextuális memória kialakulására gyakorolt hatása valóban hippokampusz függő volt.

Az NI GABAerg neuronok szerepének összefoglalása

Az epizodikus emlékek kódolása elengedhetetlen az állatok túléléséhez. A hippokampusz dorzális CA1 régiójának piramissejtjei kulcsszerepet játszanak ebben a folyamatban (*185*, *207*, *216*) azáltal, hogy a több érzékszervtől érkező kontextuális információkat összepárosítják a feltétlen inger közvetlen egyedi érzékszervi élményével, ami a sejtek szintjén hosszú távú szinaptikus plaszticitás révén valósul meg (*192*, *194*, *199*). Ha azonban túl sok piramissejt kap ugyanolyan közvetlen érzékszervi információt, akkor az általuk létrehozott memórianyom kódja nem lesz elég specifikus és az emlék elveszik (*200*). Ezért a piramissejteknek csak egy alpopulációja vesz részt az egyes memória nyomok létrehozásában. Az emlékek lenyomatát így u.n. memória engramok azaz összehangolódott piramissejtek őrzik (*195*, *199*). Ehhez azonban az entorhinális kéregből a piramissejtek disztális dendritjeire érkező közvetlen érzékszervi feltétlen ingereket el kell zárni a legtöbb piramissejttől (*200*).

A hippokampális SOM-pozitív OLM neuronok szelektíven gátolják a piramissejtek disztális dendritjeit, hogy kiszűrjék az entorhinális kéregből érkező közvetlen érzékszervi feltétlen ingereket (*43*, *187*, *200*). Az OLM sejteket, a fontos környezeti ingerek hatására, a MS glutamaterg és kolinerg sejtjei aktiválják (*43*, *187*, *200*, *203–205*), így a disztális dendriteket célzó OLM sejtek hatékonyan blokkolhatják a legtöbb piramissejt közvetlen érzékszervi bemeneteit a memória formálódás pillanatában. Ez teszi lehetővé, hogy a piramissejteknek valóban csak egy alpopulációja tud asszociációt végezni és ezek fognak engramokat képezni.

Ezen piramissejtek kiválasztásának azonban pontosan kiegyensúlyozottnak kell lennie, ugyanis ha az OLM sejtek minden piramissejt disztális dendritjét gátolnák akkor nem maradna engram alkotásra alkalmas piramissejt. Ezért feltételeztük, hogy az OLM interneuronokat szintén időben pontosan kell tudni gátolni, célszerűen kéreg alatti információk alapján (*201*, *207*, *216*). Felfedeztük, hogy a NI GABAerg neuronok kitűnően alkalmasak erre időzítetten, külső ingertől függő módon.

Bebizonyítottuk, hogy az NI GABAerg neuronok számos agyterületről mono-szinaptikus bemenetet kapnak, amelyek előre feldolgozzák a fontos környezeti ingereket. Kiderült, hogy a NI GABAerg neuronok szelektíven, közvetlenül gátolják a hippokampusz SOM-pozitív interneuronjait, amelyek messze túlnyomó többsége OLM interneuron (*200*, *202*).

Bár a bazális előagyi kolinerg sejtek a fent leírt módon felszabadítanak GABA transzmittert is, ezt azonnal követi egy erős kolinerg serkentő komponens (*99*), ami az OLM sejtek hatékony nettó aktiválását eredményezi (*99*, *200*). A fenti eredményeinkből látható,

hogy a hippokampális OLM sejtek, bazális előagyból eredő glutamáterg és kolinerg serkentéséért felelős sejtjeit a NI GABAergic neuronok szintén gátolják, ami megkönnyíti a hippokampusz OLM sejtek hatékony és pontosan időzített gátlását. Azt is bizonyítottuk, hogy ezeket a közvetlen (hippokampális) és közvetett (bazális előagyi) gátló rostokat sokszor ugyanazon NI GABAerg sejt axonjainak az elágazásai hozzák létre megkönnyítve ezáltal azok szinkron működését.

Korábbi tanulmányok alapján a dorzális CA1 OLM neuronok közvetlen gátlása gyengébb memória-formációt eredményezett (*200*, *201*). És valóban, a dorzális CA1 OLM neuronok gátolhatók az agytörzs NI GABAerg neuronok aktiválásával, így pedig a NI GABAerg neuronok pontosan ütemezett aktiválása a kontextuális félelemi emlékek teljes gátláshoz vezethet, ahogyan azt kísérleteink is bizonyították.

Ezzel szemben az NI irtás után a patkányok patológiásan erős memóriaképződést mutatnak, amit a félelmi emlékek csökkent kioltódását és fokozott generalizált szorongás kialakulását jelzi (217, 218). És valóban, a NI GABAerg neuronok gátlása után mi is a kontextuális félelemi memória erőteljesebb megmaradását figyeltünk meg.

Leírtuk, hogy az NI GABAerg neuronok több olyan agyterületről kapnak mono-szinaptikus bemeneteket, amelyek fontos környezeti ingereket dolgoznak fel. Továbbá kiderült, hogy a különböző környezeti ingerek a NI rostok különböző részét aktiválták, így az érzelmileg jelentősebb bemenetek például hatékonyabbak voltak. Ezenkívül, elemzésünk arra utalt, hogy a különböző NI sejteket részben eltérő szenzoros ingerek aktiválhatják. Ezért feltételezhető, hogy az NI GABAergic neuronok különböző populációi, a piramissejtek különböző alpopulációit válogatják ki a memória kódoláshoz szükséges engramok kódolásához.

Patkányban megfigyelték, hogy a kortikotropin-felszabadító hormon receptort (CRH-R1-et) kifejező NI GABAerg neuronokat különböző stresszorok aktiválhatják (67, 218–220). Eredményeink azt is mutatták, hogy az NI GABAerg neuronok több agyterületről kapnak stressz szabályozással kapcsolatos beidegzést, amelyek között a medián raphe régióból érkező CRH-t kifejező, általunk leírt idegsejtjeiről érkező beidegzés korábban még nem volt ismert. Ezért, a NI GABAerg neuronok CRH-függő modulációja hozzájárulhat a stresszes körülmények között megfigyelt kóros epizodikus memória rögzítéshez (221, 222).

A NI GABAerg neuronok jelentősége

A NI GABAerg neuronok esetleges neurodegenerációja hypermnézia-szerű tüneteket eredményezhet, amelyekben a mindennapi élet szükségtelenül kódolt részletes emlékei kognitív problémákat okoznak a betegekben (223, 224). Az NI GABAerg sejtek működési hibái hozzájárulhatnak az általános szorongásos szindrómákhoz vagy poszt-traumás stressz rendellenességekhez is, melyek esetében a patológiásan erős epizodikus memória kialakulása jól ismert. Másrészt az NI GABAerg neuronok rendellenesen erős aktivitása kognitív problémákat eredményezhet.

Az NI GABAerg neuronoknak fontos szerepe lehet a memóriakódolásban résztvevő engram-képző piramissejtek kiválasztásában, melyet a környezeti ingerek fontossága és/vagy jellege alapján képes pontosan elvégezni. A NI GABAerg sejtek szintén segíthetnek kiszűrni az érdektelen mindennapi élményeket, amelyekhez az állatok már hozzászoktak vagy megjegyzésük szükségtelen. Eredményeink egy olyan váratlanul specifikus agytörzsből felszálló gátló pályát tártak fel, melynek alapvető szerepe van emlékeink raktározásában.

Összefoglalás

A hippokampális formáció egy evolúciósan ősi, erősen specializálódott és egyik legjobban ismert agykéreg terület. Mégis, működésének teljes megismerése csak akkor lesz lehetséges, ha megismertük a vele összeköttetésben lévő agyterületek működését is, etc., míg el nem jutunk az agy működésének teljes modelljéhez. Azonban a hippokampusz megértésében elért haladás már most is sok inspirációt szolgáltatott más agyrégiók tanulmányozásához is, amelyek pl. a hippokampuszba vetítenek vagy melyek onnan kapnak beidegzést. A hippokampusz fontos kiinduló pontként szolgál ahhoz is, hogy megértsük az agyterületek közötti kommunikációt lehetővé tevő neuronális kommunikáció alapelemeit, és hogy azok együttműködése hogyan vezet az állat viselkedéshez.

A hippokampusz memóriában betöltött szerepe, nem jelenti, hogy a hippokampusz önmagában képes lenne a valóság vagy a megtanulható információ „megértésére”. Működéséhez nem kell önmagában értelmeznie az elraktározandó memórianyomokat. Elsődleges feladata vélhetően az, hogy az ide érkező információk sorrendisége, tér és időbeli elrendeződése alapján lenyomatot képezzen azok információinak struktúrájáról, melyet fősejtjeik kisebb populációi segítségével egyfajta kódként képes tárolni majd a nagyagykéregbe továbbítani. A hippokampális információ feldolgozás leginkább tér és időbeli viszonyítási pontokat ad az információk tárolásához. Kiterjedt kapcsolatrendszere elősegíti, hogy a események lenyomata, az események minél több aspektusát, minél több modalitását tartalmazza, hogy azt a kód egyediségének segítségével minél pontosabban el tudja helyezni kiterjedt „kognitív térképén”. Ennek a térképnek a megrajzolásához szükségesek a kéreg alatti területek, a szeptum, a mediális raphe és a nucleus incertus által előre feldolgozott információk.

Miközben évtizedekig az agytörzset főként az autonóm funkciókban és a ritmus generálásában tartották csak fontosnak, munkáink megmutatták hogy az agytörzsi NI és MRR pontosan időzített módon, gyorsan, közvetett pályákon és közvetlen hippokampális beidegzéssel is képes vezérelni a kontextuális memória nyomok kialakítását. Továbbá bemutattuk, hogy a kolinerg rendszer, mely a hippocampus egyik legintenzívebb beidegzését adja, egy pontosan időzített GABAerg gátlással is ellátja a hippokampuszt, mely GABA felszabadulás önmagában is képes a memória nyomok raktározása szempontjából kulcsfontosságú hippokampális ritmusok koordinálására.

Új sejtpopulációk vagy jelátvivő rendszerek felfedezése kapcsán mindig felmerül, ezek esetleges gyógyászati felhasználása. A modern gyógyászati és géntechnológiák ígéretével, szerencsére valóban elérhető távolságba kerülhetnek majd új megoldások. Ezek segítségével reméljük képesek leszünk a jelátvivő rendszerek módosításának vagy bizonyos specifikus sejtpopulációk aktiválásának vagy gátlásának segítségével, a szükséges minimális beavatkozás mellett kezelni, vagy akár meggyógyítani az idegrendszeri eredetű megbetegedéseket.

Köszönetnyilvánítás

Mindenekelőtt szeretném megköszönni tanítványaimnak és munkacsoportom minden korábbi és jelenlegi tagjának munkájukat és az általuk nyújtott inspiráló légkört. Mindennapi hatékony kísérletes kutatómunkájuk nélkül nem tehettünk volna ennyi izgalmas felfedezést és ez az értekezés nem születhetett volna meg. Így külön is köszönöm asszisztenseink Arszovszki Antónia, Goda Győző, Hajós Zsuzsanna, Iványi Katalin, Kriczky Andrea, Lengyel Katalin, Szépné Simon Emőke segítségét, valamint külön köszönöm közvetlen munkatársaim és diákjaim, Cserép Csaba, Bardóczi Zsuzsanna, Gönczi Roland, Hegedüs Panna, Major Ábel, Mayer Márton, Orosz Áron, Papp Péter, Pósfai Balázs, Sós Katalin Eszter, Szőnyi András, Takács Virág, Zádori Dénes, Zichó Krisztián kitűnő kutatómunkáját.

Hálás vagyok Freund Tamás akadémikus csoportvezetőnknek, hogy munkájával és folyamatos támogatásával olyan tudományos közösséget és légkört hozott létre mind a kutatóintézet, mind pedig kutatócsoportunk szorosan együttműködő munkacsoportjai számára, ami inspiráló és termékeny kereteket adott a kutatómunkának. Továbbá hálás vagyok egykori mentoraimnak Halasy Katalinnak (Állatorvostudományi Egyetem, Budapest) és Somogyi Péternek (Oxfordi Egyetem, Egyesült Királyság) is korábbi támogatásukért.

Itt bemutatott munkákhoz számos hazai és külföldi kollégám nyújtott kísérleti vagy egyéb szakmai segítséget, akik nélkül ezek a munkák nem készülhettek volna el. Ezért köszönetet szeretnék mondani Balázsfi Diána, Barth Albert, Bodor Ágnes, Borhegyi Zsolt, Dénes Ádám, Demeter, Kornél, Domonkos Andor, Gulyás Attila, Haller József, Hájos Norbert, Jelitai Márta, Katona István, Káli Szabolcs, Környei Zsuzsanna, Nyilas Rita, Schlingloff Dániel, Sipos Eszter, Török Bibiána, Varga Viktor, Zelena, Dóra munkatársaimnak a Kísérleti Orvostudományi Kutatóintézetben, illetve Watanabe Masahiko (Hokkaido University, Japan), Ken P. MacKie (Indiana University Bloomington, USA), Shigemoto Ryuichi (National Institute for Physiological Sciences, Okazaki, Japan), Jan de Vente (Maastricht University, Netherlands), Losonczy Attila (Columbia University, New York, USA), James Benjamin Priestley (Columbia University, New York, USA), Andrew Gundlach (Florey Institute of Neuroscience, Melbourne, Austrália) külföldi kollégáimnak. Továbbá szeretném megköszönni a Kísérleti Orvostudományi Kutatóintézet valamennyi központi és többi laboratóriumának munkatársainak és állatgondozói szakembereinek sokféle formában nyújtott a segítségüket.

Nem utolsósorban szeretném megköszönni szüleimnek, valamint páromnak Boglárkának és kisfiamnak Barnabásnak kitartó támogatásukat és segítő szeretetüket.

Referenciák

1. S. K. Karadimas, K. Satkunendrarajah, A. M. Laliberte, D. Ringuette, I. Weisspapir, L. Li, S. Gosgnach, M. G. Fehlings, Sensory cortical control of movement. *Nat. Neurosci.* **23**, 75–84 (2020).
2. N. G. Hatsopoulos, A. J. Suminski, Sensing with the motor cortex. *Neuron*. **72** (2011), pp. 477–487.
3. S. a Farr, J. F. Flood, J. E. Morley, The effect of cholinergic, GABAergic, serotonergic, and glutamatergic receptor modulation on posttrial memory processing in the hippocampus. *Neurobiol. Learn. Mem.* **73**, 150–167 (2000).
4. I. Morgado-Bernal, Learning and memory consolidation: Linking molecular and behavioral data. *Neuroscience*. **176** (2011), pp. 12–19.
5. F. Nazari-Serenjeh, A. Rezayof, M. R. Zarrindast, Functional correlation between GABAergic and dopaminergic systems of dorsal hippocampus and ventral tegmental area in passive avoidance learning in rats. *Neuroscience*. **196**, 104–114 (2011).
6. M. Ohno, S. Watanabe, Concurrent blockade of hippocampal metabotropic glutamate and N-methyl-D-aspartate receptors disrupts working memory in the rat. *Neuroscience*. **70**, 303–311 (1996).
7. L. Bacciottini, M. B. Passani, P. F. Mannaioni, P. Blandina, in *Behavioural Brain Research* (2001), vol. 124, pp. 183–194.
8. D. J. Watson, M. E. Stanton, Intrahippocampal administration of an NMDA-receptor antagonist impairs spatial discrimination reversal learning in weanling rats. *Neurobiol. Learn. Mem.* **92**, 89–98 (2009).
9. K. Okada, H. Okaichi, Functional differentiation and cooperation among the hippocampal subregions in rats to effect spatial memory processes. *Behav. Brain Res.* **200**, 181–191 (2009).
10. P. R. Zoladz, A. M. Campbell, C. R. Park, D. Schaefer, W. Danysz, D. M. Diamond, Enhancement of long-term spatial memory in adult rats by the noncompetitive NMDA receptor antagonists, memantine and neramexane. *Pharmacol. Biochem. Behav.* **85**, 298–306 (2006).
11. I. Izquierdo, C. da Cunha, R. Rosat, D. Jerusalinsky, M. B. C. Ferreira, J. H. Medina, Neurotransmitter receptors involved in post-training memory processing by the amygdala, medial septum, and hippocampus of the rat. *Behav. Neural Biol.* **58**, 16–26 (1992).
12. N. Axmacher, F. Mormann, G. Fernández, C. E. Elger, J. Fell, Memory formation by neuronal synchronization. *Brain Res. Rev.* **52** (2006), pp. 170–182.
13. Z. U. Khan, E. C. Muly, Molecular mechanisms of working memory. *Behav. Brain Res.* **219** (2011), pp. 329–341.
14. I. Lee, T. S. Jerman, R. P. Kesner, Disruption of delayed memory for a sequence of spatial locations following CA1- or CA3-lesions of the dorsal hippocampus. *Neurobiol. Learn. Mem.* **84**, 138–147 (2005).
15. B. P. Kirby, J. N. P. Rawlins, The role of the septo-hippocampal cholinergic projection in T-maze rewarded alternation. *Behav. Brain Res.* **143**, 41–48 (2003).
16. R. M. Ridley, C. J. Timothy, C. J. MacLean, H. F. Baker, Conditional learning and memory impairments following neurotoxic lesion of the CA1 field of the hippocampus. *Neuroscience*. **67**, 263–275 (1995).
17. G. Riedel, J. Micheau, Function of the hippocampus in memory formation: Desperately seeking resolution. *Prog. Neuro-Psychopharmacology Biol. Psychiatry*. **25** (2001), pp. 835–853.
18. G. L. Gessa, M. S. Mascia, M. A. Casu, G. Carta, Inhibition of hippocampal acetylcholine release by cannabinoids: Reversal by SR 141716A. *Eur. J. Pharmacol.* **327** (1997), , doi:10.1016/S0014-2999(97)89683-5.
19. S. E. File, P. J. Kenny, S. Cheeta, The role of the dorsal hippocampal serotonergic and cholinergic systems in the modulation of anxiety. *Pharmacol. Biochem. Behav.* **66** (2000), pp. 65–72.
20. T. Balazsa, J. Bíró, N. Gullai, C. Ledent, B. Sperlágh, CB1-cannabinoid receptors are involved in the modulation of non-synaptic [3H]serotonin release from the rat hippocampus. *Neurochem. Int.* **52**, 95–102 (2008).
21. A. Drago, C. Crisafulli, A. Sidoti, A. Serretti, The molecular interaction between the glutamatergic, noradrenergic, dopaminergic and serotoninergic systems informs a detailed genetic perspective on depressive phenotypes. *Prog. Neurobiol.* **94** (2011), pp. 418–460.
22. A. I. Gulyás, L. Acsády, T. F. Freund, in *Neurochemistry International* (1999), vol. 34, pp. 359–372.
23. H. Li, J. Zhang, W. Xiong, T. Xu, J. Cao, L. Xu, Long-term depression in rat CA1-subicular synapses depends on the G-protein coupled mACh receptors. *Neurosci. Res.* **52**, 287–294 (2005).
24. M. R. Picciotto, M. J. Higley, Y. S. Mineur, Acetylcholine as a Neuromodulator: Cholinergic Signaling Shapes Nervous System Function and Behavior. *Neuron*. **76**, 116–129 (2012).
25. J. a Dani, D. Bertrand, Nicotinic acetylcholine receptors and nicotinic cholinergic mechanisms of the central nervous system. *Annu. Rev. Pharmacol. Toxicol.* **47**, 699–729 (2007).
26. G. Calfa, D. Bussolino, V. A. Molina, Involvement of the lateral septum and the ventral Hippocampus in the emotional sequelae induced by social defeat: Role of glucocorticoid receptors. *Behav. Brain Res.* **181**, 23–34 (2007).
27. B. W. Adams, B. Moghaddam, Tactile stimulation activates dopamine release in the lateral septum. *Brain Res.* **858** (2000), pp. 177–180.
28. M. R. Lamprea, A. M. B. Garcia, S. Morato, Effects of reversible inactivation of the medial septum on rat exploratory behavior in the elevated plus-maze using a test-retest paradigm. *Behav. Brain Res.* **210**, 67–73 (2010).
29. J. F. Flood, S. A. Farr, K. Uezu, J. E. Morley, The pharmacology of post-trial memory processing in septum. *Eur. J. Pharmacol.* **350**, 31–38 (1998).
30. E. C. McNay, C. E. Canal, R. S. Sherwin, P. E. Gold, Modulation of memory with septal injections of morphine and glucose: Effects on extracellular glucose levels in the hippocampus. *Physiol. Behav.* **87**, 298–303 (2006).
31. O. Mamad, H. M. McNamara, R. B. Reilly, M. Tsanov, Medial septum regulates the hippocampal spatial representation. *Front. Behav. Neurosci.* **9**, 166 (2015).
32. A. Rashidy-Pour, F. Motamedi, Z. Motahed-Larijani, Effects of reversible inactivations of the medial septal area on reference and working memory versions of the Morris water maze. *Brain Res.* **709**, 131–140 (1996).
33. A. Degroot, D. Treit, Septal gabaergic and hippocampal cholinergic systems interact in the modulation of anxiety. *Neuroscience*. **117**, 493–501 (2003).

34. C. Furini, J. Myskiw, I. Izquierdo, The learning of fear extinction. *Neurosci. Biobehav. Rev.* **47** (2014), pp. 670–683.

35. D. C. de Paula, A. S. Torricelli, M. R. Lopreato, J. O. G. Nascimento, M. B. Viana, 5-HT 2A receptor activation in the dorsolateral septum facilitates inhibitory avoidance in the elevated T-maze. *Behav. Brain Res.* **226**, 50–55 (2012).

36. G. Ashabi, S. Oryan, R. Ahmadi, F. Valizadegan, The effects of hippocampal opioidergic and septal GABAergic system interactions on anxiety-like behavior in rats. *Life Sci.* **89**, 821–826 (2011).

37. R. M. M. de Almeida, M. Giovenardi, S. P. da Silva, V. P. de Oliveira, D. J. Stein, Maternal aggression in Wistar rats: Effect of 5-HT2A/2C receptor agonist and antagonist microinjected into the dorsal periaqueductal gray matter and medial septum. *Brazilian J. Med. Biol. Res.* **38**, 597–602 (2005).

38. F. Khakpai, M. Nasehi, A. Haeri-Rohani, A. Eidi, M. R. Zarrindast, Septo-hippocampo-septal loop and memory formation. *Basic Clin. Neurosci.* **4**, 5–23 (2013).

39. D. E. A. T. Arnolds, F. H. Lopes Da Silva, J. W. Aitink, A. Kamp, P. Boeijinga, The spectral properties of hippocampal EEG related to behaviour in man. *Electroencephalogr. Clin. Neurophysiol.* **50**, 324–328 (1980).

40. M. J. Kahana, R. Sekuler, J. B. Caplan, M. Kirschen, J. R. Madsen, Human theta oscillations exhibit task dependence during virtual maze navigation. *Nature*. **399**, 781–784 (1999).

41. R. Bódizs, S. Kántor, G. Szab??, A. Sz??cs, L. Er??ss, P. Hal??sz, Rhythmic hippocampal slow oscillation characterizes REM sleep in humans. *Hippocampus*. **11**, 747–753 (2001).

42. F. Sotty, M. Danik, F. Manseau, F. Laplante, R. Quirion, S. Williams, Distinct electrophysiological properties of glutamatergic, cholinergic and GABAergic rat septohippocampal neurons: novel implications for hippocampal rhythmicity. *J. Physiol.* **551**, 927–943 (2003).

43. F. Fuhrmann, D. Justus, L. Sosulina, H. Kaneko, T. Beutel, D. Friedrichs, S. Schoch, M. Schwarz, M. Fuhrmann, S. Remy, Locomotion, Theta Oscillations, and the Speed-Correlated Firing of Hippocampal Neurons Are Controlled by a Medial Septal Glutamatergic Circuit. *Neuron*. **86**, 1253–1264 (2015).

44. A. Szőnyi, M. I. Mayer, C. Cserép, V. T. Takács, M. Watanabe, T. F. Freund, G. Nyiri, The ascending median raphe projections are mainly glutamatergic in the mouse forebrain. *Brain Struct. Funct.* **221**, 735–751 (2016).

45. V. Varga, A. Losonczy, B. V. B. V. Zemelman, Z. Borhegyi, G. Nyiri, A. Domonkos, B. Hangya, N. Holderith, J. C. J. C. Magee, T. F. T. F. Freund, Fast synaptic subcortical control of hippocampal circuits. *Science (80-.).* **326**, 449–453 (2009).

46. M.-C. Bohut, Serotonin receptors in cognitive behaviors. *Cogn. Behav.*, 243–254 (1997).

47. R. P. Vertes, W. J. Fortin, A. M. Crane, Projections of the median raphe nucleus in the rat. *J. Comp. Neurol.* (1999), doi:10.1002/(SICI)1096-9861(19990517)407:4<555::AID-CNE7>3.3.CO;2-5.

48. V. Avanzi, M. L. Brandão, Activation of somatodendritic 5-HT1A autoreceptors in the median raphe nucleus disrupts the contextual conditioning in rats. *Behav. Brain Res.* (2001), doi:10.1016/S0166-4328(01)00254-6.

49. V. Avanzi, R. C. B. Silva, C. E. Macedo, M. L. Brandão, 5-HT mechanisms of median raphe nucleus in the conditioned freezing caused by light/foot-shock association. *Physiol. Behav.* (2003), doi:10.1016/S0031-9384(03)00029-5.

50. K. G. Borelli, A. C. Gárgaro, J. M. Dos Santos, M. L. Brandão, Effects of inactivation of serotonergic neurons of the median raphe nucleus on learning and performance of contextual fear conditioning. *Neurosci. Lett.* (2005), doi:10.1016/j.neulet.2005.07.031.

51. L. Dos Santos, T. G. C. S. De Andrade, H. Zangrossi, Serotonergic neurons in the median raphe nucleus regulate inhibitory avoidance but not escape behavior in the rat elevated T-maze test of anxiety. *Psychopharmacology (Berl).* **179**, 733–741 (2005).

52. Y. Ohmura, T. Izumi, T. Yamaguchi, I. Tsutsui-Kimura, T. Yoshida, M. Yoshioka, The serotonergic projection from the median raphe nucleus to the ventral hippocampus is involved in the retrieval of fear memory through the corticotropin-releasing factor type 2 receptor. *Neuropsychopharmacology*. **35**, 1271–1278 (2010).

53. S. Peters, D. A. Slattery, N. Uschold-Schmidt, S. O. Reber, I. D. Neumann, Dose-dependent effects of chronic central infusion of oxytocin on anxiety, oxytocin receptor binding and stress-related parameters in mice. *Psychoneuroendocrinology*. **42**, 225–236 (2014).

54. H. H. Zangrossi, F. G. Graeff, Serotonin in anxiety and panic: Contributions of the elevated T-maze. *Neurosci. Biobehav. Rev.* **46**, 397–406 (2014).

55. R. T. Fremeau, J. Burman, T. Qureshi, C. H. Tran, J. Proctor, J. Johnson, H. Zhang, D. Sulzer, D. R. Copenhagen, J. Storm-Mathisen, R. J. Reimer, F. A. Chaudhry, R. H. Edwards, The identification of vesicular glutamate transporter 3 suggests novel modes of signaling by glutamate. *Proc. Natl. Acad. Sci. U. S. A.* (2002), doi:10.1073/pnas.222546799.

56. J. A. Stamp, K. Semba, Extent of colocalization of serotonin and GABA in the neurons of the rat raphe nuclei. *BRAIN Res. ELSEVIER Brain Res.* **677**, 39–49 (1995).

57. C. Gras, E. Herzog, G. C. Bellenchi, V. Bernard, P. Ravassard, M. Pohl, B. Gasnier, B. Giros, S. El Mestikawy, A third vesicular glutamate transporter expressed by cholinergic and serotoninergic neurons. *J. Neurosci.* (2002), doi:20026583.

58. J. Jackson, B. H. Bland, M. C. Antle, Nonserotonergic projection neurons in the midbrain raphe nuclei contain the vesicular glutamate transporter VGLUT3. *Synapse*. **63**, 31–41 (2009).

59. S. M. Azmitia, C, An Autoradiographic Analysis of the Differential Ascending Projections of the Dorsal and Median Raphe Nuclei in the Rat. *J Comp Neurol.* **3**, 641–667 (1978).

60. G. G. Kinney, B. Kocsis, R. P. Vertes, Medial septal unit firing characteristics following injections of 8-OH-DPAT into the median raphe nucleus. *Brain Res.* **708**, 116–122 (1996).

61. I. S. Wang DV, Yau HJ, Broker CJ, Tsou JH, Bonci A, D. V. Wang, H.-J. J. Yau, C. J. Broker, J.-H. H. Tsou, A. Bonci, S. Ikemoto, I. S. Wang DV, Yau HJ, Broker CJ, Tsou JH, Bonci A, Mesopontine median raphe regulates hippocampal ripple oscillation and memory consolidation. *Nat. Neurosci.* **18**, 728–735 (2015).

62. A. Cervera-Ferri, Y. Rahmani, S. Martínez-Bellver, V. Teruel-Martí, J. Martínez-Ricós, Glutamatergic projection from the nucleus incertus to the septohippocampal system. *Neurosci. Lett.* **517**, 71–76 (2012).

63. S. Ma, P. Bonaventure, T. Ferraro, P. J. Shen, T. C. D. Burazin, R. a D. Bathgate, C. Liu, G. W. Tregear, S. W. Sutton, a. L. Gundlach, Relaxin-3 in GABA projection neurons of nucleus incertus suggests widespread influence on forebrain circuits via G-protein-coupled receptor-135 in the rat. *Neuroscience*. **144**, 165–190 (2007).

64. F. E. Olucha-Bordonau, V. Teruel, J. Barcia-González, A. Ruiz-Torner, A. A. Valverde-Navarro, F. Martínez-Soriano,

Cytoarchitecture and efferent projections of the nucleus incertus of the rat. *J. Comp. Neurol.* **464**, 62–97 (2003).

65. T. Stefanelli, C. Bertollini, D. Muller, T. Stefanelli, C. Bertollini, C. Lu, Hippocampal Somatostatin Interneurons Control the Size of Neuronal Memory Ensembles Article Hippocampal Somatostatin Interneurons Control the Size of Neuronal Memory Ensembles, 1–12 (2016).

66. M. Goto, L. W. Swanson, N. S. Canteras, Connections of the nucleus incertus. *J. Comp. Neurol.* **438**, 86–122 (2001).

67. S. Ma, A. Blasiak, F. E. Olucha-Bordonau, A. J. M. Verberne, A. L. Gundlach, Heterogeneous responses of nucleus incertus neurons to corticotrophin-releasing factor and coherent activity with hippocampal theta rhythm in the rat. *J. Physiol.* **591**, 3981–4001 (2013).

68. S. Ma, F. E. Olucha-Bordonau, M. A. Hossain, F. Lin, C. Kuei, C. Liu, J. D. Wade, S. W. Sutton, A. Nuñez, A. L. Gundlach, Modulation of hippocampal theta oscillations and spatial memory by relaxin-3 neurons of the nucleus incertus. *Learn. Mem.* **16**, 730–742 (2009).

69. A. M. Sánchez-Pérez, I. Arnal-Vicente, F. N. Santos, C. W. Pereira, N. Elmlili, J. Sanjuan, S. Ma, A. L. Gundlach, F. E. Olucha-Bordonau, Septal projections to nucleus incertus in the rat: Bidirectional pathways for modulation of hippocampal function. *J. Comp. Neurol.* **523**, 565–588 (2015).

70. M. M. Mesulam, E. J. Mufson, B. H. Wainer, A. I. Levey, Central cholinergic pathways in the rat: An overview based on an alternative nomenclature (Ch1-Ch6). *Neuroscience*. **10**, 1185–1201 (1983).

71. F. Eckenstein, R. Baughman, J. Quinn, An anatomical study of cholinergic innervation in rat cerebral cortex. *Neuroscience*. **25**, 457–474 (1988).

72. D. B. Rye, B. H. Wainer, M. M. Mesulam, E. J. Mufson, C. B. Saper, Cortical projections arising from the basal forebrain: a study\rof cholinergic and noncholinergic components employing\rcombined retrograde tracing and immunohistochemical\rlocalization of choline acetyltransferase. *Neuroscience*. **13**, 627–643 (1984).

73. A. J. Yu, P. Dayan, Uncertainty, neuromodulation, and attention. *Neuron*. **46**, 681–692 (2005).

74. M. E. Hasselmo, J. M. Bower, Acetylcholine and memory. *Trends Neurosci.* **16** (1993), pp. 218–222.

75. D. D. Rasmusson, R. W. Dykes, Long-term enhancement of evoked potentials in cat somatosensory cortex produced by co-activation of the basal forebrain and cutaneous receptors. *Exp. Brain Res.* **70**, 276–286 (1988).

76. B. E. Jones, The organization of central cholinergic systems and their functional importance in sleep-waking states. *Prog Brain Res*. **98**, 61–71 (1993).

77. A. M. Tata, L. Velluto, C. D'Angelo, M. Reale, Cholinergic system dysfunction and neurodegenerative diseases: cause or effect? *CNS Neurol. Disord. - Drug Targets*. **13**, 1996–3181 (2014).

78. L. Descarries, V. Gisiger, M. Steriade, Diffuse transmission by acetylcholine in the CNS. *Prog. Neurobiol.* **53**, 603–625 (1997).

79. B. Lendvai, E. S. Vizi, Nonsynaptic Chemical Transmission Through Nicotinic Acetylcholine Receptors. *Physiol. Rev.* **88**, 333–349 (2008).

80. M. Sarter, V. Parikh, W. M. Howe, Phasic acetylcholine release and the volume transmission hypothesis: time to move on. *Nat. Rev. Neurosci.* **10**, 383–390 (2009).

81. S. Arroyo, C. Bennett, S. Hestrin, Nicotinic modulation of cortical circuits. *Front. Neural Circuits*. **8**, 1–6 (2014).

82. M. Zoli, A. Jansson, E. Syková, L. F. Agnati, K. Fuxe, Volume transmission in the CNS and its relevance for neuropsychopharmacology. *Trends Pharmacol. Sci.* **20**, 142–150 (1999).

83. L. M. Teles-Grilo Ruivo, J. R. Mellor, Cholinergic modulation of hippocampal network function. *Front. Synaptic Neurosci.* **5**, 1–15 (2013).

84. D. Umbriaco, K. C. Watkins, L. Descarries, C. Cozzari, B. K. Hartman, Ultrastructural and Morphometric Features of the Acetylcholine Innervation in Adult-Rat Parietal Cortex - An Electron-Microscopic Study in Serial Sections. *J. Comp. Neurol.* **348**, 351–373 (1994).

85. D. Umbriaco, S. Garcia, C. Beaulieu, L. Descarries, Relational features of acetylcholine, noradrenaline, serotonin and GABA axon terminals in the Stratum radiatum of adult rat hippocampus (CA1). *Hippocampus*. **5**, 605–620 (1995).

86. B. Hangya, S. P. Ranade, M. Lorenc, A. Kepecs, Central Cholinergic Neurons Are Rapidly Recruited by Reinforcement Feedback. *Cell*. **162**, 1155–1168 (2015).

87. W. Muñoz, B. Rudy, Spatiotemporal specificity in cholinergic control of neocortical function. *Curr. Opin. Neurobiol.* **26**, 149–160 (2014).

88. L. M. Teles-Grilo Ruivo, K. L. Baker, M. W. Conway, P. J. Kinsley, G. Gilmour, K. G. Phillips, J. T. R. Isaac, J. P. Lowry, J. R. Mellor, Coordinated Acetylcholine Release in Prefrontal Cortex and Hippocampus Is Associated with Arousal and Reward on Distinct Timescales. *Cell Rep.* **18**, 905–917 (2017).

89. Z. Gu, J. L. Yakel, Timing-Dependent Septal Cholinergic Induction of Dynamic Hippocampal Synaptic Plasticity. *Neuron*. **71**, 155–165 (2011).

90. M. E. Hasselmo, J. McGaughy, High acetylcholine levels set circuit dynamics for attention and encoding and low acetylcholine levels set dynamics for consolidation. *Prog. Brain Res.* **145**, 207–231 (2004).

91. S. Lee, Y. Dan, Review Neuromodulation of Brain States. *Neuron*. **76**, 209–222 (2012).

92. M. Vandecasteele, V. Varga, A. Berényi, E. Papp, P. Barthó, L. Venance, T. F. Freund, G. Buzsáki, Optogenetic activation of septal cholinergic neurons suppresses sharp wave ripples and enhances theta oscillations in the hippocampus. *Proc. Natl. Acad. Sci.* **111**, 13535–13540 (2014).

93. V. T. Takács, T. F. Freund, G. Nyiri, Neuroligin 2 Is Expressed in Synapses Established by Cholinergic Cells in the Mouse Brain. *PLoS One*. **8** (2013).

94. E. R. Graf, X. Zhang, S. X. Jin, M. W. Linhoff, A. M. Craig, Neurexins induce differentiation of GABA and glutamate postsynaptic specializations via neuroligins. *Cell*. **119**, 1013–1026 (2004).

95. F. Varoqueaux, S. Jamain, N. Brose, Neuroligin 2 is exclusively localized to inhibitory synapses. *Eur. J. Cell Biol.* **83**, 449–456 (2004).

96. M. Hoon, G. Bauer, J. M. Fritschy, T. Moser, B. H. Falkenburger, F. Varoqueaux, Neuroligin 2 controls the maturation of GABAergic synapses and information processing in the retina. *J. Neurosci.* **29**, 8039–8050 (2009).

97. R. M. Hines, L. Wu, D. J. Hines, H. Steenland, S. Mansour, R. Dahlhaus, R. R. Singaraja, X. Cao, E. Sammler, S. G. Hormuzdi, M. Zhuo, A. El-Husseini, Synaptic imbalance, stereotypies, and impaired social interactions in mice with altered neuroligin 2 expression. *J. Neurosci.* **28**, 6055–6067 (2008).

98. J. Blundell, K. Tabuchi, M. F. Bolliger, C. A. Blaiss, N. Brose, X. Liu,

T. C. Südhof, C. M. Powell, Increased anxiety-like behavior in mice lacking the inhibitory synapse cell adhesion molecule neuroligin 2. *Genes, Brain Behav.* **8**, 114–126 (2009).

99. V. T. V. T. Takács, C. Cserép, D. Schlingloff, B. Pósfai, A. Szőnyi, K. E. K. E. Sos, Z. Környei, Á. Dénes, A. I. A. I. Gulyás, T. F. T. F. Freund, G. Nyiri, Co-transmission of acetylcholine and GABA regulates hippocampal states. *Nat. Commun.* **9**, 2848 (2018).

100. L. A. Bell, K. A. Bell, A. R. McQuiston, Acetylcholine release in mouse hippocampal CA1 preferentially activates inhibitory-selective interneurons via α4β2* nicotinic receptor activation. *Front. Cell. Neurosci.* **9**, 1–10 (2015).

101. N. A. Courtney, C. P. Ford, The Timing of Dopamine- and Noradrenaline-Mediated Transmission Reflects Underlying Differences in the Extent of Spillover and Pooling. *J. Neurosci.* **34**, 7645–7656 (2014).

102. S. Karunanithi, L. Marin, K. Wong, H. L. Atwood, Quantal Size and Variation Determined by Vesicle Size in Normal and Mutant Drosophila Glutamatergic Synapses. *J. Neurosci.* **22**, 10267–10276 (2002).

103. S. T. Rouse, S. M. Edmunds, H. Yi, M. L. Gilmor, A. I. Levey, Localization of M(2) muscarinic acetylcholine receptor protein in cholinergic and non-cholinergic terminals in rat hippocampus. *Neurosci Lett*. **284**, 182–186 (2000).

104. G. Nyíri, E. Szabadits, C. Cserép, K. Mackie, R. Shigemoto, T. F. Freund, GABAB and CB1 cannabinoid receptor expression identifies two types of septal cholinergic neurons. *Eur. J. Neurosci.* **21**, 3034–3042 (2005).

105. A. Scheuber, Presynaptic Cav2.1 and Cav2.2 Differentially Influence Release Dynamics at Hippocampal Excitatory Synapses. *J. Neurosci.* **24**, 10402–10409 (2004).

106. S. Lee, K. Kim, Z. J. Zhou, Role of ACh-GABA Cotransmission in Detecting Image Motion and Motion Direction. *Neuron*. **68**, 1159–1172 (2010).

107. S. F. Traynelis, R. Dingledine, Potassium-induced spontaneous electrographic seizures in the rat hippocampal slice. *J.Neurophysiol.* **59**, 259–276 (1988).

108. M. R. Karlócai, Z. Kohus, S. Káli, I. I. Ulbert, G. Szabó, Z. Máté, T. F. T. F. Freund, A. I. Gulyás, M. R. Karlocai, Z. Kohus, S. Kali, I. I. Ulbert, G. Szabo, Z. Mate, T. F. T. F. Freund, A. I. Gulyas, Physiological sharp wave-ripples and interictal events in vitro: what's the difference? *Brain*. **137**, 463–485 (2014).

109. L. F. Agnati, G. Leo, A. Zanardi, S. Genedani, A. Rivera, K. Fuxe, D. Guidolin, Volume transmission and wiring transmission from cellular to molecular networks: History and perspectives. *Acta Physiol.* **187**, 329–344 (2006).

110. F. Marrosu, C. Portas, M. S. Mascia, M. A. Casu, M. Fà, M. Giagheddu, A. Imperato, G. L. Gessa, Microdialysis measurement of cortical and hippocampal acetylcholine release during sleep-wake cycle in freely moving cats. *Brain Res.* **671**, 329–332 (1995).

111. S. Gais, J. Born, Low acetylcholine during slow-wave sleep is critical for declarative memory consolidation. *Proc. Natl. Acad. Sci.* **101**, 2140–2144 (2004).

112. G. Girardeau, K. Benchenane, S. I. Wiener, G. Buzsáki, M. B. Zugaro, Selective suppression of hippocampal ripples impairs spatial memory. *Nat. Neurosci.* **12**, 1222–1223 (2009).

113. G. Buzsáki, Hippocampal sharp wave-ripple: A cognitive biomarker for episodic memory and planning. *Hippocampus*. **25**, 1073–1188 (2015).

114. D. Schlingloff, S. Kali, T. F. Freund, N. Hajos, A. I. Gulyas, Mechanisms of Sharp Wave Initiation and Ripple Generation. *J. Neurosci.* **34**, 11385–11398 (2014).

115. J. C. Amatniek, W. a Hauser, C. DelCastillo-Castaneda, D. M. Jacobs, K. Marder, K. Bell, M. Albert, J. Brandt, Y. Stern, Incidence and predictors of seizures in patients with Alzheimer's disease. *Epilepsia*. **47**, 867–872 (2006).

116. G. Buzsáki, G. L. Ponomareff, F. Bayardo, R. Ruiz, F. H. Gage, Neuronal activity in the subcortically denervated hippocampus: A chronic model for epilepsy. *Neuroscience*. **28**, 527–538 (1989).

117. D. C. Silveira, G. L. Holmes, S. C. Schachter, C. Geula, D. L. Schomer, Increased susceptibility to generalized seizures after immunolesions of the basal forebrain cholinergic neurons in rats. *Brain Res.* **878**, 223–7 (2000).

118. I. Ferencz, G. Leanza, A. Nanobashvili, Z. Kokaia, M. Kokaia, O. Lindvall, Septal cholinergic neurons suppress seizure development in hippocampal kindling in rats: Comparison with noradrenergic neurons. *Neuroscience*. **102**, 819–832 (2001).

119. H. Zhang, S.-C. Lin, M. A. L. Nicolelis, A distinctive subpopulation of medial septal slow-firing neurons promote hippocampal activation and theta oscillations. *J. Neurophysiol.* **106**, 2749–2763 (2011).

120. A. Crespel, M. Baldy-Moulinier, P. Coubes, The relationship between sleep and epilepsy in frontal and temporal lobe epilepsies: Practical and physiopathologic considerations. *Epilepsia*. **39**, 150–157 (1998).

121. D. Minecan, A. Natarajan, M. Marzec, B. Malow, Relationship of epileptic seizures to sleep stage and sleep depth. *Sleep*. **25**, 899–904 (2002).

122. L. Turski, C. Ikonomidou, W. A. Turski, Z. A. Bortolotto, E. A. Cavalheiro, Review: Cholinergic mechanisms and epileptogenesis. The seizures induced by pilocarpine: A novel experimental model of intractable epilepsy. *Synapse*. **3**, 154–171 (1989).

123. E. S. Bromberg-Martin, M. Matsumoto, H. Nakahara, O. Hikosaka, Multiple Timescales of Memory in Lateral Habenula and Dopamine Neurons. *Neuron*. **67**, 499–510 (2010).

124. E. S. Bromberg-Martin, O. Hikosaka, Lateral habenula neurons signal errors in the prediction of reward information. *Nat. Neurosci.* **14**, 1209–1218 (2011).

125. E. S. Bromberg-Martin, M. Matsumoto, O. Hikosaka, Distinct tonic and phasic anticipatory activity in lateral habenula and dopamine neurons. *Neuron*. **67**, 144–155 (2010).

126. C. A. Orsini, D. E. Moorman, J. W. Young, B. Setlow, S. B. Floresco, Neural mechanisms regulating different forms of risk-related decision-making: Insights from animal models. *Neurosci. Biobehav. Rev.* **58**, 147–167 (2015).

127. C. M. Stopper, S. B. Floresco, What's better for me? Fundamental role for lateral habenula in promoting subjective decision biases. *Nat. Neurosci.* **17**, 33–35 (2014).

128. C. M. Stopper, M. T. L. Tse, D. R. Montes, C. R. Wiedman, S. B. Floresco, Overriding phasic dopamine signals redirects action selection during risk/reward decision making. *Neuron*. **84**, 177–189 (2014).

129. P. M. Baker, S. E. Oh, K. S. Kidder, S. J. Y. Mizumori, Ongoing behavioral state information signaled in the lateral habenula guides choice flexibility in freely moving rats. *Front. Behav. Neurosci.* **9**, 295 (2015).

130. R. Goutagny, M. Loureiro, J. Jackson, J. Chaumont, S. Williams, P. Isope, C. Kelche, J. C. Cassel, L. Lecourtier, Interactions between the lateral habenula and the Hippocampus: Implication for spatial memory processes.

Neuropsychopharmacology. **38**, 2418–2426 (2013).

131. R. Crooks, J. Jackson, B. H. Bland, Dissociable pathways facilitate theta and non-theta states in the median raphe-Septohippocampal circuit. *Hippocampus*. **22**, 1567–1576 (2012).

132. A. Domonkos, L. Nikitidou Ledri, T. Laszlovszky, C. Cserép, Z. Borhegyi, E. Papp, G. Nyiri, T. F. Freund, V. Varga, Divergent in vivo activity of non-serotonergic and serotonergic VGluT3–neurones in the median raphe region. *J. Physiol.* **594**, 3775–3790 (2016).

133. J. Jackson, C. T. Dickson, B. H. Bland, Median Raphe Stimulation Disrupts Hippocampal Theta Via Rapid Inhibition and State-Dependent Phase Reset of Theta-Related Neural Circuitry. *J. Neurophysiol.* **99**, 3009–3026 (2008).

134. G. V. Di Prisco, Z. Albo, R. P. Vertes, B. Kocsis, Discharge properties of neurons of the median raphe nucleus during hippocampal theta rhythm in the rat. *Exp. Brain Res.* **145**, 383–394 (2002).

135. H. Aizawa, S. Yanagihara, M. Kobayashi, K. Niisato, T. Takekawa, R. Harukuni, T. J. McHugh, T. Fukai, Y. Isomura, H. Okamoto, The Synchronous Activity of Lateral Habenular Neurons Is Essential for Regulating Hippocampal Theta Oscillation. *J. Neurosci.* **33**, 8909–8921 (2013).

136. T. G. C. S. Andrade, H. Zangrossi, F. G. Graeff, The median raphe nucleus in anxiety revisited. *J. Psychopharmacol.* **27**, 1107–1115 (2013).

137. D. G. D. G. Balázsfi, D. Zelena, L. Farkas, K. Demeter, I. Barna, C. Cserép, V. T. V. T. Takács, G. Nyíri, F. Gölöncsér, B. Sperlágh, T. F. T. F. Freund, J. Haller, Median raphe region stimulation alone generates remote, but not recent fear memory traces. *PLoS One*. **12**, e0181264 (2017).

138. T. F. Freund, A. I. Gulyás, L. Acsády, T. Görcs, K. Tóth, A. I. Gulyas, L. Acsady, T. Gorcs, K. Toth, Serotonergic control of the hippocampus via local inhibitory interneurons. *Proc. Natl. Acad. Sci.* **87**, 8501–8505 (1990).

139. S. J. Bang, P. Jensen, S. M. Dymecki, K. G. Commons, Projections and interconnections of genetically defined serotonin neurons in mice. *Eur. J. Neurosci.* **35**, 85–96 (2012).

140. C. Leranth, R. P. Vertes, Median raphe serotonergic innervation of medial septum/diagonal band of broca (MSDB) parvalbumin-containing neurons: possible involvement of the MSDB in the desynchronization of the hippocampal EEG. *J. Comp. Neurol.* **410**, 586–98 (1999).

141. K. E. K. E. Sos, M. I. M. I. Mayer, C. Cserép, F. S. F. S. Takács, A. Szőnyi, T. F. T. F. Freund, G. Nyiri, Cellular architecture and transmitter phenotypes of neurons of the mouse median raphe region. *Brain Struct. Funct.* **222**, 287–299 (2017).

142. A. Szo, K. Zichó, A. M. Barth, R. T. Gönczi, D. Schlingloff, B. Török, E. Sipos, A. Major, Z. Bardóczi, K. E. Sos, A. I. Gulyás, V. Varga, D. Zelena, T. F. Freund, G. Nyiri, Median raphe controls acquisition of negative experience in the mouse. *Science (80-.).* **366** (2019), doi:10.1126/science.aay8746.

143. S. Lammel, B. K. Lim, C. Ran, K. W. Huang, M. J. Betley, K. M. Tye, K. Deisseroth, R. C. Malenka, Input-specific control of reward and aversion in the ventral tegmental area. *Nature*. **491**, 212–217 (2012).

144. S. Lammel, B. K. Lim, R. C. Malenka, Reward and aversion in a heterogeneous midbrain dopamine system. *Neuropharmacology*. **76 Pt B**, 351–9 (2014).

145. L. A. Quina, L. Tempest, L. Ng, J. A. Harris, S. Ferguson, T. C. Jhou, E. E. Turner, Efferent pathways of the mouse lateral habenula. *J. Comp. Neurol.* **523**, 32–60 (2015).

146. A. Szőnyi, K. E. Sos, R. Nyilas, D. Schlingloff, A. Domonkos, V. T. Takács, B. Pósfai, P. Hegedüs, J. B. Priestley, A. L. Gundlach, A. I. Gulyás, V. Varga, A. Losonczy, T. F. Freund, G. Nyiri, Brainstem nucleus incertus controls contextual memory formation. *Science*. **364** (2019), doi:10.1126/science.aaw0445.

147. I. R. Wickersham, D. C. Lyon, R. J. O. Barnard, T. Mori, S. Finke, K.-K. Conzelmann, J. A. T. Young, E. M. Callaway, Monosynaptic restriction of transsynaptic tracing from single, genetically targeted neurons. *Neuron*. **53**, 639–47 (2007).

148. Y. Cui, Y. Yang, Z. Ni, Y. Dong, G. Cai, A. Foncelle, S. Ma, K. Sang, S. Tang, Y. Li, Y. Shen, H. Berry, S. Wu, H. Hu, Astroglial Kir4.1 in the lateral habenula drives neuronal bursts in depression. *Nature*. **554**, 323–327 (2018).

149. K. Li, T. Zhou, L. Liao, Z. Yang, C. Wong, F. Henn, R. Malinow, J. R. Yates, H. Hu, βCaMKII in lateral habenula mediates core symptoms of depression. *Science (80-.).* **341**, 1016–1020 (2013).

150. Y. Yang, Y. Cui, K. Sang, Y. Dong, Z. Ni, S. Ma, H. Hu, Ketamine blocks bursting in the lateral habenula to rapidly relieve depression. *Nature*. **554**, 317–322 (2018).

151. S. A. Golden, M. Heshmati, M. Flanigan, D. J. Christoffel, K. Guise, M. L. Pfau, H. Aleyasin, C. Menard, H. Zhang, G. E. Hodes, D. Bregman, L. Khibnik, J. Tai, N. Rebusi, B. Krawitz, D. Chaudhury, J. J. Walsh, M. H. Han, M. L. Shapiro, S. J. Russo, Basal forebrain projections to the lateral habenula modulate aggression reward. *Nature*. **534**, 688–692 (2016).

152. L. A. Martin, H. W. Neighbors, D. M. Griffith, The experience of symptoms of depression in men vs women: Analysis of the national comorbidity survey replication. *JAMA Psychiatry*. **70**, 1100–1106 (2013).

153. N. Verdolini, G. Perugi, L. Samalin, A. Murru, J. Angst, J. M. Azorin, C. L. Bowden, S. Mosolov, A. H. Young, M. Barbuti, G. Guiso, D. Popovic, E. Vieta, I. Pacchiarotti, Aggressiveness in depression: a neglected symptom possibly associated with bipolarity and mixed features. *Acta Psychiatr. Scand.* **136**, 362–372 (2017).

154. C. R. Yang, Y. Y. Bai, C. S. Ruan, H. F. Zhou, D. Liu, X. F. Wang, L. J. Shen, H. Y. Zheng, X. F. Zhou, Enhanced Aggressive Behaviour in a Mouse Model of Depression. *Neurotox. Res.* **27**, 129–142 (2014).

155. B. Li, J. Piriz, M. Mirrione, C. Chung, C. D. Proulx, D. Schulz, F. Henn, R. Malinow, Synaptic potentiation onto habenula neurons in the learned helplessness model of depression. *Nature*. **470**, 535–9 (2011).

156. G. Buzsáki, E. I. Moser, Memory, navigation and theta rhythm in the hippocampal-entorhinal system. *Nat. Neurosci.* **16**, 130–138 (2013).

157. B. Hangya, Z. Borhegyi, N. Szilagyi, T. F. Freund, V. Varga, GABAergic Neurons of the Medial Septum Lead the Hippocampal Network during Theta Activity. *J. Neurosci.* **29**, 8094–8102 (2009).

158. Z. Borhegyi, V. Varga, N. Szilágyi, D. Fabo, T. F. Freund, Phase segregation of medial septal GABAergic neurons during hippocampal theta activity. *J. Neurosci.* **24**, 8470–9 (2004).

159. D. J. Barker, J. Miranda-Barrientos, S. Zhang, D. H. Root, H. L. Wang, B. Liu, E. S. Calipari, M. Morales, Lateral Preoptic Control of the Lateral Habenula through Convergent Glutamate and GABA Transmission. *Cell Rep.* **21**, 1757–1769 (2017).

160. M. Stephenson-Jones, K. Yu, S. Ahrens, J. M. Tucciarone, A. N. Van Huijstee, L. A. Mejia, M. A. Penzo, L. H. Tai, L. Wilbrecht, B. Li, A basal ganglia circuit for evaluating action outcomes. *Nature*. **539**, 289–293 (2016).

161. J. W. de Jong, S. A. Afjei, I. Pollak Dorocic, J. R. Peck, C. Liu, C. K. Kim, L. Tian, K. Deisseroth, S. Lammel, A Neural Circuit Mechanism for Encoding Aversive Stimuli in the Mesolimbic Dopamine System. *Neuron*. **101**, 133-151.e7 (2019).

162. K. Brinschwitz, A. Dittgen, V. I. Madai, R. Lommel, S. Geisler, R. W. Veh, Glutamatergic axons from the lateral habenula mainly terminate on GABAergic neurons of the ventral midbrain. *Neuroscience*. **168**, 463–476 (2010).

163. T. C. Jhou, S. Geisler, M. Marinelli, B. A. Degarmo, D. S. Zahm, The mesopontine rostromedial tegmental nucleus: A structure targeted by the lateral habenula that projects to the ventral tegmental area of Tsai and substantia nigra compacta. *J. Comp. Neurol.* **513**, 566–596 (2009).

164. S. Hong, T. C. Jhou, M. Smith, K. S. Saleem, O. Hikosaka, Negative Reward Signals from the Lateral Habenula to Dopamine Neurons Are Mediated by Rostromedial Tegmental Nucleus in Primates. *J. Neurosci.* **31**, 11457–11471 (2011).

165. A. M. Stamatakis, G. D. Stuber, Activation of lateral habenula inputs to the ventral midbrain promotes behavioral avoidance. *Nat. Neurosci.* **15**, 1105–1107 (2012).

166. J. Tian, N. Uchida, Habenula Lesions Reveal that Multiple Mechanisms Underlie Dopamine Prediction Errors. *Neuron*. **87**, 1304–1316 (2015).

167. M. Matsumoto, O. Hikosaka, Lateral habenula as a source of negative reward signals in dopamine neurons. *Nature*. **447**, 1111–1115 (2007).

168. H. Li, D. Pullmann, T. C. Jhou, Valence-encoding in the lateral habenula arises from the entopeduncular region. *Elife*. **8**, 1–17 (2019).

169. F. J. Meye, K. Valentinova, S. Lecca, L. Marion-Poll, M. J. Maroteaux, S. Musardo, I. Moutkine, F. Gardoni, R. L. Huganir, F. Georges, M. Mameli, Cocaine-evoked negative symptoms require AMPA receptor trafficking in the lateral habenula. *Nat. Neurosci.* **18**, 376–380 (2015).

170. C. D. Proulx, O. Hikosaka, R. Malinow, Reward processing by the lateral habenula in normal and depressive behaviors. *Nat. Neurosci.* **17**, 1146–52 (2014).

171. M. Trusel, A. Nuno-Perez, S. Lecca, H. Harada, A. L. Lalive, M. Congiu, K. Takemoto, T. Takahashi, F. Ferraguti, M. Mameli, Punishment-Predictive Cues Guide Avoidance through Potentiation of Hypothalamus-to-Habenula Synapses. *Neuron*. **102**, 120-127.e4 (2019).

172. D. Wang, Y. Li, Q. Feng, Q. Guo, J. Zhou, M. Luo, Learning shapes the aversion and reward responses of lateral habenula neurons. *Elife*. **6**, 1–20 (2017).

173. D. H. Root, C. A. Mejias-Aponte, J. Qi, M. Morales, Role of glutamatergic projections from ventral tegmental area to lateral habenula in aversive conditioning. *J. Neurosci.* **34**, 13906–10 (2014).

174. D. S. Zahm, D. H. Root, Review of the cytology and connections of the lateral habenula, an avatar of adaptive behaving. *Pharmacol. Biochem. Behav.* **162**, 3–21 (2017).

175. U. Kim, Topographic commissural and descending projections of the habenula in the rat. *J. Comp. Neurol.* **513**, 173–187 (2009).

176. J. Tooley, L. Marconi, J. B. Alipio, B. Matikainen-Ankney, P. Georgiou, A. V. Kravitz, M. C. Creed, Glutamatergic Ventral Pallidal Neurons Modulate Activity of the Habenula–Tegmental Circuitry and Constrain Reward Seeking. *Biol. Psychiatry* (2018), doi:10.1016/j.biopsych.2018.01.003.

177. A. M. Stamatakis, M. Van Swieten, M. L. Basiri, G. A. Blair, P. Kantak, G. D. Stuber, Lateral Hypothalamic Area Glutamatergic Neurons and Their Projections to the Lateral Habenula Regulate Feeding and Reward. *J. Neurosci.* (2016), doi:10.1523/jneurosci.1202-15.2016.

178. J. Kaufling, Alterations and adaptation of ventral tegmental area dopaminergic neurons in animal models of depression. *Cell Tissue Res.* (2019), , doi:10.1007/s00441-019-03007-9.

179. S. F. Maier, M. E. P. P. Seligman, Learned Helplessness at Fifty: Insights from Neuroscience. **123**, 349–67 (2016).

180. I. Lazaridis, O. Tzortzi, M. Weglage, A. Märtin, Y. Xuan, M. Parent, Y. Johansson, J. Fuzik, D. Fürth, L. E. Fenno, C. Ramakrishnan, G. Silberberg, K. Deisseroth, M. Carlén, K. Meletis, A hypothalamus-habenula circuit controls aversion. *Mol. Psychiatry* (2019), doi:10.1038/s41380-019-0369-5.

181. D. Knowland, V. Lilascharoen, C. P. Pacia, S. Shin, E. H.-J. Wang, B. K. Lim, Distinct Ventral Pallidal Neural Populations Mediate Separate Symptoms of Depression. *Cell* (2017), doi:10.1016/j.cell.2017.06.015.

182. A. Friedman, E. Lax, Y. Dikshtein, L. Abraham, Y. Flaumenhaft, E. Sudai, M. Ben-Tzion, G. Yadid, Electrical stimulation of the lateral habenula produces an inhibitory effect on sucrose self-administration. *Neuropharmacology* (2011), doi:10.1016/j.neuropharm.2010.10.006.

183. G. Gangadharan, J. Shin, S.-W. Kim, A. Kim, A. Paydar, D. D.-S. Kim, T. Miyazaki, M. Watanabe, Y. Yanagawa, J. Kim, Y.-S. Kim, D. D.-S. Kim, H.-S. Shin, Medial septal GABAergic projection neurons promote object exploration behavior and type 2 theta rhythm. *Proc. Natl. Acad. Sci.* **113**, 6550–6555 (2016).

184. S. Aznar, Z. X. Qian, G. M. Knudsen, Non-serotonergic dorsal and median raphe projection onto parvalbumin- and calbindin-containing neurons in hippocampus and septum. *Neuroscience* (2004), doi:10.1016/j.neuroscience.2003.12.020.

185. H. B. Eichenbaum, The hippocampus and declarative memory: cognitive mechanisms and neural codes. *Behav. Brain Res.* **127**, 199–207 (2001).

186. Andersen P., *The Hippocampus Book* (Oxford University Press, 2007).

187. J. Haam, J. Zhou, G. Cui, J. L. Yakel, Septal cholinergic neurons gate hippocampal output to entorhinal cortex via oriens lacunosum moleculare interneurons. *Proc. Natl. Acad. Sci.* **115**, 1886–1895 (2018).

188. T. Kitamura, C. Sun, J. Martin, L. J. Kitch, M. J. Schnitzer, S. Tonegawa, Entorhinal cortical ocean cells encode specific contexts and drive context-specific fear memory. *Neuron*. **87**, 1317–1331 (2015).

189. J. E. Lisman, Relating hippocampal circuitry to function: Recall of memory sequences by reciprocal dentate-CA3 interactions. *Neuron*. **22**, 233–242 (1999).

190. J. Suh, A. J. Rivest, T. Nakashiba, T. Tominaga, S. Tonegawa, Entorhinal cortex layer III input to the hippocampus is crucial for temporal association memory. *Science (80-.).* **1415**, 1415–1421 (2013).

191. T. Kitamura, M. Pignatelli, J. Suh, K. Kohara, A. Yoshiki, K. Abe, S. Tonegawa, Island cells control temporal association memory. *Science (80-.).* **343**, 896–901 (2014).

192. K. C. Bittner, C. Grienberger, S. P. Vaidya, A. D. Milstein, J. J. Macklin, J. Suh, S. Tonegawa, J. C. Magee, Conjunctive input processing drives feature selectivity in hippocampal CA1 neurons. *Nat. Neurosci.* **18**, 1133–1142 (2015).

193. K. C. Bittner, A. D. Milstein, C. Grienberger, S. Romani, J.

C. Magee, Behavioral time scale synaptic plasticity underlies CA1 place fields. *Science (80-.).* **357**, 1033–1036 (2017).

194. J. T. Dudman, D. Tsay, S. A. Siegelbaum, A role for synaptic inputs at distal dendrites: instructive signals for hippocampal long-term plasticity. *Neuron*. **56**, 866–879 (2007).

195. D. S. Roy, T. Kitamura, T. Okuyama, S. K. Ogawa, C. Sun, Y. Obata, A. Yoshiki, S. Tonegawa, Distinct neural circuits for the formation and retrieval of episodic memories. *Cell*. **170**, 1000-1012.e19 (2017).

196. S. Maren, M. S. Fanselow, Electrolytic lesions of the fimbria/fornix, dorsal hippocampus, or entorhinal cortex produce anterograde deficits in contextual fear conditioning in rats. *Neurobiol. Learn. Mem.* **67**, 142–149 (1997).

197. R. P. Kesner, Behavioral functions of the CA3 subregion of the hippocampus. *Learn. Mem.* **14**, 771–781 (2007).

198. S. Maren, K. L. Phan, I. Liberzon, The contextual brain: Implications for fear conditioning, extinction and psychopathology. *Nat. Rev. Neurosci.* **14**, 417–428 (2013).

199. K. Z. Tanaka, H. He, A. Tomar, K. Niisato, A. J. Y. Huang, T. J. McHugh, The hippocampal engram maps experience but not place. *Science (80-.).* **361**, 392–397 (2018).

200. M. Lovett-Barron, P. Kaifosh, M. A. Kheirbek, N. Danielson, J. D. Zaremba, T. R. Reardon, G. F. Turi, R. Hen, B. V. Zemelman, A. Losonczy, Dendritic inhibition in the hippocampus supports fear learning. *Science (80-.).* **1**, 857–864 (2014).

201. S. Siwani, A. S. C. França, S. Mikulovic, A. Reis, M. M. Hilscher, S. J. Edwards, R. N. Leão, A. B. L. Tort, K. Kullander, OLMα2 Cells Bidirectionally Modulate Learning. *Neuron*. **99**, 404–412 (2018).

202. S. Royer, B. V. Zemelman, A. Losonczy, J. Kim, F. Chance, J. C. Magee, G. Buzsáki, Control of timing, rate and bursts of hippocampal place cells by dendritic and somatic inhibition. *Nat. Neurosci.* **15**, 769–775 (2012).

203. S. Nakauchi, R. J. Brennan, J. Boulter, K. Sumikawa, Nicotine gates long-term potentiation in the hippocampal CA1 region via the activation of α2* nicotinic ACh receptors. *Eur. J. Neurosci.* **25**, 2666–2681 (2007).

204. Y. Jia, Y. Yamazaki, S. Nakauchi, K. Sumikawa, α2 Nicotine receptors function as a molecular switch to continuously excite a subset of interneurons in rat hippocampal circuits. *Eur. J. Neurosci.* **29**, 1588–1603 (2009).

205. R. N. Leão, S. Mikulovic, K. E. Leão, H. Munguba, H. Gezelius, A. Enjin, K. Patra, A. Eriksson, L. M. Loew, A. B. L. Tort, K. Kullander, OLM interneurons differentially modulate CA3 and entorhinal inputs to hippocampal CA1 neurons. *Nat. Neurosci.* **15**, 1524–1530 (2012).

206. D. Justus, D. Dalügge, S. Bothe, F. Fuhrmann, C. Hannes, H. Kaneko, D. Friedrichs, L. Sosulina, I. Schwarz, D. Anthony Elliott, S. Schoch, F. Bradke, M. Karl Schwarz, S. Remy, Glutamatergic synaptic integration of locomotion speed via septoentorhinal projections. *Nat. Publ. Gr.* (2016),

207. I. Misane, A. Kruis, A. W. Pieneman, S. O. Ögren, O. Stiedl, GABA-A receptor activation in the CA1 area of the dorsal hippocampus impairs consolidation of conditioned contextual fear in C57BL/6J mice. *Behav. Brain Res.* **238**, 160–169 (2013).

208. T. F. Freund, G. Buzsáki, Interneurons of the hippocampus. *Hippocampus*. **6**, 347–470 (1996).

209. Y. Yanovsky, O. A. Sergeeva, T. F. Freund, H. L. Haas, Activation of interneurons at the stratum oriens/alveus border suppresses excitatory transmission to apical dendrites in the CA1 area of the mouse hippocampus. *Neuroscience*. **77**, 87–96 (1997).

210. C. M. Smith, P. J. Shen, A. Banerjee, P. Bonaventure, S. Ma, R. a D. Bathgate, S. W. Sutton, A. L. Gundlach, Distribution of relaxin-3 and RXFP3 within arousal, stress, affective, and cognitive circuits of mouse brain. *J. Comp. Neurol.* **518**, 4016–4045 (2010).

211. M. Haidar, G. Guèvremont, C. Zhang, R. A. D. Bathgate, E. Timofeeva, C. M. Smith, A. L. Gundlach, Relaxin-3 inputs target hippocampal interneurons and deletion of hilar relaxin-3 receptors in floxed-RXFP3 mice impairs spatial memory. *Hippocampus*. **27**, 529–546 (2017).

212. P. Kaifosh, M. Lovett-Barron, G. F. Turi, T. R. Reardon, A. Losonczy, Septo-hippocampal GABAergic signaling across multiple modalities in awake mice. *Nat. Neurosci.* **16**, 1182–4 (2013).

213. R. W. Stackman, S. J. Cohen, J. C. Lora, L. M. Rios, Temporary inactivation reveals that the CA1 region of the mouse dorsal hippocampus plays an equivalent role in the retrieval of long-term object memory and spatial memory. *Neurobiol. Learn. Mem.* **133**, 118–128 (2016).

214. R. Boyce, S. D. Glasgow, S. Williams, A. Adamantidis, Causal evidence for the role of REM sleep theta rhythm in contextual memory consolidation. *Science (80-.).* **352**, 812 (2016).

215. J. Basu, J. D. Zaremba, S. K. Cheung, F. L. Hitti, B. V. Zemelman, A. Losonczy, S. A. Siegelbaum, Gating of hippocampal activity, plasticity, and memory by entorhinal cortex long-range inhibition. *Science (80-.).* **351** (2016),

216. D. C. Drieskens, L. R. Neves, K. C. Pugliane, I. B. M. B. de Souza, Á. da C. Lima, M. G. da S. S. Salvadori, A. M. Ribeiro, R. H. Silva, F. F. Barbosa, CA1 inactivation impairs episodic-like memory in rats. *Neurobiol. Learn. Mem.* **145**, 28–33 (2017).

217. C. W. Pereira, F. N. Santos, A. M. Sánchez-Pérez, M. Otero-García, M. Marchioro, S. Ma, A. L. Gundlach, F. E. Olucha-Bordonau, Electrolytic lesion of the nucleus incertus retards extinction of auditory conditioned fear. *Behav. Brain Res.* **247**, 201–210 (2013).

218. L. C. Lee, R. Rajkumar, G. S. Dawe, Selective lesioning of nucleus incertus with corticotropin releasing factor-saporin conjugate. *Brain Res.* **1543**, 179–190 (2014).

219. M. Tanaka, N. Iijima, Y. Miyamoto, S. Fukusumi, Y. Itoh, H. Ozawa, Y. Ibata, Neurons expressing relaxin 3/INSL 7 in the nucleus incertus respond to stress. *Eur. J. Neurosci.* **21**, 1659–1670 (2005).

220. S. Ma, G. Allocca, E. K. E. Ong-Pålsson, C. E. Singleton, D. Hawkes, S. J. McDougall, S. J. Williams, R. A. D. Bathgate, A. L. Gundlach, Nucleus incertus promotes cortical desynchronization and behavioral arousal. *Brain Struct. Funct.* **222**, 515–537 (2017).

221. F. Darcet, I. Mendez-David, L. Tritschler, A. M. Gardier, J.-P. Guilloux, D. J. David, Learning and memory impairments in a neuroendocrine mouse model of anxiety/depression. *Front. Behav. Neurosci.* **8**, 1–13 (2014).

222. A. Eskildsen, L. P. Andersen, A. D. Pedersen, S. K. Vandborg, J. H. Andersen, Work-related stress is associated with impaired neuropsychological test performance: A clinical cross-sectional study. *Stress*. **18**, 198–207 (2015).

223. E. S. Parker, L. Cahill, J. L. McGaugh, A case of unusual autobiographical remembering. *Neurocase*. **12**, 35–49 (2006).

224. S. Kamiya, Relationship between frequency of involuntary autobiographical memories and cognitive failure. *Memory*. **22**, 839–851 (2014).

OPEN ACCESS Freely available online

PLOS ONE

Neuroligin 2 Is Expressed in Synapses Established by Cholinergic Cells in the Mouse Brain

Virág T. Takács, Tamás F. Freund, Gábor Nyiri*

Laboratory of Cerebral Cortex Research, Department of Cellular and Network Neurobiology, Institute of Experimental Medicine, Hungarian Academy of Sciences, Budapest, Hungary

Abstract

Neuroligin 2 is a postsynaptic protein that plays a critical role in the maturation and proper function of GABAergic synapses. Previous studies demonstrated that deletion of neuroligin 2 impaired GABAergic synaptic transmission, whereas its overexpression caused increased inhibition, which suggest that its presence strongly influences synaptic function. Interestingly, the overexpressing transgenic mouse line showed increased anxiety-like behavior and other behavioral phenotypes, not easily explained by an otherwise strengthened GABAergic transmission. This suggested that other, non-GABAergic synapses may also express neuroligin 2. Here, we tested the presence of neuroligin 2 at synapses established by cholinergic neurons in the mouse brain using serial electron microscopic sections double labeled for neuroligin 2 and choline acetyltransferase. We found that besides GABAergic synapses, neuroligin 2 is also present in the postsynaptic membrane of cholinergic synapses in all investigated brain areas (including dorsal hippocampus, somatosensory and medial prefrontal cortices, caudate putamen, basolateral amygdala, centrolateral thalamic nucleus, medial septum, vertical- and horizontal limbs of the diagonal band of Broca, substantia innominata and ventral pallidum). In the hippocampus, the density of neuroligin 2 labeling was similar in GABAergic and cholinergic synapses. Moreover, several cholinergic contact sites that were strongly labeled with neuroligin 2 did not resemble typical synapses, suggesting that cholinergic axons form more synaptic connections than it was recognized previously. We showed that cholinergic cells themselves also express neuroligin 2 in a subset of their input synapses. These data indicate that mutations in human neuroligin 2 gene and genetic manipulations of neuroligin 2 levels in rodents will potentially cause alterations in the cholinergic system as well, which may also have a profound effect on the functional properties of brain circuits and behavior.

Citation: Takács VT, Freund TF, Nyiri G (2013) Neuroligin 2 Is Expressed in Synapses Established by Cholinergic Cells in the Mouse Brain. PLoS ONE 8(9): e72450. doi:10.1371/journal.pone.0072450

Editor: Thomas H. Gillingwater, University of Edinburgh, United Kingdom

Received June 6, 2013; **Accepted** July 17, 2013; **Published** September 5, 2013

Funding: This work was supported by National Institutes of Health (NS030549, www.nih.gov); National Office for Research and Technology – Hungarian Scientific Research Fund (CNK77793, www.nih.gov.hu, www.otka.hu); European Research Council (ERC-2011-ADG-294313, SERRACO, erc.europa.eu). GN was supported by János Bolyai Research Scholarship. The funders had no role in study design, data collection and analysis, decision to publish, or preparation of the manuscript.

Competing Interests: The authors have declared that no competing interests exist.

* E-mail: nyiri.gabor@koki.mta.hu

Introduction

Neuroligins (NLGNs) are a family of postsynaptic transmembrane proteins that bind to presynaptic neurexins [1], whereby they form a trans-synaptic signal transduction complex and mediate a bidirectional signaling between the presynaptic axon and the postsynaptic target [2]. Both NLGNs and neurexins recruit proteins that are involved in synaptic communication and are able to induce pre- or postsynaptic specializations [3–5]. Experiments with NLGN-knockout (KO) mice demonstrated that NLGNs play an important role in the maturation and proper function of synapses [6,7] and appear to be dynamically regulated and therefore contribute to the activity dependent stabilization/destabilization of synapses [8–11].

Four neuroligin isoforms (NLGN1-4) were described in rodent brain, which were shown to localize to different synapse types. NLGN1 is present in glutamatergic synapses [12], whereas NLGN2 was localized to GABAergic and a small subset of glycinergic synapses [4,13,14]. NLGN3 was found in undefined subgroups of both glutamatergic and GABAergic synaptic contacts [15]; whereas NLGN4 was detected in glycinergic synapses [16]. Consistent with the location of different isoforms, manipulation (deletion or overexpression) of NLGN1 or NLGN2 resulted in alterations in glutamatergic or GABAergic transmission, respectively [17]. The distinct localization of these NLGN isoforms suggests that they fulfill different roles in distinct synapse types and may recruit different kinds of synaptic proteins.

NLGN2 was detected exclusively in inhibitory synapses so far [4,13,14] and it is of particular interest, because mutations in human NLGN2 gene were implicated in schizophrenia [18], whereas manipulations of mouse NLGN2 levels resulted in characteristic behavioral phenotypes, including an increase in anxiety levels both in NLGN2-KO and NLGN2-overexpressing mice [19–21]. Consistent with the location of NLGN2 in inhibitory synapses, NLGN2-KO mice had impairments in inhibitory synaptic transmission [20,22–24], whereas NLGN2-overexpressing animals revealed an increase in inhibition [19]. Interestingly, despite the opposite changes in the strength of GABAergic transmission detected in NLGN2-KO and NLGN2-overexpressing mice, both mice showed increased anxiety-like behavior [19,20]. This enhancement is surprising in case of NLGN2-overexpressing mouse (where the GABAergic transmission is enhanced), because positive modulation of GABAergic signaling (for example benzodiazepine treatment) generally results

in anxiolytic effects [25]. Some other behavioral and physiological effects of NLGN2-overexpression are also inconsistent with the strengthened GABAergic transmission (high level of basal activity, enhanced startle response, stereotyped jumping behavior and seizures in frontoparietal EEG [19]). These controversial results raise the possibility that besides GABAergic synapses, NLGN2 is expressed in other kinds of synapses as well. To the best of our knowledge, colocalization of NLGN2 was investigated only with glutamatergic, GABAergic and glycinergic markers, while synapses that use other types of neurotransmitters were not analyzed previously. One of the most abundant terminal type of the mammalian brain is cholinergic, and they provide a massive innervation in most brain regions [26]. They were shown to modulate almost every process in the central nervous system including development, arousal, consciousness, attention, learning and memory, anxiety and depression [27] and interestingly, in line with our hypothesis, in human, nicotine dependence was associated with neurexin-1 gene (which is one of the main binding partners of NLGNs) [28,29].

Therefore, we tested the presence of NLGN2 in cholinergic synapses of the mouse brain using serial electron microscopic sections double labeled for NLGN2 and choline acetyltransferase (ChAT), the synthesizing enzyme of acetylcholine in axon terminals. We found that NLGN2 is expressed postsynaptically at these synapses in all investigated brain areas, and for instance in the hippocampus, its density was similar to that of the GABAergic synapses. Moreover, we also found that NLGN2 was present in atypical contact sites of cholinergic axons that probably would not have been considered contact site before, suggesting that these terminals establish more synapses than it was recognized previously. In addition, we found that cholinergic cells themselves also express NLGN2 in some of their input synapses. These results provide the basis for new interpretations of data in the literature, in which the effects of the genetic manipulation of NLGN2 was tested.

Materials and Methods

Ethics statement

All experiments were performed in accordance with the Institutional Ethical Codex and the Hungarian Act of Animal Care and Experimentation guidelines, which are in concert with the European Communities Council Directive of November 24, 1986 (86/609/EEC). The Animal Care and Experimentation Committee of the Institute of Experimental Medicine of Hungarian Academy of Sciences and the Animal Health and Food Control Station, Budapest, have specifically approved the experimental design under the number of 22.1/362/3/2011.

Tissue preparation

Five male wild-type (WT) C57BL/6J mice (24–60 days old) and two neuroligin 2 knockout mice (NLGN2-KO; 49 and 67 days old) [6] were sacrificed. For perfusion, mice were anaesthetized with isoflurane followed by an intraperitoneal injection of an anesthetic mixture (containing 0.83% ketamine, 0.17% xylazin hydrochloride, 0.083% promethazinium chloride, 0.00083% benzethonium chloride, and 0.00067% hydrochinonum) to achieve deep anesthesia.

Mice were perfused transcardially with 0.9% NaCl solution for 2 min followed by a fixative containing 4% paraformaldehyde in 0.1 M phosphate buffer (PB, pH 7.4) for 35 min. In case of one WT mouse the fixative also contained 0.5% glutaraldehyde. The perfusion with fixative was followed by perfusion with PB for 10 min. The brains were then removed from the skull and coronal sections were cut on a Leica VT1200S vibratome at 50 or 60 μm. The sections were rinsed in PB, cryoprotected sequentially in 10% and 30% sucrose dissolved in PB, freezed over liquid nitrogen and stored at −70C until further processing.

Immunohistochemistry

Sections were freeze-thawed two times over liquid nitrogen in 30% sucrose dissolved in PB. After extensive washes in PB and 0.05 M Tris-buffered saline (TBS, pH 7.4) endogenous peroxidase-like activity was blocked by incubation of the sections in 1% hydrogen peroxide in TBS for 10 min. After repeated washes in TBS, sections were blocked in 1% human serum albumin (HSA, Sigma-Aldrich, in TBS) for 1 h. This was followed by a 2–3 days of incubation in a mixture of primary antibodies for choline acetyltransferase (ChAT; monoclonal mouse antibody, 1:750) [30] and for neuroligin 2 (NLGN2; polyclonal rabbit antibody, Synaptic Systems, Cat. No.: 129 203; Lot No. 10: 1:600, Lot No. 12–13: 1:300) made up in TBS containing 0.05% sodium azide. After extensive washes in TBS, sections were treated with blocking solution (Gel-BS) containing 0.2% cold water fish skin gelatin and 0.5% HSA in TBS for 1 h. This was followed by an overnight incubation in a mixture of biotinylated donkey anti-mouse antibodies (1:1000, Jackson ImmunoResearch Europe Ltd) and 1.4-nm gold-conjugated goat anti-rabbit antibodies (1:100–300; Fab' fragment, Nanoprobes) diluted in Gel-BS. After repeated washes in TBS and PB, sections were treated with 2% glutaraldehyde in PB for 15 min to fix the gold particles into the tissue. This was followed by washes in PB, TBS, and a 2–3 hours of incubation in Elite ABC (1:300, Vector Laboratories) diluted in TBS. After sections were washed in TBS and tris-buffer (pH 7.6) the immunoperoxidase reaction was developed using 3,3-diaminobenzidine (DAB) as chromogen. After repeated washes in PB and Enhancement Conditioning Solution (Aurion), gold particles were intensified using the Aurion R-Gent Silver Enhancement Solution (SE-EM) as described by the manufacturer. After subsequent washes in PB, sections were treated with 0.5% osmium tetroxide in PB for 8–15 min on ice, dehydrated in ascending ethanol series and acetonitrile and embedded in epoxy resin (Durcupan, ACM, Fluka). During dehydration sections were treated with 1% uranyl acetate in 70% ethanol for 20 min.

Electron microscopy

For electron-microscopic analysis of cholinergic terminals, resin-embedded tissue samples from the CA1 area of the dorsal hippocampus, caudate putamen (CPu), basolateral amygdala (BLA), centrolateral thalamic nucleus (CL), somatosensory (S1) and medial prefrontal cortices (PFC) were glued onto small Durcupan blocks. Series of consecutive ultrathin sections (70 nm thick, at least 14 sections/series) were cut using an ultramicrotome (Leica EM UC6) and picked up on Formvar-coated single-slot grids. Ultrathin sections were counterstained with lead citrate (Ultrostain 2, Leica) and examined in a Hitachi 7100 electron microscope equipped with a Veleta CCD camera (Olympus Soft Imaging Solutions, Germany). For evaluation of the NLGN2 content at synapses of ChAT-positive terminals, sections were systemically scanned for synapses of DAB-labeled ChAT-positive boutons. Parallel appositions between the membranes of the presynaptic bouton and the putative postsynaptic target were regarded as synapses if they displayed widening of the extracellular space at the presumptive synaptic cleft, a postsynaptic membrane thickening, and clustered synaptic vesicles in the bouton. Synapses found were followed and photographed at 30,000 magnification in every section where they were present throughout the series: thus these synapses were fully reconstructed. For the semiquantitative

analyses, we measured the length of synapses from these series of digital images using the ImageJ image analyzer software (NIH, USA) then counted the immunogold particles at the postsynaptic membrane. Gold particles were considered to be associated with the cell membrane only when they were not farther away from the membrane than 40 nm. The density of immunogold particles at extrasynaptic plasma membranes and type I synaptic membranes of the target profiles was also measured.

For comparison of NLGN2 contents of ChAT-positive and GABAergic terminals in the hippocampus, we have also measured the immunogold densities of partially or fully reconstructed somatic synapses in the pyramidal layer of the hippocampal CA1 area, because hippocampal pyramidal cells receive only GABAergic synapses onto their somata in rodents [31]. These synapses were reconstructed from the very same series of sections.

Postsynaptic targets of hippocampal cholinergic terminals were classified as described earlier [32]. Briefly, spines were recognized by their small size and specific morphology. Dendrites that have spines and do not receive type I (asymmetric) inputs on their shafts are known to be pyramidal cells [31], whereas dendrites receiving type I synapses on their shafts are interneurons [33]. The robustness of this classification method was reconfirmed recently [32]. Cell bodies from str. pyramidale that did not receive type I inputs were considered to be pyramidal cells, whereas cell bodies in other layers were classified as interneurons. In other brain areas (see above) only the dendrites and spines were discriminated.

For electron microscopic analysis of input synapses of cholinergic cells, tissue samples were taken from medial septum (MS), vertical- and horizontal limbs of the diagonal band of Broca (VDB and HDB), substantia innominata/ventral pallidum (SI/VP) and CPu. Consecutive series of ultrathin sections were systematically scanned for NLGN2-positive synapses of DAB-labeled ChAT-positive dendrites and somata. MS, VDB, HDB and SI/VP were also scanned for NLGN2-positive synapses of ChAT-positive terminals.

Specificity of antibodies

We tested the NLGN2 antibody in experiments with NLGN2-KO mice (n = 2). At the electron microscopic level, specific labeling of synapses could not be detected in these animals (Fig. 1B and C). We have also investigated 28 completely reconstructed synapses of hippocampal ChAT-positive terminals from two NLGN2-KO mice and found only one gold particle in only one synapse. Therefore, the density of synaptic labeling in WT animals was 240-fold larger than in NLGN2-KO mice (9.6±6.02 vs. 0.04±0.24 intensified gold particles/ μm) demonstrating that the background labeling is negligible. The ChAT antibody was used in several previous studies [34–39], and its specificity has been characterized previously [30].

Statistical Analysis

A statistical analysis was carried out using the software Statistica (StatSoft). When data populations had a Gaussian distribution according to the Shapiro-Wilk's W test, we reported parametric statistical features (mean ± SD). In the case of non-Gaussian distribution, we used non-parametric statistical features (median, interquartile ranges). Two groups showing Gaussian distribution were compared using the parametric t test. The Kruskal-Wallis test was used to compare the data from three groups showing non-Gaussian distribution. The differences were considered significant at $p < 0.05$.

Results

Neuroligin 2 is abundant at hippocampal cholinergic synapses

Although NLGN2 is widely considered to be present only in GABAergic synapses [2,7,40–44], we tested its presence at cholinergic synapses as well. We performed double immunogold/immunoperoxidase labeling for NLGN2 and choline acetyltransferase (ChAT), the synthesizing enzyme of acetylcholine. In the hippocampus of NLGN2-KO mice, no specific NLGN2 labeling was found (see Methods, Fig. 1B and C). First, we tested the presence of NLGN2 in GABAergic synapses. CA1 pyramidal cells were shown to receive exclusively GABAergic synapses onto their somata in rodents [31], therefore these synapses were considered to be GABAergic. We confirmed the presence of NLGN2 in these type II (symmetric) synapses of GABAergic boutons (Fig. 1A) [13,45].

Interestingly, synapses of ChAT-positive terminals were also densely labeled at the postsynaptic membrane (Fig. 1D–G). To estimate and compare the abundance of NLGN2 in cholinergic and GABAergic synapses we tested fully reconstructed synapses of ChAT-positive terminals from str. radiatum (n = 59), pyramidale (n = 13) and oriens (n = 35) and fully or partially reconstructed synapses of GABAergic somatic boutons (n = 69) on pyramidal cell bodies in the CA1 area of three mice. Hippocampal cholinergic boutons formed type II synapses that were usually very small (they were present typically only in 2–4 (2.9±1.2) 70 nm-thick sections, median of synaptic membrane area: 0.0256 μm^2, interquartile range: 0.0205–0.0369 μm^2; n = 107, three mice, pooled, Fig. 1D–I) compared to GABAergic synapses. For example, the size of parvalbumin and cannabinoid receptor 1 positive somatic synapses per contact are about 0.07 and 0.22 μm^2, respectively (our unpublished observations). Please note, that although synapses were collected in a random fashion, these are only semiquantitative measurements, nevertheless they still clearly demonstrate the tendency that cholinergic synapses are smaller than GABAergic ones.

In three WT mice, 100%; 100% and 95.8% of the GABAergic synaptic connections (n = 68 out of 69) and 94.3%; 97.1% and 86.5% of cholinergic synapses (n = 99 out of 107) were identified as NLGN2 positive on the basis of intensified immunogold particles associated with the postsynaptic membrane. The somewhat lower positivity of the cholinergic synapses may be due to the fact that they could be tested on fewer sections, because they are much smaller (see above). To test the relative density of NLGN2 in these synapses and extrasynaptically as well, we measured and calculated the relative density of the immunogold labeling. The labeling was specifically enriched in GABAergic and cholinergic synapses compared to the labeling in extrasynaptic membranes and type I synapses (for the definition of membrane associated immunogold particles, please see methods). In three mice, the linear density of labeling was 12.2±3.8; 13±3.5 and 9.4±4.7 gold particles per μm membrane (mean ± SD) in GABAergic synapses, whereas it was only 0.11±0.1; 0.12±0.06 and 0.06±0.06 gold particles per μm at extrasynaptic membrane domains of the same somata in the vicinity of these synapses. In the same animals, in cholinergic synapses, the linear density of labeling was 10.5±6.1; 10.2±6.2 and 8.2±5.7 gold particles per μm membrane, whereas it was only 0.11±0.15; 0.1±0.11 and 0.13±0.19 gold particles per μm at extrasynaptic and type I synaptic membranes of the postsynaptic targets of cholinergic boutons. The linear density values of NLGN2 labeling at GABAergic and cholinergic synapses were compared in three mice and no significant differences were found (Fig. 2). We identified the postsynaptic targets of cholinergic

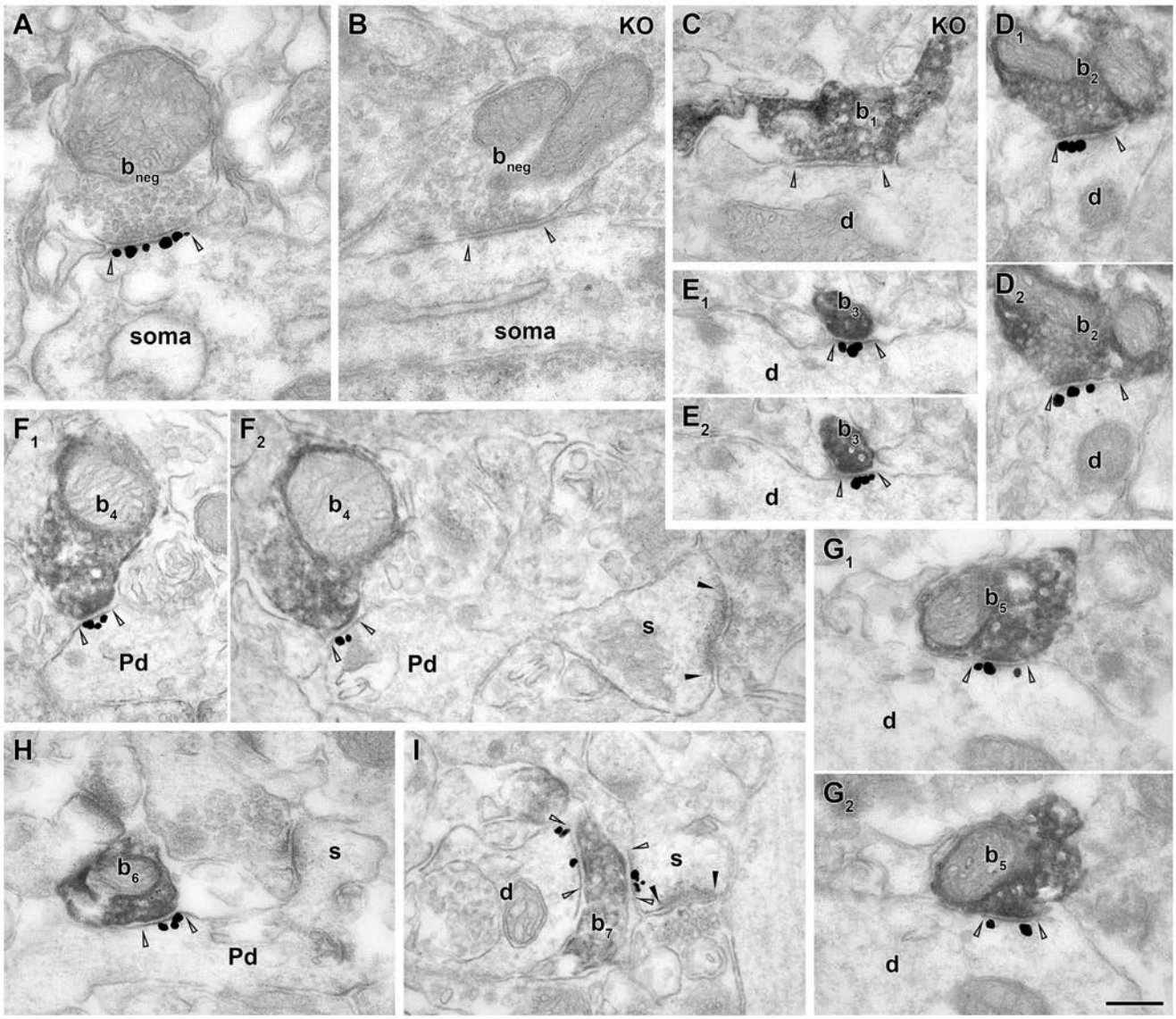

Figure 1. Neuroligin 2 is present postsynaptically at both GABAergic and cholinergic synapses in the hippocampus. Electron micrographs from combined immunogold/immunoperoxidase experiments for NLGN2 (immunogold: black particles) and ChAT (DAB: dark, homogenous reaction product) reveal the presence of NLGN2 at ChAT-negative and ChAT-positive type II synapses in the CA1 area. Arrowheads indicate synapse-edges. A, A pyramidal cell body receives a synapse from a ChAT-negative bouton (b_{neg}) that expresses NLGN2 postsynaptically in a WT mouse. B, C, In contrast, the same type of immunostaining in a NLGN2-KO mice shows no NLGN2-immunoreactive synapses, demonstrating the specificity of the antibody. A GABAergic terminal (b_{neg}) from str. pyramidale, lacking gold particles at the postsynaptic site is shown (B). An example of a synapse of a ChAT-positive bouton (b_1) on a dendrite (d) in str. radiatum that is immunonegative for NLGN2 in KO mouse (C). D–I: NLGN2 immunogold labeling is present at the postsynaptic site of synapses established by ChAT-positive axon terminals (b_{2-5}) on dendrites (d) and spines (s) in str. radiatum (D–G) and oriens (H, I) of WT mice. Serial images show the same synapse in D_1 and D_2; E_1 and E_2; F_1 and F_2; G_1 and G_2. E_{1-2} demonstrates that some of the presynaptic profiles were small-diameter, intervaricose-like segments of ChAT-positive axons (b_3). In F_{1-2} and H, the postsynaptic targets of boutons b_4 and b_6 are putative pyramidal dendrites (Pd) the latter of which is identified by the presence of spines (s). I, Occasionally, we found ChAT-positive presynaptic elements that formed synapses with two postsynaptic targets. Here, bouton b7 forms a synapse with a dendrite and a spine, which receives a type I synapse (black arrowheads). Note, that in many cases, synaptic junctions of ChAT-positive terminals are atypical (E, F, H, I). Scale bar is 200 nm for all images.
doi:10.1371/journal.pone.0072450.g001

boutons in three mice, and found that at least 48.8%; 68.6% and 48.6% of them innervated pyramidal dendritic shafts (Fig. 1F and H) and 17.1%; 20%; and 24.3% targeted spines, that also received a type I input (Fig. 1I). Only 2.9%; 0% and 8.1% of the cholinergic synapses targeted interneuron dendrites or somata (three interneuron dendrites and one interneuron soma out of 107 targets), and rarely cholinergic boutons innervated pyramidal cell somata as well (two out of 107 targets; 0%; 2.9% and 2.7% of the boutons in three mice). The rest of the postsynaptic targets could not be unequivocally classified (31.4%; 8.6% and 16.2%). Occasionally, we found cholinergic boutons that formed two synapses with different postsynaptic targets (Fig. 1I).

These data show that in the hippocampus virtually all cholinergic synapses contain NLGN2 at the postsynaptic membrane and its density is just as high in cholinergic as in GABAergic synapses.

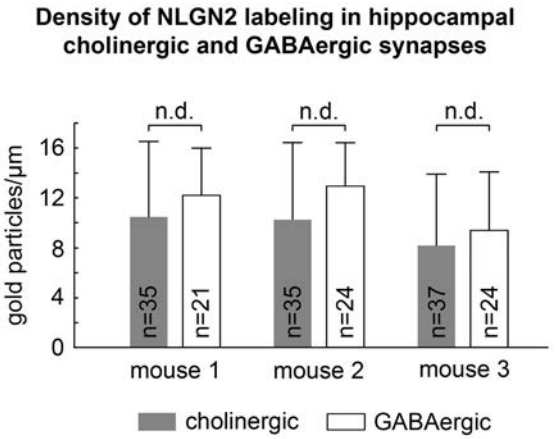

Figure 2. Hippocampal cholinergic and GABAergic synapses express a similar density of neuroligin 2. There was no significant difference in the density of NLGN2 labeling (intensified gold particles/ µm synaptic membrane) between GABAergic synapses on pyramidal cell somata (12.2±3.8, 13±3.5 and 9.4±4.7; mean and standard deviation in three mice, respectively) and ChAT-positive synapses in str. radiatum, pyramidale and oriens (10.5±6.1, 10.2±6.2 and 8.2±5.7). (n.d.: no statistical difference).
doi:10.1371/journal.pone.0072450.g002

Neuroligin 2 is also abundant in neocortical cholinergic synapses

We tested the presence of NLGN2 in the somatosensory (S1) and prefrontal cortices (PFC) using the same combined immunogold/ immunoperoxidase staining for NLGN2 and ChAT as above. In the S1 of two WT mouse, 97% and 88.6% of the cholinergic synapses (n = 33, 35) were identified as NLGN2 positive on the basis of intensified immunogold particles associated with the postsynaptic membrane (Fig. 3A, B). Cholinergic terminals formed small type II synapses on dendritic shafts (60.6% and 60% of all targets; Fig. 3A) and spines (36.4% and 37.1%; Fig. 3B) in the S1, whereas 3% and 2.9% of the postsynaptic targets remained unidentified. Many of the innervated dendritic shafts possessed spines on the recorded serial photos (21.2% and 37.1% of all targets), demonstrating that these originated presumably from pyramidal cells. In the PFC, almost all cholinergic synapses collected were NLGN2-positive (92% and 84.8%; n = 25 and 46, two mice; Fig. 3C–E). The morphology and size of synapses were also similar in these cortical areas: they formed type II synapses that were usually small. The distribution of postsynaptic targets were also similar in the S1 and PFC: in the PFC of two mice 64% and 41.3% of the cholinergic synapses were found on dendrites (Fig. 3C, D; 20% and 8.7% of all targets were on putative pyramidal dendrites, because they were spiny on the serial photos), whereas 24% and 52.2% of the cholinergic inputs innervated spines (Fig. 3E). Some (12% and 6.5%) of the targets could not be classified.

Neuroligin 2 is expressed in cholinergic synapses in several other non-cortical brain areas as well

The basolateral amygdala (BLA), the caudate putamen (CPu) and the thalamic centrolateral nucleus (CL) receive abundant cholinergic innervation [46].

In BLA, cholinergic terminals formed type II synapses that were NLGN2-positive (97.1% and 100%; n = 34 and 47, two mice; Fig. 4E–G). Cholinergic boutons innervated dendrites (76.5 and 51.1% of all targets in two mice; Fig. 4E–G) and spines (17.6% and 48.9%; Fig. 4E); 2.9 and 0% of the targets could not be classified. One of the postsynaptic targets (out of 81) was an unidentified soma. Large part of the dendritic targets possessed spines in the examined segment (35.3% and 40.4% of all targets), suggesting that they originated from pyramidal cells.

In CPu, cholinergic synapses formed type II synapses that were NLGN2-positive (92% and 97.6% n = 25 and 41, two mice; Fig. 4A–D). Approximately every second cholinergic synapse innervated dendrites in CPu (48% and 43.9% of all targets; Fig. 4A,B and D) whereas the rest of them targeted spines (36% and 36.6%; Fig. 4C); 16% and 14.6% of all targets remained unidentified. Out of 66 synapses tested, one targeted a soma and another targeted an axon initial segment. 36% and 9.8% of all targets were spiny dendrites, suggesting that they were GABAergic medium spiny neurons in CPu.

In contrast to other brain areas investigated, cholinergic synapses formed both type I and type II synapses in CL (53.3% type I, 30% type II in the first animal; 16% type I, 56% type II in the second animal; the remaining synapses could not be classified; n = 30 and 25, two mice). Most cholinergic synapses were NLGN2-positive in CL (73% and 84%; Fig. 4H, I).

We also tested the NLGN2 content of ChAT-positive synapses in basal forebrain areas and found that their cholinergic terminals formed NLGN2-positive type II synapses. The number of positive samples that were collected are as follows: the medial septum: n = 14 and 2; vertical limb of diagonal band of Broca: n = 3 and 7; horizontal limb of diagonal band of Broca: n = 4 and 10; substantia innominata/ ventral pallidum: n = 9 and 12 synapses collected from two mice, respectively).

Neuroligin 2 clusters revealed the presence of contact sites of cholinergic boutons that probably would not have been considered contact sites previously

In our preliminary experiments, we expected cholinergic terminals to establish synapses only rarely in cortical areas [34,35,38,39]. Although cholinergic synapses are known to be less prominent than GABAergic or glutamatergic synapses, we expected and searched for typical synapse features. Indeed, several cholinergic synapses had typical synaptic morphology and NLGN2 labeling. Based on data in the literature and on our own experience, NLGN2 is accumulated only in synaptic contact sites and indeed its clusters appeared in synapses with very typical morphology. However, it very soon became obvious that not all cholinergic contact sites resemble typical features of type I or II synapses. In several cases, we found clusters of NLGN2 immunogold labeling next to ChAT positive terminals, in membrane appositions that traditionally would not have been considered synaptic contact sites previously, because of an only very mild thickening of the membrane and because its size is smaller than the smallest cortical GABAergic synapses. However, based on the accumulated data, these contact sites should probably also be considered synapses.

Especially in the hippocampus and neocortex, a substantial amount of the cholinergic contact sites possessed hardly detectable thickening of the synaptic membranes (Fig. 1E, F, H, I; Fig. 3B, E). Some of these contacts were formed by small-diameter intervaricose segments of cholinergic axons (Fig. 1E). In many cases, the length of parallel appositions between membrane segments of the presumed pre- and postsynaptic profiles were also small; therefore probably none of these contact sites could have been recognized without NLGN2 labeling. However, these contacts were as densely labeled for NLGN2 as cholinergic synapses that have more prominent synaptic clefts and postsynaptic densities (Fig. 1.D, 3A, C). According to our observations, there is a continuum between clearly apparent synapse-like structures of cholinergic boutons and

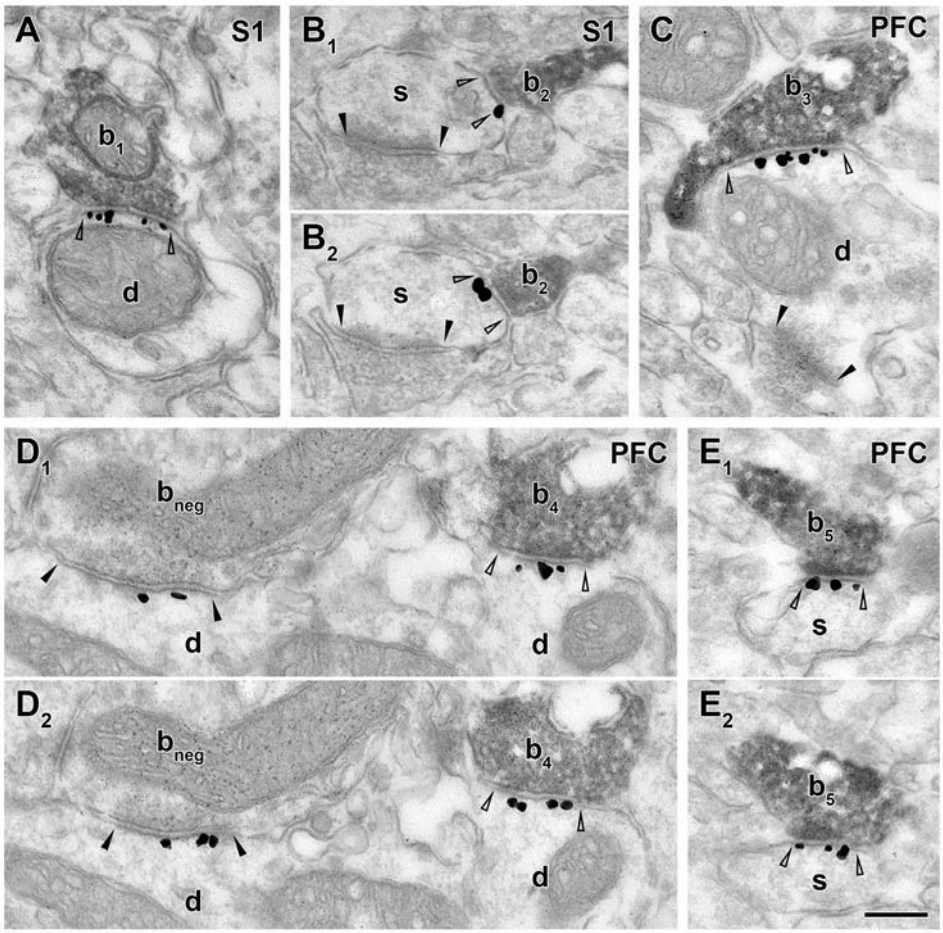

Figure 3. Neuroligin 2 is localized postsynaptically at cholinergic synapses in the neocortex. Images demonstrate double immunohistochemical reactions for ChAT (dark, homogenous DAB precipitate) combined with NLGN2 (black intensified gold particles) in somatosensory (S1) and prefrontal cortices (PFC). Serial sections of the same synapses are shown in B_{1-2}, D_{1-2} and E_{1-2}. In both areas, ChAT-positive boutons (b_{1-5}) form type II synaptic contacts on dendrites (d, A, C, D_{1-2}) and spines (s, B_{1-2}, E_{1-2}) that express NLGN2 at the postsynaptic membranes (open arrowheads label synaptic edges). The innervated spines also received a type I synapse from a ChAT-negative terminal (B_{1-2}, black arrowheads). In C the postsynaptic dendrite of bouton b_3 receive an additional, type I synaptic input (black arrowheads) from an unlabeled terminal. These type I synapses in B_{1-2} and C do not contain NLGN2. In contrast, another ChAT-negative, putative GABAergic bouton (b_{neg}) establishes a type II, NLGN2-positive synapse (black arrowheads) with a dendrite in D_{1-2}. Scale bar is 200 nm for all images.
doi:10.1371/journal.pone.0072450.g003

hardly detectable contact sites that can now be recognized based on the dense NLGN2 labeling.

Cholinergic cells themselves express neuroligin 2 in a subset of their input synapses

The majority of cholinergic afferents to most of the investigated brain areas (hippocampus, BLA, S1, PFC) arises from different parts of the basal forebrain: the medial septum (MS), the vertical and horizontal limbs of the diagonal band of Broca (VDB and HDB) and the substantia innominata/ ventral pallidum (SI/VP) [26]. We tested whether these cholinergic cells of the basal forebrain express NLGN2 at their input synapses on their dendrites and/or cell bodies. We found that a subset of their synaptic inputs were indeed NLGN2-positive (Fig. 5A–E). NLGN2-positive input synapses of cholinergic cells were collected in all of the basal forebrain areas investigated (MS: n = 24 dendritic and n = 24 somatic; VDB: n = 29 dendritic and n = 11 somatic, HDB: n = 37 dendritic and n = 14 somatic, SI/VP: n = 50 dendritic and n = 10 somatic synapses from two mice). In the MS, two of the somatic, and one of the dendritic NLGN2-positive input synapses were formed by ChAT-positive terminals, while one similar dendritic input was found in SI/VP, demonstrating that cholinergic cells can form synaptic connections with each other and these contacts also contain NLGN2.

In contrast to most of the brain areas that receive their cholinergic innervation from distant projection neurons, dense cholinergic innervation in CPu is provided by local cholinergic interneurons [47]. We found that they also express NLGN2 in a minority of their input synapses (n = 43 dendritic and n = 7 somatic NLGN2-positive synapses were collected from two mice; Fig. 5F).

Discussion

The present study provides evidence that besides GABAergic synapses, cholinergic synapses also express NLGN2 postsynaptically, in all investigated brain areas in mice. Our estimation also shows that NLGN2 density is similar in cholinergic and GABAergic synapses in the hippocampus. We identified several putative contact sites established by cholinergic axons that do not show the typical morphology of classical synapses and therefore,

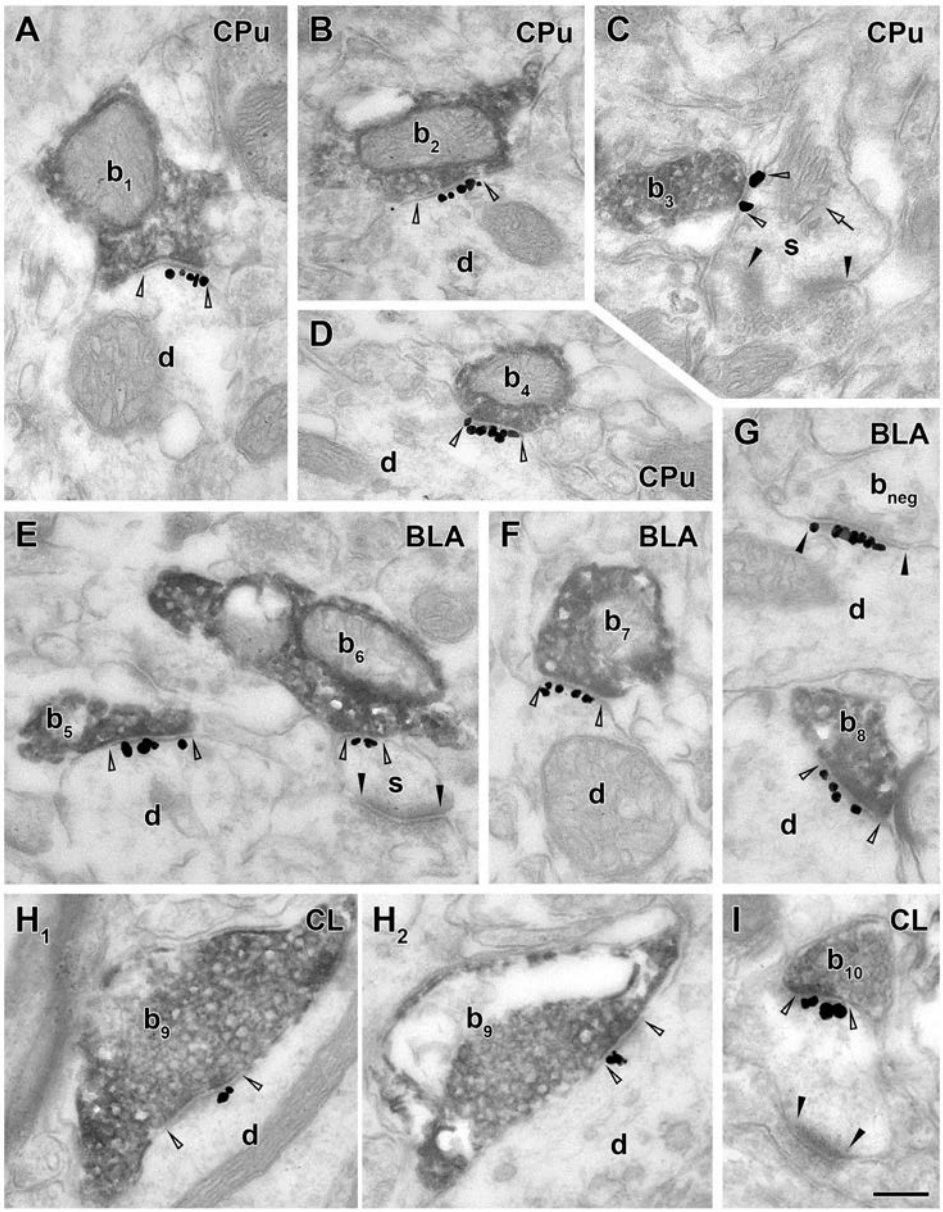

Figure 4. Neuroligin 2 is expressed postsynaptically at cholinergic synapses in the caudate putamen, basolateral amygdala and centrolateral thalamic nucleus. Electron micrographs from combined immunogold/immunoperoxidase experiments show that NLGN2 immunogold labeling (black particles) is present at the postsynaptic site of synapses (open arrowheads) established by ChAT-positive axon terminals (b_{1-10}, dark reaction product) on dendrites (d) and spines (s) in caudate putamen (CPu, A–D) basolateral amygdala (BLA, E–G), and centrolateral thalamic nucleus (CL, H–I). Note that many of these boutons form synapses that could hardly be identified without NLGN2 labeling (e.g. b_3 in C, b_6 in E or b_8 in G). In C, arrow indicates the spine apparatus. In G, a putative GABAergic bouton (b_{neg}) forming a NLGN2-positive type II synapse (black arrowheads) is also shown next to the ChAT-positive terminal. Serial sections of the same terminal are shown in H_{1-2}. Scale bar is 200 nm for all images.

doi:10.1371/journal.pone.0072450.g004

they probably could not be recognized without NLGN2 labeling. We also found that some of the input synapses of cholinergic cells contain NLGN2 postsynaptically, demonstrating that cholinergic cells themselves also express NLGN2.

NLGNs are present postsynaptically and form a trans-synaptic signal transduction complex with presynaptic neurexins; they participate in the recruitment of synaptic proteins, and thereby play an important role in the maturation and activity-dependent regulation of synaptic contacts [3,4,6,9–11]. Previous immunocytochemical experiments localized NLGN2 exclusively to GABAergic and a small subset of glycinergic synapses [13,14]. Further investigations and conclusions were based on those results in the literature and several studies demonstrated that deletion of NLGN2 caused selective impairment in inhibitory synaptic transmission [17,22–24], whereas overexpression of NLGN2 resulted in enhanced inhibition [17,19]. However, in the light of our results, previous conclusions may need to be reconsidered, because the strength of cholinergic synapses was probably also altered in NLGN2-KO and NLGN2-overexpressing animals.

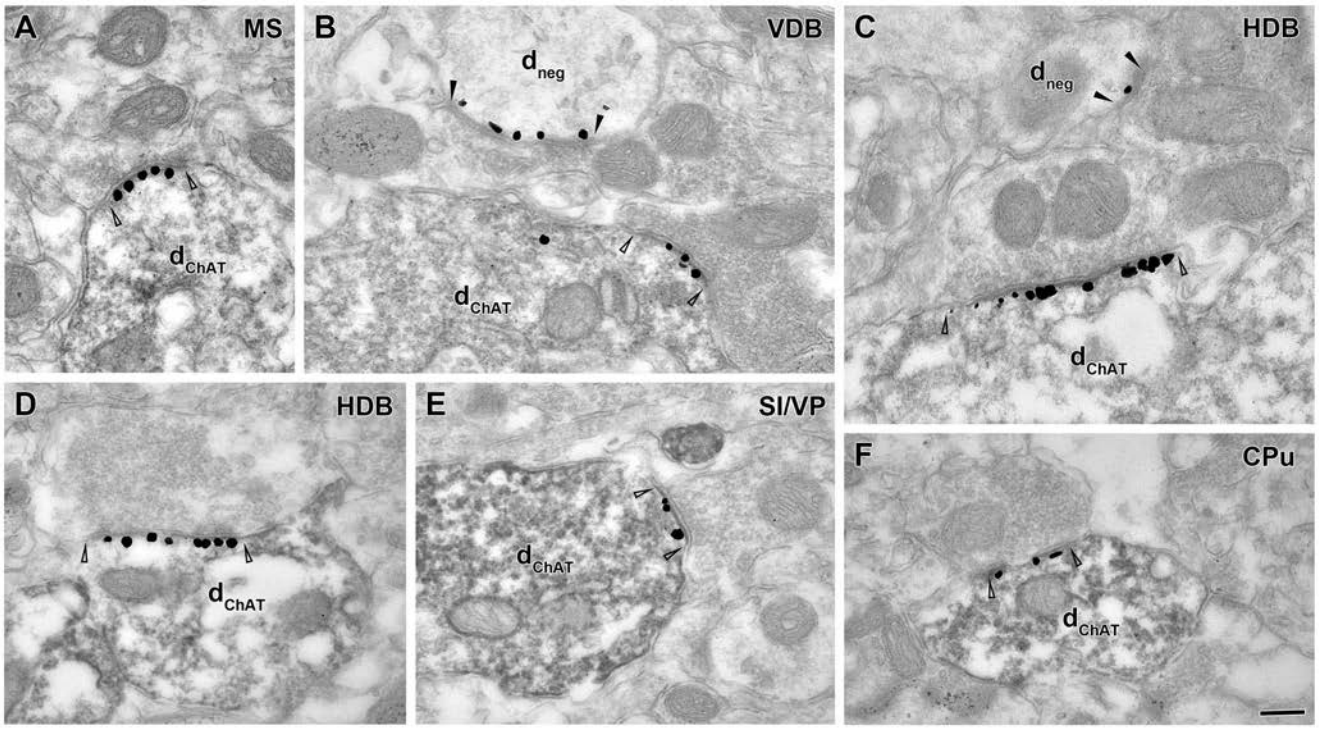

Figure 5. Cholinergic projection neurons of the basal forebrain and neostriatal cholinergic interneurons express NLGN2 in their inputs synapses. Images from combined immunogold/immunoperoxidase experiments show that dendrites of cholinergic cells (dChAT, dark, homogenous DAB precipitate) express NLGN2 (intensified gold particles) at postsynaptic membranes of type II synapses (open arrowheads) in the medial septum (A: MS), vertical- and horizontal diagonal band of Broca (B: VDB; C, D: HDB), substantia innominata/ventral pallidum (E: SI/VP) and caudate putamen (F: CPu). In B and C two unlabeled dendrites (d_{neg}) also express NLGN2 in their type II synapses (black arrowheads). Scale bar is 200 nm for all images.
doi:10.1371/journal.pone.0072450.g005

Potential molecular interactions of neuroligin 2 in cholinergic synapses

In perisomatic GABAergic synapses, NLGN2 was shown to bind to the $GABA_A$-receptor anchoring protein gephyrin and to activate collybistin, which is responsible for the membrane tethering of gephyrin [23]. Through this interaction, NLGN2 participates in the clustering of $GABA_A$ receptors at the postsynaptic side, which likely influences the properties of GABAergic synapses [23,24,48]. Cholinergic synapses are much less known than GABAergic ones, however; here, NLGN2 may also contribute to the recruitment or alignment of synaptic proteins, including acetylcholine (ACh) receptors in cholinergic synapses.

What kind of scaffolding proteins can potentially bind to NLGN2 in cholinergic synapses? The synaptic scaffolding molecule (S-SCAM; [49]) is also present and interacts with NLGN2 at inhibitory synapses [50]. Furthermore, it was demonstrated that in chicken, where only three forms of NLGN is present (NLGN1,3,4) and NLGN2 is absent [51], S-SCAM is directly associated with NLGN1 at cholinergic synapses of the ciliary ganglion [52]. In these synapses, S-SCAM indirectly interacts with the adenomatous polyposis coli protein that organizes a multimolecular protein complex which targets α3 nicotinic ACh receptors to the postsynaptic membrane [53,54]. With these interactions NLGN1 might indirectly influence the strength of these cholinergic contacts. NLGN1 also binds to β-neurexins in these cholinergic synapses, induces accumulation of presynaptic components and enhances nicotinic synaptic activity in chicken ciliary ganglionic cell culture [55]. A third known binding partner of NLGN1 in cholinergic synapses of the chicken ciliary ganglion is the scaffolding protein postsynaptic density-93 [52], which is also present in cholinergic synapses of autonomic ganglia in mouse and plays a role in stabilization of nicotinic ACh receptors at postsynaptic sites [56]. Although, to the best of our knowledge, no data is available about the presence of these three proteins in cholinergic synapses of the mammalian central nervous system, but our results suggest that they may potentially be present and interact with NLGN2 in these synapses.

It is known that different NLGN isoforms can be present in the same synapse. For instance, a subset of GABAergic synapses express both NLGN 2 and 3; while several glutamatergic synapses express both NLGN 1 and 3 [15]. Therefore, cholinergic synapses may also express other types of NLGNs. However, it is not possible to predict, whether other neuroligin isoforms are also present at these synapses, because (besides heterodimers [57]) NLGNs can also form homodimers by themselves.

Possible role of neuroligin 2 in cholinergic synapses

The behavioral phenotype of NLGN2-KO mice and NLGN2-overexpressing animals has been thoroughly described [19–21,58]. However, the interpretation of these data should be reconsidered in the light of our new results.

NLGN2-KO mice showed a marked increase in anxiety-like behavior which can be explained by an impairment in GABAergic synaptic transmission [20], because pharmacological blockade of $GABA_A$ receptors produces a similar effect [25,59]. In contrast, positive modulators of GABAergic signaling cause anxiolysis [25,59,60]. Based on these data, the expected effect of NLGN2

overexpression in GABAergic synapses would be also anxiolytic. However, global overexpression of NLGN2 resulted in an enhancement of anxiety-like behavior despite the observed potentiated GABAergic function [19]. We suggest that these controversial findings may be explained by a strengthened cholinergic tone that is due to NLGN2-overexpression, the result of which may be a subsequent strengthening of these synapses. This is supported by findings that increased ACh signaling can indeed induce anxiety-like behavior [61–63]. Nevertheless, it should also be noted that manipulations of the cholinergic system, for example nicotine administration, can also induce anxiolytic effects, depending on treatment type, dose and brain region investigated [64].

In NLGN2-overexpressing mice, high levels of basal activity, enhanced startle response, anxiety and stereotyped jumping behavior was observed [19] that may be the result of an increased level of arousal. We have detected NLGN2 postsynaptically at virtually all cholinergic synapses investigated, including those in the intralaminar thalamus, a brain area that receives cholinergic innervation from the pedunculopontine nucleus [65]. This projection is part of the cholinergic arm of the reticular activating system [65], therefore, if NLGN2 content of these synapses is increased in NLGN2-overexpressing mice, their arousal state could also be heightened.

The general effect of NLGN2 manipulation may also depend on the relative number of cholinergic terminals in different brain regions. In the hippocampus, according to data published by different groups, the density of GABAergic terminals seems to be larger (1.93×10^8 GAD-immunoreactive boutons/mm^3 in CA1 area of rat [66]) than the density of cholinergic varicosities (4.9 and 5.6×10^6 ChAT-positive varicosities/mm^3 in CA1 area of rat and mouse, respectively [37]). Since the density of NLGN2 is similar in cholinergic and GABAergic synapses, but GABAergic synapses are larger and more numerous, the majority of NLGN2 is localized in GABAergic synapses in the hippocampus. However, the relative proportion of cholinergic terminals may outnumber GABAergic terminals in other brain areas. For instance, in the striatum, cholinergic terminals are highly abundant (2×10^8 varicosities/mm^3 [36]) and in these areas manipulation of NLGN2 will probably have a higher impact on the cholinergic system. Nevertheless, the importance of a molecule at the network level is not necessarily a linear function of its abundance in the given brain area.

The incidence of seizure spiking in the frontoparietal EEG of NLGN2-overexpressing mouse [19] may also be the consequence of an increased cholinergic tone, because brain oscillations are under effective cholinergic control [67,68].

Since the cholinergic system influences also brain circuits that are responsible for regulating motor control, NLGN2 loss in cholinergic synapses might also contribute to the slightly diminished motor co-ordination described in NLGN2-KO mice [20,21]. This hypothesis is supported by the observations that gait and postural instability might be associated with cholinergic dysfunction in Parkinson's disease as well [69].

Mutations of NLGN2 gene were recently identified in schizophrenia patients [18]. Because cholinergic impairments are implicated in schizophrenia [70], NLGN2 dysfunction in cholinergic synapses may also contribute to the pathophysiology in these subjects.

Cholinergic and GABAergic cells express neuroligin 2 in their inputs synapses

We demonstrated that cholinergic neurons of the basal forebrain and striatum express NLGN2 in the postsynaptic membrane of their putative GABAergic (ChAT-negative, type II) and cholinergic (ChAT-positive) inputs synapses. In the hippocampus, a small fraction of the postsynaptic targets of NLGN2-positive cholinergic synapses were identified as GABAergic interneurons, which means that GABAergic cells also express NLGN2.

Neuroligin 2 in non-classical cholinergic contacts

Interestingly, besides classical synapses of cholinergic axons, we found NLGN2 clusters also at cholinergic contact sites that did not resemble typical synapses because of their small size and a very mild thickening of the postsynaptic membrane. Because NLGN2 is known to recruit other synaptic receptor proteins, these clusters may label membrane segments that participate in signal transmission. Therefore, these contacts might be considered synapses that do not show classical morphology. Many studies that analyzed the incidence of synaptic contacts formed by cholinergic boutons concluded that cholinergic innervation of the brain is mainly non-synaptic [34–36,38,39]. These studies provided strong support for the volume transmission hypothesis [71]. In contrast, other groups demonstrated that classical synaptic contacts predominate among cholinergic inputs [72,73]. Because we could see a continuum between clearly synapse-like contacts and those contacts that could be recognized only with the aid of NLGN2-labeling, the discrepancy between these groups of studies might be explained by a different strictness of criteria used in the morphological definition of the synaptic active zone. Because a completely different approach would be required, we did not attempt to quantify the proportion of boutons or inter-bouton (i.e. intervaricose) segments (Fig. 1E) that formed synaptic contacts in this study. Nevertheless, our results imply that cholinergic synapses are far more frequent than presumed previously, even if several of them do not show classical morphology. This may suggest the importance of synaptic transmission also in the cholinergic system. Indeed, for instance, acetylcholinesterase (that terminates the ACh signal) has a very high catalytic activity [74,75], and it is particularly abundant in the striatum [76]. These facts suggest that ACh is quickly cleared from extracellular space; therefore, synaptic transmission of ACh would be more effective in this area. New data on phasic ACh release also support this view [75].

Previously, NLGN2 was found in GABAergic and some glycinergic synapses [13,14], while we found it in cholinergic synapses in this study. However, information about the possible presence or absence of NLGN2 in dopaminergic, noradrenergic, serotonergic and some other types of synapses is still to be explored.

Acknowledgments

We thank Dr. Csaba Cserép, Panna Hegedüs and András Szőnyi for their contribution to some of the experiments, Dr. Thomas C. Südhof for providing the NLGN2-KO mouse, Dr. Costantino Cozzari for the gift of the ChAT antibody, and Dr. Henrik Martens (Synaptic Systems, Goettingen) for providing NLGN2 antibodies for testing. The technical assistance of Katalin Lengyel, Emőke Szépné Simon, Katalin Iványi and Győző Goda is also greatly acknowledged.

Author Contributions

Conceived and designed the experiments: VTT GN. Performed the experiments: VTT. Analyzed the data: VTT GN. Wrote the paper: VTT GN. Revised the article critically for important intellectual content: TFF.

References

1. Ichtchenko K, Nguyen T, Südhof TC (1996) Structures, alternative splicing, and neurexin binding of multiple neuroligins. J Biol Chem 271: 2676–2682.
2. Siddiqui TJ, Craig AM (2011) Synaptic organizing complexes. Curr Opin Neurobiol 21: 132–143.
3. Scheiffele P, Fan J, Choih J, Fetter R, Serafini T (2000) Neuroligin expressed in nonneuronal cells triggers presynaptic development in contacting axons. Cell 101: 657–669.
4. Graf ER, Zhang X, Jin SX, Linhoff MW, Craig AM (2004) Neurexins induce differentiation of GABA and glutamate postsynaptic specializations via neuroligins. Cell 119: 1013–1026.
5. Nam CI, Chen L (2005) Postsynaptic assembly induced by neurexin-neuroligin interaction and neurotransmitter. Proc Natl Acad Sci U S A 102: 6137–6142.
6. Varoqueaux F, Aramuni G, Rawson RL, Mohrmann R, Missler M, et al. (2006) Neuroligins determine synapse maturation and function. Neuron 51: 741–754.
7. Südhof TC (2008) Neuroligins and neurexins link synaptic function to cognitive disease. Nature 455: 903–911.
8. Schapitz IU, Behrend B, Pechmann Y, Lappe-Siefke C, Kneussel SJ, et al. (2010) Neuroligin 1 is dynamically exchanged at postsynaptic sites. J Neurosci 30: 12733–12744.
9. Peixoto RT, Kunz PA, Kwon H, Mabb AM, Sabatini BL, et al. (2012) Transsynaptic signaling by activity-dependent cleavage of neuroligin-1. Neuron 76: 396–409.
10. Suzuki K, Hayashi Y, Nakahara S, Kumazaki H, Prox J, et al. (2012) Activity-dependent proteolytic cleavage of neuroligin-1. Neuron 76: 410–422.
11. Zeidan A, Ziv NE (2012) Neuroligin-1 loss is associated with reduced tenacity of excitatory synapses. PLoS One 7: e42314.
12. Song JY, Ichtchenko K, Südhof TC, Brose N (1999) Neuroligin 1 is a postsynaptic cell-adhesion molecule of excitatory synapses. Proc Natl Acad Sci U S A 96: 1100–1105.
13. Varoqueaux F, Jamain S, Brose N (2004) Neuroligin 2 is exclusively localized to inhibitory synapses. Eur J Cell Biol 83: 449–456.
14. Hoon M, Bauer G, Fritschy JM, Moser T, Falkenburger BH, et al. (2009) Neuroligin 2 controls the maturation of GABAergic synapses and information processing in the retina. J Neurosci 29: 8039–8050.
15. Budreck EC, Scheiffele P (2007) Neuroligin-3 is a neuronal adhesion protein at GABAergic and glutamatergic synapses. Eur J Neurosci 26: 1738–1748.
16. Hoon M, Soykan T, Falkenburger B, Hammer M, Patrizi A, et al. (2011) Neuroligin-4 is localized to glycinergic postsynapses and regulates inhibition in the retina. Proc Natl Acad Sci U S A 108: 3053–3058.
17. Chubykin AA, Atasoy D, Etherton MR, Brose N, Kavalali ET, et al. (2007) Activity-dependent validation of excitatory versus inhibitory synapses by neuroligin-1 versus neuroligin-2. Neuron 54: 919–931.
18. Sun C, Cheng MC, Qin R, Liao DL, Chen TT, et al. (2011) Identification and functional characterization of rare mutations of the neuroligin-2 gene (NLGN2) associated with schizophrenia. Hum Mol Genet 20: 3042–3051.
19. Hines RM, Wu L, Hines DJ, Steenland H, Mansour S, et al. (2008) Synaptic imbalance, stereotypies, and impaired social interactions in mice with altered neuroligin 2 expression. J Neurosci 28: 6055–6067.
20. Blundell J, Tabuchi K, Bolliger MF, Blaiss CA, Brose N, et al. (2009) Increased anxiety-like behavior in mice lacking the inhibitory synapse cell adhesion molecule neuroligin 2. Genes Brain Behav 8: 114–126.
21. Wöhr M, Silverman JL, Scattoni ML, Turner SM, Harris MJ, et al. (2012) Developmental delays and reduced pup ultrasonic vocalizations but normal sociability in mice lacking the postsynaptic cell adhesion protein neuroligin2. Behav Brain Res.
22. Gibson JR, Huber KM, Südhof TC (2009) Neuroligin-2 deletion selectively decreases inhibitory synaptic transmission originating from fast-spiking but not from somatostatin-positive interneurons. J Neurosci 29: 13883–13897.
23. Poulopoulos A, Aramuni G, Meyer G, Soykan T, Hoon M, et al. (2009) Neuroligin 2 drives postsynaptic assembly at perisomatic inhibitory synapses through gephyrin and collybistin. Neuron 63: 628–642.
24. Jedlicka P, Hoon M, Papadopoulos T, Vlachos A, Winkels R, et al. (2011) Increased dentate gyrus excitability in neuroligin-2-deficient mice in vivo. Cereb Cortex 21: 357–367.
25. Kalueff AV, Nutt DJ (2007) Role of GABA in anxiety and depression. Depress Anxiety 24: 495–517.
26. Mesulam MM, Mufson EJ, Wainer BH, Levey AI (1983) Central cholinergic pathways in the rat: an overview based on an alternative nomenclature (Ch1–Ch6). Neuroscience 10: 1185–1201.
27. Picciotto MR, Higley MJ, Mineur YS (2012) Acetylcholine as a neuromodulator: cholinergic signaling shapes nervous system function and behavior. Neuron 76: 116–129.
28. Bierut LJ, Madden PA, Breslau N, Johnson EO, Hatsukami D, et al. (2007) Novel genes identified in a high-density genome wide association study for nicotine dependence. Hum Mol Genet 16: 24–35.
29. Nussbaum J, Xu Q, Payne TJ, Ma JZ, Huang W, et al. (2008) Significant association of the neurexin-1 gene (NRXN1) with nicotine dependence in European- and African-American smokers. Hum Mol Genet 17: 1569–1577.
30. Cozzari C, Howard J, Hartman B (1990) Analysis of epitopes on choline acetyltransferase (ChAT) using monoclonal antibodies. Soc Neurosci Abstr 16: 200.
31. Megías M, Emri Z, Freund TF, Gulyás AI (2001) Total number and distribution of inhibitory and excitatory synapses on hippocampal CA1 pyramidal cells. Neuroscience 102: 527–540.
32. Takács VT, Klausberger T, Somogyi P, Freund TF, Gulyás AI (2012) Extrinsic and local glutamatergic inputs of the rat hippocampal CA1 area differentially innervate pyramidal cells and interneurons. Hippocampus 22: 1379–1391.
33. Gulyás AI, Megías M, Emri Z, Freund TF (1999) Total number and ratio of excitatory and inhibitory synapses converging onto single interneurons of different types in the CA1 area of the rat hippocampus. J Neurosci 19: 10082–10097.
34. Umbriaco D, Watkins KC, Descarries L, Cozzari C, Hartman BK (1994) Ultrastructural and morphometric features of the acetylcholine innervation in adult rat parietal cortex: an electron microscopic study in serial sections. J Comp Neurol 348: 351–373.
35. Umbriaco D, Garcia S, Beaulieu C, Descarries L (1995) Relational features of acetylcholine, noradrenaline, serotonin and GABA axon terminals in the stratum radiatum of adult rat hippocampus (CA1). Hippocampus 5: 605–620.
36. Contant C, Umbriaco D, Garcia S, Watkins KC, Descarries L (1996) Ultrastructural characterization of the acetylcholine innervation in adult rat neostriatum. Neuroscience 71: 937–947.
37. Aznavour N, Mechawar N, Descarries L (2002) Comparative analysis of cholinergic innervation in the dorsal hippocampus of adult mouse and rat: a quantitative immunocytochemical study. Hippocampus 12: 206–217.
38. Mechawar N, Watkins KC, Descarries L (2002) Ultrastructural features of the acetylcholine innervation in the developing parietal cortex of rat. J Comp Neurol 443: 250–258.
39. Aznavour N, Watkins KC, Descarries L (2005) Postnatal development of the cholinergic innervation in the dorsal hippocampus of rat: Quantitative light and electron microscopic immunocytochemical study. J Comp Neurol 486: 61–75.
40. Craig AM, Kang Y (2007) Neurexin-neuroligin signaling in synapse development. Curr Opin Neurobiol 17: 43–52.
41. Tallafuss A, Constable JR, Washbourne P (2010) Organization of central synapses by adhesion molecules. Eur J Neurosci 32: 198–206.
42. Williams ME, de Wit J, Ghosh A (2010) Molecular mechanisms of synaptic specificity in developing neural circuits. Neuron 68: 9–18.
43. Sassoè-Pognetto M, Frola E, Pregno G, Briatore F, Patrizi A (2011) Understanding the molecular diversity of GABAergic synapses. Front Cell Neurosci 5: 4.
44. Fritschy JM, Panzanelli P, Tyagarajan SK (2012) Molecular and functional heterogeneity of GABAergic synapses. Cell Mol Life Sci 69: 2485–2499.
45. Kasugai Y, Swinny JD, Roberts JD, Dalezios Y, Fukazawa Y, et al. (2010) Quantitative localisation of synaptic and extrasynaptic GABAA receptor subunits on hippocampal pyramidal cells by freeze-fracture replica immunolabelling. Eur J Neurosci 32: 1868–1888.
46. Paxinos G, Franklin KBJ (2001) The Mouse Brain in Stereotaxic Coordinates. San Diego: Academic Press.
47. McGeer PL, McGeer EG, Fibiger HC, Wickson V (1971) Neostriatal choline acetylase and cholinesterase following selective brain lesions. Brain Res 35: 308–314.
48. Dong N, Qi J, Chen G (2007) Molecular reconstitution of functional GABAergic synapses with expression of neuroligin-2 and GABAA receptors. Mol Cell Neurosci 35: 14–23.
49. Hirao K, Hata Y, Ide N, Takeuchi M, Irie M, et al. (1998) A novel multiple PDZ domain-containing molecule interacting with N-methyl-D-aspartate receptors and neuronal cell adhesion proteins. J Biol Chem 273: 21105–21110.
50. Sumita K, Sato Y, Iida J, Kawata A, Hamano M, et al. (2007) Synaptic scaffolding molecule (S-SCAM) membrane-associated guanylate kinase with inverted organization (MAGI)-2 is associated with cell adhesion molecules at inhibitory synapses in rat hippocampal neurons. J Neurochem 100: 154–166.
51. Ross BS, Conroy WG (2008) Capabilities of neurexins in the chick ciliary ganglion. Dev Neurobiol 68: 409–419.
52. Rosenberg MM, Yang F, Mohn JL, Storer EK, Jacob MH (2010) The postsynaptic adenomatous polyposis coli (APC) multiprotein complex is required for localizing neuroligin and neurexin to neuronal nicotinic synapses in vivo. J Neurosci 30: 11073–11085.
53. Temburni MK, Rosenberg MM, Pathak N, McConnell R, Jacob MH (2004) Neuronal nicotinic synapse assembly requires the adenomatous polyposis coli tumor suppressor protein. J Neurosci 24: 6776–6784.
54. Rosenberg MM, Yang F, Giovanni M, Mohn JL, Temburni MK, et al. (2008) Adenomatous polyposis coli plays a key role, in vivo, in coordinating assembly of the neuronal nicotinic postsynaptic complex. Mol Cell Neurosci 38: 138–152.
55. Conroy WG, Nai Q, Ross B, Naughton G, Berg DK (2007) Postsynaptic neuroligin enhances presynaptic inputs at neuronal nicotinic synapses. Dev Biol 307: 79–91.
56. Parker MJ, Zhao S, Bredt DS, Sanes JR, Feng G (2004) PSD93 regulates synaptic stability at neuronal cholinergic synapses. J Neurosci 24: 378–388.
57. Poulopoulos A, Soykan T, Tuffy LP, Hammer M, Varoqueaux F, et al. (2012) Homodimerization and isoform-specific heterodimerization of neuroligins. Biochem J 446: 321–330.

58. Kohl C, Riccio O, Grosse J, Zanoletti O, Fournier C, et al. (2013) Hippocampal neuroligin-2 overexpression leads to reduced aggression and inhibited novelty reactivity in rats. PLoS One 8: e56871.
59. Dalvi A, Rodgers RJ (1996) GABAergic influences on plus-maze behaviour in mice. Psychopharmacology (Berl) 128: 380–397.
60. Zarrindast M, Rostami P, Sadeghi-Hariri M (2001) GABA(A) but not GABA(B) receptor stimulation induces antianxiety profile in rats. Pharmacol Biochem Behav 69: 9–15.
61. Zarrindast MR, Homayoun H, Babaie A, Etminani A, Gharib B (2000) Involvement of adrenergic and cholinergic systems in nicotine-induced anxiogenesis in mice. Eur J Pharmacol 407: 145–158.
62. Irvine EE, Cheeta S, File SE (2001) Tolerance to nicotine's effects in the elevated plus-maze and increased anxiety during withdrawal. Pharmacol Biochem Behav 68: 319–325.
63. Mineur YS, Obayemi A, Wigestrand MB, Fote GM, Calarco CA, et al. (2013) Cholinergic signaling in the hippocampus regulates social stress resilience and anxiety- and depression-like behavior. Proc Natl Acad Sci U S A 110: 3573–3578.
64. Picciotto MR, Brunzell DH, Caldarone BJ (2002) Effect of nicotine and nicotinic receptors on anxiety and depression. Neuroreport 13: 1097–1106.
65. Reese NB, Garcia-Rill E, Skinner RD (1995) The pedunculopontine nucleus – auditory input, arousal and pathophysiology. Prog Neurobiol 47: 105–133.
66. Shi L, Argenta AE, Winseck AK, Brunso-Bechtold JK (2004) Stereological quantification of GAD-67-immunoreactive neurons and boutons in the hippocampus of middle-aged and old Fischer 344 x Brown Norway rats. J Comp Neurol 478: 282–291.
67. Song C, Murray TA, Kimura R, Wakui M, Ellsworth K, et al. (2005) Role of alpha7-nicotinic acetylcholine receptors in tetanic stimulation-induced gamma oscillations in rat hippocampal slices. Neuropharmacology 48: 869–880.
68. Siok CJ, Rogers JA, Kocsis B, Hajós M (2006) Activation of alpha7 acetylcholine receptors augments stimulation-induced hippocampal theta oscillation. Eur J Neurosci 23: 570–574.
69. Yarnall A, Rochester L, Burn DJ (2011) The interplay of cholinergic function, attention, and falls in Parkinson's disease. Mov Disord 26: 2496–2503.
70. Miwa JM, Freedman R, Lester HA (2011) Neural systems governed by nicotinic acetylcholine receptors: emerging hypotheses. Neuron 70: 20–33.
71. Vizi ES, Kiss JP, Lendvai B (2004) Nonsynaptic communication in the central nervous system. Neurochem Int 45: 443–451.
72. Smiley JF, Morrell F, Mesulam MM (1997) Cholinergic synapses in human cerebral cortex: an ultrastructural study in serial sections. Exp Neurol 144: 361–368.
73. Turrini P, Casu MA, Wong TP, De Koninck Y, Ribeiro-da-Silva A, et al. (2001) Cholinergic nerve terminals establish classical synapses in the rat cerebral cortex: synaptic pattern and age-related atrophy. Neuroscience 105: 277–285.
74. Zimmerman G, Soreq H (2006) Termination and beyond: acetylcholinesterase as a modulator of synaptic transmission. Cell Tissue Res 326: 655–669.
75. Sarter M, Parikh V, Howe WM (2009) Phasic acetylcholine release and the volume transmission hypothesis: time to move on. Nat Rev Neurosci 10: 383–390.
76. Hoover DB, Muth EA, Jacobowitz DM (1978) A mapping of the distribution of acetycholine, choline acetyltransferase and acetylcholinesterase in discrete areas of rat brain. Brain Res 153: 295–306.

nature COMMUNICATIONS

ARTICLE

DOI: 10.1038/s41467-018-05136-1 OPEN

Co-transmission of acetylcholine and GABA regulates hippocampal states

Virág T. Takács[1], Csaba Cserép[1,4], Dániel Schlingloff[1,2], Balázs Pósfai[1], András Szőnyi[1,2], Katalin E. Sos[1,2], Zsuzsanna Környei[3], Ádám Dénes[3], Attila I. Gulyás[1], Tamás F. Freund[1] & Gábor Nyiri[1]

The basal forebrain cholinergic system is widely assumed to control cortical functions via non-synaptic transmission of a single neurotransmitter. Yet, we find that mouse hippocampal cholinergic terminals invariably establish GABAergic synapses, and their cholinergic vesicles dock at those synapses only. We demonstrate that these synapses do not co-release but co-transmit GABA and acetylcholine via different vesicles, whose release is triggered by distinct calcium channels. This co-transmission evokes composite postsynaptic potentials, which are mutually cross-regulated by presynaptic autoreceptors. Although postsynaptic cholinergic receptor distribution cannot be investigated, their response latencies suggest a focal, intra- and/or peri-synaptic localisation, while $GABA_A$ receptors are detected intra-synaptically. The GABAergic component alone effectively suppresses hippocampal sharp wave-ripples and epileptiform activity. Therefore, the differentially regulated GABAergic and cholinergic co-transmission suggests a hitherto unrecognised level of control over cortical states. This novel model of hippocampal cholinergic neurotransmission may lead to alternative pharmacotherapies after cholinergic deinnervation seen in neurodegenerative disorders.

[1] Laboratory of Cerebral Cortex Research Institute of Experimental Medicine, Hungarian Academy of Sciences, Szigony u 43, Budapest 1083, Hungary. [2] János Szentágothai Doctoral School of Neurosciences, Semmelweis University, Budapest 1085, Hungary. [3] Momentum Laboratory of Neuroimmunology, Institute of Experimental Medicine, Hungarian Academy of Sciences, Szigony u 43, Budapest 1083, Hungary. [4] Present address: Momentum Laboratory of Neuroimmunology, Institute of Experimental Medicine, Hungarian Academy of Sciences, Szigony u 43, Budapest 1083, Hungary. These authors contributed equally: Virág T. Takács, Csaba Cserép, Dániel Schlingloff. Correspondence and requests for materials should be addressed to G.N. (email: nyiri@koki.hu)

The cholinergic system arising from the basal forebrain[1,2] has a fundamental role in controlling cortical functions including attention[3], learning and memory[4], plasticity[5], sleep–wake alternation[6], and is implicated in neurodegenerative diseases[7].

Contemporary models of the basal forebrain cholinergic system and efforts to develop pro-cholinergic treatments have been based largely on the assumption that cholinergic cells release only a single transmitter and it is released non-synaptically[8–13]. The seemingly rare synapses on cholinergic fibres (see Supplementary Discussion) supported the concept of non-synaptic transmission. However, highly precise cholinergic transmission during reward and punishment[14], recordings of phasic release[10,15,16], and the dependence of hippocampal synaptic plasticity on the millisecond-scale timing of the cholinergic input[17] challenge this textbook model of non-synaptic transmission by cholinergic fibres.

Therefore, we hypothesised that all cholinergic terminals establish synapses. After immunolabeling, we analysed the real incidence of synapses, localised vesicle pools using STORM super-resolution imaging and we also localised membrane-docked neurotransmitter vesicles using electron tomography. Because previous data suggested the co-localisation of acetylcholine and GABA in retina and other brain areas[18–23], we also hypothesised that hippocampal cholinergic fibres may be GABAergic as well. Using immunolabelling and optogenetics combined with in vitro electrophysiology, we investigated the possible presence and subcellular regulation of hippocampal co-transmission of acetylcholine and GABA, and the role of its GABAergic component in controlling hippocampal network activity.

Challenging a decades-old model, we show that all hippocampal cholinergic terminals establish GABAergic synapses, where cholinergic vesicles are released as well, and these synapses evoke composite (hyperpolarising and depolarising) postsynaptic potentials. Our data suggest synaptic release and action of GABA and synaptic release and a focal, synaptic and/or peri-synaptic action of acetylcholine. GABA and acetylcholine transmissions are modulated by distinct calcium channels and were mutually regulated by presynaptic autoreceptors. We demonstrate here that synaptic release of GABA from cholinergic terminals alone can suppress hippocampal sharp wave-ripples effectively and it can attenuate hippocampal epileptiform activity as well.

Our data urge the re-interpretation of previous studies about the basal forebrain cholinergic system and offer a new explanation for the emergence of hippocampal epileptiform activity associated with Alzheimer's disease-related loss of cholinergic innervation.

Results

All hippocampal cholinergic axon terminals form synapses. Previous studies concluded that few cholinergic terminals form synapses (see Discussion and Supplementary Discussion). We hypothesised that all cholinergic terminals form synapses. By identifying synapses with neuroligin 2 (NL2) labelling (Fig. 1, Supplementary Figure 1[24],) on cholinergic fibres, we could test the incidence of synapses with three-dimensional serial electron microscopic reconstructions in the hippocampus. We reconstructed randomly selected, long axonal segments [6–33 µm, average: 21 µm, $n = 17$, labelled either with anti-choline acetyltransferase (ChAT) antibody in wild-type (WT) mice or with eYFP-adeno-associated viruses (AAV) injected in ChAT-Cre mice, Fig. 1, Supplementary Figure 1, Supplementary Table 4, for controls see Supplementary Note 7 and Supplementary Figure 2] and identified their synapses with NL2 or gephyrin immunogold labelling. All of them established synapses abundantly (Fig. 1, Supplementary Figure 1, Supplementary Note 1). The average density of synapses was 42 synapses/100 µm. Some of these contact sites would not have been considered synapses earlier, because of their weak membrane thickening and narrower intercellular synaptic gap (e.g. Figure 1a, synapse 2–3);[24] however, NL2 and gephyrin labelling clearly identified their active zones. For comparison, we have also reconstructed GABAergic axonal segments (labelled for cannabinoid receptor type-1, CB_1; $n = 2$, 18 and 29 µm, Supplementary Figure 1, Supplementary Table 4), which are known to establish synapses abundantly. Having verified that all hippocampal cholinergic terminals originate from basal forebrain cholinergic cells (for controls see Supplementary Note 7 and Supplementary Figure 2), we found that practically all hippocampal cholinergic terminals examined established one or more NL2-positive synapses (Fig. 1, Supplementary Figure 1; Supplementary Table 4, Supplementary Note 1). As a consequence, the linear density of synapses along cholinergic axons was similar to that along GABAergic axons (Supplementary Figure 1, Supplementary Table 4, number of synapses per 100 µm cholinergic axons: 42 in CA1, 40 in S1, number of synapses per 100 µm CB_1-positive axons: 51).

Using electron microscopy in hippocampal CA1, we found that NL2 and gephyrin positive cholinergic synapses ($n = 107$, collected from four mice) predominantly innervated pyramidal dendritic shafts (63%) and spine-necks (27%), and they also innervated interneuron dendrites (5%), while some (6%) postsynaptic targets could not be classified (Fig. 1o, Supplementary Table 4).

All innervated spines received another, putatively glutamatergic asymmetric, type-I input from an unlabelled terminal, suggesting that, contrary to previous suggestion[25], cholinergic synapses alone do not induce spine formation. These data suggest that about 90% of these synapses target pyramidal cells in CA1, whereas they also innervate interneurons (at least 5%), which ratio is close to the neuronal ratios in CA1.

We tested whether these synapses are GABAergic as well. First, we localised the elements of postsynaptic GABAergic signalling machinery in these contacts. We localised gephyrin first, because it is known to interact with both $GABA_A$ receptors and NL2. We found, that at least 81% of synapses on hippocampal cholinergic fibres contained gephyrin postsynaptically, on dendrites and spine-necks (Fig. 1, Supplementary Note 2, Supplementary Table 3). In addition, we found that at least 80% of these synapses showed $GABA_A$ receptor gamma2 subunit labelling that was also readily detected on both dendrites and spine-necks (Fig. 1, Supplementary Figure 1, Supplementary Table 3, and Supplementary Note 2).

Then, we localised the elements of presynaptic GABAergic and cholinergic signalling machinery in these terminals. By crossing a zsGreen fluorescent reporter mouse-line with a vesicular GABA transporter (vGAT)-Cre mouse line and labelling the medial septum for ChAT, we found that all septo-hippocampal cholinergic cells are also vGAT positive (Fig. 2a, b, Supplementary Note 3). Hippocampal cholinergic terminals expressed the GABA-synthesising enzyme, glutamate decarboxylase 65 (GAD65) as well (Supplementary Note 3, Fig. 2c). In addition, at least 83% of cholinergic septo-hippocampal terminals were vGAT positive (Fig. 2d, Supplementary Note 3), whereas vesicular acetylcholine transporter (vAChT) was detected in 64% of the septo-hippocampal cholinergic terminals (Supplementary Note 4, 5). Finally, using postembedding immunogold staining, we showed that GABA is detectable in cholinergic terminals (Fig. 2e, f, Supplementary Note 3).

Composite GABAergic–cholinergic postsynaptic responses. We investigated the electrophysiological properties of these

dc_1777_20

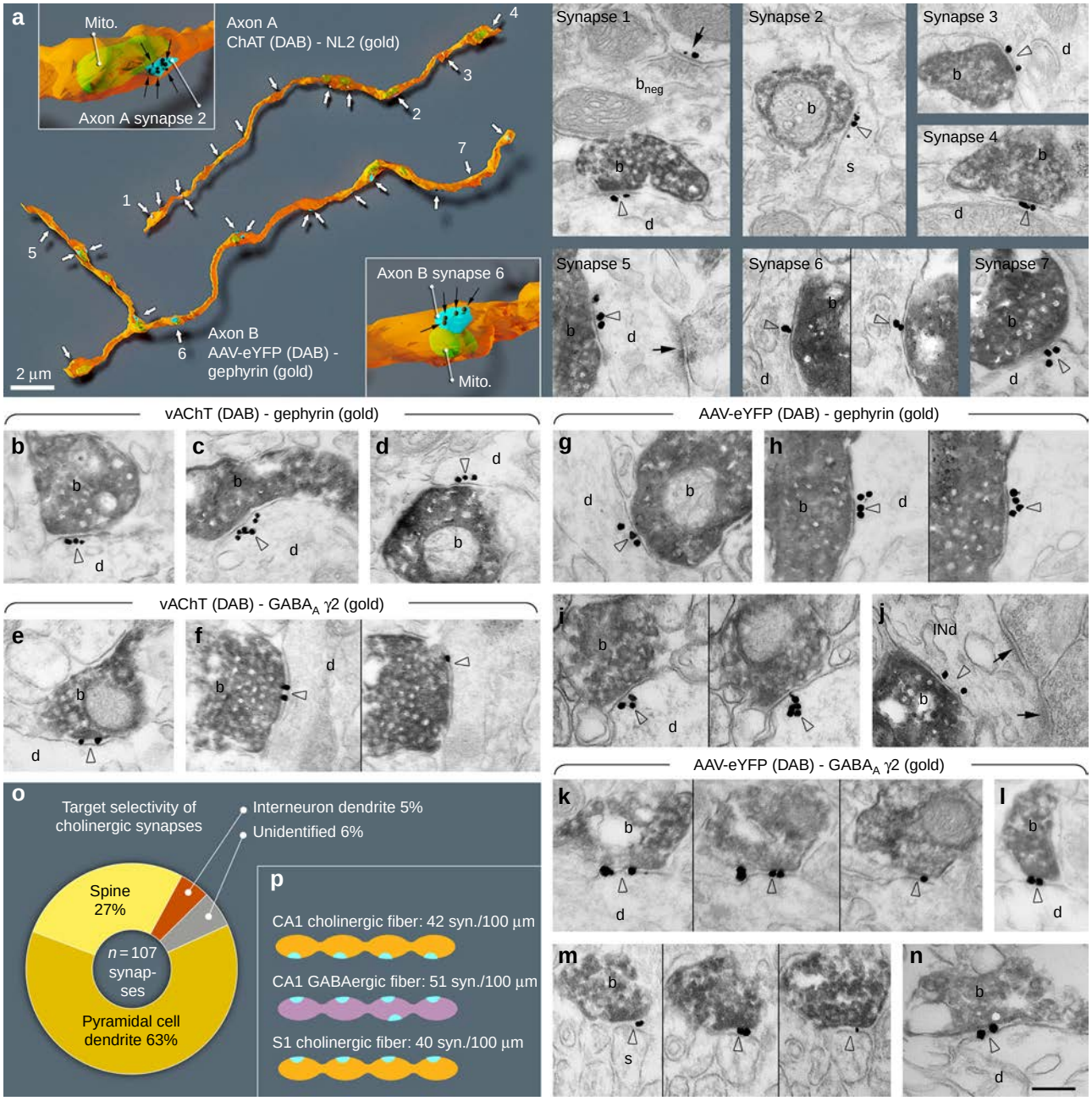

Fig. 1 All cholinergic terminals establish synapses, express GABAergic markers and innervate pyramidal cells or interneurons. **a** Three-dimensional EM reconstructions show that hippocampal cholinergic fibres form synapses (arrows) frequently. Axon A is labelled for ChAT in a WT mouse. Axon B is an AAV-eYFP virus-labelled septo-hippocampal fibre in a ChAT-Cre mouse. Insets show two typical terminals with synapses (blue). The plasma membrane was made partially transparent to reveal mitochondria (mito, green). Gold labellings of NL2 (axon A, synapse 1–4) or gephyrin (axon B, synapse 5–7) were used to recognise synapses (black dots and arrows in the insets). EM images show terminal boutons (b) of the reconstructed axonal segments establishing synapses 1–7 (arrowheads, indicated by the same numbers on the left) on dendrites (d) and a spine (s). Next to synapse 1, a ChAT-negative, putative GABAergic terminal bouton (b_{neg}) forming a NL2-positive synapse (arrow) is also shown. **b**–**n** EM images reveal the presence of gephyrin (arrowheads, gold; **b**–**d**; **g**–**j**) and GABA$_A$ γ2 receptor subunits (arrowheads, gold; **e**–**f**; **k**–**n**) postsynaptically in synapses established by vAChT-positive terminals in WT mice (**b**–**f**; DAB, b) or by AAV-eYFP-labelled septo-hippocampal terminals in ChAT-Cre mice (**g**–**n**; DAB, b). Images of consecutive sections are separated by thin black lines. Terminals innervate dendrites (d) or spines (s). In **j**, the postsynaptic target is an interneuron dendrite (INd) that receives type-I synapses as well (arrows). Synapses are from str. ori. (**a**, **b**–**e**, **g**–**j**, **l**, **m**), str. rad. (**k**, **n**) and str. l-m (**f**). Scale bar is 200 nm for all EM images. **o** Postsynaptic target selectivity of reconstructed cholinergic axonal segments from str. oriens and radiatum. Spine: 27.1%, pyramidal cell dendrite: 62.6%, interneuron dendrite: 4.7%, unidentifiable: 5.6%. **p** Comparison of the number of synapses per 100 µm cholinergic axonal segments in CA1 and S1 cortex and GABAergic fibres in CA1

cholinergic responses in target neurons. We injected Cre-dependent, channelrhodopsin-2 (ChR2) expressing adeno-associated virus (AAV-ChR2) into the medial septum of ChAT-Cre knock-in mice (Fig. 3a, see Methods) and recorded hippocampal cells. AAV-ChR2 labelled only cholinergic cells in the septo-hippocampal pathway (see Supplementary Note 7) and cells of wild-type mice did not respond to illumination, proving that membrane potential responses in ChAT-Cre mice were

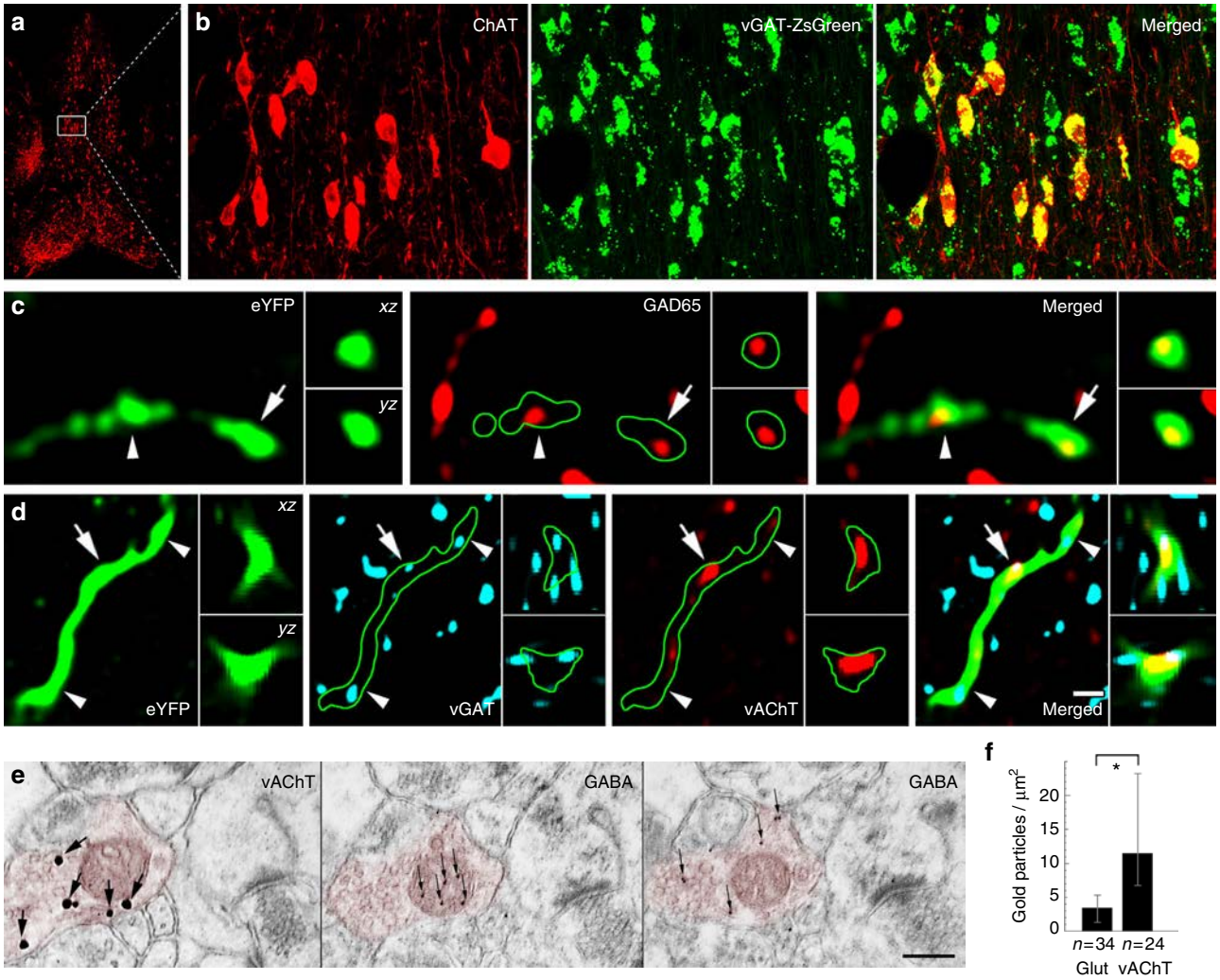

Fig. 2 Cholinergic cells express the molecular machinery required for GABA release. **a**, **b** The cholinergic neurons of the MS are GABAergic. White box in **a** contains area enlarged in **b**. Images show neurons stained for ChAT in red, while the green labelling marks the vGAT-expressing neurons in vGAT-ZsGreen reporter mouse. **c**, **d** AAV-eYFP virus-traced septo-hippocampal fibres express GAD65 (**c**). AAV-eYFP virus-traced septo-hippocampal fibres express vGAT and vAChT (**d**). Insets show *xz* and *yz* projections of the terminal labelled with an arrow. Arrowhead points to another terminal. Green line marks the fibre outline. (Scale bar on **d** is 210, 14, 2 and 1 µm for **a**, **b**, **c** and **d**, respectively.) **e**, **f** Hippocampal cholinergic terminals contain GABA. Three consecutive EM sections of a vAChT-positive terminal (**e**, red pseudocolor) are shown. vAChT was visualised by pre-embedding immunogold method (the first panel of **e**, silver-intensified gold particles, large arrows), whereas on the next ultrathin sections (the second and third panels of **e**) postembedding GABA immunostaining was performed (smaller gold particles, thin arrows, some GABA molecules penetrate into mitochondria during fixation). vAChT signal is absent in postembedding images, because of the etching procedure. Scale bar is 200 nm for all EM images. **f** Cholinergic terminals contained significantly higher immunogold signal than glutamatergic ones ($p < 0.05$) suggesting the presence of GABA in cholinergic terminals (median and interquartile ranges, Supplementary Note 8)

caused only by cholinergic fibres. NMDA- and AMPA-type glutamate receptors were blocked to prevent polysynaptic recruitment of neuronal activity in all in vitro recordings presented in Fig. 3.

We recorded the membrane potential of inhibitory neurons in CA1 str. lacunosum-moleculare, because they are known to display cholinergic responses[26]. Cells were recorded using whole-cell patch-clamp in responses to 1 ms optical stimulation (Fig. 3a) that resulted in a composite membrane potential response: a $GABA_A$ receptor-dependent hyperpolarization (peak @ 13.8 ms), and a slightly delayed (peak @ 92 ms) acetylcholine receptor-dependent depolarisation (Fig. 3c–e, Supplementary Figure 3A–C). Although these synaptically released transmitters may act on non-synaptic receptors as well, both responses had relatively short onset latency (2.8 and 7.4 ms, Supplementary Figure 3A–C) compared to typical non-synaptic transmission that has a typical evoked onset latency of about 60–160 ms[27]. Together with our anatomical data these suggest synaptic release and action of GABA and synaptic release and a very focal, synaptic and/or peri-synaptic action of acetylcholine. Synaptic spill-over of GABA and acetylcholine may act extrasynaptically as well.

Next, we blocked both nicotinic and muscarinic acetylcholine receptors (AChR) and recorded inhibitory postsynaptic currents (IPSC) on pyramidal cells (PCs) and interneurons (INs) after optical stimulation of cholinergic fibres (Fig. 3f–i). Single IPSC kinetics and short-term plasticity in PCs and INs were tested using five short light pulses at physiologically relevant firing rates (at 2, 5, 10 and 20 Hz) measured in vivo[28,29]. The amplitude of the evoked inhibitory currents (calculated for the first stimulus) was larger on INs than on PCs, but their rise time (20–80%) was not significantly different. IPSCs evoked in INs had a shorter decay time (Fig. 3h). The series of light pulses revealed strong short-term depression (STD) of inhibitory currents onto both PCs and INs (Fig. 3g, i). GABAergic STD was observed in every tested

dc_1777_20

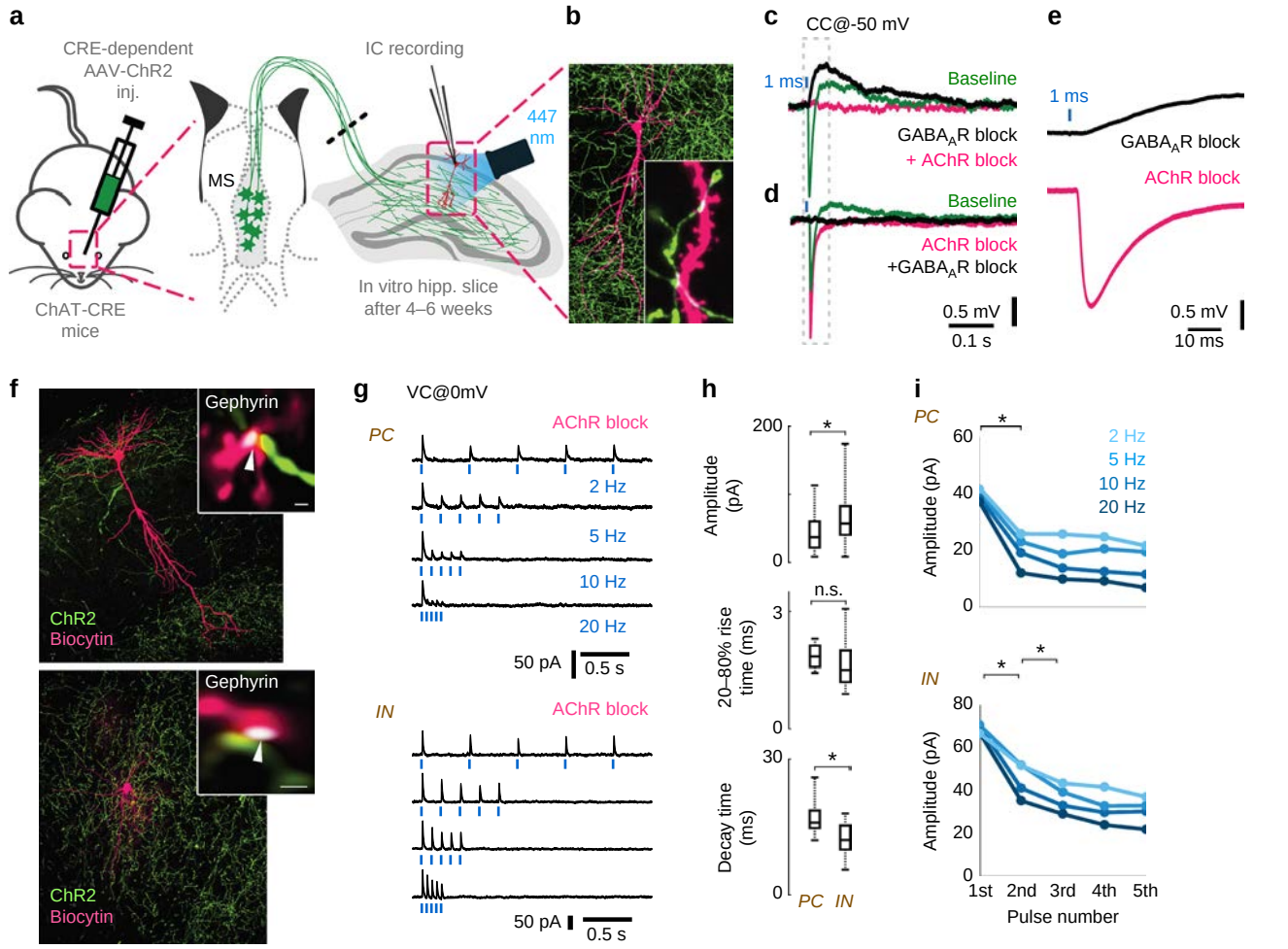

Fig. 3 Optogenetic stimulation of cholinergic fibres elicits composite GABAergic and cholinergic postsynaptic responses. **a** Medial septum (MS) of ChAT-Cre mice were injected with Cre-dependent AAV containing Channelrhodopsin-2 (ChR2). Using whole-cell patch-clamp in horizontal hippocampal slices, we recorded voltage or current response from hippocampal neurons upon optical excitation of septo-hippocampal cholinergic fibres. NMDA and AMPA receptors were blocked with AP5 (50 µM) and NBQX (20 µM) in all experiments presented in Figs. 3 and 5. **b** Representative post-hoc visualised CA1 pyramidal cell (magenta) and the surrounding cholinergic fibres (green) with putative contacts (inset, white arrowheads). **c** Blue light pulses elicited a composite membrane potential response from str. lacunosum-moleculare inhibitory neurons (green, average of 50 stimulations). Inhibition of $GABA_A$Rs (10 µM gabazine) abolishes the hyperpolarising component (nine from nine tested cells), resulting in a putative cholinergic excitatory potential (black). Inhibition of all AChRs (1 µM MLA, 1 µM DHβE, 10 µM atropine, four from four tested cells) blocks the remaining depolarising response (magenta). **d** Conversely, first blocking the AChRs, resulted in a putative GABAergic IPSP (magenta), which was blocked by $GABA_A$Rs inhibitor gabazine (black). The increase of IPSP amplitude for AChR block is addressed in Fig. 5. **e** Magnified cholinergic EPSP (black) from **c**, and GABAergic IPSP from **d** (magenta) demonstrate their short latency (see also Supplementary Figure 3). **f** A representative recorded pyramidal cell (PC, top) and an inhibitory neuron (IN, bottom) post-hoc visualised in magenta and ChR2 positive cholinergic axons in green. Insets: Immunostaining for gephyrin (white) identify their putative synapses (white arrows). **g** We blocked both nicotinic and muscarinic AChRs (1 µM MLA, 1 µM DHβE, 10 µM atropine) and recorded inhibitory postsynaptic currents (IPSC) evoked by cholinergic fibre illumination. Traces show IPSC response of a PC and an IN to five light pulses (1 ms) at increasing stimulation frequencies (2, 5, 10, 20 Hz, cells were recorded in VC@0 mV). **h** Amplitude and decay time of unitary GABAergic IPSCs from pyramidal cells ($n = 5$) and inhibitory neurons ($n = 16$) were statistically different ($p < 0.05$), while their rise time was not different (median values, interquartile ranges and min/max values, see Supplementary Note 8). **i** Averages of IPSC amplitudes for the five pulses presented on **g** shows strong short-term depression (STD) of GABAergic transmission evoked by stimulating cholinergic fibres (for details see Supplementary Note 8 and Supplementary Figure 3)

neuron and was accompanied by a decrease in transmission probability during the stimulation sequence (Supplementary Figure 3), suggesting a presynaptic mechanism for STD.

Calcium influx through ChR2 expressed on axon terminals can alter intrinsic short-term plasticity of the synapses[30]. To exclude this possibility, we used a digital micro-mirror device (DMD) inserted into the optical path of the microscope, to illuminate cholinergic axons running towards the recorded cell, but not the terminals (Supplementary Figure 3D). This resulted in STD similar to that recorded with optic fibre illumination (Supplementary Figure 3E–F), excluding the possibility of ChR2-mediated Ca^{2+} influx, as the reason for the observed STD. A series of stimuli could also decrease the driving force of chloride through $GABA_A$Rs, resulting in apparent STD[31,32]. In this case, the putative site of STD would be postsynaptic instead of presynaptic. When we used a high Cl^- intracellular solution to prevent shifts in Cl^- reversal, a series of stimuli resulted in STD similar to that shown above (Supplementary Figure 3G and H).

Cholinergic and GABAergic vesicle docking is restricted to synapses. Our physiological and anatomical data showed that cholinergic terminals establish synapses. Non-synaptic

acetylcholine release, however, might still be possible, if cholinergic vesicles could be docked and fused outside of the synaptic active zones as well. Using advanced electron tomography tools, we were able to reconstruct cholinergic fibre segments, to localise vesicles with 1 nm resolution and to analyse the precise distribution of synaptic vesicles in hippocampal cholinergic terminals. We identified terminals using vAChT immunogold labelling and reconstructed them using electron tomography (Fig. 4a–d). Three-dimensional reconstruction revealed that synaptic vesicles clustered close to the active zones (Fig. 4d). We measured the distances of vesicles to the closest (synaptic or non-synaptic) cell membranes, and compared their density at different distance intervals from the membranes (Fig. 4f). The density of the vesicles within 60 nm from the membranes was 6.5 times higher in the synaptic active zone than extrasynaptically (Fig. 4d, f). We did not find any docked (<5 nm from the membrane) or fused (undergoing exocytotic fusion) vesicles non-synaptically, but we detected both of these at synapses (Fig. 4b, c, f). The distribution of vesicles in cholinergic terminals was similar to that found at other glutamatergic or GABAergic terminals, arguing against non-synaptic vesicular docking or release in cholinergic terminals.

Vesicular volume can correlate with its transmitter content[33]. Therefore, using electron tomography, we compared the vesicular morphology between cholinergic and GABAergic terminals (Fig. 4e). Vesicles of cholinergic terminals were significantly ($p < 0.001$), about 60% larger than those in GABAergic terminals (Fig. 4e, Supplementary Note 4) and their volumes were significantly more variable as well ($p < 0.001$). Smaller (putatively GABAergic) vesicles of cholinergic terminals were similar to those in purely GABAergic terminals (Fig. 4e, see Supplementary Note 4), suggesting an even larger difference between the two types of vesicles.

Acetylcholine and GABA in different vesicles and same vesicle pool. To further confirm that the two transmitter systems use the same active zones, we used confocal fluorescent imaging in mouse hippocampus and found that vAChT-positive vesicles were concentrated at gephyrin-labelled synapses (Fig. 4g, h, Supplementary Note 5). Scale-free analysis confirmed that the likelihood of vAChT labelling was the highest at the gephyrin-labelled synaptic active zones (Fig. 4i, Supplementary Note 5).

Using super-resolution STORM imaging of vGAT and vAChT immunolabelling, combined with correlated fluorescent confocal laser-scanning microscopy (CLSM) of cholinergic fibres, we demonstrated that cholinergic–GABAergic vesicle pools were mixed and were confined to a small volume of the AAV-eYFP-labelled septo-hippocampal terminals (Fig. 4j, Supplementary Note 5).

Using isolated mouse cortical synaptic vesicles (neocortex and hippocampus, in ~4:1 ratio), we found that acetylcholine and GABA are packed into different vesicles (Supplementary Figure 4A, Supplementary Note 6). Both flow cytometry (Supplementary Figure 4B) and electron microscopy data (Supplementary Figure 4C, E) confirmed the purity of our sample (see also Supplementary Note 6 and Methods). All vesicles were labelled with synaptophysin (SYP). After quadruple-immunolabelling of the isolated synaptic vesicles, 29% were only SYP-positive, 45% were double labelled for vesicular glutamate transporter 1 and SYP, 14% were double labelled for vGAT and SYP, 11% were double labelled for vAChT and SYP. Only a negligible amount of vesicles (0.9%) were triple labelled with any combinations and only 0.14% of all vesicles were co-labelled for vAChT and vGAT, suggesting that vesicular transporters for GABA and acetylcholine are expressed by distinct vesicle populations in cortical samples (Supplementary Figure 4H; Supplementary Note 6).

Different Ca-channel and mutual autoreceptor modulation. Our anatomical data indicated that acetylcholine and GABA are stored in, and thus likely released from different vesicles. First, we investigated presynaptic modulation of this vesicular release. Blocking AChRs increased the amplitude of GABAergic hyperpolarization (Fig. 3d), for which presynaptic muscarinic receptors may be responsible[26]. We held CA1 interneurons at −50 mV, to record GABAergic hyperpolarization and cholinergic depolarisation concurrently (Fig. 5a, NMDA- and AMPA-type glutamate receptors were blocked to prevent polysynaptic recruitment of neuronal activity in all in vitro recordings presented in Fig. 5). Muscarinic receptor blocker atropine (10 µM) significantly increased the amplitude of both GABAergic IPSPs and cholinergic EPSPs (Fig. 5b). By blocking M2-type AChRs, reported abundant in hippocampal cholinergic terminals[26,34], we reproduced PSP increases evoked by atropine (Fig. 5c). This confirms the role of M2-type AChRs in regulating both acetylcholine and GABA release from cholinergic terminals.

Previously, we described the presence of presynaptic $GABA_B$ autoreceptors in septal cholinergic cells[35]. To test their role in regulating synaptic co-transmission, we blocked $GABA_B$ receptors. This led to a significant increase in the amplitude of both GABAergic IPSPs and cholinergic EPSPs (Fig. 5d). However, we did not see $GABA_B$ receptor-dependent postsynaptic hyperpolarization in response to cholinergic fibre stimulation in our recordings. Overall, these experiments revealed that GABA and acetylcholine cross- and auto-regulate their co-transmission from cholinergic–GABAergic terminals, presynaptically.

Dynamics of vesicle release likely depends on the type of voltage-dependent calcium channels (VDCCs), which mediate Ca^{2+}-triggered vesicle release[36]. However, different VDCCs in the same cell[20] can be associated with distinct types of vesicles. Indeed, we found that selective blockade of P/Q-type calcium channels decreased GABAergic IPSPs significantly, but caused no change in the cholinergic components (Fig. 5e). Conversely, the cholinergic component was robustly decreased after the selective blockade of N-type calcium channels, while GABAergic IPSPs showed no significant change (Fig. 5f). Besides confirming the presence of different vesicular pools, this revealed different molecular pathways for their regulation during co-transmission.

Distinct vesicle pools of the same terminals can couple to different release mechanisms with different short-term plasticity[20]. Because GABAergic transmission always showed strong STD in cholinergic terminals (Fig. 3g, i), we examined, whether cholinergic responses display similar short-term dynamics. We recorded inhibitory neurons in the physiologically relevant current clamp ($I = 0$) situation, and repeatedly light-stimulated ChR2-expressing cholinergic axons (Supplementary Figure 3J). The net depolarisation for a series of five stimuli did not decrease. Also, the area under the voltage curve increased with frequency (Supplementary Figure 3J–K). In current clamp (more than in voltage clamp) even a non-depressing transmission could be seen as depressing due to reduction of driving force. Therefore, based on our current clamp measurements, it is highly unlikely that the cholinergic component would show such a strong STD as the GABAergic component.

GABA release of cholinergic cells shape hippocampal states. Septal cholinergic neurons control hippocampal activity states[37,38] and suppress in vivo sharp wave-ripples (SWR) in the hippocampus[39]. However, the effect of their hippocampal GABA release has not been investigated. We recorded spontaneous

dc_1777_20

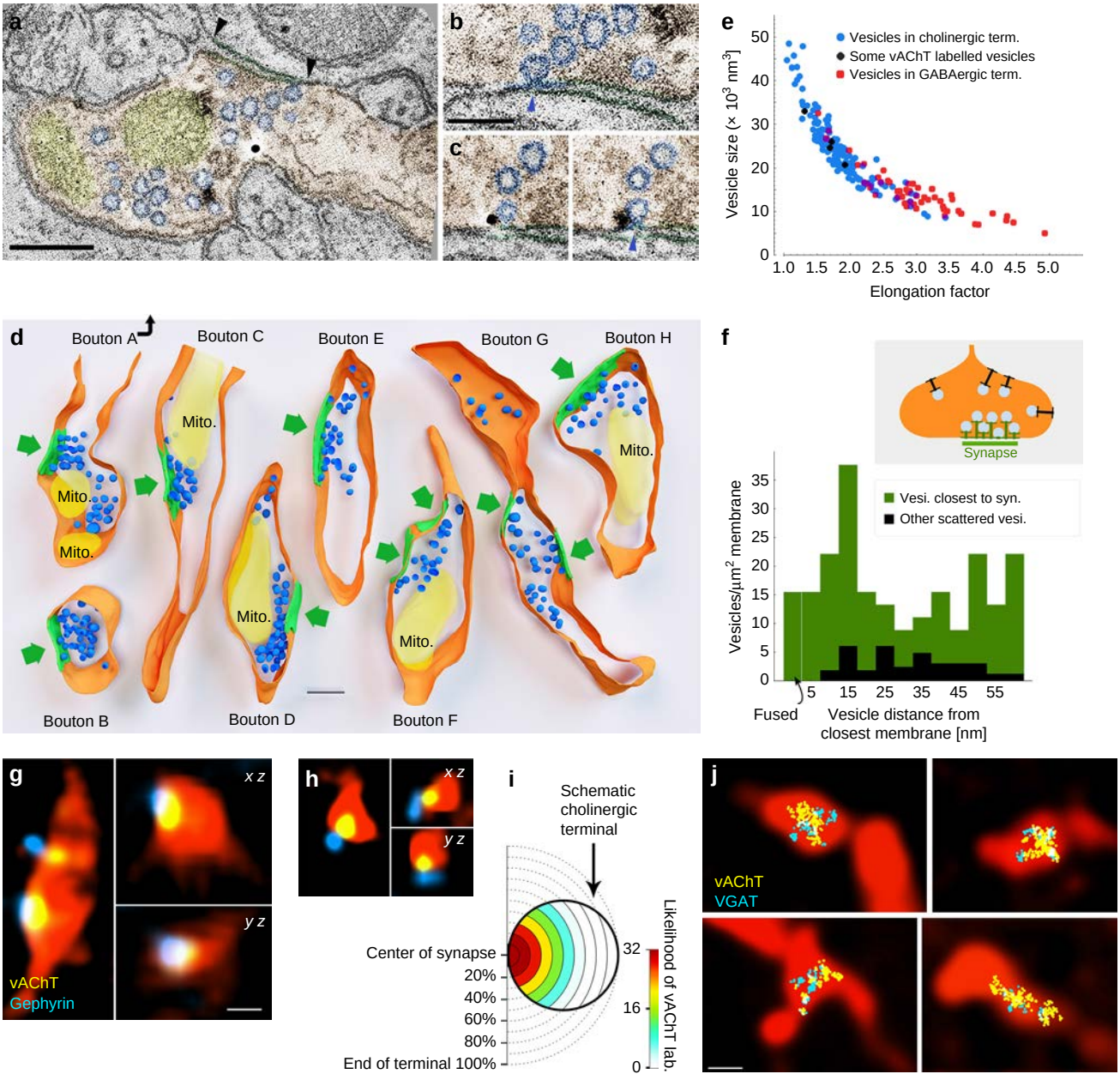

Fig. 4 Separate vesicular release of acetylcholine and GABA from the same synaptic active zones. **a**–**c** About 0.5 nm-thick virtual sections from electron tomographic reconstructions of cholinergic terminals. Terminal is orange, mitochondria are yellow, synaptic vesicles are blue. Black arrowheads point to the edges of the synapse. Scale bar is 200 nm. **b** Active zone is enlarged from **a**. The omega-shaped vesicle is being fused with the terminal membrane (blue arrowhead). **c** Two serial virtual sections showing a portion of the active zone of another terminal. A fused synaptic vesicle (blue arrowhead) is labelled for vesicular acetylcholine transporter (black immunogold particle). Scale bar for **b** and **c** is 100 nm. **d** Three-dimensional models of reconstructed terminals. Terminal membranes are orange, mitochondria are yellow, synaptic vesicles are blue and synapses are green. Green arrows point to the synapses. Scale bar is 200 nm. The association of the vesicle pools to the active zones is evident. **e** Scatterplot shows the relationship of vesicle size (volume) and elongation factor in the sampled vesicles. Vesicles in the cholinergic terminals had a broader size-distribution than vesicles of purely GABAergic terminals, which were smaller and more elongated (Supplementary Note 4). Some vesicles (black markers) could be identified as vAChT-positive because immunogold particles clearly labelled them. **f** The density of the vesicles within a 60-nm-wide band from the membrane is plotted as a function of distance from the terminal membrane at synaptic (green) and extra-synaptic (black) areas. Vesicle density was 6.5 times higher (in the first 60 nm from the membrane) in the synaptic active zone than extrasynaptically ($n = 183$ vesicles from 8 terminals in 2 mice). Docked (closer to the membrane than 5 nm) or fused (undergoing exocytotic fusion) vesicles were absent extrasynaptically, but were present in the active zones. **g**, **h** vAChT labelling was confined to synaptic active zones in cholinergic fibres. CLSM images show terminals of virus-traced septo-hippocampal fibres (red pseudocolor) containing vAChT-positive vesicle pools (yellow), localised to the synaptic active zones that are identified by gephyrin labelling (blue). Scale bar is 500 nm for **g** and **h**. **i** Scale-free analysis confirms that the likelihood of vAChT labelling is the highest at the synaptic active zones ($n = 32$ synapses, 2 mice). **j** Correlated CLSM-STORM super-resolution microscopy images show that vAChT (yellow) and vGAT (cyan) vesicle pools are overlapping and are confined to small portions within AAV-eYFP virus-traced septo-hippocampal fibres (red pseudocolor)

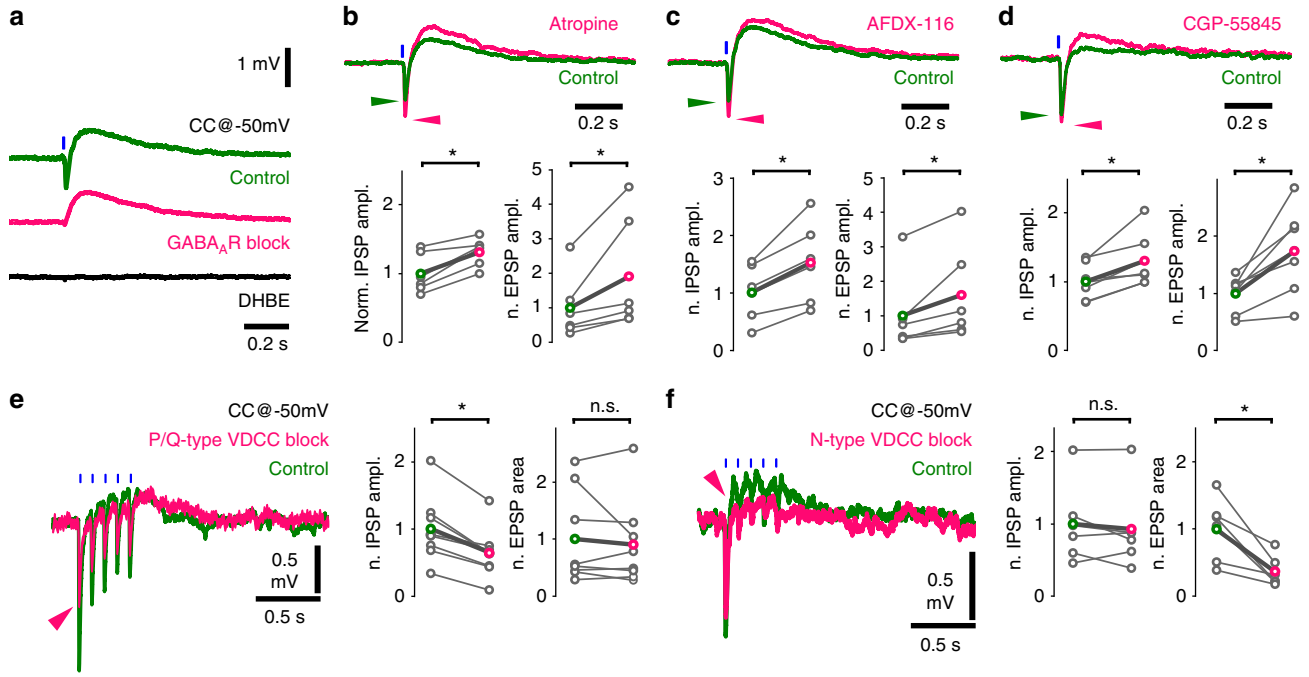

Fig. 5 Co-transmission of GABA and acetylcholine is cross-regulated by autoreceptors and mediated by distinct calcium channels. **a** Optical stimulations of cholinergic fibres trigger composite membrane potential responses (average of 50 traces) of an inhibitory neuron recorded in str. lacunosum-moleculare (green). Cells were held at approximately −50 mV to record hyperpolarising and depolarising components concurrently. Early hyperpolarization was confirmed to be of GABAergic origin by bath application of the GABA$_A$R blocker gabazine (magenta, 10 µM, which abolished quick hyperpolarization in 9 out of 9 tested cells), while the late depolarisation was confirmed to be cholinergic by the application of the alpha4-type nicotinic acetylcholine receptor blocker DHβE (black, 1 µM, which abolished depolarisation in 5 out of 5 tested cells). Cells with identifiable nicotinic responses were used to further investigate the properties of GABA and acetylcholine release from cholinergic fibres. **b** Increase in GABAergic response after AChR block (Fig. 3d) suggested that presynaptic muscarinic receptors cross-modulated GABA (and possibly ACh) release from cholinergic fibres. Therefore, putative presynaptic muscarinic receptors were selectively inhibited via bath application of atropine ($n = 6$), which led to a significant increase in amplitude of both the GABAergic hyperpolarization and nicotinic depolarisation (green, see Supplementary Note 8). **c** Bath application of the selective M2 antagonist AFDX-116 (10 µM, $n = 6$) resulted in changes similar to that of atropine application (for data see Supplementary Note 8). **d** Blocking GABA$_B$Rs with CGP-55845 (1 µM, $n = 7$) also resulted in increased GABAergic and cholinergic responses suggesting a dual modulatory role (for data see Supplementary Note 8). **e**, **f** Testing roles of distinct voltage-dependent calcium channels (VDCC) in release of GABA and ACh . **e** Blockade of P/Q-type VDCC, using selective antagonist ω-agatoxin (1 µM, puff application), reliably decreased GABAergic response component but did not alter cholinergic component. At control conditions, 5 short (1 ms) light pulses at 10 Hz evoked a composite event of GABAergic hyperpolarization and cholinergic depolarisation (green, average of 20 traces). In response to ω-agatoxin application (magenta, $n = 9$), the GABAergic component (measured as IPSP amplitude) decreased robustly (magenta arrowhead) and the cholinergic component (measured as EPSP area) showed no change (for details see Supplementary Note 8). **f** Blockade of N-type VDCC, using selective blocker ω-conotoxin (1 µM), reliably reduced cholinergic response component ($n = 6$) but left GABAergic component unchanged (for details see Supplementary Note 4)

SWRs in hippocampal slices (Fig. 6, Methods). Illumination of control slices without ChR2 expression caused no change in SWR activity. In AAV-ChR2-infected ChAT-Cre mice, we found that without blocking cholinergic transmission, optical stimulation of cholinergic fibres decreased SWR rate significantly (Fig. 6c, d), followed by a transient increase in SWR rate after the cessation of optical stimuli. However, when cholinergic transmission was blocked, the same optical stimulation caused a similar decrease in SWR rate (Fig. 6e, f), with no rebound after stimulation. Although cholinergic fibres have been reported to be responsible for inhibiting SWRs[39], here we demonstrated that GABA release from cholinergic synapses alone is sufficient to downregulate the rate of SWRs.

The GABA release from septo-hippocampal cholinergic fibres may also affect the occurrence of hippocampal epileptiform activity. Therefore, we examined the effect of GABA release from cholinergic axons in the in vitro high potassium epilepsy model (Fig. 6g–k)[40,41]. Optical stimulation of cholinergic fibres reduced the rate of epileptiform events (Fig. 6h, i) and a similar reduction was present, when AChRs were blocked (Fig. 6j, k). These results demonstrated that synaptic transmission of GABA from cholinergic fibres alone can effectively control hippocampal epileptiform activity.

Discussion

Our results challenge the model of non-synaptic single transmitter release from cholinergic fibres in the hippocampus and demonstrate that all cholinergic terminals establish synapses, where GABA and acetylcholine are released into the same synaptic gap. Our results also show non-synaptic action of these synaptically released transmitters. We showed that hippocampal cholinergic terminals established effective GABAergic synapses as well. Cholinergic fibres are among the densest and most influential subcortical pathways in hippocampus; therefore, our findings suggest a fundamental change in our view of the regulation of hippocampal states. We also found that acetylcholine and GABA were not co-released but co-transmitted from the same synaptic active zone. We confirmed this by showing that (i) isolated cortical transmitter vesicles do not co-express vGAT and vAChT, (ii) they are preferentially modulated by distinct voltage-

dc_1777_20

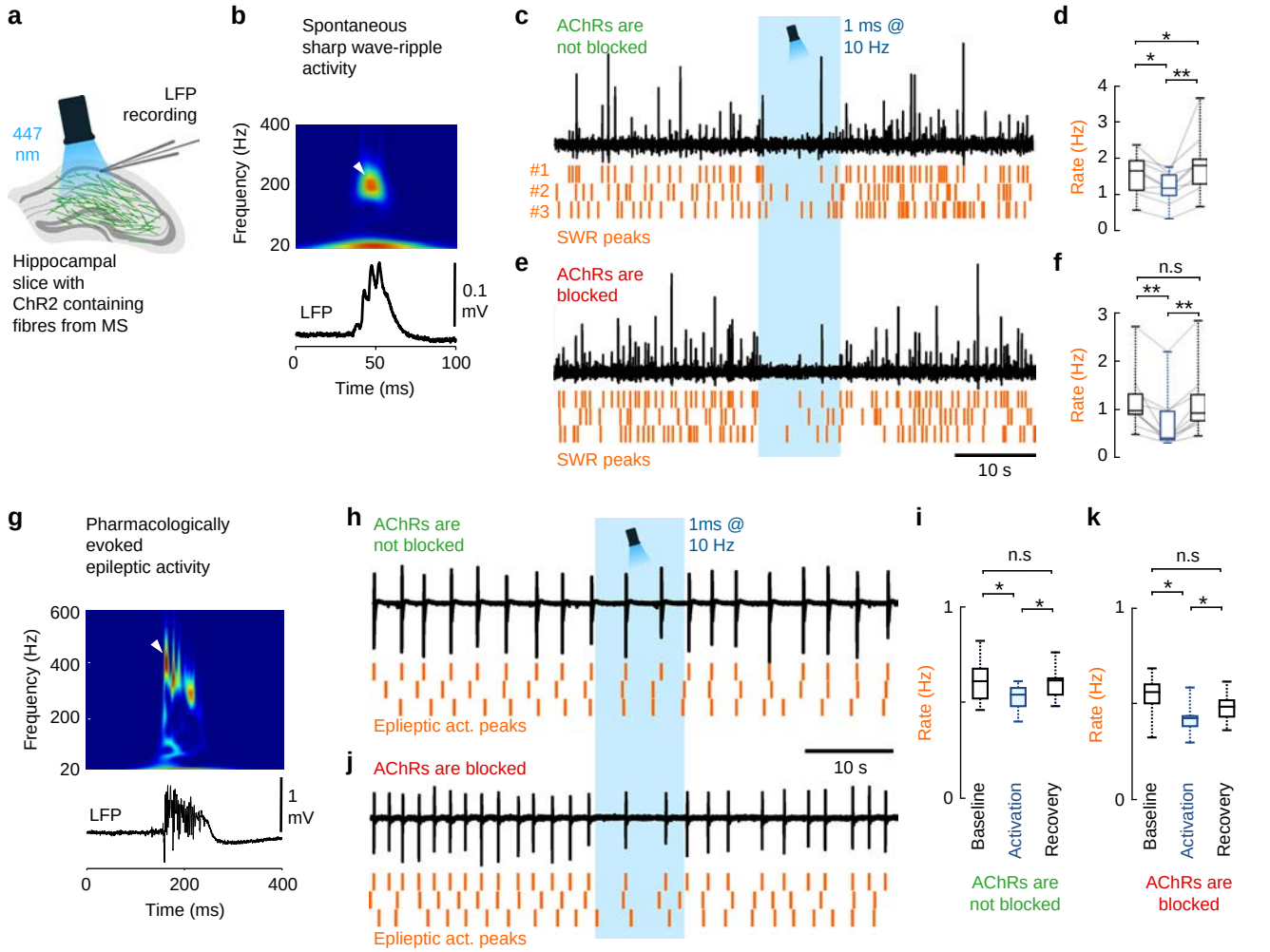

Fig. 6 GABA release from cholinergic terminals controls healthy and pathological hippocampal network activity. **a** To understand the functional impact of GABA and acetylcholine co-transmission onto cortical network oscillations, local field potential (LFP) was recorded with standard patch pipettes from the CA1 area of thick hippocampal slices. These slices generated healthy and pathological in vivo like activity patterns. Cholinergic fibres expressing ChR2 were illuminated with blue light in the presence, or in the absence of AChR blockers parallel with LFP recordings. **b** A spontaneous sharp wave-ripple (SWR) LFP signature (bottom), and its wavelet transform (top) highlighting the characteristic ripple-band frequency component (~200 Hz, white arrowhead). **c**, **d** LFP recording from hippocampal CA1 in the absence of AChR blockers ($n = 9$). Orange raster indicate SWR peaks for three consecutive stimulation periods. Optical stimulation decreased SWR rate significantly (**d**), then SWR rate increased temporarily after the cessation of optical stimulation (median values, interquartile ranges and min/max values, for data see Supplementary Note 8). **e**, **f** After we blocked AChRs (1 µM MLA, 1 µM DHβE, 10 µM atropine), LFP recording from CA1 ($n = 9$) showed that GABA release from cholinergic fibres alone could decrease SWR rate even more effectively (**f**). There was no SWR rate increase after the cessation of optical stimulation (median values, interquartile ranges and min/max values, for data see Supplementary Note 8). **g** Epileptiform activity was evoked by elevating K^+ concentration in the ACSF to 8.5 mM in slices. LFP (bottom) and its wavelet transform (top) shows the signature of a pharmacologically evoked epileptiform events. Note the robust differences in amplitude, length and frequency components compared to physiological SWR activity (Fig. 6b) that is consistent with literature data[41]. **h**, **i** Epileptic activity recorded in CA1 in the absence of AChR blockers ($n = 7$). Orange raster indicate detected epileptic activity peaks for three consecutive stimulation periods. Illumination of cholinergic fibres reduced the rate of epileptic events (**i**), which recovers after the cessation of optical stimulation (for data see Supplementary Note 8). **j**, **k** Epileptic activity recorded in CA1 in the presence of AChR blockers ($n = 8$). Even in the presence of AChR blockers, illumination of cholinergic fibres reduced the rate of epileptic discharges (**k**), which recovers after the stimulation (median values, interquartile ranges and min/max values, for data see Supplementary Note 8), suggesting a crucial role for GABA release in controlling epileptiform activity

dependent calcium channels and (iii) electron tomography suggested differences in the volume of GABA and acetylcholine containing vesicles. This co-transmission (similar to that in retina[20]) may require nanoscale sub-synaptic organisation of presynaptic molecules, as proposed before[42,43]. Emphasising the functional role of GABA release, we also demonstrated that synaptic GABA release from cholinergic terminals alone can effectively suppress hippocampal sharp wave-ripples and per se can attenuate hippocampal epileptiform activity. These confirmed the functional importance of this GABAergic–cholinergic co-transmission in healthy and pathological states and led to a novel model of the septo-hippocampal cholinergic neurotransmission.

For decades, the predominant form of cholinergic communication was thought to be a form of non-synaptic release[8–10,12,44], which was seemingly supported by studies showing cholinergic fibres with few synapses (for details see Supplementary Discussion). Originally, the presence of extra-synaptic acetylcholine receptors and micro-dialysis experiments seemed to support a non-synaptic release hypothesis; however, later, sensitive microelectrodes showed faster changes in extracellular acetylcholine

levels (Supplementary Discussion). In addition, basal forebrain cholinergic neurons were also shown to respond to reward and punishment with extremely high speed and precision[14], and recent data suggested that cholinergic cells may regulate cortical information processing with a remarkable, millisecond-scale temporal precision[15,17,45–48]. These data urged the re-examination of whether acetylcholine release is synaptic[49]. Using electron tomography and direct labelling of synapses for neuroligin 2, we showed that, all terminals of the dense meshwork of hippocampal cholinergic fibres established (one or more) synapses and no docked or fused vesicles were detectable non-synaptically. Most of these synapses were missed previously, probably, because of their weak membrane thickening and narrower synaptic gap. Furthermore, we found that vAChT-labelled vesicle pools associated only with synaptic active zones (Fig. 7).

Non-synaptic transmission has a typical delayed onset latency of about 60–160 ms[27], while synaptic onset latencies are typically more than an order of magnitude faster. For instance, the average latency with optogenetic stimulation can be as long as 6.4[50] or 5.6 ms[51] for monosynaptic glutamate transmission. Our data show the release of acetylcholine into the synaptic active zone and a 7.4 ms onset cholinergic response latency. These response latencies suggest a focal, intra- and/or peri-synaptic localisation of nicotinic receptors, while $GABA_A$ receptors are detected intra-synaptically. However, future work will be required to resolve the contribution of intra- and/or peri-synaptic receptors to the cholinergic response, because measured, relatively fast latency alone cannot reveal the distribution of postsynaptic receptors around synapses. Although none of our data suggests "volume transmission" of acetylcholine or GABA, they may still act on extra-synaptic receptors as well, in a "volume transmission" fashion. In fact, the most likely resolution for the mismatch between our and the classic non-synaptic volume transmission hypothesis is a strong "spill-over" of transmitters from these frequently occurring synapses that would allow transmitters to reach extra-synaptic receptors as well. In fact, the much larger cholinergic vesicles that we found could contain more acetylcholine to counteract its effective extra-synaptic removal by extracellular acetylcholine esterase.

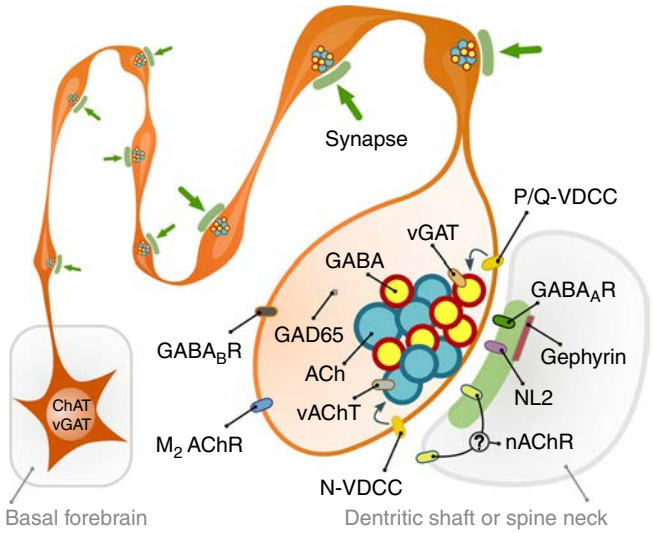

Fig. 7 Illustration of cholinergic terminals and their synaptic architecture. Summary illustration of some of the findings. All cholinergic terminals establish synapses, they are fully equipped with GABAergic–cholinergic co-transmission signalling machinery. GABAergic and cholinergic vesicles are regulated by different VDCCs. Although postsynaptic cholinergic receptor distribution cannot be investigated, their response latencies (that are at least and order of magnitude faster that typical non-synaptic transmission) suggest a focal, intra- and/or peri-synaptic localisation, while $GABA_A$ receptors are detected intra-synaptically. Synapses are established on both dendritic shafts and spines in hippocampus

Co-transmission can significantly increase the efficacy of information transfer[52–54]. Using purified vesicle preparation, we showed that GABA and acetylcholine are not "co-released" from the same vesicles, but "co-transmitted" from separate vesicles, sequentially inhibiting and exciting hippocampal neurons. To unlock the full potential of co-transmission, these coexisting vesicle pools need complex regulation. Indeed, we showed that the release of GABAergic vesicles are preferentially regulated by P/Q-type calcium channels, while the cholinergic ones are more affected by N-type calcium channels in the same synapses (Fig. 7), similar to that of retinal co-transmission of GABA and acetylcholine[20], therefore, an activity-dependent segregation in their release is also possible. Under special circumstances one of these transmitters may even be depleted earlier (GABAergic transmission shows strong STD). Differential calcium channel regulation may be achieved by sub-synaptic nanoscale organisation of presynaptic molecules[42,43], while the presence of two different kinds of presynaptic channel "slots" have already been suggested at excitatory synapses: one accepting N-type channels but rejecting P/Q-type (N-specific) and the other preferring P/Q-type but also accepting N-type (PQ preferring[53],).

Negative feedback via presynaptic autoreceptors could provide a further level of control (Fig. 7). Previously, we demonstrated that septo-hippocampal cholinergic neurons express $GABA_B$-receptors[35], while the expression of muscarinic M2 receptors was also described in these cells[34]. Indeed, we confirmed that blocking either M2- or $GABA_B$-receptors increased the release of both acetylcholine and GABA, suggesting the presence of tonically active autoreceptor regulation of these transmitters, presynaptically. In addition, our results, verified by a series of control experiments, suggested that GABAergic STD is an intrinsic property of synapses established by cholinergic fibres in the mouse hippocampus.

The timing of this co-transmission seems crucially important in hippocampal Schaffer collateral (SC) to CA1 synaptic plasticity. If the cholinergic input was activated 100 or 10 ms before SC stimulation, it resulted in ionotropic AChR-dependent long-term potentiation (LTP) or short-term depression, respectively, while delaying cholinergic stimulation until 10 ms after SC stimulation resulted in metabotropic AChR-dependent LTP[17]. Here, we found that the GABAergic and cholinergic components of this co-transmission reach their IPSP and EPSP peak about 13.8 and 92 ms after stimulation, respectively, which suggest that synaptic plasticity may depend on the coincidence of SC stimulation with the GABAergic or cholinergic component of PSPs from these basal forebrain fibres. Nevertheless, the GABAergic component seems to have its own inhibitory role in the target network, making basal forebrain cholinergic fibres an unorthodox but effective source of GABAergic inhibitory control of the hippocampus, as suggested by our demonstration of its effect on network dynamics.

Basal forebrain cholinergic cells play a pivotal role in transforming activity states in the hippocampus[37]. High cholinergic cell activity is associated with theta oscillation and the fast, yet unstable storage of external information in the hippocampus, while low cholinergic activity accompanies sharp wave-ripple (SWR) activity[55], which seems important for the consolidation and relocation of unstable memory traces from the hippocampus to the neocortex[56,57]. Classic theories of cholinergic modulation presume that diffusely released acetylcholine would slowly retune cortical network activity, enabling the appearance of distinct network dynamics[8,58,59]. Indeed, a recent study demonstrated

that medial septal cholinergic cells suppress SWR activity in vivo[39]. The authors suspected an M2 cholinergic receptor-mediated suppression of GABAergic interneurons. We re-examined that hypothesis and confirmed that cholinergic fibre activation indeed suppressed SWRs; however, we also showed that GABA (without acetylcholine) release from cholinergic fibres alone was able to achieve that. This GABAergic inhibition could lower the probability of concurrently active pyramidal cells in a given time-window, which is required for stochastic SWR initiation[60]. Blocking all GABA receptors would have eliminated SWRs[61], therefore the effect of acetylcholine release alone, without the contribution of GABA co-transmission could not be addressed. The presence of a transient increase in SWR rate after the cessation of optical stimuli, might reflect longer-lasting changes in network or cell excitability, mediated by "synaptic spill-over" of acetylcholine, while the effect of GABA release from smaller vesicles is likely confined to synaptic (and presynaptic) receptors. However, this transient effect was not reported in vivo[39], therefore, it could have been the result of a relatively low acetylcholine esterase activity in our dual-superfusion system.

Degeneration of the cholinergic system is a typical characteristic of Alzheimer's disease pathology[7], and these patients often develop epileptic seizures[62]. Indeed, selective lesion of medial septal cholinergic projection increases seizure incidence in the hippocampus[63–65], while REM-sleep, which is associated with enhanced cholinergic cell activity[29], has a suppressing effect on epileptic seizures[66,67]. The mechanisms, however, were unclear, because several cholinergic agonists were shown to trigger epileptic discharges[68]. Therefore, we hypothesise that degeneration of basal forebrain cholinergic cells leads to epileptiform activity primarily, because it deprives the hippocampus of a massive GABAergic input. Indeed, our results supported this idea, because GABA release from basal forebrain cholinergic fibres alone was sufficient to decrease the occurrence of epileptiform activity in the hippocampus.

Our results, showing a tightly regulated, effective, synaptic GABA co-transmission from hippocampal cholinergic fibres urge the re-interpretation of previous models and can lead to alternative pharmacotherapies to treat Alzheimer's disease-related loss of cholinergic innervation.

Methods

Animals and surgery. A total of 21 (25–80 days old) male C57BL/6J mice, 51 (30–200 days old) ChAT-IRES-Cre mice from either sex (Jackson Laboratory, RRID: IMSR_JAX:006410, postnatal day 30–200) and 4 (30–50 days old) VGAT-IRES-Cre/Gt(ROSA)26Sor_CAG/ZsGreen1 mice were used in the present study. All experiments were performed in accordance with the Institutional Ethical Codex, Hungarian Act of Animal Care and Experimentation (1998, XXVIII, section 243/1998) and the European Union guidelines (directive 2010/63/EU), and with the approval of the Institutional Animal Care and Use Committee of the Institute of Experimental Medicine of the Hungarian Academy of Sciences. All efforts were made to minimise potential pain or suffering and to reduce the number of animals used.

ChAT-Cre mice were anaesthetised with isoflurane followed by an intraperitoneal injection of an anaesthetic mixture (containing 8.3 mg/ml ketamine, 1.7 mg/ml xylazine-hydrochloride in 0.9 % saline, 10 ml/kg bodyweight) and then were mounted in a stereotaxic frame. For selective labelling of septo-hippocampal cholinergic axons, we injected 30–60 nl AAV2/5-EF1a-DIO-eYFP (UNC Vector Core) or AAV2/5-EF1a-DIO-ChR2(H134R)-eYFP-WPRE-hGH (plasmid: Addgene 20298, Penn Vector Core) into the medial septal area. The coordinates for the injection were based on the atlas by Paxinos, G and Franklin, (2012)[69]: 1 mm anterior from the bregma, in the midline, and 4.3 mm below the level of the horizontal plane defined by the bregma and the lambda (zero level). For a control experiment, 100 nl injections of the same virus were delivered into the hippocampus (both hemispheres) of a ChAT-Cre mouse (coordinates: −2.7 mm from the bregma, ±2.5 mm from the midline, 2.5 mm from the zero level and −3.1 from the bregma, ±3 mm from the midline and 3 mm from the zero level). For the injections, we used a Nanoject 2010 precision microinjector pump (WPI, Sarasota, FL 34240). We used borosilicate micropipettes (Drummond, Broomall, PA) for the injections with tips broken to 40–50 µm. After the surgeries, the animals received 0.5–0.7 ml saline for rehydration and 0.03–0.05 mg/kg meloxicam as nonsteroidal anti-inflammatory drug (Metacam, Boehringer Ingelheim, Germany) intraperitoneally to support recovery, and we placed them into separate cages to survive for at least three weeks before decapitations or perfusions.

Slice preparation and recording conditions. After 3–6 weeks following injection (to reach an appropriate expression level in long-range projecting axons) horizontal slices were prepared. In all cases, mice were decapitated under deep isoflurane anaesthesia. The brain was removed into ice-cold cutting solution, which had been bubbled with 95% O_2–5% CO_2 (carbogen gas) for at least 15 min before use. The cutting solution contained the following (in mM): 205 sucrose, 2.5 KCl, 26 $NaHCO_3$, 0.5 $CaCl_2$, 5 $MgCl_2$, 1.25 NaH_2PO_4, 10 glucose, saturated with 95% O_2–5% CO_2. Horizontal hippocampal slices of 300 µm or 450 µm thicknesses (for whole-cell and LFP recordings, respectively) were cut using a vibratome (Leica VT1000S). After acute slice preparation the slices were placed into an interface-type holding chamber for recovery. This chamber contained standard artificial cerebrospinal fluid (ACSF) at 35 °C that gradually cooled down to room temperature. The ACSF had the following composition (in mM): 126 NaCl, 2.5 KCl, 26 $NaHCO_3$, 2 $CaCl_2$, 2 $MgCl_2$, 1.25 NaH_2PO_4, 10 glucose, saturated with 95% O_2–5% CO_2. After incubation for at least 1.5 h, slices were transferred individually into a submerged-style recording chamber equipped with a single superfusion system. In case of LFP recording of hippocampal network activities, a double superfusion system was used for improved slices maintenance conditions[60,70]. In the latter design, the slices were placed on a metal mesh and two separate fluid inlets allowed ACSF to flow both above and below the slices with a rate of 3–5 ml/min for each flow channel at 30–32 °C (Supertech Instruments; www.super-tech.eu). The composition of the modified ACSF (mACSF) used in experiment presented in Fig. 6g–k was the following (in mM): 126 NaCl, 3.5 KCl, 26 $NaHCO_3$, 1.6 $CaCl_2$, 1.2 $MgCl_2$, 1.25 NaH_2PO_4, 10 glucose saturated with 95% O_2–5% CO_2. Epileptic events were evoked by further increasing the potassium concentration from 3.5 to 8.5 mM after 15 min spent in mACSF in the recording chamber. Slices were visualised with an upright microscope (Nikon Eclipse FN1 or Olympus BX61WI) with infrared-differential interference contrast optics. Standard patch electrodes were used in all recording configurations (i.e., in whole-cell patch-clamp and field potential recordings). Pipette resistances were 3–6 MΩ when filled either with the intracellular solution or with ACSF. ACSF filled pipettes placed into CA1 pyramidal layer were used for local field potential (LFP) recordings. The composition of the intracellular pipette solution was the following (in mM): 110 K-gluconate, 4 NaCl, 20 HEPES, 0.1 EGTA, 10 phosphocreatine, 2 ATP, 0.3 GTP, 3 mg/ml biocytin adjusted to pH 7.3–7.35 using KOH (285–295 mOsm/L). Where indicated, high-chloride containing intracellular solution was used: 54 K-gluconate, 4 NaCl, 56 KCl, 20 HEPES, 0.1 EGTA, 10 phosphocreatine, 2 ATP, 0.3 GTP, 3 mg/ml biocytin adjusted to pH 7.3–7.35 using KOH (285–295 mOsm/L). Whole-cell series resistance was in the range of 5–15 MΩ. Series resistance was not compensated but was frequently monitored, and cells where the values changed more than 25% during recording were discarded from further analysis. Voltage measurements were not corrected for the liquid junction potential.

Drugs. To avoid polysynaptic effects in response to optical stimulation of cholinergic fibres, glutamatergic excitatory currents were blocked by 20 µM NBQX and 50 µM AP5 in all experiments presented on Figs. 3, 5 and Supplementary Figure 3. The following drug concentrations were used in the specified experiments (wash application): 20 µM NBQX, 50 µM AP5, 10 µM atropine, 1 µM MLA, 1 µM DHBE, 10 µM gabazine, 1 µM CGP-55845. For puff application of ω-conotoxin (1 µM) and ω-agatoxin (1 µM), a glass capillary was placed adjacent to the recorded cell. These drugs were injected by mouth-applied pressure for 1–2 min during the stimulation protocol following the control period. Drugs were dissolved in HEPES-based buffer with a composition in mM: 126 NaCl, 10 glucose, 2.5 KCl, 1.25 NaH_2PO_4, 2 $CaCl_2$, 2 $MgCl_2$, 26 HEPES, pH 7.3. Gabazine (SR 95531 hydrobromide), CGP-55845, MLA (Methyllycaconitine citrate), DhβE (dihydro-β-erythroidine hydrobromide) and AFDX-116 were purchased from Tocris Bioscience, ω-conotoxin and ω-agatoxin were purchased from Almone labs, and NBQX (2,3-Dioxo-6-nitro-1,2,3,4-tetrahydrobenzo[f]quinoxaline-7-sulfonamide) and AP5 were purchased from Hello Bio. All other salts and drugs were obtained from Sigma-Aldrich or Molar Chemicals KFT.

Anatomical identification. The recorded cells were filled with biocytin. After the recording, the slices were fixed in 4% paraformaldehyde in 0.1 M phosphate buffer (PB; pH 7.4) for at least 3 h, followed by washout with PB several times. Then, sections were blocked with normal goat serum (NGS; 10%) diluted in Tris-buffered saline (pH 7.4), followed by incubations in Alexa Fluor 594-conjugated streptavidin (1:1000; Invitrogen). Sections were then mounted on slides in Vectashield (Vector Laboratories) and were morphologically identified on the basis of their location, dendritic and axonal arborisation.

Optogenetic illumination. For illumination, we used a blue laser diode (447 nm, Roithner LaserTechnik GmbH) attached to a single optic fibre (Thorlabs) positioned above the hippocampal slice. In all cases, 1 ms pulse length was used. In case of structured illumination (Supplementary Figure 3), the same laser was used with a digital micro-mirror device (Polygon400, Mightex Systems, Toronto, Canada)

integrated into the optical path of the microscope. We have used Polygon400 for the illumination of the slice at a remote location (~5–600 µm), to avoid direct illumination of ChR2-expressing terminals on the recorded cell.

Electrophysiological recordings and analysis. Both whole-cell and LFP recordings were performed with a Multiclamp 700A or 700B amplifier (Molecular Devices) and were low-pass filtered at 3 kHz using the built-in Bessel filter of the amplifier. Data were digitised at 10 kHz with a PCI-6042E board (National Instruments) and recorded with EVAN 1.3 software (courtesy of Prof. I. Mody, University of California Los Angeles, Los Angeles, CA). All data were analysed off-line using custom-made programmes written in MATLAB 8.5.0, Python 2.7 by D.S. and Delphi 6.0 by A.I.G.

The kinetic properties (20–80% rise times, decay time constant, latency) were calculated on stimulus triggered averaged events. Fitting of a single exponential function to the decaying phase of averaged responses and statistical analyses were performed in OriginPro, version 9.2.214 (OriginLab Corporation, Northampton, MA, USA). Latency from stimulation start to PSP onset was calculated as the time when the signal crossed three times standard deviation of baseline. Transmission probability was defined, as the probability of detectable IPSC in response to the optical stimulation. For characterising short-term plasticity, each stimulation frequency was repeated 20 times with an interval of 3 s. To record in parallel the changes in cholinergic EPSP and GABAergic IPSPs (for the drug applications presented on Fig. 5) cells were measured at −50 mV in current clamp mode. Since the amplitude of both PSPs increased, qualitative changes in amplitude could be measured, however in this way, we may have underestimated the changes in amplitude due to conductances overlapping in time and acting in the opposite directions. In the case of VDCC blocker application, we used five pulses to evoke larger cholinergic responses. We quantified EPSP area changes for ω-agatoxin and ω-conotoxin application after low-pass filtering (at 2 Hz) the response (e.g. subtracting GABAergic component).

Figure 5 data were normalised for visualisation (all values were divided by the mean of the control sample)[71]. LFP signals were filtered with a two way RC filter to preserve phase. SWRs were pre-detected on 30 Hz low-pass-filtered field recordings using a threshold value of four times the SD of the signal. The pre-detected SWRs were then redetected using a programme that detected SWR peaks and eliminated recording artefacts similar to SWRs. Epileptic event peaks were detected similarly. Event rates were calculated with equal time periods for control, stimulation and recovery phases. All automatic detection steps were manually supervised.

Perfusion. For perfusion, mice were deeply anaesthetised as above. Mice for electron microscopical reconstruction of axonal segments and immunofluorescent labellings were perfused transcardially first with 0.9% NaCl in 0.1 M phosphate buffer (PBS) solution for 2 min followed by 4% paraformaldehyde (PFA) in 0.1 M phosphate buffer (pH = 7.4; PB) for 40 min and finally with PBS for 10 min. In the case of one WT mouse for reconstruction, the fixative also contained 0.5% glutaraldehyde. Two WT mice for postembedding GABA-labelling and electron tomography were perfused first with PBS for 2 min followed by a fixative containing 2% PFA and 2% glutaraldehyde in 0.1 M sodium acetate buffer (pH 6.5) for 2 min, and then by 2% PFA/2% glutaraldehyde in 0.1 M sodium borate buffer (pH 8.5) for 1 h[72]. Brains were removed from the skull and postfixed overnight at 4 °C in 2% PFA/2% glutaraldehyde in 0.1 M sodium borate buffer (pH 8.5). Mice for electron microscopical or immunfluorescent detection of gephyrin and $GABA_A$ receptors were perfused transcardially with ice-cold, oxygenated artificial cerebrospinal fluid [containing (mM) NaCl 125, KCl 2.5, $CaCl_2$ 2.5, $MgCl_2$ 2, $NaHCO_3$ 26, NaH_2PO_4 1.25, glucose 25[73]]. Then the brain was removed from the skull and cut in blocks containing the hippocampal formation (separated hemispheres) and the medial septal area. The blocks were incubated in a fixative containing 4% PFA and 0.2% glutaraldehyde in PB for 90 min at 4 °C and then embedded in 2% agarose for sectioning. Coronal sections were cut on a Leica VT1200S vibratome at 50 µm. All series of sections were rinsed in PB, cryoprotected sequentially in PB containing 10 and 30% sucrose, frozen in liquid nitrogen and stored at −70 °C until further processing.

Antibodies. We have summarised the primary antibodies used, their concentrations and information on their specificity in Supplementary Table 1. The secondary antibodies (Supplementary Table 2) were extensively tested for possible cross-reactivity with the other secondary or primary antibodies, and possible tissue labelling without primary antibodies was also tested to exclude auto-fluorescence or specific background labelling by the secondary antibodies. No specific-like staining was observed under these control conditions.

Single- and double-labelling pre-embedding immunoelectron microscopy. Sections were freeze-thawed two times over liquid nitrogen and washed in PB. Sections for gephyrin immunolabelling were treated with 1% sodium borohydride in PB for 10 min. For detection of $GABA_A$ receptors, the sections were incubated in 0.2 M HCl solution containing 2 mg/ml pepsin (Dako) at 37 °C for 2–4 min. After extensive washes in PB and 0.05 M Tris-buffered saline (pH 7.4; TBS) sections were blocked in 1% human serum albumin (HSA; Sigma-Aldrich) in TBS. Then, they were incubated in a mixture of primary antibodies (Supplementary Table 1) diluted in TBS containing 0.05% sodium azide for 2–3 days. After repeated washes in TBS, the sections were incubated in blocking solution (Gel-BS) containing 0.2% cold water fish skin gelatine and 0.5% HSA in TBS for 1 h. Next, sections were incubated in gold-conjugated and biotinylated secondary antibodies (Supplementary Table 1) diluted in Gel-BS overnight. After extensive washes in TBS the sections were treated with 2% glutaraldehyde in 0.1 M PB for 15 min to fix the gold particles into the tissue. This was followed by incubation in avidin–biotinylated horseradish peroxidase complex (Elite ABC; 1:300; Vector Laboratories) diluted in TBS for 3 h at room temperature or overnight at 4 °C. The immunoperoxidase reaction was developed using 3,3-diaminobenzidine (DAB; Sigma-Aldrich) as chromogen. To enlarge immunogold particles, sections were incubated in silver enhancement solution (SE-EM; Aurion) for 40–60 min at room temperature. The sections were then treated with 1% (for electron tomography) or 0.5% OsO_4 in 0.1 M PB, at room temperature (for electron tomography) or on ice, dehydrated in ascending alcohol series and in acetonitrile and embedded in Durcupan (ACM; Fluka). During dehydration, the sections were treated with 1% uranyl acetate in 70% ethanol for 20 min. For electron microscopic analysis, tissue samples from the CA1 area of dorsal hippocampus/somatosensory cortex (S1) were glued onto Durcupan blocks. Consecutive 70 nm-thick (for conventional electron microscopic analysis) or 150 nm-thick (for electron tomography) sections were cut using an ultramicrotome (Leica EM UC6) and picked upon Formvar-coated single-slot grids. Ultrathin sections for conventional electron microscopic analysis were counterstained with lead citrate (Ultrostain 2, Leica) and examined in a Hitachi 7100 electron microscope equipped with a Veleta CCD camera (Olympus Soft Imaging Solutions, Germany). 150 nm-thick electron tomography sections were examined in FEI Tecnai Spirit G2 BioTwin TEM equipped with an Eagle 4k HS camera.

Combination of pre- and postembedding immunocytochemistry. vAChT was visualised using the pre-embedding gold method as described above. Alternate serial 70 nm-thick sections were mounted on copper and nickel grids (5–6 sections/grid). Postembedding GABA immunostaining was carried out on nickel grids according to a modified protocol[74]. Incubations of sections were performed on droplets of solutions in humid Petri dishes in the following order: 0.5% periodic acid (H_5IO_6) for 5 min at room temperature; three times at 2 min wash in distilled water; 3 min in TBS; 15 min in 1% ovalbumin dissolved in TBS at 37 °C; 8 min in TBS, 90 min rabbit anti-GABA antiserum (1:10,000 in TBS) at 37 °C; two times at 10 min TBS; 10 min in TBS containing 1% BSA and 0.05% Tween 20; 90 min at room temperature in 10 nm colloidal gold-conjugated goat anti-rabbit IgG (BBI solutions; 1:1000 in the same solution as before); three times at 5 min wash in distilled water; 20 min in 10% saturated uranyl acetate; 4 wash in distilled water; staining with lead citrate; wash in distilled water. The etching procedure of post-embedding GABA immunostaining removes the silver precipitate of the pre-embedding vAChT labelling (Fig. 2e); therefore, only every second electron microscope grid was reacted for GABA and the analysis of vACHT-positive terminals were carried out using the so called mirror technique. Sections on copper grids adjacent to the first sections on nickel grids were systemically scanned for pre-embedding immunogold-labelled vAChT-positive terminals. These terminals were identified in the next, GABA-labelled section, followed in consecutive serial sections and digital images were taken at 50,000 times magnification in each serial section. Postembedding immunogold particles were counted on these GABA-labelled terminals and the examined surface area was measured using the Reconstruct software[75]. For comparison, we have also measured the immunogold densities of putative glutamatergic terminals using the same method, in the same series of images. Terminals forming type-I (asymmetric) synapses were considered glutamatergic. Although periodic acid-etching of the sections is known to remove pre-embedding antibodies together with immunogold and silver precipitation, we confirmed this again in a control experiment because, here, both the pre-embedding labelling and the postembedding GABA staining was performed using rabbit antibodies. In these control experiments, the postembedding GABA immunostaining was carried out without the primary anti-GABA antibody, in which case practically no postembedding gold particles were detected, confirming the specificity of the method.

Electron microscopy analysis of synapses of cholinergic fibres. For evaluation of the gephyrin and $GABA_A$ receptor content at synapses of cholinergic axons, we performed pre-embedding double labelling. vAChT (in wild-type mice) or eYFP (in ChAT-Cre mice, see above) was labelled with DAB, while gephyrin or $GABA_A$ γ2 subunit was labelled with immunogold (see above, Supplementary Tables 1–2). Electron microscopic serial sections were systemically scanned for synapses of DAB-labelled terminals. Parallel appositions between the membranes of a DAB-containing terminal and a putative postsynaptic target were regarded as a synapse if they displayed widening of the extracellular space at the presumptive synaptic cleft and clustered synaptic vesicles in the terminal. Synapses found were followed and photographed at 30,000 magnification in every section, where they were present throughout the series: thus they were fully reconstructed. Since the background labelling (measured in putative glutamatergic synapses in the same series of sections) was negligible, synapses containing at least one gold particle were regarded as positive.

3D reconstruction of axonal segments. Cholinergic axonal segments ($n = 17$) were reconstructed using consecutive serial 70 nm-thick sections double labelled for choline acetyltransferase (ChAT; DAB) and neuroligin 2 (NL2; immunogold) in wild-type mice ($n = 2$) or eYFP (DAB) and gephyrin (immunogold) in ChAT-Cre animals, in which the medial septum was injected with Cre-dependent eGFP-containing virus ($n = 2$). CB_1-positive axons were reconstructed from a series of 70 nm-thick sections double labelled for CB_1 (DAB) and NL2 (immunogold). DAB-containing axons were followed in consecutive serial sections and digital images were taken at 30,000 times magnification in each serial section. Three-dimensional reconstructions of plasma membranes, mitochondria, putative synapses of DAB-containing axons and postsynaptic gold particles were made using the Reconstruct software[75]. For preparing figures of reconstructed axons and measuring their 3D length, Blender software (www.blender.org) was used. Postsynaptic targets of cholinergic axons were classified as described earlier[76]. Briefly, spines were recognised by their small size and specific morphology. In CA1 str. oriens and radiatum, dendrites that have spines and do not receive type-I (asymmetric) inputs on their shafts are known to be pyramidal cells[77], whereas dendrites receiving type-I synapses on their shafts are interneurons[78]. The robustness of this classification method was reconfirmed recently[76]. Because in str. lacunosum-moleculare the shafts of pyramidal dendrites may receive type-1 inputs[77] they were not distinguished from interneuron dendritic shafts. Also, the dendritic shafts in somatosensory cortex S1 could not be identified based on morphological features.

Immunofluorescent labelling and confocal laser-scanning microscopy. Before the immunofluorescent staining, the 50 µm thick sections were washed in PB and Tris-buffered saline (TBS). This was followed by blocking for 1 h in 1% human serum albumin (HSA) and 0.1% Triton X-100 dissolved in TBS. After this, sections were incubated in mixtures of primary antibodies overnight at room temperature. After incubation, sections were washed in TBS, and were incubated overnight at 4 °C in the mixture of, all diluted in TBS. Secondary antibody incubation was followed by washes in TBS, PB, the sections were mounted on glass slides and coverslipped with Aqua-Poly/Mount (Polysciences). Immunofluorescence was analysed using a Nikon Eclipse Ti-E inverted microscope (Nikon Instruments Europe B.V., Amsterdam, The Netherlands), with a CFI Plan Apochromat VC 60XH oil immersion objective (numerical aperture: 1.4) and an A1R laser confocal system. We used 405, 488, 561 and 647 nm lasers (CVI Melles Griot), and scanning was done in line serial mode. Image stacks were obtained with NIS-Elements AR software, and deconvolved using Huygens Professional software (www.svi.nl).

STORM super-resolution microscopy. Before the immunofluorescent staining for the super-resolution experiments, the 20 µm thick sections were washed in PB and TBS. This was followed by blocking for 1 h in 1% HSA dissolved in TBS. After this, sections were incubated in mixtures of primary antibodies; overnight at room temperature. After incubation, sections were washed in TBS, and sections were incubated overnight at 4 °C in the mixtures of secondary antibodies. Secondary antibody incubation was followed by washing in TBS, PB; then hippocampi were cut out with scalpels in buffer, sections were dried on clean coverslips, and stored for maximum 3 weeks at room temperature in a dry environment before imaging. 3D direct-STORM (direct Stochastic Optical Reconstruction Microscopy) acquisition protocol was used as described before[79]. The imaging setup was built around a Nikon Ti-E inverted microscope equipped with a Perfect Focus System, with an Andor iXon Ultra 897 EMCCD camera, a C2 confocal head, 405, 488 and 561 nm lasers (Melles Griot 56RCS/S2780, Coherent Sapphire), and a high power 647 nm laser (300 mW, MPB Communications VFL-P-300-647). A high NA ×100 oil immersion objective (Nikon CFI SR Apochromat TIRF ×100 oil, 1.49 NA) was used for imaging. During STORM acquisition the emitted light was let through 582/636 nm and 670/760 nm bandpass filters to reach the detector for the 561 and 647 channels, respectively. We used the NIS-Elements AR 4.3 with N-STORM 3.4 software for acquisition and analysis. Imaging medium was mixed from 80 µl DPBS (Dulbecco's phosphate-buffered saline), 10 µl MEA (mercaptoethylamine) solution, 10 µl 50% glucose solution and 1 µl GLOX (glucose oxidase) solution. Coverslips with the dried sections were mounted onto microscope slides with 25 µl of freshly prepared imaging medium, and sealed with nail-polish. After selecting the region of interest, confocal image stacks were acquired containing 15 focal planes with $80 \times 80 \times 150$ nm voxel size in x, y and z, respectively. This was followed by bleaching the fluorophores in the STORM channels (561 and 647) with high intensity laser illumination, and running dSTORM acquisition using oblique (near-TIRF) illumination. The acquisition in the two channels was done in sequential mode. Confocal stacks were deconvolved (Huygens Professional), and – together with the STORM molecule lists – processed for further analysis in VividSTORM software (see "Analysis"). Imaging was performed with identical parameters (depth in the section, laser intensities, etc.) for all samples.

Electron tomography. For the electron tomographic investigation we used 150 nm-thick sections from the hippocampal CA1 region from the anti-vAChT immunogold stained material (see: "Pre-embedding immunoelectron-microscopy"). Before electron tomography, serial sections on single-slot copper grids were photographed with a Hitachi H-7100 electron microscope and a Veleta CCD camera. Serial sections were examined at lower magnification, and vAChT-positive synaptic terminals from the CA1 area selected. For each terminal, the section containing the largest synaptic cross section was chosen for electron tomography. After this, grids were put on drops of 10% HSA in TBS for 10 min, dipped in distilled water (DW), put on drops of 10 nm gold-conjugated Protein-A in DW (1:3) and washed in DW. Finally, we deposited 5 and 5 nm-thick layers of carbon on both sides of the grids. Electron tomography was performed using a Tecnai T12 BioTwin electron microscope equipped with a computer-controlled precision stage (CompuStage, FEI). Acquisition was controlled via the Xplore3D software (FEI). Regions of interest were pre-illuminated for 4–6 min to prevent further shrinkage. Dual-axis tilt series were collected at 2 degree increment steps between −65 and +65 degrees at 120 kV acceleration voltage and ×23,000 magnification with −1.6 to −2 µm objective lens defocus. Reconstruction was performed using the IMOD software package[80]. Isotropic voxel size was 0.49 nm in the reconstructed volumes. After combining the reconstructed tomograms from the two axes, the nonlinear anisotropic diffusion (NAD) filtering algorithm was applied to the volumes. Segmentation of the terminals has been performed on the virtual sections using the 3Dmod software, and measurements were done on the scaled 3D models.

Isolation of synaptic vesicles. Synaptic vesicles were isolated according to ref. [81], with some modifications (Supplementary Figure 4A). Briefly, cortices and hippocampi (neocortex and hippocampus, in 4:1 ratio) of ten C57Bl6 mice (80 days old, mixed gender) were pulverised mechanically after freezing in liquid nitrogen. The resulting fine powder was then homogenised using a Teflon-glass homogeniser in 0.3 M sucrose-containing HEPES buffer (0.3 M sucrose, 50 mM HEPES, pH 7.4, 2 mM EGTA). The homogenate was centrifuged at 100,000×g (1 h, 4 °C). The supernatant was laid onto a 0.6 M/1.5 M sucrose step gradient and centrifuged at 260,000×g (2 h, 4 °C). Synaptic vesicles were collected from the 0.6 M/1.5 M sucrose solution interface. The vesicles were either immediately used or were frozen in liquid nitrogen and stored at −20 °C for later use.

Immunostaining and flow cytometry analysis. The vesicles were dialysed overnight, at 4 °C, in phosphate-buffered saline (PBS; 800 ml). For dialysis a 300kD MWCO membrane was used (Biotech CE Dialysis Tubing). All solutions used during the dialysis or subsequent immunostaining were thoroughly filtered through either 0.2 µm (Millipore) or 0.02 µm pore diameter filters (Anodisc-47; GE Healthcare/Whatman). The vesicles were incubated with primary antibody in the presence of 0.1% BSA (RT, 1 h) followed by incubation with secondary antibody (RT, 1 h), under constant shaking. Prior to FACS analysis the stained vesicle suspensions were dialysed again against PBS (800 ml, at RT, for 1 h). FACS analysis was performed on a BD FACSVerse instrument.

Electron and confocal microscopy of isolated synaptic vesicles. Isolated synaptic vesicle suspension was diluted 10× in TBS, and 100 µl was dropped onto ultra-clean coverslips. After 10 min, 100 µl 4% PFA in 0.1 M PB was added to the drops. For a further 15 min the coverslips were washed gently in distilled water (DW), and processed for TEM and CLSM analysis. For the electron microscopic investigation, vesicles fixed to the coverslips were treated with 1% OsO_4 in 0.1 M PB at room temperature, dehydrated in ascending alcohol series and in acetonitrile, and embedded in Durcupan (ACM; Fluka). During dehydration, the coverslips were treated with 1% uranyl acetate in 70% ethanol for 20 min. After resin polymerisation, small pieces were cut and removed from the coverslip surface, glued onto plastic blocks, and 40 nm-thick sections were prepared using an ultramicrotome (Leica EM UC6) and picked upon Formvar-coated single-slot grids. Ultrathin sections were examined in a Hitachi 7100 electron microscope equipped with a Veleta CCD camera (Olympus Soft Imaging Solutions, Germany). For CLSM analysis coverslips were washed in PB and Tris-buffered saline (TBS). This was followed by blocking for 1 h in 1% human serum albumin (HSA) dissolved in TBS. After this, sections were incubated in mixtures of primary antibodies for 1 h at room temperature. After incubation, sections were washed in TBS, and were incubated for 1 h at room temperature in the mixture of secondary antibodies, all diluted in TBS. Secondary antibody incubation was followed by washes in TBS, PB, DW and the coverslips were mounted on glass slides with Aqua-Poly/Mount (Polysciences). Immunofluorescence was analysed using a Nikon Eclipse Ti-E inverted microscope (Nikon Instruments Europe B.V., Amsterdam, The Netherlands), with a CFI Plan Apochromat VC 60XH oil immersion objective (numerical aperture: 1.4) and an A1R laser confocal system. The possible influence of chromatic aberration on PSF-position was controlled using fluorescent TetraSpeck™ Microspheres (0.1 µm diameter, blue/green/orange/dark red, ThermoFisher Scientific). We used 405, 488, 561 and 647 nm lasers (CVI Melles Griot), and scanning was done in line serial mode. Image stacks were obtained with NIS-Elements AR software, and deconvolved using Huygens Professional software (www.svi.nl).

Statistical analysis. During segmentation of tomographic volumes, z-scaling was calculated from the thickness difference of the reconstructed volume and the original section thickness, and applied to the 3D models. Mesh surface areas and volumes inside meshed objects were measured with the "imodinfo" programme.

In STORM imaging "molecule lists" were exported from NIS in txt format, and the three image planes of the ics-ids file pairs from the deconvolved confocal stacks

matching the STORM-volume were converted to the ome-tiff format using Fiji software. Confocal and corresponding STORM images were fitted in VividSTORM[82].

When data populations in this work had a Gaussian distribution according to the Shapiro–Wilks *W* test, we reported parametric statistical features (mean ± SD), otherwise we reported non-parametric statistical features (median, interquartile range). For the presentation of electrophysiological data, we used median and interquartile range, because the data did not show Gaussian distribution. Two non-parametric groups were compared using the Mann–Whitney *U* test. Wilcoxon signed-rank test was used for calculating significance between dependent non-parametric data groups. *F*-test was used to compare the variability of data groups. The types of statistical tests used in different investigations are indicated in the text. We always used two-tailed statistical tests. All statistical analyses were carried out using the software package Statistica (StatSoft, Tulsa, OK, USA) or OriginPro 9.2.214 (OriginLab Corporation, Northampton, MA, USA). Adequate sample sizes were chosen based on experience with similar measurements to ensure adequate power to detect a specified effect size. The number of animals used was minimised as much as possible. No animals or measurements were excluded from the measurements after data were collected. Samples from tissue slices or from anatomical sections were collected randomly. The investigator was not blinded to any group allocations, because we investigated only a healthy group of mice. The differences were considered significant at $p < 0.05$.

Code availability. Custom written codes for sharp wave-ripple and epileptic event detection, and electron tomographic analysis are available upon request.

Data availability. The data generated during the current study are available from the corresponding author on reasonable request.

Received: 2 January 2018 Accepted: 12 June 2018
Published online: 20 July 2018

References

1. Eckenstein, F., Baughman, R. & Quinn, J. An anatomical study of cholinergic innervation in rat cerebral cortex. *Neuroscience* **25**, 457–474 (1988).
2. Rye, D. B., Wainer, B. H., Mesulam, M. M., Mufson, E. J. & Saper, C. B. Cortical projections arising from the basal forebrain: a study/rof cholinergic and noncholinergic components employing/rcombined retrograde tracing and immunohistochemical/rlocalization of choline acetyltransferase. *Neuroscience* **13**, 627–643 (1984).
3. Yu, A. J. & Dayan, P. Uncertainty, neuromodulation, and attention. *Neuron* **46**, 681–692 (2005).
4. Hasselmo, M. E. & Bower, J. M. Acetylcholine and memory. *Trends Neurosci.* **16**, 218–222 (1993).
5. Rasmusson, D. D. & Dykes, R. W. Long-term enhancement of evoked potentials in cat somatosensory cortex produced by co-activation of the basal forebrain and cutaneous receptors. *Exp. Brain Res.* **70**, 276–286 (1988).
6. Jones, B. E. The organization of central cholinergic systems and their functional importance in sleep-waking states. *Prog. Brain Res.* **98**, 61–71 (1993).
7. Tata, A. M., Velluto, L., D'Angelo, C. & Reale, M. Cholinergic system dysfunction and neurodegenerative diseases: cause or effect? *CNS Neurol. Disord. Drug Targets* **13**, 1996–3181 (2014).
8. Descarries, L., Gisiger, V. & Steriade, M. Diffuse transmission by acetylcholine in the CNS. *Prog. Neurobiol.* **53**, 603–625 (1997).
9. Lendvai, B. & Vizi, E. S. Nonsynaptic chemical transmission through nicotinic acetylcholine receptors. *Physiol. Rev.* **88**, 333–349 (2008).
10. Sarter, M., Parikh, V. & Howe, W. M. Phasic acetylcholine release and the volume transmission hypothesis: time to move on. *Nat. Rev. Neurosci.* **10**, 383–390 (2009).
11. Arroyo, S., Bennett, C. & Hestrin, S. Nicotinic modulation of cortical circuits. *Front. Neural Circuits* **8**, 1–6 (2014).
12. Zoli, M., Jansson, A., Syková, E., Agnati, L. F. & Fuxe, K. Volume transmission in the CNS and its relevance for neuropsychopharmacology. *Trends Pharmacol. Sci.* **20**, 142–150 (1999).
13. Teles-Grilo Ruivo, L. M. & Mellor, J. R. Cholinergic modulation of hippocampal network function. *Front. Synaptic Neurosci.* **5**, 1–15 (2013).
14. Hangya, B., Ranade, S. P., Lorenc, M. & Kepecs, A. Central cholinergic neurons are rapidly recruited by reinforcement feedback. *Cell* **162**, 1155–1168 (2015).
15. Muñoz, W. & Rudy, B. Spatiotemporal specificity in cholinergic control of neocortical function. *Curr. Opin. Neurobiol.* **26**, 149–160 (2014).
16. .Teles-Grilo Ruivo, L. M. et al. Coordinated acetylcholine release in prefrontal cortex and hippocampus is associated with arousal and reward on distinct timescales. *Cell Rep.* **18**, 905–917 (2017).
17. Gu, Z. & Yakel, J. L. Timing-dependent septal cholinergic induction of dynamic hippocampal synaptic plasticity. *Neuron* **71**, 155–165 (2011).
18. Fisher, R. S. & Levine, M. S. Transmitter cosynthesis by corticopetal basal forebrain neurons. *Brain Res.* **491**, 163–168 (1989).
19. Beaulieu, C. & Somogyi, P. Enrichment of cholinergic synaptic terminals on GABAergic neurons and coexistence of immunoreactive GABA and choline acetyltransferase in the same synaptic terminals in the striate cortex of the cat. *J. Comp. Neurol.* **304**, 666–680 (1991).
20. Lee, S., Kim, K. & Zhou, Z. J. Role of ACh-GABA cotransmission in detecting image motion and motion direction. *Neuron* **68**, 1159–1172 (2010).
21. Saunders, A. et al. A direct GABAergic output from the basal ganglia to frontal cortex. *Nature* **521**, 85–89 (2015).
22. Saunders, A., Granger, A. J. & Sabatini, B. L. Corelease of acetylcholine and GABA from cholinergic forebrain neurons. *Elife* **2015**, 1–13 (2015).
23. Granger, A. J., Mulder, N., Saunders, A. & Sabatini, B. L. Cotransmission of acetylcholine and GABA. *Neuropharmacology* **100**, 40–46 (2016).
24. Takács, V. T., Freund, T. F. & Nyiri, G. Neuroligin 2 is expressed in synapses established by cholinergic cells in the mouse brain. *PLoS ONE* **8**, e72450 (2013).
25. Frotscher, M. & Leranth, C. Cholinergic innervation of the rat hippocampus as revealed by choline acetyltransferase immunocytochemistry: a combined light and electron microscopic study. *J. Comp. Neurol.* **239**, 237–246 (1985).
26. Bell, L. A., Bell, K. A. & McQuiston, A. R. Acetylcholine release in mouse hippocampal CA1 preferentially activates inhibitory-selective interneurons via α4β2* nicotinic receptor activation. *Front. Cell Neurosci.* **9**, 1–10 (2015).
27. Courtney, N. A. & Ford, C. P. The timing of dopamine- and noradrenaline-mediated transmission reflects underlying differences in the extent of spillover and pooling. *J. Neurosci.* **34**, 7645–7656 (2014).
28. Pascale Simon, A. Firing properties of anatomically identified neurons in the medial septum of anesthetized and unanesthetized restrained rats. *J. Neurosci.* **26**, 9038–9046 (2006).
29. Zhang, H., Lin, S.-C. & Nicolelis, M. A. L. A distinctive subpopulation of medial septal slow-firing neurons promote hippocampal activation and theta oscillations. *J. Neurophysiol.* **106**, 2749–2763 (2011).
30. Jackman, S. L., Beneduce, B. M., Drew, I. R. & Regehr, W. G. Achieving high-frequency optical control of synaptic transmission. *J. Neurosci.* **34**, 7704–7714 (2014).
31. Staley, K. J. & Proctor, W. R. Modulation of mammalian dendritic GABA A receptor function by the kinetics of Cl ⧖ and HCO 3 ⧖ transport. *J. Physiol.* **519**, 693–712 (1999).
32. McCarren, M. & Alger, B. E. Use-dependent depression of IPSPs in rat hippocampal pyramidal cells in vitro. *J. Neurophysiol.* **53**, 557–571 (1985).
33. Karunanithi, S., Marin, L., Wong, K. & Atwood, H. L. Quantal size and variation determined by vesicle size in normal and mutant drosophila glutamatergic synapses. *J. Neurosci.* **22**, 10267–10276 (2002).
34. Rouse, S. T., Edmunds, S. M., Yi, H., Gilmor, M. L. & Levey, A. I. Localization of M(2) muscarinic acetylcholine receptor protein in cholinergic and non-cholinergic terminals in rat hippocampus. *Neurosci. Lett.* **284**, 182–186 (2000).
35. Nyíri, G. et al. GABAB and CB1 cannabinoid receptor expression identifies two types of septal cholinergic neurons. *Eur. J. Neurosci.* **21**, 3034–3042 (2005).
36. Scheuber, A. Presynaptic Cav2.1 and Cav2.2 differentially influence release dynamics at hippocampal excitatory synapses. *J. Neurosci.* **24**, 10402–10409 (2004).
37. Hasselmo, M. E. & McGaughy, J. High acetylcholine levels set circuit dynamics for attention and encoding and low acetylcholine levels set dynamics for consolidation. *Prog. Brain Res.* **145**, 207–231 (2004).
38. Lee, S. & Dan, Y. Review neuromodulation of brain states. *Neuron* **76**, 209–222 (2012).
39. Vandecasteele, M. et al. Optogenetic activation of septal cholinergic neurons suppresses sharp wave ripples and enhances theta oscillations in the hippocampus. *Proc. Natl. Acad. Sci. USA* **111**, 13535–13540 (2014).
40. Traynelis, S. F. & Dingledine, R. Potassium-induced spontaneous electrographic seizures in the rat hippocampal slice. *J. Neurophysiol.* **59**, 259–276 (1988).
41. Karlócai, M. R. et al. Physiological sharp wave-ripples and interictal events in vitro: what's the difference? *Brain* **137**, 463–485 (2014).
42. Tang, A.-H. et al. A trans-synaptic nanocolumn aligns neurotransmitter release to receptors. *Nature* **536**, 210–214 (2016).
43. Chamberland, S. & Tóth, K. Functionally heterogeneous synaptic vesicle pools support diverse synaptic signalling. *J. Physiol.* **594**, 825–835 (2016).
44. Agnati, L. F. et al. Volume transmission and wiring transmission from cellular to molecular networks: history and perspectives. *Acta Physiol.* **187**, 329–344 (2006).
45. Letzkus, J. J. et al. A disinhibitory microcircuit for associative fear learning in the auditory cortex. *Nature* **480**, 331–335 (2011).
46. Gritton, H. J. et al. Cortical cholinergic signaling controls the detection of cues. *Proc. Natl. Acad. Sci. USA* **113**, E1089–E1097 (2016).
47. Sun, Y.-G. et al. Biphasic cholinergic synaptic transmission controls action potential activity in thalamic reticular nucleus neurons. *J. Neurosci.* **33**, 2048–2059 (2013).

48. Bennett, C., Arroyo, S., Berns, D. & Hestrin, S. Mechanisms generating dual-component nicotinic EPSCs in cortical interneurons. *J. Neurosci.* **32**, 17287–17296 (2012).
49. Yamasaki, M., Matsui, M. & Watanabe, M. Preferential localization of muscarinic M1 receptor on dendritic shaft and spine of cortical pyramidal cells and its anatomical evidence for volume transmission. *J. Neurosci.* **30**, 4408–4418 (2010).
50. Assous, M. et al. Differential processing of thalamic information via distinct striatal interneuron circuits. *Nat. Commun.* **8**, 15860 (2017).
51. Schone, C. et al. Optogenetic probing of fast glutamatergic transmission from hypocretin/orexin to histamine neurons in situ. *J. Neurosci.* **32**, 12437–12443 (2012).
52. Somogyi, J. Functional significance of co-localization of GABA and Glu in nerve terminals: a hypothesis. *Curr. Top. Med. Chem.* **6**, 969–973 (2006).
53. Sethuramanujam, S. et al. A central role for mixed acetylcholine/GABA transmission in direction coding in the retina. *Neuron* **90**, 1243–1256 (2016).
54. Vaaga, C. E., Borisovska, M. & Westbrook, G. L. Dual-transmitter neurons: functional implications of co-release and co-transmission. *Curr. Opin. Neurobiol.* **29**, 25–32 (2014).
55. Marrosu, F. et al. Microdialysis measurement of cortical and hippocampal acetylcholine release during sleep-wake cycle in freely moving cats. *Brain Res.* **671**, 329–332 (1995).
56. Gais, S. & Born, J. Low acetylcholine during slow-wave sleep is critical for declarative memory consolidation. *Proc. Natl Acad. Sci. USA* **101**, 2140–2144 (2004).
57. Girardeau, G., Benchenane, K., Wiener, S. I., Buzsáki, G. & Zugaro, M. B. Selective suppression of hippocampal ripples impairs spatial memory. *Nat. Neurosci.* **12**, 1222–1223 (2009).
58. Picciotto, M. R., Higley, M. J. & Mineur, Y. S. Acetylcholine as a neuromodulator: cholinergic signaling shapes nervous system function and behavior. *Neuron* **76**, 116–129 (2012).
59. Buzsáki, G. Hippocampal sharp wave-ripple: a cognitive biomarker for episodic memory and planning. *Hippocampus* **25**, 1073–1188 (2015).
60. Schlingloff, D., Kali, S., Freund, T. F., Hajos, N. & Gulyas, A. I. Mechanisms of sharp wave initiation and ripple generation. *J. Neurosci.* **34**, 11385–11398 (2014).
61. Maier, N., Nimmrich, V. & Draguhn, A. Cellular and network mechanisms underlying spontaneous sharp wave-ripple complexes in mouse hippocampal slices. *J. Physiol.* **550**, 873–887 (2003).
62. Amatniek, J. C. et al. Incidence and predictors of seizures in patients with Alzheimer's disease. *Epilepsia* **47**, 867–872 (2006).
63. Buzsáki, G., Ponomareff, G. L., Bayardo, F., Ruiz, R. & Gage, F. H. Neuronal activity in the subcortically denervated hippocampus: a chronic model for epilepsy. *Neuroscience* **28**, 527–538 (1989).
64. Silveira, D. C., Holmes, G. L., Schachter, S. C., Geula, C. & Schomer, D. L. Increased susceptibility to generalized seizures after immunolesions of the basal forebrain cholinergic neurons in rats. *Brain Res.* **878**, 223–227 (2000).
65. Ferencz, I. et al. Septal cholinergic neurons suppress seizure development in hippocampal kindling in rats: comparison with noradrenergic neurons. *Neuroscience* **102**, 819–832 (2001).
66. Crespel, A., Baldy-Moulinier, M. & Coubes, P. The relationship between sleep and epilepsy in frontal and temporal lobe epilepsies: practical and physiopathologic considerations. *Epilepsia* **39**, 150–157 (1998).
67. Minecan, D., Natarajan, A., Marzec, M. & Malow, B. Relationship of epileptic seizures to sleep stage and sleep depth. *Sleep* **25**, 899–904 (2002).
68. Turski, L., Ikonomidou, C., Turski, W. A., Bortolotto, Z. A. & Cavalheiro, E. A. Review: cholinergic mechanisms and epileptogenesis. The seizures induced by pilocarpine: a novel experimental model of intractable epilepsy. *Synapse* **3**, 154–171 (1989).
69. Paxinos, G. & Franklin, K. B. J. *Paxinos and Franklin's the Mouse Brain in Stereotaxic Coordinates* (Academic Press, São Paulo, 2012).
70. Hájos, N. et al. Maintaining network activity in submerged hippocampal slices: importance of oxygen supply. *Eur. J. Neurosci.* **29**, 319–327 (2009).
71. Valcu, M. & Valcu, C.-M. Data transformation practices in biomedical sciences. *Nat. Methods* **8**, 104–105 (2011).
72. Berod, A., Hartman, B. K. & Pujol, J. F. Importance of fixation in immunohistochemistry: use of formaldehyde solutions at variable pH for the localization of tyrosine hydroxylase. *J. Histochem. Cytochem.* **29**, 844–850 (1981).
73. Notter, T., Panzanelli, P., Pfister, S., Mircsof, D. & Fritschy, J. M. A protocol for concurrent high-quality immunohistochemical and biochemical analyses in adult mouse central nervous system. *Eur. J. Neurosci.* **39**, 165–175 (2014).
74. Somogyi, P. & Hodgson, A. J. Antisera to gamma-aminobutyric acid. III. Demonstration of GABA in Golgi-impregnated neurons and in conventional electron microscopic sections of cat striate cortex. *J. Histochem. Cytochem.* **33**, 249–257 (1985).
75. Fiala, J. C. Reconstruct: a freeeditor for serial section microscopy. *J. Microsc.* **218**, 52–61 (2005).
76. Takács, V. T., Klausberger, T., Somogyi, P., Freund, T. F. & Gulyás, A. I. Extrinsic and local glutamatergic inputs of the rat hippocampal CA1 area differentially innervate pyramidal cells and interneurons. *Hippocampus* **22**, 1379–1391 (2012).
77. Megias Emri, Z., Freund, T. F. & Gulyas, A. I. M. Total number and distribution of inhibitory and excitatory synapses on hippocampal CA1 pyramidal cells. *Neuroscience* **102**, 527–540 (2001).
78. Gulyás, A. I., Megías, M., Emri, Z. & Freund, T. F. Total number and ratio of excitatory and inhibitory synapses converging onto single interneurons of different types in the CA1 area of the rat hippocampus. *J. Neurosci.* **19**, 10082–10097 (1999).
79. Dudok, B. et al. Cell-specific STORM super-resolution imaging reveals nanoscale organization of cannabinoid signaling. *Nat. Neurosci.* **18**, 75–86 (2014).
80. Kremer, J. R., Mastronarde, D. N. & McIntosh, J. R. Computer visualization of three-dimensional image data using IMOD. *J. Struct. Biol.* **116**, 71–76 (1996).
81. Mutch, S. A. et al. Protein quantification at the single vesicle level reveals that a subset of synaptic vesicle proteins are trafficked with high precision. *J. Neurosci.* **31**, 1461–1470 (2011).
82. Barna, L. et al. Correlated confocal and super-resolution imaging by VividSTORM. *Nat. Protoc.* **11**, 163–183 (2015).

Acknowledgements

This work was supported by the European Research Council (ERC-2011-ADG-294313, SERRACO), National Institutes of Health, USA (NS030549), National Research, Development and Innovation Office, Hungary (OTKA K119521, OTKA K115441, OTKA KH124345 and VKSZ_14-1-2O15-0155), Human Brain Project, EU (EU H2020 720270); B.P. is supported by UNKP-16-2-13 and D.S. is supported by the UNKP-16-3-IV New National Excellence Program of the Ministry of Human Capacities, Hungary. Á. D. is supported by the Hungarian Brain Research Program KTIA_13_NAP-A-I/2, the 'Momentum' Program of the Hungarian Academy of Sciences and ERC-CoG 724994. We thank László Barna, the Nikon Microscopy Center at IEM, Nikon Austria GmbH and Auro-Science Consulting Ltd for technical support for fluorescent and STORM imaging. We thank Emőke Szépné Simon, Katalin Lengyel, Katalin Iványi, Győző Goda and Nándor Kriczky for assistance, and Anna Jász for help in scripting. We thank Dr. David Mastronarde (Univ. of Colorado Boulder) for help with electron tomography software IMOD. We thank Drs László Acsády, Julian Budd, Balázs Hangya, and Liset Menendez de la Prida for their comment on an earlier version of the manuscript.

Author contributions

Conceptualisation, V.T., C.C., D.S., G.N.; Methodology, V.T., C.C., D.S., G.N., Z.K., A.D, A.I.G.; Investigation, V.T., C.C., D.S., B.P., A.S., K.E.S., Z.K.; Writing—original draft, V. T., C.C., D.S., G.N.; Writing—editing, V.T., C.C., D.S., G.N, A.D., A.I.G, T.F.F.; Funding acquisition and supervision, T.F.F., G.N., A.I.G., A.D.

Additional information

Supplementary Information accompanies this paper at https://doi.org/10.1038/s41467-018-05136-1.

Competing interests: The authors declare no competing interests.

Reprints and permission information is available online at http://npg.nature.com/reprintsandpermissions/

Publisher's note: Springer Nature remains neutral with regard to jurisdictional claims in published maps and institutional affiliations.

SUPPLEMENTARY INFORMATION FOR

Co-transmission of acetylcholine and GABA regulates hippocampal states

Virág T. Takács, Csaba Cserép, Dániel Schlingloff, Balázs Pósfai, András Szőnyi, Katalin E. Sos, Zsuzsanna Környei, Ádám Dénes, Attila I. Gulyás, Tamás F. Freund, Gábor Nyiri

Correspondence to: Gabor Nyiri, nyiri@koki.hu

This PDF file includes:

- Supplementary Note 1-8:
- Supplementary Discussion
- Supplementary Figures 1-4
- Supplementary Tables 1-4
- Supplementary References

Supplementary Note 1:

Cortical S1 cholinergic axon terminals also form synapses

In somatosensory cortex S1, similar to hippocampal cholinergic fibres all cholinergic terminals established synapses (Supplementary Figure 1A, axon J-L). In somatosensory cortex S1, differentiation of pyramidal and interneuronal dendritic shafts is not possible based on electron microscopic profiles. In S1 cortex, cholinergic terminals targeted dendrites (54%), spines (38%), while 8% of their synaptic targets remained unidentified (Supplementary Table 4).

Supplementary Note 2:

Synapses established by cholinergic fibres express $GABA_A$ receptors and its scaffolding protein postsynaptically

Previously, we demonstrated that synapses established by cholinergic fibres (in CA1, S1 somatosensory cortex, prefrontal cortex, basolateral amygdala and centrolateral thalamic nucleus) expressed the postsynaptic protein NL2 [1]. This protein directly interacts with gephyrin, a core scaffolding protein of inhibitory postsynaptic densities [2] and their complex is implicated in the anchoring and clustering of $GABA_A$ receptors postsynaptically [3–5]. Here, we labelled cholinergic fibres either with vesicular acetylcholine transporter (vAChT, in WT mice) or eYFP (in ChAT-Cre mice, where medial septum was injected with a Cre-dependent eYFP-expressing AAV). Latter labelings were developed with DAB, while gephyrin or $GABA_A$ receptor γ2 subunits were labelled with immunogold particles. Using electron microscopy, we tested fully reconstructed synapses of vAChT or eYFP-AAV labelled terminals for the presence of immunogold particles. Data from vAChT and AAV-eYFP labelled samples were not statistically different; therefore, they were pooled.

We found that at least 81% of 188 synapses collected in the CA1 area of two WT and two ChAT-Cre mice contained gephyrin postsynaptically (Supplementary Table 3). Immunogold particles in these synapses were associated with the cytoplasmic side of the postsynaptic membrane of the innervated pyramidal cell dendrites (Figure 1B-D, G-I) and spines (Supplementary Figure 1B) or interneuron dendrites (Figure 1J). The antibody used for $GABA_A$ receptor-labelling was directed against an extracellular epitope of the γ2 subunit [6,7] and labelled synaptic clefts accordingly. In the CA1 of three WT and two ChAT-Cre mice, at least 80% of the synapses established by cholinergic fibres (out of 172) showed $GABA_A$ receptor γ2 subunit labelling (Supplementary Table 3). Cholinergic fibres established $GABA_A$ receptor containing synapses on both dendrites (Figure 1E,F,K,L,N; Supplementary Figure 1 C, D) and spine-necks (Figure 1M). In addition, we found that at least 83% of synapses of vAChT-positive terminals in the somatosensory cortex S1 (n=36, Supplementary Figure 1 E-F) contained these $GABA_A$ receptor γ2 subunits. Because reliable nicotinic receptor antibodies are not available, they could not be localized directly.

Supplementary Note 3:

Cholinergic terminals possess the molecular machinery for GABA-release

By crossing a zsGreen fluorescent reporter-mouse-line with a vesicular GABA transporter (vGAT)-Cre mouse line, we created mice, in which all GABAergic cells are zsGreen labelled (vGAT-zsGreen mice). After co-labelling medial septum sections for ChAT, we found that all cholinergic cells were also positive for zsGreen (n=243 cells in 2 mice, Figure 2A, B), while many of the cells were positive only for zsGreen, corresponding to the non-cholinergic, GABAergic neurons of the

medial septum. These results confirmed that all hippocampal projecting cholinergic cells express vGAT.

To confirm that septo-hippocampal cholinergic fibres can synthetize GABA, we performed immunofluorescent reactions against glutamate-decarboxylase (GAD65) and eYFP on hippocampal sections of ChAT-Cre mice, in which medial septal cholinergic fibres were labelled with Cre-dependent eYFP-AAV. We confirmed the GAD65 expression in eYFP positive terminals (Figure 2C) as well.

To confirm vGAT protein expression in cholinergic terminals we performed vGAT-eYFP and vAChT-eYFP multiple labelings, and found that vGAT was present in the majority of the eYFP positive cholinergic terminals (at least 82.9%, n=311 in 3 mice Figure 2D). We also quantified vAChT expression, which was found to be present in at least 63.6% of the eYFP positive cholinergic terminals (n=364 in 3 mice).

Using postembedding GABA-immunogold staining, we also tested, whether cholinergic terminals contain GABA itself (Figure 2 E-F). We measured postembedding GABA-immunogold labelling densities in preembedding labelled vAChT-positive terminals (n=2 mice, 24 terminals). Background level was estimated measuring gold particles on vAChT-negative, putative glutamatergic terminals that formed asymmetric synapses in the vicinity of the examined vAChT-positive terminals (n=2 mice, 34 terminals). Data from two mice were not different statistically; therefore, they were pooled. We found a significantly higher level of immunogold labelling for GABA in vAChT-positive terminals than in glutamatergic terminals (3.3 times higher density; Figure 2F), suggesting the presence of GABA in these terminals.

Supplementary Note 4:

Synaptic vesicles of cholinergic terminals are highly heterogeneous and relatively large

We analysed the volume and elongation of vesicles [8,9] in cholinergic terminals along with similar data from purely GABAergic terminals (Figure 4E). As expected, GABAergic vesicles were small and elongated (median volume: 13730 nm^3, 11174-16434 nm^3 interquartile range; median of elongation factor: 2.90, 2.52-3.41 interquartile range; n=54 vesicles from 2 mice). However, the volume of cholinergic vesicles were significantly larger (Mann-Whitney test, $p<0.001$). The volume of the vesicles in cholinergic terminals showed a significantly higher variability as well (F-test, $p<0.001$), ranging from the very large and round ones to the small and elongated vesicles (median volume: 23267 nm^3, 19160-27539 nm^3 interquartile range; median elongation factor: 1.80, 1.57-2.04 interquartile range; n=140 vesicles from two mice, Figure 4E). The small and elongated vesicles in the cholinergic terminals were similar to the purely GABAergic ones from GABAergic interneuron terminals (Figure 4E). These data suggest that cholinergic terminals contain both smaller, more elongated GABAergic vesicles and larger, rounder cholinergic vesicles, both of which are released from the same synaptic active zone. Interestingly, some vesicles that were directly labelled with vAChT-immunogold particles were rather large and round (Figure 4E). We also observed a vAChT-labelled vesicle, fused to the synaptic membrane, likely releasing its transmitter into the synaptic cleft (Figure 4C). In subsequent experiments, we collected further evidence that acetylcholine and GABA are filled into different vesicles allowing their separately-regulated co-transmission.

Supplementary Note 5:

Acetylcholine and GABA are released at the same active zone in cholinergic terminals

We also tested, whether the two transmitter systems use the same or distinct active zones. We performed multiple immunofluorescent labelling experiments on virus labelled (eYFP) cholinergic fibres in ChAT-Cre mice for gephyrin, vAChT and eYFP, followed by confocal fluorescent imaging. We observed gephyrin-labelled puncta opposed to eYFP-positive terminals (Figure 4G, H), identifying the postsynaptic active zones of these fibres. vAChT-labelling was clearly concentrated opposite to the gephyrin-puncta, proving a tight association to the synaptic active zones (Figure 4G, H). Scale-free analysis confirmed that the likelihood of vAChT labelling was the highest at the synaptic active zones (Figure 4I; n=32 synapses from two mice). To directly examine the existence of a mixed cholinergic/GABAergic vesicle pool, we labelled brain slices for vGAT, vAChT and eYFP, and performed correlated fluorescent confocal laser scanning microscopy (CLSM) and superresolution STORM imaging (Figure 4J). The superresolution images confirmed that vAChT- and vGAT-labelled vesicle pools overlap, and were localized to the same small, confined portions of the eYFP septo-hippocampal terminals.

Supplementary Note 6:

Acetylcholine and GABA are released from different vesicles in cholinergic terminals

Although a previous study in rat has suggested that GABA-containing synaptic vesicles do not contain acetylcholine [10], using a highly specific method, we confirmed that GABA and acetylcholine vesicular transporters are localized on different vesicles in mouse cortical axon terminals. We used isolated synaptic vesicles to test whether acetylcholine and GABA are packed into the same vesicles. Isolation from neocortex and hippocampus was performed according to Mutch et al. (Supplementary Figure 4A,[11]). Isolated vesicles were investigated by flow cytometry for synaptophysin (SYP) expression. Labelling with a specific SYP antibody resulted in an about two orders of magnitude higher mean fluorescent intensity of vesicle preparations compared to the labelling with the secondary antibody alone (Supplementary Figure 4B), suggesting a highly purified preparation. After fixation and dehydration of vesicle preparations, we confirmed the presence of synaptic vesicles surrounded by lipid bilayer on electron microscopic images (Supplementary Figure 4E). The analysis confirmed that the diameter of the isolated vesicles was 37.55 nm (median, 33.78-40.21 nm interquartile range, n=100 vesicles; Supplementary Figure 4C), in accordance with literature data [12]. Next, we performed immunolabelling experiments on isolated synaptic vesicles fixed onto coverslips. Prior to CLSM imaging, we labelled the samples for SYP, vGAT, vAChT and vesicular glutamate transporter (VG1). As expected, we observed well separated fluorescent dots (point-spread functions, PSF) of the fluorophores in one single focal plane (Supplementary Figure 4F), but most PSFs showed vesicular co-localization of one of the vesicular transporters and SYP. Control experiments of the immunolabelling confirmed the lack of unspecific staining (Supplementary Figure 4I). In the absence of vesicle suspension, no PSFs were found in the CLSM scans, and the exclusion of any primary antibody led to the selective disappearance of PSFs in the corresponding channel. We also tested the distribution of fluorescent PSFs on the CLSM images. SYP-labelled vesicles were usually more than 1 µm away from each other as nearest-neighbor analysis of PSF centroids confirmed (median: 1.16 µm, 0.82-1.59 µm interquartile range, 0.46-3.92 min-max, n=149 vesicles; Supplementary Figure 4D). When PSFs in different channels colocalized, their centroids were never farther away from each other than 0.130 µm (median: 0.03 µm, 10-50 µm interquartile range, 0-0.13 min-max, n=92 vesicles; Supplementary Figure 4D). These experiments confirmed that co-localizing PSFs correspond to a

single vesicle. Next, we analysed co-localizations of the PSFs in different channels (Supplementary Figure 4G) and found that 29.2% of vesicles were labelled only for SYP, 44.5% were double-labelled for VG1 and SYP, 14.3% were double-labelled for vGAT and SYP, 11.1% were double-labelled for vAChT and SYP. Only a negligible amount of vesicles (0.9%) were triple labelled with any combinations, whereas only a sub-fraction of these vesicles (0.14% of all) were co-labelled for vAChT and vGAT. Only 0.98% of all vGAT/SYP positive vesicles were labelled for vAChT, and only 1.26% of all vAChT/SYP positive vesicles were labelled for vGAT. These numbers are in the range of false positive labelling as confirmed in the control experiments, where primary antibodies were omitted (Supplementary Figure 4I). These data suggest that vesicular transporters for glutamate, GABA and acetylcholine are expressed by distinct vesicle populations in cortical samples (Supplementary Figure 4H; n=353 vesicles). Therefore, acetylcholine and GABA may be released at the same active zones, but from different vesicles.

Supplementary Note 7:

Identification of basal forebrain cholinergic fibres in the hippocampus: control experiments

We either used immunolabelling against the vesicular acetylcholine transporter (vAChT), or performed anti-eYFP staining on sections from ChAT-Cre mice, the medial septal areas of which have previously been injected with Cre-dependent eYFP-adeno associated virus (AAV). Both of these methods had to be verified for selectivity and specificity, thus we completed a comprehensive set of control experiments. The cholinergic innervation of the hippocampus is reported to originate exclusively from the basal forebrain. Although the presence of a local cholinergic cell population in the mouse hippocampus was reported to be an artefact [13] we also tested for it. We injected Cre-dependent eYFP-AAV into the hippocampi of ChAT-Cre mice (Supplementary Figure 2C, inset), and stained hippocampal sections for eYFP, vAChT and vGAT (Supplementary Figure 2E, F). We found a few eYFP positive cells in the hippocampus. They were extremely rare and resembled dentate gyrus granule cells and CA3 pyramidal cells. We also found some sparsely distributed eYFP positive fibres originating from them, but vAChT or vGAT immunoreactivity was never found in these eYFP positive terminals (0 out of 323 terminals, from 2 mice, Supplementary Figure 2F). We also tested vAChT positive terminals in the same samples, and never found any eYFP-positivity in them (0 out of 3673 from 2 mice, Supplementary Figure 2F). Thus, we confirmed that there are no cholinergic cells in the hippocampus, only some extremely rare ectopic expression of the Cre enzyme. These results also confirmed that we can reliably label the septo-hippocampal cholinergic fibres with vAChT labelling.

To verify the other approach, we injected eYFP-AAV into the medial septal areas of ChAT-Cre mice (Supplementary Figure 2C), and performed PV/ChAT/eYFP triple labelings (Supplementary Figure 2D). 97.6% of all tested eYFP positive cells in the MS were also positive for ChAT (the few % of false negative cells are likely due to not perfectly efficient antibody penetration), but none of them were positive for PV (n=212 in 2 mice). We also tested the fibres of these cells in the hippocampus, and performed a PV/vAChT/eYFP triple labelling (Supplementary Figure 2A, B). We found that eYFP positive terminals colocalized with vAChT-labelling, but were never positive for PV (n=252 terminals from 2 mice). These results confirmed that eYFP positive fibres in these animals originate exclusively from cholinergic cells.

Supplementary Note 8:

Statistical details for Figures

Figure 2F: Medians (columns) and interquartile ranges (bars) of immunogold densities of GABA labelling in glutamatergic (Glut, median: 3.5 gold particles/ μm2, interquartile ranges: 1.5-5.3) and in VAChT-positive terminals (VAChT, median: 11.5 gold particles/ μm2, interquartile ranges: 6.8-22.7). Asterisk indicates significant difference (Mann-Whitney Test: $p< 0.05$). vAChT-negative terminals forming type I synapses were considered to be glutamatergic.

Figure 3H: Amplitude, 20-80% rise time and decay time of unitary GABAergic IPSCs from pyramidal cells (n=5) and inhibitory neurons (n=16). Box plots represent median values, with interquartile ranges, whiskers represent min/max values. Amplitude in pA: PCs: 37.28 (20.94, 61.61); INs: 61.56(46.78, 98.39), Mann-Whitney Test: $p<0.05$. Rise time (in ms) in PCs: 2.06 (1.62, 2.29), INs: 1.29 (1.12, 1.83); Mann-Whitney Test: not significant. Decay time (in ms): PCs: 16.29 (15.72, 25.94), INs: 11.35 (8.68, 14.10), Mann-Whitney Test: $p<0.05$.

Figure 3I: Averages of IPSC amplitudes for the 5 pulses presented on panel G show strong short-term depression (STD) of GABAergic transmission evoked by stimulating cholinergic fibers. **PCs:** 2 Hz: 1^{st} –42.89 (±21.79); 2^{nd} –25.74 (±13.7); 3^{rd} –25.63 (±14.85); 4^{th} –24.65 (±18.64); 5^{th} – 21.54 (±17.04). 5 Hz: 1^{st} – 40.12(±18.32); 2^{nd} – 22.96(±12.17); 3^{rd} –18.68 (±10.9); 4^{th} – 20.45 (±14.9); 5^{th} – 19.36 (±17.28). 10 Hz: 1^{st} – 38.59(±13.62); 2^{nd} – 19.04(±12.67); 3^{rd} – 13.65(±8.57); 4^{th} – 12.44(±7.5); 5^{th} – 11.46(±7.44). 20 Hz: 1^{st} –37.10 (±24.18); 2^{nd} –11.98 (±12.24); 3^{rd} –9.82 (±10.35); 4^{th} – 9.13(±8.92); 5^{th} – 6.78 (±8.06). **INs**: 2 Hz: 1^{st} – 66.72(±18.33); 2^{nd} – 51.53(±19.44); 3^{rd} – 43.19(±15.35); 4^{th} – 41.44(±13.34); 5^{th} – 36.78(±13.36). 5 Hz: 1^{st} – 70.55(±18.31); 2^{nd} – 51.73(±16.27); 3^{rd} – 39.02(±15.12); 4^{th} – 32.58(±15.49); 5^{th} – 32.76(±13.22). 10 Hz: 1^{st} – 70.01(±14.75); 2^{nd} – 50.89(±14.89); 3^{rd} – 32.75(±14.93); 4^{th} – 29.50(±13.82); 5^{th} – 30.02(±14.41). 20 Hz: 1^{st} – 67.1(±15.22); 2^{nd} –35.0 (±15.22); 3^{rd} –28.76 (±15.07); 4^{th} – 23.68(±14.38); 5^{th} – 21.55(±13.14).

Figure 5B: IPSP amplitude at control (median (interquartile range)): 0.88 mV (0.78-1.29), atropine: 1.35 mV (1.13-1.38); Wilcoxon-sign rank test: $p<0.05$. EPSP amplitude at control: 0.42 mV (0.27-0.77), atropine: 0.65 mV (0.45-2.22); Wilcoxon-sign rank test: $p<0.05$.

Figure 5C: IPSP amplitude at control: 0.74 mV (0.43-1.05), AFDX-116: 1.08 mV (0.58-1.42); Wilcoxon-sign rank test: $p<0.05$; EPSP amplitude at control: 0.17 mV (0.1-0.27), AFDX-116: 0.29 mV (0.18-0.74); Wilcoxon-sign rank test: $p<0.05$.

Figure 5D: IPSP amplitude at control: 0.79 mV (0.57-1.05), CGP: 0.9 mV (0.79-1.24); Wilcoxon sign rank test: $p<0.05$; EPSP amplitude at control: 0.24 mV (0.13-0.25), CGP: 0.37 mV (0.23-0.46); Wilcoxon sign rank test: $p<0.05$.

Figure 5E: IPSP amplitude at control: 1.21 mV (1.01-1.56), ω-agatoxin: 0.85 mV (0.59-0.96); Wilcoxon sign rank test: $p<0.05$. EPSP integral at control: 0.29 mV*s (0.24-0.94); agatoxin: 0.34 mV*s (0.21-0.64), Wilcoxon sign rank test: $p=0.63$.

Figure 5F: EPSP integral at control: 0.55 mV*s (0.25-0.59); conotoxin: 0.13 mV*s (0.11-0.25); Wilcoxon sign rank test: $p<0.05$. IPSP amplitude at control: 0.74 mV (0.49-0.91), conotoxin: 0.68 mV (0.51-0.72); Wilcoxon sign rank test: $p=0.52$.

Figure 6D: SWR rate in the absence of cholinergic blockers: 1.65 Hz (1.18-1.78) at control, 1.18 Hz (0.99-1.27) during illumination and 1.78 Hz (1.27-1.95) during recovery period, Wilcoxon-sign rank test: control-stimulation, $p<0.05$; stimulation-recovery, $p<0.01$; control-recovery, $p<0.05$.

Figure 6F: SWR rate in cholinergic blockers: 1.0 Hz (0.93-1.34) at control, 0.44 Hz (0.40-0.99) during illumination, 0.95 Hz (0.79-1.33) during recovery period, Wilcoxon-sign rank test: control-stimulation, $p<0.01$; stimulation-recovery, $p<0.01$; control-recovery, not significant.

Figure 6I: Epileptic discharge rate in the absence of AChR blockers: 0.61 Hz (0.47-0.68) at control, 0.54 Hz (0.44-0.58) during illumination, 0.62 Hz (0.5-0.63) during recovery period, Wilcoxon-sign rank test: control-stimulation, $p<0.05$; stimulation-recovery, $p<0.05$; control-recovery, not significant.

Figure 6K: Epileptic discharge rate in the presence of AChR blockers: 0.56 Hz (0.49-0.60) at control, 0.43 Hz (0.37-0.44) during illumination, 0.48 Hz (0.42-0.54) during recovery period, Wilcoxon-sign rank test: control-stimulation, $p<0.01$; stimulation-recovery, $p<0.05$; control-recovery, not significant.

Supplementary Discussion:

Cholinergic non-synaptic neurotransmission.

For decades, the predominant form of cholinergic communication was thought to be a form of “non-synaptic volume transmission" [14–20], which was supported by electron microscopic studies showing that cholinergic terminals form few synapses [3-17%: in cat striate cortex [21], rat parietal cortex [22,23], rat hippocampus [24,25], mouse hippocampus [26]], while some papers reported more frequent synapses [44-67%: in macaque prefrontal cortex [27], human temporal lobe [28], rat parietal cortex [29]]. Although acetylcholine esterase (AChE) was known to be highly effective in terminating extracellular cholinergic signal, the presence of certain extrasynaptic acetylcholine receptors (”receptor mismatch“,[26,30]) suggested that extracellular diffusion of acetylcholine occurs. Micro-dialysis experiments [31] and the localization of AChE, distant from cholinergic terminals, also seemed to support a non-synaptic “volume” transmission hypothesis [14]. However, later, highly sensitive microelectrodes showed faster, phasic changes in extracellular acetylcholine levels that facilitated cue detection and cortical information processing [20,32–35]. Basal forebrain cholinergic neurons were also shown to respond to reward and punishment with extremely high speed and precision [36], and recent data suggested that cholinergic cells may regulate cortical information processing with a remarkable, millisecond-scale temporal precision [34,37–39]. However, such a delicate temporal precision is hard to imagine without synapses and it remained inconclusive, whether the mode of acetylcholine signalling is synaptic “wired” transmission or “non-synaptic volume” transmission by ambient acetylcholine [26].

GABAergic markers in cholinergic cells

Basal forebrain cholinergic cells share a common developmental origin with different populations of cortical, striatal and basal forebrain GABAergic neurons [40–43]. Previous studies have suggested that less than 2% of cholinergic cells express GABAergic markers [44,45], while about 8% of ChAT-positive boutons in the cat striate cortex was shown to contain GABA [46]. The recognition of GABAergic signalling in the BF cholinergic system may have been hampered by its lack of GAD67 [47] and GABA transporter 1 [48]. Although the associations of cholinergic terminals with gephyrin [49] and NL2 [1] suggested the capability of GABAergic signalling from these terminals. While, for example, GABA is released together with glutamate or aspartate in the hippocampus, or with dopamine in periglomerular cells [50,51], and acetylcholine is released with glutamate in striatum [52]; GABA and acetylcholine were also shown to be released together in retina and frontal cortex [45,47,53,54]. However, the precise architecture, the mechanism of the dual cholinergic/GABAergic transmission and their hippocampal synaptic physiological and network effects have not yet been investigated.

SUPPLEMENTARY FIGURES 1-4:

Supplementary Figure 1,

Cholinergic axons establish synaptic contacts just as frequently as other GABAergic fibers and express GABAergic postsynaptic markers

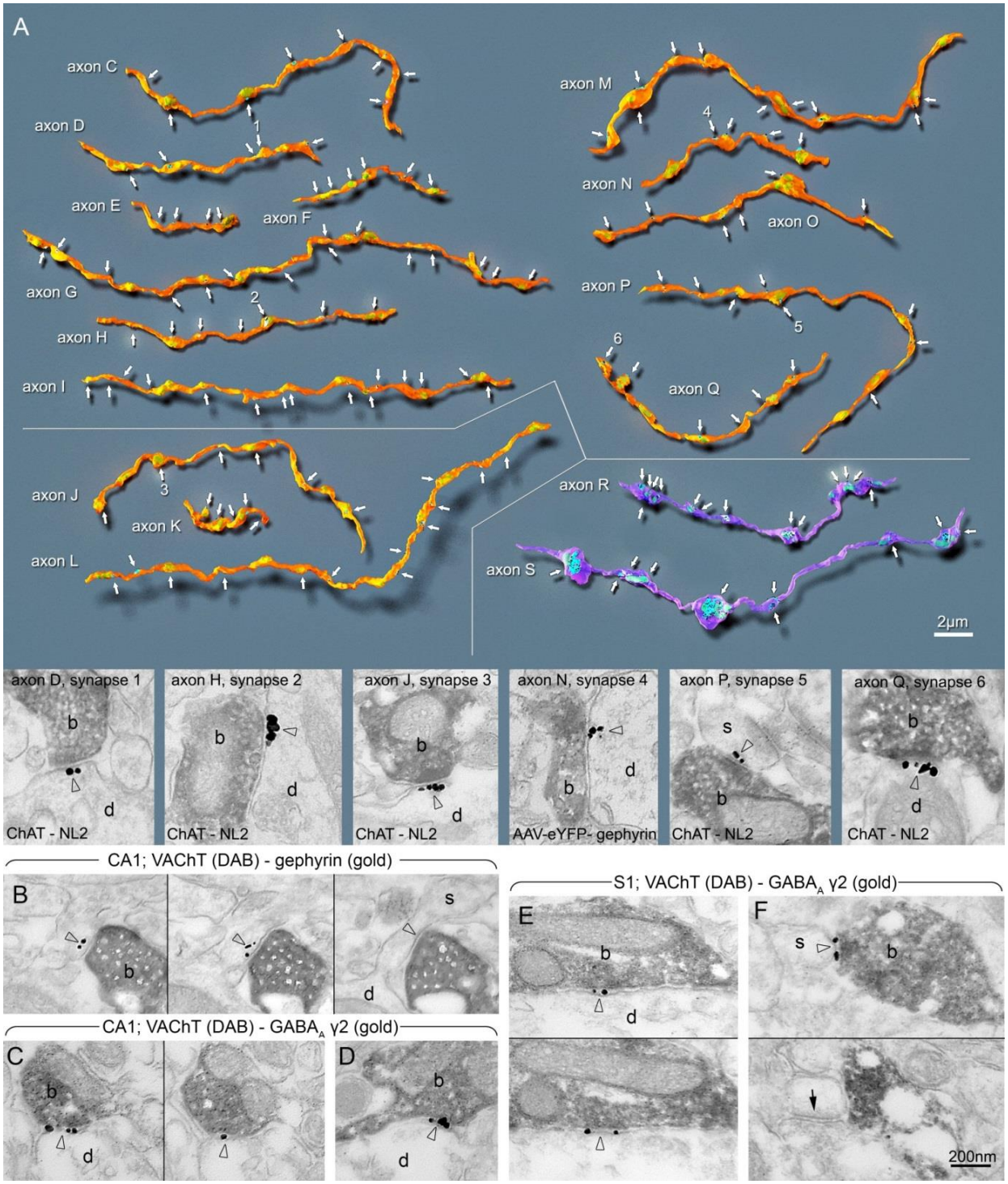

A: 3D EM reconstructions of DAB-labelled ChAT-positive (axons C-L; P,Q), AAV-eYFP virus-traced septo-hippocampal (axons M-O) and CB_1-positive (axons R, S) axonal segments from the hippocampus (str. ori: axons C-F, M-O, R; str. rad: G-I, S; str. l-m: P,Q) and layer I-III of the somatosensory cortex (axons J-L). Gold

labelings of NL2 (axons C-L; P-S) or gephyrin (axons M-O) were used to recognize synapses (arrows). Notice, that the linear density of synapses along cholinergic (C-Q) and CB_1-positive GABAergic axons (R,S) are not different (see also data in Figure 1). Electron micrographs show cholinergic terminal boutons (b) forming synapses 1-6 (arrowheads, indicated by the same numbers in the 3D-reconstructions) on dendrites (d) and a spine (s).

B-F: Electron micrographs from combined preembedding immunogold/immunoperoxidase experiments for gephyrin or $GABA_A\gamma2$ receptor subunit (immunogold) and vAChT (DAB: dark, homogenous reaction product) reveal the presence of gephyrin postsynaptically (B, arrowheads) and $GABA_A\gamma2$ receptor subunit (C, D; arrowheads) in the synaptic cleft of synapses established by vAChT-positive axons in the hippocampus (CA1, str. l-m: B, str. ori: C, D). E-F: vAChT-positive terminals (DAB) establish synapses with $GABA_A\gamma2$ receptor subunits (immunogold, arrowheads) in the neocortex S1 area (E-F). Two or three consecutive sections of the same synapses are shown in B, C, E, and F. Labelled terminals shown in the EM images innervate dendrites (d) or spines (s). Spine in F receives a type I synapse (arrow in the lower panel) from an unlabelled terminal. Scale bars are 2 µm for all reconstructions and 200 nm for all EM images.

Supplementary Figure 2,
Control experiments for the labelling of septo-hippocampal cholinergic cells and fibres with Cre-dependent viral and immunolabelling techniques

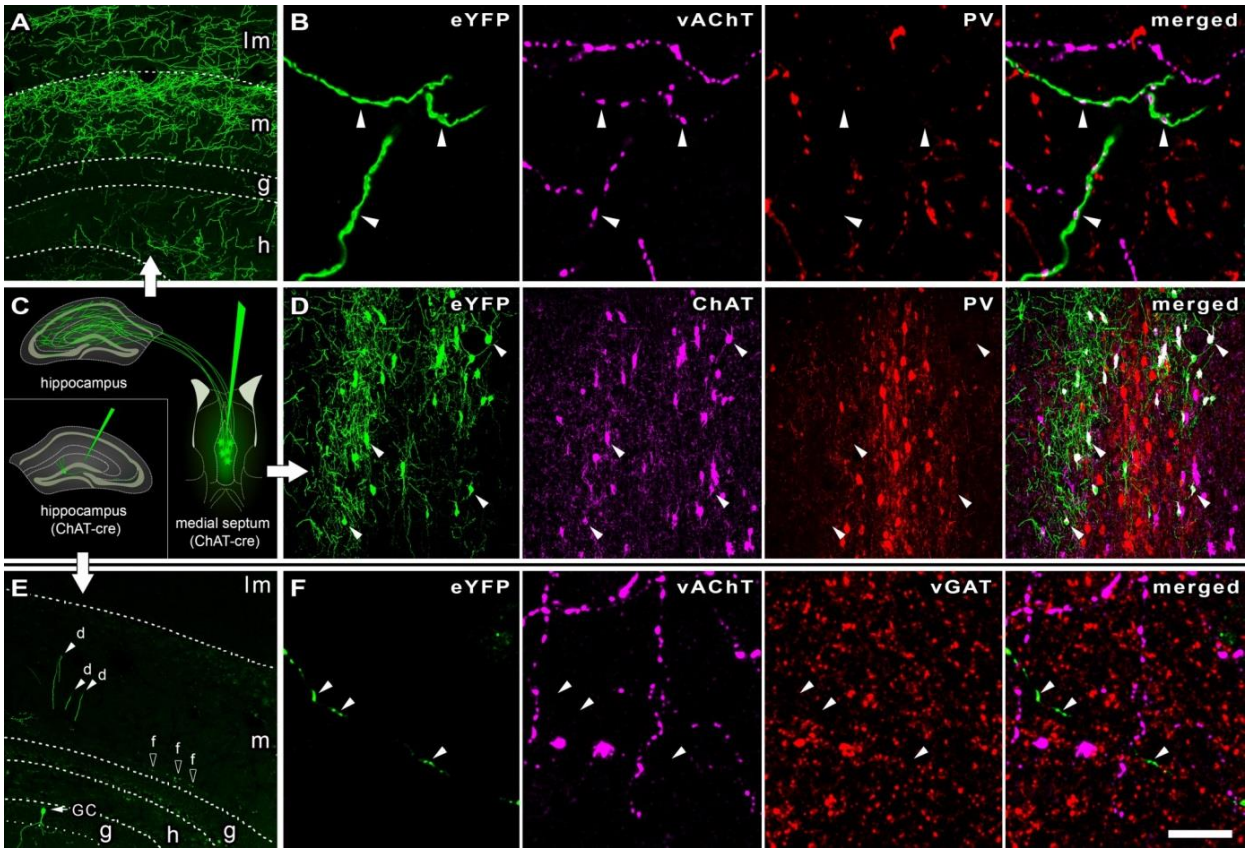

A: A robust network of eYFP-expressing cholinergic fibres is present in the hippocampus after AAV-injection into the MS of ChAT-Cre mouse. (lm: laconosum-moleculare, m: moleculare, g: granule-cell layer, h: hilus)
B: Confocal laser scanning microscopy images confirm that AAV-eYFP virus-traced septo-hippocampal fibres contain vAChT, but not parvalbumin (PV) in the hippocampus, demonstrating that septal GABAergic PV cells did not express Cre-dependent fluorescent protein. vAChT-labelling is localized to the terminals of the fibres. (Arrowheads mark the position of some terminals.)
C: Schematic diagram showing the AAV-eYFP-injections into the MS or hippocampus (inset) of ChAT-Cre mice.
D: All eYFP-expressing MS neurons were positive for ChAT, while none of them contained PV. (Arrowheads mark the position of some cell bodies.)
E: After AAV-eYFP-injection into the hippocampus of ChAT-Cre mice, a negligible amount of cells could be detected to express eYFP. eYFP-expressing granule cell can be seen with some dendrite-segments and few scattered fibres. (d: dendrite, f: fibre, GC: granule-cell)
F: Local eYFP-expressing fibres in the hippocampus do not contain vAChT or vGAT (Arrowheads mark some terminals, scale bar on F is 150 µm for A, D, E, and 6 µm for B and F), demonstrating the lack of cholinergic fibres originating from inside the hippocampus.

Supplementary Figure 3,
GABAergic short-term depression is a presynaptic property of cholinergic fibers.

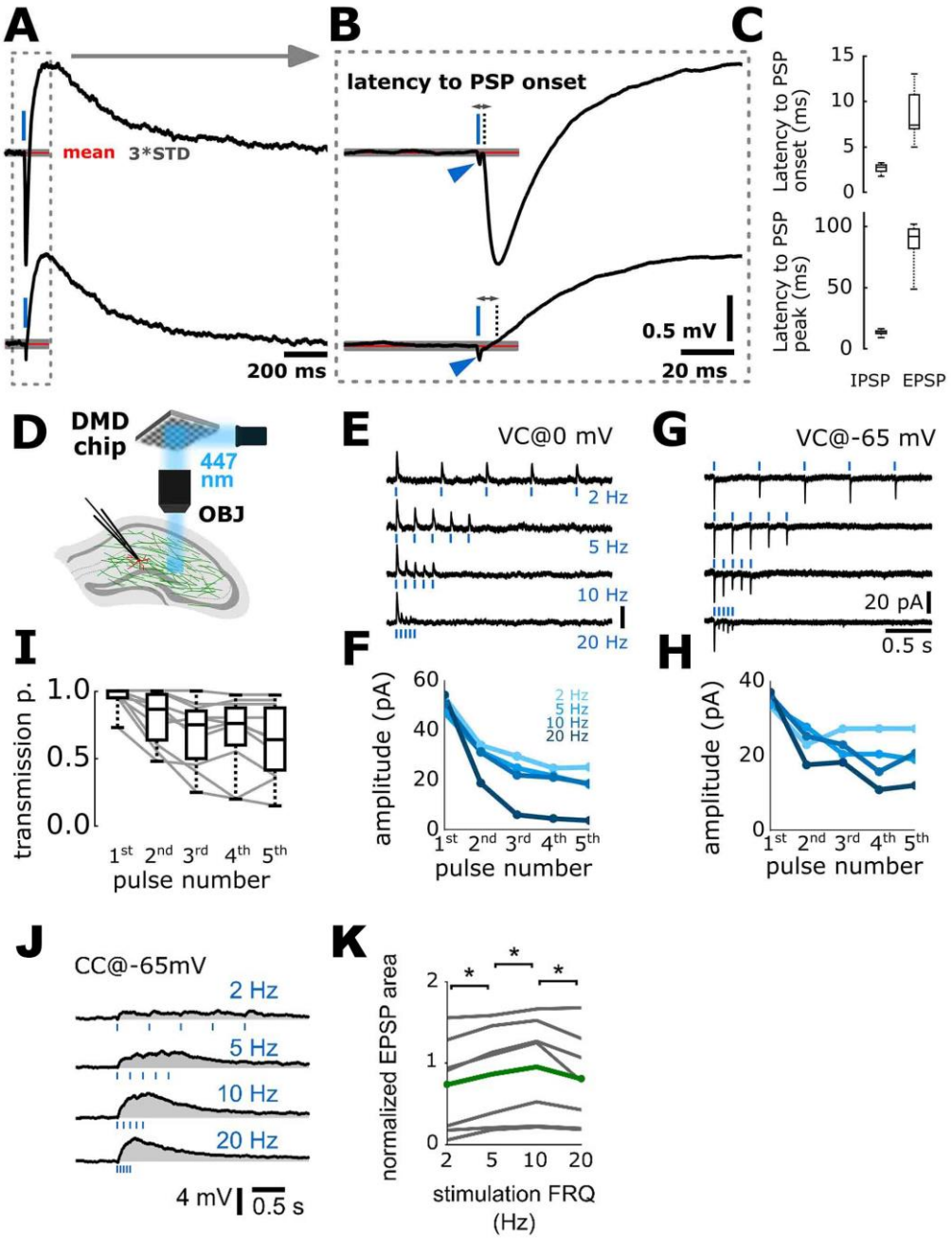

A: Average membrane potential response of an inhibitory neuron recorded in str. lacunosum-moleculare for cholinergic fiber stimulation (top). Latency from stimulation start to PSP onset was calculated as the time when the signal crosses 3 times standard deviation of baseline (orange line and grey shaded area represent mean and 3 times STD of the baseline). Inhibition of $GABA_AR$s (10 µM gabazine) blocks hyperpolarization (bottom) and the latency of the cholinergic response can be calculated similarly as well. **B:** Responses are magnified in time (from panel A). Blue arrowheads mark photoelectric artefacts evoked by 1 ms optical stimulus (blue bar). Note the short latency to rise (dotted line) in both the GABAergic IPSP and cholinergic EPSP.

C: Latency from stimulus start to PSP onset (top) and PSP peak (bottom) are shown. IPSP time to onset (n = 7, in ms): 2.8 (2.2, 3.1), time to peak: 13.8 (12.7, 14.9). EPSP time to onset (n = 6, in ms): 7.4(7.0, 11.7), time to peak: 92.0 (80.5, 98.0).
D: Channelrhodopsin 2 expression in axon terminals could change the short-term plasticity of the examined synapse by illumination driven calcium entry through the light activated channels. To exclude this possibility, with the help of a digital micro-mirror device (DMD), we have illuminated only axons running towards the measured cell, but not the axon terminals themselves.
E: We have recorded from inhibitory neurons in str. lacunosum moleculare (n=5), and illuminated the slice far (~500 µm) from the cells. Similarly as in Figure 3, we applied 5 pulses at different frequencies (2, 5, 10 and 20 Hz). Averaged traces from one cell are shown.
F: Mean amplitudes for different frequencies are shown from 5 cells. GABAergic currents evoked by light stimulation using the DMD device show similar short-term depression as presented on Figure 3. Amplitudes in pA (mean±std): 2 Hz: 1^{st} – 53.41(±23.66); 2^{nd} – 34.05(±17.79); 3^{rd} – 29.59(±11.54); 4^{th} – 24.80(±9.47); 5^{th} – 25.20(±11.54). 5 Hz: 1^{st} – 47.05(±21.15); 2^{nd} – 31.53(±15.58); 3^{rd} – 24.87(±12.68); 4^{th} – 21.69(±10.39); 5^{th} – 18.20(±9.58). 10 Hz: 1^{st} – 50.66(±19.43); 2^{nd} – 31.22(±13.31); 3^{rd} – 22.00(±8.16); 4^{th} – 21.10(±10.21); 5^{th} – 18.63(±4.71). 20 Hz: 1^{st} – 54.21(±18.28); 2^{nd} – 18.80(±3.95); 3^{rd} – 6.07(±1.8); 4^{th} – 4.55(±1.82); 5^{th} – 3.75(±2.11).
G: Another factor, which can contribute to short-term depression is postsynaptic chloride loading and subsequent reduction of chloride drive, due to series of stimuli. This phenomenon can be explored with reversing chloride gradient, as demonstrated here by using a high chloride content intracellular solution. Average GABAergic responses are shown from one cell.
H: Mean amplitudes for different frequencies are shown from 5 cells. GABAergic responses show similar short-term depression as described previously. Amplitudes in pA (mean±std): 2 Hz: 1^{st} – 33.27(±19.16); 2^{nd} – 23.02(±23.76); 3^{rd} – 27.28(±16.80); 4^{th} – 27.33(±20.33); 5^{th} – 26.31(±25.86). 5 Hz: 1^{st} – 33.27(±14.57); 2^{nd} – 27.76(±17.51); 3^{rd} – 20.46(±9.24); 4^{th} – 22.48(±10.67); 5^{th} – 10.00(±13.91). 10 Hz: 1^{st} – 36.23(±24.69); 2^{nd} – 25.29(±20.18); 3^{rd} – 23.02(±20.10); 4^{th} – 15.79(±10.36); 5^{th} – 20.76(±17.03). 20 Hz: 1^{st} – 37.09(±33.27); 2^{nd} – 17.61(±20.65); 3^{rd} – 18.29(±24.65); 4^{th} – 10.95(±10.16); 5^{th} – 12.10(±11.49).
I: Transmission probability is shown for 10 Hz stimulation from the 10 cells presented on Figure E-H. The decrease in transmission probability support presynaptic mechanism for STD. Transmission probability: 1^{st} pulse 1(0.95, 1), 2^{nd} pulse: 0.87 (0.60, 1), 3^{rd} pulse: 0.75 (0.45, 0.87), 4^{th} pulse: 0.76 (0.55, 0.90), 5^{th} pulse: 0.64 (0.37, 0.90). Wilcoxon-sign rank test: 1^{st}–2^{nd}: $p<0.05$, 2^{nd}–3^{rd}: $p<0.05$, 3^{rd}–4th and 4^{th}-5^{th}: not significant. In some cells, transmission probability remained stable despite the observed STD in IPSC amplitude, suggesting that multiple contacts were excited and “averaged” by optical illumination. These results support our hypothesis that GABAergic short-term depression emerges presynaptically, and not the result of channelrhodopsin-2 expression or postsynaptic chloride loading.
J: Short-term dynamics of cholinergic EPSPs recorded from inhibitory neurons in str. lac.-mol. in response to 5 light pulses at different frequencies (top; 2, 5, 10, 20 Hz, n = 7). Cholinergic events overlap, not allowing reliable EPSP peak detection. Therefore, STP was quantified as the integral of the evoked events.
K: The relative change in EPSP integral for the stimulations at different frequencies (n=7, average is green). Unlike the GABAergic component (Figure 3), short-term depression was not observed in cholinergic responses. Slight increase in EPSP area from 2 to 10 Hz suggests some form of a weak facilitation of the cholinergic component. EPSP integral at 2 Hz: 2.19 mV*s (0.41-3.63), 5 Hz: 2.56 mV*s (0.49-3.70), 10 Hz: 2.92 mV*s (0.53-3.88), 20 Hz: 1.82 mV*s (0.46-3.92); Wilcoxon-sign rank test: $p<0.05$; 0.05; 0.03.

Supplementary Figure 4,
Vesicular acetylcholine and GABA transporters are localized on different vesicles

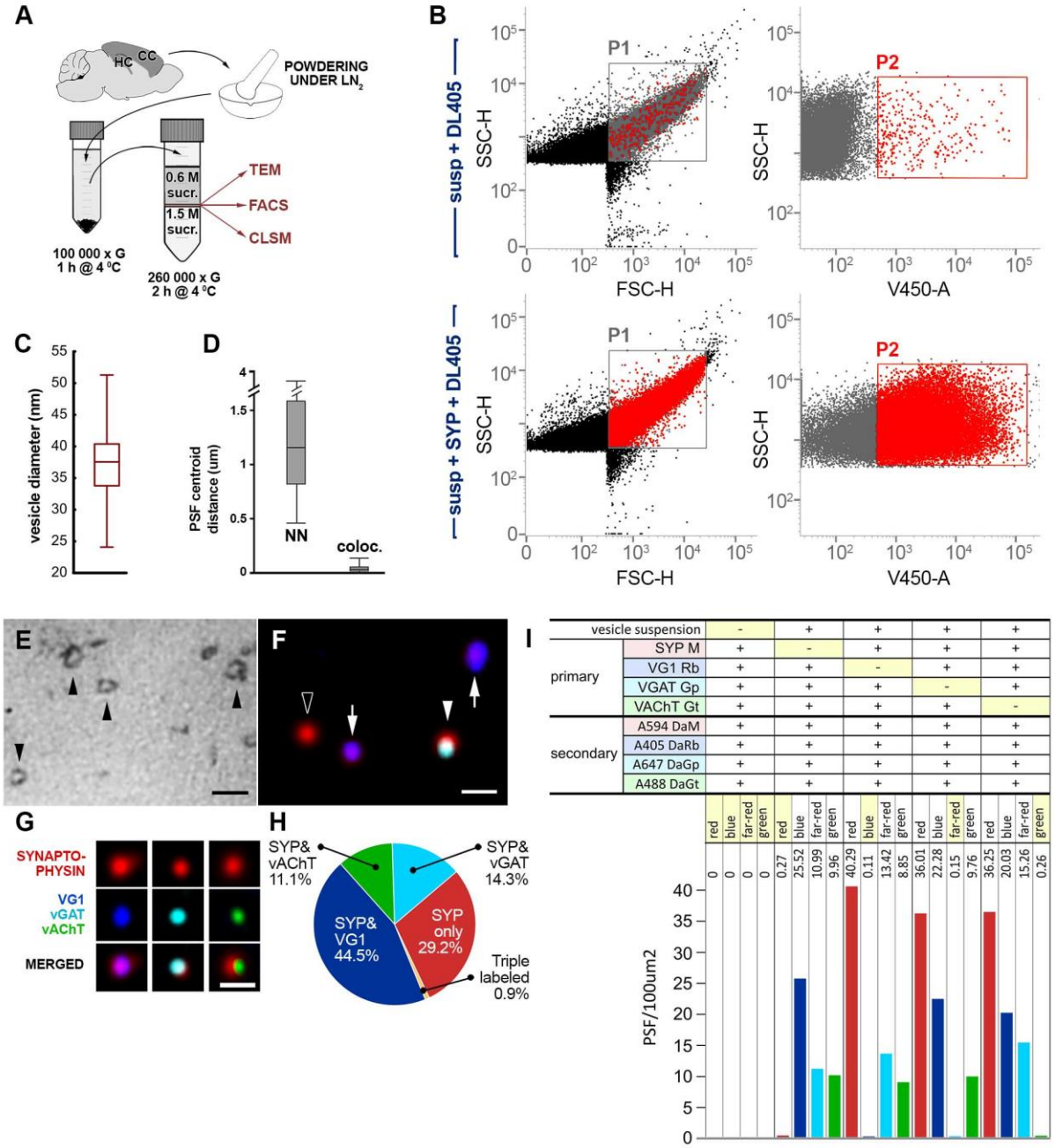

A: Schematic drawing depicts the main steps of synaptic vesicle isolation. Cerebral cortices (CC) and hippocampi (HC) of mice were frozen and powdered under liquid nitrogen. After homogenization, the sample was centrifuged at 100 000 G (1h, 4°C). The supernatant was laid onto a 0,6M/1,5M sucrose step gradient and centrifuged at 260 000 G (2h, 4°C). Synaptic vesicles were collected from the 0,6M/1,5M sucrose solution interface, and processed for transmission electron microscopy (TEM), flow cytometry (FACS) and confocal laser scanning microscopy (CLSM).
B: Flow cytometric analysis of isolated synaptic vesicles from mouse hippocampal and neocortical areas show the purity of our vesicular sample preparations. Dot plot diagrams show putative vesicles

investigated without (upper row) and with (lower row) synaptophysin (SYP) primary antibody labelling, followed by fluorescent secondary antibody labelling in both cases. Dot plots on the right, show strong fluorescence signal of SYP immunolabelled putative vesicles (SSC/V450), gated also on the SSC/FSC dot plots [P1], suggesting that the isolated sample is highly purified.

C: Diameter distribution of isolated synaptic vesicles on the TEM images show typical vesicular diameters.

D: Distribution of fluorescent point-spread functions on the CLSM images. SYP labelled vesicles were usually more than 1 μm away from each other as nearest-neighbor analysis of PSF centroids confirmed. Centroids of PSF in different channels belonging to one vesicle were never farther away from each other than 130 nm.

E: Electron micrograph of fixed and dehydrated synaptic vesicles isolated (see A) from cerebral cortex and hippocampus. Arrows point to individual vesicles, scale bar is 100 nm.

F: CLSM image of fixed and immunolabelled isolated synaptic vesicles. Arrows point to point spread functions (PSF) of VG1 and SYP co-labelled vesicles, arrowhead marks PSF of vGAT and SYP co-labelled vesicle, empty arrowhead shows PSF of vesicle positive only for SYP. Scale bar is 400 nm.

G: CLSM images of individual PSFs representing synaptic vesicles from quadruple labelling experiments. Scale bar is 600 nm.

H: Percentages of differently labelled synaptic vesicles (n=350 individual vesicles). Frequency of triple labelled vesicles were less than 1 percent, confirming that vesicular transporters for glutamate, GABA and acetylcholine are expressed by distinct vesicle populations.

I: Control experiments of the immunolabelling method confirm the lack of non-specific staining. In the absence of vesicle suspension no PSF-s were found in the CLSM scans, and the exclusion of each primary antibody led to the selective disappearance of PSFs in the corresponding channel.

SUPPLEMENTARY TABLES 1-4:

Supplementary Table 1 (primary antibodies)

RAISED AGAINST	RAISED IN	DILUTION* (APPLICATION)	SOURCE	CATALOG NUMBER / CODE	SPECIFICITY
CHOLINE ACETYL TRANSFERASE (CHAT)	mouse	1:750 (DAB), 1:400-500 (fluorescent)	Dr. Costantino Cozzari		Characterized in [55]
GABA	rabbit	1:10 000 (postembedding immunogold)	Dr. Peter Somogyi	GABA9	Characterized in [56]
GABA A RECEPTOR GAMMA 2 SUBUNIT	rabbit	1:1000 (preembedding immunogold)	Synaptic Systems	224 003	Immunolabelling is abolished by virus-mediated gene-knock-out of GABAA receptors [57]
GEPHYRIN	mouse	1:100 (preembedding immunogold), 1:500 (fluorescent)	Synaptic Systems	147,021	Specific for the brain specific 93 kDa splice variant; KO verified (manufacturer's information)
GREEN FLUORESCENT PROTEIN	chicken	1:2000 (DAB, fluorescent)	Molecular Probes	A10262	no labelling in animals that were not injected with eGFP-expressing viruses
NEUROLIGIN 2 (NL2)	rabbit	1:600 (preembedding immunogold)	Synaptic Systems	129,203	No cross reactivity to neuroligins 1, 3, 4 (manufacturer's information); KO verified by our laboratory [1];
TYPE 1 CANNABINOID RECEPTOR (CB1)	goat	1:2000 (DAB)	Dr. Masahiko Watanabe		KO verified in [58]
VESICULAR ACETYLCHOLINE TRANSPORTER (VACHT)	rabbit	1:5000 (DAB, preembedding immunogold), 1:3000 (fluorescent)	Synaptic Systems	139 103	KO verified (manufacturer's information)
VESICULAR ACETYLCHOLINE TRANSPORTER (VACHT)	goat	1:10 000 (DAB, fluorescent)	Immunostar	1308002	Immunolabelling is completely abolished by preadsorption with synthetic rat VAT (vAChT) (511–530). Immunolabelling of transfected cells demonstrates no cross reactivity with vesicular monoamine transporters (manufacturer's information)

VESICULAR GABA TRANSPORTER (VGAT)	guinea-pig	1:2000 (fluorescent)	Synaptic Systems	131004	KO verified (manufacturer's information)
GFP	rabbit	1:2000 (fluorescent)	Molecular Probes	A11122	no labelling in animals that were not injected with eGFP-expressing viruses
PV	mouse	1:1000 (fluorescent)	Dr. Kenneth Baimbridge	-	stains the same as the KO-verified mouse ab
PV	rabbit	1:2000 (fluorescent)	SWANT	235	KO verified (manufacturer's information)
GAD65	mouse	1:250 (fluorescent)	Millipore (clone: GAD6)	MAB351	Recognizes the lower molecular weight isoform of the two GAD isoforms identified in brain [59].
GEPHYRIN	rabbit	1:2000 (fluorescent)	Synaptic Systems	147008 RbmAB7a	KO verified (manufacturer's information)
VACHT	guinea-pig	1:1000 (fluorescent)	Synaptic Systems	139 105	Gives identical staining to the K.O. verified 139 103 rabbit-anti-vAChT antibody
SYNAPTO-PHYSIN	mouse	1:1000 (fluorescent)	Sigma Aldrich, clone: SVP-38	S5768	[60]
VESICULAR GLUTAMATE TRANSPORTER 1	rabbit	1:1000 (fluorescent)	Synaptic Systems	135 302	KO verified (manufacturer's information)

* WHOLE SERUM WAS DILUTED OR STOCK SOLUTION WAS RECONSTITUTED AS DESCRIBED BY THE MANUFACTURER

Supplementary Table 2 (secondary antibodies)

CONJUGATED WITH	RAISED IN	RAISED AGAINST	DILUTION* (PROCEDURE)	SOURCE	CATALOG NUMBER
1.4-NM NANOGOLD	goat	rabbit	1:100-1:300 (preembedding immunogold)	Nanoprobes	#2004
10-NM GOLD	goat	rabbit	1:1000 (postembedding immunogold)	BBI solutions	EM.GAR10
ULTRA SMALL GOLD	goat	mouse	1:50 (preembedding immunogold)	Aurion	100.022
BIOTIN-SP	donkey	goat	1:1000 (DAB)	JIL Inc. (Jackson Immunoresearch Laboratories, Inc.)	705-066-147
BIOTIN-SP	donkey	mouse	1:1000 (DAB)	JIL Inc.	715-066-151
BIOTIN-SP	donkey	goat	1:1000 (DAB)	JIL Inc.	705-066-147
BIOTIN-SP	donkey	rabbit	1:500 (DAB)	JIL Inc.	711-065-152
BIOTIN	goat	chicken	1:200 (DAB)	Vector Laboratories	BA-9010
DYLIGHT 405	donkey	mouse	1:200 Flow cytometry	JIL Inc.	715-475-151
DYLIGHT 405	donkey	rabbit	1:1000 (confocal)	JIL Inc.	711-475-152
ALEXA 488	goat	chicken	1:1000 (confocal), 1:500 (STORM)	Vector Laboratories	A-11039
ALEXA 488	donkey	rabbit	1:500 (confocal)	Invitrogen	A21206
ALEXA 488	donkey	chicken	1:1000 (confocal)	JIL Inc.	703-545-155
ALEXA 488	donkey	goat	1:1000 (confocal)	JIL Inc.	705-475-147
CY-3	donkey	mouse	1:500 (confocal)	JIL Inc.	715-165-151
ALEXA 594	donkey	rabbit	1:500 (confocal)	Invitrogen	A21207
DYLIGHT 549	donkey	guinea-pig	1:500 (confocal)	JIL Inc.	706-505-148
ALEXA 594	donkey	mouse	1:500 (confocal)	Life Technologies	A21203
CF 568	donkey	guinea-pig	1:500 (STORM)	Biotium	20377-500uL
ALEXA 647	donkey	guinea-pig	1:500 (confocal)	JIL Inc.	706-605-148
CY-5	donkey	goat	1:500 (confocal)	JIL Inc.	705-175-147
ALEXA 647	donkey	rabbit	1:500 (confocal, STORM)	JIL Inc.	711-605-152
ALEXA 647	donkey	mouse	1:500 (confocal)	JIL Inc.	715-605-151

Supplementary Table 3.,
The ratio of synapses of cholinergic fibres expressing gephyrin and $GABA_AR$ γ2 subunit in different brain areas.

Mouse, area, labeling*	No. of synapses	No. of positive synapses	% of positive synapses
CA1, Gephyrin labelling in synapses of cholinergic fibres			
WT3 ori (vAChT labelling)	29	23	79
WT3 pyr (vAChT labelling)	5	5	100
WT3 l-m (vAChT labelling)	18	15	83
WT4 ori (vAChT labelling)	22	20	91
WT4 pyr (vAChT labelling)	2	2	100
WT4 l-m (vAChT labelling)	25	21	84
ChAT-Cre1 ori (AAV-eYFP labelling)	26	21	81
ChAT-Cre1 pyr (AAV-eYFP labelling)	1	1	100
ChAT-Cre1 rad (AAV-eYFP labelling)	22	15	68
ChAT-Cre2 ori (AAV-eYFP labelling)	37	29	78
ChAT-Cre2 pyr (AAV-eYFP labelling)	1	1	100
all	**188**	**153**	**81**
CA1, $GABA_AR$ γ2 labelling in synapses of cholinergic fibres			
WT3 l-m (vAChT labelling)	31	24	77
WT5 ori (vAChT labelling)	27	20	74
WT6 ori (vAChT labelling)	16	11	69
WT6 pyr (vAChT labelling)	3	2	67
WT6 l-m (vAChT labelling)	20	16	80
ChAT-Cre2 ori (AAV-eYFP labelling)	32	27	84
ChAT-Cre2 pyr (AAV-eYFP labelling)	9	8	89
ChAT-Cre2 rad (AAV-eYFP labelling)	5	4	80
ChAT-Cre3 ori (AAV-eYFP labelling)	26	25	96
ChAT-Cre3 pyr (AAV-eYFP labelling)	3	1	33
all	**172**	**138**	**80**
S1, $GABA_AR$γ2 labelling in synapses of cholinergic fibres			
WT6 all (vAChT labelling)	**36**	**30**	**83**

* WT3-6: indicates 4 wild type mice, ChAT-Cre1-3: indicates 3 different mice, ori: stratum oriens, pyr: stratum pyramidale, rad: stratum radiatum, l-m: stratum lacunosum-moleculare

Supplementary Table 4.
Measured parameters of reconstructed axonal segments

							Postsynaptic targets			
Axon ID [a]	**Labelling (DAB-gold)**	**mouse**	**Length (µm)**	**No. of mitochondria**	**No. of synapses**	**Synapse density (syn./ 100 µm)**	**Pyramidal dendrite**	**Interneuron dendrite**	**Spine**	**Unidentified**
A (in CA1 ori)	ChAT-NL2	WT1	22.0	4	12	54.5	8	1	3	0
C (in CA1 ori)	ChAT-NL2	WT2	21.5	3	8	37.2	3	1	4	0
D (in CA1 ori)	ChAT-NL2	WT2	14.8	4	5	33.8	5	0	0	0
E (in CA1 ori)	ChAT-NL2	WT2	6.8	1	4	58.5	2	1	0	1
F (in CA1 ori)	ChAT-NL2	WT2	10.0	4	6	60.1	5	1	0	0
B (in CA1 ori)	eYFP-gephyrin	ChAT-Cre1	38.1	11	15	39.4	10	0	3	2
M (in CA1 ori)	eYFP-gephyrin	ChAT-Cre1	27.0	7	10	37.0	6	1	0	3
N (in CA1 ori)	eYFP-gephyrin	ChAT-Cre2	12.3	2	4	32.6	4	0	0	0
O (in CA1 ori)	eYFP-gephyrin	ChAT-Cre2	18.4	4	6	32.7	4	0	2	0
CA1 ori (cholinergic) all			**170.9**	**40**	**70**	**41.0**	**47 (67.1%)**	**5 (7.1%)**	**12 (17.1%)**	**6 (8.6%)**
G (in CA1 rad)	ChAT-NL2	WT1	33.1	12	15	45.3	8	0	7	0
H (in CA1 rad)	ChAT-NL2	WT2	17.2	4	7	40.8	4	0	3	0
I (in CA1 rad)	ChAT-NL2	WT1	25.4	9	15	59.0	8	0	7	0
CA1 rad (cholinergic) all			**75.8**	**25**	**37**	**48.8**	**20 (54.1%)**	**0 (0%)**	**17 (45.9%)**	**0 (0%)**
CA1 ori+rad (cholinergic) all			**246.7**	**65**	**107**	**43.4**	**67 (62.6%)**	**5 (4.7%)**	**29 (27.1%)**	**6 (5.6%)**
P (in CA1 l-m)	ChAT-NL2	WT2	26.2	7	8	30.5	2[b]		5	1
Q (in CA1 l-m)	ChAT-NL2	WT2	17.0	5	6	35.3	2[b]		3	1
CA1 l-m (cholinergic) all			**43.2**	**12**	**14**	**32.4**	**4[b] (28.6%)**		**8 (57.1%)**	**2 (14.3%)**
CA1 cholinergic fibers in all layers			**289.9**	**77**	**121**	**41.7**	**76[b] (62.8%)**		**37 (30.6%)**	**8 (6.6%)**
J (in S1 LI)	ChAT-NL2	WT2	22.0	7	6	27.3	4[b]		2	0
K (in S1 LII/LIII)	ChAT-NL2	WT2	6.1	3	5	82.7	1[b]		3	1
L (in S1 LII)	ChAT-NL2	WT2	32.6	10	13	39.9	8[b]		4	1
S1 cholinergic fibers in all layers			**60.6**	**20**	**24**	**39.6**	**13[b] (54.2%)**		**9 (37.5%)**	**2 (8.3%)**
R (in CA1 ori)	CB_1-NL2	WT1	18.0	6	14	77.6	13	0	1	0
S (in CA1 rad)	CB_1-NL2	WT1	29.2	7	10	34.2	8	0	0	2
CA1 CB_1-positive fibers in all layers			**47.2**	**13**	**24**	**50.8**	**21 (87.5%)**	**0 (0%)**	**1 (4.2%)**	**2 (8.3%)**

[a]: WT3-6: indicates 4 wild type mice, ChAT-Cre1-3: indicates 3 different mice, ori: stratum oriens, pyr: stratum pyramidale, rad: stratum radiatum, l-m: stratum lacunosum-moleculare; [b]: We did not identify the cell types that established the dendritic shafts in CA1 lacunosum-moleculare and S1 (see Supplemental Experimental Procedures).

Supplementary References:

1. Takács, V. T., Freund, T. F. & Nyiri, G. Neuroligin 2 Is Expressed in Synapses Established by Cholinergic Cells in the Mouse Brain. *PLoS One* **8,** (2013).
2. Tyagarajan, S. K. & Fritschy, J.-M. Gephyrin: a master regulator of neuronal function? *Nat. Rev. Neurosci.* **15,** 141–156 (2014).
3. Dong, N., Qi, J. & Chen, G. Molecular reconstitution of functional GABAergic synapses with expression of neuroligin-2 and GABAA receptors. *Mol. Cell. Neurosci.* **35,** 14–23 (2007).
4. Poulopoulos, A. *et al.* Neuroligin 2 Drives Postsynaptic Assembly at Perisomatic Inhibitory Synapses through Gephyrin and Collybistin. *Neuron* **63,** 628–642 (2009).
5. Jedlicka, P. *et al.* Increased dentate gyrus excitability in neuroligin-2-deficient mice in vivo. *Cereb. Cortex* **21,** 357–367 (2011).
6. Essrich, C., Lorez, M., Benson, J. A., Fritschy, J.-M. & Lüscher, B. Postsynaptic clustering of major GABAA receptor subtypes requires the γ2 subunit and gephyrin. *Nat. Neurosci.* **1,** 563–571 (1998).
7. Schweizer, C. *et al.* The ??2 subunit of GABAA receptors is required for maintenance of receptors at mature synapses. *Mol. Cell. Neurosci.* **24,** 442–450 (2003).
8. Zhang, B., Ganetzky, B., Bellen, H. J. & Murthy, V. N. Tailoring uniform coats for synaptic vesicles during endocytosis. *Neuron* **23,** 419–422 (1999).
9. Karunanithi, S., Marin, L., Wong, K. & Atwood, H. L. Quantal Size and Variation Determined by Vesicle Size in Normal and Mutant Drosophila Glutamatergic Synapses. *J. Neurosci.* **22,** 10267–10276 (2002).
10. Takamori, S., Riedel, D. & Jahn, R. Immunoisolation of GABA-specific synaptic vesicles defines a functionally distinct subset of synaptic vesicles. *J. Neurosci.* **20,** 4904–4911 (2000).
11. Mutch, S. A. *et al.* Protein Quantification at the Single Vesicle Level Reveals That a Subset of Synaptic Vesicle Proteins Are Trafficked with High Precision. *J. Neurosci.* **31,** 1461–1470 (2011).
12. Qu, L., Akbergenova, Y., Hu, Y. & Schikorski, T. Synapse-to-synapse variation in mean synaptic vesicle size and its relationship with synaptic morphology and function. *J. Comp. Neurol.* **514,** 343–352 (2009).
13. Blusztajn, J. K. & Rinnofner, J. Intrinsic cholinergic neurons in the hippocampus: Fact or artifact? *Front. Synaptic Neurosci.* **8,** 6–11 (2016).
14. Descarries, L., Gisiger, V. & Steriade, M. Diffuse transmission by acetylcholine in the CNS. *Prog. Neurobiol.* **53,** 603–625 (1997).
15. Lendvai, B. & Vizi, E. S. Nonsynaptic Chemical Transmission Through Nicotinic Acetylcholine Receptors. *Physiol. Rev.* **88,** 333–349 (2008).
16. Vizi, E. S., Kiss, J. P. & Lendvai, B. Nonsynaptic communication in the central nervous system. *Neurochem. Int.* **45,** 443–451 (2004).
17. Zoli, M., Jansson, A., Syková, E., Agnati, L. F. & Fuxe, K. Volume transmission in the CNS and its relevance for neuropsychopharmacology. *Trends Pharmacol. Sci.* **20,** 142–150 (1999).
18. Vizi, E. S. Role of high-affinity receptors and membrane transporters in nonsynaptic communication and drug action in the central nervous system. *Pharmacol. Rev.* **52,** 63–89 (2000).
19. Agnati, L. F. *et al.* Volume transmission and wiring transmission from cellular to molecular networks: History and perspectives. *Acta Physiol.* **187,** 329–344 (2006).
20. Sarter, M., Parikh, V. & Howe, W. M. Phasic acetylcholine release and the volume transmission hypothesis: time to move on. *Nat. Rev. Neurosci.* **10,** 383–390 (2009).
21. De Lima, a D. & Singer, W. Cholinergic innervation of the cat striate cortex: a choline acetyltransferase immunocytochemical analysis. *J. Comp. Neurol.* **250,** 324–38 (1986).
22. Aznavour, N., Mechawar, N. & Descarries, L. Comparative analysis of cholinergic innervation in the dorsal hippocampus of adult mouse and rat: A quantitative immunocytochemical study. *Hippocampus* **12,** 206–217 (2002).

23. Umbriaco, D., Watkins, K. C., Descarries, L., Cozzari, C. & Hartman, B. K. Ultrastructural and Morphometric Features of the Acetylcholine Innervation in Adult-Rat Parietal Cortex - An Electron-Microscopic Study in Serial Sections. *J. Comp. Neurol.* **348,** 351–373 (1994).
24. Umbriaco, D., Garcia, S., Beaulieu, C. & Descarries, L. Relational features of acetylcholine, noradrenaline, serotonin and GABA axon terminals in the Stratum radiatum of adult rat hippocampus (CA1). *Hippocampus* **5,** 605–620 (1995).
25. Aznavour, N., Watkins, K. C. & Descarries, L. Postnatal development of the cholinergic innervation in the dorsal hippocampus of rat: Quantitative light and electron microscopic immunocytochemical study. *J. Comp. Neurol.* **486,** 61–75 (2005).
26. Yamasaki, M., Matsui, M. & Watanabe, M. Preferential Localization of Muscarinic M1 Receptor on Dendritic Shaft and Spine of Cortical Pyramidal Cells and Its Anatomical Evidence for Volume Transmission. *J. Neurosci.* **30,** 4408–4418 (2010).
27. Mrzljak, L., Pappy, M., Leranth, C. & Goldman???Rakic, P. S. Cholinergic synaptic circuitry in the macaque prefrontal cortex. *J. Comp. Neurol.* **357,** 603–617 (1995).
28. Smiley, J. F., Morrell, F. & Mesulam, M. M. Cholinergic synapses in human cerebral cortex: an ultrastructural study in serial sections. *Exp. Neurol.* **144,** 361–8 (1997).
29. Turrini, P. *et al.* Cholinergic nerve terminals establish classical synapses in the rat cerebral cortex: Synaptic pattern and age-related atrophy. *Neuroscience* **105,** 277–285 (2001).
30. Rouse, S. T., Edmunds, S. M., Yi, H., Gilmor, M. L. & Levey, A. I. Localization of M(2) muscarinic acetylcholine receptor protein in cholinergic and non-cholinergic terminals in rat hippocampus. *Neurosci Lett* **284,** 182–186 (2000).
31. Pepeu, G. & Giovannini, M. G. Changes in Acetylcholine Extracellular Levels During Cognitive Processes. 21–27 (2004). doi:10.1101/lm.68104.)
32. Parikh, V., Kozak, R., Martinez, V. & Sarter, M. Prefrontal Acetylcholine Release Controls Cue Detection on Multiple Timescales. *Neuron* **56,** 141–154 (2007).
33. Howe, W. M. *et al.* Prefrontal Cholinergic Mechanisms Instigating Shifts from Monitoring for Cues to Cue-Guided Performance: Converging Electrochemical and fMRI Evidence from Rats and Humans. *J. Neurosci.* **33,** 8742–8752 (2013).
34. Muñoz, W. & Rudy, B. Spatiotemporal specificity in cholinergic control of neocortical function. *Curr. Opin. Neurobiol.* **26,** 149–160 (2014).
35. Teles-Grilo Ruivo, L. M. *et al.* Coordinated Acetylcholine Release in Prefrontal Cortex and Hippocampus Is Associated with Arousal and Reward on Distinct Timescales. *Cell Rep.* **18,** 905–917 (2017).
36. Hangya, B., Ranade, S. P., Lorenc, M. & Kepecs, A. Central Cholinergic Neurons Are Rapidly Recruited by Reinforcement Feedback. *Cell* **162,** 1155–1168 (2015).
37. Letzkus, J. J. *et al.* A disinhibitory microcircuit for associative fear learning in the auditory cortex. *Nature* **480,** 331–335 (2011).
38. Gritton, H. J. *et al.* Cortical cholinergic signaling controls the detection of cues. *Proc. Natl. Acad. Sci.* **113,** E1089–E1097 (2016).
39. Gu, Z. & Yakel, J. L. Timing-Dependent Septal Cholinergic Induction of Dynamic Hippocampal Synaptic Plasticity. *Neuron* **71,** 155–165 (2011).
40. Allaway, K. C. & Machold, R. Developmental specification of forebrain cholinergic neurons. *Dev. Biol.* **421,** 1–7 (2017).
41. Fragkouli, A., van Wijk, N. V., Lopes, R., Kessaris, N. & Pachnis, V. LIM homeodomain transcription factor-dependent specification of bipotential MGE progenitors into cholinergic and GABAergic striatal interneurons. *Development* **136,** 3841–3851 (2009).
42. Bachy, I. & Rétaux, S. GABAergic specification in the basal forebrain is controlled by the LIM-hd factor Lhx7. *Dev. Biol.* **291,** 218–226 (2006).
43. Liodis, P. *et al.* Lhx6 Activity Is Required for the Normal Migration and Specification of Cortical Interneuron Subtypes. *J. Neurosci.* **27,** 3078–3089 (2007).

44. Fisher, R. S. & Levine, M. S. Transmitter cosynthesis by corticopetal basal forebrain neurons. *Brain Res.* **491,** 163–168 (1989).
45. Granger, A. J., Mulder, N., Saunders, A. & Sabatini, B. L. Cotransmission of acetylcholine and GABA. *Neuropharmacology* **100,** 40–46 (2016).
46. Beaulieu, C. & Somogyi, P. Enrichment of cholinergic synaptic terminals on GABAergic neurons and coexistence of immunoreactive GABA and choline acetyltransferase in the same synaptic terminals in the striate cortex of the cat. *J. Comp. Neurol.* **304,** 666–680 (1991).
47. Saunders, A., Granger, A. J. & Sabatini, B. L. Corelease of acetylcholine and GABA from cholinergic forebrain neurons. *Elife* **2015,** 1–13 (2015).
48. Pang, K. C. H., Jiao, X., Sinha, S., Beck, K. D. & Servatius, R. J. Damage of GABAergic neurons in the medial septum impairs spatial working memory and extinction of active avoidance: Effects on proactive interference. *Hippocampus* **21,** 835–846 (2011).
49. Henny, P. & Jones, B. E. Projections from basal forebrain to prefrontal cortex comprise cholinergic, GABAergic and glutamatergic inputs to pyramidal cells or interneurons. *Eur. J. Neurosci.* **27,** 654–670 (2008).
50. Münster-Wandowski, A., Gómez-Lira, G. & Gutiérrez, R. Mixed neurotransmission in the hippocampal mossy fibers. *Front. Cell. Neurosci.* **7,** 1–19 (2013).
51. Gundersen, V., Holten, A. T. & Storm-Mathisen, J. GABAergic synapses in hippocampus exocytose aspartate on to NMDA receptors: Quantitative immunogold evidence for co-transmission. *Mol. Cell. Neurosci.* **26,** 156–165 (2004).
52. Kljakic, O., Janickova, H., Prado, V. F. & Prado, M. A. M. Cholinergic/glutamatergic co-transmission in striatal cholinergic interneurons: New mechanisms regulating striatal computation. *J. Neurochem.* 1–13 (2017). doi:10.1111/jnc.14003
53. Lee, S., Kim, K. & Zhou, Z. J. Role of ACh-GABA Cotransmission in Detecting Image Motion and Motion Direction. *Neuron* **68,** 1159–1172 (2010).
54. Saunders, A. *et al.* A direct GABAergic output from the basal ganglia to frontal cortex. *Nature* **521,** 85–89 (2015).
55. Cozzari, C., Howard, J. & Hartman, B. Analysis of epitopes on choline acetyltransferase (ChAT) using monoclonal antibodies. in *Soc Neurosci Abstr 16* 200 (1990).
56. Somogyi, P. & Hodgson, A. J. Antisera to gamma-aminobutyric acid. III. Demonstration of GABA in Golgi-impregnated neurons and in conventional electron microscopic sections of cat striate cortex. *J. Histochem. Cytochem.* **33,** 249–257 (1985).
57. Rovo, Z. *et al.* Phasic, Nonsynaptic GABA-A Receptor-Mediated Inhibition Entrains Thalamocortical Oscillations. *J. Neurosci.* **34,** 7137–7147 (2014).
58. Uchigashima, M. *et al.* Subcellular Arrangement of Molecules for 2-Arachidonoyl-Glycerol-Mediated Retrograde Signaling and Its Physiological Contribution to Synaptic Modulation in the Striatum. *J. Neurosci.* **27,** 3663–3676 (2007).
59. Gottlieb, I. Characterization of the Proteins Purified with Monoclonal to Glutamic Acid Decarboxylase. **8,** 2123–2130 (1988).
60. Obata, K. *et al.* Four synaptic vesicle-specific proteins: identification by monoclonal antibodies and distribution in the nervous tissue and the adrenal medulla. *Brain Res.* **404,** 169–179 (1987).

Brain Struct Funct
DOI 10.1007/s00429-016-1217-x

ORIGINAL ARTICLE

Cellular architecture and transmitter phenotypes of neurons of the mouse median raphe region

Katalin E. Sos[1,2] · Márton I. Mayer[1] · Csaba Cserép[1] · Flóra S. Takács[1] · András Szőnyi[1,2] · Tamás F. Freund[1] · Gábor Nyiri[1]

Received: 14 August 2015 / Accepted: 16 March 2016

Abstract The median raphe region (MRR, which consist of MR and paramedian raphe regions) plays a crucial role in regulating cortical as well as subcortical network activity and behavior, while its malfunctioning may lead to disorders, such as schizophrenia, major depression, or anxiety. Mouse MRR neurons are classically identified on the basis of their serotonin (5-HT), vesicular glutamate transporter type 3 (VGLUT3), and gamma-aminobutyric acid (GABA) contents; however, the exact cellular composition of MRR regarding transmitter phenotypes is still unknown. Using an unbiased stereological method, we found that in the MR, 8.5 % of the neurons were 5-HT, 26 % were VGLUT3, and 12.8 % were 5-HT and VGLUT3 positive; whereas 37.2 % of the neurons were GABAergic, and 14.4 % were triple negative. In the whole MRR, 2.1 % of the neurons were 5-HT, 7 % were VGLUT3, and 3.6 % were 5-HT and VGLUT3 positive; whereas 61 % of the neurons were GABAergic. Surprisingly, 25.4 % of the neurons were triple negative and were only positive for the neuronal marker NeuN. PET-1/ePET-Cre transgenic mouse lines are widely used to specifically manipulate only 5-HT containing neurons. Interestingly, however, using the ePET-Cre transgenic mice, we found that far more VGLUT3 positive cells expressed ePET than 5-HT positive cells, and about 38 % of the ePET cells contained only VGLUT3, while more than 30 % of 5-HT cells were ePET negative. These data should facilitate the reinterpretation of PET-1/ePET related data in the literature and the identification of the functional role of a putatively new type of triple-negative neuron in the MRR.

Keywords Median raphe · Paramedian raphe · Stereology · Serotonin · 5-HT · ePET · PET-1 · VGLUT3 · VGAT · Immunohistochemistry

Introduction

The median raphe region (MRR) plays a fundamental role in regulating cortical network activity, as well as subcortical functions (Bohut 1997; Vertes et al. 1999). It participates in several aspects of fear behavior, its lesion disrupts the acquisition of conditioned fear memory, and it is associated with specific subtypes of anxiety disorders (Avanzi and Brandão 2001; Avanzi et al. 2003; Silva et al. 2004; Borelli et al. 2005; Dos Santos et al. 2005; Ohmura et al. 2014; Peters et al. 2014; Zangrossi and Graeff 2014). Its functional alterations may also lead to disorders, such as schizophrenia or major depression (Aghajanian and Marek 2000; Hensler 2006). However, its precise cellular composition with regard to transmitter phenotypes is still unknown.

The MRR is located in the midline of the brainstem and consists of the MR and the paramedian raphe (PMR) subregions. The MRR used to be known as a serotonergic nucleus; however, several studies have already reported the presence of non-serotonergic neurons (Gras et al. 2002; Jackson et al. 2009) as well. Four cell populations can be distinguished based on 5-HT, glutamate, and gamma-aminobutyric acid (GABA) contents: (1) some neurons

✉ Gábor Nyiri
nyiri.gabor@koki.mta.hu

[1] Laboratory of Cerebral Cortex Research, Institute of Experimental Medicine, Hungarian Academy of Sciences, Budapest 1083, Hungary

[2] János Szentágothai Doctoral School of Neurosciences, Semmelweis University, Budapest 1085, Hungary

Published online: 04 April 2016

contain only 5-HT (serotonin only, SO cells); (2) others show only vesicular glutamate transporter type 3 expression (VGLUT3 only, GO cells); (3) in the third group, both molecules are detectable (serotonin and VGLUT3, SG cells) (Fremeau et al. 2002; Shutoh et al. 2008); (4) while the fourth group of cells is GABAergic (Stamp and Semba 1995; Serrats et al. 2003; Calizo et al. 2011) and only contains vesicular GABA transporter (VGAT). No studies have investigated the possible occurrence of cells that would express none of these molecules or the ratios of these four cell types in the MRR.

Serotonergic and glutamatergic MRR cells project densely to several forebrain areas (Vertes et al. 1999; Azmitia 1978; Köhler 1982; Aznar et al. 2004; Varga et al. 2009). Serotonergic neurons desynchronize the hippocampal activity and disrupt rhythmic discharge of septal cholinergic and GABAergic neurons (Assaf and Miller 1978; Kinney et al. 1996; Vertes and Kocsis 1997). VGLUT3 containing glutamatergic neurons suppress the hippocampal ripple activity and disrupt memory consolidation (Wang et al. 2015), and both of these cells can innervate more forebrain areas simultaneously (Szőnyi et al. 2014). Although serotonergic and glutamatergic neurons are frequently investigated, it is unknown how many of them possess both transmitters.

Efforts to genetically identify and modify serotonergic cells led to the discovery of the E26 transformation-specific transcription factor PET-1 and its enhancer region ePET (Hendricks et al. 1999). The generation of PET-1-Cre and ePET-Cre transgenic mouse lines promised efficient manipulation of the 5-HT containing neurons and provided tools for numerous studies (Braz et al. 2009; Hodges et al. 2009; Hawthorne et al. 2010; Liu et al. 2010; Depuy et al. 2011, 2013; Spaethling et al. 2014; Wang et al. 2015).

In this study, we investigated the number of cells of different cell populations in the MRR. In the whole MRR, 2.1 % of the neurons were 5-HT, 7 % were VGLUT3, and 3.6 % were 5-HT and VGLUT3 positive; whereas 61 % of the neurons were GABAergic. Surprisingly, 25.4 % of the MRR neurons were only positive for the neuronal marker NeuN and were negative for 5-HT, VGLUT3, and VGAT, and because of several reasons detailed below, these cells are highly unlikely to be false negative. Furthermore, using one specific commonly used ePET-Cre transgenic mouse line (Jackson Laboratories), we show that more than half of the SO neurons are negative for ePET, and about 38 % of the ePET cells only contain VGLUT3. Therefore, ePET is not specific to serotonergic cells, since it is present in a portion of SO, GO, SG cells, and also in some of the unidentified neuronal population.

Materials and methods

Animals and perfusions

All experiments were performed in accordance with the Institutional Ethical Codex and the Hungarian Act of Animal Care and Experimentation guidelines, which are in concert with the European Communities Council Directive of September 22, 2010 (2010/63/EU). The Animal Care and Experimentation Committee of the Institute of Experimental Medicine of the Hungarian Academy of Sciences and the Animal Health and Food Control Station, Budapest, have also approved the experiments.

VGAT-IRES-Cre mice were crossed with Gt(ROSA)26Sor_CAG/ZsGreen1 or with Gt(ROSA)26Sor_CAG/tdTomato reporter mice, and ePET-IRES-Cre mice were crossed with Gt(ROSA)26Sor_CAG/ZsGreen1 mice (Jackson Laboratories). Their offspring showed genetically coded specific fluorescent labeling in VGAT or ePET expressing neurons. Scott et al. (2005) described in detail the construction of this ePET-Cre mouse line. Three 42 days old male VGAT-ZsGreen1 offspring mice (named GM1; GM2; and GM3), one 42 days old male VGAT-tdTomato mouse (named GM4), one 42 days old male C57BL/6J wild-type mouse (named WT), and three 49 days old male ePET-ZsGreen1 mice (named PM1; PM2; and PM3) were used. For perfusion, mice were anesthetized with isoflurane, followed by intraperitoneal injection of an anesthetic mixture (containing 8.3 mg/ml ketamine, 1.7 mg/ml xylazine-hydrochloride, and 0.8 mg/ml promethazinium-chloride) to achieve deep anesthesia. Then, mice were transcardially perfused first with PBS (0.9 % NaCl in 0.1 M phosphate buffer) solution for 2 min, followed by 4 % paraformaldehyde for 40 min, and finally with 0.1 M phosphate buffer (PB) for 10 min.

Fluorescent immunohistochemistry

After perfusion of mice and removal of their brains from the skull, coronal sections were cut on a Leica VT1200S vibratome at 60 μm from the whole MRR and collected in stereological order into eight vials. This was followed by washing out the fixative in 0.1 M (PB) for 1 h. Then, the sections were cryoprotected sequentially in 10 % (overnight) and 30 % (2 h) sucrose in PB and freeze–thawed five times over liquid nitrogen. This was followed by several washing in 0.1 M PB (3 × 10 min) and tris-buffered saline solution (TBS, 3 × 10 min). Then, sections were incubated in TBS containing 1 % human serum albumin, 0.1 % Triton™ X-100, and 700 μg/ml Digitonin (all from Sigma-Aldrich) for 1 h to achieve better penetration.

Vials were separated into two groups (even and odd sections) that were used for experiment type A and B, respectively (Table 2). Even-numbered sections were used to demonstrate the ratios between the 5-HT and/or VGLUT3 positive neurons, while odd-numbered sections were used for determining the number of other neurons.

Antibodies

Table 1 summarizes information about the primary and secondary antibodies. Previously, we extensively tested the rabbit anti-VGLUT3 antibody in experiments using VGLUT3 knock out animals (Szőnyi et al. 2014). Immunostaining of VGLUT3 in raphe neurons was also tested by others (Mintz and Scott 2006; Shutoh et al. 2008). The mouse anti-NeuN antibody labels a neuron specific DNA binding nuclear protein and is widely used to identify neurons (Mullen et al. 1992). To increase the accuracy of the measurements, we counted only the DAPI stained nuclei of cells. The rat and rabbit anti-5-HT antibodies were characterized before (Amilhon et al. 2010; Fox and Deneris 2012), they labeled the same cells, and also labeled the expected population of neurons, which further confirm their specificity. In the experiment, where the expression pattern of ePET was analyzed, we found a mismatch between ePET and 5-HT expression. These surprising results prompted us to test whether it is possible that some cells only express the synthesizing enzyme of serotonin, but the enzyme does not produce detectable levels of serotonin. Therefore, we tested whether all cells that are positive for the 5-HT synthesizing enzyme, tryptophan hydroxylase (TPH), are also positive for 5-HT. We colocalized rabbit anti-5-HT and mouse anti-TPH labeling (Fig. 2). We found that all 160 examined TPH labeled cells were also positive for 5-HT; consequently, 5-HT was always detected in TPH expressing cells. This shows that the sensitivity of 5-HT labeling cannot be responsible for the lack of labeling in some cells, because cells that express its synthesizing enzyme, TPH, always express detectable levels of 5-HT as well.

The antibody penetration into 60 µm-thick sections was examined rigorously using confocal imaging, and was found to be perfect even in the middle of the section. Secondary antibodies were extensively tested for possible cross-reactivity with other primary or secondary antibodies, but no cross-reactivity was found.

Confocal microscopy

Image stacks were recorded by using a Nikon A1R confocal laser-scanning system built on a Ti-E inverted microscope with 0.45 NA CFI Super Plan Fluor ELWD 20XC Nikon objective and operated by NIS-Elements AR 4.3 software. Argon ion laser (457–514 nm, 40 mW), yellow DPSS laser (561 nm, 20 mW), violet diode laser (405 nm), and diode laser system (647 nm, 100 mW) were used as excitation lasers with appropriate filters. Images were acquired at a z-separation of 1 µm. Each section plane was identified by using the Mouse Brain Atlas (Paxinos and Franklin 2012).

Table 1 Antibody specifications

Raised against	Raised in	Protein cc. of stock solution	Dilution	Source	Catalog number	Lot number	Characterized
VGLUT3	Rabbit	1 µg/µl	1:500	Synaptic Systems	135203		Szonyi et al. (2014)
NeuN	Mouse	1 mg/ml	1:500	Chemicon	MAB 377	LV 1359479	Mullen et al. (1992)
Serotonin	Rat	Not available	1:500	Merck Millipore	MAB 352	2168248	Amilhon et al. (2010)
Serotonin	Rabbit	25 µg/ml	1:10000	ImmunoStar	20080	1431001	Fox and Deneris (2012)
TPH	Mouse		1:3000	Sigma-Aldrich	T0678		Calizo et al. (2011)

Conjugated with	Raised in	Raised against	Dilution	Source	Catalog number	Molecule
Alexa 594	Donkey	Mouse	1:500	Life technologies	A-21203	Full IgG
Alexa 647	Chicken	Rat	1:500	Life technologies	A-21472	Full IgG
Alexa 647	Donkey	Rabbit	1:500	Jackson immuno-research	711-605-152	Full IgG
Cy3	Donkey	Rabbit	1:500	Jackson immuno-research	711-165-152	Full IgG
Alexa 488	Donkey	Mouse	1:500	Life technologies	A21206	Full IgG
Alexa 488	Donkey	Rabbit	1:500	Life technologies	A 21202	Full IgG
DAPI	–	–	1:10.000	Sigma-Aldrich	D9564	–

Stereology measurement

Unbiased design-based stereological measurements were carried out using the optical fractionator method (Sterio 1984; Gundersen 1986; West and Slomianka 1991; Schmitz and Hof 2005), which is based on the principle that one can accurately define the number of cells in the volume of interest by counting them in a predetermined fraction of the given volume (Dorph-Petersen et al. 2001). To get the total cell numbers, the number of counted cells is multiplied by the reciprocal of three different fractions: section, area, and thickness sampling fractions (West and Slomianka 1991). Using systematic random sampling in each experiment, every second section of the MRR was used; therefore, section sampling fraction was 0.5. In mounted sections, cells were counted only within a fraction of a predefined grid area. In the MR, this fraction was $15^2/40^2$ μm in experiment type A and $15^2/80^2$ μm in experiment type B. In the PMR, this fraction was $10^2/80^2$ μm for both types of experiments. Finally, thickness sampling fraction was about 15/28 μm, because the average mounted section thickness was about 28 μm and counting performed only in a 15-μm-high counting cube. We used a guard zone of minimum 5 μm of tissue above and below the counting cube; however, for maximum accuracy, thickness sampling fractions were determined at every sampling site. Cells were counted inside the counting cubes or if they touched one of the inclusion planes of the counting cubes. Using these parameters, we directly identified the phenotype of about 13 % of the MR neurons and altogether counted about 12,300 nuclei in MRR in these animals. Cell counting was carried out in Stereo Investigator 10.0 stereology software (MBF Bioscience), while cells were identified parallel using NIS-Elements AR 4.2 software.

Results

Cell types of the MRR

Using immunohistochemistry combined with stereological methods, we identified ten different types of neuronal phenotypes in the MRR. We used three kinds of genetically modified mouse strains and one wild-type mouse. We carried out two types of experiments, because we could use a maximum of four different fluorescent channels per experiment. In experiment type A, we focused on the identification of SO, GO, SG, VGAT, or ePET positive cells, while in experiment type B, we primarily focused on NeuN positive neurons that were negative for all other labeling (see Table 2). To label 5-HT, VGLUT3, and NeuN, we used immunohistochemistry; to stain the nuclei, we performed DAPI histochemistry and we used genetically expressed fluorescent markers for the visualization of VGAT and ePET. Using an unbiased stereological method, the combination of different mice and two types of experiments allowed the estimation of the absolute number of different cells in the MRR. The general labeling pattern of neuronal markers distributed in the MRR as expected, and neuronal markers could be clearly distinguished (Figs. 1, 2, 3, 4). We found that the genetic background did not have any effect on the estimated cell numbers.

In all mouse strains, genetically determined fluorescent markers showed intensive expression in the soma of VGAT or ePET containing neurons (Figs. 3a3–d3, 4a3, b3). Some neurons expressed only these genetically determined markers: these are only VGAT positive (Fig. 3a3, c3, asterisk) or only ePET positive cells (Fig. 4b3, asterisk). In experiment type B, to determine the total number of neurons, we used Neu-N staining (Fig. 3a1, c1), which labeled all neuronal nuclei and with a lower intensity also the cytoplasm. Some

Table 2 Experiment types, primary and secondary antibody combinations, and animals from different mouse strains

Mice (genetic background)	Experiment type A (here 5-HT and VGLUT3 cells could be distinguished, using different fluorescent channels)	Experiment type B (here 5-HT and VGLUT3 cells could not be distinguished, but other neurons could be detected in a separate channel with NeuN)
GM1, GM2, GM3 (strain: *VGAT-IRES-Cre-ZsGreen*) PM1, PM2, PM3—tested only with type A (strain: *ePet-ZsGreen*) WT—tested only with type A (strain*: C57BL/6J*)	Rat anti-5-HT/Alexa 647 Rabbit anti-VGLUT3/Cy3 DAPI	Rat anti-5-HT/Alexa 647 Rabbit anti-VGLUT3/A647 Mouse anti-NeuN/Alexa 594 DAPI
GM4 (strain: *VGAT-IRES-Cre-tdTomato*)	Rat anti-5-HT/Alexa 647 Rabbit anti-VGLUT3/Alexa 488 DAPI	Rat anti-5-HT/Alexa 647 Rabbit anti-VGLUT3/Alexa647 Mouse anti-NeuN/Alexa 488 DAPI

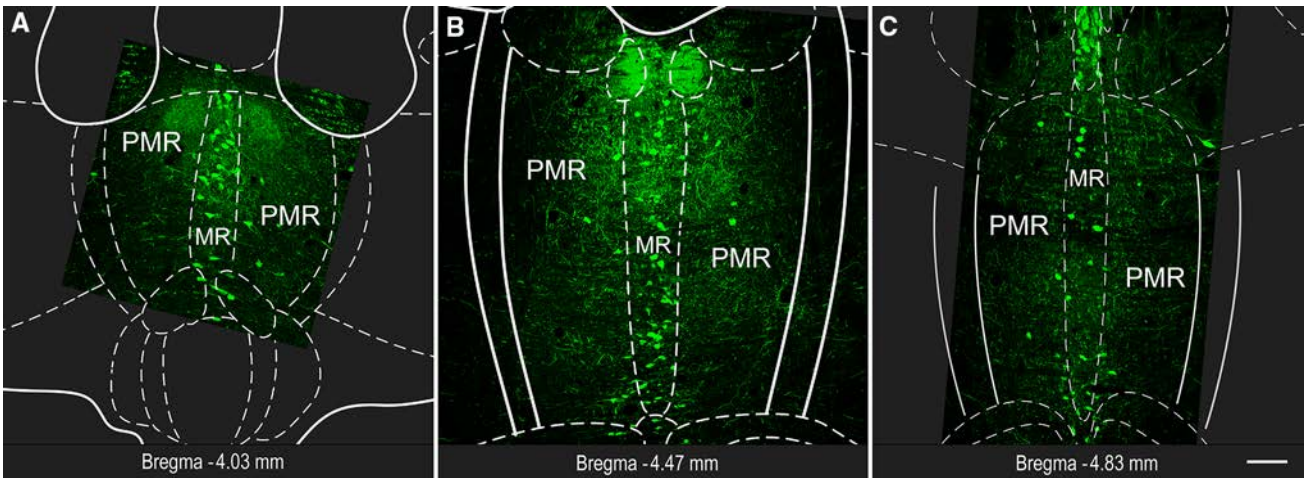

Fig. 1 Fluorescent micrographs show representative MRR sections with 5-HT labeling. Subregions (MR and PMR) are defined based on the Mouse Brain Atlas (Paxinos and Franklin 2012). Position of the coronal section is indicated in each image, relative to the Bregma. *Scale bar* 100 μm for all images

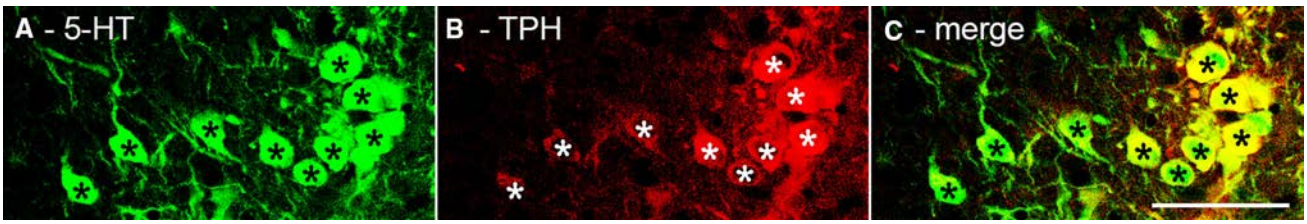

Fig. 2 Confocal laser scanning images (**a**–**c**) show 100 % colocalization between the labeling of 5-HT and its synthesizing enzyme, TPH, in representative MR neurons (*asterisk*). *Scale bar* 50 μm for all images

cells were only NeuN positive, which were marked with filled circle in Fig. 3. In experimental type B, 5-HT and/or VGLUT3 positive cells were visualized in the same fluorescent channel (Fig. 3a2, c2). Some cells were positive for 5-HT and/or VGLUT3 (filled square in Fig. 3), while some were only NeuN positive or VGAT positive.

In experiment type A, 5-HT positive (Figs. 3b1, d1, 4a1, b1) and VGLUT3 positive (Figs. 3b2, d2, 4a2, b2) cells were visualized separately. Both of the markers showed intensive labeling in the somata and axon terminals. In the case of VGAT-Cre animals (Fig. 3), SO cells (filled circle), GO cells (filled square), SG cells (empty circle), VGLUT3 and VGAT positive cells (empty square), and VGAT-positive (GABAergic) cells could be differentiated. In the case of ePET-Cre animals (Fig. 4), some SO cells expressed ePET (filled circle), while some were ePET negative (empty circle). Some GO cells were ePET positive (filled square), while some were ePET negative (empty square). Most SG cells were ePET positive (filled diamond), but some were ePET negative (empty diamond). In both types of experiment, we performed DAPI staining, which labelled the nuclei in the blue fluorescent channel.

Stereological results are shown in Table 3 for MR and in Table 4 for PMR and the whole MRR. Based on these data, we calculated the ratios of the different cells types and plotted all results in Fig. 5. Briefly, in the MR, we found that only about 8.5 % of the neurons are SO cells, 26 % are GO cells, and about 12.8 % are SG double positive cells; whereas 37.2 % of the neurons are GABAergic, and 14.4 % of all MR neurons were triple negative for 5-HT, VGLUT3, and VGAT. In the PMR, we found that only 6.4 % of all neurons expressed 5-HT and/or VGLUT3, but these cells appeared only very close to the MR border, which was defined according to the Mouse Brain Atlas (Paxinos and Franklin 2012). 66.8 % of all PMR neurons expressed VGAT, while 27.7 % of the neurons were triple negative for 5-HT, VGLUT3, and VGAT. We never found that colocalization between 5-HT and VGAT and colocalization between VGLUT3 and VGAT occurred only very rarely (see Tables 3, 4; Fig. 5 for details).

The mouse MRR is a relatively small area. Dendritic trees of cells in MR or PMR cross their putative borders as well, making specific activation or deactivation of these putative subregions even more difficult. In addition, separate manipulation of the MR and PMR with optogenetic, electrical, and/or pharmacological tools would currently be a considerable challenge, if possible at all. Although genetic tagging can be used to selectively target a

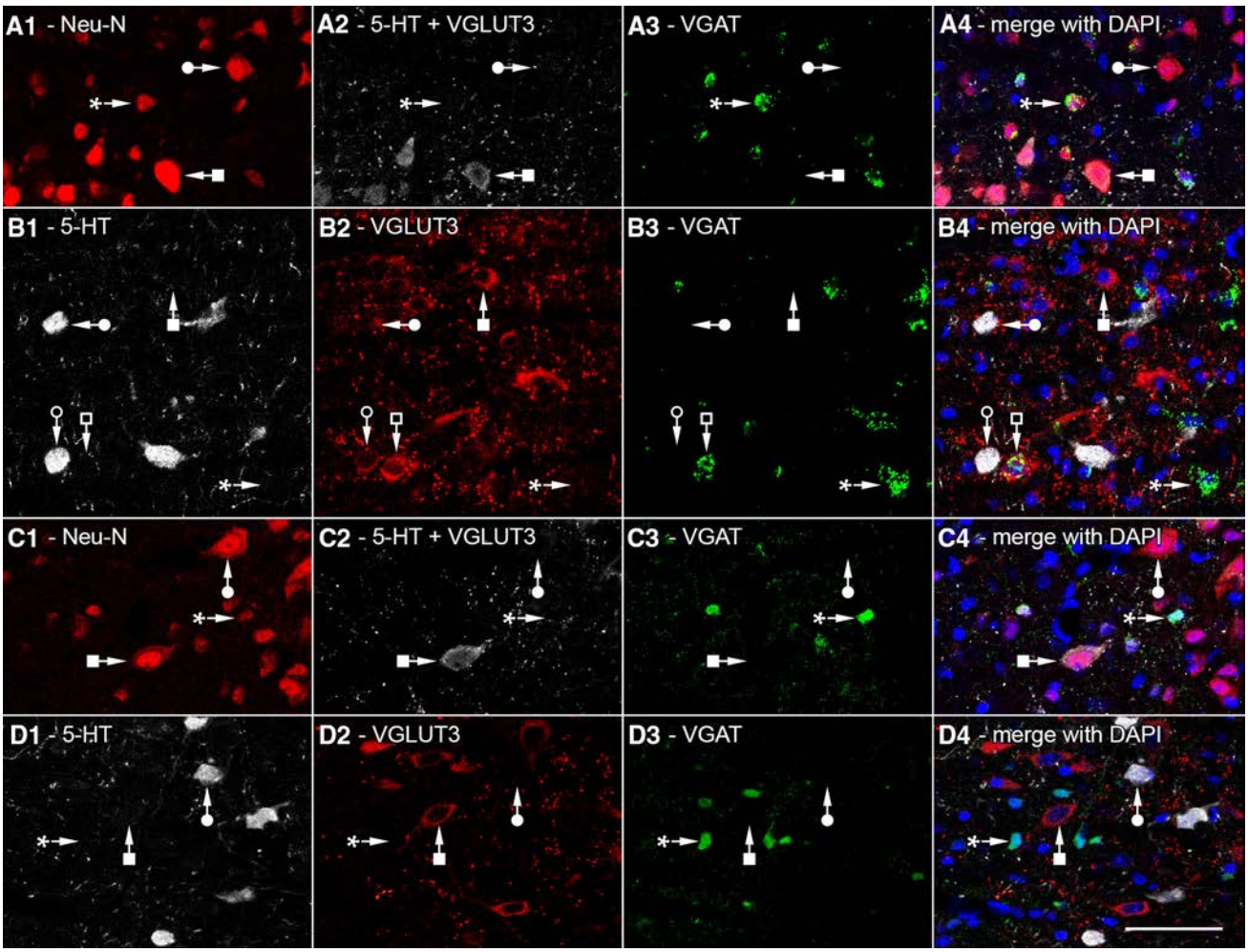

Fig. 3 Confocal laser scanning images used for stereological measurement of different cell types of MRR in VGAT-IRES-Cre-ZsGreen (**a**, **b**) and VGAT-IRES-Cre-tdTomato mice (**c**, **d**). In both strains, genetically determined fluorescent markers labeling VGAT are shown in *green* in **a3**–**d3**. Nuclei were always labeled with DAPI (*blue*). In "experiment type B" (**a1**–**a4**; **c1**–**c4**), neurons were identified with Neu-N staining (*red*), while 5-HT and/or VGLUT3 positive cells were visualized in the same fluorescent channel (*white*). Some cells were only NeuN positive (*filled circles*), and some were positive for 5-HT and/or VGLUT3 (*filled square*); while some of them only VGAT positive (*asterisk*). In "experiment type A" (**b1**–**b4**; **d1**–**d4**), 5-HT positive (*white*) and VGLUT3 positive (*red*) cells were visualized separately. SO cells (*filled circle*), GO cells (*filled square*), SG cells (*empty circle*), VGLUT3 and VGAT positive cells (*empty square*), and only VGAT-positive cells (*asterisk*) could be differentiated. *Scale bar* 50 μm for all images

subpopulation of neurons, available methods would still manipulate cell in both MR and PMR together. Therefore, separation of MR and PMR is impossible even with optogenetic methods. Therefore, we calculated the number of cells for the whole MRR as well. We found that 13.5 % of the MRR neurons contained 5-HT and/or VGLUT3, while 61.8 % expressed VGAT, and 25.4 % belongs to the unidentified cell type (see Tables 3, 4; Fig. 5 for details).

Distribution of ePET positive cells in the MRR

Previously, the PET-1 enhancer region, ePET, was thought to be expressed exclusively in serotonergic cells. However, we found a mismatch between ePET and 5-HT expression in MRR, as shown in Figs. 4, 5 and Tables 3, 4. We also found triple-negative NeuN positive neurons that were labeled with ePET. Although, in this experimental design, colocalization between the genetic markers (ePET and VGAT) is not possible, it is highly unlikely that these markers would colocalize, because ePET positive cells are mostly localized in MR, and most GABAergic cells are in the PMR. In addition, SO and SG cells that are partly ePET positive were never GABAergic. Furthermore, generally, excitatory and inhibitory neurons derive from different cell lines; therefore, it is highly unlikely that ePET would be localized in GABAergic cells as well. Therefore, we classified triple-negative and ePET positive cells as VGAT negative. Results clearly show that ePET is partially

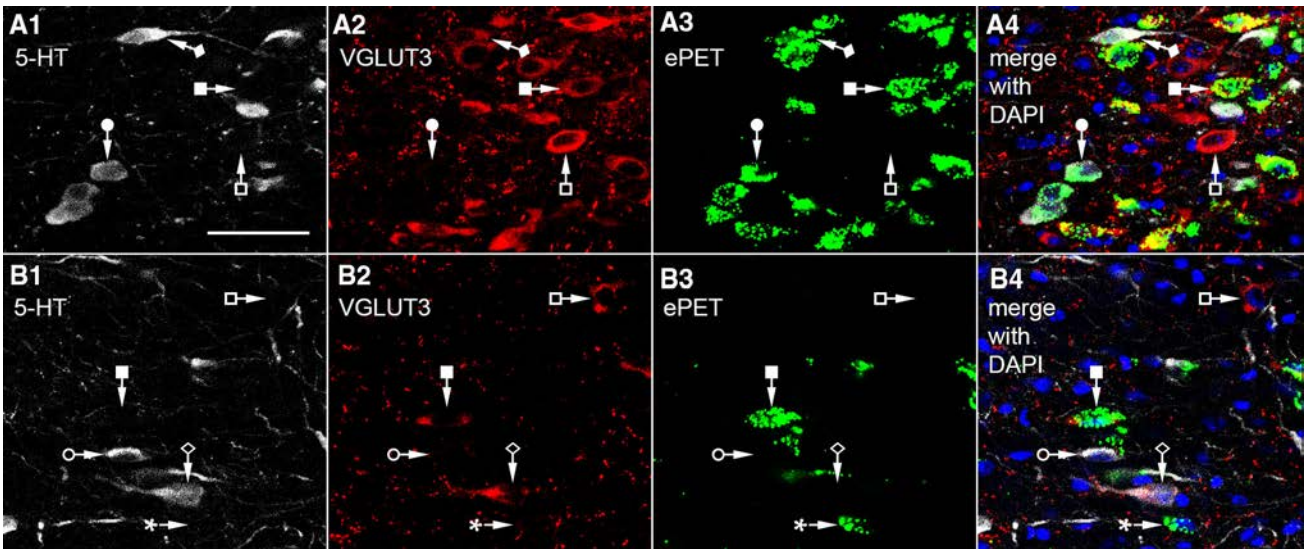

Fig. 4 Confocal laser scanning images used for stereological measurement of different cell types of MRR in ePET-IRES-Cre-ZsGreen mice (**a**, **b**) in "experiment type A". ePET labeling is *green*, nuclear DAPI labeling is *blue*, while 5-HT (*white*) and VGLUT3 (*red*) positive cells were visualized separately. Some SO cells express ePET (*filled circle*), while some are ePET negative (*empty circle*). Some GO cells were ePET positive (*filled square*), while some are ePET negative (*empty square*). Most SG cells are ePET positive (*filled diamond*), but some are ePET negative (*empty diamond*). Some cells expressed only ePET without any other labeling (*asterisk*). *Scale bar* 50 μm for all images

Table 3 Number of cells in median raphe

The number of cells in median raphe in eight mice									
Labelled cell types	GM1	GM2	GM3	GM4	WT	PM1	PM2	PM3	Mean
Non-neuronal cells, only DAPI positive	11269	10449	10672	11928	–	–	–	–	11079
All neurons (calculated, using all mice, from the mean number of all labelled neurons)									8160
All 5-HT positive cells, without VGLUT3 labeling—abbreviated as "SO"	1310	515	573	662	640	807	351	697	695
And from these, ePET positive cells are:	–	–	–	–	–	380	240	378	333
All VGLUT3 positive cells, without 5-HT labeling—abbreviated as "GO"	1840	2078	2209	2055	2041	2209	2591	1957	2123
And from these, ePET positive cells are:	–	–	–	–	–	906	886	959	917
All 5-HT and VGLUT3 double positive cells—abbreviated as "SG"	627	890	904	940	1408	1427	1014	1126	1042
And from these, ePET positive cells are:	–	–	–	–	–	1002	705	891	866
All 5-HT and/or VGLUT3positive cells	3655	3450	3426	3620	4089	4862	3957	3780	3855
All VGAT positive cells, without 5-HT and VGLUT3 labeling	3105	3190	2619	3222	–	–	–	–	3034
All VGAT and VGLUT3 double positive cells, without 5-HT labeling	35	149	93	65	–	–	–	–	86
All NeuN positive cells (triple negative), without 5-HT, VGLUT3 and VGAT labeling	597	712	1632	1782	–	–	–	–	910
All ePET positive cells, without 5-HT and/or VGLUT3 labeling	–	–	–	–	–	68	451	296	271

expressed in four different populations of neurons (Table 3; Fig. 5).

Because the "border" between MR and PMR is artificial, we have all reason to believe that all SO cells in MRR belong to the same neuronal population, regardless of their localization in MR or PMR, and the same is true for all other cell types. Therefore, the ratio of ePET positive cells in the PMR was calculated based on the ratios found in MR. However, to further confirm that ePET positive cells indeed comprise the same cell types at a similar distribution in the PMR, we defined the phenotype of the counted ePET positive cells in the PMR in experimental type A of one mouse. In that case, we used a semiquantitative approach that allowed the testing of colocalization of other

Table 4 Number of cells in paramedian raphe and median raphe region

The number of cells in paramedian raphe						The number of cells in MRR (sum of the means of MR and PMR cells)
Labelled cell types	GM1	GM2	GM3	GM4	Mean	
Non-neuronal cells, only DAPI positive	69924	59634	71573	71472	68151	79230
All neurons (calculated, using all mice, from the mean number of all labelled neurons)					39298	47458
All 5-HT positive cells, without VGLUT3 labeling—abbreviated as "SO"	264	0	795	221	320	1015
And from these, ePET positive cells (calculated based on the proportions in Fig. 5b) are:					153	486
All VGLUT3 positive cells, without 5-HT labeling—abbreviated as "GO"	751	1143	2094	899	1222	3344
And from these, ePET positive cells (calculated based on the proportions in Fig. 5b) are:					528	1445
All 5-HT and VGLUT3 double positive cells—abbreviated as "SG"	1438	217	555	460	668	1710
And from these, ePET positive cells (calculated based on the proportions in Fig. 5b) are:					555	1421
All 5-HT and/or VGLUT3positive cells	2514	1535	3013	1785	2212	6067
All VGAT positive cells, without 5-HT and VGLUT3 labeling	33486	25728	25035	19445	25924	28958
All VGAT and VGLUT3 double positive cells, without 5-HT labeling	244	578	234	130	297	383
All NeuN positive cells(triple-negative cells), without 5-HT, VGLUT3 and VGAT labeling	9017	8646	11991	13820	10710	12049
All ePET positive cells, without 5-HT and/or VGLUT3 labeling (calculated based on the proportions in Fig. 5b)					159	430

markers with ePET positive cell on a larger number of cells. We collected ePET positive cells in PMR from a representative series of sections (a sample size was 425 ePET+ cells) in experimental type A. This was more optimal in this case, because ePET positive cells are rare in the PMR, and testing with the fully quantitative method would have provided an unacceptably small sample. The result is shown in Fig. 5d lower pie chart. This proportion is very similar to the ratio in the MR (Fig. 5d upper pie chart) that further confirms that these regions contain the same type of cells.

Discussion

Using an unbiased stereological method, first, we estimated the average numbers of different cell types of the mouse MR and PMR areas. Second, we found that about a quarter of the neurons are negative for 5-HT, VGLUT3, and VGAT, which indicates the existence of a so far unrecognized cell population. Third, we found that ePET is not specific for 5-HT, because it is not present in all SO neurons, and it is expressed in GO and triple-negative neurons as well.

Ratios of cell types in MR and PMR

MRR is a widely investigated brain area, and several physiological experimental manipulations (excitation, inhibition or lesions) target the whole MRR. The physiological role of individual cell populations could be studied using optogenetic manipulation of cells with certain neurochemical phenotypes; however, even this method cannot be cell type specific, because MRR neurons form neurochemically overlapping cell populations that hamper their separate investigation. Although intersectional genetics might help to separate these cells in the future, it is important to know their ratios; otherwise, even intersectional genetic experiments may be misinterpreted. In addition, our results can help to define the absolute number of cells that are modulated in optogenetic experiments.

5-HT and VGLUT3 neurons are abundant in the center of the MRR, and they are getting gradually less and less abundant outward from the center, and the steepness of the decrease in abundance is variable between mice. Therefore, there is no way to unbiasedly draw a border between MR/PMR based on staining pattern. Dendritic trees of cells in MR or PMR cross their putative borders as well making specific activation or deactivation of these putative subregions even more difficult, if possible at all. The mouse MRR is relatively small; therefore, even from the practical point of view, the separation of the MR and PMR may also seems to be less useful, because most types of experimental interventions would affect both MR and PMR in mice. These subregions contain the same types of cells, and during experiments using optical fibers the lateral and the conical light spread is about 500–1000 μm from the optical fiber tip (Adamantidis et al. 2007; Yizhar et al. 2011), which would affect the whole volume of median raphe region; therefore, at least in mice, data for the whole MRR seem to be more useful. However, because of historical reasons and also to allow a certain level of comparison with

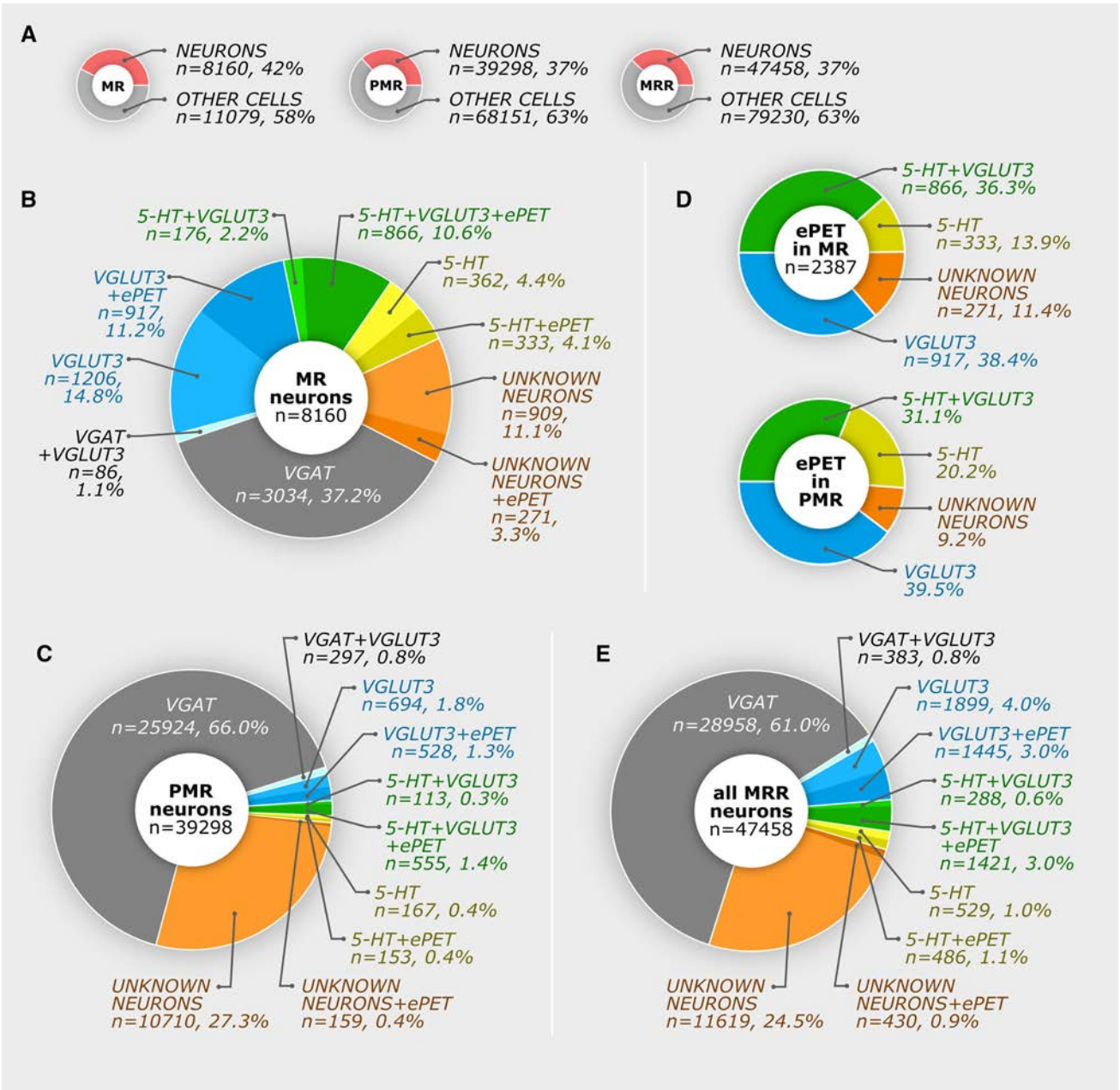

Fig. 5 Number of cells and ratios in the median raphe region. Using original data presented in Tables 3, 4, these pie charts show calculated results originating from eight mice. **a** Ratios between neurons and non-neuronal cells in the MR, PMR, and MRR. **b**, **c** Different neuron types and ePET expression in the MR and PMR, respectively. **d** Distribution of 5-HT and VGLUT3 contents in ePET expressing neurons in the MR and PMR. Ratios of PMR neurons were defined with a semiquantitative method; therefore, the number of cells is not shown, but could be calculated from the other pie charts. **e** Summary pie chart about the whole MRR neurons

other species, we analyzed MR and PMR separately as well, for which the only unbiased and reproducible method was to use the stereotaxic Mouse Brain Atlas as reference (Paxinos and Franklin 2012).

Interestingly, based on these criteria, more than a third of the 5-HT and/or VGLUT3 containing neurons are in the PMR—mostly closer to the MR border. We found that about half of the serotonergic cells contained VGLUT3, whereas a third of the VGLUT3 neurons were positive for 5-HT as well. It is important to note that, while the MRR contains about 47,500 neurons, only about 13 % of them are investigated regularly, because these 5-HT and/or VGLUT3 positive cells are known to project to forebrain areas.

One-third of MR neurons and two-thirds of PMR neurons are GABAergic, and these cells never contained 5-HT.

Although it may seem insignificant, we found that about 0.8 % of MRR neurons showed VGAT and VGLUT3 double positivity. This type of colocalization is also known in a population of hippocampal GABAergic interneuron (Somogyi et al. 2004), but their connections and role in the MRR is unknown.

The quarter of MRR neurons belong to an unknown population

We found a previously unidentified cell population, which constituted more than 25 % of the MRR neurons. This group was triple negative for 5-HT, VGLUT3, and VGAT labeling, and was positive only for the neuronal NeuN staining.

These cells are highly unlikely to be false negative, because: (1) they were just as numerous close to the section surface, where no antibody penetration problems occur, (2) they were surrounded by other strongly positive cells, also indicating appropriate antibody penetration; furthermore, (3) these triple-negative cells were distributed homogeneously in the tissue, which means that it is not due to regional penetration differences. In addition, (4) about 28 % of neurons belong to this triple-negative population also in the PMR, where SO, GO, and SG cells are rare, so they are highly unlikely to be false negative of those populations. (5) We proved that 5-HT can indeed label all serotonergic cells, because all TPH positive cells were 5-HT positive. (6) Genetic labeling was always very strong, and the specificity of genetically labeled VGAT expression was extensively tested (Madisen et al. 1993; Vong et al. 2011).

This triple-negative cell type was completely overlooked in the literature, because only SO, GO, SG, and GABAergic neurons were investigated, and to the best of our knowledge, these markers have never been investigated in the same experiment. Triple-negative cells are unlikely to be glutamatergic, because other vesicular glutamate transporter (VGLUT1 or VGLUT2) positive cells have not yet been shown in the MRR (Hioki et al. 2010). Dopaminergic neurons of negligible density were observed in the rat MRR (Jahanshahi et al. 2013), and although its colocalization with 5-HT or VGLUT3 was not tested, triple-negative cells are much more abundant, therefore, highly unlikely to be dopaminergic. In the MRR, most neurokinin-1 receptor labeling did not colocalize with VGLUT3 (Commons and Serock 2009), but other neurons of the MRR were not tested. Somatostatin and galanin positive neurons were also observed in the MRR (Araneda et al. 1999), but their localization in VGLUT3 and/or all 5-HT positive cells was not tested. To the best of our knowledge, so far, no other types of neurons were identified in the MRR that could account for the amount of this new triple-negative type of neuron.

Possible neurotransmitter phenotype plasticity of 5-HT and/or VGLUT3 containing neurons

Neurotransmitter phenotype plasticity has already been described in several areas of the mammalian brain (Baudry et al. 2010; Dulcis et al. 2013). For instance, during the normal development (between P15 and P90), dopamine neurons lose their VGLUT2 contents completely in ventral tegmental area and substantia nigra (Bérubé-Carrière et al. 2009). In the medial nucleus of the trapezoid body, GABAergic neurons transiently release glutamate, and then switch to glycine as a primary neurotransmitter (Demarque and Spitzer 2012). Glutamatergic granule cells of the dentate gyrus are initially GABAergic, and then express a dual GABAergic/glutamatergic phenotype before becoming purely glutamatergic, but they can transiently express a GABAergic phenotype when a state of hyperexcitability is induced in the adult rat (Gutiérrez et al. 2003). Interestingly, in the MRR in this study, the number of 5-HT and/or VGLUT3 containing neurons shows high variability among mice. Although their ages were similar, 5-HT could be detected in more cells in mouse GM1 compared with GM2; on the other hand, GM2 had more VGLUT3 positive GO and GS cells. However, the total numbers of 5-HT and/or VGLUT3 containing neurons are fairly stable among animals, which suggest that in some mice, serotonergic/glutamatergic ratios would change without changing the total number of main forebrain projection neurons: SO, GO, and SG cells. These shifts in ratios are unlikely to be due to technical reasons, because we used all sections of the MRR and collected a large systematic random sample; therefore, uneven or topographic cell distributions could not account for this variability. We may hypothesize that these SO, GO, and SG cells belong to the same neuronal population, which can change its transmitter phenotype, as a function of activity in MRR inputs. Other data also support this hypothesis. First, ePET was expressed in all these three types of neurons, and we found some triple-negative cells that were also labeled with ePET, which may represent either a transitional cell population or a developmental side-branch. Second, VGLUT3 accelerates 5-HT transmission at specific 5-HT terminals; its deletion decreased 5-HT tone in projection areas and decreased serotonin autoreceptor-mediated transmission in raphe, further suggesting a close cooperation of these transmitter systems in the same cells (Amilhon et al. 2010). Third, a robust change in serotonin content of raphe neurons has already been detected between postnatal day 22 and 61 (Rind et al. 2000). Our mice (P42, P49) had slightly different housing

environments; some of them had many littermates, and others had less that may have caused a variation in regulation of their MRR.

Expression of ePET is not restricted to serotonergic neurons

A large body of the literature, partly summarized by Deneris (2011), is based on the assumption that PET-1/ePET can faithfully identify serotonergic neurons. PET-1 was identified as a key factor that triggers the appearance of serotonergic phenotype (Hendricks et al. 1999). PET-1 was thought to play a role in the 5-HT neuron development and is required for anxiety-like and aggressive behavior (Hendricks et al. 2003). Based on those results, ePET (an enhancer region upstream of mouse PET-1-transcribed sequences) was identified and was thought to be a reliable marker for serotonergic cells (Scott et al. 2005).

Using a commonly used ePET-Cre transgenic mouse line that was described by Scott et al. (2005) and is now supplied by Jackson Laboratories; here, we studied the expression of ePET in different types of MRR neurons. Surprisingly, ePET is expressed not only in SO cells, but in GO and SG neurons as well. More than half of SO cells showed a lack of ePET expression, while almost half of GO neurons were also ePET positive. More than a tenth of all ePET expressing neurons were negative for both 5-HT and VGLUT3 labeling. In fact, a previous study has already also shown that 5-HT positive neurons are present in the raphe even in PET-1 knock-out mice, and they were estimated to be about 20–30 % of the 5-HT neuron population in wild-type mice (Kiyasova et al. 2011). PET-1-independent and dependent serotonergic cells have been shown to project to different brain areas (Kiyasova et al. 2011). Furthermore, non-serotonergic neurons were also found to be positive for PET-1 in several raphe nuclei (Pelosi et al. 2014).

Our results can be used to estimate the number and ratios of modulated neurons in previous and future studies, employing ePET/PET-1 transgenic mice, and facilitate the reinterpretations of data in the literature.

Acknowledgments We thank Emőke Szépné Simon, Katalin Lengyel and Katalin Iványi for the excellent technical assistance. The authors wish to thank László Barna, the Nikon Microscopy Center at IEM, Nikon Austria GmbH and Auro-Science Consulting Ltd for kindly providing technical support for fluorescent microscopy. This work was supported by the European Research Council (Grant number ERC-2011-ADG-294313, SERRACO) and the National Institutes of Health (Grant number NS030549). Gábor Nyiri was supported by a János Bolyai Research Scholarship. András Szőnyi was supported by the European Union and the State of Hungary, cofinanced by the European Social Fund in the framework of TÁMOP 4.2.4. A/1-11-1-2012-0001 "National Excellence Program".

Compliance with ethical standards

Conflict of interest The authors declare that they have no conflict of interest.

References

Adamantidis AR, Zhang F, Aravanis AM et al (2007) Neural substrates of awakening probed with optogenetic control of hypocretin neurons. Nature 450:420–424. doi:10.1038/nature06310

Aghajanian GK, Marek GJ (2000) Serotonin model of schizophrenia: emerging role of glutamate mechanisms. Brain Res Rev 31:302–312

Amilhon B, Lepicard E, Renoir T et al (2010) VGLUT3 (vesicular glutamate transporter type 3) contribution to the regulation of serotonergic transmission and anxiety. J Neurosci 30:2198–2210. doi:10.1523/JNEUROSCI.5196-09.2010

Araneda S, Gysling K, Calas A (1999) Raphe serotonergic neurons projecting to the olfactory bulb contain galanin or somatostatin but not neurotensin. Brain Res Bull 49:209–214. doi:10.1016/S0361-9230(99)00055-6

Assaf SY, Miller JJ (1978) The role of a raphe serotonin system in the control of septal unit activity and hippocampal desynchronization. Neuroscience 3:539–550. doi:10.1016/0306-4522(78)90018-0

Avanzi V, Brandão ML (2001) Activation of somatodendritic 5-HT1A autoreceptors in the median raphe nucleus disrupts the contextual conditioning in rats. Behav Brain Res 126:175–184. doi:10.1016/S0166-4328(01)00254-6

Avanzi V, Silva RCB, Macedo CE, Brandão ML (2003) 5-HT mechanisms of median raphe nucleus in the conditioned freezing caused by light/foot-shock association. Physiol Behav 78:471–477. doi:10.1016/S0031-9384(03)00029-5

Azmitia CSM (1978) An Autoradiographic analysis of the differential ascending projections of the dorsal and median raphe nuclei in the rat. J Comp Neurol 3:641–667

Aznar S, Qian ZX, Knudsen GM (2004) Non-serotonergic dorsal and median raphe projection onto parvalbumin- and calbindin-containing neurons in hippocampus and septum. Neuroscience 124:573–581. doi:10.1016/j.neuroscience.2003.12.020

Baudry A, Mouillet-Richard S, Schneider B et al (2010) miR-16 targets the serotonin transporter: a new facet for adaptive responses to antidepressants. Science 329:1537–1541. doi:10.1126/science.1193692

Bérubé-Carrière N, Riad M, Dal Bo G et al (2009) The dual dopamine-glutamate phenotype of growing mesencephalic neurons regresses in mature rat brain. J Comp Neurol 517:873–891. doi:10.1002/cne.22194

Bohut M-C (1997) Serotonin receptors in cognitive behaviors. Cogn Behav 7:243–254

Borelli KG, Gárgaro AC, Dos Santos JM, Brandão ML (2005) Effects of inactivation of serotonergic neurons of the median raphe nucleus on learning and performance of contextual fear conditioning. Neurosci Lett 387:105–110. doi:10.1016/j.neulet.2005.07.031

Braz JM, Enquist LW, Basbaum AI (2009) Inputs to serotonergic neurons revealed by conditional viral transneuronal tracing. J Comp Neurol 514:145–160. doi:10.1002/cne.22003

Calizo LH, Akanwa A, Ma X et al (2011) Raphe serotonin neurons are not homogenous: electrophysiological, morphological and neurochemical evidence. Neuropharmacology 61:524–543. doi:10.1016/j.neuropharm.2011.04.008

Commons KG, Serock MR (2009) Coincidence of neurokinin 1 receptor with the vesicular glutamate transporter 3 (VGLUT3) in the rat forebrain. Neurosci Lett 464:188–192. doi:10.1016/j.neulet.2009.08.042

Demarque M, Spitzer NC (2012) Neurotransmitter phenotype plasticity: an unexpected mechanism in the toolbox of network activity homeostasis. Dev Neurobiol 29:997–1003. doi:10.1016/j.biotechadv.2011.08.021.Secreted

Deneris ES (2011) Molecular genetics of mouse serotonin neurons across the lifespan. Neuroscience 197:17–27. doi:10.1016/j.neuroscience.2011.08.061

Depuy SD, Kanbar R, Coates MB et al (2011) Control of breathing by raphe obscurus serotonergic neurons in mice. J Neurosci 31:1981–1990. doi:10.1523/JNEUROSCI.4639-10.2011

DePuy SD, Stornetta RL, Bochorishvili G et al (2013) Glutamatergic neurotransmission between the C1 neurons and the parasympathetic preganglionic neurons of the dorsal motor nucleus of the vagus. J Neurosci 33:1486–1497. doi:10.1523/JNEUROSCI.4269-12.2013

Dorph-Petersen KA, Nyengaard JR, Gundersen HJG (2001) Tissue shrinkage and unbiased stereological estimation of particle number and size. J Microsc 204:232–246. doi:10.1046/j.1365-2818.2001.00958.x

Dos Santos L, De Andrade TGCS, Zangrossi H (2005) Serotonergic neurons in the median raphe nucleus regulate inhibitory avoidance but not escape behavior in the rat elevated T-maze test of anxiety. Psychopharmacology 179:733–741. doi:10.1007/s00213-004-2120-3

Dulcis D, Jamshidi P, Leutgeb S, Spitzer NC (2013) Neurotransmitter switching in the adult brain regulates behavior. Science 340:449–453. doi:10.1126/science.1234152

Fox SR, Deneris ES (2012) Engrailed is required in maturing serotonin neurons to regulate the cytoarchitecture and survival of the dorsal raphe nucleus. J Neurosci 32:7832–7842. doi:10.1523/JNEUROSCI.5829-11.2012

Fremeau RT, Burman J, Qureshi T et al (2002) The identification of vesicular glutamate transporter 3 suggests novel modes of signaling by glutamate. Proc Natl Acad Sci USA 99:14488–14493. doi:10.1073/pnas.222546799

Gras C, Herzog E, Bellenchi GC et al (2002) A third vesicular glutamate transporter expressed by cholinergic and serotoninergic neurons. J Neurosci 22:5442–5451

Gundersen HJG (1986) Stereology of arbitrary shaped particles: unbiased estimation of number and size. Science on form. In: Proceeding of the first international symposium for science on form, pp 509–516

Gutiérrez R, Romo-Parra H, Maqueda J et al (2003) Plasticity of the GABAergic phenotype of the "glutamatergic" granule cells of the rat dentate gyrus. J Neurosci 23:5594–5598

Hawthorne AL, Wylie CJ, Landmesser LT et al (2010) Serotonergic neurons migrate radially through the neuroepithelium by dynamin-mediated somal translocation. J Neurosci 30:420–430. doi:10.1523/JNEUROSCI.2333-09.2010

Hendricks T, Francis N, Fyodorov D, Deneris ES (1999) The ETS domain factor Pet-1 is an early and precise marker of central serotonin neurons and interacts with a conserved element in serotonergic genes. J Neurosci 19:10348–10356

Hendricks TJ, Fyodorov DV, Wegman LJ et al (2003) Pet-1 ETS gene plays a critical role in 5-HT neuron development and is required for normal anxiety-like and aggressive behavior. Neuron 37:233–247. doi:10.1016/S0896-6273(02)01167-4

Hensler JG (2006) Serotonergic modulation of the limbic system. Neurosci Biobehav Rev 30:203–214. doi:10.1016/j.neubiorev.2005.06.007

Hioki H, Nakamura H, Ma YF et al (2010) Vesicular glutamate transporter 3-expressing nonserotonergic projection neurons constitute a subregion in the rat midbrain raphe nuclei. J Comp Neurol 518:668–686. doi:10.1002/cne.22237

Hodges MR, Wehner M, Aungst J et al (2009) Transgenic mice lacking serotonin neurons have severe apnea and high mortality during development. J Neurosci 29:10341–10349. doi:10.1523/JNEUROSCI.1963-09.2009

Jackson J, Bland BH, Antle MC (2009) Nonserotonergic projection neurons in the midbrain raphe nuclei contain the vesicular glutamate transporter VGLUT3. Synapse 63:31–41. doi:10.1002/syn.20581

Jahanshahi A, Steinbusch HWM, Temel Y (2013) Distribution of dopaminergic cell bodies in the median raphe nucleus of the rat brain. J Chem Neuroanat 53:60–63. doi:10.1016/j.jchemneu.2013.09.002

Kinney GG, Kocsis B, Vertes RP (1996) Medial septal unit firing characteristics following injections of 8-OH-DPAT into the median raphe nucleus. Brain Res 708:116–122

Kiyasova V, Fernandez SP, Laine J et al (2011) A genetically defined morphologically and functionally unique subset of 5-HT neurons in the mouse raphe nuclei. J Neurosci 31:2756–2768. doi:10.1523/JNEUROSCI.4080-10.2011

Köhler CC-PV (1982) Somatostatin-like immunoreactive neurons in the hippocampus: an immunocytochemical study in the rat. Neurosci Lett 34:259–264

Liu C, Maejima T, Wyler SC et al (2010) Pet-1 is required across different stages of life to regulate serotonergic function. Nat Neurosci 13:1190–1198. doi:10.1038/nn.2623

Madisen L et al (1993) Regulation of fatty acid synthase gene expression: an approach for reducing fat accumulation. J Anim Sci 71:1957–1965. doi:10.1038/nn.2467

Mintz EM, Scott TJ (2006) Colocalization of serotonin and vesicular glutamate transporter 3-like immunoreactivity in the midbrain raphe of Syrian hamsters (*Mesocricetus auratus*). Neurosci Lett 394:97–100. doi:10.1016/j.neulet.2005.10.033

Mullen RJ, Buck CR, Smith AM (1992) NeuN, a neuronal specific nuclear protein in vertebrates. Development 116:201–211

Ohmura Y, Tanaka KF, Tsunematsu T et al (2014) Optogenetic activation of serotonergic neurons enhances anxiety-like behaviour in mice. Int J Neuropsychopharmacol. doi:10.1017/S1461145714000637

Paxinos, G and Franklin KBJ (2012) Paxinos and Franklin's the mouse brain in stereotaxic coordinates, 4th edn, Academic Press, ISBN:9780123910578

Pelosi B, Migliarini S, Pacini G et al (2014) Generation of Pet1210-Cre transgenic mouse line reveals non-serotonergic expression domains of Pet1 both in CNS and periphery. PLoS One 9:e104318. doi:10.1371/journal.pone.0104318

Peters S, Slattery DA, Uschold-Schmidt N et al (2014) Dose-dependent effects of chronic central infusion of oxytocin on anxiety, oxytocin receptor binding and stress-related parameters in mice. Psychoneuroendocrinology 42:225–236. doi:10.1016/j.psyneuen.2014.01.021

Rind HB, Russo AF, Whittemore SR (2000) Developmental regulation of tryptophan hydroxylase messenger RNA expression and enzyme activity in the raphe and its target fields. Neuroscience 101:665–677. doi:10.1016/S0306-4522(00)00402-4

Schmitz C, Hof PR (2005) Design-based stereology in neuroscience. Neuroscience 130:813–831. doi:10.1016/j.neuroscience.2004.08.050

Scott MM, Wylie CJ, Lerch JK et al (2005) A genetic approach to access serotonin neurons for in vivo and in vitro studies. Proc Natl Acad Sci USA 102:16472–16477. doi:10.1073/pnas.0504510102

Serrats J, Artigas F, Mengod G, Cortés R (2003) GABA B receptor mRNA in the raphe nuclei: co-expression with serotonin transporter and glutamic acid decarboxylase. J Neurochem 84:743–752. doi:10.1046/j.0022-3042.2003.01557.x

Shutoh F, Ina A, Yoshida S et al (2008) Two distinct subtypes of serotonergic fibers classified by co-expression with vesicular glutamate transporter 3 in rat forebrain. Neurosci Lett 432:132–136. doi:10.1016/j.neulet.2007.12.050

Silva RCB, Gárgaro AC, Brandão ML (2004) Differential regulation of the expression of contextual freezing and fear-potentiated startle by 5-HT mechanisms of the median raphe nucleus. Behav Brain Res 151:93–101. doi:10.1016/j.bbr.2003.08.015

Somogyi J, Baude A, Omori Y et al (2004) GABAergic basket cells expressing cholecystokinin contain vesicular glutamate transporter type 3 (VGLUT3) in their synaptic terminals in hippocampus and isocortex of the rat. Eur J Neurosci 19:552–569. doi:10.1111/j.0953-816X.2003.03091.x

Spaethling JM, Piel D, Dueck H et al (2014) Serotonergic neuron regulation informed by in vivo single-cell transcriptomics. FASEB J 28:771–780. doi:10.1096/fj.13-240267

Stamp JA, Semba K (1995) Extent of colocalization of serotonin and GABA in the neurons of the rat raphe nuclei. Brain Res 677:39–49

Sterio D (1984) The unbiased estimation of number and sizes of arbitrary particles using the disector. J Microsc 134:127–136

Szőnyi A, Mayer MI, Cserép C et al (2014) The ascending median raphe projections are mainly glutamatergic in the mouse forebrain. Brain Struct Funct. doi:10.1007/s00429-014-0935-1

Varga V, Losonczy A, Zemelman BV et al (2009) Fast synaptic subcortical control of hippocampal circuits. Science 326:449–453. doi:10.1126/science.1178307

Vertes RP, Kocsis B (1997) Brainstem-diencephalo-septohippocampal systems controlling the theta rhythm of the hippocampus. Neuroscience 81:893–926

Vertes RP, Fortin WJ, Crane AM (1999) Projections of the median raphe nucleus in the rat. J Comp Neurol 407:555–582. doi:10.1002/(SICI)1096-9861(19990517)407:4<555:AID-CNE7>3.3.CO;2-5

Vong L, Ye C, Yang Z et al (2011) Leptin action on GABAergic neurons prevents obesity and reduces inhibitory tone to POMC neurons. Neuron 71:142–154. doi:10.1016/j.neuron.2011.05.028

Wang DV, Yau HJ, Broker CJ, Tsou JH, Bonci AIS (2015) Mesopontine median raphe regulates hippocampal ripple oscillation and memory consolidation. Nat Neurosci 18:728–735. doi:10.1038/nn.3998

West MJ, Slomianka LGH (1991) Unbiased stereological estimation of the total number of neurons in the subdivisions of the rat hippocampus using the optical fractionator. Anat Rec 231:482–497. doi:10.1002/ar.1092310411

Yizhar O, Fenno LE, Davidson TJ et al (2011) Optogenetics in neural systems. Neuron 71:9–34. doi:10.1016/j.neuron.2011.06.004

Zangrossi H, Graeff FG (2014) Serotonin in anxiety and panic: contributions of the elevated T-maze. Neurosci Biobehav Rev 46:397–406. doi:10.1016/j.neubiorev.2014.03.007

RESEARCH ARTICLE SUMMARY

NEUROSCIENCE

Median raphe controls acquisition of negative experience in the mouse

András Szőnyi*, Krisztián Zichó*, Albert M. Barth, Roland T. Gönczi, Dániel Schlingloff, Bibiána Török, Eszter Sipos, Abel Major, Zsuzsanna Bardóczi, Katalin E. Sos, Attila I. Gulyás, Viktor Varga, Dóra Zelena, Tamás F. Freund, Gábor Nyiri†

INTRODUCTION: Coping with negative experience is essential for survival. Animals must quickly recognize a harmful situation, produce an adequate response, and learn its context, so that they can predict the reoccurrences of similar experiences. This process requires the lateral habenula (LHb) and the medial ventral tegmental area (mVTA) for evaluating and predicting aversive stimuli. LHb neurons promote encoding of aversive behavior, learn to respond to cues that predict aversive stimuli, and activate negative experience–processing mVTA dopaminergic (DA) neurons. Overexcitation of LHb neurons leads to depression-like symptoms, whereas their inactivation has an antidepressant effect. Coping with negative experience also requires the septohippocampal system to record and recall contextual memories of events. This process necessitates increased firing of pacemaker parvalbumin (PV)–positive neurons in the medial septum and the vertical limbs of the diagonal bands of Broca (MS/VDB) and subsequent theta oscillations in the hippocampus. However, how all these brain centers coordinate their activity during adverse events is poorly understood.

RATIONALE: Because the LHb does not project directly to the septohippocampal system, the brainstem median raphe region (MRR) has been proposed to coordinate their activity. Although MRR plays an important role in regulating mood, fear, and anxiety, and neuronal projections from it have been extensively studied for decades, it is still unclear how MRR neurons process these negative experiences. Using cell type–specific neuronal tract tracing, monosynaptic rabies tracing, block-face scanning immunoelectron microscopy, and in vivo and in vitro electrophysiological methods, we investigated the neurons of mouse MRR that are responsible for these functions. We used in vivo optogenetics combined with behavioral experiments or electrophysiological recordings to explore the role of MRR neurons responsible for the acquisition of negative experience.

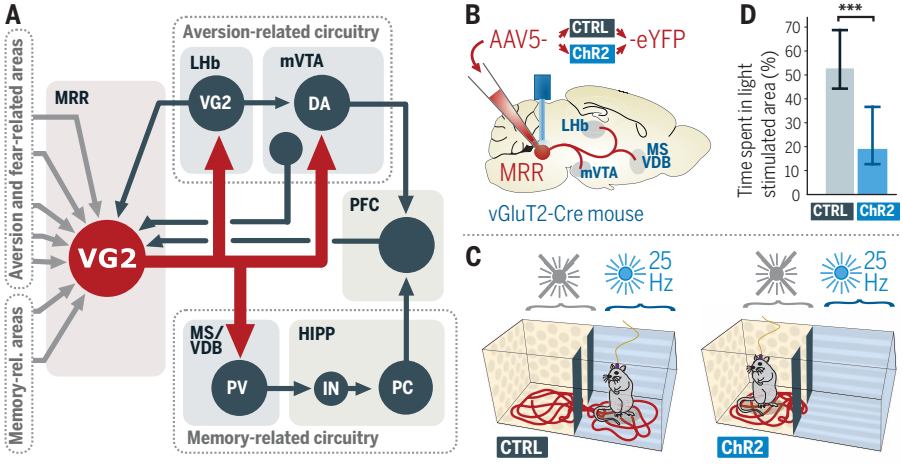

MRR vGluT2 neurons serve as a key hub for aversive behavior. (**A**) MRR vGluT2 (VG2) neurons process aversive events by activating LHb and mVTA neurons and hippocampus (HIPP)–projecting memory acquisition–promoting PV-positive cells in MS/VDB. PFC, prefrontal cortex; IN, interneuron; PC, pyramidal cell. After viruses made MRR vGluT2 neurons light-sensitive (**B**), mice were light-stimulated in a specific area (**C**), which caused significant avoidance of that area compared with response in control mice (**D**). Medians and interquartile ranges; ***P = 0.00034; Mann-Whitney U test. AAV5, adeno-associated virus serotype 5; CTRL, control; ChR2, channelrhodopsin 2; eYFP, enhanced yellow fluorescent protein.

RESULTS: We discovered that the MRR harbors a vesicular glutamate transporter 2 (vGluT2)–positive cell population that gives rise to the largest ascending output of the MRR. These neurons received extensive inputs from negative sensory experience–related brain centers, whereas their excitatory fibers projected to the LHb, mVTA, and MS/VDB (see figure). MRR vGluT2 neurons mainly innervated MRR- or mVTA-projecting cells in the medial (limbic) LHb, creating a direct feedback in the MRR-LHb-mVTA axis. MRR vGluT2 neurons were selectively activated by aversive but not rewarding stimuli in vivo. Stimulation of MRR vGluT2 neurons induced strong aversion (see figure), agitation, and aggression and suppressed reward-seeking behavior, whereas their chronic activation induced depression-related anhedonia. The latter can at least partly be explained by our three-dimensional electron microscopy data showing highly effective synaptic targeting of LHb neurons and by our in vitro data showing that MRR vGluT2 terminals can trigger depressive behavior–related bursting activity of LHb neurons. MRR vGluT2 neurons seem to be involved in active responses to negative experience, therefore inducing aggression or avoidance, classical fight-or-flight responses. Suppression of MRR vGluT2 neurons precisely at the moment of the aversive stimulus presentation strongly disrupted the expression of both contextual and cued fear memories and prevented fear generalization. MRR vGluT2 neurons could facilitate the learning of negative experience, because their LHb-projecting axons bifurcated and selectively innervated pacemaker MS/VDB PV-positive neurons that projected to the hippocampus. Consequently, in vivo stimulation of MRR vGluT2 neurons instantly evoked memory acquisition–promoting hippocampal theta oscillations in mice.

ON OUR WEBSITE

Read the full article at http://dx.doi.org/10.1126/science.aay8746

CONCLUSION: Our results revealed that the MRR harbors a previously unrecognized brainstem center that serves as a key hub for the acquisition of negative experience. MRR vGluT2 neurons could activate the aversion- and negative prediction–related LHb-mVTA axis and could swiftly transform the state of the septohippocampal system for immediate acquisition of episodic memories of the negative experience. Maladaptations in processing negative experience form the basis of several types of mood disorders, which have a huge social and economic impact on individuals and society. Selective targeting of this neural hub may form the basis of new therapies. ■

The list of author affiliations is available in the full article online.
*These authors contributed equally to this work.
†Corresponding author. Email: nyiri.gabor@koki.mta.hu
Cite this article as A. Szőnyi *et al.*, *Science* **366**, eaay8746 (2019). DOI: 10.1126/science.aay8746

RESEARCH ARTICLE

NEUROSCIENCE

Median raphe controls acquisition of negative experience in the mouse

András Szőnyi[1]*†‡, Krisztián Zichó[1]*, Albert M. Barth[1], Roland T. Gönczi[1], Dániel Schlingloff[1,2], Bibiána Török[2,3], Eszter Sipos[3], Abel Major[1], Zsuzsanna Bardóczi[1], Katalin E. Sos[1,2], Attila I. Gulyás[1], Viktor Varga[1], Dóra Zelena[3], Tamás F. Freund[1], Gábor Nyiri[1]§

Adverse events need to be quickly evaluated and memorized, yet how these processes are coordinated is poorly understood. We discovered a large population of excitatory neurons in mouse median raphe region (MRR) expressing vesicular glutamate transporter 2 (vGluT2) that received inputs from several negative experience–related brain centers, projected to the main aversion centers, and activated the septohippocampal system pivotal for learning of adverse events. These neurons were selectively activated by aversive but not rewarding stimuli. Their stimulation induced place aversion, aggression, depression-related anhedonia, and suppression of reward-seeking behavior and memory acquisition–promoting hippocampal theta oscillations. By contrast, their suppression impaired both contextual and cued fear memory formation. These results suggest that MRR vGluT2 neurons are crucial for the acquisition of negative experiences and may play a central role in depression-related mood disorders.

To survive, animals must quickly recognize a harmful situation, produce an adequate response, and learn its context to help predict the occurrence of similar negative experiences in the future (*1*–*6*). This process requires the lateral habenula (LHb) and medial ventral tegmental area (mVTA) for evaluating and predicting aversive stimuli and also requires the septohippocampal system to record and recall memories of these adverse events. Yet how these brain centers coordinate their activity during adverse events is poorly understood. Because the LHb does not project directly to the septohippocampal system, the brainstem median raphe region (MRR) has been proposed to coordinate their activity (*7*–*14*). Although the MRR plays an important role in regulating mood, fear, and anxiety, its role in processing negative experience remains elusive (*13*, *15*, *16*). It contains projection neurons expressing serotonin [5-hydroxytryptamine (5-HT)] and/or type 3 vesicular glutamate transporter (vGluT3), yet after decades of studies, it is still unclear how MRR neurons can support these functions (*17*–*19*). Although projections from the MRR to the LHb, mVTA, and medial septum and the vertical limbs of the diagonal bands of Broca (MS/VDB) must be crucial to understanding negative experience–related behavior, the identity of key MRR neurons responsible for these connections remains unknown (*20*, *21*).

[1]Laboratory of Cerebral Cortex Research, Department of Cellular and Network Neurobiology, Institute of Experimental Medicine, Hungarian Academy of Sciences, Budapest, Hungary. [2]János Szentágothai Doctoral School of Neurosciences, Semmelweis University, Budapest, Hungary. [3]Laboratory of Behavioral and Stress Studies, Department of Behavioral Neurobiology, Institute of Experimental Medicine, Hungarian Academy of Sciences, Budapest, Hungary.
*These authors contributed equally to this work.
†Present address: Laboratory for Cellular Mechanisms of Learning and Memory, Friedrich Miescher Institute for Biomedical Research, Basel, Switzerland.
‡Present address: Laboratory of Cellular Neurophysiology, Department of Cellular and Network Neurobiology, Institute of Experimental Medicine, Hungarian Academy of Sciences, Budapest, Hungary.
§Corresponding author. Email: nyiri.gabor@koki.mta.hu

Most MRR projection neurons are vGluT2-positive

In mice, the transmitter phenotypes and targets of almost 25% of MRR neurons are unknown (*22*). In this study, injections of the Cre-dependent tracer virus AAV5-eYFP (AAV5, adeno-associated virus serotype 5; eYFP, enhanced yellow fluorescent protein) into the MRR of vGluT2-Cre mice, together with complete stereological measurements, revealed that at least 20% of the MRR neurons are vGluT2-positive (Fig. 1, A to C; table S5; and supplementary materials). MRR vGluT2-positive neurons were evenly distributed both in the median and the paramedian part of the MRR. Fluorescent immunohistochemistry demonstrated that this group of cells was distinct from 5-HT– and/or vGluT3-positive neurons in the MRR (Fig. 1B). Terminals of eYFP-expressing MRR neurons of vGluT2-Cre mice were positive for vGluT2 (fig. S1, A and B), but they do not express the plasma membrane serotonin transporter, vesicular GABA transporter (vGAT), or vGluT3 (fig. S1C).

MRR vGluT2 neurons are linked to negative experience–related brain regions

Viral labeling of vGluT2 neurons with Cre-dependent AAV5-eYFP in vGluT2-Cre mice revealed that they strongly innervate the LHb and the mVTA (Fig. 1, E and F), as well as other neurons locally (fig. S1D). We did not observe similar innervation patterns after injecting surrounding brain areas in vGluT2-Cre mice, nor after injecting AAV5-eYFP into the MRR of tryptophan hydroxylase (TpH)–Cre, vGluT3-Cre, or vGAT-Cre mice [labeling serotonergic, vGluT3-positive, and γ-aminobutyric acid–releasing (GABAergic) MRR neurons, respectively] (fig. S3, A to I).

Injections of Cre-dependent AAV5-eYFP into the MRR of vGluT2-Cre mice showed that MRR vGluT2 neuronal projections avoided positive reinforcement–related lateral VTA dopaminergic (DA) cells (Fig. 1G). Instead, they innervated mVTA DA neurons (Fig. 1, G and H). Glutamatergic LHb neurons also innervate mVTA DA cells to regulate negative reward predictions and aversive behavior (*1*–*3*, *23*). Indeed, when we simultaneously injected AAV5-mCherry into the LHb and AAV5-eYFP into the MRR of the same vGluT2-Cre mice, we detected that both LHb and MRR vGluT2 neurons targeted the mVTA specifically (Fig. 1, G and H).

Aversion-related mVTA DA cells target the medial prefrontal cortex (mPFC) (*23*, *24*). We injected the retrograde tracer choleratoxin B subunit (CTB) into the mPFC and Cre-dependent AAV5-eYFP into the MRR of vGluT2-Cre mice (fig. S1E). vGluT2-positive MRR terminals established synaptic contacts with those mVTA DA neurons that project to the mPFC (fig. S1, F and G), showing that vGluT2-positive MRR neurons target DA cells related to negative reward predictions.

Glutamatergic LHb neurons (primarily in the medial part of the LHb) also innervate the MRR (*25*), but the identity of their target cells is unknown. We injected Cre-dependent AAV5-eYFP into the MRR and AAV5-mCherry into the LHb of vGluT2-Cre mice and found that MRR vGluT2 neurons primarily targeted the medial part of the LHb (Fig. 1E), whereas at least 39% of LHb terminals innervated vGluT2-positive neurons in the MRR (Fig. 1, I to L). Serotonergic and vGluT3-positive MRR neurons were also targeted by LHb vGluT2 neurons (for the exact ratios, see fig. S2, F and G). Using combined anterograde and retrograde tracing, we also found that there is a direct reciprocal connection between the LHb-projecting vGluT2-positive MRR neurons and the MRR-projecting vGluT2-positive LHb neurons (Fig. 1I) (for measured ratios, see figs. S1, H to J, and S2, A to E, and supplementary materials). vGluT2-positive MRR neurons also innervate LHb neurons that project to the mVTA (fig. S1, H to J). These results indicate an excitatory positive-feedback loop between the vGluT2 neurons of the MRR and LHb. Both of these neuronal populations project to the aversion-encoding mVTA as well.

To identify upstream brain areas that synaptically target the MRR vGluT2-positive neurons, we used mono-transsynaptic rabies tracing (*26*). We used a Cre-dependent helper

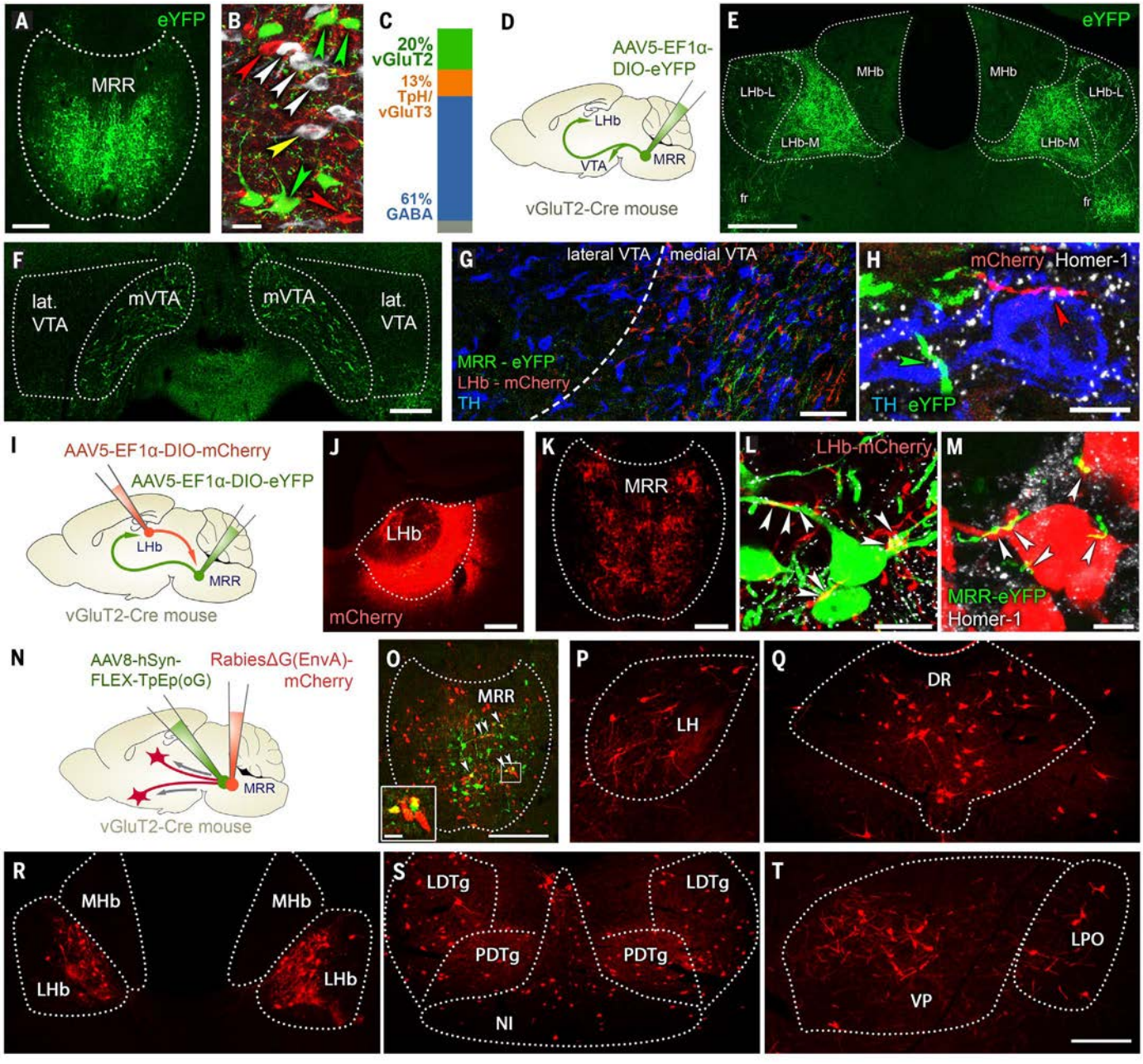

Fig. 1. vGluT2 neurons are the largest population of projection cells in the MRR. (**A**) AAV5-eYFP labeling in the MRR in vGluT2-Cre mice. Scale bar: 200 μm. (**B**) eYFP-labeled vGluT2-positive (green arrows), immunolabeled TpH-positive (white arrows), vGluT3-positive (red arrows), and TpH/vGluT3 double positive (yellow arrow) cells in MRR. Scale bar: 20 μm. (**C**) At least 20% of the MRR neurons are vGluT2-positive. (For stereological statistical details, see table S5). (**D**) AAV2/5-EF1α-DIO-eYFP was injected into the MRR of vGluT2-Cre mice (n = 3). (**E** and **F**) Virally labeled vGluT2-positive MRR fibers innervate the LHb (primarily the medial part) and mVTA. fr, fasciculus retroflexus; LHb-L, lateral habenula, lateral division; LHb-M, lateral habenula, medial division; MHb, medial habenula; VTA, ventral tegmental area. Scale bars: 200 μm. (**G**) vGluT2-positive fibers from MRR (green) and LHb (red) innervate the same medial VTA but not the lateral VTA. DA cells were labeled with anti–tyrosine hydroxylase (TH, blue). Scale bar: 50 μm. Statistical details for all figures are provided in the supplementary text section of the supplementary materials. (**H**) vGluT2-positive MRR axon terminal (green) and an LHb terminal (red) establish Homer-1 (white) positive synaptic contacts with the same dopaminergic cell (TH, blue) in mVTA. Scale bar: 5 μm. (**I**) AAV2/5-EF1α-DIO-eYFP was injected into the MRR and AAV2/5-EF1α-DIO-mCherry was injected into the LHb of vGluT2-Cre mice bilaterally (n = 2). (**J** and **K**) Injection site in the LHb (J) and its vGluT2-positive fibers in the MRR (K). Scale bar: 200 μm. (**L**) vGluT2-positive LHb fibers (red) establish Homer-1 (white) positive synaptic contacts (white arrowheads) with vGluT2-positive MRR neurons (green). Scale bar: 10 μm. (**M**) vGluT2-positive MRR fibers (green) establish Homer-1 (white) positive synaptic contacts (white arrowheads) with vGluT2-positive LHb neurons (red). Scale bar: 5 μm. (**N**) A helper AAV2/8-hSyn-FLEX-TpEp(oG) was injected into the MRR of vGluT2-Cre mice, followed by an injection of Rabies(ΔG)-EnvA-mCherry 2 weeks later (n = 3 mice). (**O**) Injection site of helper (green) and rabies (red) viruses into the MRR of vGluT2-Cre mice. Inset shows some starter neurons expressing both viruses. Scale bar: 100 μm (main image), 10 μm (inset). (**P** to **T**) Rabies-labeled neurons in different brain areas establish synapses on vGluT2-positive MRR neurons. Scale bar: 100 μm. LDTg, laterodorsal tegmental nucleus; LPO, lateral preoptic area; PDTg, posterodorsal tegmental nucleus; VP, ventral pallidum. For detailed analysis, see table S6.

virus encoding both an avian tumor virus receptor A (TVA) and an optimized rabies glycoprotein, and we used a TVA-receptor-dependent and glycoprotein-deleted rabies virus in vGluT2-Cre mice (supplementary materials and Fig. 1, N and O)—the specificity of this virus combination was validated in our previous study (*27*). Brain areas that play an essential role in negative experience–related behavior, including the dorsal raphe (DR), lateral hypothalamus (LH), periaqueductal gray, and zona incerta, showed a strong convergence onto vGluT2-positive MRR cells (Fig. 1, P to T; for details, see table S6). The LHb accounts for most of the monosynaptically labeled input cells (Fig. 1R). Areas related to the encoding of aversive memories [such as the mammillary areas, the pontine reticular nucleus, or the nucleus incertus (NI)] also sent strong projections onto vGluT2-positive MRR neurons (table S6).

MRR vGluT2 neurons establish multiple burst-promoting synapses on LHb neurons

Negative experience–related behavior and subsequent depression-like symptoms are strongly promoted by the excitatory inputs of LHb neurons (*28*–*30*). Using block-face scanning electron microscopy, we revealed that MRR vGluT2 neurons provide an extensive synaptic coverage on LHb neurons (Fig. 2, A, B, E, and F), and most of the axon terminals of MRR vGluT2 neurons established more than one synapse on the same or different target cells (Fig. 2D). *N*-methyl-D-aspartate (NMDA) receptor–dependent burst-firing in LHb neurons play a key role in the development of depression (*28*, *30*). We found that MRR vGluT2 neurons established NMDA receptor–containing excitatory glutamatergic synapses on LHb neurons (Fig. 2C). In the LHb, astroglia cooperate with excitation to regulate neuronal bursting and depression-like symptoms (*28*). These glial processes enwrapped most synapses of MRR vGluT2 terminals in the LHb (Fig. 2, B, E, and F).

To test the physiological effect of MRR vGluT2 neurons on the activity of the LHb neurons, we selectively activated MRR vGluT2 fibers in the LHb in vitro using channelrhodopsin 2 (ChR2)–containing Cre-dependent AAV5-ChR2-eYFP in optogenetic experiments (Fig. 3A). Light stimulation of ChR2-containing MRR vGluT2-positive fibers reliably evoked glutamatergic excitatory postsynaptic currents (EPSCs) in voltage-clamped neurons of the LHb (Fig. 3B and fig. S4, A and B), which

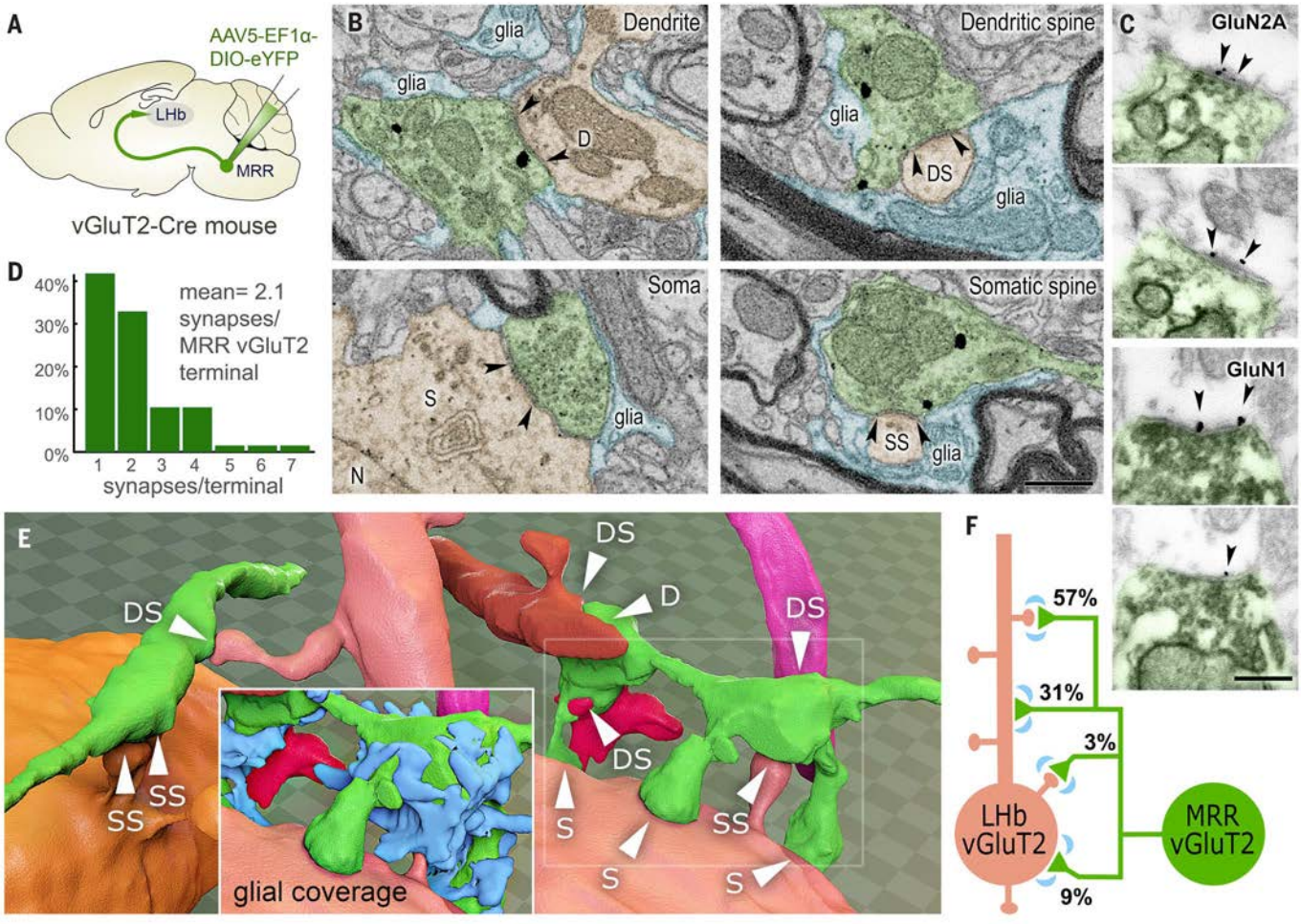

Fig. 2. MRR vGluT2 neurons establish glia-enwrapped glutamatergic synapses on LHb neurons. (**A**) AAV2/5-EF1α-DIO-eYFP was injected into the MRR of vGluT2-Cre mice. (**B**) Scanning electron micrographs represent different types of synaptic contacts established by eYFP-positive MRR terminals (immunogold labeling, black spheres) on different subcellular compartments of LHb neurons. Arrows indicate synaptic edges. D, dendrite; DS, dendritic spine; N, nucleus; S, soma; SS, somatic spine. Scale bar: 500 nm. (**C**) AAV-eYFP positive terminals [serial sections of immunoperoxidase labeling, dark 3,3′ diaminobenzidine (DAB) precipitate] establish synapses on LHb neurons that contain the GluN2A (top two images) or GluN1 (bottom two images) NMDA-receptor subunits (immunogold particles indicated with arrowheads). Scale bar: 300 nm. (**D**) MRR vGluT2 terminals establish more than one synapse on LHb neurons (from two mice). (**E**) 3D reconstruction of MRR vGluT2 fibers (green) shows their synapses with different membrane domains of LHb neurons. Inset shows the abundant glial coverage around MRR vGluT2 terminals (blue). (**F**) Schematic illustration of the proportion of MRR vGluT2 synapses on different membrane domains of LHb neurons (from two mice).

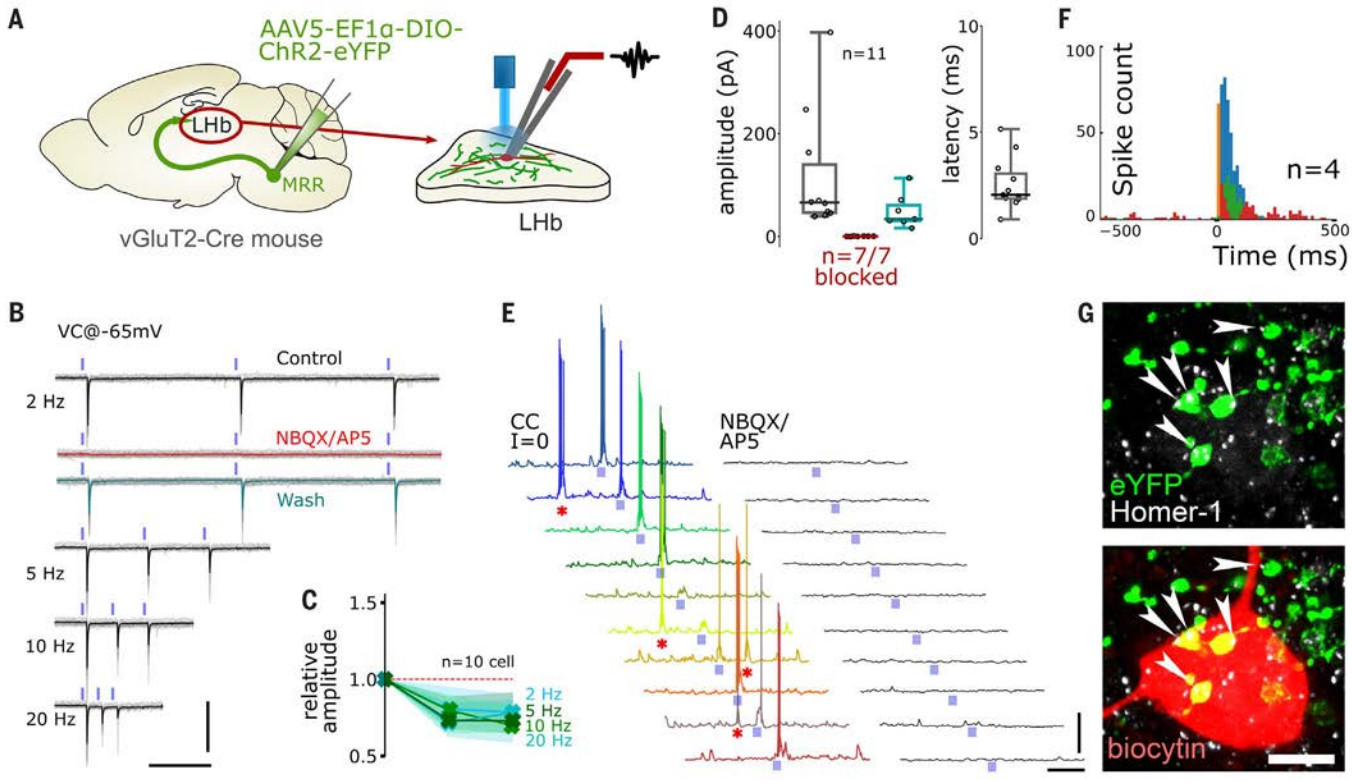

Fig. 3. Fibers of MRR vGluT2 neurons evoke burst firing in LHb neurons. (**A**) AAV2/5-EF1α-DIO-ChR2-eYFP was injected into the MRR of vGluT2-Cre mice (n = 3). Six weeks later, 300-μm-thick horizontal in vitro slices were prepared from the LHb. Neurons in the LHb were whole-cell patch clamped in voltage-clamp mode (see supplementary methods). (**B**) Light stimulations of MRR vGluT2 fibers evoked EPSCs in LHb neurons. The average responses to 2-ms light pulses are shown above individual gray traces. Responses are strong in control conditions (black); they were completely abolished (red trace) by 20-μM NBQX (AMPA/kainite receptor antagonists) and 50-μM AP5 (NMDA antagonist) and partially recovered after washout (teal). Scale bars: 200 ms, 200 pA. (**C**) Cells displayed short-term depression of EPSC amplitudes at all stimulation frequencies (averages from 10 cells). (**D**) EPSC amplitude and latency distributions from all 11 recorded neurons (in gray). Excitatory postsynaptic potentials were sensitive to glutamatergic antagonists in 7 out of 7 tested cells (red) and partially recovered after washout (teal). (**E**) Traces show representative current-clamped (I = 0) LHb neurons displaying spontaneous (asterisks) and light-evoked (pale blue lines, 5 pulses at 20 Hz) bursts. Ten consecutive stimulations are shown. Both spontaneous and light-evoked bursts were abolished by application of NBQX and AP5 (traces on the right). Scale bars: 1 s, 20 mV. (**F**) Peristimulus time histogram shows action potential distributions upon light stimuli (n = 4 cells). (**G**) A representative, recorded LHb cell (biocytin labeling, red) receives Homer-1–positive (white) synaptic contacts (white arrowheads) from eYFP-positive MRR fibers (green). Scale bar: 5 μm.

received MRR vGluT2 terminals (Fig. 3G). These EPSCs showed strong short-term depression and were abolished by the simultaneous blockade of α-amino-3-hydroxy-5-methyl-4-isoxazolepropionic acid (AMPA)– and NMDA-type glutamate receptors (Fig. 3, B to D). After activating ChR2-expressing vGluT2-positive MRR terminals in the LHb, we frequently observed the induction of burst-firing in LHb neurons (Fig. 3, E and F), whereas some spontaneous burst-firing was also present in these neurons. Bursting disappeared after the combined blockade of AMPA- and NMDA-type glutamate receptors (Fig. 3E).

MRR vGluT2 neurons are selectively activated by aversive stimuli in vivo

We explored the in vivo response of identified MRR vGluT2 neurons to aversive and rewarding stimuli. We used a combination of multichannel recording and optogenetic tagging in the MRR of Cre-dependent, AAV-ChR2-eYFP–injected vGluT2-Cre mice. Awake mice were head-fixed on top of an air-supported spherical treadmill, while multiple single units were simultaneously recorded from the MRR using a multichannel silicone probe. Light pulses that were used to tag vGluT2 neurons were delivered through an optic fiber positioned above the MRR (Fig. 4, A and B). Tagged neurons reliably responded to brief blue laser light pulses with short latency and small jitter (Fig. 4C). A large set of optogenetically identified vGluT2-positive MRR neurons were robustly activated by strongly aversive air puffs (Fig. 4, D to F). By contrast, MRR vGluT2 neurons were practically never affected by rewarding stimuli (water drops) (Fig. 4, D to F). Mildly aversive light-emitting diode (LED) flashes triggered a slight, transient elevation of activity in a small subgroup of vGluT2-positive MRR neurons, partially overlapping with the air-puff activated group (fig. S4, G and H), but this effect was significantly lower than that of air-puff stimulation (Fig. 4, D to F).

Optogenetic activation of MRR vGluT2 neurons causes strongly aversive behavior

The rapid, adverse experience–specific in vivo activity of MRR vGluT2 neurons suggests that they specifically process negative experience. To light-activate MRR vGluT2 neurons selectively in vivo, we injected ChR2-containing Cre-dependent AAV5-ChR2-eYFP into the MRR of vGluT2-Cre mice ("ChR2 mice"). Control mice were injected with a control virus that expressed no ChR2 ("CTRL mice"). Then, we implanted an optic fiber over the MRR (supplementary materials, Fig. 5A, and fig. S5). After handling, mice were placed in a chamber containing two different areas with different visual cues (Fig. 5A). In the habituation session, mice did not show a preference for one

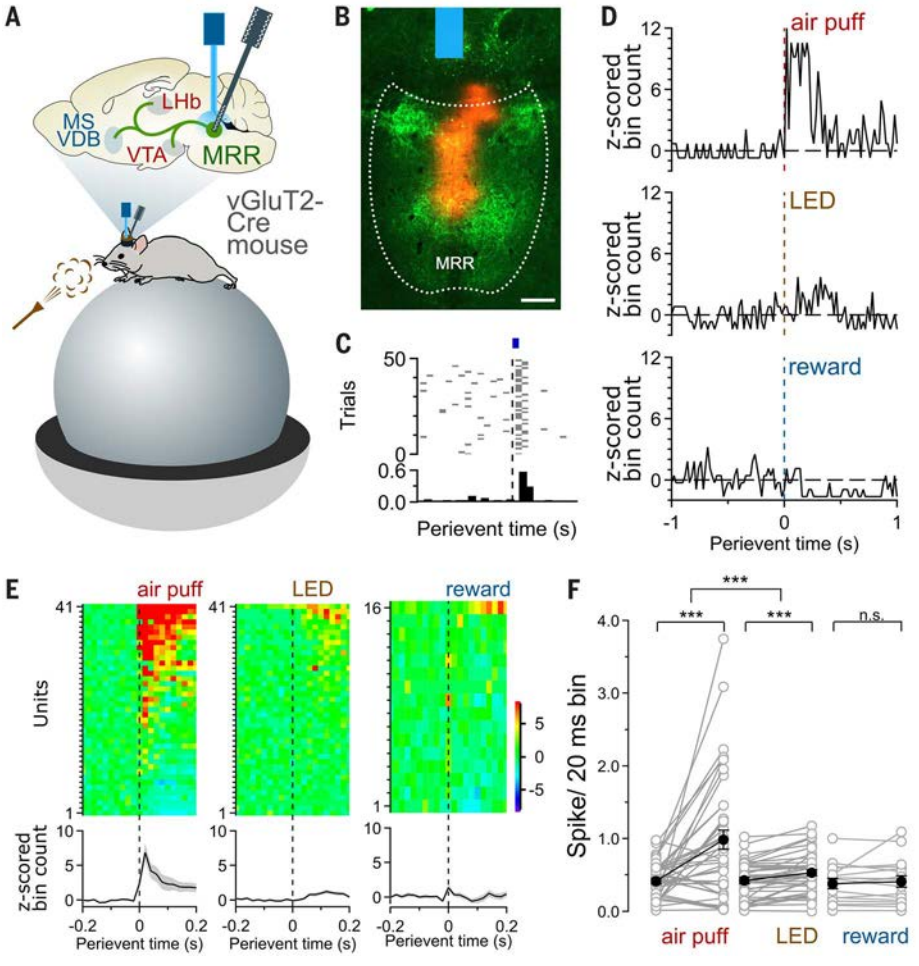

Fig. 4. In vivo, MRR vGluT2 neurons selectively respond to aversive stimuli. (**A**) AAV2/5-EF1α-DIO-ChR2-eYFP was injected into the MRR of vGluT2-Cre mice. A silicone probe was inserted into and an optical fiber was placed above the MRR. Mice were head-fixed on top of an air-supported spherical treadmill, and strongly aversive (air puff), mildly aversive (LED flash), and rewarding (water drops) stimuli were randomly presented to the awake animals (eight mice). (**B**) A representative image of virus expression (green) and the position of the implanted optic fiber (blue) and silicone probe (red DiI labeling) in the MRR of a vGluT2-Cre mouse. Scale bar: 200 μm. (**C**) A raster plot and a peristimulus time histogram, corresponding to an optogenetically tagged vGluT2 neuron in the MRR, shows short latency, high success rate, and low jitter of the responses. The blue square indicates the light pulse. (**D**) A representative MRR vGluT2 neuron was robustly activated by an aversive air puff, was only weakly activated by a slightly aversive LED stimulus, and showed no response to water reward. (**E**) Top matrices show the reaction of individual MRR vGluT2 neurons to different stimuli (each row is one neuron's *z*-scored peristimulus time histogram), sorted by descending response magnitudes. Bottom plots show average response across all tagged units (from eight animals, mean ± SEM). (**F**) Paired plots of cells [same as those displayed in (E)] show the baseline versus stimulus-evoked firing activity of MRR vGluT2 neurons (gray, individual tagged neurons; black, mean ± SEM). Air puffs evoked significantly larger responses than did LED flashes. Reward induced no significant population response.

area over the other (fig. S6, A and B). Twenty-four hours later, mice were returned to the same chamber and received optogenetic stimulation (25 Hz) only in one area of the chamber (area selection was systematically random). ChR2 mice, but not CTRL mice, showed a powerful and immediate real-time place aversion to the stimulation-linked area (Fig. 5, A and B, and fig. S6, A and B). The following day, previously stimulated ChR2 mice, but not CTRL mice, showed a strong conditioned aversion to the area that was previously linked to stimulation (Fig. 5, A and B, and fig. S6, A and B).

We investigated whether the activity of MRR vGluT2 neurons is powerful enough to counteract the strongly positive expectation of a motivated, food-seeking animal. The above-mentioned ChR2 and CTRL mice were food-restricted and trained for 10 days in an operant conditioning task to nose-poke for food rewards (Fig. 5C and supplementary materials). On the last day of their training, both groups of mice reached a plateau in the total number of nose-pokes during the 30-min-long operant conditioning session (Fig. 5C). Twenty-four hours later, mice received blue laser stimulation that started after each rewarded nose-poke during the entire 30-min-long session. ChR2 mice, but not CTRL mice, poked significantly less for reward pellets during the day of the stimulation experiment compared with the frequency of poking on the last day of their training (Fig. 5, D and E).

We also tested whether the activation of these cells can induce passive coping. We performed an optogenetic contextual fear conditioning experiment with the same cohort of mice that participated in the operant conditioning task (fig. S6C). Mice were allowed 3 days to rest and regain their original weight, and on the 25th day they were placed in a novel environment, where they received 15-s-long laser stimulation 10 times. Twenty-four hours later, mice were tested in the same environment. Neither ChR2 mice nor CTRL mice showed any sign of freezing behavior during light stimulation or 24 hours later in the same environment (fig. S6C).

Activation of MRR vGluT2 neurons induces aggression and depressive symptoms

Neuronal activity in the LHb is related to aggressive behavior (*31*). Therefore, we investigated whether activation of MRR vGluT2 neurons induces the prediction of negative experience in a social context and whether it promotes an aggressive behavior in mice during these social interactions. We used a DREADD (designer receptors exclusively activated by designer drugs)–containing AAV-based chemogenetic tool that expresses mutant receptors that activates cells upon binding to clozapine-*N*-oxide (CNO). We injected either Cre-dependent excitatory DREADD virus AAV8-h3MDq-mCherry ("hM3Dq mice") or Cre-dependent AAV8-mCherry virus ("CTRL mice") into the MRR of vGluT2-Cre mice. Then, both hM3Dq and CTRL mice received intraperitoneal injections of CNO (Fig. 6A and supplementary materials) and performed two behavioral tests. In the social interaction test, mice were placed in a novel environment 30 min after CNO injections, together with an unfamiliar mouse. CTRL mice showed mostly prosocial behavior toward the conspecific (Fig. 6B). In contrast, hM3Dq mice became highly aggressive (Fig. 6B and fig. S4, C to F). Five days later, we carried out a resident-intruder test. Thirty minutes after CNO injections, a subordinate intruder mouse was placed into the home cage of the CTRL or hM3Dq mice. Again, hM3Dq mice became highly aggressive

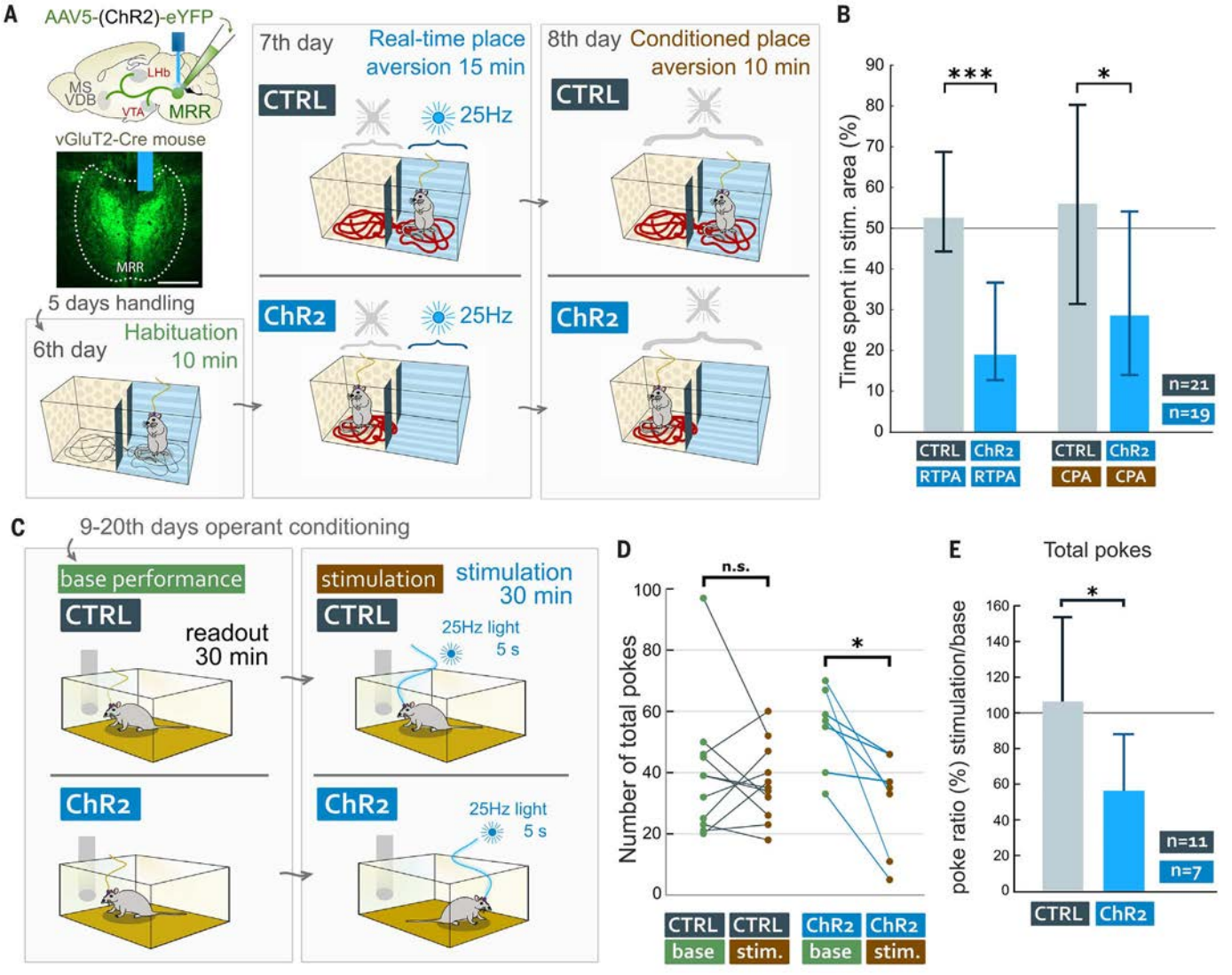

Fig. 5. MRR vGluT2 neurons induce active avoidance of negative experience. (**A**) After injecting ChR2-containing AAV2/5-EF1α-DIO-ChR2-eYFP ("ChR2 mice") or control (only eYFP-containing) Cre-dependent AAV5 ("CTRL mice") into the MRR of vGluT2-Cre mice, we implanted an optic fiber over the MRR. Image represents an injection site in MRR and the position of the optic fiber (blue). Scale bar: 500 μm. Four weeks later, mice were habituated to a chamber with two areas. On day 7, mice received 25-Hz light illumination in one of the areas of the chamber. ChR2 mice showed immediate, significant real-time place aversion (RTPA) of the stimulated area. On day 8, no light was presented, but ChR2 mice displayed a significant conditioned place aversion (CPA), suggesting that the activity of MRR vGluT2 neurons can directly induce real-time and learned active contextual avoidance (see also fig. S6A). (**B**) RTPA and CPA tests show significant effects (medians and interquartile ranges). (**C**) Between days 9 and 21, mice were food-restricted and learned to nose-poke for reward pellets. On day 22, mice received 5-s 25-Hz light stimulation on nose-pokes. Compared with base performance (on day 21), ChR2 mice performed significantly fewer nose-pokes when nose-pokes were paired with laser stimulation (on day 22). (**D**) The total number of nose-pokes for rewards during the base and stimulation performance in the operant conditioning task. (**E**) Nose-poke ratios of stimulation/base performance in the operant conditioning task (mean and SD).

toward the intruder (Fig. 6C and fig. S4, C to F). In a separate experiment, chemogenetic activation of AAV8-h3MDq-expressing MRR vGluT2 neurons by CNO injections also induced significantly higher motor activities in a Y-maze compared with CTRL mice (fig. S4I).

Aggressive behavior frequently accompanies the depressive state (*32*–*34*), which is also promoted by chronic overactivation and burst-firing of LHb neurons (*28*–*31*, *35*). Using the above-mentioned types of CTRL and hM3Dq mice, we tested whether chronic activation of MRR vGluT2 neurons promoted depression-like symptoms. Mice received intraperitoneal injections of the DREADD-agonist CNO three times a week for 3 weeks (Fig. 6A and supplementary materials). On day 19, mice were tested in a sucrose preference test, which can detect anhedonia, a classic symptom of depression (*36*). CTRL mice preferred the 1% sucrose solution over water significantly more than hM3Dq mice did (Fig. 6D). The postmortem weight of the adrenal glands of hM3Dq mice was significantly higher than that of CTRL mice (fig. S4J).

MRR vGluT2 neurons activate memory acquisition–promoting MS/VDB neurons

Fast and effective processing of negative experience requires the immediate induction of memory acquisition, which necessitates a rapid change in the state of the MS/VDB-hippocampal system (*37*). After AAV5-eYFP labeling of MRR vGluT2 neurons, we observed

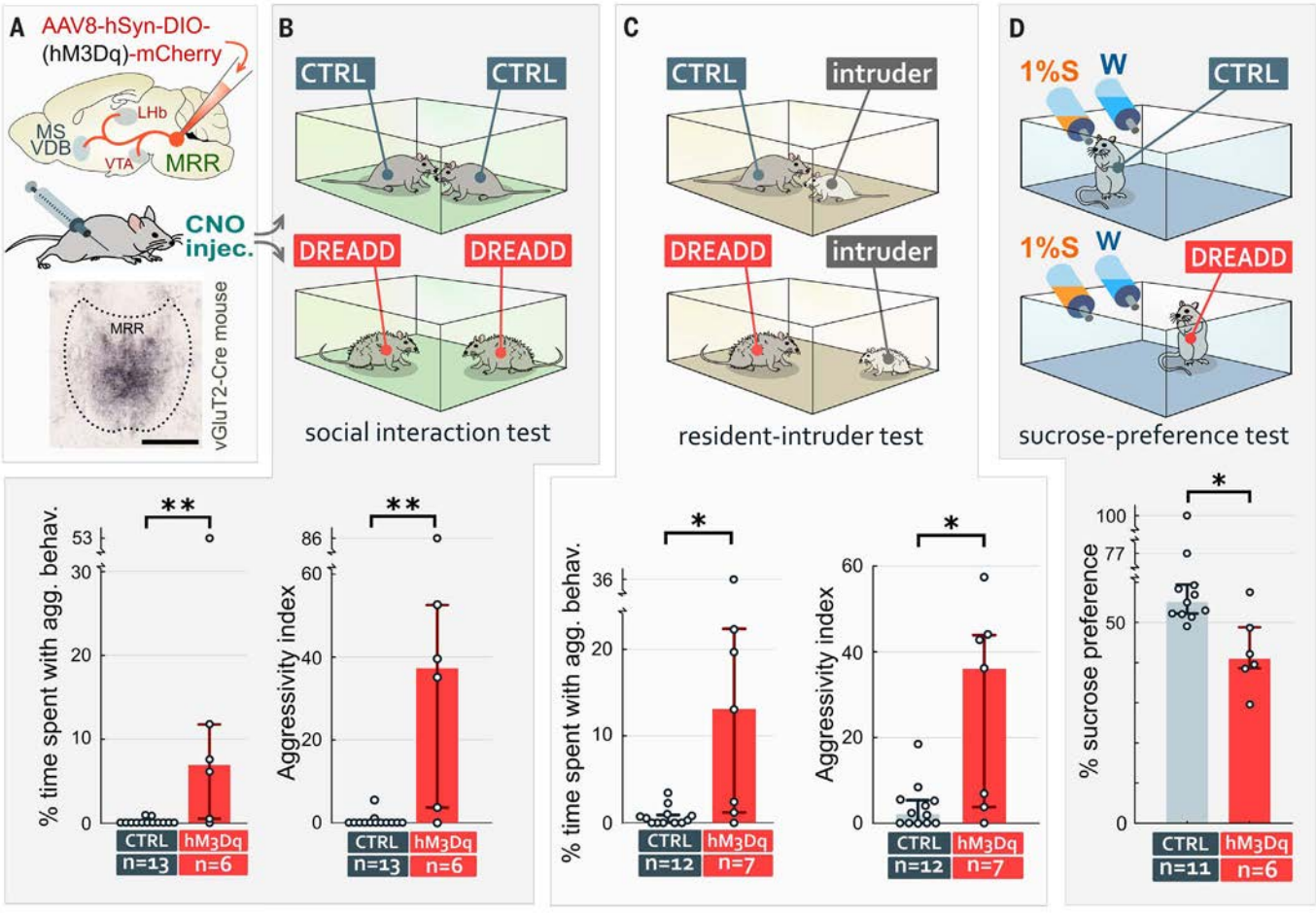

Fig. 6. Chronic overactivation of MRR vGluT2 neurons induces aggression and anhedonia. (**A**) AAV2/8-hSyn-DIO-hM3D(Gq)-mCherry or control AAV2/8-hSyn-DIO-mCherry was injected into the MRR of vGluT2-Cre mice (14 CTRL mice and 8 hM3Dq mice). All mice received hM3Dq-agonist clozapine-*N*-oxide (CNO, 1 mg 10 ml^{-1} kg^{-1} intraperitoneally, 30 min before testing). Image represents a DAB-labeled injection site in the MRR. Scale bar: 500 μm. (**B** and **C**) Social interaction (B) and resident-intruder (C) tests. Percentage of time spent with aggressive interactions and aggressivity index are shown at the bottom. Chemogenetic stimulation of MRR vGluT2 neurons led to highly aggressive behavior, suggesting the induction of active coping with a perceived strongly negative experience. (**D**) Testing anhedonia in a sucrose preference test (see supplementary methods for details). Chronic stimulation of MRR vGluT2 neurons in hM3Dq mice led to a significant difference in sucrose preference compared to CTRL mice, suggesting the induction of depression-related anhedonia. Graphs show medians and 25%–75% quartiles.

an abundant axonal labeling in the MS/VDB (Fig. 7, A and B). MRR vGluT2 neurons established NMDA receptor–containing excitatory synapses selectively with parvalbumin (PV)–positive GABAergic cells in the MS/VDB (Fig. 7, A to E; fig. S1K; and supplementary text). Using hippocampal injections of the retrograde tracer FluoroGold, in combination with AAV5-mCherry, into the MRR of vGluT2-Cre mice, we found that MRR vGluT2 neurons directly innervate hippocampus-projecting PV neurons in MS/VDB (Fig. 7, F to H). These PV neurons are the pacemakers of memory acquisition–promoting hippocampal theta rhythm (*38*, *39*).

The theta-rhythmic activity of LHb neurons and the hippocampal network are phase-locked, and their concerted activity is necessary for proper memory formation (*8*, *14*). Therefore, we investigated whether individual axons of MRR vGluT2 neurons bifurcate and target both areas. We performed double retrograde tracing by injecting CTB into the LHb and FluoroGold into the MS/VDB of vGluT2-Cre mice, and we labeled vGluT2-positive MRR cells with AAV5-mCherry (Fig. 7, I and J). At least 61% of MRR vGluT2 neurons retrogradely labeled from the MS/VDB were retrogradely labeled from the LHb as well (Fig. 7K).

We also investigated the effect of activation of MRR vGluT2 neurons on hippocampal network activity in vivo. Using AAV5-ChR2-eYFP, we expressed ChR2 in MRR vGluT2 neurons and implanted an optic fiber over the MRR and a Buzsaki probe into the dorsal CA1 (Fig. 8A). Ten-second-long stimulation of MRR vGluT2 neurons by a 25-Hz light train triggered some movement (possibly related to the above-mentioned active avoidance of the stimuli) and it triggered hippocampal theta oscillations (Fig. 8, B to D) known to facilitate the formation of memories.

MRR vGluT2 neurons are necessary for fear memory acquisition

MRR vGluT2 neurons are specifically excited by negative experience, which they relay to aversion centers and to the septohippocampal system, likely promoting memory encoding. We injected Cre-dependent Archaerhodopsin T-3 (ArchT 3.0)–containing AAV5-ArchT-GFP (ArchT mice) or control Cre-dependent AAV5-eYFP (CTRL mice) into the MRR of vGluT2-Cre mice and implanted an optic fiber over the MRR (Fig. 8E and fig. S5). After handling, mice were tested in a delay cued fear conditioning paradigm. First, we placed mice into a novel environment "A," where they received three

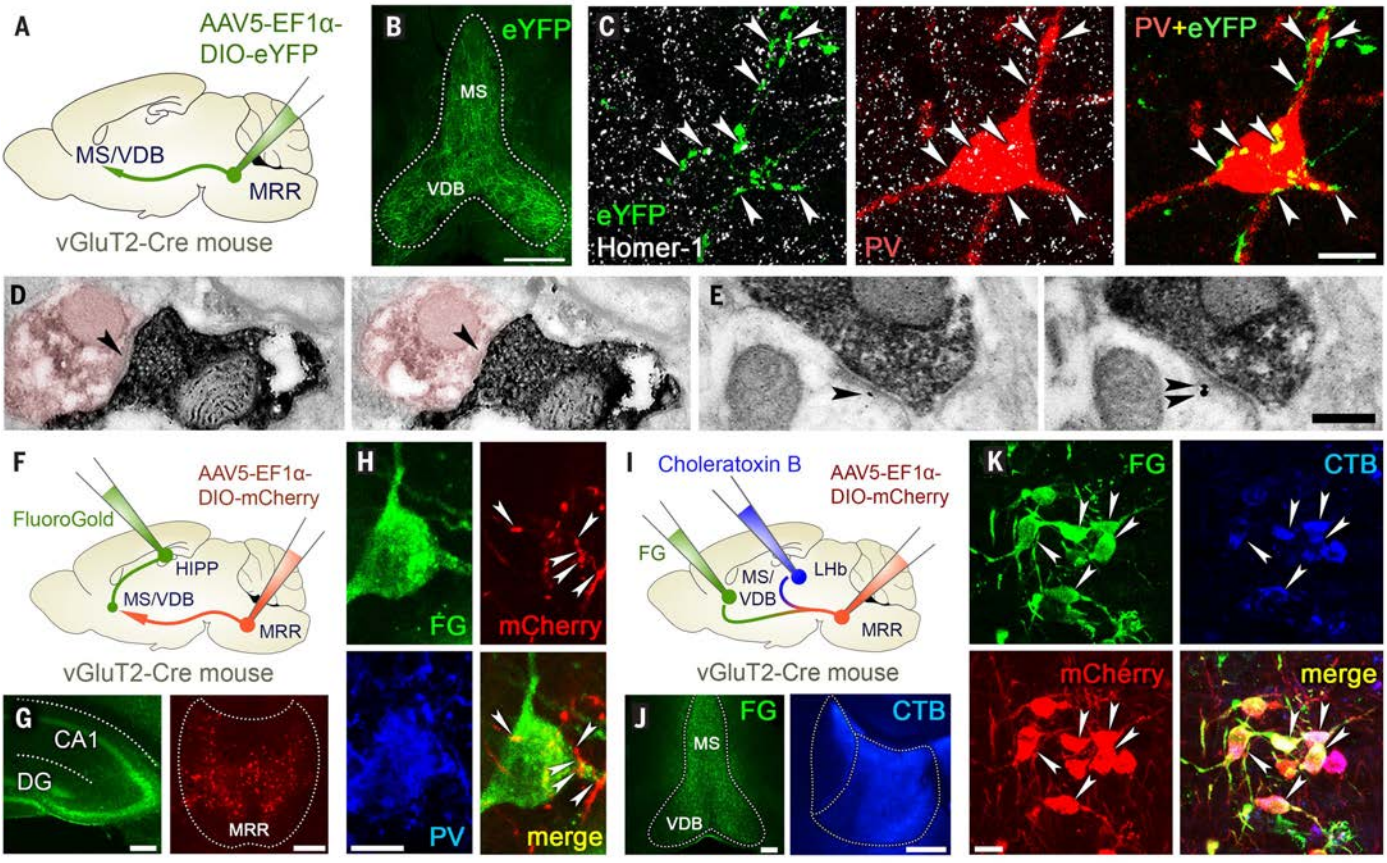

Fig. 7. MRR vGluT2 neurons selectively innervate PV-positive MS/VDB neurons. (**A**) AAV2/5-EF1α-DIO-eYFP was injected into the MRR of vGluT2-Cre mice (n = 3). (**B**) MRR vGluT2 neuronal fibers innervate the MS/VDB. Scale bar: 200 μm. (**C**) A representative MS/VDB PV-positive neuron (red) is innervated by basket-like multiple synapses of vGluT2-positive MRR fibers (green), establishing Homer 1-positive (white) synaptic contacts (white arrowheads). Scale bar: 10 μm. (**D** and **E**) Electron microscopic images show serial sections of synapses of vGluT2-positive MRR terminals (dark SI-DAB). (D) PV-positive dendrite (false red colored, DAB-Ni precipitate) in the VDB received synaptic contacts (at least 12 synapses were reconstructed; black arrowheads). (E) Synapses contained GluN2A subunit of the NMDA receptors (immunogold labeling, black arrowheads) postsynaptically. Scale bar: 300 nm. (**F**) AAV2/5-EF1α-DIO-mCherry was injected into the MRR and FluoroGold into the bilateral hippocampi of vGluT2-Cre mice (n = 2). (**G**) Representative injection sites in the hippocampus [green FluoroGold (FG) labeling] and MRR (red AAV-mCherry). Scale bars: 200 μm. (**H**) AAV-mCherry containing vGluT2-positive MRR terminals (red) establish several putative contacts (white arrowheads) with a FG-positive (green) septohippocampal PV-positive (blue) neuron. Scale bar: 10 μm. (**I**) Double retrograde tracing was performed by injecting FG into the MS/VDB and CTB into the LHb, bilaterally, and AAV2/5-EF1α-DIO-mCherry was injected into the MRR to virally label vGluT2-positive neurons in vGluT2-Cre mice (n = 2). (**J**) Representative injection sites in the MS/VDB (FG labeling) and in the LHb (CTB labeling). Scale bars: 200 μm. (**K**) MRR vGluT2 neurons (red) contain both FG (green) and CTB retrograde labeling (blue), which shows that bifurcating axons of these neurons simultaneously target both the MS/VDB and LHb. Scale bar: 20 μm.

auditory tones, at the end of which they received foot shocks and light illuminations. Light delivery was precisely aligned to foot shocks (Fig. 8E). All mice displayed equally strong immediate reactions to foot shocks. In the tests that followed, mice received no light illumination. Twenty-four hours later, mice were placed into the same environment "A" to test their contextual memories. CTRL mice expressed strong contextual freezing behavior, whereas ArchT mice showed almost no freezing behavior (Fig. 8E). The next day, we placed mice into a different, neutral environment (environment "B"), where ArchT mice showed significantly lower generalized fear compared with CTRL mice (Fig. 8E). Then, in the same neutral environment, we presented mice with an auditory cue. CTRL mice showed very high levels of freezing. In contrast, light-inhibited ArchT mice showed significantly diminished freezing, indicating impaired fear memory formation (Fig. 8E). Even after cue presentation was completed, the difference between the fear levels of ArchT and CTRL mice remained significant (fig. S6D).

MRR vGluT2 neurons serve as a key hub for the acquisition of negative experience

Animals must recognize adverse events quickly and decide whether to fight or flee, while at the same time efficiently learning the context of that event so that they can predict it in the future. The LHb and mVTA are activated during the acquisition of negative experience (*7*, *23*, *24*, *40*), which initiates the encoding of "negative reward prediction errors" and aversion in these nuclei (*5*, *41*). Activation of mVTA DA neurons is also aversive (*23*, *42*), whereas the activity of lateral VTA neurons plays a role in positive reinforcement. The LHb contains nearly exclusively glutamatergic neurons, which encode aversive behavior and activate DA neurons of the mVTA (*23*–*25*, *43*). LHb activity also indirectly inhibits encoding of positive reinforcement in the lateral VTA (*23*, *44*). These processes fine-tune future strategies in similar situations (*5*, *41*, *45*–*48*). The LHb and mVTA convey information related to negative predictions and learn to respond to cues that predict aversive stimuli (*3*, *42*, *49*–*53*).

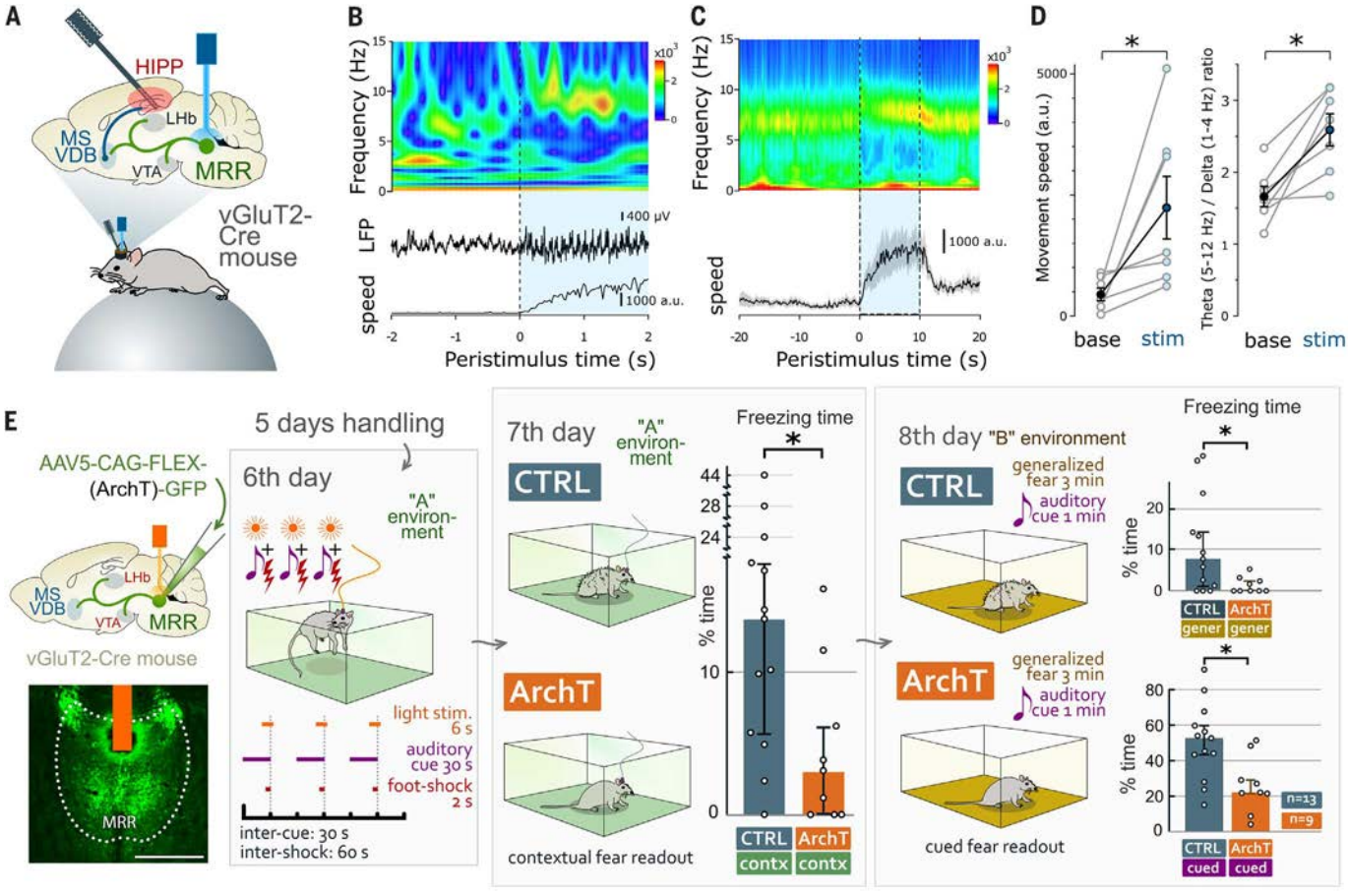

Fig. 8. MRR vGluT2 neurons promote hippocampal theta rhythm and are necessary for fear memory formation. (**A**) AAV2/5-EF1α-DIO-ChR2-eYFP was injected into the MRR of vGluT2-Cre mice. An optical fiber was inserted into the MRR and a silicone probe was implanted into the hippocampal CA1 region to measure concurrent hippocampal network activity (n = 7 mice). Mice were head-fixed on top of an air-supported spherical treadmill and their behavior was monitored. (**B**) Running speed (bottom), local field potential (LFP) recordings from the pyramidal layer of the dorsal hippocampal CA1 region (middle), and corresponding wavelet spectrogram (top). Vertical dashed line indicates the onset of laser stimulation, which rapidly induced a switch to theta oscillation. (**C**) Average running speed (mean ± SEM) (bottom) and corresponding averaged wavelet spectrogram (seven mice) (top). Vertical dashed lines highlight the MRR laser illumination period. (**D**) Paired plots indicating movement speed (left) and theta/delta ratios (right) during baseline (10-s window before laser onset) versus stimulation (10-s window after laser onset) periods (gray, individual animals; black, mean ± SEM). (**E**) Design of cued fear conditioning experiments with optogenetic inhibition of MRR vGluT2 neurons. Fluorescent image represents one of the injection sites to label MRR vGluT2 neurons, and the orange area represents the position of the optic fiber. Scale bar: 500 µm. After handling, light illumination of MRR was switched on precisely during foot shocks that mice received at the end of the auditory cue presentation on day 6. On days 7 and 8, mice received no more light. On day 7, contextual freezing behavior in ArchT mice in the same environment was almost completely diminished (below the 5% threshold) compared with CTRL mice, which received virus without ArchT. On day 8, ArchT mice showed significantly less generalized fear and cued fear in a novel environment compared with CTRL mice. Medians and interquartile ranges are shown on the graphs.

Meanwhile, the MS/VDB-hippocampal system must also be switched into the state optimal for memory acquisition to record the context of such events (*8*, *14*). These processes are also necessary for the prediction and prevention of negative experience in the future. Yet it was not clear which neuronal pathway orchestrates the coordinated activation of these networks. Although the MRR was known to play a central role in processing negative experience (*13*, *15*), its known cell types did not project to the LHb, and the transmitter phenotypes and targets of almost 25% of the MRR neurons were not even known (*22*).

We discovered that these previously unrecognized vGluT2-positive MRR neurons project heavily into the LHb, mVTA, and MS/VDB (fig. S7). They are the largest population of projection neurons from the MRR, are glutamatergic, and do not express 5-HT, vGluT3, or vGAT. We detected an extensive convergence of monosynaptic inputs to MRR vGluT2 neurons from several environmental experience–related brain centers (fig. S7) (*7*, *40*, *54*). MRR vGluT2 neurons predominantly innervate the medial (limbic) division of the LHb that projects to the MRR and mVTA, but they mostly avoid lateral (pallidal) division of the LHb that receives a different set of inputs (*25*, *51*, *55*, *56*). MRR vGluT2 neurons directly innervate MRR- or mVTA-projecting LHb cells, creating a direct feedback in the MRR-LHb-mVTA axis.

Our in vivo physiological measurements confirmed the central and specific role of MRR vGluT2 neurons in the formation of negative experience. MRR vGluT2 neurons were strongly and specifically activated by strong aversive stimuli, mildly activated by weak aversive stimuli, and unaffected by rewarding stimuli. This suggests that these neurons are primarily responsible and necessary for relaying negative experience in the brainstem. Indeed, specific optogenetic inhibition

of these neurons precisely during the presentation of adverse stimuli eliminated or significantly decreased hippocampus-dependent contextual or hippocampus-independent cued fear memories, respectively. These data showed that this neural hub is essential for processing negative experience.

The elevation of excitatory transmission in the LHb and the stimulation of the mVTA have similar effects (*23*, *46*, *57*, *58*). MRR vGluT2 neurons heavily project to the LHb and also selectively innervate mVTA DA neurons (but do not innervate neurons in lateral VTA that are mostly reward-related), suggesting that they can effectively activate negative prediction centers. Indeed, their optogenetic activation triggered immediate behavioral changes by inducing acute place aversion. The adverse event was effectively memorized because it induced conditioned place aversion. Furthermore, the selective activation of MRR vGluT2 neurons could negate an otherwise strongly rewarding behavior in an operant conditioning task. The activation of MRR vGluT2 neurons did not induce passive freezing behavior directly; instead, MRR vGluT2 neurons seem to be involved in active responses to negative experience, and therefore they induce avoidance or flight-or-fight behavior.

Depression is thought to be a result of a learning mechanism based on chronically sustained negative experiences (*59*, *60*). Glutamatergic synapses on LHb neurons show long-term plasticity mechanisms, and LHb neurons can learn to respond to cues preceding aversive events (*28*, *29*, *50*, *61*). The chronic elevation of glutamatergic transmission in the LHb causes depressive disorder through the promotion of burst-firing of LHb neurons, which is also regulated by adjacent glial cell coverage (*28*–*30*, *50*, *62*, *63*). MRR vGluT2 neurons massively innervate LHb neurons with different types of NMDA receptor–containing excitatory contacts that are mostly covered by glial processes on LHb neurons. They can also evoke burst-firing of LHb neurons. We revealed an abundant reciprocal excitatory connection between vGluT2-positive glutamatergic neurons of the LHb and MRR that may result in a reverberation and may support pathological learning and excessive activation of LHb neurons if the loop is not controlled effectively. To mimic a chronically maladapted circuitry, we chemogenetically induced chronic overactivation of vGluT2-positive MRR neurons and it caused anhedonia in the sucrose-preference test, which is a typical sign of depressive disorder in mice.

Aggression is another well-known symptom of depression in mice and humans (*32*–*34*), and both the LHb and MS/VDB play a role in the emotional processing of aggressive behavior (*31*). The activation of MRR vGluT2 neurons also promoted aggressive behavior. Aggression is commonly associated with agitation, the most distinguishing features of which include restlessness, pacing, and motor activities. We observed elevated locomotor activity and exploration in chemogenetically stimulated mice, which together suggest that activation of vGluT2-positive MRR neurons promotes agitation and active aversive behaviors (flight-or-fight responses) in neutral or social situations.

MRR has a complex effect on MS/VDB-hippocampal activity and the formation of contextual fear memories, although its mechanism is not well understood (*9*, *11*). In vivo optogenetic activation of MRR promoted memory acquisition–related theta rhythm through a mechanism conveyed by a non-serotonergic and non-GABAergic MRR cell population (*13*). Activation of pacemaker PV-positive MS/VDB neurons is essential for the generation of hippocampal theta rhythm and proper episodic memory formation (*38*, *39*, *64*). PV-positive MS/VDB neurons are innervated by glutamatergic cells of the MRR (*18*, *65*, *66*), but the identity of those neurons was unknown. We discovered that MRR vGluT2 neurons not only project to the LHb-mVTA aversion axis, but the axons of most of these MRR vGluT2-positive excitatory neurons bifurcate and simultaneously innervate PV-positive neurons in the MS/VDB and can instantly and reliably promote hippocampal theta rhythm generation necessary for memory acquisition. MRR vGluT2 neurons increased theta rhythm–related exploratory behavior, while animals exhibited conditioned place aversion on the day after stimulation, suggesting the facilitation of strong memory formation. MRR vGluT2 neurons may also facilitate the phase-locking of theta rhythm in the LHb and the hippocampus.

Our data revealed that the MRR vGluT2-positive neuronal population is a previously unrecognized neural hub of the brain that is both necessary and sufficient for the acquisition of negative experience, but which is not activated by positive rewarding experience. MRR vGluT2 neurons receive extensive convergence of inputs from sensory experience–related brain areas, their inhibition disrupts aversive memory formation, and their activation promotes agitated and aversive behavior and flight, which quickly negates motivated behavior. If flight is not an option during social interaction, MRR vGluT2 neurons provoke fight and aggression. MRR vGluT2 neurons also facilitate long-term memory formation related to negative experience, and their chronic activation produces a depression-like phenotype, likely through inducing long-term bursting activity in LHb neurons (*28*, *30*), which we showed in our in vitro experiments. Therefore, vGluT2-positive MRR neurons control the acquisition of negative experience by simultaneously triggering the activity of brain aversion centers and hippocampal episodic memory encoding. Maladaptations in processing negative experience are the basis of several types of mood disorders, which have a huge social and economic impact on individuals and society. Selective targeting of this neural hub may form the basis of new therapies.

Materials and methods summary

Ethical considerations and mouse strains

All experiments were performed in accordance with regulations. For details, see the supplementary methods section of the supplementary materials. We used male and female vGluT2-iRES-Cre, vGAT-iRES-Cre, BAC-vGluT3/iCre, and TpH2/iCre-ERT2 mice and males C57Bl/6 wild-type mice. We used adult (at least 6-week-old) mice.

Viral gene transfer, retrograde and mono-transsynaptic rabies tracing, and optic fiber implantations

Mice were anesthetized and mounted in an animal stereotaxic frame. A microinjector pump was used for injections. For anterograde tracing, optogenetic and chemogenetic experiments, we injected different amounts of viruses into the target brain areas. For retrograde tracing experiments, we injected FluoroGold or choleratoxin B subunit into the target areas. For behavioral experiments, 4 to 6 weeks after virus injections, optic fibers were implanted over the MRR. Positions of the optic fibers are illustrated in fig. S5. See (*26*) for a detailed description of the monosynaptic rabies tracing technique used.

Perfusions

Mice were anesthetized and were perfused transcardially with different solutions, depending on the experiments. After perfusions, brains were cut into 30-μm-thick sections using a sliding microtome or into 50-, 60-, or 100-μm-thick sections using a vibratome.

Immunohistochemistry and antibodies

Generally, perfusion-fixed sections were cryoprotected, and after antigen retrieval they were incubated in a blocking medium, and sections were incubated in a mixture of primary antibodies. This was followed by extensive washes and incubation in the mixture of appropriate secondary antibodies. Then, sections were placed on slides and covered with mounting medium. Fluorescent immunohistochemistry for laser-scanning confocal microscopy, immunoperoxidase labeling for localization of virus injections, immunogold-immunoperoxidase double labeling for electron microscopy, silver-gold intensified and nickel-intensified immunoperoxidase double

labeling, and sample preparation for 3D block-face scanning electron microscopy required different procedures, which are described in detail in the supplementary methods.

The list and specifications of the primary and secondary antibodies used can be found in tables S1 and S2. Combinations of the used primary and secondary antibodies in the different experiments are listed in tables S3 and S4.

Block-face scanning electron microscopy and image analysis

We used an FEI Apreo VolumeScope. Images in the z-stacks measured 16,384 pixels × 16,383 pixels with 70 nm thickness, and the final z-stacks contained 300 slices. Voxel size was 4 nm × 4 nm × 70 nm. All image post-processing was done in FIJI ImageJ. Segmentation was performed manually. Data were analyzed using Tibco Statistica 13.4. After segmentation, the models were exported in .obj format and imported into Blender (Blender Foundation, Amsterdam, the Netherlands) for further investigation and visualization.

Stereology measurements

Unbiased design-based stereological measurements were carried out using the optical fractionator method. Cell counting was carried out in Stereo Investigator 10.0 stereology software, while cells were identified parallel using NIS Elements AR 4.3 software.

In vitro electrophysiological experiments

In all slice experiments, mice were decapitated under deep isoflurane anesthesia. The brain was removed, and coronal slices of 300 μm thickness were cut using a vibratome. Slices were placed into an interface-type holding chamber, and cells were recorded. Drugs were administered from stock solutions via pipettes into the ACSF-containing superfusion system. All data were processed and analyzed off-line using standard built-in functions of Python 2.7.0. Latency was defined as a time between light stimulus onset and time of reaching 10% of maximal EPSC amplitude. Throughout this article, for in vitro electrophysiology data, we used median, first, and third quartiles for the description of data groups because they did not show Gaussian distribution.

In vivo electrophysiological recordings in head-fixed mice

Animals were anesthetized and mounted in a stereotaxic frame. After surgery, mice were continuously monitored. After a recovery period of 3 to 7 days, mice were water-restricted and habituated for 10 to 14 days to the spherical treadmill setup with their head fixed. Animal weight was monitored, and when a mouse reached 85% of the initially measured baseline weight, the daily volume of water supplement was individually adjusted in order to maintain this 85% target weight. Habituation is described in the supplementary methods. On the day of the experiment, the animal was head-fixed above the air-supported spherical treadmill. Hippocampal and median raphe silicone probes were lowered through the cranial window. Ground electrode was placed above the cerebellum. Electrophysiological recordings were performed by a signal multiplexing headstage. At the end of each recording session, brief laser pulses were applied for offline identification of responsive units. Units (i.e., neurons) were categorized as "tagged" if their firing followed the laser pulse with short latency (within 4 ms) and >50% success rate.

The mean baseline firing rate values and standard deviations were calculated from a 4-s time window preceding stimulus onset. A change in firing rate was declared significant if it deviated more than 2 standard deviations from the mean baseline value (z-score larger than 2 or smaller than −2) in a 200-ms time window after stimulus onset. Both responsive neurons (which increased their firing frequency) and nonresponsive neurons distributed across animals. All statistical analyses were performed with standard Igor Pro 8 functions.

Optogenetic behavioral experiments

After optic fiber implantations, mice were transferred to the animal room of the behavioral unit of the institute to rest and then received 5 days of handling. We carried out real-time place-aversion tests (RTPA), conditioned place-aversion tests (CPA), operant conditioning tests, optogenetic contextual fear conditioning tests (Opto-CFC), and delayed cued-fear conditioning tests (CuedFC). The experimenters evaluating behavioral experiments were blind to the conditions and treatment of the mice. Experimental data were collected and analyzed using the Noldus EthoVision 13.0 and Tibco Statistica 13.4 software.

Behavioral test battery for chemogenetic experiments

We carried out a series of behavioral tests with mice that were injected either with the hM3Dq-containing virus [that expressed a clozapine-*N*-oxide (CNO)–sensitive, excitatory G protein–coupled receptor plus a fluorescent protein] or with a control virus (that expressed only a fluorescent protein). Mice were allowed 48 to 72 hours of rest between tests. To activate the hM3Dq virus, CNO (1 mg/kg in 10 ml saline, Tocris) was injected intraperitoneally 30 min before each behavioral test. Tests were video recorded and analyzed later by an observer blind to the treatment protocols. After this battery of behavioral tests, mice were sacrificed, and their adrenal glands were removed and weighed.

REFERENCES AND NOTES

1. E. S. Bromberg-Martin, M. Matsumoto, H. Nakahara, O. Hikosaka, Multiple timescales of memory in lateral habenula and dopamine neurons. *Neuron* **67**, 499–510 (2010). doi: 10.1016/j.neuron.2010.06.031; pmid: 20696385
2. E. S. Bromberg-Martin, O. Hikosaka, Lateral habenula neurons signal errors in the prediction of reward information. *Nat. Neurosci.* **14**, 1209–1216 (2011). doi: 10.1038/nn.2902; pmid: 21857659
3. E. S. Bromberg-Martin, M. Matsumoto, O. Hikosaka, Distinct tonic and phasic anticipatory activity in lateral habenula and dopamine neurons. *Neuron* **67**, 144–155 (2010). doi: 10.1016/j.neuron.2010.06.016; pmid: 20624598
4. C. A. Orsini, D. E. Moorman, J. W. Young, B. Setlow, S. B. Floresco, Neural mechanisms regulating different forms of risk-related decision-making: Insights from animal models. *Neurosci. Biobehav. Rev.* **58**, 147–167 (2015). doi: 10.1016/j.neubiorev.2015.04.009; pmid: 26072028
5. C. M. Stopper, S. B. Floresco, What's better for me? Fundamental role for lateral habenula in promoting subjective decision biases. *Nat. Neurosci.* **17**, 33–35 (2014). doi: 10.1038/nn.3587; pmid: 24270185
6. C. M. Stopper, M. T. L. Tse, D. R. Montes, C. R. Wiedman, S. B. Floresco, Overriding phasic dopamine signals redirects action selection during risk/reward decision making. *Neuron* **84**, 177–189 (2014). doi: 10.1016/j.neuron.2014.08.033; pmid: 25220811
7. P. M. Baker, S. E. Oh, K. S. Kidder, S. J. Y. Mizumori, Ongoing behavioral state information signaled in the lateral habenula guides choice flexibility in freely moving rats. *Front. Behav. Neurosci.* **9**, 295 (2015). doi: 10.3389/fnbeh.2015.00295; pmid: 26582981
8. R. Goutagny *et al.*, Interactions between the lateral habenula and the hippocampus: Implication for spatial memory processes. *Neuropsychopharmacology* **38**, 2418–2426 (2013). doi: 10.1038/npp.2013.142; pmid: 23736315
9. R. Crooks, J. Jackson, B. H. Bland, Dissociable pathways facilitate theta and non-theta states in the median raphe—Septohippocampal circuit. *Hippocampus* **22**, 1567–1576 (2012). doi: 10.1002/hipo.20999; pmid: 22180148
10. A. Domonkos *et al.*, Divergent in vivo activity of non-serotonergic and serotonergic VGluT3-neurones in the median raphe region. *J. Physiol.* **594**, 3775–3790 (2016). doi: 10.1113/JP272036; pmid: 27028801
11. J. Jackson, C. T. Dickson, B. H. Bland, Median raphe stimulation disrupts hippocampal theta via rapid inhibition and state-dependent phase reset of theta-related neural circuitry. *J. Neurophysiol.* **99**, 3009–3026 (2008). doi: 10.1152/jn.00065.2008; pmid: 18436639
12. G. Viana Di Prisco, Z. Albo, R. P. Vertes, B. Kocsis, Discharge properties of neurons of the median raphe nucleus during hippocampal theta rhythm in the rat. *Exp. Brain Res.* **145**, 383–394 (2002). doi: 10.1007/s00221-002-1123-8; pmid: 12136388
13. D. V. Wang *et al.*, Mesopontine median raphe regulates hippocampal ripple oscillation and memory consolidation. *Nat. Neurosci.* **18**, 728–735 (2015). doi: 10.1038/nn.3998; pmid: 25867120
14. H. Aizawa *et al.*, The synchronous activity of lateral habenular neurons is essential for regulating hippocampal theta oscillation. *J. Neurosci.* **33**, 8909–8921 (2013). doi: 10.1523/JNEUROSCI.4369-12.2013; pmid: 23678132
15. T. G. C. S. Andrade, H. Zangrossi Jr., F. G. Graeff, The median raphe nucleus in anxiety revisited. *J. Psychopharmacol.* **27**, 1107–1115 (2013). doi: 10.1177/0269881113499208; pmid: 23999409
16. D. G. Balázsfi *et al.*, Median raphe region stimulation alone generates remote, but not recent fear memory traces. *PLOS ONE* **12**, e0181264 (2017). doi: 10.1371/journal.pone.0181264; pmid: 28708877
17. T. F. Freund, A. I. Gulyás, L. Acsády, T. Görcs, K. Tóth, Serotonergic control of the hippocampus via local inhibitory interneurons. *Proc. Natl. Acad. Sci. U.S.A.* **87**, 8501–8505 (1990). doi: 10.1073/pnas.87.21.8501; pmid: 1700433
18. J. Jackson, B. H. Bland, M. C. Antle, Nonserotonergic projection neurons in the midbrain raphe nuclei contain the vesicular glutamate transporter VGLUT3. *Synapse* **63**, 31–41 (2009). doi: 10.1002/syn.20581; pmid: 18925658

19. V. Varga *et al*., Fast synaptic subcortical control of hippocampal circuits. *Science* **326**, 449–453 (2009). doi: 10.1126/science.1178307; pmid: 19833972
20. S. J. Bang, P. Jensen, S. M. Dymecki, K. G. Commons, Projections and interconnections of genetically defined serotonin neurons in mice. *Eur. J. Neurosci.* **35**, 85–96 (2012). doi: 10.1111/j.1460-9568.2011.07936.x; pmid: 22151329
21. C. Leranth, R. P. Vertes, Median raphe serotonergic innervation of medial septum/diagonal band of broca (MSDB) parvalbumin-containing neurons: Possible involvement of the MSDB in the desynchronization of the hippocampal EEG. *J. Comp. Neurol.* **410**, 586–598 (1999). doi: 10.1002/(SICI)1096-9861(19990809)410:4<586::AID-CNE6>3.0.CO;2-H; pmid: 10398050
22. K. E. Sos *et al*., Cellular architecture and transmitter phenotypes of neurons of the mouse median raphe region. *Brain Struct. Funct.* **222**, 287–299 (2017). doi: 10.1007/s00429-016-1217-x; pmid: 27044051
23. S. Lammel *et al*., Input-specific control of reward and aversion in the ventral tegmental area. *Nature* **491**, 212–217 (2012). doi: 10.1038/nature11527; pmid: 23064228
24. S. Lammel, B. K. Lim, R. C. Malenka, Reward and aversion in a heterogeneous midbrain dopamine system. *Neuropharmacology* **76**, 351–359 (2014). doi: 10.1016/j.neuropharm.2013.03.019; pmid: 23578393
25. L. A. Quina *et al*., Efferent pathways of the mouse lateral habenula. *J. Comp. Neurol.* **523**, 32–60 (2015). doi: 10.1002/cne.23662; pmid: 25099741
26. I. R. Wickersham *et al*., Monosynaptic restriction of transsynaptic tracing from single, genetically targeted neurons. *Neuron* **53**, 639–647 (2007). doi: 10.1016/j.neuron.2007.01.033; pmid: 17329205
27. A. Szőnyi *et al*., Brainstem nucleus incertus controls contextual memory formation. *Science* **364**, eaaw0445 (2019). doi: 10.1126/science.aaw0445; pmid: 31123108
28. Y. Cui *et al*., Astroglial Kir4.1 in the lateral habenula drives neuronal bursts in depression. *Nature* **554**, 323–327 (2018). doi: 10.1038/nature25752; pmid: 29446379
29. K. Li *et al*., βCaMKII in lateral habenula mediates core symptoms of depression. *Science* **341**, 1016–1020 (2013). doi: 10.1126/science.1240729; pmid: 23990563
30. Y. Yang *et al*., Ketamine blocks bursting in the lateral habenula to rapidly relieve depression. *Nature* **554**, 317–322 (2018). doi: 10.1038/nature25509; pmid: 29446381
31. S. A. Golden *et al*., Basal forebrain projections to the lateral habenula modulate aggression reward. *Nature* **534**, 688–692 (2016). doi: 10.1038/nature18601; pmid: 27357796
32. L. A. Martin, H. W. Neighbors, D. M. Griffith, The experience of symptoms of depression in men vs women: Analysis of the National Comorbidity Survey Replication. *JAMA Psychiatry* **70**, 1100–1106 (2013). doi: 10.1001/jamapsychiatry.2013.1985; pmid: 23986338
33. N. Verdolini *et al*., Aggressiveness in depression: A neglected symptom possibly associated with bipolarity and mixed features. *Acta Psychiatr. Scand.* **136**, 362–372 (2017). doi: 10.1111/acps.12777; pmid: 28741646
34. C. R. Yang *et al*., Enhanced aggressive behaviour in a mouse model of depression. *Neurotox. Res.* **27**, 129–142 (2015). doi: 10.1007/s12640-014-9498-4; pmid: 25367807
35. B. Li *et al*., Synaptic potentiation onto habenula neurons in the learned helplessness model of depression. *Nature* **470**, 535–539 (2011). doi: 10.1038/nature09742; pmid: 21350486
36. S. J. Russo, E. J. Nestler, The brain reward circuitry in mood disorders. *Nat. Rev. Neurosci.* **14**, 609–625 (2013). doi: 10.1038/nrn3381; pmid: 23942470
37. G. Buzsáki, E. I. Moser, Memory, navigation and theta rhythm in the hippocampal-entorhinal system. *Nat. Neurosci.* **16**, 130–138 (2013). doi: 10.1038/nn.3304; pmid: 23354386
38. B. Hangya, Z. Borhegyi, N. Szilágyi, T. F. Freund, V. Varga, GABAergic neurons of the medial septum lead the hippocampal network during theta activity. *J. Neurosci.* **29**, 8094–8102 (2009). doi: 10.1523/JNEUROSCI.5665-08.2009; pmid: 19553449
39. Z. Borhegyi, V. Varga, N. Szilágyi, D. Fabo, T. F. Freund, Phase segregation of medial septal GABAergic neurons during hippocampal theta activity. *J. Neurosci.* **24**, 8470–8479 (2004). doi: 10.1523/JNEUROSCI.1413-04.2004; pmid: 15456820
40. D. J. Barker *et al*., Lateral preoptic control of the lateral habenula through convergent glutamate and GABA transmission. *Cell Rep.* **21**, 1757–1769 (2017). doi: 10.1016/j.celrep.2017.10.066; pmid: 29141211
41. M. Stephenson-Jones *et al*., A basal ganglia circuit for evaluating action outcomes. *Nature* **539**, 289–293 (2016). doi: 10.1038/nature19845; pmid: 27652894
42. J. W. de Jong *et al*., A neural circuit mechanism for encoding aversive stimuli in the mesolimbic dopamine system. *Neuron* **101**, 133–151.e7 (2019). doi: 10.1016/j.neuron.2018.11.005; pmid: 30503173
43. K. Brinschwitz *et al*., Glutamatergic axons from the lateral habenula mainly terminate on GABAergic neurons of the ventral midbrain. *Neuroscience* **168**, 463–476 (2010). doi: 10.1016/j.neuroscience.2010.03.050; pmid: 20353812
44. T. C. Jhou, S. Geisler, M. Marinelli, B. A. Degarmo, D. S. Zahm, The mesopontine rostromedial tegmental nucleus: A structure targeted by the lateral habenula that projects to the ventral tegmental area of Tsai and substantia nigra compacta. *J. Comp. Neurol.* **513**, 566–596 (2009). doi: 10.1002/cne.21891; pmid: 19235216
45. S. Hong, T. C. Jhou, M. Smith, K. S. Saleem, O. Hikosaka, Negative reward signals from the lateral habenula to dopamine neurons are mediated by rostromedial tegmental nucleus in primates. *J. Neurosci.* **31**, 11457–11471 (2011). doi: 10.1523/JNEUROSCI.1384-11.2011; pmid: 21832176
46. A. M. Stamatakis, G. D. Stuber, Activation of lateral habenula inputs to the ventral midbrain promotes behavioral avoidance. *Nat. Neurosci.* **15**, 1105–1107 (2012). doi: 10.1038/nn.3145; pmid: 22729176
47. J. Tian, N. Uchida, Habenula lesions reveal that multiple mechanisms underlie dopamine prediction errors. *Neuron* **87**, 1304–1316 (2015). doi: 10.1016/j.neuron.2015.08.028; pmid: 26365765
48. M. Matsumoto, O. Hikosaka, Lateral habenula as a source of negative reward signals in dopamine neurons. *Nature* **447**, 1111–1115 (2007). doi: 10.1038/nature05860; pmid: 17522629
49. H. Li, D. Pullmann, T. C. Jhou, Valence-encoding in the lateral habenula arises from the entopeduncular region. *eLife* **8**, e41223 (2019). doi: 10.7554/eLife.41223; pmid: 30855228
50. F. J. Meye *et al*., Cocaine-evoked negative symptoms require AMPA receptor trafficking in the lateral habenula. *Nat. Neurosci.* **18**, 376–378 (2015). doi: 10.1038/nn.3923; pmid: 25643299
51. C. D. Proulx, O. Hikosaka, R. Malinow, Reward processing by the lateral habenula in normal and depressive behaviors. *Nat. Neurosci.* **17**, 1146–1152 (2014). doi: 10.1038/nn.3779; pmid: 25157511
52. M. Trusel *et al*., Punishment-predictive cues guide avoidance through potentiation of hypothalamus-to-habenula synapses. *Neuron* **102**, 120–127.e4 (2019). doi: 10.1016/j.neuron.2019.01.025; pmid: 30765165
53. D. Wang *et al*., Learning shapes the aversion and reward responses of lateral habenula neurons. *eLife* **6**, e23045 (2017). doi: 10.7554/eLife.23045; pmid: 28561735
54. D. H. Root, C. A. Mejias-Aponte, J. Qi, M. Morales, Role of glutamatergic projections from ventral tegmental area to lateral habenula in aversive conditioning. *J. Neurosci.* **34**, 13906–13910 (2014). doi: 10.1523/JNEUROSCI.2029-14.2014; pmid: 25319687
55. D. S. Zahm, D. H. Root, Review of the cytology and connections of the lateral habenula, an avatar of adaptive behaving. *Pharmacol. Biochem. Behav.* **162**, 3–21 (2017). doi: 10.1016/j.pbb.2017.06.004; pmid: 28647565
56. U. Kim, Topographic commissural and descending projections of the habenula in the rat. *J. Comp. Neurol.* **513**, 173–187 (2009). doi: 10.1002/cne.21951; pmid: 19123238
57. J. Tooley *et al*., Glutamatergic ventral pallidal neurons modulate activity of the habenula-tegmental circuitry and constrain reward seeking. *Biol. Psychiatry* **83**, 1012–1023 (2018). doi: 10.1016/j.biopsych.2018.01.003; pmid: 29452828
58. A. M. Stamatakis *et al*., Lateral hypothalamic area glutamatergic neurons and their projections to the lateral habenula regulate feeding and reward. *J. Neurosci.* **36**, 302–311 (2016). doi: 10.1523/JNEUROSCI.1202-15.2016; pmid: 26758824
59. J. Kaufling, Alterations and adaptation of ventral tegmental area dopaminergic neurons in animal models of depression. *Cell Tissue Res.* **377**, 59–71 (2019). doi: 10.1007/s00441-019-03007-9; pmid: 30848354
60. S. F. Maier, M. E. P. Seligman, Learned helplessness at fifty: Insights from neuroscience. *Psychol. Rev.* **123**, 349–367 (2016). doi: 10.1037/rev0000033; pmid: 27337390
61. I. Lazaridis *et al*., A hypothalamus-habenula circuit controls aversion. *Mol. Psychiatry* **24**, 1351–1368 (2019). doi: 10.1038/s41380-019-0369-5; pmid: 30755721
62. D. Knowland *et al*., Distinct ventral pallidal neural populations mediate separate symptoms of depression. *Cell* **170**, 284–297.e18 (2017). doi: 10.1016/j.cell.2017.06.015; pmid: 28689640
63. A. Friedman *et al*., Electrical stimulation of the lateral habenula produces an inhibitory effect on sucrose self-administration. *Neuropharmacology* **60**, 381–387 (2011). doi: 10.1016/j.neuropharm.2010.10.006; pmid: 20955718
64. G. Gangadharan *et al*., Medial septal GABAergic projection neurons promote object exploration behavior and type 2 theta rhythm. *Proc. Natl. Acad. Sci. U.S.A.* **113**, 6550–6555 (2016). doi: 10.1073/pnas.1605019113; pmid: 27208094
65. S. Aznar, Z. X. Qian, G. M. Knudsen, Non-serotonergic dorsal and median raphe projection onto parvalbumin- and calbindin-containing neurons in hippocampus and septum. *Neuroscience* **124**, 573–581 (2004). doi: 10.1016/j.neuroscience.2003.12.020; pmid: 14980728
66. A. Szőnyi *et al*., The ascending median raphe projections are mainly glutamatergic in the mouse forebrain. *Brain Struct. Funct.* **221**, 735–751 (2016). doi: 10.1007/s00429-014-0935-1; pmid: 25381463
67. A. M. Barth, LFP_analysis, software, Figshare (2019); https://doi.org/10.6084/m9.figshare.8924771.v1.

ACKNOWLEDGMENTS

We thank S. Arthaud (INSERM, Lyon, France) for help with vGluT2-Cre mice. We thank L. Barna, the Nikon Microscopy Center at IEM, Nikon Austria GmbH, and Auro-Science Consulting Ltd. for fluorescent imaging technical support. We thank K. Demeter, C. Fazekas, D. Várkonyi, and the Behavior Studies Unit of IEM-HAS for behavioral experiment support. We thank É. Mikics, M. Aliczki, and Z. Balogh for help in planning and evaluating the operant conditioning experiments. We thank Z. Erdélyi, F. Erdélyi, and the staff of the Animal Facility and the Medical Gene Technology Unit of IEM-HAS for expert technical help with the breeding and genotyping of the mouse strains used in this study. We thank Z. Hajós, E. Szépné Simon, M. Mayer, and N. Kriczky for help with experiments and A. Kriczky, K. Iványi, and G. Goda for other assistance. We thank J. Budd and L. Acsady for comments on an earlier version of this manuscript.
Funding: This work was supported by the European Research Council (ERC-2011-ADG-294313, SERRACO); the National Research, Development and Innovation Office, Hungary (OTKA K119521, OTKA K115441, OTKA K109790, OTKA KH124345, OTKA NN125643, FK129019, PD121248, EFOP-3.6.3-VEKOP-16-2017-00009, NKFIH K120311, and VKSZ_14-1-2015-0155); the U.S. National Institutes of Health (NS030549); the Human Brain Project of the EU (EU H2020 720270); and the Hungarian Brain Research Program (2017-1.2.1-NKP-2017-00002). The New National Excellence Program of the Ministry of Human Capacities, Hungary, supported D.S. (UNKP-16-3-IV), A.S. (UNKP-17-3-III-SE-9), A.M. (UNKP-18-02-I-SE-20), A.M.B. (UNKP-18-4-SE-126), and K.Z. (UNKP-18-2-I-SE-22). A.M.B. was supported by the Bolyai János Research Fellowship of the Hungarian Academy of Sciences. **Author contributions:** Conceptualization, A.S., K.Z., and G.N.; Investigation: A.S., K.Z., R.T.G., Z.B., and K.E.S. performed and analyzed fluorescent and transmission electron microscopy experiments, supervised by G.N.; A.M. and Z.B. performed and analyzed the scanning electron microscopy experiments, supervised by G.N.; A.S., K.Z., and R.T.G. performed and analyzed the optogenetic behavioral experiments, supervised by G.N.; A.M.B. performed and analyzed the in vivo optogenetic tagging in head-fixed EEG recording experiments, supervised by V.V.; D.S. planned the in vitro experiments and recorded and analyzed the data, supervised by A.I.G.; B.T., E.S., and D.Z. performed and analyzed the chemogenetic behavioral experiments, supervised by D.Z.; Writing – Original Draft, A.S., K.Z., T.F.F., and G.N.; Writing – Review & Editing, all authors; Funding Acquisition, A.M.B., A.I.G., V.V., D.Z., G.N., and T.F.F.
Competing interests: The authors have no competing interests.
Data and materials availability: Viruses used in this study were obtained under material transfer agreements, as follows: AAV2/5-EF1α-DIO-eYFP, AAV2/5-EF1α-DIO-mCherry, and AAV2/5-CAG-FLEX-ArchT-GFP from the UNC Vector Core; AAV2/5-EF1α-DIO-hChR2 (H134R)-eYFP from the Penn Vector Core; AAV2/8-hSyn-DIO-mCherry and AAV2/8-hSyn-DIO-hM3D(Gq)-mCherry from Addgene; and AAV2/8-hSyn-FLEX-TVA-p2A-eGFP-p2A-oG and Rabies(ΔG)-EnvA-mCherry from the Salk GT3 Vector Core. Data generated and analyzed during this study are presented in the manuscript or in the supplementary materials, and additional custom written codes for in vivo electrophysiological recordings are available online (*67*).

SUPPLEMENTARY MATERIALS

science.sciencemag.org/content/366/6469/eaay8746/suppl/DC1
Supplementary Methods
Supplementary Text
Figs. S1 to S7
Tables S1 to S6
References (*68*–*79*)

View/request a protocol for this paper from *Bio-protocol*.

25 July 2019; accepted 8 October 2019
10.1126/science.aay8746

Science

Median raphe controls acquisition of negative experience in the mouse

András Szonyi, Krisztián Zichó, Albert M. Barth, Roland T. Gönczi, Dániel Schlingloff, Bibiána Török, Eszter Sipos, Abel Major, Zsuzsanna Bardóczi, Katalin E. Sos, Attila I. Gulyás, Viktor Varga, Dóra Zelena, Tamás F. Freund and Gábor Nyiri

Science **366** (6469), eaay8746.
DOI: 10.1126/science.aay8746

Keeping tabs on bad experiences

Identifying the neural basis underlying how we acquire, process, and store negative experiences could help the search for effective treatments for mood disorders. Szonyi *et al.* used a range of neuroscientific tools to elucidate the role of a specific neural circuit that originates in the median raphe region of the murine brainstem (see the Perspective by Ikemoto). A subpopulation of excitatory neurons projected to aversive brain areas and received recurrent feedback from the lateral habenula and convergent feedback from a range of fear-related circuitry. These neurons were activated by aversive stimuli, and artificial stimulation promoted aversion or anxiety-related behavior. This group of cells thus plays a pivotal role in a network that helps to mediate aversive motivation.

Science, this issue p. eaay8746; see also p. 1071

Science (print ISSN 0036-8075; online ISSN 1095-9203) is published by the American Association for the Advancement of Science, 1200 New York Avenue NW, Washington, DC 20005. The title *Science* is a registered trademark of AAAS.

science.sciencemag.org/content/366/6469/eaay8746/suppl/DC1

Supplementary Materials for

Median raphe controls acquisition of negative experience in the mouse

András Szőnyi*, Krisztián Zichó*, Albert M. Barth, Roland T. Gönczi, Dániel Schlingloff, Bibiána Török, Eszter Sipos, Abel Major, Zsuzsanna Bardóczi, Katalin E. Sos, Attila I. Gulyás, Viktor Varga, Dóra Zelena, Tamás F. Freund, Gábor Nyiri§

*These authors contributed equally to this work.
§Corresponding author. Email: nyiri.gabor@koki.mta.hu

Published 29 November 2019, *Science* **366**, eaay8746 (2019)
DOI: 10.1126/science.aay8746

This PDF file includes:

Supplementary Methods

Ethical considerations

All experiments were performed in accordance with the Institutional Ethical Codex and the Hungarian Act of Animal Care and Experimentation guidelines (40/2013, II.14), which are in concert with the European Communities Council Directive of September 22, 2010 (2010/63/EU). The Animal Care and Experimentation Committee of the Institute of Experimental Medicine of Hungarian Academy of Sciences and the Animal Health and Food Control Station, Budapest, have also approved the experiments under the project numbers PEI/001/33-4/2013, PE/EA/2553-6/2016 and PE/EA/254-7/2019.

Mice

The following mice were used in the experiments: males and females of vGluT2-iRES-Cre, vGAT-iRES-Cre, BAC-vGluT3/iCre, TpH2/iCre-ERT2 (The Jackson Laboratory) and males of C57Bl/6 wild type (Charles River). We used adult, at least 6 weeks-old mice. Mice had access to food and water ad libitum and were housed in a vivarium (3-5 mice/cage) until used in experiments, after which they were single-housed. Mice used for optogenetic behavioral experiments were maintained on a normal 12h light-dark cycle, with experiments performed during the light phase of the cycle. Mice used for chemogenetic behavioral experiments were maintained on a reversed 12h light-dark cycle, with experiments performed during the dark phase of the cycle.

Stereotaxic surgeries for viral gene transfer, retrograde tracing and optic fiber implantations

Mice were anesthetized with 2% isoflurane followed by an intraperitoneal injection of an anesthetic mixture (containing 8.3 mg/ml ketamine and 1.7 mg/ml xylazine-hydrochloride in 0.9% saline, 10 ml/kg body weight); and were then mounted in a small animal stereotaxic frame (David Kopf Instruments, CA, USA) and the skull surface was exposed. A Nanoject II precision microinjector pump (Drummond, Broomall, PA) was used for the microinjections. For anterograde tracing, optogenetic and chemogenetic experiments, we injected 10-100 nl and for stereological measurements 1000-1200nl of one of the following viruses into the target brain areas: AAV2/5-EF1α-DIO-eYFP; AAV2/5-EF1α-DIO-mCherry; AAV2/5-EF1α-DIO-hChR2(H134R)-eYFP; AAV2/5-CAG-FLEX-ArchT-GFP (UNC Vector Core for the viruses above), AAV2/8-hSyn-DIO-mCherry and AAV2/8-hSyn-DIO-hM3D(Gq)-mCherry (Addgene; 4.4-21×1012 colony forming units/ml for all viruses). For retrograde tracing experiments we injected 20-40 nl of 2% FluoroGold (Fluorochrome, Denver, CO, USA) or 0.5% Choleratoxin B subunit (List Biologicals, Campbell, CA, USA) into the target areas. The coordinates for the injections were defined by a stereotaxic atlas (Paxinos & Watson 2012); the null coronal plane of the anteroposterior (AP) axis was defined by the position of Bregma; the null sagittal plane of the mediolateral (ML) axis was defined by the sagittal suture; the null horizontal plane of the dorso-ventral (DV) axis was defined by the bregma and lambda. The median raphe region (MRR) was defined as the median raphe and the para-median raphe areas together. The injection coordinates were the following (always given in mm at the AP, ML and DV axes, respectively): median raphe region: -4.5, 0.0, -4.5 or -4.1,

0.0, -4.6; median raphe region for stereology (4 injections altogether): -4.3, 0.0, -4.3 and -4.8 and -4.7, 0.0, -4.1 and -4.6; lateral habenula: -1.5; +/- 0.5; -2.8; hippocampus: (2-2 injections bilaterally) -2.0, +/- 1,5, -2 and -2.7, +/- 2.5, -2.7; VTA: -3.4, +/- 0.2, -4.5; medial septum: +1.0, 0.0, -4.3; vertical limb of the diagonal bands of Broca (VDB): +1.0, 0.0, -5.2; medial prefrontal cortex (1-1 injection bilaterally): + 1.8, +/- 0.3 and -2.7.

For behavioral experiments, during a second, similar surgical procedure 4-6 weeks after virus injections, optic fibers (105 μm core diameter, 0.22 NA, Thorlabs GmbH, Dachau/Munich, Germany) were implanted into the MRR with the tip at the following coordinates: -4.5, 0.0, -4.4. Positions of the optic fibers are illustrated in Suppl. Fig. 5. After the surgeries, mice received 0.3-0.5 ml saline and 0.03-0.05 mg/kg meloxicam (Metacam, Boehringer Ingelheim, Germany) intraperitoneally or 0.1 ml buprenorphine (0.1 mg/kg; Bupaq) subcutaneously and were placed into separate cages to rest, until further experiments or perfusions. Following two weeks of recovery, animals used in chemogenetic experiments were moved to the behavioral examination unit and adapted to reversed lighting cycle for another 2 weeks before behavioral experiments started.

Mono-trans-synaptic rabies tracing

A detailed description of the monosynaptic rabies tracing technique used has already been published by (26). Briefly, vGluT2-Cre mice were prepared for stereotaxic surgeries as described above, and 30 nl of the virus AAV2/8-hSyn-FLEX-TVA-p2A-eGFP-p2A-oG (Salk GT3 Core, 4.5×1012 colony forming units/ml) was injected into the MRR at the coordinates given above. These Cre-dependent viruses contain an avian tumor virus receptor A (TVA), which is necessary for them to be infected by the rabies viruses and they contain an upgraded version of the rabies glycoprotein (oG) that provides an increased trans-synaptic labeling potential for the rabies viruses (68). After 2-3 weeks of survival, mice were injected with the genetically modified Rabies(ΔG)-EnvA-mCherry (Salk GT3 Core, 3.5×107 colony forming units/ml) at the same coordinates. After 10 days of survival, mice were prepared for perfusions.

Perfusions

Mice were anesthetized with 2% isoflurane followed by an intraperitoneal injection of an anesthetic mixture (containing 8.3 mg/ml ketamine, 1.7 mg/ml xylazine-hydrochloride, 0.8 mg/ml promethazinium-chloride) to achieve deep anesthesia. The mice were then perfused transcardially with 0.1M phosphate-buffered saline (PBS, pH 7.4) solution for 2 min, followed by of 4% freshly depolymerized paraformaldehyde (PFA) solution for 40 min, followed by PBS for 10 min, then the brains were removed from the skull (protocol A). Animals used in chemogenetic behavioral experiments were perfused with 0.1M phosphate buffered saline (PBS) for 1 minutes, then with 4% PFA in PBS for 20 minutes. Brains were taken out and post-fixed for 24 h in fixative at 4°C then cryoprotected by 20% glucose-PBS solution for 24 hours at 4°C (protocol B). For block-face scanning electron microscopy, mice were perfused with 0.1M phosphate-buffered saline (PBS, pH 7.4) solution for 30 sec, followed by a fixative solution containing 2% PFA and 1% glutaraldehyde (GA) and 15% picric acid for 5 minutes (all salts were obtained from Sigma-Aldrich); the brains were then removed from the skull on ice, cut sagittally and coronally into 5 pieces and immersion fixed in 4% PFA and 0,1% GA in 0.1 M phosphate-buffer (PB, pH 7.4) for 4 hours at room temperature, then the fixative

was washed out with 0.1 M PB (protocol C). After perfusions brains were cut into 30 µm-thick sections using a sliding microtome or to 50, 60 or 100 µm-thick sections using a vibrating microtome (Leica VT1200S or Vibratome 3000).

Antibodies

The list and specifications of the primary and secondary antibodies used can be found in Suppl. Table S1-S2. The specificities of the primary antibodies were extensively tested, using either knock-out mice or other reliable methods. Secondary antibodies were extensively tested for possible cross-reactivity with the other antibodies used, and possible tissue labeling without primary antibodies was also tested to exclude auto-fluorescence or specific background labeling. No specific-like staining was observed under these control conditions. Combinations of the used primary and secondary antibodies in the different experiments are listed in Supplementary Table S3-S4.

Fluorescent immunohistochemistry and laser-scanning confocal microscopy

Perfusion-fixed sections were washed in 0.1 M PB (pH 7.4), and incubated in 30% sucrose overnight for cryoprotection. Sections were then freeze-thawed over liquid nitrogen three times for antigen retrieval. Sections were subsequently washed in PB and Tris-buffered saline (TBS, pH 7.4) and blocked in 1% human serum albumin in TBS (HSA; Sigma-Aldrich) and then incubated in a mixture of primary antibodies for 48-72 h. This was followed by extensive washes in TBS, and incubation in the mixture of appropriate secondary antibodies overnight. We used DAPI staining (Sigma-Aldrich) to visualize cell nuclei. Then, sections were washed in TBS and PB, dried on slides and covered with Aquamount (BDH Chemicals Ltd) or with Fluoromount-G Mounting Medium (Invitrogen). For the viral anterograde and retrograde tracing experiments, each injection site was reconstructed from 50 µm sections using a Zeiss Axioplan2 microscope. Every part of the injected tissue containing even low levels of tracer was considered as part of the injection site. Sections were evaluated using a Nikon A1R confocal laser-scanning microscope system built on a Ti-E inverted microscope with a 10× air objective or with a 0.45 NA CFI Super Plan Fluor ELWD 20XC or with a 1.4 NA CFI Plan Apo VC 60× oil objective or with a Nikon Ni-E C2+ confocal system equipped with a 0.75 NA Plan Apo VC DIC 20× objective, both operated by NIS-Elements AR 4.3 software. Regions of interests were reconstructed in z-stacks; distance between the focal planes was 0.5 µm for examined synaptic contacts and 2 µm for examined neuronal somata. In case of the monosynaptic rabies tracing experiments, coronal sections spaced at 300 µm were prepared from the whole brain for confocal laser-scanning microscopy, and every trans-synaptically labeled cell was scanned using a Nikon Ni-E C2+ confocal system equipped with a 0.13 NA Plan Fluor 4× objective operated by NIS-Elements AR 4.3 software. The cell counting was performed using the Adobe Photoshop CS6 software.

Immunoperoxidase labeling for virus injection localization in chemogenetic experiments

Red fluorescent protein (RFP) was labeled with a rabbit polyclonal antibody (Rockland Immunochemicals, Inc., Pennsylvania, USA). The primary antibody was detected by biotinylated anti-rabbit goat serum (Rockland Immunochemicals, Inc., Pennsylvania, USA) and avidin–biotin complex diluted in TBS (1:1000, Vectastain ABC Kit, Vector Laboratories, USA). The peroxidase reaction was developed in the presence

of diaminobenzidine tetrahydrochloride (0.2mg/ml), nickel–ammonium sulphate (0.1%) and hydrogen peroxide (0.003%) dissolved in TBS. The sections were mounted on glass slides and covered by a DPX mounting medium.

For identification of virus location, microscopic images were digitized by an OLYMPUS CCD camera using a 4x magnification lens. The extent and anatomical localization of viral gene expression was determined by the atlas of Paxinos and Franklin (2012).

Immunogold-immunoperoxidase double labeling and electron microscopy

Perfusion-fixed sections were washed in 0.1 M PB for 1 hour, then cryoprotected by incubation in 30% sucrose overnight and freeze-thawed three times over liquid nitrogen. For synaptic detection of N-methyl-D-aspartate (NMDA) receptor GluN1 or GluN2A subunit, sections were pretreated with 0.2 M HCl solution containing 2 mg/ml pepsin (Dako) at 37°C for 6 min. Then sections were blocked in 1% HSA in TBS, followed by incubation in a mixture of primary antibodies. After repeated washes in TBS, sections were incubated in blocking solution (Gel-BS) containing 0.2% cold water fish skin gelatin (Aurion) and 0.5% HSA in TBS for 1 h. Sections were then incubated in mixtures of secondary antibody solutions overnight. After intensive washes in TBS, the sections were treated with 2% glutaraldehyde in 0.1 M PB for 15 min to fix the gold particles in the tissue. To develop the labeling for MRR vGluT2 fibers, this was followed by incubation in avidin-biotinylated horseradish peroxidase complex (Elite ABC; 1:300; Vector Laboratories) diluted in TBS for 3 h. The immunoperoxidase reaction was developed using 3-3′-diaminobenzidine (DAB; Sigma-Aldrich) as chromogen. To enlarge immunogold particles, this was followed by incubation in silver enhancement solution (SE-EM; Aurion) for 40-70 min at room temperature. The sections were treated with 0.5% osmium tetroxide in 0.1 M PB on ice and they were dehydrated in ascending ethanol series and in acetonitrile and embedded in Durcupan (ACM; Fluka). During dehydration, the sections were treated with 1% uranyl-acetate in 70% ethanol for 20 min. After this, 70-100nm serial sections were prepared using an ultramicrotome (Leica EM UC6) and collected on single-slot copper grids. Sections were examined using a Hitachi H-7100 electron microscope and a Veleta CCD camera driven by the iTEM 5.0 software (Olympus). Randomly sampled terminals of the MRR establishing synaptic contacts in the LHb and MS/VDB were always fully reconstructed.

Silver-gold intensified and nickel-intensified immunoperoxidase double labeling (SI-DAB/DAB-Ni)

Perfusions, sectioning and incubations of sections in primary antibody solutions were performed as described above. In the SI-DAB reaction, it was followed by subsequent washes in the appropriate secondary antibody solutions for 24h in TBS. After subsequent washes in TBS and incubation in avidin-biotin-peroxidase complex for 3 h (ABC Elite 1:300, Vector Laboratories), ammonium nickel sulphate-intensified 3-3'-diaminobenzidine (DAB-Ni) was used for the development of immunoperoxidase reaction. This reaction was further intensified with silver-gold (SI-DAB) as described in detail in Dobó et al. 2011. This intensification step converts the labeling from homogenous to granular by loading fine gold particles onto the DAB-Ni deposit. After washes in TBS, sections were blocked in 1% HSA for 1 h and incubated in primary

antibody solutions for the second DAB-Ni reaction for 48-72 h. This step was followed by incubation with an ImmPRESS secondary antibody solution overnight. The second immunoperoxidase reaction was developed by DAB-Ni, resulting in a homogenous deposit, which was clearly distinguishable from the silver-gold intensified SI-DAB at the electron microscopic level (69). Further dehydration, contrasting and processing of the sections for electron microscopy was performed as described above.

Sample preparation for 3D block face scanning electron microscopy (BF-SEM)

Virally injected vGluT2-Cre mice, 4-6 weeks after the injection, were sacrificed for BF-SEM experiments. Mice were anesthetized and perfused according to "protocol C" as described above. 100 µm-thick sections were cut using a vibrating microtome from the blocks containing the lateral habenula and 50 µm-thick sections were cut from the blocks containing the MRR. Sections were washed in PB for 1 hour, then cryoprotected by incubation in 30% sucrose overnight and freeze-thawed three times over liquid nitrogen. Then, sections were blocked in 1% HSA in TBS, followed by incubation in a mixture of primary antibodies. After repeated washes in TBS, sections were incubated in blocking solution (Gel-BS) containing 0.2% cold water fish skin gelatin (Aurion) and 0.5% HSA in TBS for 2 h. Sections were then incubated in mixtures of secondary antibody solutions for 2 days. After intensive washes in TBS, the sections were treated with 2% glutaraldehyde in 0.1 M PB for 30 min to fix the gold particles in the tissue. Then gold conjugated secondary was intensified with GOLDENHANCE™ EM Plus Kit (Nanoprobes). To get high contrast for BF-SEM equipped with field emission gun, we used a modified protocol of Deerinck et al. (70). Briefly, sections were postfixed in 1% osmium-tetroxide reduced with 0,75% potassium ferrocyanide, on ice for 1 hour, followed by thiocarbohydrazide (TCH) incubation for 30 minutes. Then sections were treated with 1% osmium-tetroxide solution for 30 minutes, and then for another 30 minutes with 1% aqueous uranyl-acetate in dark. Then, en bloc Walton's lead aspartate staining was performed at 60°C for 30 minutes. After each step, sections were washed 5 x 3 minutes in distilled water. Finally, the sections were dehydrated through ascending ethanol series on ice (from 30% to absolute ethanol for 2x5 minutes) and then infiltrated with acetonitrile for 2 x 10 minutes (first on ice, second at room temperature). The sections were transferred into aluminum boats and infiltrated with embedding resin (Epoxy Embedding Medium Kit, Sigma-Aldrich, hard mixture) overnight. The next day, sections were mounted on glass slides, covered and baked at 60°C for 48 hours. After baking, a small region of interest was cut out with razor blade and mounted on an aluminum specimen pin with Silver Conductive Epoxy, H2OE EPO-TEK® (Ted Pella) and baked at 60°C for 48 hours. After the conductive epoxy was polymerized, samples were trimmed with an ultracut (EM UC6, Leica, Wetzlar, Germany) to create a cube with a glass knife. The cube shaped block (~ 400 µm x 400 µm x 75 µm) was sputter coated with gold using a Rotary-Pumped Sputter Coater (Quorum Technologies, Q150R ES). The samples were stored in dust free holders and they were transferred into the vacuum chamber for at least one night before using them for BF-SEM imaging.

BF-SEM imaging and image analysis

We used a FEI Apreo field emission gun (FEG) SEM equipped with an in situ ultramicrotome (VolumeScope, FEI, Eindhoven, The Netherlands) and a T1 "in column"

detector to record the backscattered electrons (BSE) from each voxel. For all image stacks, we collected BSE images with MAPs software from 6,5 mm working distance at high vacuum with fixed 0,1 nA beam current, 2.27 kV high voltage, 1,25 µs pixel dwell time, with a voxel size of 4 nm x 4 nm x 70 nm. The images in the z-stacks measured 16384x16383 pixels with 70 nm thickness, and the final z-stacks contained 300 such slices, so the overall volume for each animal was cca. 90 200 µm3. All image post-processing was done in Fiji. The BF-SEM stacks were imported into FIJI ImageJ TrakEM2 and fine aligned. For segmentation, we used area lists for axonal profiles, mitochondria, and profile lists for synapses. Manual segmentation was performed on a Wacom Cintiq 27QHD Creative Pen and display tablet. After, synaptic surface measurements were finished using the built-in plugin of TrakEM2, data were retrieved by custom made excel datasheet and analyzed with Tibco Statistica 13.4. After segmentation, the models were exported in .obj format and imported into Blender (Blender Foundation, Amsterdam, The Netherlands) for further investigation and visualization.

Stereology measurements

Unbiased design-based stereological measurements were carried out using the optical fractionator method (71–73), which is based on the principle that one can accurately define the number of cells in the volume of interest by counting them in a predetermined fraction of the given volume (74). To get the total cell numbers, the number of counted cells is multiplied by the reciprocal of three different fractions: section, area, and thickness sampling fractions (75). Using systematic random sampling in each experiment, every second section of the MRR was used; therefore, section sampling fraction was 0.5. In mounted sections, cells were counted only within a fraction of a predefined grid area. In the MRR, this fraction was 152/802 µm, in the para-median raphe, this fraction was 102/802 µm. Finally, thickness sampling fraction was 15/28 µm, because the average mounted section thickness was 28 µm and counting was performed only in a 15-µm-high counting cube. We used a guard zone of minimum 5 µm of tissue above and below the counting cube; however, for maximum accuracy, thickness sampling fractions were determined at every sampling site. Cells were counted inside the counting cubes or if they touched one of the 3 inclusion planes of the counting cubes. Cell counting was carried out in Stereo Investigator 10.0 stereology software (MBF Bioscience), while cells were identified parallel using NIS Elements AR 4.3 software.

In vitro slice preparation

In all slice studies, mice were decapitated under deep isoflurane anesthesia. The brain was removed and placed into an ice-cold cutting solution, which had been bubbled with 95% O2/5% CO2 (carbogen gas) for at least 30 min before use. The cutting solution contained the following (in mM): 205 sucrose, 2.5 KCl, 26 NaHCO3, 0.5 CaCl2, 5 MgCl2, 1.25 NaH2PO4, 10 glucose. Then, coronal slices of 300 µm thickness were cut using a Vibratome (Leica VT1000S). After acute slice preparation, slices were placed into an interface-type holding chamber for recovery. This chamber contained standard ACSF at 35°C that gradually cooled down to room temperature. The ACSF solution contained the following (in mM): 126 NaCl, 2.5 KCl, 26 NaHCO3, 2 CaCl2, 2 MgCl2, 1.25 NaH2PO4, 10 glucose saturated with carbogen gas. NBQX was ordered from Hello

Bio Inc., and AP-5 was from Tocris Bioscience. Drugs were administered from stock solutions via pipettes into the ACSF containing superfusion system. All other salts were obtained from Sigma-Aldrich or Molar Chemicals KFT.

Intracellular recordings

The composition of the intracellular pipette solution was the following (in mM): 110 K-gluconate, 4 NaCl, 20 HEPES, 0.1 EGTA, 10 phosphocreatine, 2 ATP, 0.3 GTP, 3 mg/ml biocytin adjusted to pH 7.3–7.35 using KOH (285–295 mOsm/L). Whole-cell series resistance was in the range of 5–15 MΩ. Series resistance was not compensated, but was frequently monitored, and cells, where the values changed more than 25% during recording were discarded from further analysis. Voltage measurements were not corrected for the liquid junction potential. To record glutamatergic currents, membrane potential was clamped far (~ 65 mV) from α-amino-3-hydroxy-5-methyl-4-isoxazolepropionic acid (AMPA)/NMDA-R reversal potential. To block AMPA and NMDA currents, NBQX (20 μM) and AP-5 (50 μM) were added to the recording solution. For illumination, we used a blue laser diode (447 nm, Roithner LaserTechnik GmbH) attached to a single optic fiber (Thorlabs) positioned above the lateral habenula.

Digital signal processing, analysis and statistics for in vitro experiments

All data were processed and analyzed off-line using standard built-in functions of Python 2.7.0. Latency was defined as a time between light stimulus onset and time of reaching 10% of maximal EPSC amplitude. Throughout this manuscript, for in vitro electrophysiology data, we used median, first, and third quartiles for the description of data groups because they did not show Gaussian distribution.

Stereotaxic surgeries for electrophysiological recordings in head-fixed mice

Animals were anesthetized with isoflurane and mounted in a stereotaxic frame (David Kopf Instruments, Tujunga, CA). The cranium was exposed, the bone was dried. For the future hippocampal and median raphe recording sites, 2 cranial windows (1.5 mm width), and for the optical fiber, a hole (0.5 mm diameter) were drilled into the cranium (from Bregma: 2.5 mm caudal and 2.5 mm lateral for the hippocampal window; 6.2 mm caudal and 0 mm lateral for median raphe window and 4.5 mm caudal and 0 mm lateral for the optical fiber). A hole was drilled above the cerebellum for the insertion of the ground electrode. A head-plate was fixed to the skull surface using dental acrylate (Paladur). Finally, the skull surface and the holes were covered with a silicone sealant. After surgery, the mouse was continuously monitored until recovered, as demonstrated by their ability to maintain sternal recumbence and to exhibit purposeful movement.

In vivo electrophysiological recording

After a recovery period of 3-7 days, the mice were water restricted and habituated for 10 to 14 days to the spherical treadmill setup with their head fixed. The animal weights were monitored and when a mouse reached 85% of the initially measured baseline weight, the daily volume of water supplement was individually adjusted in order to maintain this 85 % target weight. During the habituation period the animals learned to took water drops from a lick port positioned in front of the animals' mouth.

On the day of the experiment the animal was head-fixed above the air supported spherical treadmill. Hippocampal silicone probe (Buzsaki32 or Buzsaki64 type silicon probe, NeuroNexus, Ann-Arbor, MI) was lowered through the cranial window into the hippocampal CA1 pyramidal layer. The pyramidal layer was identified physiologically by increased unit activity and the occurrence of ripple events. The optical fiber was lowered to a 4.2 mm depth from the skull surface. The median raphe probe (Buzsaki32 or Poly5 type silicon probe, NeuroNexus, Ann-Arbor, MI) was inserted and lowered to a depth of 4.4 mm in an angle of 20 degree from caudal. Before the insertion of the probe and the optical fiber, they were coated with the lipophilic fluorescent dye, Dil (Thermo Fischer Scientific) for later histological verification of their location. Ground electrode was placed above the cerebellum.

The median raphe probe was advanced by a micromanipulator until multiple median raphe unit activity was detected in a depth of 4-8-5.2 mm. Once the probes were positioned at their final position, recording was started. Following a 10-15 minutes baseline recording period LED flash (200 ms, yellow), air puff (200 ms) and rewarding water drops were applied at random intervals. Electrophysiological recordings were performed by a signal multiplexing head-stage. Signals were acquired at 20k sample/s (KJE-1001, Amplipex Ltd, Hungary). Mouse locomotor activity was recorded with an optical computer mouse positioned close to the spherical treadmill at the equator.

To represent the spectral components of hippocampal LFP activity on Fig. 4 we obtained the Morlet wavelet decomposition of the hippocampal recording. For calculating the theta to delta ratio, hippocampal LFP oscillations (delta: 1-4 Hz, theta: 5-12 Hz) were separated on the basis of the Hilbert magnitude of the band-pass-filtered signal. The average Hilbert magnitudes were calculated before and during the laser stimulation (in 10 s long windows) and ratios (average theta / average delta magnitudes) were calculated in each period. All in vivo data were analyzed in Igor Pro 8 (Wavemetrics).

Optogenetical tagging

At the end of each recording session brief laser pulses were applied (n = 30, 1 ms at 4 Hz, 473 nm) for offline identification of responsive units. Units were categorized as "tagged" if followed the laser pulse with short latency (within 4 ms) and more than 50 % success rate.

Neuronal spikes were detected and automatically sorted from the high-pass filtered local field potential recordings (0.5–5 kHz) by a template matching algorithm Spyking-Circus (76), followed by manual adjustment of the clusters using the Phy software (77) to obtain well-isolated single units. Cluster isolation quality was estimated by calculating the interspike interval index for each cluster (78); poor quality clusters were discarded.

Quantification and statistical analysis of in vivo physiological experiments

The mean baseline firing rate values and standard deviations were calculated from a 4 second time window preceding stimulus onset. Changes in firing rate was declared significant if it deviated more than 2 standard deviations from the mean baseline value (z-score larger than 2 or smaller than -2) in a 200 ms time window after stimulus onset. Both responsive and non-responsive neurons distributed across animals.

All statistical analyses were performed with standard Igor Pro 8 functions. For paired comparisons the Wilcoxon signed rank test was used. All graphs indicate mean +/- SEM. For significance, $p = 0.05$ was used.

Real time place aversion (RTPA) and conditioned place aversion (CPA) tests

After optic fiber implantations, mice were transferred to the animal room of the behavioral unit of the institute to rest, then they received 5 days of handling. On the 6th day (habituation day), mice were placed into a chamber (40 cm x 20 cm x 20cm, divided into two areas with striped walls and floor on the one side and dotty walls and floor on the other side) for habituation for 10 min. After each experiment, the chamber was washed with "macadamia-scented" soap. On the 7th day (real-time place aversion), mice were placed in into the non-stimulated side of the chamber and left moving freely for 15 min. Blue laser stimulation (5 ms pulses at 25Hz with 10-15mW intensity, 473 nm) started when the animal entered the stimulation side. On the 8th day (conditioned place aversion) mice were tested without laser stimulation for 5 min in the same chamber. The experiments were performed in a counter-balanced way, some mice received stimulation in the striped side, while others in the dotty side, to exclude the possibility of innate aversion for any context. The behavior of the mice was recorded with a Basler acA1300-60gc camcorder. Experimental data were collected and analyzed using the Noldus EthoVision 13.0 and Tibco Statistica 13.4 software.

Statistical analysis and evaluation of RTPA and CPA data

To precisely examine whether mice distinguished the stimulated and non-stimulated sides in the RTPA and CPA paradigms, the chamber was divided into three virtual areas: a stimulation area, a non-stimulated area and a so-called decision zone. The decision zone was a rectangle with an area of 14 cm x 8 cm (14% of the total chamber area of 800 cm2) placed in the middle of the chamber. We excluded the time spent in the decision zone to exclude any possible uncertainty of the detection of the position of the mice in the middle of the chamber. To define the percentage of time spent by the mice in the different contexts, we divided the time spent in the stimulation area with the sum of the time spent in the stimulation area plus the non-stimulated area.

Operant conditioning

On the 9th day (after RTPA and CPA tests), mice were started to be kept on a diet to keep their body weight between 80%-90% of the original. They were also habituated to the reward pellets (Bio-Serv, NJ, USA) used in the operant conditioning paradigm for 3 days. The diet was held for the whole duration of the operant conditioning tests to support the motivational drive to poke for pellet rewards.

On the 12th day (Fig. 5C), mice were put in an automatized operant conditioning chamber system (Med Associates Inc., VT, USA), and they were conditioned to nose-poke for pellet rewards (45mg) for 30 minutes/day for 10 days. The chamber was put in a dark box, but it was lit by a house light. Every correct nose-poke was followed by a 15 seconds-long interval, when the house light turned off and mice did not receive pellet rewards even if they performed nose-pokes. This interval was inserted into the experiment to help the mice learn the conditioning rule, and to allow them time to consume the pellets. After this interval, mice could perform a correct nose-poke again to

receive pellets. The number of total nose-pokes was defined as the sum of the correct nose-pokes and the interval nose-pokes.

The operant conditioning chambers were washed after every individual mouse with distilled water. From the 20th day, mice were connected to a dummy fiber patch for habituation. On the 22th day (poke stimulation), mice received 5 seconds blue laser stimulation (5 ms pulses at 25Hz with 10-15mW intensity, 473 nm), after every correct nose-poke. After the 30 min stimulation period, mice were placed back into their home cages and received food ad libitum again for 3 days to regain their original weight.

Statistical analysis and evaluation of operant conditioning tests

We compared the number of total-nose pokes performed by the individual mice in a pairwise manner between the 21th (poke baseline) and 22th (poke stimulation) days of the experiment. Then, we normalized the number of the total nose-pokes performed by a mouse on the 22th day to the number of the total nose-pokes performed by the same mouse on the 21th day, respectively (Poke ratio, stimulation/base). These ratios were compared between the groups of ChR2-expressing and CTRL virus expressing mice.

Optogenetic contextual fear conditioning (Opto-CFC)

After operant conditioning, mice rested for 3 days to regain their original weight. On the 25th day, mice were placed into a plexiglass foot-shocking chamber (Suppl. Fig. 6C, 25 cm × 25 cm × 31 cm) that was enriched with a specific combination of olfactory (baby soap scent), visual (grey wall), spatial (rectangular chamber walls) and tactile (metal bars on the floor) cues. Mice were allowed to freely move in the environment for 3 minutes to record baseline freezing levels. After this, mice received 15 seconds of blue laser stimulation (5 ms pulses at 25Hz with 10-15mW intensity, 473 nm) that was repeated 10 times with 15 seconds inter-stimulation interval. After receiving the last stimulation, mice were kept in the context for another 3 minutes. 24 hours later, on the 26th day, mice were placed back to the same context to read out freezing levels. The behavior of mice was recorded with a Basler acA1300-60gc camcorder, and freezing behavior was analyzed manually using the Solomon Coder (https://solomoncoder.com) software. The experimenter evaluating freezing levels was blind to the conditions and treatment of the mice. Mice displaying higher than 5% baseline freezing levels were excluded from further analysis.

Delayed cued fear conditioning (CuedFC)

After optic fiber implantations, mice were transferred to the animal room of the behavioral unit, where they received 5 days of handling. On the 6th day, mice were placed into the first environmental context (environment “A”) in a plexiglass shocking chamber (25 cm × 25 cm × 31 cm) that was enriched with a specific combination of olfactory (macadamia nut scent), visual (black dotted wall with white background), spatial (bended chamber walls), auditory (white noise) and tactile (metal bars on the floor) cues. Mice were allowed to freely move in the first environment for 3 minutes to record baseline freezing levels. After this, mice received 3 shocks (2 seconds, 2 mA intensity, 60 seconds inter-shock interval) that were paired with an auditory cue (30s long sound at 7500 Hz). The footshocks and the auditory cues were co-terminated each time. Footshocks were paired with 6 seconds-long yellow laser light illumination (10-15 mW

intensity at the tip of the optic fiber at 593 nm wavelength), which was precisely aligned with the shocks, starting 2 seconds before the shock onset and finishing 2 seconds after shock offset. After receiving the last shock, mice were kept in the context for another 30 seconds. After 3 successfully delivered shocks, mice were placed back into their home cages for 24 h. On the 7th day, mice were placed back into the environment "A" for 3 minutes to record freezing behavior related to the contextual fear memories. 24 hours later, on the 8th day, mice were placed into a second environmental context (environment "B") with distinct olfactory (citrus scent), visual (black and white striped wall), spatial (square shaped chamber), auditory (no noise) and tactile (plastic floor) cues. For 3 minutes, generalized fear levels were recorded in environment "B". After this, mice were presented with the auditory cue for 1 minute to record freezing behavior related to the cued fear memories. After the termination of the auditory cue, mice were kept in the environment "B" for 1 minute to read out post-cue freezing levels. The behavior of mice was recorded with a Basler acA1300-60gc camcorder and freezing behavior was analyzed manually using the Solomon Coder software. The experimenter evaluating freezing levels was blind to the conditions and treatment of the mice. Mice displaying higher than 5% baseline freezing levels in environment "A" were excluded from the further analysis.

Behavioral test battery for chemogenetic experiments

We carried out a series of behavioral tests with mice that were injected either with the hM3Dq-containing virus (that expressed a clozapine-N-oxide (CNO)-sensitive, excitatory G-protein-coupled receptor plus a fluorescent protein) or with a control virus (that expressed only a fluorescent protein). All behavioral tests were done between 9:00 am – 1:00 pm, at the early phase of the active period under reversed 12h light-dark cycle. 48-72h rest was left for the mice between each tests. The test cages were cleaned with 20% ethanol between animals in each test. In order to activate the hM3Dq-virus CNO (1mg/kg in 10ml saline, Tocris) was injected intraperitoneally 30 minutes before each behavioral test. Not all tests were conclusive either because of technical difficulties and/or because of insufficient number of animals for the given test. We briefly describe all tests, but give all details only about those that were fully evaluated and reported in this study. On day 1, mice were tested in a sociability test, in which two small cylinders were placed in the cage and after habituation, an unfamiliar mouse was placed in one of the cylinders. Then a familiar mouse was placed into one cylinder and an unfamiliar new mouse was put in the other cylinder. These tests were inconclusive. On day 3, we carried out a social interaction test, as described below. On day 5, we tested mice in an elevated plus maze test apparatus that had two open and two closed arms, crossed in the middle, perpendicularly with each other. Mice were put into the center and could freely explore the apparatus for 5 minutes. These tests were inconclusive. On day 8, we carried out a resident intruder test, as described below. On day 10, we tested locomotor activity in a Y-maze test, as described below. On day 12, we explored behavioral changes to cat odor. A perforated plastic bottle (50ml) filled with used cat litter was put into one of the corners of the test arena and mice could freely explore. These tests were inconclusive. On day 15, we carried out a self-care test, in which a few drops of 10% sucrose solution was splashed onto the back of the mice. These tests were inconclusive. On day 17, mice were forced to swim for 6 minutes individually in an open glass cylinder with 20 cm of fresh

water at 23–25□C. They could not reach the bottom of the tank and were unable to escape. These tests were inconclusive. On day 19, we carried out an anhedonia test, as described below. Tests were video recorded and analyzed later by an observer blind to the treatment protocols using Ethovision 10.0 (Noldus Information Technology, The Netherlands), Solomon Coder (https://solomoncoder.com) or H77 (Mihály Dobos-Kovács, 2017) software. After this battery of behavioral tests, mice were sacrificed, and their adrenal glands were removed and their weight measured.

Social interaction test

Social interaction test measures social and anxiety-like and aggressive behavior, and it was performed on the day 3 of the battery. Mice were confronted with an unknown conspecific with the same size and treatment, in a new environment, with bright illumination, which increases the anxiety-like behavior of mice. The day before the test, habituation was carried out for 2x15 min consisting of single housing in the test cage (41.3 × 26 × 29.8 cm, GeoMaxi, Ferplast, Italy). This reduced the novelty of the environment, with the aim to enhance social behavior during the test. During the test phase, two mice with the same treatment were taken together into the test cage for 10 minutes. Duration, frequency and percentage of the following behaviors were recorded: social (direct sniffing of the conspecific), aggressive, (biting, chasing, boxing, aggressive grooming, offensive upright posture and mounting), defensive (escape from conspecific) and other (exploring, grooming).

Resident intruder test

Resident intruder test was conducted to measure territorial aggression and it was performed on the day 8 of the battery (79). A 20% smaller intruder mouse was placed into the subject's home cage for 10 minutes. The same parameters were measured as in the social interaction test. These tests were performed under red light illumination.

Locomotor activity in Y-maze

In a Y-maze, we observed the locomotor activity of mice (Suppl. Fig. 4I), and it was performed on the day 10 of the battery. The apparatus had three arms (25 cm x 5 cm x 21 cm) at 120 degrees. Mice could freely explore the maze for 5 min.

Sucrose preference test

Anhedonia, a typical symptom of depression, is reflected by neglect of the rewarding sucrose. This test was performed on the day 19 of the battery. The experiment started with a habituation phase. On the first day, two identical bottles of water were available. One day later, both of the bottles were filled with 1% sucrose solution. Then, after 15-hour liquid deprivation, we tested mice for 5 hours in a cage with one bottle of water and another one with 1% sucrose solution. Pre-weighted bottles were used. The sucrose preference was the percentage of sucrose solution consumed, relative to the total liquid consumption. The formula was as follows: SP = (sucrose intake/[sucrose consumption + water consumption]) × 100%

Statistics for behavioral and in vivo experiments

In case of data groups that did not display a Gaussian distribution, we used median and 25%-75% interquartile range to describe data. We used means and standard deviations to describe data groups that displayed Gaussian distribution. To test for statistical differences, we used the non-parametric Mann-Whitney U-test or parametric Student's t-test in independent data populations, and we used the Wilcoxon's signed-rank test in non-parametric dependent data populations. Statistical difference have always been tested using two-sided tests. Homogeneity of variance was tested using F-test and if it was significant then populations were compared using nonparametric tests. For indicating significance levels on figures, we used the following rules, *: $p<0.05$, **: $p<0.01$, ***: $p<0.001$.

Supplementary Text for Main Figures 1 to 8

Supplementary Data for Figure 1:

Fig. 1G: Our measurements in 2 mice showed that at least 47% (369/780) of eYFP-positive MRR terminals established synaptic contacts with TH-positive profiles, while at least 61% (97/160) of TH-positive cells received at least one synaptic contact from eYFP-positive MRR terminals.

Fig. 1L: Our measurements in 2 mice showed that at least 39% (201/518) of vGluT2-positive LHb fibers established synaptic contacts with vGluT2-positive MRR profiles, and at least 55% (48/88) of MRR vGluT2-positive cells received at least one synaptic contact from mCherry-labelled LHb terminals.

Fig. 1P-T: Abbreviations: DR: dorsal raphe; LH: lateral hypothalamus; LDTg: laterodorsal tegmental nucleus; LHb: lateral habenula; LPO: lateral preoptic area; MHb: medial habenula; NI: nucleus incertus; PDTg: posterodorsal tegmental nucleus; VP: ventral pallidum.

Supplementary Data for Figure 2:

Fig. 2C: At least 81% (22/27, n=2 mice) of vGluT2-positive MRR synapses established in the LHb contain the GluN2A subunit, and 81% (9/11, n=1 mouse) contain the GluN1 subunit of the NMDA-receptors, postsynaptically.

Supplementary Data for Figure 3:

Fig. 3C: Population data showing relative second and third EPSC amplitude distributions compared to the first EPSC for 10 cells are as follows (median [25%-75% quartiles]): 2 Hz: 0.80 [0.79-0.94]; 0.78 [0.73-0.90]; 5 Hz: 0.73 [0.67-0.88]; 0.73 [0.64-0.91]; 10 Hz: 0.79[0.64-0.90]; 0.69 [0.65-0.82]; 20 Hz: 0.71 [0.62-0.84]; 0.78 [0.58-0.86].

Fig. 3D: Population data showing EPSC amplitude distributions in pA are as follows (median [25%-75% quartiles]): control conditions: 65.78 [46.29-139.79]; NBQX/AP5: 0 [0-0.15], washout: 33.89 [30.24-60.54]. Population data showing latency distributions of the recorded cells in msec are as follows (median [25%-75% quartiles]): 2.05 [1.87, 3.05].

Supplementary Data for Figure 4:

Fig. 4F: Population data for the activity of tagged MRR vGluT2-neurons in baseline (4 s window before stimulus onset) and stimulated conditions (0.5 s window after stimulus onset), respectively are as follows (mean +/- SEM). Air puff: 0.41 +/- 0.04 vs 0.99 +/- 0.13, n=41 neurons, p=1.1*10-4. LED flash: CTRL: 0.43 +/- 0.04; STIM: 0.53 +/- 0.04, n=41 neurons, p=6.9*10-5. Reward: CTRL: 0.38 +/- 0.07; STIM: 0.41 +/- 0.08, n=16 neurons, p=0.98; Wilcoxon signed-rank test. Air puff evoked significantly larger response than LED flash (comparing percentage elevation of baseline activity, LED: 57.9+/-20.0% vs air puff: 340.9+/-133.3%, n=41, p=4.3*10-4, Wilcoxon signed-rank test). By analyzing them separately, we found that no neuron decreased its firing. Firing frequency increased in 18 out of 41 neurons for air puffs, in 3 out of 41 for LED and with a longer latency in 1 out of 16 neurons for reward.

Supplementary Data for Figure 5:

Fig. 5B: Population data for the time spent in the stimulated area (% of the sum of the time spent in the stimulated area). Results for RTPA test and CPA test for 21 CTRL- and 19 ChR2-mice that received light above the MRR (median [25%-75% quartiles]). During habituation (see Fig. S5B) CTRL: 44.10 [32.60-56.19]; ChR2: 52.84 [43.76-59.03]. During RTPA test, CTRL: 52.52 [44.27-68.72]; ChR2: 18.86 [12.70-36.64]. During CPA test, CTRL: 55.98 [37.37-80.27]; ChR2: 28.50 [13.95-54.11]. *: p=0.045, ***: p=3.4x10-4, Mann-Whitney U-test.

Fig. 5D: Population data for the total number of nose-pokes for rewards at the base and stimulation performance for 11 CTRL- and 7 ChR2-mice in the operant conditioning task are as follows (median [25%-75% quartiles]). During base performance, CTRL: 39 [23-46]; ChR2: 57 [40-67]. During stimulation performance, CTRL: 35 [26-47]; ChR2: 35 [11-46]. *: p=0.018, Wilcoxon signed-rank test.

Fig. 5E: Population data for the ratios of stimulation/base performance of 11 CTRL- and 7 ChR2-mice are as follows: (mean, +/- SD): CTRL: 1.06, +/- 0.47; ChR2: 0.56, +/- 0.31. *: p=0.025, Student's t-test.

Supplementary Data for Figure 6:

Fig. 6B: Population data for the percentage of time spent with aggressive behavior in the social interaction test for CTRL- and h3MDq-mice, respectively are as follows (median [25%-75% quartiles]): CTRL: 0.00 [0.00-0.00]; h3MDq: 6.89 [0.53-11.77]; **: p=0.002, Mann-Whitney U-test.

Population data for the aggressivity index in the social interaction test for CTRL- and h3MDq-mice, respectively are as follows (median [25%-75% quartiles]): CTRL: 0.00 [0.00-0.00]; h3MDq: 37.28 [3.68-52.56]; **: p=0.002, Mann-Whitney U-test.

Fig. 6C: Population data for the percentage of time spent with aggressive behavior in the resident-intruder test for CTRL- and h3MDq-mice, respectively are as follows (median [25%-75% quartiles]): CTRL: 0.42 [0.00-0.89]; h3MDq: 13.10 [1.17-22.37]. *: p=0.013, Mann-Whitney U-test.

Population data for the aggressivity index in the resident-intruder test for CTRL- and h3MDq-mice, respectively are as follows (median [25%-75% quartiles]): CTRL: 2.14 [0.00-5.37]; h3MDq: 36.05 [3.79-43.89]. *: p=0.032, Mann-Whitney U-test.

Fig. 6D: Population data in the sucrose preference test for CTRL- and h3MDq-mice, respectively are as follows (median [25%-75% quartiles]): CTRL: 55.11 [52.21-59.42]; h3MDq: 40.93 [38.60-48.80]. *: p=0.010, Mann-Whitney U-test.

Supplementary Data for Figure 7:

Fig. 7C: Our measurements in 2 mice showed that at least 79% (497/626) of vGluT2-positive MRR terminals targeted PV-positive profiles, while at least 53% (35/66) of PV-positive cells received at least one contact from these vGluT2-positive MRR terminals.

Fig. 7E: Our measurements in 2 mice showed that at least 67% (14/21) of the synapses of MRR vGluT2-neurons contain the GluN2A subunit of the NMDA-receptors, postsynaptically in the MS/VDB.

Fig. 7K: Our measurements in 2 mice showed that at least 61% (138/225) of the cells projecting to the MS/VDB projected to the LHb as well.

Supplementary Data for Figure 8:

Fig. 8D: Population data in 7 mice for the movement speed of the mice and theta/delta ratios of the hippocampal network activity during baseline (10 s long window before laser onset) and stimulation (10 s long window after laser onset) periods in arbitrary units are as follows (mean +/- SEM): speed: base: 445.0 +/- 128.9; stim: 2235.3 +/- 646.2, p=0.016, Wilcoxon signed-rank test; theta/delta ratios: base: 1.7 +/- 0.1; stim: 2.6 +/- 0.2, p=0.016, Wilcoxon signed-rank test.

Fig. 8E: Population data for the contextual freezing levels (% of total time) in the "A" environment for 13 CTRL- and 9 ArchT-mice are as follows (median [25%-75% quartiles]), CTRL: 13.68 [5.67-17.57]; ArchT: 3.00 [0.00-6.11]. *: p=0.025, Mann-Whitney U-test.

Population data for the generalized freezing levels (% of total time) in the "B" environment for 13 CTRL- and 9 ArchT-mice are as follows (median [25%-75% quartiles]), CTRL: 7.77 [1.11-14.33]; ArchT: 0.00 [0.00-2.44]. *: p=0.026, Mann-Whitney U-test.

Population data for the cued freezing levels (% of total time) in the "B" environment for 13 CTRL- and 9 ArchT-mice are as follows (median [25%-75% quartiles]), CTRL: 52.67 [43.33-59.67]; ArchT: 22.00 [21.33-29.00]. *p=0.011, Mann-Whitney U-test.

Fig. S1. Supplementary anatomical details of MRR vGluT2-neuronal projections

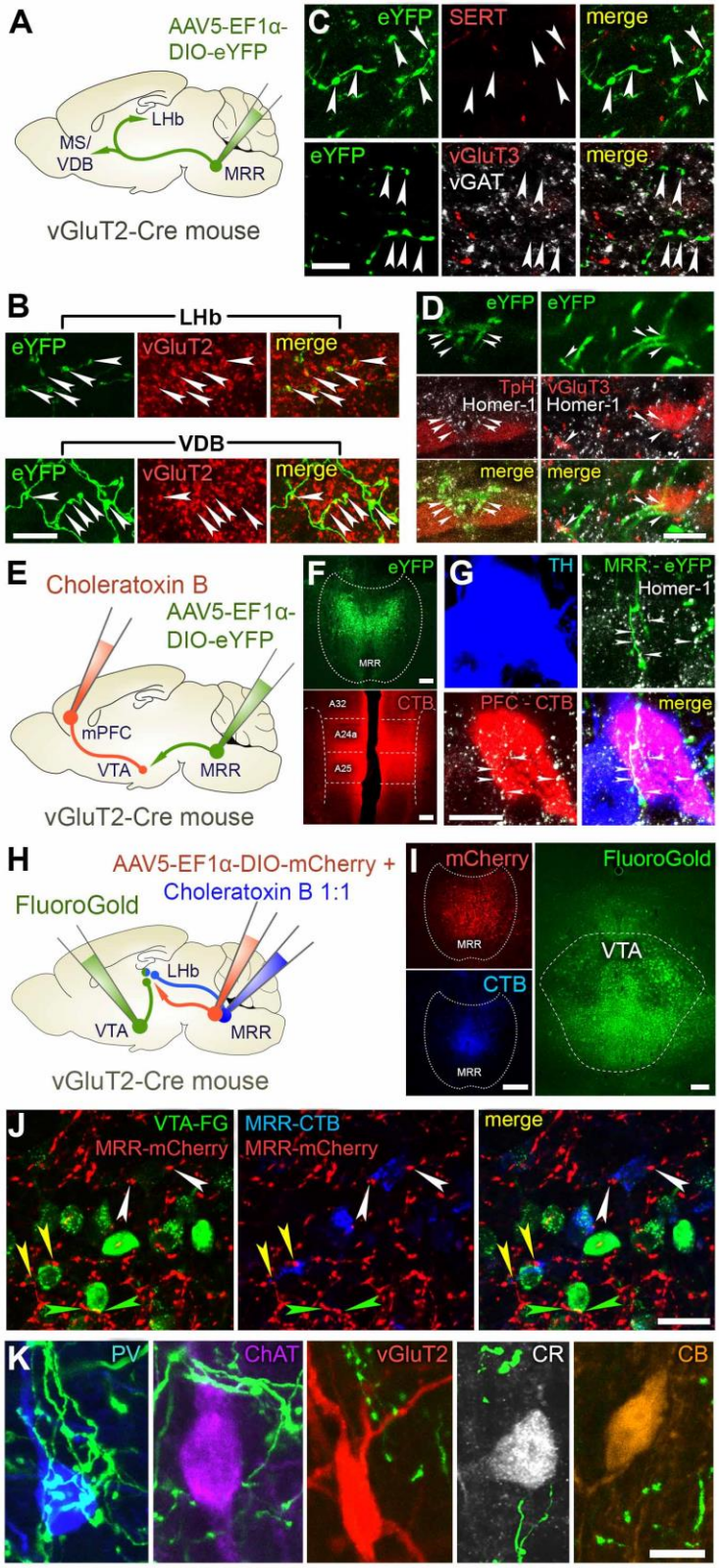

A: AAV2/5-EF1α-DIO-eYFP was injected into the MRR of vGluT2-Cre mice (n=2).
B: Representative images from LHb (upper panel) and VDB (lower panel) show that eYFP-labelled MRR fibers (green) are indeed immunopositive for vGluT2 (red). Double immunopositive terminals are labelled with white arrowheads. At least 93% (339/367) of LHb and at least 97% (284/293) of VDB eYFP-labelled MRR terminals were clearly immunopositive for vGluT2. Scale bar for both panels: 10 µm.
C: Upper panel: representative images show that eYFP-labelled MRR terminals (green, white arrowheads) in the LHb are negative for SERT (red). Lower panel: representative images show that eYFP-labelled MRR terminals in the LHb (green, white arrowheads) are negative for vGluT3 (red) or vGAT (white). In the LHb, only 4% (8/200) of eYFP-labelled terminals seemed positive for either vGluT3 or vGAT. In the VDB, only 8% (17/200) of eYFP-labelled MRR terminals seemed positive for either vGluT3 or vGAT. These few positive looking terminals were probably false positive due to detection issues. Scale bar for both panels: 10 µm.

D: Left panel: confocal fluorescent images show that eYFP-labelled MRR fibers (green) establish synaptic contacts (white arrowheads), marked by Homer-1 (white), with TpH positive (serotonergic) cells (red) in the MRR. Our measurements showed that at least 17% (113/680) of eYFP-labeled terminals established synaptic contacts on TpH-positive profiles, and at least 68% (90/132) of TpH-positive cells received at least one synaptic contact from eYFP-labelled terminals (white arrowheads).
Right panel: confocal fluorescent images show that eYFP-labelled MRR fibers (green) establish synaptic contacts (white arrowheads), marked by Homer-1 (white), with vGluT3-positive cells (red) in the MRR. Our measurements showed that at least 17% (132/797) of eYFP-labeled terminals established synaptic contacts on vGluT3-positive profiles, and at least 36% (48/135) of vGluT3-positive cells received at least one synaptic contact from eYFP-labelled terminals (white arrowheads). Scale bar for both panels: 10 μm.
E: Anterograde tracer AAV2/5-EF1α-DIO-eYFP was injected into the MRR, and retrograde tracer CTB into the medial prefrontal cortex (PFC) of vGluT2-Cre mice (n=2).
F: Fluorescent images show representative injection sites in the MRR and mPFC, respectively. Scale bars: 200 μm.
G: Confocal laser-scanning microscopy images show a medial VTA dopaminergic neuron (blue), retrogradely labeled with CTB (red) from the mPFC, receiving several Homer-1 (white) positive synaptic contacts from eYFP-containing vGluT2-positive MRR fibers (green). Scale bar: 10 μm.
H: Anterograde tracer AAV2/5-EF1α-DIO-mCherry and retrograde tracer CTB (diluted 1:1) was injected into the MRR and retrograde tracer FluoroGold (FG) was injected into the VTA of vGluT2-Cre mice (n=2).
I: Fluorescent images show representative injection sites in the MRR and VTA, respectively.
Scale bars: 200 μm.
J: mCherry-containing vGluT2-positive MRR fibers (red) establish putative contacts with FG-positive (green) VTA projecting neurons (green arrows), with CTB-positive (blue) MRR projecting neurons (white arrows) and with FG-CTB-positive double projecting neurons (yellow arrows) in the LHb, respectively. Altogether, we counted 466 cells in the LHb that projected to the VTA and/or to the MRR, 70% (325/466) of which projected only to the VTA, 17% (78/466) only to the MRR and 13% (63/466) was double-projecting cells. 45% (63/141) of the cells that projected to the MRR, also projected to the VTA. Furthermore, 78% (254/325) of the cells projecting only to the VTA, 69% (54/78) of the cells projecting only to MRR and 78% (49/63) of the double-projecting cells received at least 5 appositions from mCherry-containing MRR terminals. These data show that MRR vGluT2-neurons target LHb neurons, irrespectively from their preferences of targeting MRR or VTA. Scale bar: 20 μm.
K: Representative confocal fluorescent microscopic images show that only PV-positive, but not ChAT, vGluT2, calretinin (CR) or calbindin (CB)-positive MS/VDB cells received dense basket-like innervation from vGluT2-positive MRR cells. Scale bar: 10 μm.

Fig. S2. Interconnections of MRR and LHb

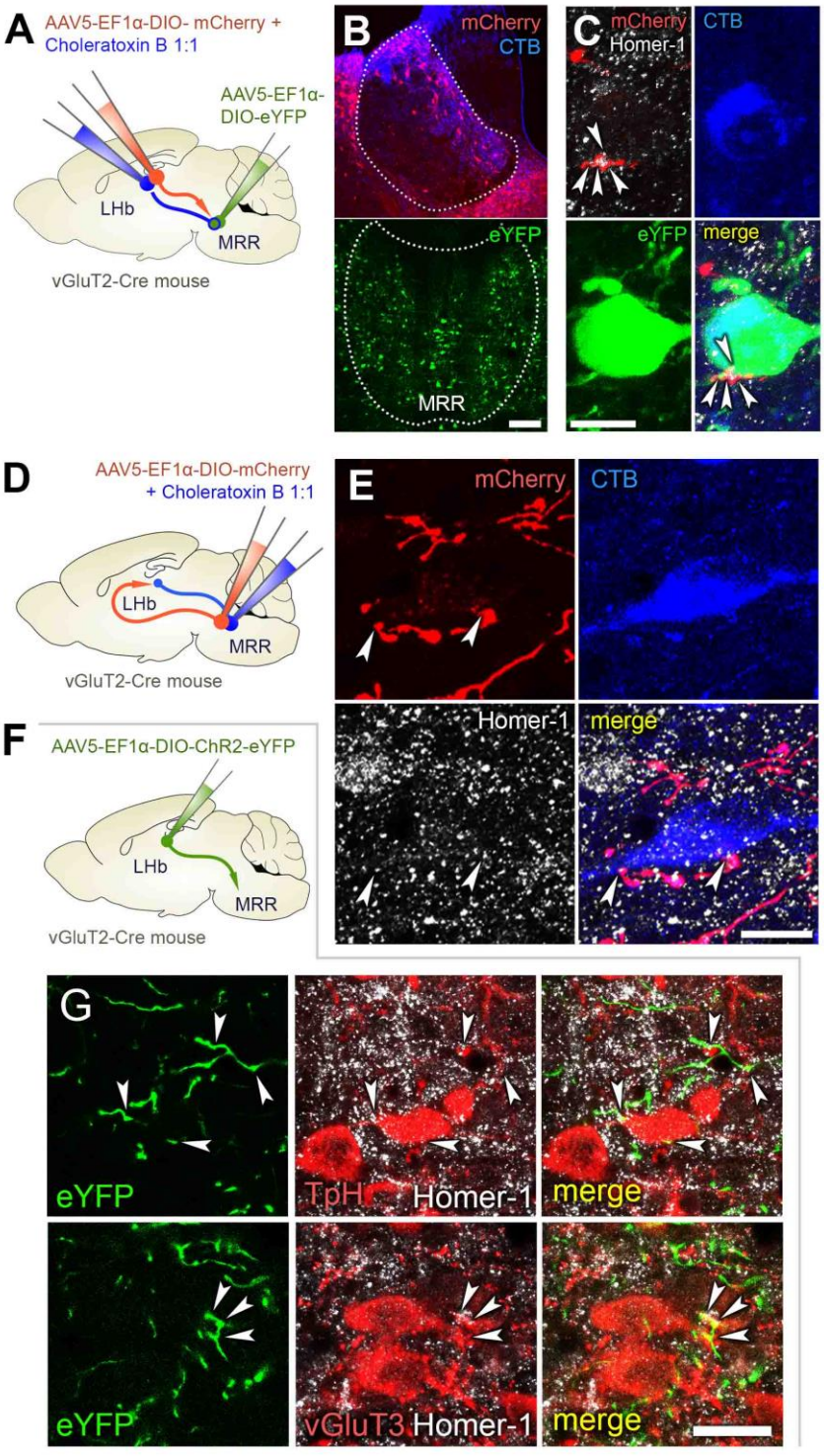

A: The anterograde tracer AAV2/5-EF1α-DIO-mCherry and the retrograde tracer CTB was injected into the bilateral LHb and anterograde tracer AAV2/5-EF1α-DIO-eYFP was injected into the MRR of vGluT2-Cre mice (n=2). **B**: Fluorescent images showing representative injection sites in the LHb and MRR, respectively. Scale bar: 100 µm. **C**: Confocal laser scanning microscopic images show that LHb vGluT2-positive fibers (red) establish synaptic contacts, marked by Homer-1 (white), on a CTB-positive (blue), LHb-projecting vGluT2-positive MRR neuron (green). At least 53% (32/60) of LHb-projecting vGluT2-positive MRR cells received altogether 122 Homer-1 positive synaptic contacts from vGluT2-positive LHb neurons. Scale bar: 10 µm. **D**: Anterograde tracer AAV2/5-EF1α-DIO-mCherry and retrograde tracer CTB was injected into the MRR of vGluT2-Cre mice (n=2). **E**: Confocal laser scanning microscopic images show that MRR vGluT2-positive fibers (red)

establish synaptic contacts, marked by the scaffolding protein Homer-1 (white), with CTB-positive MRR-projecting LHb neurons (blue). At least 58% (71/122) of MRR-projecting LHb cells received altogether 268 Homer-1 positive synaptic contacts from vGluT2-positive MRR cells. Scale bar: 10 μm.
F: AAV2/5-EF1α-DIO-ChR2-eYFP was injected into the bilateral LHb of vGluT2-Cre mice (n=2). **G**: Upper panel: vGluT2-positive LHb fibers (green) establish Homer-1 (white) positive synaptic contacts with TpH-positive neurons (red) in the MRR. Our measurements showed that at least 12% (35/306) of eYFP labeled LHb terminals established synapses on TpH-positive profiles, while at least 57% (29/51) of TpH-positive cells received at least one synaptic contact from eYFP-labelled terminals (white arrowheads). Lower panel: vGluT2-positive LHb fibers (green) establish Homer-1 (white) positive synaptic contacts with vGluT3-positive neurons (red) in the MRR. Our measurements showed that at least 5% (11/223) of eYFP labeled LHb terminals established synapses on vGluT3-positive profiles, while at least 28% (10/36) of vGluT3-positive cells received at least one synaptic contact from eYFP-labelled terminals (white arrowheads). Scale bar for both panels: 20 μm.

Fig. S3. Projection patterns of brainstem vGluT2 neurons and surrounding nuclei

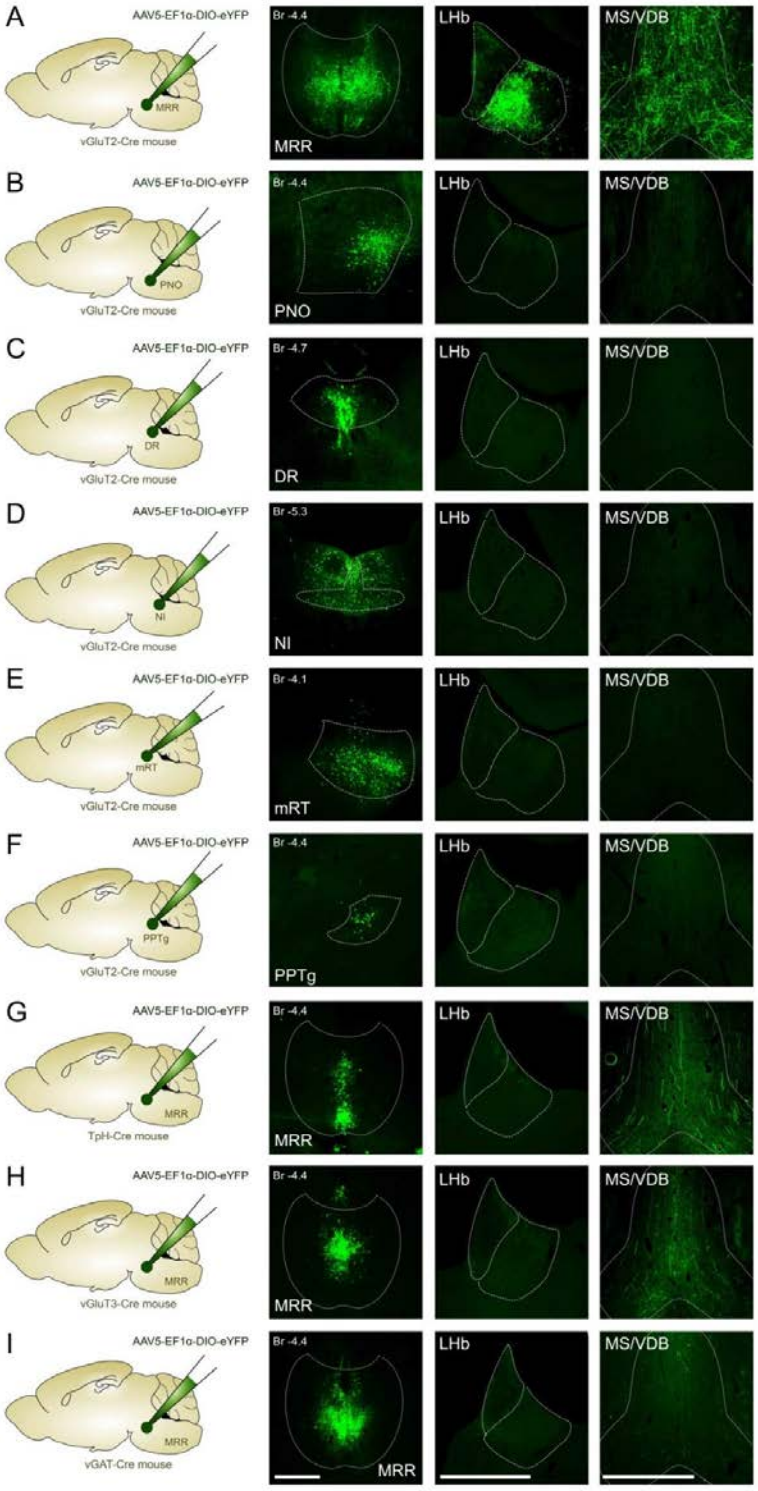

A-I: AAV2/5-EF1α-DIO-eYFP was injected into various adjacent areas in the brainstem in vGluT2-Cre mice to confirm that the pathway described here originates selectively from the MRR (A-F). Furthermore, AAV2/5-EF1α-DIO-eYFP was injected into the MRR of TpH-Cre (labeling serotonergic cells), vGluT3-Cre (labeling vesicular glutamate transporter type 3 positive glutamatergic cells) and vGAT-Cre mice (labeling GABAergic cells) to illustrate that the pathway described here originates selectively from vGluT2-positive neurons in MRR (G-I). The images illustrate representative coronal sections from the regions of different injection sites and from the LHb and MS-VDB. The centers of the injection sites were also identified and defined by their anteroposterior coordinates from Bregma, as seen in the images. In LHb and MS/VDB, vGluT2-positive fibers can only be observed if viruses were injected into MRR (A), and they are absent in experiments, where the AAV-eYFP was injected into the neighboring brain areas (B-F) or into the MRR of TpH-Cre or vGluT3-Cre or GAT-Cre mice (G-I). All combinations of tracings were confirmed in at least 2 mice. Scale bars in panel I are 500 μm for all image columns. [Median raphe region (MRR), nucleus pontis oralis (PNO), dorsal raphe (DR), nucleus incertus (NI), mesencephalic reticular formation (mRT), pontine peduncular tegmentum (PPTg)]

Fig. S4. Supplementary data for behavioral, in vitro and in vivo electrophysiological experiments

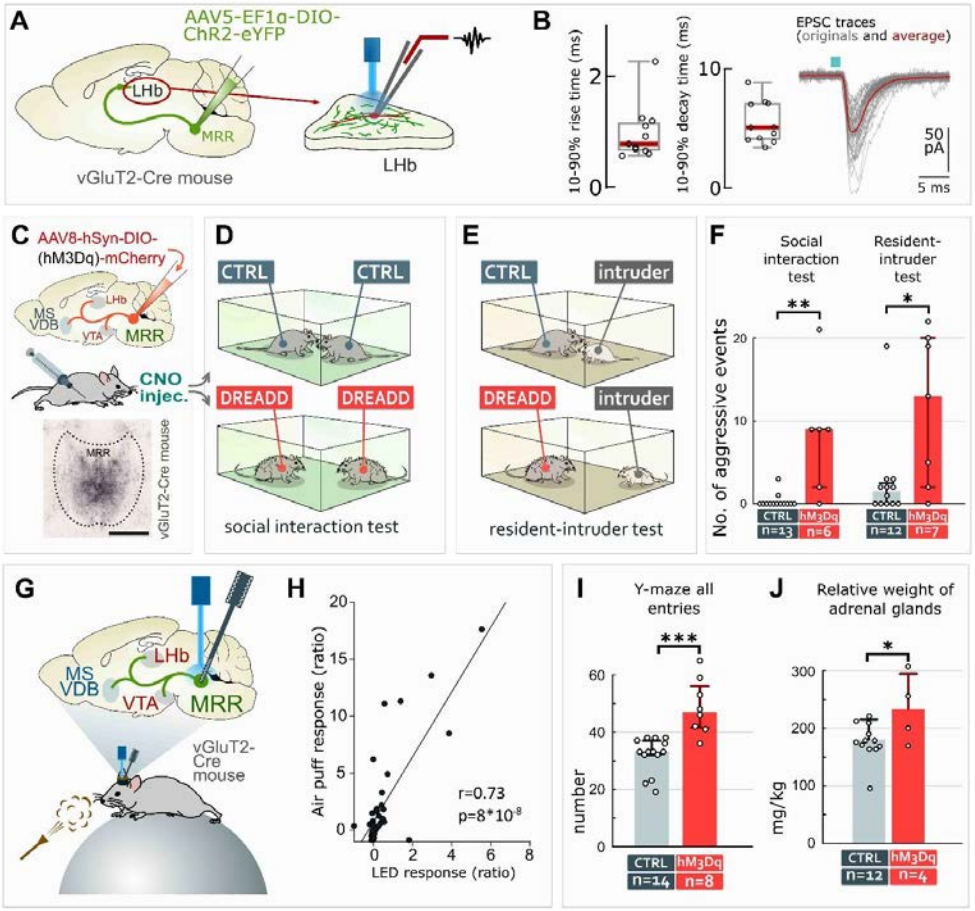

A-B: Additional data for Fig. 3A. Population data for 10-90% rise and decay time distributions respectively in ms are as follows (median [25%-75% quartiles]), 10-90% rise time: 0.77 [0.66-1.14]; 10-90% decay time 5.06 [4.10-7.03]. Original and averaged individual traces are also shown.

C-F: Additional data for Fig. 6A-C. The number of aggressive events in the social interaction and resident-intruder tests for CTRL- and h3MDq-mice, respectively are as follows (median [25%-75% quartiles]), social interaction test: CTRL: 0.00 [0.00-0.00]; h3MDq: 9.00 [2.00-9.00]; resident intruder test: CTRL: 0.00 [0.00-0.00]; h3MDq: 13.00 [2.00-20.00]. *: p=0.031, **: p=0.002, Mann-Whitney U-test.

G-H: Additional data for Fig. 4A. Air puff-triggered change of firing was significantly correlated with the effect of LED flashes on the activity of the vGLuT2-positive MRR neurons (r=0.73, p=8*10-8).

I: Population data for the number of total entries in the exploration of a Y-maze for CTRL- and h3MDq-mice are as follows (median [25%-75% quartiles]), CTRL: 33 [32-37]; h3MDq: 47 [41-56].

***: p=4.71x10-4, Mann-Whitney U-test.

J: Population data for the relative weight of adrenal glands to the body weight for CTRL- and h3MDq-mice, respectively are as follows, in mg/kg (mean +/- SD), CTRL: 180.661 +/- 34.88; h3MDq: 233.41 +/- 61.37. *: p=0.047, Student's t-test.

Fig. S5. Injection sites and optic fiber localizations

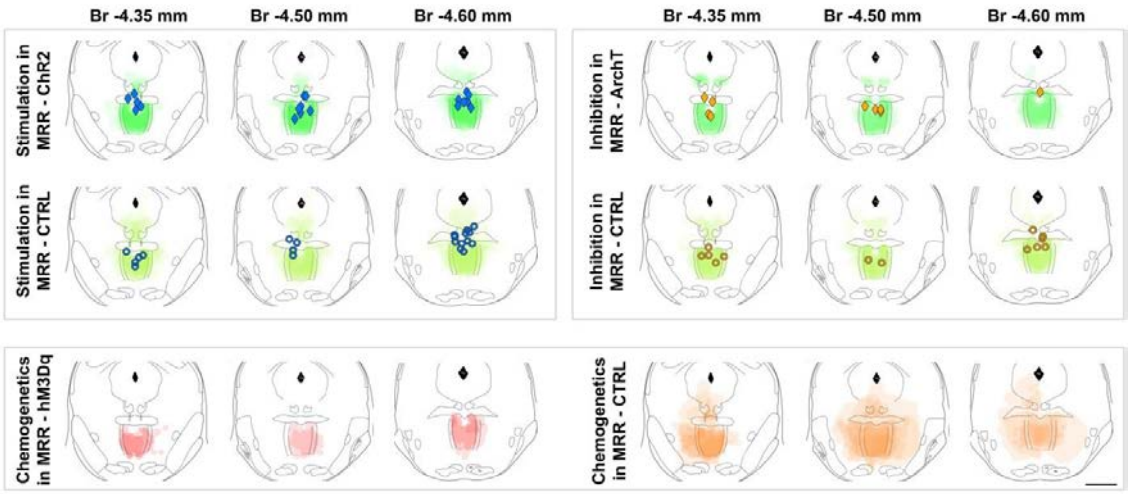

Summary of virus injection sites in every mouse used in the behavioral opto- and chemogenetic experiments. The virus injection sites in the different mice participating in the different experiments were checked one-by-one and overlaid onto each other in these images. AAV2/5-EF1a-DIO-ChR2-eYFP (ChR2) or AAV2/5-CAG-FLEX-ArchT-GFP (ArchT) expression is labeled with green, AAV2/5-EF1a-DIO-eYFP (CTRL) expression is labeled with yellow, AAV2/8-hSyn-DIO-hM3Dq-mCherry is labeled with red and AAV2/8-hSyn-DIO-mCherry is labeled with orange in the area of MRR and adjacent structures at 3 different coronal levels (Bregma -4.35, -4.50 and -4.60 mm, respectively). The tips of the optic fibers positioned over the MRR are also labeled as follows: In experiments comparing ChR2 stimulation vs. CTRL in the MRR (described in Fig. 5A-D), blue rhombs show the tip of optic fibers in ChR2-expressing mice, whereas blue circles show the tip of optic fibers in CTRL-mice. In experiments comparing ArchT inhibition vs. CTRL (described in Fig. 8E), orange rhombs show the tip of optic fibers in ArchT-expressing mice, whereas orange circles show the tip of optic fibers in CTRL-mice.

Fig. S6. Supplementary data for behavioral experiments

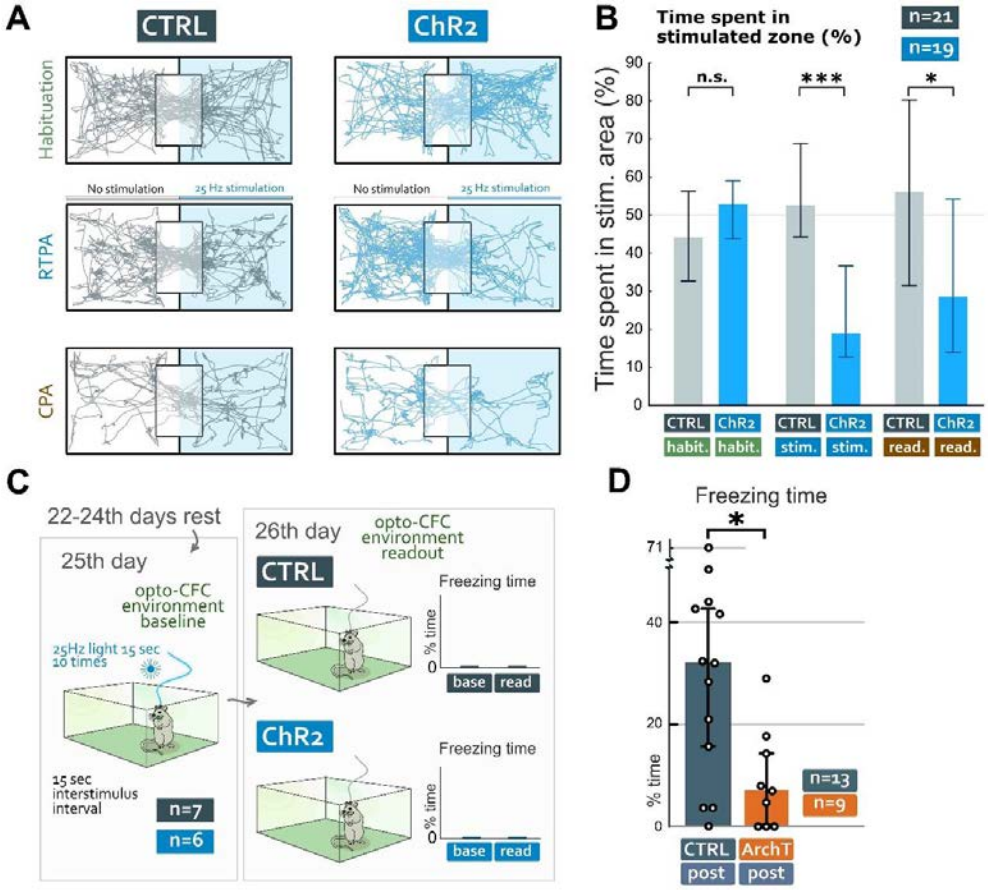

A: Animal movement traces of a representative CTRL- and ChR2-mouse during the habituation, real time place aversion (RTPA) and conditioned place aversion (CPA) experiments. Mice were light stimulated in the blue shaded area of the test chamber. The CTRL-mouse spent equal time in the two sides of the chamber, whereas the ChR2-mouse avoided the stimulation area during and 24 hours after the 25 Hz blue laser light stimulation of the vGluT2-positive MRR cells. We found no statistical difference either in the velocity of locomotion (Mann-Whitney U-test, p=0.1293) or in distance travelled (Mann-Whitney U-test, p=0.1363) during RTPA experiments.

B: Population data for the time spent in the two areas during habituation, RTPA and CPA tests (the latter two graphs are the same as in Fig. 5B). Medians and interquartile range shown on the graphs. (For statistical details see Suppl. Data for Fig. 5).

C: Additional data for Fig. 5. Experimental design of optogenetic stimulation of vGluT2-positive MRR cells. During the 3 days following operant conditioning, animals gained back their original body weight. Mice were then placed into a new "opto-CFC" environment, and after 3 min of baseline freezing recording, they were light-stimulated for 10 times 15 seconds, with 15 seconds interstimulus interval. 24 hours later mice were placed back into the same environment to detect freezing levels. Freezing behavior was absent in both groups (n=7 CTRL and n=6 ChR2-mice) during both conditions.

D: Additional data for Fig. 8E. Population data for the post-cue freezing levels (% of total time) in environment "B" for 13 CTRL- and 9 ArchT-mice are as follows: (median [25%-75% quartiles]), CTRL: 32.00 [15.67-42.67]; ArchT: 0.00 [0.00-14.33]. *p=0.021, Mann-Whitney U-test.

Fig. S7. MRR vGluT2-neurons provide a neural hub for processing negative experiences

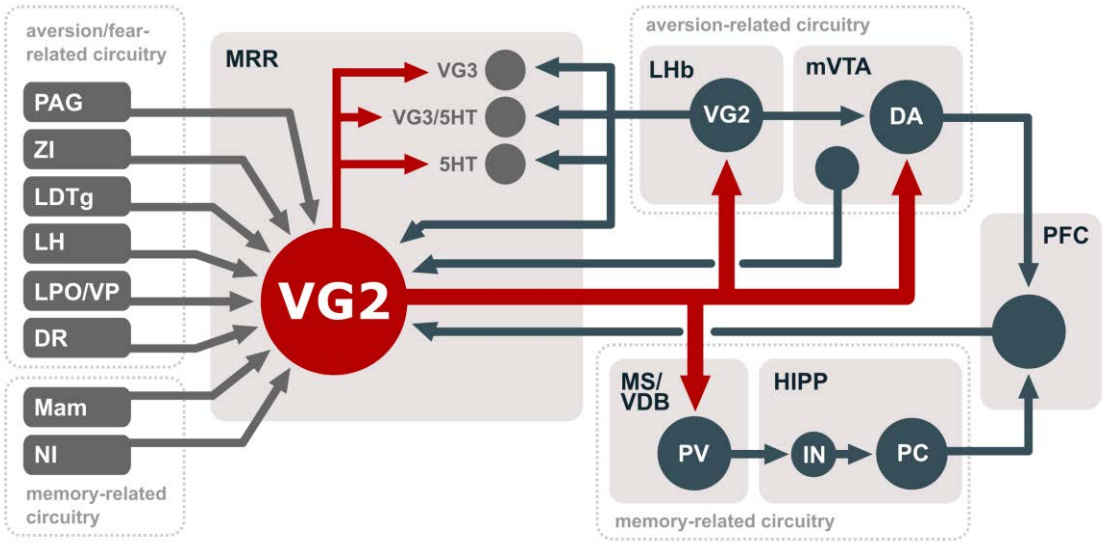

Illustration of the input and output connections of the MRR vGluT2-neurons (VG2). MRR vGluT2-neurons receive extensive inputs both from aversion-, freezing-, fear-related brain areas (see on the left) and from areas related to the memorization of negative experience (see on the left). In addition, MRR vGluT2-neurons project to LHb and mVTA, which are centers for aversion and for the prediction of negative experience, whereas they also project to the MS/VDB that induces hippocampal theta-rhythm activity, which is essential for contextual memory formation of negative experience. PAG: periaqueductal gray, ZI: zona incerta, LDTg: laterodorsal tegmental nucleus, LH: lateral hypothalamus, LPO/VP: lateral preoptic area & ventral pallidum, DR: dorsal raphe, Mam: mammillary complex, NI: nucleus incertus, MRR: median raphe region, VG2: vesicular glutamate transporter 2-positive neurons, VG3: vesicular glutamate transporter 3-positive neurons, 5TH: serotonergic neurons, LHb: lateral habenula, mVTA: medial ventral tegmental nucleus, DA: dopaminergic neurons, PFC: prefrontal cortex, MS/VDB: medial septum & vertical limb of the diagonal band of Broca, PV: parvalbumin-positive neurons, HIPP: hippocampus, IN: interneurons, PC: pyramidal cells.

Table S1. Characterization of the primary antibodies and retrograde tracers used.

Antigen or reagent	Host	Dilution	Source	Catalog number	Charac-terization	Specificity
Calbindin	Rabbit	1:2000	Kind gift from K. Baimbridge	-	**1**	The antibody recognizes one major broad band of the expected molecular weight (28 kDa) on western blots from rat cerebellum samples and immunostaining was abolished by preadsorption with the immunogen
Calretinin	Mouse	1:3000	Swant	6B3	**17**	KO verified
Choline Acetyltransferase (ChAT)	Mouse	1:300	Kind gift from C. Cozzari	-	**2,3**	Staining is typical for cholinergic cells; complete overlap of staining with eYFP-positive cells in ChAT-iRES-Cre mice injected with AAV-EF1a-DIO-eYFP
Choleratoxin B subunit	Goat	1:20000	List Biologicals	#703	**4**	No staining in non-injected animals
Choleratoxin B subunit	Mouse	1:2000	Abcam	ab1003	**5**	No staining in non-injected animals
Choleratoxin B subunit	Mouse	1:500	Abcam	ab35988	**6**	No staining in non-injected animals
eGFP	Chicken	1:2000	Thermo Fisher Scientific	A10262	**17**	No staining in animals not injected with eGFP-expressing virus
eGFP	Rabbit	1:1000	Thermo Fisher Scientific	A11122	**17**	No staining in animals not injected with eGFP-expressing virus
Fluoro Gold	Rabbit	1:500	Chemicon	AB153-i	**7**	No staining in non-injected animals
Fluoro Gold	Guinea pig	1:5000	Protos Biotech Corp	NM-101	**17**	No staining in non-injected animals

Homer-1	Rabbit	1:2000	Synaptic Systems	160 003	**17**	Specific for Homer 1. Cross-reactivity of the serum to Homer 2 and 3 was removed by pre-adsorption with Homer 2 (aa 1 - 176) and Homer 3 (aa 1 - 177).
mCherry	Rabbit	1:2000	BioVision	5993-100	**17**	No staining in animals not injected with mCherry-expressing virus
NMDA receptor GluN1 subunit	Rabbit	1:200	Kind gift from Watanabe M.	-	**8**	KO verified
NMDA receptor GluN2A subunit	Rabbit	1:200	Kind gift from Watanabe M.	-	**8**	KO verified
Parvalbumin	Guinea pig	1:10000	Synaptic Systems	195 004	**17, 9**	Labels the same cell populations in the brain as other antibodies to parvalbumin
Parvalbumin	Rabbit	1:2000	Kind gift from K. Baimbridge	-	**10, 11**	Labels the same cell populations in the brain as other antibodies to parvalbumin
Parvalbumin	Mouse	1:2000	Swant	235	**17**	KO verified
RFP	Rabbit	1:4000	Rockland Immuno-chemicals Inc.	600-401-379	**17**	No staining in animals not injected with mCherry-expressing virus
RFP	Rat	1:2000-1:5000	Chromotek	5F8	**17**	No staining in animals not injected with mCherry-expressing virus
SERT	Guinea pig	1:1000	Frontier Institute	2571777	**12**	Immunoblot detects a single protein band at 67-69 kDa. This selectively stains serotonergic neurons and fibers.
TH	Mouse	1:2000	Immuno Star	22941	**13**	Staining is typical for TH-positive cells
TpH	Mouse	1:3000	Sigma-Aldrich	T0678	**17, 14**	Staining is typical for TpH-positive cells

vesicular GABA transporter (vGAT)	Guinea pig	1:2000	Synaptic Systems	131 004	**17**	KO verified
vesicular glutamate transporter, type 2 (vGluT2)	Guinea pig	1:2000	Synaptic Systems	135 404	**17, 15**	The antibody recognizes one major broad band of the expected molecular weight (65 kDa) on western blots of a synaptic vesicle fraction of rat brain and immunostaining was abolished by preadsorption with the immunogen
vesicular glutamate transporter, type 3 (vGluT3)	Rabbit	1:300	Synaptic Systems	135 203	**17**	KO verified
vesicular glutamate transporter, type 3 (vGluT3)	Guinea pig	1:500-1:1000	Frontier Institute	522 588	**17**	Immunoblot detects a single protein band at 60-62 kDa. This stains distinct neuronal populations, which have not been classified as glutamatergic neurons.
DAPI		1:10000	Sigma-Aldrich		-	nuclear marker
Choleratoxin B subunit		0,5%	List Biologicals	#104	**16**	retrograde tracer
FluoroGold		2%	Fluoro Chrome Inc.	-	**16**	retrograde tracer

References: **1.** Buchan, A. M. et al., Peptides 9, 333–8; **2.** Chédotal, A. et al., Brain Res. (1994); **3.** Takács, V. T. et al., Nat. Commun. 9, 2848 (2018); **4.** Dederen, P. J. et al., Histochem. J. 26, 856–62 (1994); **5.** Hamorsky, K. T. et al., PLoS Negl. Trop. Dis. (2013); **6.** Dautan, D. et al., Nat. Neurosci. (2016). **7.** Varga, C. et al., J. Neurosci. 22, 6186–94 (2002). **8.** Watanabe, M. et al. Eur. J. Neurosci. 10, 478–87 (1998), **9.** Hartwich, K. et al., J. Neurosci. (2012). **10.** Mascagni, F. et al., Neuroscience 158, 1541–50 (2009), **11.** Condé, F. et al., J. Comp. Neurol. 341, 95–116 (1994), **12.** Somogyi, J. et al., Eur. J. Neurosci. 19, 552–69 (2004), **13.** Chermenina, M. et al., Parkinsons. Dis. (2015), **14.** Kodani, S. et al., J. Neurosci. 37, 7164–7176 (2017). **15.** Broms, J. et al., J. Comp. Neurol. (2015), **16.** Lanciego, J. L. et al., Journal of Chemical Neuroanatomy (2011). **17.** Information is provided by the distributor.

Table S2. Secondary antibodies

Raised in	Raised against	Conjugated with	Dilution	Source	Catalog number
Donkey	Rabbit	Alexa 647	1:500	Jackson Immunoresearch	711-605-152
Donkey	Mouse	Alexa 647	1:500	Jackson Immunoresearch	715-605-151
Donkey	Guinea pig	Alexa 647	1:500	Jackson Immunoresearch	706-605-148
Goat	Chicken	Alexa 488	1:1000	ThermoFisher Scientific	A11039
Donkey	Rabbit	Alexa 488	1:1000	ThermoFisher Scientific	A21206
Donkey	Mouse	Alexa 488	1:500	ThermoFisher Scientific	A21202
Goat	Guinea pig	Alexa 488	1:500	ThermoFisher Scientific	A11073
Donkey	Rabbit	Alexa 594	1:500	ThermoFisher Scientific	A21207
Donkey	Rat	Alexa 594	1:500	ThermoFisher Scientific	A21209
Donkey	Guinea pig	Alexa 594	1:500	Jackson Immunoresearch	706-585-148
Donkey	Mouse	Alexa 594	1:500	ThermoFisher Scientific	A21203
-	-	DyLight405	1:500	Jackson Immunoresearch	016-470-084
Goat	Rabbit	1.4 nm gold	1:100	Nanoprobes	#2004
Goat	Chicken	biotinylated	1:200	Vector Laboratories	BA-9010
Donkey	Mouse	biotinylated	1:1000	Jackson Immunoresearch	715-066-151
Goat	Rabbit	biotinylated	1:1000	Rocklan Immunochemicals Inc.	611-106-B76
Horse	Mouse	Horseradish peroxidase (ImmPress)	1:3	Vector Laboratories	MP-7402

Table S3. Primary and secondary antibody combinations used in immunofluorescent experiments

mouse strain	experiment types	used primary antibodies or reagents	used secondary antibodies	note
vGluT2-Cre	Stereology	DAPI	-	Stereological measurement
		chicken-anti-eGFP	Alexa 488-conjugated goat-anti-chicken	
		rabbit-anti-vGluT3	Alexa 594-conjugated donkey-anti-rabbit	
		mouse-anti-TpH	Alexa 647 conjugated donkey-anti-mouse	
vGluT2-Cre	viral anterograde tracing	chicken-anti-eGFP	Alexa 488-conjugated goat-anti-chicken	Labeling the injection sites and ascending fibers from MRR in vGluT2-Cre mice
vGluT2-Cre	viral anterograde tracing, monosynaptic rabies tracing	chicken-anti-eGFP	Alexa 488-conjugated goat-anti-chicken	Labeling the injection sites and ascending fibers from DR, NI, mRT, PnO, PPTg in vGluT2-Cre mice. Injection site analysis and identification of monosynaptically labeled cells in the forebrain and in the brainstem
		rat-anti-RFP	Alexa 594-conjugated donkey-anti-rat	
vGAT-Cre, vGluT3-Cre, TpH-Cre	viral anterograde tract-tracing	chicken-anti-eGFP	Alexa 488-conjugated goat-anti-chicken	Labeling the injection sites and ascending fibers from MRR in vGAT-Cre, vGluT3-Cre, TpH-Cre mouse
vGluT2-Cre	Analysis of the neurochemical identity of MRR fibers	chicken-anti-eGFP	Alexa 488-conjugated goat-anti-chicken	vGluT2-labeling and MRR fibers identification in the forebrain
		guinea pig anti-vGluT2	Alexa 594-conjugated donkey-anti-guinea pig	

vGluT2-Cre	Analysis of the neurochemical identity of MRR fibers	chicken-anti-eGFP	Alexa 488-conjugated goat-anti-chicken	vGluT3 and vGAT-labeling and MRR fibers identification in the forebrain
		rabbit anti-vGluT3	Alexa 594-conjugated donkey-anti-rabbit	
		guinea pig anti-VGAT	Alexa 647 conjugated donkey-anti-guinea pig	
vGluT2-Cre	Analysis of the neurochemical identity of MRR fibers	chicken-anti-eGFP	Alexa 488-conjugated goat-anti-chicken	SERT-labeling and MRR fibers identification in the forebrain
		guinea pig anti-SERT	Alexa 594-conjugated donkey-anti-guinea pig	
vGluT2-Cre	Target cell selectivity of LHb fibers in the MRR; Local connections of MRR vGluT2 fibers to vGluT3+ cells	chicken-anti-eGFP	Alexa 488-conjugated goat-anti-chicken	Labeling vGluT3 cells in the MRR
		guinea pig-anti-vGluT3	Alexa 594-conjugated donkey-anti-guinea pig	
		rabbit-anti-Homer	Alexa 647-conjugated donkey-anti-rabbit	
vGluT2-Cre	Target cell selectivity of LHb fibers in the MRR; Local connections of MRR vGluT2 fibers to serotonergic cells	chicken-anti-eGFP	Alexa 488-conjugated goat-anti-chicken	Labeling serotonergic cells in the MRR
		mouse-anti-TpH	Alexa 594 conjugated donkey-anti-mouse	
		rabbit-anti-Homer	Alexa 647-conjugated donkey-anti-rabbit	
vGluT2-Cre	Target cell selectivity of MRR fibers in the LHb and LHb fibers in the MRR	chicken-anti-eGFP	Alexa 488-conjugated goat-anti-chicken	Viraly labeling vGluT2 cells in LHb and MRR
		rat-anti-RFP	Alexa 594-conjugated donkey-anti-rat	
		rabbit-anti-Homer	Alexa 647-conjugated donkey-anti-rabbit	

vGluT2-Cre	Target cell selectivity of LHb fibers in MRR	chicken-anti-eGFP	Alexa 488-conjugated goat-anti-chicken	Measurement from retrogradely traced vGluT2-positive cells from LHb in the MRR
		rat-anti-RFP	Alexa 594-conjugated donkey-anti-rat	
		rabbit-anti-Homer	Alexa 647-conjugated donkey-anti-rabbit	
		mouse-anti-Choleratoxin B	biotinylated donkey-anti-mouse + DyLight405 conjugated streptavidin	
vGluT2-Cre	Target cell selectivity of MRR fibers in the LHb	guinea pig-anti-FluoroGold	Alexa 488-conjugated goat-anti-guinea pig	Retrograde tracing from VTA and MRR in the LHb
		rabbit-anti-mCherry	Alexa 594-conjugated donkey-anti-rabbit	
		mouse-anti-Choleratoxin B	Alexa 647-conjugated donkey-anti-mouse	
vGluT2-Cre	Target cell selectivity of MRR fibers in the LHb	mouse-anti-Choleratoxin B	Alexa 488-conjugated donkey-anti-mouse	Measurement from retrograde tracing from MRR in the LHb
		rat-anti-RFP	Alexa 594-conjugated donkey-anti-rat	
		rabbit-anti-Homer	Alexa 647-conjugated donkey-anti-rabbit	
vGluT2-Cre	Target cell selectivity of MRR fibers in the mVTA	chicken-anti-eGFP	Alexa 488-conjugated goat-anti-chicken	LHb and MRR vGluT2-neurons target medial VTA DA neurons
		rat-anti-RFP	Alexa 594-conjugated donkey-anti-rat	
		rabbit-anti-Homer	Alexa 647-conjugated donkey-anti-rabbit	
		mouse-anti-TH	biotinylated donkey-anti-mouse + DyLight405 conjugated streptavidin	
vGluT2-Cre	Target cell selectivity of MRR fibers in the mVTA	chicken-anti-eGFP	Alexa 488-conjugated donkey-anti-chicken	MRR vGluT2-neurons target medial VTA DA neurons that project to PFC
		goat-anti-CTB	Alexa 594-conjugated donkey-anti-goat	
		rabbit-anti-Homer	Alexa 647-conjugated donkey-anti-rabbit	
		mouse-anti-TH	biotinylated donkey-anti-mouse + DyLight405 conjugated streptavidin	

vGluT2-Cre	Target cell selectivity of MRR fibers in the VDB	chicken-anti-eGFP	Alexa 488-conjugated goat-anti-chicken	Labeling PV positive cells in the VDB
		mouse-anti-Parvalbumin	Alexa 594 conjugated donkey-anti-mouse	
		rabbit-anti-Homer	Alexa 647-conjugated donkey-anti-rabbit	
vGluT2-Cre	Target cell selectivity of MRR fibers in the VDB	chicken-anti-eGFP	Alexa 488-conjugated goat-anti-chicken	Labeling PV and ChAT positive cells in the VDB
		rabbit-anti-Parvalbumin	Alexa 594 conjugated donkey-anti-rabbit	
		mouse-anti-ChAT	Alexa 647 conjugated donkey-anti-mouse	
vGluT2-Cre	Target cell selectivity of MRR fibers in the VDB	chicken-anti-eGFP	Alexa 488-conjugated goat-anti-chicken	Labeling CR positive cells in the VDB
		mouse-anti-Calretinin	Alexa 647 conjugated donkey-anti-mouse	
vGluT2-Cre	Target cell selectivity of MRR fibers in the VDB	chicken-anti-eGFP	Alexa 488-conjugated goat-anti-chicken	Labeling vGluT2+ and CB positive cells in the VDB
		rat-anti-RFP	Alexa 594-conjugated donkey-anti-rat	
		rabbit-anti-calbindin	Alexa 647-conjugated donkey-anti-rabbit	
vGluT2-Cre	Target cell selectivity of MRR fibers in the LHb	guinea pig-anti-FluoroGold	Alexa 488-conjugated goat-anti-guinea pig	Measurement from retrograde tracing from HIPP in the VDB
		rabbit-anti-mCherry	Alexa 594-conjugated donkey-anti-rabbit	
		mouse-anti-Parvalbumin	Alexa 647-conjugated donkey-anti-mouse	
vGluT2-Cre	Post-hoc anatomical identification of in vitro labeled cells in the LHb	chicken-anti-eGFP	Alexa 488-conjugated donkey-anti-rabbit	Labeling of MRR fibers and in vitro labeled cells in LHb
		Alexa 594-conjugated Streptavidin	Alexa 594-conjugated Streptavidin	
		rabbit-anti-Homer	Alexa 647-conjugated donkey-anti-rabbit	
vGluT2-Cre	VDB-LHb double retrograde tracing	rabbit-anti-FluoroGold	Alexa 488-conjugated donkey-anti-rabbit	Identification of the retrogradely labeled cells in the MRR
		rat-anti-RFP	Alexa 594-conjugated donkey-anti-rat	
		mouse-anti-Choleratoxin B	Alexa 647-conjugated donkey-anti-mouse	

Table S4. Primary and secondary antibody combinations used in immunoperoxidase and electron microscopic experiments

vGluT2-Cre	Analysis of NMDA receptor GluN2A subunit positivity of MRR fibers in the LHb and MS	chicken-anti-eGFP	biotinylated goat-anti-chicken	Correlated double immunogold-immuno-peroxidase electron microscopy for glutamatergic molecular machinery analysis in MRR vGluT2 fibers
		rabbit-anti-NMDA receptor NR2A subunit	1.4 nm gold conjugated goat-anti-rabbit	
vGluT2-Cre	Analysis of NMDA receptor GluN1 subunit positivity of MRR fibers in the LHb	chicken-anti-eGFP	biotinylated goat-anti-chicken	
		rabbit-anti-NMDA receptor NR1 subunit	1.4 nm gold conjugated goat-anti-rabbit	
vGluT2-Cre	Parvalbumin-specificity of MRR fibers in the VDB	chicken-anti-eGFP	biotinylated goat-anti-chicken	Correlated double SI-DAB/DAB-Ni electron microscopy for target specificity of MRR fibers in the MS/VDB
		mouse-anti-Parvalbumin	ImmPress horse-anti-mouse	
vGluT2-Cre	Experiment for BFSEM	rabbit-anti-eGFP	1.4 nm gold conjugated goat-anti-rabbit	MRR terminal reconstruction in LHb
vGluT2-Cre	Chemogenetic virus injection site identification	rabbit-anti-RFP	biotinylated goat-anti-rabbit	Chemogenetic virus injection site identification

Table S5. Stereological estimation of MRR neurons

	Mouse1	Mouse2	Mouse3	Average
Total counted vGluT2 positive neurons	8524	7014	4826	**6788**
Total counted TpH or/and vGluT3 positive neurons	5886	3362	3995	**4414**
vGluT2 positive neurons / TpH and-or vGluT3 positive neurons	1,45	2,09	1,21	**1,58**
All TpH and/or vGluT3 positive neurons (*22*)				**6067**
Total neurons (*22*)				**47458**
vGluT2 positive neurons in MRR				**1,58*6067 = 9586**
vGluT2 positive neurons ratios in MRR				**20,20%**

Table S6. Quantification of monosynaptically-labeled neurons with rabies virus in the different brain areas projecting onto MRR vGluT2 neurons.

Brain area /Nucleus	Median %	Estimation of cell numbers per brain area			Behavioral relevance	Ref.
		Mouse1	Mouse2	Mouse3		
Lateral habenular nucleus	10,0%	588	456	756	aversion center, depression	**1–4**
Mammillary region	8,5%	504	396	252	memory formation	**5,6**
Dorsal raphe nucleus	7,8%	468	354	678	Anti-aversion, antidepressant	**7,8**
VTA together	7,4%	438	384	384	aversion, reward	**9**
Lateral hypothalamic area	6,6%	408	300	510	cued-dependent aversion	**10,11**
PAG together	6,0%	354	342	324	freezing behavior	**12**
Laterodorsal tegmental nucleus	5,9%	348	174	721	innate fear, reward processing	**13,14**
Nucleus pontis oralis	5,2%	198	234	846	REM sleep, theta generation	**15**
Zona incerta	4,0%	258	24	360	fear, freezing, attention	**16–18**
PFC together	2,3%	138	108	78	fear, reward, aversion	**14,19**
Nucleus incertus	1,7%	300	78	126	memory formation	**20**
Raphe magnus nucleus	1,6%	108	42	144	pain inhibition	**21**
Lateral preoptic area	1,5%	90	144	78	aversion, reward	**22**
Ventral pallidum	1,3%	102	60	84	reward seeking	**23**
Posterior hypothalamic nucleus	1,2%	72	42	192	theta rhythm, spatial memory	**24,25**
Dorsomedial hypothalamic nucleus	1,1%	6	66	96	circadian rhythms	**26**
Substantia nigra, reticular part	1,1%	66	12	156	motor control	**27,28**
Rostral linear nucleus	1,0%	60	78	0	olfactory-guided behavior	**29**
TOTAL	74,43%	4506	3294	5785		

References: 1. Stephenson-Jones et al., Proc. Natl. Acad. Sci. 109, E164–E173 (2012), **2.** Stopper et al., Nat. Neurosci. 17, 33–35 (2014), **3.** Li et al., Elife 8, 1–17 (2019). **4.** Yang, Y. et al., Nature 554, 317–322 (2018), **5**. Dillingham et al., Neurosci. Biobehav. Rev. 54, 108–119 (2015), **6.** Vann, S. D. et al., Nat. Rev. Neurosci. 5, 35–44 (2004). **7**. Luo, M. et al., Learn. Mem. 22, 452–460 (2015), **8**. Zhang, H. et al., Brain Struct. Funct. 223, 2243–2258 (2018), **9**. Lammel, S. et al., Neuropharmacology 76 Pt B, 351–9 (2014), **10**. de Jong, J. W. et al., Neuron (2019), **11**. Lazaridis, I. et al., Mol. Psychiatry (2019), **12.** Tovote, P. et al. Nature 534, 206–212 (2016), **13**. Yang, H. et al., Nat. Neurosci. 19, 283–9 (2016), **14**. Lammel, S. et al., Nature 491, 212–217 (2012), **15**. Sanford, L. D. et al., J. Neurophysiol. 90, 938–945 (2006). **16**. Chou, X. L. et al. Nat. Commun. 9, 1–12 (2018), **17**. Watson et al., J. Neurosci. 35, 9463–9476 (2015), **18**. Chometton, S. et al., Brain Struct. Funct. (2017), **19**. Rozeske et al., Genes, Brain Behav. 14, 22–36 (2015), **20**. Szőnyi, A. et al., Science 364, (2019), **21**. Brodie et al., Brain Res. (1986), **22**. Barker, D. J. et al., Cell Rep. 21, 1757–1769 (2017), **23**. Tooley, J. et al., Biol. Psychiatry (2018), **24**. Bocian, R. et al., Hippocampus 26, 1354–1369 (2016), **25**. Gutiérrez-Guzmán, B. E. et al., Eur. J. Pharmacol. 682, 99–109 (2012), **26**. Chou, T. C. et al., J. Neurosci. (2003), **27**. Hikosaka, O. et al., J. Neurophysiol. (1983), **28**. Sato, M. et al., J. Neurosci. (2002), **29**. Del-Fava, F. et al., Neuroscience (2007).

References and Notes

1. E. S. Bromberg-Martin, M. Matsumoto, H. Nakahara, O. Hikosaka, Multiple timescales of memory in lateral habenula and dopamine neurons. *Neuron* **67**, 499–510 (2010). doi:10.1016/j.neuron.2010.06.031 Medline

2. E. S. Bromberg-Martin, O. Hikosaka, Lateral habenula neurons signal errors in the prediction of reward information. *Nat. Neurosci.* **14**, 1209–1216 (2011). doi:10.1038/nn.2902 Medline

3. E. S. Bromberg-Martin, M. Matsumoto, O. Hikosaka, Distinct tonic and phasic anticipatory activity in lateral habenula and dopamine neurons. *Neuron* **67**, 144–155 (2010). doi:10.1016/j.neuron.2010.06.016 Medline

4. C. A. Orsini, D. E. Moorman, J. W. Young, B. Setlow, S. B. Floresco, Neural mechanisms regulating different forms of risk-related decision-making: Insights from animal models. *Neurosci. Biobehav. Rev.* **58**, 147–167 (2015). doi:10.1016/j.neubiorev.2015.04.009 Medline

5. C. M. Stopper, S. B. Floresco, What's better for me? Fundamental role for lateral habenula in promoting subjective decision biases. *Nat. Neurosci.* **17**, 33–35 (2014). doi:10.1038/nn.3587 Medline

6. C. M. Stopper, M. T. L. Tse, D. R. Montes, C. R. Wiedman, S. B. Floresco, Overriding phasic dopamine signals redirects action selection during risk/reward decision making. *Neuron* **84**, 177–189 (2014). doi:10.1016/j.neuron.2014.08.033 Medline

7. P. M. Baker, S. E. Oh, K. S. Kidder, S. J. Y. Mizumori, Ongoing behavioral state information signaled in the lateral habenula guides choice flexibility in freely moving rats. *Front. Behav. Neurosci.* **9**, 295 (2015). doi:10.3389/fnbeh.2015.00295 Medline

8. R. Goutagny, M. Loureiro, J. Jackson, J. Chaumont, S. Williams, P. Isope, C. Kelche, J. C. Cassel, L. Lecourtier, Interactions between the lateral habenula and the hippocampus: Implication for spatial memory processes. *Neuropsychopharmacology* **38**, 2418–2426 (2013). doi:10.1038/npp.2013.142 Medline

9. R. Crooks, J. Jackson, B. H. Bland, Dissociable pathways facilitate theta and non-theta states in the median raphe—Septohippocampal circuit. *Hippocampus* **22**, 1567–1576 (2012). doi:10.1002/hipo.20999 Medline

10. A. Domonkos, L. Nikitidou Ledri, T. Laszlovszky, C. Cserép, Z. Borhegyi, E. Papp, G. Nyiri, T. F. Freund, V. Varga, Divergent in vivo activity of non-serotonergic and serotonergic VGluT3-neurones in the median raphe region. *J. Physiol.* **594**, 3775–3790 (2016). doi:10.1113/JP272036 Medline

11. J. Jackson, C. T. Dickson, B. H. Bland, Median raphe stimulation disrupts hippocampal theta via rapid inhibition and state-dependent phase reset of theta-related neural circuitry. *J. Neurophysiol.* **99**, 3009–3026 (2008). doi:10.1152/jn.00065.2008 Medline

12. G. Viana Di Prisco, Z. Albo, R. P. Vertes, B. Kocsis, Discharge properties of neurons of the median raphe nucleus during hippocampal theta rhythm in the rat. *Exp. Brain Res.* **145**, 383–394 (2002). doi:10.1007/s00221-002-1123-8 Medline

13. D. V. Wang, H. J. Yau, C. J. Broker, J. H. Tsou, A. Bonci, S. Ikemoto, Mesopontine median raphe regulates hippocampal ripple oscillation and memory consolidation. *Nat. Neurosci.* **18**, 728–735 (2015). doi:10.1038/nn.3998 Medline

14. H. Aizawa, S. Yanagihara, M. Kobayashi, K. Niisato, T. Takekawa, R. Harukuni, T. J. McHugh, T. Fukai, Y. Isomura, H. Okamoto, The synchronous activity of lateral

habenular neurons is essential for regulating hippocampal theta oscillation. *J. Neurosci.* **33**, 8909–8921 (2013). doi:10.1523/JNEUROSCI.4369-12.2013 Medline

15. T. G. C. S. Andrade, H. Zangrossi Jr., F. G. Graeff, The median raphe nucleus in anxiety revisited. *J. Psychopharmacol.* **27**, 1107–1115 (2013). doi:10.1177/0269881113499208 Medline

16. D. G. Balázsfi, D. Zelena, L. Farkas, K. Demeter, I. Barna, C. Cserép, V. T. Takács, G. Nyíri, F. Gölöncsér, B. Sperlágh, T. F. Freund, J. Haller, Median raphe region stimulation alone generates remote, but not recent fear memory traces. *PLOS ONE* **12**, e0181264 (2017). doi:10.1371/journal.pone.0181264 Medline

17. T. F. Freund, A. I. Gulyás, L. Acsády, T. Görcs, K. Tóth, Serotonergic control of the hippocampus via local inhibitory interneurons. *Proc. Natl. Acad. Sci. U.S.A.* **87**, 8501–8505 (1990). doi:10.1073/pnas.87.21.8501 Medline

18. J. Jackson, B. H. Bland, M. C. Antle, Nonserotonergic projection neurons in the midbrain raphe nuclei contain the vesicular glutamate transporter VGLUT3. *Synapse* **63**, 31–41 (2009). doi:10.1002/syn.20581 Medline

19. V. Varga, A. Losonczy, B. V. Zemelman, Z. Borhegyi, G. Nyiri, A. Domonkos, B. Hangya, N. Holderith, J. C. Magee, T. F. Freund, Fast synaptic subcortical control of hippocampal circuits. *Science* **326**, 449–453 (2009). doi:10.1126/science.1178307 Medline

20. S. J. Bang, P. Jensen, S. M. Dymecki, K. G. Commons, Projections and interconnections of genetically defined serotonin neurons in mice. *Eur. J. Neurosci.* **35**, 85–96 (2012). doi:10.1111/j.1460-9568.2011.07936.x Medline

21. C. Leranth, R. P. Vertes, Median raphe serotonergic innervation of medial septum/diagonal band of broca (MSDB) parvalbumin-containing neurons: Possible involvement of the MSDB in the desynchronization of the hippocampal EEG. *J. Comp. Neurol.* **410**, 586–598 (1999). doi:10.1002/(SICI)1096-9861(19990809)410:4<586:AID-CNE6>3.0.CO;2-H Medline

22. K. E. Sos, M. I. Mayer, C. Cserép, F. S. Takács, A. Szőnyi, T. F. Freund, G. Nyiri, Cellular architecture and transmitter phenotypes of neurons of the mouse median raphe region. *Brain Struct. Funct.* **222**, 287–299 (2017). doi:10.1007/s00429-016-1217-x Medline

23. S. Lammel, B. K. Lim, C. Ran, K. W. Huang, M. J. Betley, K. M. Tye, K. Deisseroth, R. C. Malenka, Input-specific control of reward and aversion in the ventral tegmental area. *Nature* **491**, 212–217 (2012). doi:10.1038/nature11527 Medline

24. S. Lammel, B. K. Lim, R. C. Malenka, Reward and aversion in a heterogeneous midbrain dopamine system. *Neuropharmacology* **76**, 351–359 (2014). doi:10.1016/j.neuropharm.2013.03.019 Medline

25. L. A. Quina, L. Tempest, L. Ng, J. A. Harris, S. Ferguson, T. C. Jhou, E. E. Turner, Efferent pathways of the mouse lateral habenula. *J. Comp. Neurol.* **523**, 32–60 (2015). doi:10.1002/cne.23662 Medline

26. I. R. Wickersham, D. C. Lyon, R. J. O. Barnard, T. Mori, S. Finke, K.-K. Conzelmann, J. A. T. Young, E. M. Callaway, Monosynaptic restriction of transsynaptic tracing from single, genetically targeted neurons. *Neuron* **53**, 639–647 (2007). doi:10.1016/j.neuron.2007.01.033 Medline

27. A. Szőnyi, K. E. Sos, R. Nyilas, D. Schlingloff, A. Domonkos, V. T. Takács, B. Pósfai, P. Hegedüs, J. B. Priestley, A. L. Gundlach, A. I. Gulyás, V. Varga, A. Losonczy, T. F.

Freund, G. Nyiri, Brainstem nucleus incertus controls contextual memory formation. *Science* **364**, eaaw0445 (2019). doi:10.1126/science.aaw0445 Medline

28. Y. Cui, Y. Yang, Z. Ni, Y. Dong, G. Cai, A. Foncelle, S. Ma, K. Sang, S. Tang, Y. Li, Y. Shen, H. Berry, S. Wu, H. Hu, Astroglial Kir4.1 in the lateral habenula drives neuronal bursts in depression. *Nature* **554**, 323–327 (2018). doi:10.1038/nature25752 Medline

29. K. Li, T. Zhou, L. Liao, Z. Yang, C. Wong, F. Henn, R. Malinow, J. R. Yates 3rd, H. Hu, βCaMKII in lateral habenula mediates core symptoms of depression. *Science* **341**, 1016–1020 (2013). doi:10.1126/science.1240729 Medline

30. Y. Yang, Y. Cui, K. Sang, Y. Dong, Z. Ni, S. Ma, H. Hu, Ketamine blocks bursting in the lateral habenula to rapidly relieve depression. *Nature* **554**, 317–322 (2018). doi:10.1038/nature25509 Medline

31. S. A. Golden, M. Heshmati, M. Flanigan, D. J. Christoffel, K. Guise, M. L. Pfau, H. Aleyasin, C. Menard, H. Zhang, G. E. Hodes, D. Bregman, L. Khibnik, J. Tai, N. Rebusi, B. Krawitz, D. Chaudhury, J. J. Walsh, M. H. Han, M. L. Shapiro, S. J. Russo, Basal forebrain projections to the lateral habenula modulate aggression reward. *Nature* **534**, 688–692 (2016). doi:10.1038/nature18601 Medline

32. L. A. Martin, H. W. Neighbors, D. M. Griffith, The experience of symptoms of depression in men vs women: Analysis of the National Comorbidity Survey Replication. *JAMA Psychiatry* **70**, 1100–1106 (2013). doi:10.1001/jamapsychiatry.2013.1985 Medline

33. N. Verdolini, G. Perugi, L. Samalin, A. Murru, J. Angst, J. M. Azorin, C. L. Bowden, S. Mosolov, A. H. Young, M. Barbuti, G. Guiso, D. Popovic, E. Vieta, I. Pacchiarotti; BRIDGE-II-Mix Study Group, Aggressiveness in depression: A neglected symptom possibly associated with bipolarity and mixed features. *Acta Psychiatr. Scand.* **136**, 362–372 (2017). doi:10.1111/acps.12777 Medline

34. C. R. Yang, Y. Y. Bai, C. S. Ruan, H. F. Zhou, D. Liu, X. F. Wang, L. J. Shen, H. Y. Zheng, X. F. Zhou, Enhanced aggressive behaviour in a mouse model of depression. *Neurotox. Res.* **27**, 129–142 (2015). doi:10.1007/s12640-014-9498-4 Medline

35. B. Li, J. Piriz, M. Mirrione, C. Chung, C. D. Proulx, D. Schulz, F. Henn, R. Malinow, Synaptic potentiation onto habenula neurons in the learned helplessness model of depression. *Nature* **470**, 535–539 (2011). doi:10.1038/nature09742 Medline

36. S. J. Russo, E. J. Nestler, The brain reward circuitry in mood disorders. *Nat. Rev. Neurosci.* **14**, 609–625 (2013). doi:10.1038/nrn3381 Medline

37. G. Buzsáki, E. I. Moser, Memory, navigation and theta rhythm in the hippocampal-entorhinal system. *Nat. Neurosci.* **16**, 130–138 (2013). doi:10.1038/nn.3304 Medline

38. B. Hangya, Z. Borhegyi, N. Szilágyi, T. F. Freund, V. Varga, GABAergic neurons of the medial septum lead the hippocampal network during theta activity. *J. Neurosci.* **29**, 8094–8102 (2009). doi:10.1523/JNEUROSCI.5665-08.2009 Medline

39. Z. Borhegyi, V. Varga, N. Szilágyi, D. Fabo, T. F. Freund, Phase segregation of medial septal GABAergic neurons during hippocampal theta activity. *J. Neurosci.* **24**, 8470–8479 (2004). doi:10.1523/JNEUROSCI.1413-04.2004 Medline

40. D. J. Barker, J. Miranda-Barrientos, S. Zhang, D. H. Root, H. L. Wang, B. Liu, E. S. Calipari, M. Morales, Lateral preoptic control of the lateral habenula through convergent glutamate and GABA transmission. *Cell Rep.* **21**, 1757–1769 (2017). doi:10.1016/j.celrep.2017.10.066 Medline

41. M. Stephenson-Jones, K. Yu, S. Ahrens, J. M. Tucciarone, A. N. van Huijstee, L. A. Mejia, M. A. Penzo, L. H. Tai, L. Wilbrecht, B. Li, A basal ganglia circuit for evaluating action outcomes. *Nature* **539**, 289–293 (2016). doi:10.1038/nature19845 Medline

42. J. W. de Jong, S. A. Afjei, I. Pollak Dorocic, J. R. Peck, C. Liu, C. K. Kim, L. Tian, K. Deisseroth, S. Lammel, A neural circuit mechanism for encoding aversive stimuli in the mesolimbic dopamine system. *Neuron* **101**, 133–151.e7 (2019). doi:10.1016/j.neuron.2018.11.005 Medline

43. K. Brinschwitz, A. Dittgen, V. I. Madai, R. Lommel, S. Geisler, R. W. Veh, Glutamatergic axons from the lateral habenula mainly terminate on GABAergic neurons of the ventral midbrain. *Neuroscience* **168**, 463–476 (2010). doi:10.1016/j.neuroscience.2010.03.050 Medline

44. T. C. Jhou, S. Geisler, M. Marinelli, B. A. Degarmo, D. S. Zahm, The mesopontine rostromedial tegmental nucleus: A structure targeted by the lateral habenula that projects to the ventral tegmental area of Tsai and substantia nigra compacta. *J. Comp. Neurol.* **513**, 566–596 (2009). doi:10.1002/cne.21891 Medline

45. S. Hong, T. C. Jhou, M. Smith, K. S. Saleem, O. Hikosaka, Negative reward signals from the lateral habenula to dopamine neurons are mediated by rostromedial tegmental nucleus in primates. *J. Neurosci.* **31**, 11457–11471 (2011). doi:10.1523/JNEUROSCI.1384-11.2011 Medline

46. A. M. Stamatakis, G. D. Stuber, Activation of lateral habenula inputs to the ventral midbrain promotes behavioral avoidance. *Nat. Neurosci.* **15**, 1105–1107 (2012). doi:10.1038/nn.3145 Medline

47. J. Tian, N. Uchida, Habenula lesions reveal that multiple mechanisms underlie dopamine prediction errors. *Neuron* **87**, 1304–1316 (2015). doi:10.1016/j.neuron.2015.08.028 Medline

48. M. Matsumoto, O. Hikosaka, Lateral habenula as a source of negative reward signals in dopamine neurons. *Nature* **447**, 1111–1115 (2007). doi:10.1038/nature05860 Medline

49. H. Li, D. Pullmann, T. C. Jhou, Valence-encoding in the lateral habenula arises from the entopeduncular region. *eLife* **8**, e41223 (2019). doi:10.7554/eLife.41223 Medline

50. F. J. Meye, K. Valentinova, S. Lecca, L. Marion-Poll, M. J. Maroteaux, S. Musardo, I. Moutkine, F. Gardoni, R. L. Huganir, F. Georges, M. Mameli, Cocaine-evoked negative symptoms require AMPA receptor trafficking in the lateral habenula. *Nat. Neurosci.* **18**, 376–378 (2015). doi:10.1038/nn.3923 Medline

51. C. D. Proulx, O. Hikosaka, R. Malinow, Reward processing by the lateral habenula in normal and depressive behaviors. *Nat. Neurosci.* **17**, 1146–1152 (2014). doi:10.1038/nn.3779 Medline

52. M. Trusel, A. Nuno-Perez, S. Lecca, H. Harada, A. L. Lalive, M. Congiu, K. Takemoto, T. Takahashi, F. Ferraguti, M. Mameli, Punishment-predictive cues guide avoidance through potentiation of hypothalamus-to-habenula synapses. *Neuron* **102**, 120–127.e4 (2019). doi:10.1016/j.neuron.2019.01.025 Medline

53. D. Wang, Y. Li, Q. Feng, Q. Guo, J. Zhou, M. Luo, Learning shapes the aversion and reward responses of lateral habenula neurons. *eLife* **6**, e23045 (2017). doi:10.7554/eLife.23045 Medline

54. D. H. Root, C. A. Mejias-Aponte, J. Qi, M. Morales, Role of glutamatergic projections from ventral tegmental area to lateral habenula in aversive conditioning. *J. Neurosci.*

34, 13906–13910 (2014). doi:10.1523/JNEUROSCI.2029-14.2014 Medline

55. D. S. Zahm, D. H. Root, Review of the cytology and connections of the lateral habenula, an avatar of adaptive behaving. *Pharmacol. Biochem. Behav.* **162**, 3–21 (2017). doi:10.1016/j.pbb.2017.06.004 Medline

56. U. Kim, Topographic commissural and descending projections of the habenula in the rat. *J. Comp. Neurol.* **513**, 173–187 (2009). doi:10.1002/cne.21951 Medline

57. J. Tooley, L. Marconi, J. B. Alipio, B. Matikainen-Ankney, P. Georgiou, A. V. Kravitz, M. C. Creed, Glutamatergic ventral pallidal neurons modulate activity of the habenula-tegmental circuitry and constrain reward seeking. *Biol. Psychiatry* **83**, 1012–1023 (2018). 10.1016/j.biopsych.2018.01.003 Medline

58. A. M. Stamatakis, M. Van Swieten, M. L. Basiri, G. A. Blair, P. Kantak, G. D. Stuber, Lateral hypothalamic area glutamatergic neurons and their projections to the lateral habenula regulate feeding and reward. *J. Neurosci.* **36**, 302–311 (2016). doi:10.1523/JNEUROSCI.1202-15.2016 Medline

59. J. Kaufling, Alterations and adaptation of ventral tegmental area dopaminergic neurons in animal models of depression. *Cell Tissue Res.* **377**, 59–71 (2019). doi:10.1007/s00441-019-03007-9 Medline

60. S. F. Maier, M. E. P. Seligman, Learned helplessness at fifty: Insights from neuroscience. *Psychol. Rev.* **123**, 349–367 (2016). doi:10.1037/rev0000033 Medline

61. I. Lazaridis, O. Tzortzi, M. Weglage, A. Märtin, Y. Xuan, M. Parent, Y. Johansson, J. Fuzik, D. Fürth, L. E. Fenno, C. Ramakrishnan, G. Silberberg, K. Deisseroth, M. Carlén, K. Meletis, A hypothalamus-habenula circuit controls aversion. *Mol. Psychiatry* **24**, 1351–1368 (2019). doi:10.1038/s41380-019-0369-5 Medline

62. D. Knowland, V. Lilascharoen, C. P. Pacia, S. Shin, E. H.-J. Wang, B. K. Lim, Distinct ventral pallidal neural populations mediate separate symptoms of depression. *Cell* **170**, 284–297.e18 (2017). doi:10.1016/j.cell.2017.06.015 Medline

63. A. Friedman, E. Lax, Y. Dikshtein, L. Abraham, Y. Flaumenhaft, E. Sudai, M. Ben-Tzion, G. Yadid, Electrical stimulation of the lateral habenula produces an inhibitory effect on sucrose self-administration. *Neuropharmacology* **60**, 381–387 (2011). doi:10.1016/j.neuropharm.2010.10.006 Medline

64. G. Gangadharan, J. Shin, S.-W. Kim, A. Kim, A. Paydar, D. S. Kim, T. Miyazaki, M. Watanabe, Y. Yanagawa, J. Kim, Y.-S. Kim, D. Kim, H.-S. Shin, Medial septal GABAergic projection neurons promote object exploration behavior and type 2 theta rhythm. *Proc. Natl. Acad. Sci. U.S.A.* **113**, 6550–6555 (2016). doi:10.1073/pnas.1605019113 Medline

65. S. Aznar, Z. X. Qian, G. M. Knudsen, Non-serotonergic dorsal and median raphe projection onto parvalbumin- and calbindin-containing neurons in hippocampus and septum. *Neuroscience* **124**, 573–581 (2004). doi:10.1016/j.neuroscience.2003.12.020 Medline

66. A. Szőnyi, M. I. Mayer, C. Cserép, V. T. Takács, M. Watanabe, T. F. Freund, G. Nyiri, The ascending median raphe projections are mainly glutamatergic in the mouse forebrain. *Brain Struct. Funct.* **221**, 735–751 (2016). doi:10.1007/s00429-014-0935-1 Medline

67. A. M. Barth, LFP_analysis, software, Figshare (2019); https://doi.org/10.6084/m9.figshare.8924771.v1.

68. E. J. Kim, M. W. Jacobs, T. Ito-Cole, E. M. Callaway, Improved monosynaptic neural circuit tracing using engineered rabies virus glycoproteins. *Cell Rep.* **15**, 692–699 (2016). doi:10.1016/j.celrep.2016.03.067 Medline

69. E. Dobó, V. T. Takács, A. I. Gulyás, G. Nyiri, A. Mihály, T. F. Freund, New silver-gold intensification method of diaminobenzidine for double-labeling immunoelectron microscopy. *J. Histochem. Cytochem.* **59**, 258–269 (2011). doi:10.1369/0022155410397998 Medline

70. J. B. West, Z. Fu, T. J. Deerinck, M. R. Mackey, J. T. Obayashi, M. H. Ellisman, Structure-function studies of blood and air capillaries in chicken lung using 3D electron microscopy. *Respir. Physiol. Neurobiol.* **170**, 202–209 (2010). doi:10.1016/j.resp.2009.12.010 Medline

71. D. C. Sterio, The unbiased estimation of number and sizes of arbitrary particles using the disector. *J. Microsc.* **134**, 127–136 (1984). doi:10.1111/j.1365-2818.1984.tb02501.x Medline

72. H. J. G. Gundersen, in *Science on Form: Proceeding of the First International Symposium for Science on Form*, S. Ishizaka, Y. Kato, R. Takaki, J. Toriwaki, Eds. (Springer, 1986), pp. 509–516.

73. C. Schmitz, P. R. Hof, Design-based stereology in neuroscience. *Neuroscience* **130**, 813–831 (2005). doi:10.1016/j.neuroscience.2004.08.050 Medline

74. K. A. Dorph-Petersen, J. R. Nyengaard, H. J. G. Gundersen, Tissue shrinkage and unbiased stereological estimation of particle number and size. *J. Microsc.* **204**, 232–246 (2001). doi:10.1046/j.1365-2818.2001.00958.x Medline

75. M. J. West, L. Slomianka, H. J. Gundersen, Unbiased stereological estimation of the total number of neurons in thesubdivisions of the rat hippocampus using the optical fractionator. *Anat. Rec.* **231**, 482–497 (1991). doi:10.1002/ar.1092310411 Medline

76. P. Yger, G. L. B. Spampinato, E. Esposito, B. Lefebvre, S. Deny, C. Gardella, M. Stimberg, F. Jetter, G. Zeck, S. Picaud, J. Duebel, O. Marre, A spike sorting toolbox for up to thousands of electrodes validated with ground truth recordings in vitro and in vivo. *eLife* **7**, e34518 (2018). doi:10.7554/eLife.34518 Medline

77. C. Rossant, S. N. Kadir, D. F. M. Goodman, J. Schulman, M. L. D. Hunter, A. B. Saleem, A. Grosmark, M. Belluscio, G. H. Denfield, A. S. Ecker, A. S. Tolias, S. Solomon, G. Buzsáki, M. Carandini, K. D. Harris, Spike sorting for large, dense electrode arrays. *Nat. Neurosci.* **19**, 634–641 (2016). doi:10.1038/nn.4268 Medline

78. N. Schmitzer-Torbert, J. Jackson, D. Henze, K. Harris, A. D. Redish, Quantitative measures of cluster quality for use in extracellular recordings. *Neuroscience* **131**, 1–11 (2005). doi:10.1016/j.neuroscience.2004.09.066 Medline

79. M. Aliczki, Z. K. Varga, Z. Balogh, J. Haller, Involvement of 2-arachidonoylglycerol signaling in social challenge responding of male CD1 mice. *Psychopharmacology* **232**, 2157–2167 (2015). doi:10.1007/s00213-014-3846-1 Medline

RESEARCH ARTICLE SUMMARY

NEUROSCIENCE

Brainstem nucleus incertus controls contextual memory formation

András Szőnyi, Katalin E. Sos, Rita Nyilas, Dániel Schlingloff, Andor Domonkos, Virág T. Takács, Balázs Pósfai, Panna Hegedüs, James B. Priestley, Andrew L. Gundlach, Attila I. Gulyás, Viktor Varga, Attila Losonczy, Tamás F. Freund, Gábor Nyiri*

INTRODUCTION: Associative learning is essential for survival, and the mammalian hippocampal neurocircuitry has been shown to play a central role in the formation of specific contextual memories. Contrary to the slow, neuromodulatory role commonly associated with brainstem systems, we discovered a highly specific, spatiotemporally precise, inhibitory ascending brainstem pathway that effectively controls hippocampal fear memory formation. Pyramidal neurons of the dorsal hippocampus CA1 region pair multisensory contextual information (see the figure, panel A, CA3) with direct sensory-related inputs (see the figure, panel A, EntCx). Each memory trace is encoded by a specific subset of pyramidal neurons. Remaining pyramidal cells must be actively excluded from the given memory-encoding process by direct dendritic inhibition, which is executed by somatostatin-positive (SOM) dendrite-targeting interneurons. SOM interneurons are activated by excitatory inputs from the medial septum (MS) upon salient environmental stimuli. Previous models suggested that the subset of memory-forming pyramidal cells escape this dendritic inhibition only by a stochastic, self-regulatory process, in which some SOM interneurons become inactive. However, we hypothesized that this process must be regulated more actively, and SOM interneurons should be inhibited precisely in time, on the basis of subcortical information; otherwise, underrecruitment of pyramidal neurons would lead to unstable memory formation.

RATIONALE: γ-aminobutyric acid (GABA)–releasing inhibitory neurons of the brainstem nucleus incertus (NI) seemed well suited to counterbalance the activation of SOM interneurons, as they specifically project to the stratum oriens of the hippocampus, where most SOM cells arborize. Using cell type–specific neuronal tract tracing, immunoelectron microscopy, and electrophysiological methods, we investigated the targets of NI in the mouse hippocampus, and in the MS, where excitation of SOM cells originates. We also used monosynaptic rabies tracing to identify the inputs of GABAergic NI neurons. Two-photon calcium imaging was used to analyze the response of GABAergic NI fibers to sensory stimuli in vivo. Finally, we used in vivo optogenetics combined with behavioral experiments or electrophysiological recordings to explore the role of the NI in contextual memory formation and hippocampal network activity.

RESULTS: We discovered that NI GABAergic neurons selectively inhibit hippocampal SOM interneurons in the stratum oriens both directly and also indirectly through inhibition of excitatory neurons in the MS (see the figure, panels A and B). We observed that NI GABAergic neurons receive direct inputs from several brain areas that process salient environmental stimuli, including the prefrontal cortex and lateral habenula, and that these salient sensory stimuli (e.g., air puffs, water rewards) rapidly activated hippocampal fibers of NI GABAergic neurons in vivo. Behavioral experiments revealed that optogenetic stimulation of NI GABAergic neurons or their fibers in hippocampus, precisely at the moment of aversive stimuli (see the figure, panel C), prevented the formation of fear memories, whereas this effect was absent if light stimulation was not aligned with the stimuli. However, optogenetic inhibition of NI GABAergic neurons during fear conditioning resulted in the formation of excessively enhanced contextual memories. Optogenetic stimulation of NI GABAergic neurons also changed memory encoding–related hippocampal theta rhythms.

ON OUR WEBSITE

Read the full article at http://dx.doi.org/10.1126/science.aaw0445

CONCLUSION: A role of NI GABAergic neurons may be fine-tuning of the selection of memory-encoding pyramidal cells, on the basis of the relevance and/or modality of environmental inputs. They may also help filter nonrelevant everyday experiences (e.g., those to which animals have already accommodated), by regulating the sparsity of memory-encoding dorsal CA1 pyramidal neurons. NI GABAergic neuron dysfunction may also contribute to dementia-like disorders or pathological memory formation in certain types of anxiety or stress disorders. Our data represent an unexpectedly specific role of an ascending inhibitory pathway from a brainstem nucleus in memory encoding. ■

The list of author affiliations is available in the full article online.
*Corresponding author Email: nyiri.gabor@koki.mta.hu
Cite this article as A. Szőnyi *et al.*, *Science* **364**, eaaw0445 (2019). DOI: 10.1126/science.aaw0445

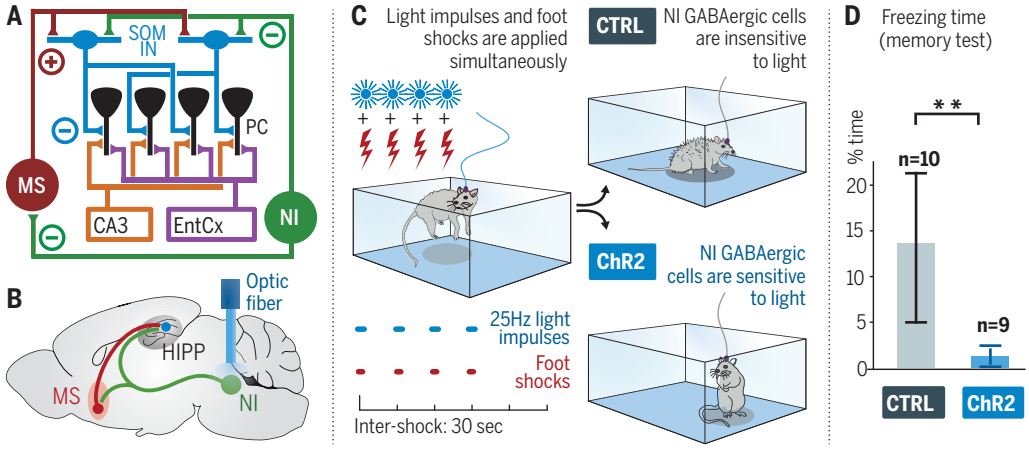

Nucleus incertus (NI) activation prevents memory formation. NI GABAergic neurons regulate contextual memory formation by inhibiting somatostatin interneurons (SOM IN) directly in hippocampus (HIPP) (**A**) and indirectly through inhibition of their excitatory inputs in the medial septum (MS). Pairing optical stimulation (**B**) with aversive stimuli (**C**) eliminates fear memory formation, whereas control mice display normal fear (freezing) after exposure to the same environment a day later (**D**).

RESEARCH ARTICLE

NEUROSCIENCE

Brainstem nucleus incertus controls contextual memory formation

András Szőnyi[1,2], Katalin E. Sos[1,2], Rita Nyilas[3], Dániel Schlingloff[1,2], Andor Domonkos[1], Virág T. Takács[1], Balázs Pósfai[1,2], Panna Hegedüs[1,2], James B. Priestley[3], Andrew L. Gundlach[4], Attila I. Gulyás[1], Viktor Varga[1], Attila Losonczy[3], Tamás F. Freund[1], Gábor Nyiri[1]*

Hippocampal pyramidal cells encode memory engrams, which guide adaptive behavior. Selection of engram-forming cells is regulated by somatostatin-positive dendrite-targeting interneurons, which inhibit pyramidal cells that are not required for memory formation. Here, we found that γ-aminobutyric acid (GABA)–releasing neurons of the mouse nucleus incertus (NI) selectively inhibit somatostatin-positive interneurons in the hippocampus, both monosynaptically and indirectly through the inhibition of their subcortical excitatory inputs. We demonstrated that NI GABAergic neurons receive monosynaptic inputs from brain areas processing important environmental information, and their hippocampal projections are strongly activated by salient environmental inputs in vivo. Optogenetic manipulations of NI GABAergic neurons can shift hippocampal network state and bidirectionally modify the strength of contextual fear memory formation. Our results indicate that brainstem NI GABAergic cells are essential for controlling contextual memories.

Fear memories, which allow mice to avoid future aversive events, are formed by associating aversive stimuli (unconditioned stimulus, US) with their environmental context. The dorsal hippocampus (HIPP) plays an essential role in contextual memory encoding and transmits this information mainly by way of CA1 pyramidal neurons to the cortex (*1*–*3*). Dorsal CA1 pyramidal neurons receive the unified representation of the multisensory context at their proximal dendrites from the CA3 subfield inputs (*4*), whereas the discrete sensory attribute of the aversive stimulus (US) is primarily conveyed by the direct temporo-ammonic pathway to their distal dendrites (*5*–*7*). At the cellular level, the dendritic interactions of these inputs may result in long-term synaptic plasticity in CA1 pyramidal neurons (*8*–*10*), a subset of which can form memory engrams to encode contextual fear memories (*11*). Both intact contextual information processing and direct sensory information–related inputs are required for precise episodic memory formation (*12*–*14*).

The number of dorsal CA1 pyramidal neurons participating in the formation of a given memory engram component must be delicately balanced (*15*). The majority of pyramidal cells must be inhibited, (i.e., excluded from memory encoding at the moment of memory formation), because if the US information reaches too many pyramidal cells, engrams may lack specificity, which may engender memory interference (*16*, *17*). Exclusion of US information in hippocampal CA1 is achieved by somatostatin (SOM)–expressing oriens-lacunosum moleculare (OLM) inhibitory interneurons (*16*). OLM cells establish by far the most abundant local SOM-positive synapses (*16*, *18*). OLM cells selectively inhibit the distal dendrites of CA1 pyramidal neurons, which receive the primary sensory-related inputs from the entorhinal cortex, representing the US (*19*–*22*). Indeed, artificial silencing of dorsal CA1 SOM-positive neurons at the moment of US presentation disrupts fear learning (*16*, *17*). OLM cell activity is synchronized with the US through cholinergic and glutamatergic excitatory inputs from the medial septum (MS) and diagonal bands of Broca. Cholinergic neurons are rapidly and reliably recruited by salient environmental stimuli (*16*, *23*) and strongly innervate hippocampal OLM neurons (*3*, *16*, *21*), whereas MS glutamatergic neurons display locomotion-related activity increases and also innervate hippocampal OLM cells (*22*, *24*).

Conversely, if too many pyramidal neurons are inhibited, allocation to engrams may be insufficient and memory formation would be impaired (*25*). Thus, to balance the sparsity of hippocampal engrams, activation of OLM neurons must be adequately controlled. Inhibitory regulation of OLM neurons would ideally arise also from an extrahippocampal area that integrates relevant environmental information, yet the source of such balancing inhibitory input to OLM neurons was, until now, unknown.

The pontine nucleus incertus (NI), characterized by expression of the neuropeptide relaxin-3 (*26*–*28*), sends an ascending γ-aminobutyric acid (GABA)–mediated pathway to the septo-hippocampal system. NI neurons display activity related to hippocampal theta rhythm and are thought to play an important role in stress and arousal (*29*–*34*).

Here, using cell type–specific neuronal tract tracing, immunogold receptor localization, and electrophysiological methods, we discovered that NI GABAergic neurons selectively inhibit hippocampal SOM-positive neurons both monosynaptically and also indirectly through inhibition of excitatory glutamatergic and cholinergic neurons in the MS. Using monosynaptic rabies tracing, we observed that NI receives direct inputs from several brain areas that process salient environmental stimuli, and indeed, using in vivo two-photon calcium imaging in head-fixed awake mice, we demonstrated that such stimuli rapidly activated hippocampal fibers of NI GABAergic neurons. Behavioral conditioned fear experiments revealed that optogenetic stimulation of NI GABAergic cells or their fibers in the dorsal HIPP, precisely at the moment of US presentation, prevented the formation of contextual fear memories. In parallel, optogenetic stimulation of NI GABAergic neurons decreased the power and frequency of the encoding-related hippocampal theta rhythm in vivo. By contrast, optogenetic inhibition of NI GABAergic neurons during fear conditioning resulted in the formation of excessively enhanced contextual memories. These findings demonstrate the fundamental importance of NI GABAergic neurons in hippocampus-dependent episodic memory formation.

Results

NI GABAergic neurons selectively inhibit hippocampal SOM-positive interneurons

We injected Cre-dependent adeno-associated tracer virus (AAV5, see supplementary materials and methods) into the NI of vesicular GABA transporter (vGAT)–Cre mice to reveal the projections of GABAergic neurons of NI (Fig. 1A). It demonstrated that NI GABAergic fibers selectively project to the stratum oriens of the HIPP and the hilus of the dentate gyrus (Fig. 1B). SOM neurons are typically found only in these subregions of HIPP (*35*). GABAergic NI nerve terminals were all positive for the neuropeptide relaxin-3 (Fig. 1C). Double retrograde tracing in wild-type (WT) mice, using the retrograde tracers FluoroGold (FG) and cholera toxin B (CTB), revealed that NI and HIPP are connected almost exclusively ipsilaterally (fig. S1, A to C). Using Cre-dependent AAV5 viral tracing, we also confirmed that brainstem areas surrounding NI do not send GABAergic projections to the HIPP (fig. S2, A to F) and NI GABAergic neurons do not use glutamate, glycine, acetylcholine, serotonin, or other monoamines as neurotransmitters (fig. S2, G to J).

To identify the targets of NI GABAergic fibers in the HIPP, we injected Cre-dependent AAV5 tracer virus into the NI of vGAT-Cre-tdTomato

[1]Laboratory of Cerebral Cortex Research, Department of Cellular and Network Neurobiology, Institute of Experimental Medicine, Hungarian Academy of Sciences, Budapest, Hungary. [2]János Szentágothai Doctoral School of Neurosciences, Semmelweis University, Budapest, Hungary. [3]Department of Neuroscience, Mortimer B. Zuckerman Mind Brain Behavior Institute, Kavli Institute for Brain Science, Columbia University, New York, NY, USA. [4]Peptide Neurobiology Laboratory, The Florey Institute of Neuroscience and Mental Health, Parkville, Victoria, Australia.
***Corresponding author. Email: nyiri.gabor@koki.mta.hu**

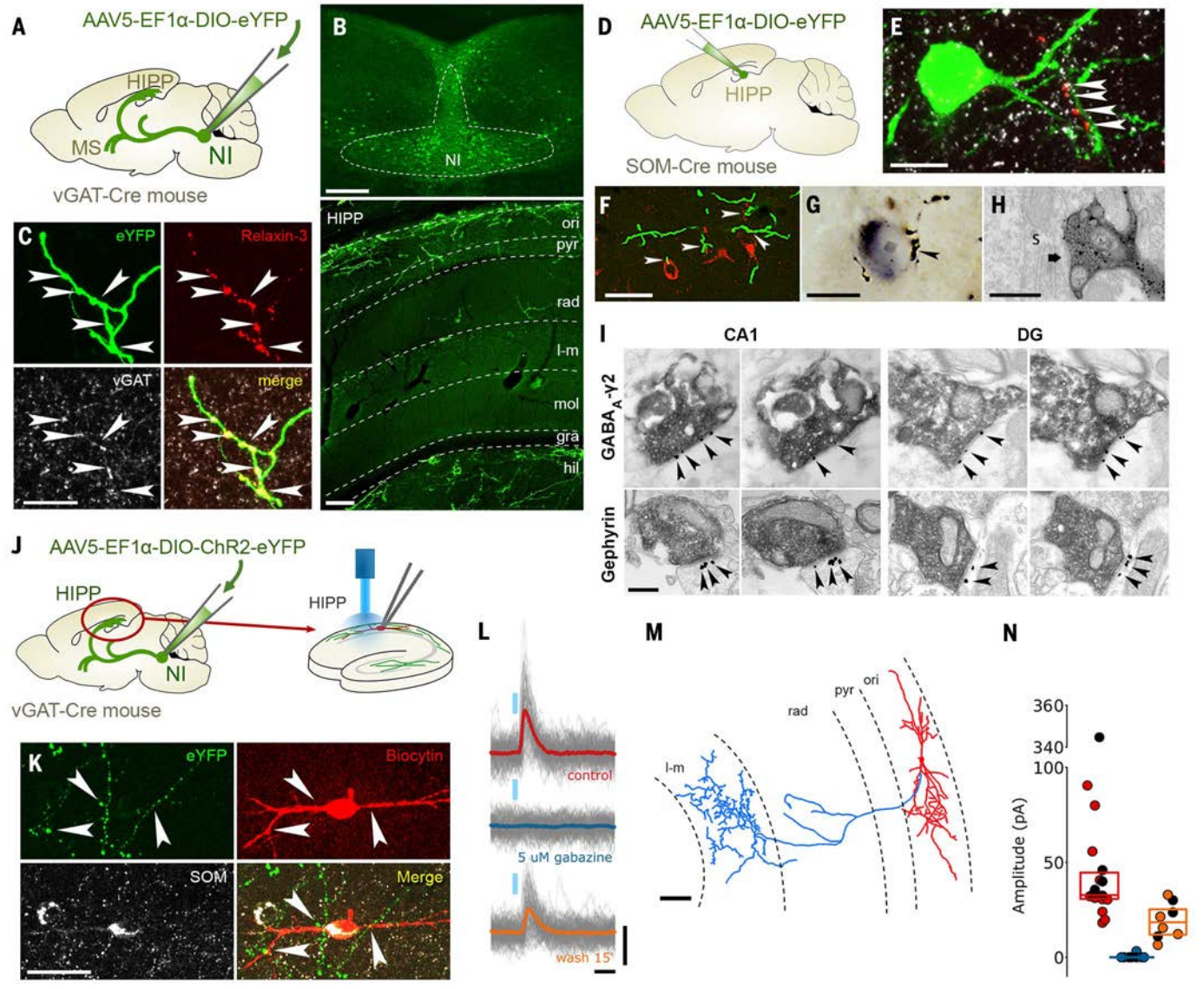

Fig. 1. NI neurons target HIPP SOM-positive neurons with GABAergic synapses. (**A**) AAV2/5-EF1α-DIO-eYFP or AAV2/5-EF1α-DIO-mCherry was injected into the NI of vGAT-Cre mice (n = 7). (**B**) Images illustrate an injection site (upper panel) and the layer-specific distribution pattern of GABAergic NI fibers in the hippocampus (HIPP) stratum oriens and hilus (lower panel) where SOM neurons are known to be abundant. Scale bars: 200 μm. (**C**) NI fibers (green) in the HIPP are immunopositive for relaxin-3 (red) and vGAT (white). Scale bar: 10 μm. (See supplementary text for Fig. 1.) (**D**) AAV2/5-EF1α-DIO-eYFP was injected into the bilateral hippocampus of SOM-Cre mice (n = 2). (**E**) Relaxin-3–positive NI fibers (red) establish synaptic contacts, marked by gephyrin (white), on SOM-positive interneurons (green) in the HIPP. Scale bar: 10 μm. (See supplementary text for Fig. 1.) (**F**) eYFP-positive NI GABAergic fibers (green) in the HIPP establishing putative contacts (white arrowheads) with SOM-positive interneurons (red). Scale bar: 20 μm. (**G**) NI GABAergic fibers (labeled with brown silver-gold-intensified-DAB precipitate) establish synaptic contact with a SOM-positive interneuron (labeled with black DAB-Ni precipitate) in the stratum oriens of dorsal CA1. Black arrowhead indicates the NI nerve terminal shown in (G). Scale bar: 10 μm. (**H**) The same terminal marked in (F) establishing a symmetrical synaptic contact (black arrow) on the soma (s) of the SOM-positive interneuron. Scale bar: 600 nm. (**I**) Electron microscopy (EM) images of serial sections of AAV-eYFP–positive NI terminals (immunoperoxidase labeling, black DAB precipitate) that establish symmetrical synaptic contacts in the CA1 stratum oriens or in the hilus (DG), containing the $GABA_A$ receptor γ2 subunit (upper row) and the scaffolding protein gephyrin (lower row). The immunogold particles labeling the postsynaptic proteins are marked by black arrowheads. Scale bar: 300 nm. (See supplementary text for Fig. 1). (**J**) For in vitro recordings, AAV2/5-EF1α-DIO-ChR2-eYFP was injected into the NI of vGAT-Cre mice (n = 9). After 6 weeks, 300-μm-thick horizontal slices were prepared from the HIPP and transferred into a dual superfusion chamber. Interneurons located in the stratum oriens were whole-cell patch-clamped in voltage-clamp mode, and inhibitory postsynaptic currents (IPSCs) evoked by the optogenetic stimulation of NI GABAergic fibers were measured. (See supplementary materials and methods and supplementary text for Fig. 1.) (**K**) A representative recorded cell (biocytin labeling, red) identified as a SOM-positive interneuron (white). Note that the eYFP-positive NI GABAergic fibers (green) with putative contacts target this neuron (arrowheads). Scale bar: 30 μm. (**L**) Optogenetically evoked GABAergic IPSCs of interneuron in (K). One hundred consecutive traces evoked by 2-ms light pulses are overlaid with gray in each condition. Responses are strong in controls (average in red) but were completely abolished by 5 μM gabazine (average in blue) and partially recovered after 15 min of washout (average in orange). Scale bars: 10 ms, 40 pA. (**M**) Morphological reconstruction of the OLM cell shown in (K). Scale bar: 50 μm. (**N**) Postsynaptic current amplitude distribution from all 18 recorded neurons. Identified O-LM cells are filled black dots. (See supplementary text for Fig. 1.)

reporter mice (supplementary materials and methods and fig. S1D). Double immunoperoxidase reactions and correlated light- and electron microscopy revealed that NI fibers establish synaptic contacts with tdTomato-expressing GABAergic interneurons in the HIPP (at least 87% were identified as interneurons, fig. S1E). Then, using Cre-dependent AAV5 viral labeling of SOM interneurons in SOM-Cre mice, we found that most of the relaxin-3–positive NI terminals (at least 62%) targeted SOM-positive cells (Fig. 1, D and E). The vast majority of SOM-positive CA1 fibers are present in stratum lacunosum-moleculare, which clearly indicated that they originate from OLM cells as described before (*16*, *18*, *36*). Using Cre-dependent AAV5 viral labeling in vGAT-Cre mice, we observed that NI GABAergic fibers establish symmetrical synapses typically with SOM-positive interneurons (Fig. 1, F to H) that also contain the previously identified markers (*37*) metabotropic glutamate receptor 1α (mGluR1α) and parvalbumin (PV; fig. S1, F to H). These results demonstrate that the primary target of NI fibers in the HIPP is the dendrite-targeting SOM-positive interneurons, the local effect of which mostly originate from OLM cells. Using a combination of CTB and Cre-dependent AAV5 in vGAT-Cre mice, we observed that some SOM-positive GABAergic interneurons in the HIPP, which project to the subiculum or the MS (*38*, *39*), also receive contacts from the NI (supplementary materials and methods and fig. S1, I to P).

Using correlated light- and immunoelectron microscopic analysis, we found that the synapses of NI fibers are symmetrical and contain $GABA_A$ receptor γ2 subunits and the GABAergic synapse-specific scaffolding protein gephyrin, postsynaptically in the HIPP (Fig. 1I).

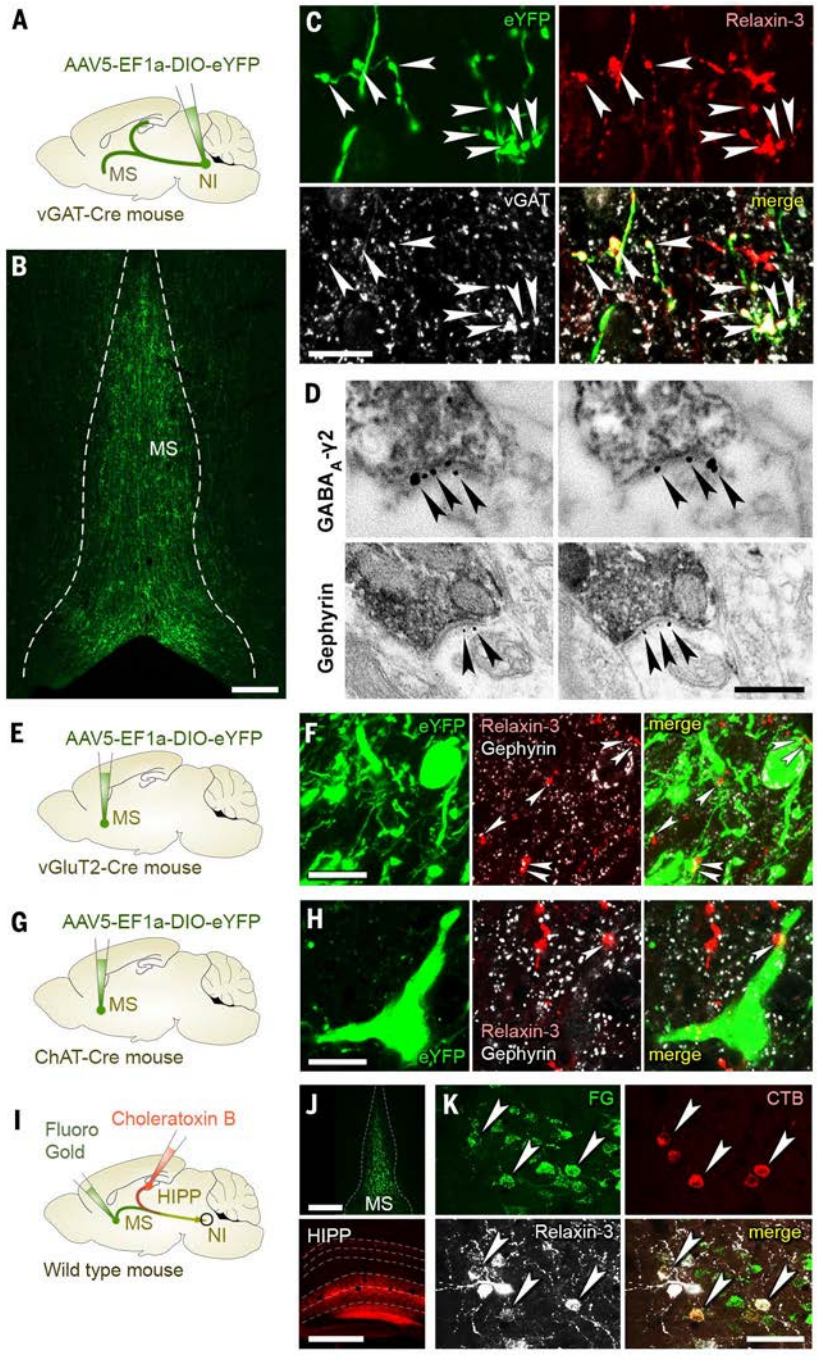

Fig. 2. NI GABAergic neurons innervate excitatory medial septal neurons and HIPP simultaneously. (**A**) AAV2/5-EF1α-DIO-eYFP or AAV2/5-EF1α-DIO-mCherry was injected into the NI of vGAT-Cre mice (n = 7). (**B**) NI GABAergic fibers strongly innervate the medial septum (MS). Scale bar: 200 μm. (**C**) NI GABAergic fibers in the MS (green) are immunopositive for relaxin-3 (red) and vGAT (white), indicated by white arrowheads. Scale bar: 10 μm. (For statistical data, see supplementary text for Fig. 2.) (**D**) EM images of serial sections of relaxin-3–positive NI terminals (immunoperoxidase labeling, black DAB precipitate) reveal the presence of symmetrical synapses in the MS, containing the $GABA_A$ receptor γ2 subunit (upper row) or the scaffolding protein gephyrin (lower row). The immunogold particles labeling the postsynaptic proteins are marked by black arrowheads. Scale bar: 300 nm. (See supplementary text for Fig. 2). (**E**) AAV2/5-EF1α-DIO-eYFP was injected into the NI of vGluT2-Cre mice (n = 2). (**F**) vGluT2-positive neurons (green) are frequently innervated by relaxin-3–positive fibers (red), establishing gephyrin-positive (white) synaptic contacts (white arrowheads) on their dendrites. Scale bar: 10 μm. (See supplementary text for Fig. 2.) (**G**) AAV2/5-EF1α-DIO-eYFP was injected into the NI of ChAT-Cre mice (n = 2). (**H**) ChAT-positive neurons (green) were innervated by relaxin-3–positive fibers (red), establishing gephyrin-positive (white) synaptic contacts (white arrowhead) on their dendrites. Scale bar: 10 μm. (See supplementary text for Fig. 2.) (**I**) Double retrograde tracing using FG in the MS and CTB in the bilateral hippocampi, respectively, in wild-type mice (n = 3). (**J**) Representative injection sites revealing green FG labeling in the MS and red CTB labeling in the hippocampus, respectively. The border of the MS and the hippocampal layers are labeled with white dashed lines. Scale bars: 500 μm. (**K**) Dual projecting neurons containing FG labeling (green) and CTB labeling (red) were frequently detected in the NI, most of which were relaxin-3 positive (white neurons, indicated by white arrowheads). Although retrograde tracers cannot fill the entire HIPP or MS, at least 50 out of 135 HIPP-projecting neurons also projected to the MS, and most of these neurons (at least 34 out of 50) were positive for relaxin-3. Scale bar: 50 μm.

dc_1777_20

To investigate the functional properties of these GABAergic synapses, we injected channelrhodopsin (ChR2)–containing Cre-dependent AAV5 into the NI of vGAT-Cre mice and, 6 to 12 weeks later, we cut horizontal slices from the HIPP for in vitro optogenetic experiments (Fig. 1J, supplementary materials and methods, and figs. S3A and S4A). Light stimulation of hippocampal NI GABAergic fibers reliably evoked gabazine-sensitive inhibitory postsynaptic potentials (IPSCs) from voltage-clamped interneurons located in the stratum oriens of CA1 (Fig. 1, K to N, and fig. S3, B and C), indicating $GABA_A$-receptor–dependent GABAergic neurotransmission in these synapses. Although NI GABAergic neurons express relaxin-3 and HIPP SOM neurons express its receptor (*28*, *40*), gabazine could block all currents at these time scales. Recorded neurons

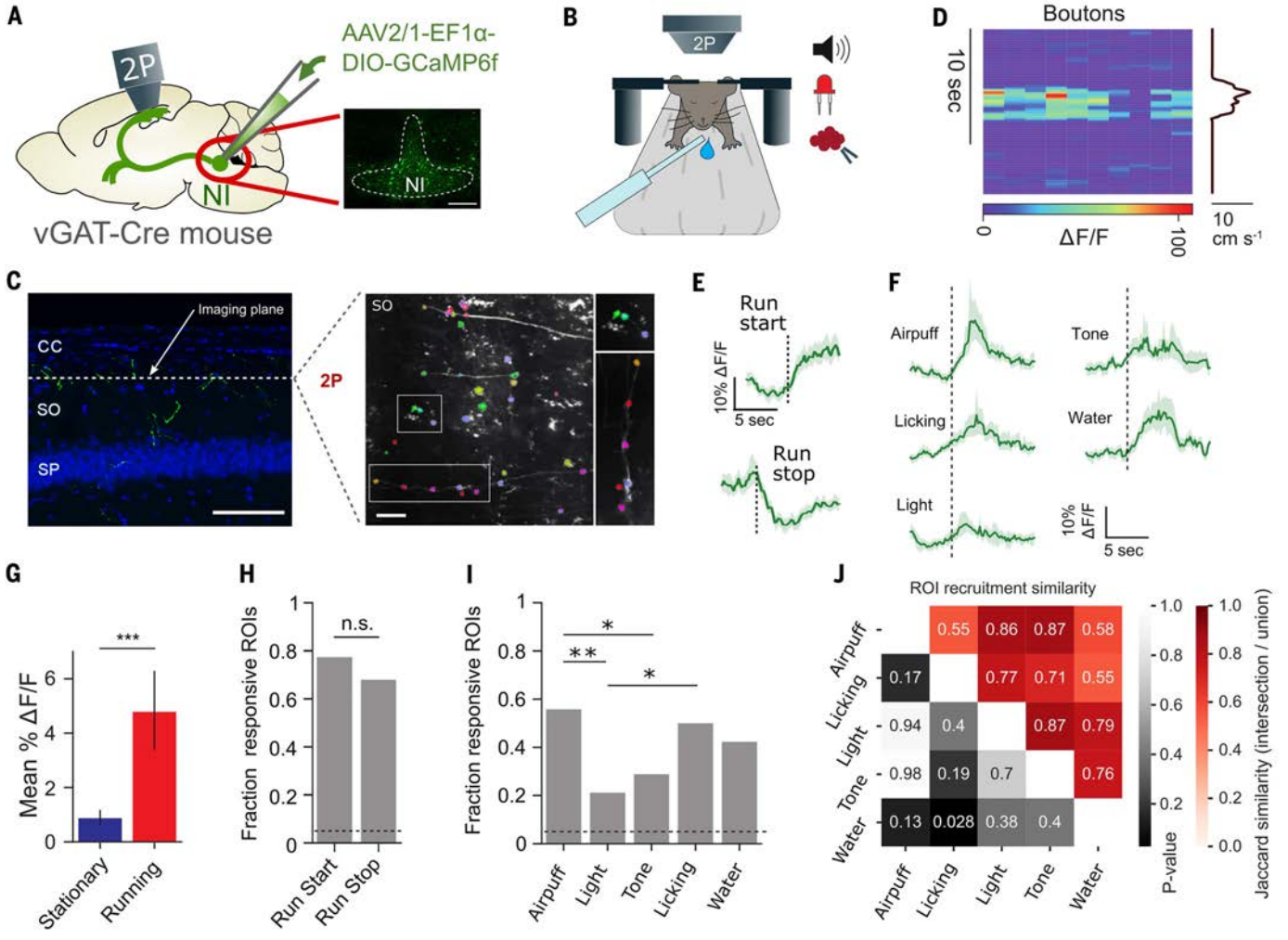

Fig. 3. NI fibers are activated by relevant sensory stimuli in vivo. (**A**) Experimental design of the in vivo 2P calcium-imaging experiments. AAV2/1-EF1a-DIO-GCaMP6f was injected into the NI of vGAT-Cre mice (n = 5). After recovery, a cranial window implant was placed over the HIPP, and 2P imaging was performed. The inset on the right illustrates a representative virus injection site in the NI. Scale bar: 200 μm. (**B**) Schematic of 2P imaging and behavioral apparatus. Mice were head-fixed under a 2P microscope on a linear treadmill and permitted to move freely during random foraging experiments. During salience experiments, mice were immobilized and randomly presented with sensory stimuli (water, air puffs, auditory tone, and light). (**C**) Left: Laser scanning confocal microscopic image of GCaMP6f-expressing fibers (green) along with cell nuclei (blue) in the dorsal CA1 region of the HIPP. Scale bar: 100 μm. CC: corpus callosum, SO: stratum oriens, SP: stratum pyramidale. Right: 2P field of view of GCaMP6f-expressing NI GABAergic axons in hippocampal CA1. Exemplary fibers with ROIs (colored polygons around axonal boutons) are enlarged on the right. Scale bar: 20 μm. (**D**) A representative random foraging experiment. Left: Fluorescence calcium signal in NI GABAergic axonal boutons; right: animal velocity. (**E**) Running event–triggered signal averages during random foraging experiments (grand mean of ROIs + 99% confidence interval (CI), for ROIs with significant responses to each event, bootstrap test, n = 3 mice). (**F**) Signal averages triggered by delivery of sensory stimuli during movement-restrained salience experiments (grand mean of ROIs + 99% CI, for ROIs with significant responses to each stimulus, bootstrap test, n = 3 mice). (**G**) Average fluorescence during stationary and running periods differed significantly. We measured 54 responsive boutons (***p < 0.001, Wilcoxon signed-rank test). (**H**) Fraction of ROIs responsive to the onset and offset of running. Dashed line indicates the 0.05 chance level of the PETH bootstrap test. There was no statistically significant difference between the two data groups (n.s.: not significant, p > 0.05, Z-test). (**I**) Fraction of ROIs responsive to sensory stimuli. Dashed line indicates the 0.05 chance level of the PSTH bootstrap test. Light stimuli recruited significantly fewer boutons than licking and air puff, and auditory tones also recruited a smaller fraction of boutons compared to air puff (*p < 0.05, **p <0.01, ***p < 0.001, Z-test between groups, Bonferroni-corrected p value). (**J**) Measure of overlap between the set of ROIs with significant responses to each stimulus (Jaccard similarity values indicated in red boxes). Differences among the fractions of responding ROIs depending on different stimuli were tested using permutation test (p values indicated in grayscale-colored boxes).

Nyiri Gábor MTA doktori értekezés oldalszáma : 162

were filled with biocytin, and post-hoc neurochemical analysis of filled neurons revealed that at least 12 of 18 cells were clearly SOM-positive (Fig. 1K). Although not all recorded neurons could be fully morphologically reconstructed, six of them were unequivocally identified as typical dendrite-targeting OLM neurons (Fig. 1M). Altogether we found that 14 out of 18 randomly recorded and NI GABAergic cells targeted neurons that were either SOM-positive or SOM-false-negative OLM cells, suggesting that at least 78% of the target cells are SOM-positive. In the immunohistochemistry described above, this number was at least 62%. Because only 14% of CA1 interneurons are SOM-positive (*41*), these numbers suggest a very high target specificity for SOM-containing interneurons. Light stimulation suggested that NI GABAergic synapses display short-term synaptic depression at higher stimulation frequencies (30 to 50 Hz, fig. S3C) that was not observed at lower frequencies (5 to 20 Hz, fig. S3C). These data clearly demonstrate that NI fibers directly target SOM–positive dendrite-targeting OLM interneurons in the HIPP with functional GABAergic synapses.

NI GABAergic neurons inhibit MS neurons that excite OLM interneurons

HIPP SOM neurons receive their main extrahippocampal excitatory inputs from glutamatergic and cholinergic neurons of the MS (*16*, *21*, *22*). We hypothesized that NI may also inhibit HIPP SOM-positive OLM cells indirectly, by inhibition of these excitatory input neurons in the MS.

Using Cre-dependent AAVs to label GABAergic NI neurons in vGAT-Cre mice (Fig. 2A), we determined that MS is strongly innervated by relaxin-3–positive NI GABAergic fibers (Fig. 2, B and C). NI neurons established $GABA_A$ receptor γ2 subunit-positive and gephyrin-positive symmetrical synapses in MS (Fig. 2D). Using Cre-dependent AAV5 viral tracing, we also confirmed that brainstem areas surrounding NI do not send GABAergic projections to the MS (fig. S2, A to H).

To investigate whether GABAergic NI fibers target the glutamatergic or cholinergic cells in the MS, we injected Cre-dependent AAV5 into the NI of vesicular glutamate transporter 2 (vGluT2)–Cre (Fig. 2E) or choline acetyltransferase (ChAT)–Cre (Fig. 2G) mice. These experiments revealed that relaxin-3–positive terminals of the NI frequently establish gephyrin-positive synapses on glutamatergic (at least 55%, Fig. 2F) and cholinergic (at least 8%, Fig. 2H) cells in the MS, indicating that NI projections can also inhibit the main extrahippocampal excitatory input to hippocampal OLM cells.

In addition, we performed double retrograde tracing by injecting FG into the MS and CTB into the HIPP of WT mice bilaterally (Fig. 2, I and J). We observed that many (at least 37%) of the individual NI GABAergic neurons that target HIPP also send axon collaterals to the MS (Fig. 2K). These data indicate that NI GABAergic neurons can synchronously inhibit HIPP OLM cells both directly in HIPP and indirectly by inhibition of their excitatory afferents in the MS.

NI GABAergic fibers in HIPP are rapidly activated by salient environmental stimuli in vivo

These anatomical and in vitro physiological data indicated that NI GABAergic neurons would be ideal to counterbalance the MS activation of OLM cells, which would permit fine-tuned regulation of pyramidal cell participation in memory formation. To test whether NI GABAergic neurons indeed respond to sensory stimuli and behavioral state, we combined two-photon (2P) calcium imaging with behavioral monitoring in awake mice. We injected AAV2/1-EF1a-DIO-GCaMP6f into the NI of vGAT-Cre mice and implanted a chronic imaging window superficial to the dorsal CA1 of the HIPP (Fig. 3A). After recovery, water restriction, and habituation to head restraint, we engaged mice in two different behavioral paradigms while imaging the fluorescent activity of GCaMP6f-positive NI boutons in the stratum oriens of the dorsal CA1 (Fig. 3, B and C).

In the first experiment, the random foraging task, mice ran on a cue-less burlap belt in search of water rewards, which were delivered at three random locations on each lap. Bouton fluorescence was increased during periods of running (Fig. 3D), consistent with previous observations of increased neural activity in the NI during hippocampal theta rhythm (*32*). To investigate how calcium dynamics in NI GABAergic axon terminals are modulated by locomotion state transitions, we examined GCaMP6f fluorescence changes in NI-GABAergic boutons in relation to the onset and offset of locomotion. We calculated peri-event time histograms (PETHs) aligned to running-start and running-stop events (Fig. 3E) and found that the majority of dynamic NI boutons were similarly modulated by the onset and offset of running (Fig. 3H).

In the second behavioral paradigm, the salience task, we explored whether discrete stimuli of various sensory modalities also modulate the activity of NI GABAergic axonal boutons in the HIPP, while the mouse was stationary (*16*, *42*). The movements of mice were restrained while different sensory cues (aversive air puffs, water rewards, auditory tones, and light flashes) were randomly presented to them (Fig. 3, B and F). We calculated peristimulus time histograms (PSTHs) and observed calcium responses in NI boutons to all types of stimuli. Salient stimuli with special valence such as aversive air puff and water reward had particularly strong effects on bouton calcium dynamics (Fig. 3F) and also activated a larger fraction of NI boutons (Fig. 3I).

Finally, to determine the stimulus-dependent variability of the responses of NI terminals in the HIPP, we analyzed the Jaccard similarity of boutons in the salience experiments, on the basis of their stimulus preference. Although all stimuli recruited an overlapping population of boutons, we detected some differences among the activated bouton populations (Fig. 3J).

NI GABAergic neurons receive monosynaptic inputs from areas processing salient environmental stimuli

The above-mentioned data demonstrate that NI GABAergic neurons transmit information on salient environmental modalities from the brainstem to the HIPP. To directly identify upstream brain areas containing neurons that synaptically target the GABAergic neurons of NI, we used mono-transsynaptic rabies tracing (*43*). We used Cre-dependent helper viruses and G protein–deleted rabies virus in vGAT-Cre mice (supplementary materials and methods and Fig. 4A). These studies assessed the level of convergence onto NI GABAergic neurons, and thus the type of inputs that can fine-tune HIPP memory formation through the modulation of NI GABAergic cells. The specificity of the virus expression was tested in WT mice (Fig. 4B).

We detected an extensive convergence of inputs onto NI GABAergic neurons, with prominent synaptic inputs from several brain areas highly relevant to associated behaviors, including the prefrontal cortex, lateral habenula, zona incerta, mammillary areas, and raphe regions. These afferent regions play essential roles in movement, aversive or rewarding stimulus processing, and memory encoding (Fig. 4C; for details, see table S6). We did not find rabies-labeled neurons in the HIPP, confirming the lack of direct output from HIPP to NI.

Rabies labeling revealed that NI GABAergic neurons are targeted by the lateral habenula (LHb; Fig. 4C), which plays a fundamental role in aversive behavior (*44*, *45*). To confirm that the glutamatergic neurons of the LHb target the NI, we injected Cre-dependent AAV5 into the LHb of vGluT2-Cre mice (Fig. 4, D and E) and detected strong fiber labeling in NI (Fig. 4F).

Rabies tracing also revealed that NI GABAergic neurons receive a strong monosynaptic input from the median raphe region (MRR; Fig. 4C and table S6). HIPP memory formation is sensitive to stress, and NI neurons express functional corticotrophin-releasing hormone (CRH) receptor 1 that plays a role in stress processing (*32*, *46*). MRR contains a small CRH-positive cell population (*47*). Injection of Cre-dependent AAV5 into the MRR of CRH-Cre mice (Fig. 4, G and H) revealed that MRR is a prominent source of CRH signaling in the NI (Fig. 4I).

MS cholinergic neurons are known to transmit a rapid and precisely timed attention signal to cortical areas (*23*), whereas the activity of MS glutamatergic (vGluT2-positive) neurons is correlated with movement and HIPP theta rhythm (*22*, *24*). We observed that virtually none of the NI projecting rabies-labeled MS neurons were positive for ChAT, parvalbumin, or calbindin (table S7). Injections of Cre-dependent AAV5 into the MS of ChAT-Cre mice confirmed the lack of cholinergic innervation of NI from MS.

Because vGluT2 is not detectable in neuronal cell bodies, we directly labeled MS vGluT2-positive glutamatergic cells, using injections of Cre-dependent AAV5 into the MS of vGluT2-Cre mice (Fig. 4, J and K), and observed that MS

glutamatergic neurons provide a strong input into the NI (Fig. 4L).

NI GABAergic cells regulate hippocampal network activity

HIPP theta activity is essential for contextual memory formation (*25*, *48*) and typical during exploration (*49*, *50*); therefore, we investigated the effects of NI GABAergic neurons on HIPP theta activity. We injected ChR2-containing Cre-dependent AAV5 into the NI of vGAT-Cre mice. Later, we implanted an optic fiber over the NI (fig. S4A) and placed a multichannel linear probe into the dorsal HIPP (Fig. 5, A to D). After recovery and habituation, HIPP rhythmic activities were recorded in an open field or on a linear track, where mice could behave freely (Fig. 5B). Blue light stimulation was triggered by the experimenter during every recording condition, while electrophysiological activity in HIPP was continuously recorded.

As revealed by wavelet analysis of the HIPP local field potentials (LFP), stimulation of NI GABAergic neurons significantly decreased the power of HIPP theta activity (Fig. 5, E to G, and fig. S5, A to D), whereas no such effect occurred after introduction of light into a dummy fiber implanted in the same mice (supplementary materials and methods; Fig. 5, E to G; and fig. S5, C and D). The effect was most prominent in the high-theta range (8 to 12 Hz) and less so in the low-theta range (5 to 8 Hz), and it was generally stronger when mice actively explored their environment (Fig. 5G). Stimulation of NI GABAergic neurons also reduced HIPP theta power during REM sleep (fig. S5, D and E). Current source

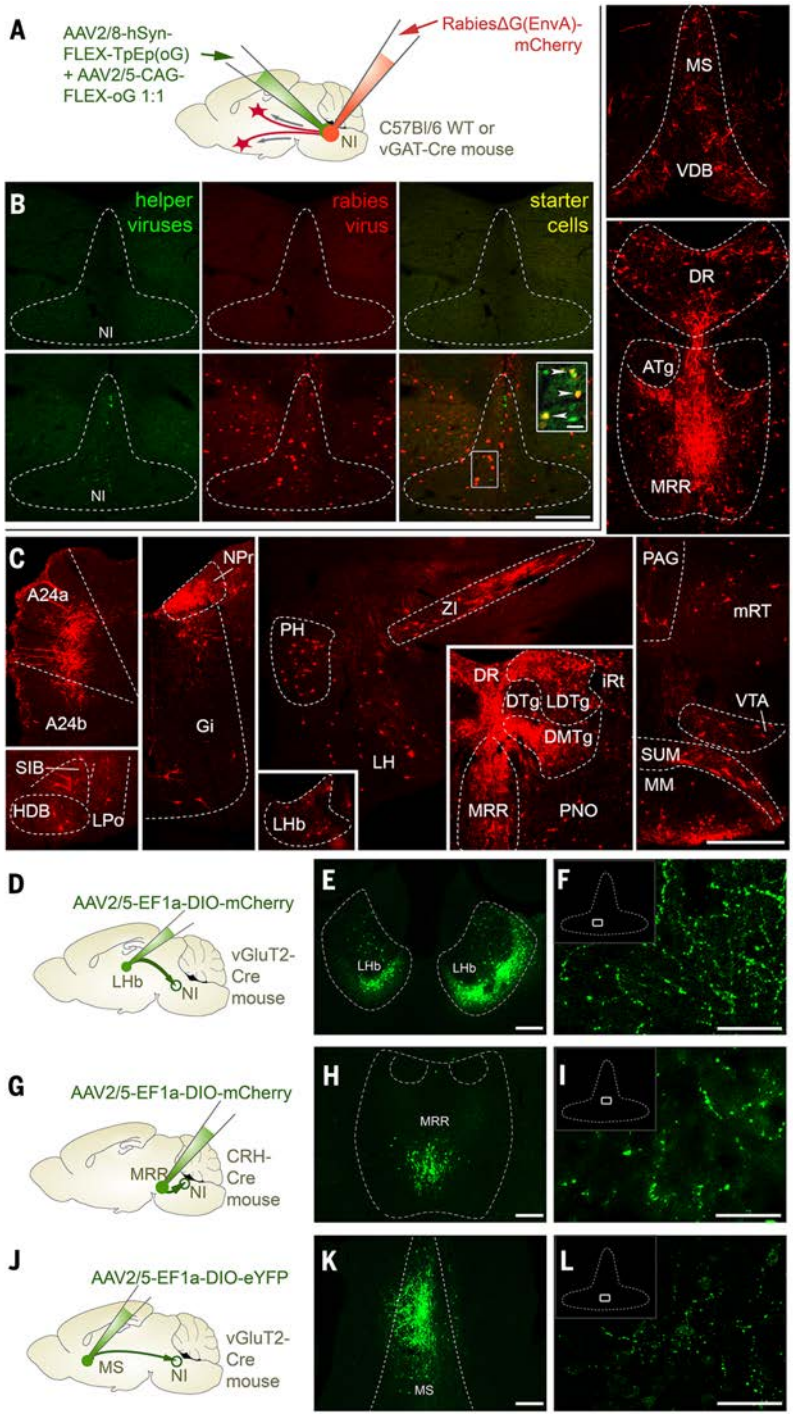

Fig. 4. NI receives monosynaptic input from brain areas processing salient environmental stimuli. (**A**) A cocktail of helper viruses [AAV2/8-hSyn-FLEX-TpEp(oG) + AAV2/5-CAG-FLEX-oG in a ratio of 1:1] was injected into the NI of vGAT-Cre (*n* = 3) or C57Bl/6 WT (*n* = 2) mice, followed by an injection of RabiesΔG(EnvA)-mCherry 2 weeks later. (**B**) Representative injection sites show the lack of virus expression in WT mice upper images, and there is strong helper (green) and rabies (red) virus expression present in the NI of vGAT-Cre mice lower images. Inset illustrates some starter neurons expressing both viruses, indicated by white arrowheads. Scale bar for large images: 200 μm. Scale bar for inset: 20 μm. (**C**) Confocal images illustrate neurons in different brain areas that establish synapses on NI GABAergic neurons. (For abbreviations, see supplementary text for Fig. 4.) (**D**) AAV2/5-EF1α-DIO-mCherry was injected into the LHb of vGluT2-Cre mice (*n* = 2). (**E**) A representative injection site reveals mCherry expression in the vGluT2-positive neurons of the bilateral LHb. Visualized in green for better visibility. Scale bar: 200 μm. (**F**) Fibers of LHb vGluT2-positive cells heavily innervate NI. Scale bar: 100 μm. (**G**) AAV2/5-EF1α-DIO-mCherry was injected into the MRR of CRH-Cre mice (*n* = 3). (**H**) A representative injection site illustrates mCherry expression in the CRH-positive neurons of the MRR. Visualized in green for better visibility. Scale bar: 200 μm. (**I**) Fibers of MRR CRH-positive neurons heavily innervate NI. Scale bar: 100 μm. (**J**) AAV2/5-EF1α-DIO-eYFP was injected into the MS of vGluT2-Cre mice (*n* = 2). (**K**) A representative injection site reveals eYFP expression in the vGluT2-positive neurons of the MS. Scale bar: 200 μm. (**L**) Fibers of MS vGluT2-positive neurons extensively innervate NI. Scale bar: 100 μm.

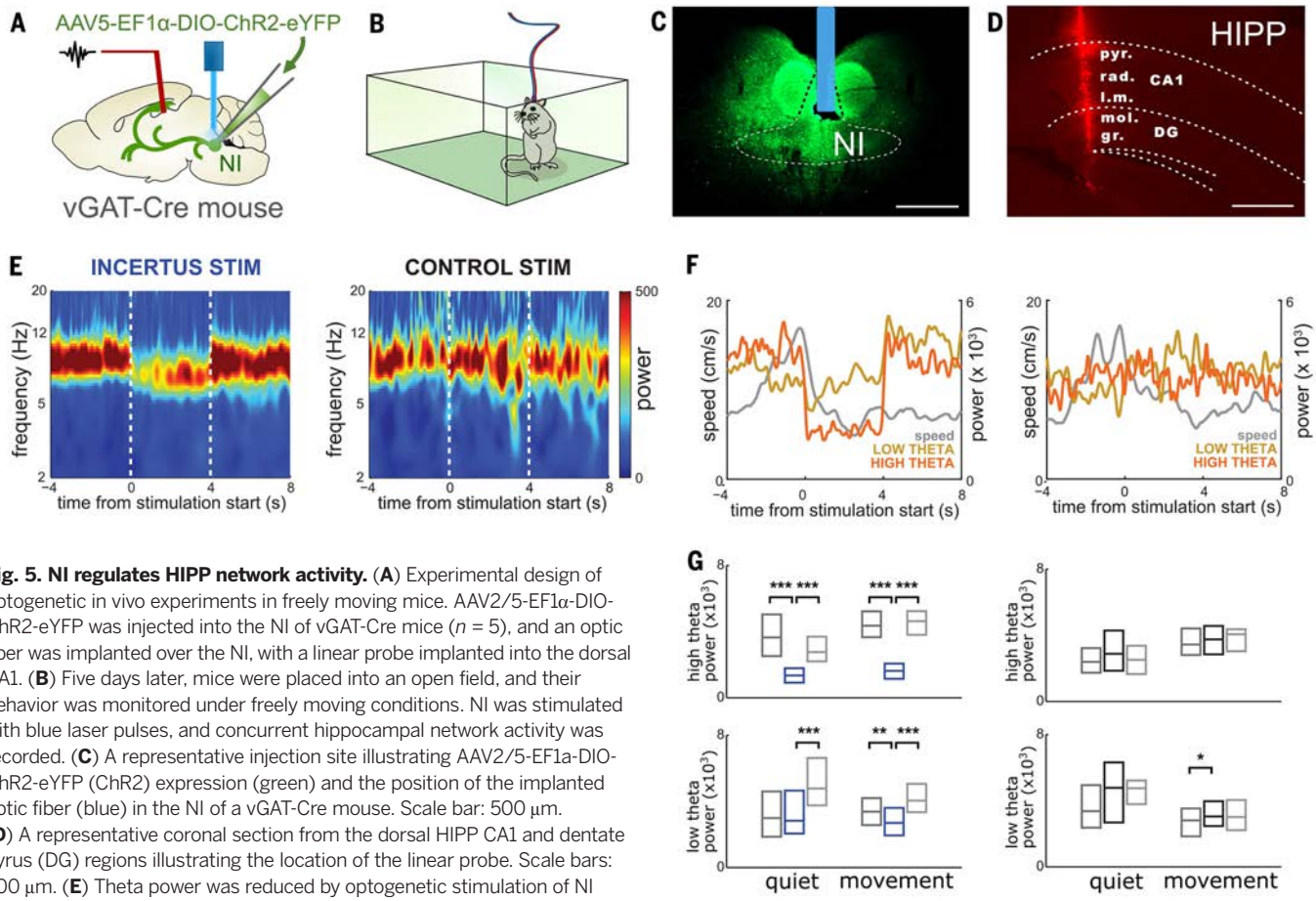

Fig. 5. NI regulates HIPP network activity. (**A**) Experimental design of optogenetic in vivo experiments in freely moving mice. AAV2/5-EF1α-DIO-ChR2-eYFP was injected into the NI of vGAT-Cre mice (n = 5), and an optic fiber was implanted over the NI, with a linear probe implanted into the dorsal CA1. (**B**) Five days later, mice were placed into an open field, and their behavior was monitored under freely moving conditions. NI was stimulated with blue laser pulses, and concurrent hippocampal network activity was recorded. (**C**) A representative injection site illustrating AAV2/5-EF1a-DIO-ChR2-eYFP (ChR2) expression (green) and the position of the implanted optic fiber (blue) in the NI of a vGAT-Cre mouse. Scale bar: 500 μm. (**D**) A representative coronal section from the dorsal HIPP CA1 and dentate gyrus (DG) regions illustrating the location of the linear probe. Scale bars: 500 μm. (**E**) Theta power was reduced by optogenetic stimulation of NI GABAergic cells in ChR2-expressing mice, as revealed by the time-frequency decomposition of pyramidal LFP with continuous wavelet transform. Frequency range of 1 to 20 Hz is shown; for expanded scale, see fig. S5C. Averages of all NI GABAergic neurons (left) and control (right) stimulation sessions in one representative mouse during running are shown. Boundaries of the stimulation periods are marked with white dashed lines. (**F**) Separate analysis of NI stimulation on low-theta (5 to 8 Hz, yellow graph) and high-theta (8 to 12 Hz, orange graph) band power with concurrent speed (gray graph). NI GABAergic cell stimulation was controlled manually, while mice were running on a linear track, and tests started when mice started to demonstrate active exploratory behavior. NI stimulation strongly reduced high-theta band power and also moderately reduced low-theta band power, independently from the speed of the animal (left). This effect was absent in control stimulations (left). The mean of all stimulation sessions in four mice is shown. (**G**) High- (top) and low-theta (bottom) power during quiet (speed < 4 cm/s) and movement (speed > 4 cm/s) periods of stimulation sessions. Theta power during 4-s stimulation versus 4-s pre- and poststimulation segments was compared. Medians and interquartile ranges are shown. The instant power values were averaged per stimulation sessions. Statistical difference between the segments was tested by two-sided Wilcoxon signed-rank test (*p < 0.05, **p < 0.01, ***p < 0.001).

Fig. 6. NI regulates the establishment of contextual fear memories. (**A**) Experimental design of contextual fear-conditioning experiments with optogenetic stimulation of NI GABAergic neurons. ChR2 expressing mice spent significantly less time freezing in environment A and significantly more time in the open arm of the elevated plus maze than CTRL mice. Confocal image represents one of the injection sites used to label NI GABAergic neurons, and the blue area represents the position of the optic fiber. Scale bar: 200 μm. Medians and interquartile ranges are shown on the graphs. (For statistical details see supplementary text for Fig. 6). (**B**) Experimental design of contextual fear-conditioning experiments with light stimulation of NI GABAergic fibers in the bilateral HIPP. Illustration of the two sets of experiments in environments A and B with and without light stimulation of the HIPP fibers of NI GABAergic neurons. Pairwise comparison reveals that ChR2-expressing mice displayed significantly more freezing in environment B, where they received no light stimulation, than in environment A. This was not observed in CTRL mice. Insets illustrate a representative injection site and optic fiber localization; white arrowheads mark NI GABAergic fibers in the HIPP stratum oriens. Scale bars: 200 μm. Data from individual mice are shown in the graphs. (For statistical details, see supplementary text for Fig. 6.) (**C**) Experimental design of contextual fear conditioning experiments with optogenetic stimulation of NI GABAergic neurons "aligned" to or 15-s "shifted" after foot shocks. "Light-aligned" mice displayed significantly less freezing than "light-shifted" mice, demonstrating the importance of timing. The inset illustrates a representative injection site and optic fiber localization. Scale bar: 200 μm. Medians and interquartile ranges are shown on the graphs. (For statistical details, see supplementary text for Fig. 6.) (**D**) Experimental design of delayed cued fear-conditioning experiments with optogenetic inhibition of NI GABAergic neurons. Light inhibition of NI GABAergic neurons caused significantly stronger contextual freezing behavior in ArchT-mice in environment A compared to CTRL mice. However, there was no difference in HIPP-independent cued fear freezing levels between the two groups in environment B. The inset illustrates a representative injection site and optic fiber localization. Scale bar: 200 μm. Medians and interquartile ranges are shown on the graphs. (For statistical details, see supplementary text for Fig. 6.)

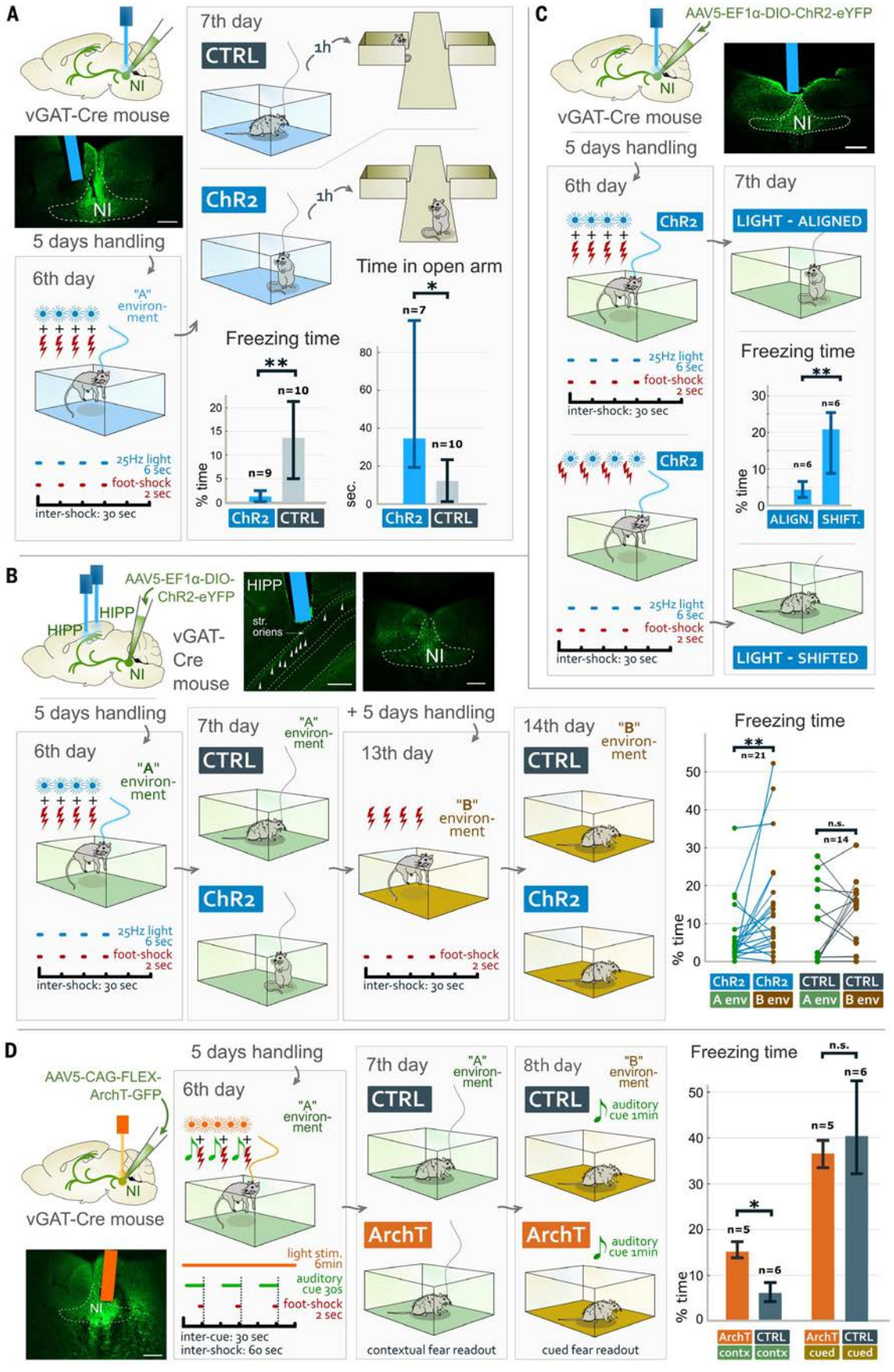

density analysis revealed a prominent effect on the magnitude of apical dendritic sinks and sources, excluding the possibility of general silencing of CA1 and instead implying a stimulus-triggered alteration of excitation–inhibition balance (fig. S5, F to I). Notably, none of these effects were observed when we stimulated the NI GABAergic neurons in urethane-anesthetized mice.

NI GABAergic neurons bidirectionally regulate hippocampus-dependent contextual memory formation

Our findings above indicated that NI GABAergic neurons can integrate behavioral modalities from several key brain areas and are activated by salient environmental inputs, whereas they inhibit HIPP OLM cells both directly and indirectly. These findings suggest that this brainstem projection is ideally suited to provide the subcortical inhibition of these HIPP SOM-positive dendrite-targeting neurons for balancing the selection of HIPP pyramidal cells that participate in memory formation.

To test this possibility, first we injected ChR2-containing Cre-dependent AAV5 (ChR2 mice) or control Cre-dependent AAV5 (CTRL mice) into the NI of vGAT-Cre mice and implanted an optic fiber over the NI (Fig. 6A and fig. S4A). After handling, mice were placed into a new multisensory context (environment "A"), where they received four foot shocks and light stimulation of NI precisely aligned to foot shocks (supplementary materials and methods and Fig. 6A). All mice displayed equally strong immediate reactions to foot shocks. Twenty-four hours later, mice were placed into the same environment A, where CTRL mice displayed strong freezing behavior, as expected, whereas ChR2 mice displayed almost no freezing behavior (Fig. 6A). An elevated plus-maze test, 1 hour later, revealed significantly lower anxiety levels in ChR2 mice compared to CTRL mice (Fig. 6A). These findings indicated that contextual fear memory formation can be severely impaired or blocked if NI GABAergic neurons are strongly activated precisely at the time of US presentation.

In an additional control experiment, we conducted the same contextual fear-conditioning experiment with the same cohorts of ChR2 and CTRL mice 1 week later, in a different environment ("B" environment, fig. S6A) without light stimulations. On the second day of the experiment, both ChR2 and CTRL mice displayed high freezing behavior (fig. S6, A and B), confirming that ChR2 mice could also display appropriate fear behavior.

To confirm that NI GABAergic cells act directly on HIPP SOM-positive cells, we created a second cohort of ChR2 and CTRL mice, as described above (Fig. 6B). However, in these mice, optic fibers were implanted bilaterally above the dorsal HIPP (Fig. 6B and fig. S4, A and B). In similar contextual fear-conditioning experiments described above, ChR2 mice again displayed significantly lower freezing levels in environment A, where they received NI light stimulation during foot shocks, than in environment B, where NI was not stimulated (Fig. 6B). This effect was absent in CTRL mice (Fig. 6B). These results suggest that dorsal HIPP fibers of NI GABAergic neurons can inhibit the formation of contextual memory directly in the HIPP.

The balancing of the selection of pyramidal cells that associate US with environmental context should be timed precisely during US presentation. To test the importance of timing, we injected ChR2-containing Cre-dependent AAV5 into the NI of vGAT-Cre mice and implanted an optic fiber over the NI (Fig. 6C and Fig. S4A). Mice were divided into two groups: One group received NI GABAergic neuron stimulation aligned to foot shocks as described above ("light-aligned-mice"), and a second group received light stimulation exactly between foot shocks (i.e., 15 s after each foot shock; "light-shifted-mice," Fig. 6C). Light-shifted-mice displayed significantly higher freezing levels compared to light-aligned-mice, indicating that activation of NI GABAergic neurons needs to occur precisely during US presentation to be effective (Fig. 6C).

Finally, we investigated whether inhibition of NI GABAergic neurons during contextual fear conditioning induced opposite effects, i.e., whether it can create inadequately strong fear. We injected archaerhodopsinT-3 (ArchT 3.0)–containing Cre-dependent AAV5 (ArchT mice) or control Cre-dependent AAV5 (CTRL mice) into the NI of vGAT-Cre mice and implanted an optic fiber over the NI (Fig. 6D and figs. S3D and S4A). After handling, mice were tested in a delay cued fear-conditioning paradigm. First, we placed mice into environment A, where they received three auditory tones, at the end of which mice received foot shocks. NI received a constant yellow light during the experiments. Twenty-four hours later, mice were placed back into environment A to test their hippocampus-dependent contextual fear memories. We observed that ArchT mice displayed significantly stronger freezing behavior than CTRL mice (Fig. 6D). The auditory cue–dependent fear component of established fear memories is known to be hippocampus independent (*51*). Therefore, on the next day, we placed these mice into a different neutral environment B and presented them with the auditory cues (Fig. 6D). At this time, however, we found no difference between the freezing levels of the two groups, further suggesting that the effect of NI GABAergic neurons on contextual memory formation was hippocampus dependent.

Discussion

Encoding of episodic memories is essential for the survival of animals. HIPP pyramidal neurons of the dorsal CA1 region play a key role in this process (*1*, *25*, *52*), by pairing multisensory contextual information with direct sensory-related inputs (e.g., an US) at the cellular level, via long-term synaptic plasticity mechanisms (*8*, *10*, *15*). However, if too many pyramidal neurons receive the same direct sensory-related inputs, information pairing is not specific enough and the memory trace will be lost (*16*). Therefore, only a subpopulation of pyramidal neurons participate in this process by forming cell assemblies that encode memory engrams (*11*, *15*), whereas the direct sensory-related input must be excluded from most of the pyramidal neurons (*16*).

HIPP SOM-positive OLM neurons selectively inhibit the distal dendrites of pyramidal neurons to filter out direct sensory-related excitatory inputs from the entorhinal cortex (*3*, *16*, *22*). Upon salient environmental stimuli, OLM cells are activated by glutamatergic and cholinergic inputs from the MS (*3*, *16*, *19*–*22*); therefore, dendrite-targeting OLM cells can efficiently block direct sensory-related inputs to most pyramidal cells at the time of memory formation, thereby leaving only a subpopulation of pyramidal neurons to form engrams.

However, the selection of these pyramidal neurons must be precisely balanced. We hypothesized that dorsal CA1 dendrite-targeting OLM interneurons should also be precisely inhibited in time, depending on subcortical states; otherwise, underrecruitment of pyramidal neurons will lead to unstable engrams (*17*, *25*, *52*). We discovered that NI GABAergic neurons are well suited to counterbalance the activation of OLM cells in a time- and sensory stimulus–dependent manner.

We demonstrated that NI GABAergic neurons receive monosynaptic inputs from several brain areas that process salient environmental stimuli and that they are activated rapidly by such stimuli in vivo. We revealed that these NI GABAergic neurons provide a selective, direct inhibition of HIPP SOM-positive interneurons, the vast majority of which are dendrite-targeting OLM interneurons (*16*, *18*). Although other types of HIPP neurons have little contribution to the local SOM-positive innervation of the CA1 area, some SOM-positive bistratified interneurons may also support the inhibition of pyramidal cell dendrites, in addition to extrahippocampal-projecting GABAergic neurons, the rare local collaterals of which also target pyramidal cell dendrites (*53*).

MS cholinergic cells release GABA, immediately followed by a strong cholinergic excitatory component (*54*), which results in an effective net activation of OLM cells (*16*). Here we revealed that medial septal glutamatergic and cholinergic excitatory inputs to OLM neurons are also inhibited by NI GABAergic neurons simultaneously, which facilitates the effective and precisely timed inhibition of hippocampal OLM cells. We also demonstrated that many of these direct and indirect inhibitory actions are provided by collaterals of the same NI GABAergic neurons, further facilitating a highly synchronous inhibition.

Although OLM cells in intermediate and ventral HIPP seem to regulate memory formation differently (*17*), previous studies agree that direct inhibition of dorsal CA1 OLM neurons resulted in weaker memory formation (*16*, *17*). Indeed, we found that dorsal CA1 OLM neurons can be inhibited by activating brainstem NI GABAergic neurons. Our behavioral data revealed that the precisely timed activation of NI GABAergic neurons could lead to an almost complete inhibition of the formation of contextual fear memories.

By contrast, NI-lesioned rats display pathologically strong memory formation, indicated by impaired fear extinction and increased fear generalization (*55*, *56*). In this regard, we also observed stronger contextual fear memory formation after inhibition of GABAergic NI neurons.

We described that NI GABAergic neurons receive monosynaptic inputs from several brain areas that process salient environmental stimuli, and our analysis of our 2P calcium imaging data revealed that different environmental inputs activated different fractions of NI fibers. Emotionally more salient inputs were more effective. Furthermore, our Jaccard similarity analysis suggested that NI fibers may be activated by different sensory stimuli. Previous studies have also shown heterogeneity among the NI cells on the basis of their activity patterns or their CRH receptor or relaxin-3 content (*30*, *32*). Therefore, one may speculate that a different subset of NI GABAergic neurons could enforce the disinhibition of a different subset of pyramidal neurons, leading to the selection of different sets of memory-encoding pyramidal cell populations, which would be beneficial to encode different contextual memories more specifically.

The activity of medial septal glutamatergic neurons is positively correlated with the running speed of the animal and with the frequency of hippocampal theta rhythm (*22*, *24*, *57*). NI neurons also display firing phase-locked to HIPP theta rhythm (*32*, *58*, *59*). Our results reveal that MS glutamatergic neurons innervate the NI and that the activity of NI GABAergic fibers is increased during running, active exploration, and new episodic memory formation. Therefore, MS glutamatergic neurons may support the phase-locking of NI GABAergic neurons to HIPP theta rhythm.

We observed that activation of NI GABAergic neurons partly inhibited and reorganized HIPP theta rhythmic activity, which is known to be essential for episodic memory formation (*25*), further suggesting a role of NI GABAergic neurons in memory formation. This effect on theta activity may be facilitated by one of the different populations of septohippocampal parvalbumin-positive GABAergic neurons (*60*–*63*). Although it is unclear which one of these neuronal populations receives GABAergic synapses from NI, some of them express metabotropic relaxin-3 receptors and may be inhibited by NI (*64*, *65*). Different types of MS parvalbumin cells target different HIPP interneurons in a rhythmic fashion, and they primarily target HIPP basket cells that are known to be fundamental in modulating HIPP theta rhythms (*63*, *66*–*68*).

In the rat, NI GABAergic neurons that express CRH-R1 are activated by different stressors (*29*, *32*, *33*, *56*). Our results demonstrate that NI GABAergic neurons receive inputs from several brain areas, some of which are related to stress regulation, and among which the projection from CRH-expressing neurons of the median raphe region was previously unknown. Therefore, CRH-dependent activation of NI GABAergic neurons might contribute to impaired episodic memory formation observed under stressful conditions (*46*, *69*).

Pathological neurodegeneration of NI GABAergic neurons may result in hyperthymesia-like symptoms, in which the unnecessarily encoded detailed memories of everyday life cause cognitive problems in patients (*70*, *71*). NI GABAergic neuron dysfunction may also contribute to general anxiety-like syndromes or posttraumatic stress disorders, in which pathologically strong episodic memory formation is present. In addition, overactivity of NI GABAergic neurons may lead to dementia-like disorders.

An important physiological role of NI GABAergic neurons may be the fine-tuning of the selection of memory-encoding pyramidal cells, based on the relevance and/or modality of environmental inputs. NI GABAergic neurons may also help filter out nonrelevant everyday experiences, to which animals have already accommodated, by regulating the population sparsity of memory-encoding dorsal CA1 pyramidal neurons. Our data represent an unexpectedly specific role of an ascending inhibitory pathway from a brainstem nucleus in memory encoding.

Methods summary

Ethical considerations and used mouse strains

All experiments were performed in accordance with the Institutional Ethical Codex and the Hungarian Act of Animal Care and Experimentation guidelines (40/2013, II.14), which are in concert with the European Communities Council Directive of 22 September 2010 (2010/63/EU). All two-photon (2P) imaging experiments were conducted in accordance with the U.S. National Institutes of Health guidelines and with the approval of the Columbia University Institutional Animal Care and Use Committee. The following mouse strains were used in the experiments: C57Bl/6J wild type, ChAT-iRES-Cre, CRH-iRES-Cre, vGAT-iRES-Cre, vGAT-iRES-Cre::Gt(ROSA26)Sor-CAG/tdTomato, vGluT2-iRES-Cre (*72*), GlyT2-iRES-Cre and SOM-iRES-Cre. We used male and female mice that were at least 6 weeks old in our experiments.

Stereotaxic surgeries for viral gene transfer and retrograde tracing

Mice were deeply anesthetized and were then mounted and microinjected using a stereotaxic frame. We used one of the following viruses: AAV2/1-EF1a-DIO-GCaMP6f; AAV2/5-EF1α-DIO-eYFP; AAV2/5-EF1α-DIO-mCherry; AAV2/5-CAG-FLEX-ArchT-GFP; AAV2/5-EF1α-DIO-hChR2(H134R)-eYFP. For retrograde tracing experiments we injected 2% FluoroGold or 0.5% cholera toxin B subunit into the target areas. The coordinates for the injections were defined by a stereotaxic atlas (*73*).

Hippocampal cranial window implants for two-photon imaging experiments

We implanted an imaging window/head-post as described previously (*16*). Briefly, under anesthesia, a 3-mm-diameter craniotomy was made in the exposed skull over the left dorsal hippocampus and the underlying cortex was slowly aspirated. A custom-made sterilized cylindrical steel imaging cannula with a glass cover slip window [3-mm diameter × 1.5-mm height, as described in (*42*)] was inserted into the craniotomy and was cemented to the skull. Analgesia was administered during and after the procedure for 3 days.

Optic fiber implantations for behavioral experiments

For behavioral experiments, optic fibers were implanted into the brain. Their positions are illustrated in fig. S4, A and B. After the surgeries, mice received meloxicam analgesia and were placed into separate cages until experiments or perfusions.

Stereotaxic surgeries for electrophysiological recordings in freely moving mice

AAV2/5-EF1a-DIO-hChR2(H134R)-YFP transfected vGAT-IRES-Cre male mice received optical fibers above their nucleus incertus and a multichannel (16 or 32) linear type silicon probe into the dorsal hippocampus. Stainless steel wires above the cerebellum served as reference for the electrophysiological recordings. An additional optical fiber with the tip in the dental acrylate above the skull was used for control illumination sessions. Analgesia was administered during and after the procedures.

Mono-transsynaptic rabies tracing

We used the monosynaptic rabies tracing technique published by Wickersham *et al.* (*43*). Briefly, C57Bl/6 and vGAT-Cre mice were prepared for stereotaxic surgeries as described above, and 30 nl of the 1:1 mixture of the following viruses was injected into the NI: AAV2/8-hSyn-FLEX-TVA-p2A-eGFP-p2A-oG and AAV2/5-CAG-FLEX-oG. These viruses contain an upgraded version of the rabies glycoprotein (oG) that has increased trans-synaptic labeling potential (*74*). After 2 to 3 weeks of survival, mice were injected with the genetically modified Rabies(ΔG)-EnvA-mCherry at the same coordinates. After 10 days of survival, mice were prepared for perfusions.

Antibodies and perfusions

The list and specifications of the primary and secondary antibodies used can be found in tables S1 to S3. Combinations of the used primary and secondary antibodies in the different experiments are listed in tables S4 and S5. Mice were anesthetized and perfused transcardially with 0.1M phosphate-buffered saline solution for 2 min followed by 4% freshly depolymerized paraformaldehyde solution; or with artificial cerebrospinal fluid (ACSF) for 2 min. After perfusion, brains were removed from the skull and were immersion-fixed in 4% PFA with or without 0.2% glutaraldehyde (GA) for 2 hours. Brains were cut into 50- or 60-μm sections using a vibrating microtome.

Fluorescent immunohistochemistry and laser-scanning confocal microscopy

Perfusion-fixed sections were washed in 0.1 M phosphate buffer (PB) and then incubated in a mixture of primary antibodies for 48 to 72 hours. This was followed by extensive washes in tris-buffered saline (TBS), and incubation in the mixture of appropriate secondary antibodies overnight. For visualizing cell layers in the hippocampus, nuclear counterstaining was done on forebrain sections using Draq5 according to the manufacturer's protocol. Following this, sections were washed in TBS and PB, dried on slides, and covered with Aquamount (BDH Chemicals Ltd) or with Fluoromount-G Mounting Medium (Invitrogen). Sections were evaluated using a Nikon A1R confocal laser-scanning microscope system built on a Ti-E inverted microscope operated by NIS-Elements AR 4.3 software. Regions of interests were reconstructed in z-stacks. For the monosynaptic rabies tracing experiments, coronal sections were prepared from the whole brain for confocal laser-scanning microscopy, and labeled cells were scanned using a Nikon Ni-E C2+ confocal system.

Immunogold-immunoperoxidase double labeling and electron microscopy

For synaptic detection of $GABA_A$-receptor γ2 subunit, sections were pepsin-treated mildly and were blocked in 1% HSA in TBS, followed by incubation in a mixture of primary antibodies. After washes in TBS, sections were incubated in blocking solution and in mixtures of secondary antibody solutions overnight. After washes in TBS, the sections were treated with 2% glutaraldehyde. The immunoperoxidase reaction was developed using 3-3′-diaminobenzidine as chromogen. Immunogold particles were silver-enhanced. The sections were contrasted using osmium tetroxide solution, dehydrated, and embedded in Durcupan. Serial sections (70 to 100 nm) were prepared using an ultramicrotome and documented in electron microscope.

Silver-gold intensified and nickel-intensified immunoperoxidase double labeling (SI-DAB/DAB-Ni)

Perfusions, sectioning and incubations of sections in primary antibody solutions were performed as described above. The SI-DAB reaction was followed by subsequent washes and incubation in secondary antibody solutions. Labeling was developed using ammonium nickel sulfate-intensified 3-3′-diaminobenzidine (DAB-Ni) and intensified with silver-gold (SI/DAB) as described in detail in Dobó *et al.* (*75*). After washes in TBS, sections were blocked in 1% HSA and incubated in primary antibody solutions for the second DAB-Ni reaction. This was followed by incubation with ImmPRESS secondary antibody solutions overnight. The second immunoperoxidase reaction was developed by DAB-Ni, resulting in a homogeneous deposit, which was clearly distinguishable from the silver-gold intensified SI-DAB at the electron microscopic level (*75*). Further dehydration, contrasting, and processing of the sections for electron microscopy was performed as described above.

In vitro slice preparation

In all slice studies, brains were removed and placed into an ice-cold cutting solution, which had been bubbled with 95% O_2–5% CO_2 (carbogen gas) for at least 30 min before use. Then 300- to 450-μm horizontal slices of ventral hippocampi or 300-μm coronal brainstem slices containing the nucleus incertus were cut using a vibrating microtome. After acute slice preparation, slices were placed in an interface-type holding chamber for recovery (*76*). This chamber contained standard ACSF at 35°C that was gradually cooled to room temperature, and saturated with carbogen gas.

Intracellular recordings

To record GABAergic currents, membrane potential was clamped far (~0 mV) from GABA reversal potential. For the intracellular recordings, fast glutamatergic transmission was blocked by adding the α-amino-3-hydroxy-5-methyl-4-isoxazolepropionic acid (AMPA)–receptor antagonist NBQX and the *N*-methyl-D-aspartate (NMDA)-receptor antagonist AP-5 to the recording solution. To test $GABA_A$-receptor dependent synaptic transmission, we administered the $GABA_A$-receptor antagonist gabazine into the ACSF. All drugs were administered from stock solutions via pipettes into the ACSF containing superfusion system. For ChR2 illumination, we used a blue laser diode attached to a single optic fiber positioned above the hippocampal slice. For ArchT illumination, we used a red laser diode with optic fiber positioned above NI. Cells recorded in current-clamp configuration were depolarized above firing threshold to test the effectivity of ArchT-mediated inhibition on action potential generation.

In vivo two-photon calcium imaging

Calcium imaging in head-fixed, behaving mice was performed using a two-photon microscope equipped with an 8-kHZ resonant scanner and a Ti:Sapphire laser tuned to 920 nm. For image acquisition, we used a Nikon 40× NIR Apo water-immersion objective (0.8 NA, 3.5 mm WD) coupled to a piezo-electric crystal. Fluorescent signals were collected by a GaAsP photomultiplier tube.

Behavior for two-photon calcium imaging

For the in vivo head-fixed 2P calcium-imaging experiments, behavioral training of the mice was started 3 days after implantation surgery. Mice were hand habituated, water restricted (>90% of their predeprivation body weight), and trained for 5 to 7 days to run on a 2-m-long cue-less burlap belt on a treadmill for water rewards, while being head-fixed. Mice were also habituated to the 2P setup and the scanner and shutter sounds before the actual 2P imaging experiments. The treadmill was equipped with a lick-port for water delivery and lick detection. Locomotion was recorded by tracking the rotation of the treadmill wheel using an optical rotary encoder. Stimulus presentation and behavioral readout were driven by microcontroller systems, using custom made electronics. During random foraging experiments, three water rewards were presented per lap in random locations, while mice were running on a cue-less burlap belt. In salience experiments, discrete stimuli were presented as described (*42*), with slight modifications. Stimuli were repeated 10 times for each modality in a pseudorandom order during one experiment. The acquired 2P imaging data were preprocessed for further analysis using the SIMA software package (*77*). Motion correction and extraction of dynamic GCaMP6f fluorescent signals were conducted as described (*78*). Regions of interest (ROIs) were drawn manually over the time-averages of motion corrected time-series to isolate the bouton calcium signals of GCaMP6f-expressing axons.

Optogenetics and contextual fear conditioning (CFC)

After optic fiber implantations, mice received 5 days of handling. On the 6th day, mice were placed into the first environmental context (environment A) in a plexiglass shock chamber, where they received four foot shocks. Optogenetic stimulation was precisely aligned with the shocks, starting 2 s before shock onset and finishing 2 s after shock offset. For the "ChR2-shifted" group, this laser stimulation was shifted by 15 s after shock onset. On the 7th day, mice were placed back into the first environment for 3 min to record freezing behavior. This was followed by 5 days of extensive handling to achieve full fear extinction that reset freezing behavior to a normal baseline. On the 13th day, mice were placed into the second environmental context (environment B), composed of another set of cues. Baseline freezing levels were recorded for 3 min, followed by four shocks without optogenetic stimulation. Twenty-four hours later, freezing behavior was recorded in the second environment for 3 min. The behavior of the mice was recorded and freezing behavior was analyzed manually. Freezing behavior was recorded when mice displayed only respiration-related movements for at least 2 s.

Optogenetics and delay cued fear conditioning (CuedFC)

After optic fiber implantations, mice received 5 days of handling. On the 6th day, mice were placed into the first environmental context (environment A) in a plexiglass shocking chamber, where they received three shocks paired with an auditory cue. The foot shocks and the auditory cues were coterminated each time. During the experiment, lasting 6 min, mice received a continuous yellow laser light illumination. On the 7th day, mice were placed back into the first environment for 3 min to record freezing behavior related to the contextual fear memories. Twenty-four hours later, on the 8th day, mice were placed into a second environmental context (environment B). Here, mice were presented with the

auditory cue for 1 min to record freezing behavior related to the cued fear memories.

Elevated plus maze (EPM) after optogenetic CFC

One hour after freezing behavior assessment in the first environment (7th day) we placed the mice into an EPM to test their anxiety levels. The cross-shaped EPM apparatus consisted of two open arms with no walls and two closed arms and was on a pedestal 50 cm above floor level (Fig. 6A). The behavior of the mice was recorded camcorder and evaluated using an automated system (Noldus Ethovision 10.0; Noldus Interactive Technologies). Behavior was measured as total time in the open and closed arms.

In vivo electrophysiological recordings in freely behaving mice

Electrophysiological recordings commenced 7 days after surgery and habituation to connections to the head-stage. The signal from the silicon probe was multiplexed and sampled at 20 kHz. The movement of the mouse was tracked by a marker-based, high speed four-camera motion capture system and reconstructed in 3D. After home cage recording, mice were placed into an open arena and into a linear track. Recordings were repeated 1 to 7 days later. In each recording situation, blue light stimulation was triggered manually by the experimenter. Mice were recorded in –three to nine sessions for 2 to 5 weeks. Then, mice were processed for histological verification of the viral transduction zone and implantation. The analysis was performed in MATLAB environment by custom-written functions and scripts. Time-frequency decomposition of pyramidal local field potential (LFP) with continuous wavelet transform (*79*) and subsequent bias correction of spectral power (*80*) was used to calculate instant power.

Data and code availability

Data generated and analyzed during the current study are presented in the manuscript or in the Supplementary Materials file, while additional datasets and custom written codes for in vivo electrophysiological recordings, 2P-imaging and data analysis are available from the following links: https://figshare.com/s/9fb345fc23ac2ac94fcd and https://figshare.com/s/5b0c6be2431caf10272b

REFERENCES AND NOTES

1. H. Eichenbaum, The hippocampus and declarative memory: Cognitive mechanisms and neural codes. *Behav. Brain Res.* **127**, 199–207 (2001). doi: 10.1016/S0166-4328(01)00365-5; pmid: 11718892
2. P. Andersen, *The Hippocampus Book* (Oxford University Press, 2007).
3. J. Haam, J. Zhou, G. Cui, J. L. Yakel, Septal cholinergic neurons gate hippocampal output to entorhinal cortex via oriens lacunosum moleculare interneurons. *Proc. Natl. Acad. Sci. U.S.A.* **115**, E1886–E1895 (2018). doi: 10.1073/pnas.1712538115; pmid: 29437952
4. T. Kitamura *et al.*, Entorhinal cortical ocean cells encode specific contexts and drive context-specific fear memory. *Neuron* **87**, 1317–1331 (2015). doi: 10.1016/j.neuron.2015.08.036; pmid: 26402611
5. J. E. Lisman, Relating hippocampal circuitry to function: Recall of memory sequences by reciprocal dentate-CA3 interactions. *Neuron* **22**, 233–242 (1999). doi: 10.1016/S0896-6273(00)81085-5; pmid: 10069330
6. J. Suh, A. J. Rivest, T. Nakashiba, T. Tominaga, S. Tonegawa, Entorhinal cortex layer III input to the hippocampus is crucial for temporal association memory. *Science* **334**, 1415–1420 (2011). pmid: 22052975
7. T. Kitamura *et al.*, Island cells control temporal association memory. *Science* **343**, 896–901 (2014). doi: 10.1126/science.1244634; pmid: 24457215
8. K. C. Bittner *et al.*, Conjunctive input processing drives feature selectivity in hippocampal CA1 neurons. *Nat. Neurosci.* **18**, 1133–1142 (2015). doi: 10.1038/nn.4062; pmid: 26167906
9. K. C. Bittner, A. D. Milstein, C. Grienberger, S. Romani, J. C. Magee, Behavioral time scale synaptic plasticity underlies CA1 place fields. *Science* **357**, 1033–1036 (2017). doi: 10.1126/science.aan3846; pmid: 28883072
10. J. T. Dudman, D. Tsay, S. A. Siegelbaum, A role for synaptic inputs at distal dendrites: Instructive signals for hippocampal long-term plasticity. *Neuron* **56**, 866–879 (2007). doi: 10.1016/j.neuron.2007.10.020; pmid: 18054862
11. D. S. Roy *et al.*, Distinct neural circuits for the formation and retrieval of episodic memories. *Cell* **170**, 1000–1012.e19 (2017). doi: 10.1016/j.cell.2017.07.013; pmid: 28823555
12. S. Maren, M. S. Fanselow, Electrolytic lesions of the fimbria/fornix, dorsal hippocampus, or entorhinal cortex produce anterograde deficits in contextual fear conditioning in rats. *Neurobiol. Learn. Mem.* **67**, 142–149 (1997). doi: 10.1006/nlme.1996.3752; pmid: 9075242
13. R. P. Kesner, Behavioral functions of the CA3 subregion of the hippocampus. *Learn. Mem.* **14**, 771–781 (2007). doi: 10.1101/lm.688207; pmid: 18007020
14. S. Maren, K. L. Phan, I. Liberzon, The contextual brain: Implications for fear conditioning, extinction and psychopathology. *Nat. Rev. Neurosci.* **14**, 417–428 (2013). doi: 10.1038/nrn3492; pmid: 23635870
15. K. Z. Tanaka *et al.*, The hippocampal engram maps experience but not place. *Science* **361**, 392–397 (2018). doi: 10.1126/science.aat5397; pmid: 30049878
16. M. Lovett-Barron *et al.*, Dendritic inhibition in the hippocampus supports fear learning. *Science* **343**, 857–863 (2014). doi: 10.1126/science.1247485; pmid: 24558155
17. S. Siwani *et al.*, OLMα2 Cells Bidirectionally Modulate Learning. *Neuron* **99**, 404–412.e3 (2018). doi: 10.1016/j.neuron.2018.06.022; pmid: 29983324
18. S. Royer *et al.*, Control of timing, rate and bursts of hippocampal place cells by dendritic and somatic inhibition. *Nat. Neurosci.* **15**, 769–775 (2012). doi: 10.1038/nn.3077; pmid: 22446878
19. S. Nakauchi, R. J. Brennan, J. Boulter, K. Sumikawa, Nicotine gates long-term potentiation in the hippocampal CA1 region via the activation of α2* nicotinic ACh receptors. *Eur. J. Neurosci.* **25**, 2666–2681 (2007). doi: 10.1111/j.1460-9568.2007.05513.x; pmid: 17466021
20. Y. Jia, Y. Yamazaki, S. Nakauchi, K. Sumikawa, α2 nicotine receptors function as a molecular switch to continuously excite a subset of interneurons in rat hippocampal circuits. *Eur. J. Neurosci.* **29**, 1588–1603 (2009). doi: 10.1111/j.1460-9568.2009.06706.x; pmid: 19385992
21. R. N. Leão *et al.*, OLM interneurons differentially modulate CA3 and entorhinal inputs to hippocampal CA1 neurons. *Nat. Neurosci.* **15**, 1524–1530 (2012). doi: 10.1038/nn.3235; pmid: 23042082
22. F. Fuhrmann *et al.*, Locomotion, theta oscillations, and the speed-correlated firing of hippocampal neurons are controlled by a medial septal glutamatergic circuit. *Neuron* **86**, 1253–1264 (2015). doi: 10.1016/j.neuron.2015.05.001; pmid: 25982367
23. B. Hangya, S. P. Ranade, M. Lorenc, A. Kepecs, Central cholinergic neurons are rapidly recruited by reinforcement feedback. *Cell* **162**, 1155–1168 (2015). doi: 10.1016/j.cell.2015.07.057; pmid: 26317475
24. D. Justus *et al.*, Glutamatergic synaptic integration of locomotion speed via septoentorhinal projections. *Nat. Publ. Gr.* (2016). doi: 10.1038/nn.4447
25. I. Misane, A. Kruis, A. W. Pieneman, S. O. Ögren, O. Stiedl, GABA(A) receptor activation in the CA1 area of the dorsal hippocampus impairs consolidation of conditioned contextual fear in C57BL/6J mice. *Behav. Brain Res.* **238**, 160–169 (2013). doi: 10.1016/j.bbr.2012.10.027; pmid: 23098796
26. M. Goto, L. W. Swanson, N. S. Canteras, Connections of the nucleus incertus. *J. Comp. Neurol.* **438**, 86–122 (2001). doi: 10.1002/cne.1303; pmid: 11503154
27. S. Ma *et al.*, Relaxin-3 in GABA projection neurons of nucleus incertus suggests widespread influence on forebrain circuits via G-protein-coupled receptor-135 in the rat. *Neuroscience* **144**, 165–190 (2007). doi: 10.1016/j.neuroscience.2006.08.072; pmid: 17071007
28. C. M. Smith *et al.*, Distribution of relaxin-3 and RXFP3 within arousal, stress, affective, and cognitive circuits of mouse brain. *J. Comp. Neurol.* **518**, 4016–4045 (2010). doi: 10.1002/cne.22442; pmid: 20737598
29. M. Tanaka *et al.*, Neurons expressing relaxin 3/INSL 7 in the nucleus incertus respond to stress. *Eur. J. Neurosci.* **21**, 1659–1670 (2005). doi: 10.1111/j.1460-9568.2005.03980.x; pmid: 15845093
30. A. Nuñez, A. Cervera-Ferri, F. Olucha-Bordonau, A. Ruiz-Torner, V. Teruel, Nucleus incertus contribution to hippocampal theta rhythm generation. *Eur. J. Neurosci.* **23**, 2731–2738 (2006). doi: 10.1111/j.1460-9568.2006.04797.x; pmid: 16817876
31. V. Teruel-Martí *et al.*, Anatomical evidence for a ponto-septal pathway via the nucleus incertus in the rat. *Brain Res.* **1218**, 87–96 (2008). doi: 10.1016/j.brainres.2008.04.022; pmid: 18514169
32. S. Ma, A. Blasiak, F. E. Olucha-Bordonau, A. J. M. Verberne, A. L. Gundlach, Heterogeneous responses of nucleus incertus neurons to corticotrophin-releasing factor and coherent activity with hippocampal theta rhythm in the rat. *J. Physiol.* **591**, 3981–4001 (2013). doi: 10.1113/jphysiol.2013.254300; pmid: 23671163
33. S. Ma *et al.*, Nucleus incertus promotes cortical desynchronization and behavioral arousal. *Brain Struct. Funct.* **222**, 515–537 (2017). doi: 10.1007/s00429-016-1230-0; pmid: 27206427
34. C. García-Díaz *et al.*, Nucleus incertus ablation disrupted conspecific recognition and modified immediate early gene expression patterns in 'social brain' circuits of rats. *Behav. Brain Res.* **356**, 332–347 (2019). doi: 10.1016/j.bbr.2018.08.035; pmid: 30195021
35. T. F. Freund, G. Buzsáki, Interneurons of the hippocampus. *Hippocampus* **6**, 347–470 (1996). doi: 10.1002/(SICI)1098-1063(1996)6:4<347::AID-HIPO1>3.0.CO;2-I; pmid: 8915675
36. Y. Yanovsky, O. A. Sergeeva, T. F. Freund, H. L. Haas, Activation of interneurons at the stratum oriens/alveus border suppresses excitatory transmission to apical dendrites in the CA1 area of the mouse hippocampus. *Neuroscience* **77**, 87–96 (1997). doi: 10.1016/S0306-4522(96)00461-7; pmid: 9044377
37. F. Ferraguti *et al.*, Immunolocalization of metabotropic glutamate receptor 1α (mGluR1α) in distinct classes of interneuron in the CA1 region of the rat hippocampus. *Hippocampus* **14**, 193–215 (2004). doi: 10.1002/hipo.10163; pmid: 15098725
38. A. I. Gulyás, N. Hájos, I. Katona, T. F. Freund, Interneurons are the local targets of hippocampal inhibitory cells which project to the medial septum. *Eur. J. Neurosci.* **17**, 1861–1872 (2003). doi: 10.1046/j.1460-9568.2003.02630.x; pmid: 12752786
39. S. Jinno *et al.*, Neuronal diversity in GABAergic long-range projections from the hippocampus. *J. Neurosci.* **27**, 8790–8804 (2007). doi: 10.1523/JNEUROSCI.1847-07.2007; pmid: 17699661
40. M. Haidar *et al.*, Relaxin-3 inputs target hippocampal interneurons and deletion of hilar relaxin-3 receptors in "floxed-RXFP3" mice impairs spatial memory. *Hippocampus* **27**, 529–546 (2017). doi: 10.1002/hipo.22709; pmid: 28100033
41. S. Jinno, T. Kosaka, Cellular architecture of the mouse hippocampus: A quantitative aspect of chemically defined GABAergic neurons with stereology. *Neurosci. Res.* **56**, 229–245 (2006). doi: 10.1016/j.neures.2006.07.007; pmid: 16930755
42. P. Kaifosh, M. Lovett-Barron, G. F. Turi, T. R. Reardon, A. Losonczy, Septo-hippocampal GABAergic signaling across multiple modalities in awake mice. *Nat. Neurosci.* **16**, 1182–1184 (2013). doi: 10.1038/nn.3482; pmid: 23912949
43. I. R. Wickersham *et al.*, Monosynaptic restriction of transsynaptic tracing from single, genetically targeted neurons. *Neuron* **53**, 639–647 (2007). doi: 10.1016/j.neuron.2007.01.033; pmid: 17329205
44. O. Hikosaka, The habenula: From stress evasion to value-based decision-making. *Nat. Rev. Neurosci.* **11**, 503–513 (2010). doi: 10.1038/nrn2866; pmid: 20559337
45. A. M. Stamatakis, G. D. Stuber, Activation of lateral habenula inputs to the ventral midbrain promotes behavioral avoidance. *Nat. Neurosci.* **15**, 1105–1107 (2012). doi: 10.1038/nn.3145; pmid: 22729176

46. F. Darcet *et al*., Learning and memory impairments in a neuroendocrine mouse model of anxiety/depression. *Front. Behav. Neurosci.* **8**, 136 (2014). doi: 10.3389/fnbeh.2014.00136; pmid: 24822041
47. J. Peng *et al*., A quantitative analysis of the distribution of CRH neurons in whole mouse brain. *Front. Neuroanat.* **11**, 63 (2017). doi: 10.3389/fnana.2017.00063; pmid: 28790896
48. R. W. Stackman Jr., S. J. Cohen, J. C. Lora, L. M. Rios, Temporary inactivation reveals that the CA1 region of the mouse dorsal hippocampus plays an equivalent role in the retrieval of long-term object memory and spatial memory. *Neurobiol. Learn. Mem.* **133**, 118–128 (2016). doi: 10.1016/j.nlm.2016.06.016; pmid: 27330015
49. G. Buzsáki, E. I. Moser, Memory, navigation and theta rhythm in the hippocampal-entorhinal system. *Nat. Neurosci.* **16**, 130–138 (2013). doi: 10.1038/nn.3304; pmid: 23354386
50. R. Boyce, S. D. Glasgow, S. Williams, A. Adamantidis, Causal evidence for the role of REM sleep theta rhythm in contextual memory consolidation. *Science* **352**, 812–816 (2016). doi: 10.1126/science.aad5252; pmid: 27174984
51. J. Basu *et al*., Gating of hippocampal activity, plasticity, and memory by entorhinal cortex long-range inhibition. *Science* **351**, aaa5694 (2016). doi: 10.1126/science.aaa5694; pmid: 26744409
52. D. C. Drieskens *et al*., CA1 inactivation impairs episodic-like memory in rats. *Neurobiol. Learn. Mem.* **145**, 28–33 (2017). doi: 10.1016/j.nlm.2017.08.008; pmid: 28843666
53. V. T. Takács, T. F. Freund, A. I. Gulyás, Types and synaptic connections of hippocampal inhibitory neurons reciprocally connected with the medial septum. *Eur. J. Neurosci.* **28**, 148–164 (2008). doi: 10.1111/j.1460-9568.2008.06319.x; pmid: 18662340
54. V. T. Takács *et al*., Co-transmission of acetylcholine and GABA regulates hippocampal states. *Nat. Commun.* **9**, 2848 (2018). doi: 10.1038/s41467-018-05136-1; pmid: 30030438
55. C. W. Pereira *et al*., Electrolytic lesion of the nucleus incertus retards extinction of auditory conditioned fear. *Behav. Brain Res.* **247**, 201–210 (2013). doi: 10.1016/j.bbr.2013.03.025; pmid: 23538065
56. L. C. Lee, R. Rajkumar, G. S. Dawe, Selective lesioning of nucleus incertus with corticotropin releasing factor-saporin conjugate. *Brain Res.* **1543**, 179–190 (2014). doi: 10.1016/j.brainres.2013.11.021; pmid: 24287211
57. G.-W. Zhang *et al*., Transforming Sensory Cues into Aversive Emotion via Septal-Habenular Pathway. *Neuron* **99**, 1016–1028. e5 (2018). pmid: 30122379
58. S. Martínez-Bellver *et al*., Regular theta-firing neurons in the nucleus incertus during sustained hippocampal activation. *Eur. J. Neurosci.* **41**, 1049–1067 (2015). doi: 10.1111/ejn.12884; pmid: 25817317
59. S. Martínez-Bellver *et al*., Causal relationships between neurons of the nucleus incertus and the hippocampal theta activity in the rat. *J. Physiol.* **595**, 1775–1792 (2017). doi: 10.1113/JP272841; pmid: 27880004
60. Z. Henderson, G. Fiddler, S. Saha, A. Boros, K. Halasy, A parvalbumin-containing, axosomatic synaptic network in the rat medial septum: Relevance to rhythmogenesis. *Eur. J. Neurosci.* **19**, 2753–2768 (2004). doi: 10.1111/j.0953-816X.2004.03399.x; pmid: 15147309
61. A. Joshi, M. Salib, T. J. Viney, D. Dupret, P. Somogyi, Behavior-Dependent Activity and Synaptic Organization of Septo-hippocampal GABAergic Neurons Selectively Targeting the Hippocampal CA3 Area. *Neuron* **96**, 1342–1357.e5 (2017). doi: 10.1016/j.neuron.2017.10.033; pmid: 29198757
62. G. Gangadharan *et al*., Medial septal GABAergic projection neurons promote object exploration behavior and type 2 theta rhythm. *Proc. Natl. Acad. Sci. U.S.A.* **113**, 6550–6555 (2016). doi: 10.1073/pnas.1605019113; pmid: 27208094
63. Z. Borhegyi, V. Varga, N. Szilágyi, D. Fabo, T. F. Freund, Phase segregation of medial septal GABAergic neurons during hippocampal theta activity. *J. Neurosci.* **24**, 8470–8479 (2004). doi: 10.1523/JNEUROSCI.1413-04.2004; pmid: 15456820
64. H. Albert-Gascó *et al*., Central relaxin-3 receptor (RXFP3) activation increases ERK phosphorylation in septal cholinergic neurons and impairs spatial working memory. *Brain Struct. Funct.* **222**, 449–463 (2017). doi: 10.1007/s00429-016-1227-8; pmid: 27146679
65. F. E. Olucha-Bordonau *et al*., Distribution and targets of the relaxin-3 innervation of the septal area in the rat. *J. Comp. Neurol.* **520**, 1903–1939 (2012). doi: 10.1002/cne.23018; pmid: 22134882
66. A. I. Gulyás, T. J. Görcs, T. F. Freund, Innervation of different peptide-containing neurons in the hippocampus by GABAergic septal afferents. *Neuroscience* **37**, 31–44 (1990). doi: 10.1016/0306-4522(90)90189-B; pmid: 1978740
67. T. F. Freund, M. Antal, GABA-containing neurons in the septum control inhibitory interneurons in the hippocampus. *Nature* **336**, 170–173 (1988). doi: 10.1038/336170a0; pmid: 3185735
68. B. Hangya, Z. Borhegyi, N. Szilágyi, T. F. Freund, V. Varga, GABAergic neurons of the medial septum lead the hippocampal network during theta activity. *J. Neurosci.* **29**, 8094–8102 (2009). doi: 10.1523/JNEUROSCI.5665-08.2009; pmid: 19553449
69. A. Eskildsen, L. P. Andersen, A. D. Pedersen, S. K. Vandborg, J. H. Andersen, Work-related stress is associated with impaired neuropsychological test performance: A clinical cross-sectional study. *Stress* **18**, 198–207 (2015). doi: 10.3109/10253890.2015.1004629; pmid: 25556981
70. E. S. Parker, L. Cahill, J. L. McGaugh, A case of unusual autobiographical remembering. *Neurocase* **12**, 35–49 (2006). doi: 10.1080/13554790500473680; pmid: 16517514
71. S. Kamiya, Relationship between frequency of involuntary autobiographical memories and cognitive failure. *Memory* **22**, 839–851 (2014). doi: 10.1080/09658211.2013.838630; pmid: 24161129
72. L. Borgius, C. E. Restrepo, R. N. Leao, N. Saleh, O. Kiehn, A transgenic mouse line for molecular genetic analysis of excitatory glutamatergic neurons. *Mol. Cell. Neurosci.* **45**, 245–257 (2010). doi: 10.1016/j.mcn.2010.06.016; pmid: 20600924
73. K. F. George Paxinos, Paxinos and Franklin's the Mouse Brain in Stereotaxic Coordinates. *São Paulo, Acad. Press* (2012), p. 360 p., (available at https://www.elsevier.com/books/paxinos-and-franklins-the-mouse-brain-in-stereotaxic-coordinates/paxinos/978-0-12-391057-8).
74. E. J. Kim, M. W. Jacobs, T. Ito-Cole, E. M. Callaway, Improved Monosynaptic Neural Circuit Tracing Using Engineered Rabies Virus Glycoproteins. *Cell Reports* **15**, 692–699 (2016). doi: 10.1016/j.celrep.2016.03.067; pmid: 27149846
75. E. Dobó *et al*., New silver-gold intensification method of diaminobenzidine for double-labeling immunoelectron microscopy. *J. Histochem. Cytochem.* **59**, 258–269 (2011). doi: 10.1369/0022155410397998; pmid: 21378280
76. N. Hájos *et al*., Maintaining network activity in submerged hippocampal slices: Importance of oxygen supply. *Eur. J. Neurosci.* **29**, 319–327 (2009). doi: 10.1111/j.1460-9568.2008.06577.x; pmid: 19200237
77. P. Kaifosh, J. D. Zaremba, N. B. Danielson, A. Losonczy, SIMA: Python software for analysis of dynamic fluorescence imaging data. *Front. Neuroinform.* **8**, 80 (2014). doi: 10.3389/fninf.2014.00080; pmid: 25295002
78. N. B. B. Danielson *et al*., Distinct contribution of adult-born hippocampal granule cells to context encoding. *Neuron* **90**, 101–112 (2016). doi: 10.1016/j.neuron.2016.02.019; pmid: 26971949
79. C. Torrence, G. P. Compo, A Practical Guide to Wavelet Analysis. *Bull. Am. Meteorol. Soc.* **79**, 61–78 (2010). doi: 10.1175/1520-0477(1998)079<0061:APGTWA>2.0.CO;2
80. Y. Liu, X. San Liang, R. H. Weisberg, Rectification of the bias in the wavelet power spectrum. *J. Atmos. Ocean. Technol.* **24**, 2093–2102 (2007). doi: 10.1175/2007JTECHO511.1

ACKNOWLEDGMENTS

We thank T. Reardon (CTRL-Labs, NY) for the AAV2/1-EF1a-DIO-GCaMP6f virus (*I6*) used in this study and D. S. Peterka and L. Hammond (ZI Cellular Imaging, CU, New York) for providing microscopy support. We thank D. Zelena for help with CRH-Cre mice; S. Arthaud (INSERM, Lyon, France) for help with vGluT2-Cre mice; H. Ulrich Zeilhofer (UZ, Zürich) for help with GlyT2-IRES-Cre mice; and J. Huang (CSHL, New York) for help with SOM-IRES-Cre mice. We thank L. Barna, the Nikon Microscopy Center at IEM, Nikon Austria GmbH, and Auro-Science Consulting Ltd. for technical support for fluorescent imaging. We thank K. Demeter and the Behavior Studies Unit of the IEM-HAS for support for behavioral experiments. We thank Z. Erdélyi and F. Erdélyi and the staff of the Animal Facility and the Medical Gene Technology Unit of the IEM-HAS for expert technical help with the breeding and genotyping of the several mouse strains used in this study. We thank Z. Bardóczi, Z. Hajós, E. Szépné Simon, K. Lengyel, M. Mayer, and N. Kriczky for help with experiments and A. Kriczky, K. Iványi, and G. Goda for other assistance. **Funding:** This work was supported by the European Research Council (ERC-2011-ADG-294313, SERRACO); the National Research, Development and Innovation Office, Hungary (OTKA K119521, OTKA K115441, OTKA K109790, OTKA KH124345 and VKSZ_14-1-2015-0155); the U.S. National Institutes of Health (NS030549); the Human Brain Project; EU (EU H2020 720270); and the Hungarian Brain Research Program (2017-1.2.1-NKP-2017-00002). B.P. is supported by UNKP-16-2-13 and D.S. is supported by the UNKP-16-3-IV New National Excellence Program of the Ministry of Human Capacities, Hungary. A.S. was supported by the ÚNKP-17-3-III-SE-9 New National Excellence Program of the Ministry of Human Capacities. A.L. is supported by NIMH 1R01MH100631, 1U19NS104590, and 1R01NS094668 and by the Zegar Family Foundation Award. **Author contributions:** Conceptualization, A.S. and G.N.; Investigation, A.S., K.E.S., R.N., D.S., A.D., V.T.T., B.P., P.H., and J.B.P.; Essential reagents: A.L.G.; Writing - original draft, A.S. and G.N.; Writing - editing, A.S., A.L.G., A.I.G, V.V., A.L., T.F.F., and G.N.; Funding acquisition and supervision: A.I.G., V.V., A.L., T.F.F., and G.N. **Competing interests:** The authors have no competing interests. **Data and materials availability:** Viruses AAV2/5-EF1α-DIO-eYFP, AAV2/5-EF1α-DIO-mCherry, and AAV2/5-CAG-FLEX-ArchT-GFP were obtained under a materials transfer agreement (MTA) with the UNC Vector Core. Virus AAV2/5-EF1α-DIO-hChR2(H134R)-eYFP was obtained under an MTA with the Penn Vector Core. Viruses AAV2/8-hSyn-FLEX-TVA-p2A-eGFP-p2A-oG, AAV2/5-CAG-FLEX-oG, and Rabies(ΔG)-EnvA-mCherry were obtained under an MTA with the Salk GT3 Vector Core. The GlyT2-iRES-Cre mouse strain was obtained under an MTA with the University of Zürich. Data generated and analyzed during this study are presented in the manuscript or in the supplementary materials; additional datasets and custom written codes for in vivo electrophysiological recordings, 2P-imaging, and data analysis are available at the following sites: https://figshare.com/s/9fb345fc23ac2ac94fcd and https://figshare.com/s/5b0c6be2431caf10272b.

SUPPLEMENTARY MATERIALS

science.sciencemag.org/content/364/6442/eaaw0445/suppl/DC1
Materials and Methods
Supplementary Text
Figs. S1 to S6
Tables S1 to S7

13 November 2018; accepted 5 April 2019
10.1126/science.aaw0445

Science

Brainstem nucleus incertus controls contextual memory formation

András Szonyi, Katalin E. Sos, Rita Nyilas, Dániel Schlingloff, Andor Domonkos, Virág T. Takács, Balázs Pósfai, Panna Hegedüs, James B. Priestley, Andrew L. Gundlach, Attila I. Gulyás, Viktor Varga, Attila Losonczy, Tamás F. Freund and Gábor Nyiri

Science **364** (6442), eaaw0445.
DOI: 10.1126/science.aaw0445

What inhibits the inhibitors?

In the hippocampus, each memory trace is encoded by a specific subset of pyramidal cells. The other pyramidal cells must be actively excluded from the memory encoding process by inhibition, which is done by selective dendrite-targeting interneurons. Szonyi *et al.* found that γ-aminobutyric acid–releasing (GABAergic) cells located in a small region in the brain stem called the nucleus incertus project to the hippocampus. The nucleus incertus again is innervated by several regions that respond to salient stimuli. Its GABAergic cells preferentially inhibit the dendrite-targeting interneurons in the hippocampus. The nucleus incertus is thus a central mediator between brain regions that are highly responsive to salient stimuli and the hippocampal circuitry involved in memory formation.

Science, this issue p. eaaw0445

science.sciencemag.org/content/364/6442/eaaw0445/suppl/DC1

Supplementary Materials for

Brainstem nucleus incertus controls contextual memory formation

András Szőnyi, Katalin E. Sos, Rita Nyilas, Dániel Schlingloff, Andor Domonkos, Virág T. Takács, Balázs Pósfai, Panna Hegedüs, James B. Priestley, Andrew L. Gundlach, Attila I. Gulyás, Viktor Varga, Attila Losonczy, Tamás F. Freund, Gábor Nyiri*

*Corresponding author Email: nyiri.gabor@koki.mta.hu

Published 24 May 2019, *Science* **364**, eaaw0445 (2019)
DOI: 10.1126/science.aaw0445

This PDF file includes:

Supplementary Materials and Methods

Ethical considerations

All experiments were performed in accordance with the Institutional Ethical Codex and the Hungarian Act of Animal Care and Experimentation guidelines (40/2013, II.14), which are in concert with the European Communities Council Directive of September 22, 2010 (2010/63/EU). The Animal Care and Experimentation Committee of the Institute of Experimental Medicine of Hungarian Academy of Sciences and the Animal Health and Food Control Station, Budapest, have also approved the experiments under the project number PE/EA/2553-6/2016. All two-photon (2P) imaging experiments were conducted in accordance with the United States of America, National Institutes of Health guidelines and with the approval of the Columbia University Institutional Animal Care and Use Committee.

Mice

The following mouse strains were used in the experiments: C57Bl/6J wild type, ChAT-iRES-Cre, CRH-iRES-Cre, vGAT-iRES-Cre, vGAT-iRES-Cre::Gt(ROSA26)Sor-CAG/tdTomato (all strains from The Jackson Laboratory), vGluT2-iRES-Cre (received from Dr Sébastien Arthaud) (71), GlyT2-iRES-Cre (courtesy of Prof Hanns Ulrich Zeilhofer) and SOM-iRES-Cre (courtesy of Prof Josh Huang). We used adult (at least 6 weeks-old) mice from both genders in our experiments. Mice had ad libitum access to food and water. Mice were housed in a vivarium (3-5 mice/cage) until used in experiments. Mice used for 2P-experiments were maintained on a reversed 12h light-dark cycle, with experiments performed during the dark phase of the cycle. Mice used for all other experiments were maintained on a normal 12h light-dark cycle, with experiments performed during the light phase of the cycle.

Stereotaxic surgeries for viral gene transfer and retrograde tracing

Mice were anesthetized with 2% isoflurane followed by an intraperitoneal injection of an anesthetic mixture (containing 8.3 mg/ml ketamine and 1.7 mg/ml xylazine-hydrochloride in 0.9% saline, 10 ml/kg body weight); and were then mounted in a small animal stereotaxic frame (David Kopf Instruments, CA, USA) and the skull surface was exposed. A Nanoject II precision microinjector pump (Drummond, Broomall, PA) was used for the microinjections. For 2P-microscopic, anterograde tracing and optogenetic experiments 10-100 nl of one of the following viruses were injected into the target brain areas: AAV2/1-EF1a-DIO-GCaMP6f (courtesy of Dr Thomas Reardon); AAV2/5-EF1α-DIO-eYFP; AAV2/5-EF1α-DIO-mCherry; AAV2/5-CAG-FLEX-ArchT-GFP (UNC Vector Core); AAV2/5-EF1α-DIO-hChR2(H134R)-eYFP (Penn Vector Core; 4.4-8.5×1012 colony forming units/ml for all viruses). For retrograde tracing experiments we injected 20-40 nl of 2% FluoroGold (Fluorochrome, Denver, CO, USA) or 0.5% Cholera toxin B subunit (List Biologicals, Campbell, CA, USA) into the target areas. The coordinates for the injections were defined by a stereotaxic atlas (72); the null coronal plane of the anteroposterior axis was defined by the position of Bregma; the null sagittal plane of the mediolateral axis was defined by the sagittal suture; the null horizontal plane of the dorso-ventral axis was defined by the bregma and lambda. The injection

coordinates were the following (always given in mm at the anteroposterior, mediolateral and dorsoventral axes, respectively): nucleus incertus: -5.0, 0.0, -4.2; hippocampus: (SOM-Cre, 4-4 injections bilaterally) -2.5, +/- 1.5, -2.1 and -1.5; or -2.0, +/-1.3, -2.0 and -1.5; (WT HIPP-HIPP retrograde tracing, 3-3 injections unilaterally per tracer) -2.0, +/-1.5, -1.7; or -2.7, +/-2.2, -1.8; or -3.3, +/-3.0, -2.7; (WT MS-HIPP retrograde tracing, 2-2 injections bilaterally) -2.0, +/-1.5, -1.7; or -3.0, +/-3.0, -3.0; MS: +1.0, 0.0, -4.3; subiculum: -4.2, +/-3.0, and -3.5.

Definition of the area of nucleus incertus

In the brainstem reticular formation, borders of "nuclei" are not well-defined. For instance, NI is best defined by neurons expressing relaxin-3 mRNA/peptide (28, Figure 1). Although relaxin-3 immunostaining is better detected in nerve terminals in the region, relaxin-3 positive neurons are scattered several tens of micrometers outside the NI "borders" defined by the Allen Brain Atlas (28, Figure 1), while dendritic arrays of NI neurons cross all these putative borders as well. However, in mice the NI is still a relatively small area located below the 4th ventricle, occupying about 500 and 1000 μm in antero-posterior and lateral axes, respectively, which functionally belong to the same cell population. Putative borders, defined by the Allen Brain Atlas, indicated here are given only as a reference, because the region is recognized more easily this way.

Hippocampal cranial window implants for two-photon imaging experiments

Mice spent at least 3 days post injection in their home cages to recover, and then were surgically implanted with an imaging window/head-post implant as described (16). Briefly, under isoflurane anesthesia, a 3-mm diameter craniotomy was made in the exposed skull over the left dorsal hippocampus. After gentle removal of the dura, the underlying cortex was slowly aspirated with continuous irrigation with chilled ACSF until fibers of the corpus callosum were exposed. A custom-made sterilized cylindrical steel imaging cannula with a glass cover slip window (3-mm diameter × 1.5-mm height, as described in (41) was inserted into the craniotomy and was cemented to the skull with dental acrylic (Unifast Trad) along with a stainless-steel headpost for head-fixation. Buprenorphine analgesia (0.05-0.1 mg/kg, sc.) was administered during the procedure and for three days after the surgery to minimize post-operative discomfort.

Optic fiber implantations for behavioral experiments

The highly-specific manipulation of GABAergic neurons in the NI area was achieved by the combination of three factors: (1) we infected only GABAergic cells in vGAT-Cre mice, (2) we infected only the area of the NI (which was confirmed anatomically), and (3) optic fibers targeted only the NI or the hippocampus (Fig. S4). The highly restricted infection or specific optic stimulations would have been sufficiently selective individually, but their combination ensures the best possible specificity.

For behavioral experiments, during a second surgical procedure 5-6 weeks after virus injections, optic fibers (105 μm core diameter, 0.22 NA, Thorlabs GmbH, Dachau/Munich, Germany) were implanted into the brain with the tip at the following coordinates: nucleus incertus: -5.0, 0.0, -4.1; hippocampus: -2.5, +/-2.2, -1.7. For secure fixture of the implantable optic fiber, 3 screws were inserted into the skull followed by disinfection and drying the surface with 70% ethanol and finally, dental cement (Paladur,

M+W Dental, Hungary) was added between the skull and the base of the ceramic ferrule of the fiber implant (Precision Fiber Products, CA, USA). Positions of the optic fibers are illustrated in Fig. S4A-B. After the surgeries, mice received 0.5-0.7 ml saline and 0.03-0.05 mg/kg meloxicam (Metacam, Boehringer Ingelheim, Germany) intraperitoneally, and were placed into separate cages until further experiments or perfusions.

Stereotaxic surgeries for electrophysiological recordings in freely moving mice

Anesthesia of AAV2/5-EF1a-DIO-hChR2(H134R)-YFP-WPRE transfected vGAT-IRES-Cre male mice (time interval between virus injection and surgery: 102±42 days) was induced by intraperitoneal injection of ketamine-xylazine (4 to 1) combination diluted (1:6) in Ringer's lactate solution (10 ml/kg body weight) and maintained by isoflurane during head fixation in the stereotaxic frame. After local disinfection by Betadine and local analgesia by 10% lidocaine-spray (both from Egis Pharmaceuticals PLC, Budapest, Hungary), the cranium was exposed and cleaned for application of adhesive agent (OptiBond XTR, Kerr Corporation, Orange, CA). After photocuration, stereotaxically-guided craniotomies were performed for implantation of the optical fiber (105 μm core diameter, 0.22 NA, Thorlabs GmbH, Dachau/Munich, Germany) above the nucleus incertus (-5.4, 0.0 with tip -3.1 mm from the brain surface) and a multichannel (16 or 32) linear type silicon probe (Neuronexus, Ann-Arbor, MI) into the dorsal hippocampus (AP -2.5, +2 with tip -2.1 mm from brain surface). Two additional small holes were drilled above the cerebellum for stainless steel wires serving as ground and reference for the electrophysiological recordings. The optical fiber and a custom-made microdrive holding the silicon probe were fixed to the skull using dental acrylate (Paladur, Heraeus Kulzer GmbH, Hanau, Germany). The craniotomy above the hippocampus was sealed with artificial dura (Cambridge NeuroTech Ltd, Cambridge, UK). The probe-microdrive assembly was shielded by a copper mesh preventing the contamination of the recordings by environmental electric noise. The mesh was also covered by dental acrylate. An additional optical fiber with the tip limited to the dental acrylate above the skull was used for control illumination sessions. Before finishing the surgery, buprenorphine (0.045 mg/kg body weight) was subcutaneously injected. Following all surgeries, the mice were continuously monitored until recovered as demonstrated by their ability to exhibit purposeful movements.

Mono-trans-synaptic rabies tracing

A detailed description of the monosynaptic rabies tracing technique used has already been published by Wickersham et al. (42). Briefly, C57Bl/6 and vGAT-Cre mice were prepared for stereotaxic surgeries as described above, and 30 nl of the 1:1 mixture of the following viruses was injected into the NI at the coordinates given above: AAV2/8-hSyn-FLEX-TVA-p2A-eGFP-p2A-oG and AAV2/5-CAG-FLEX-oG (4.5×1012 colony forming units/ml). These viruses contain an upgraded version of the rabies glycoprotein (oG) that has increased trans-synaptic labeling potential (73). After 2-3 weeks of survival, mice were injected with the genetically modified Rabies(ΔG)-EnvA-mCherry (3.5×107 colony forming units/ml) at the same coordinates. After 10 days of survival, mice were prepared for perfusions. Cells can be the initiators of transsynaptic spread (starter cells) only if they contain both helper viruses (green color) and the rabies viruses (red color). We used only those mice, in which starter cells could be found strictly in the area of NI

only, therefore the transsynaptic spread from the surrounding areas could be excluded, as illustrated in the representative image of Figure 4B. Theoretically, in the area of the helper virus injection site, trans-synaptic jumps are possible between cells that are interconnected and express the G-protein. It is unknown if these jumps would be able to create an efficient starter cell. However, the helper virus injection site is confined to the NI area and infected cells can be only GABAergic neurons, because the G-protein expressing helper virus is also Cre-dependent. Therefore, initial trans-synaptic jumps are theoretically possible only within the area of NI, and it may even be beneficial for slightly amplifying starter cell number within NI, however frequently or otherwise it occurs.

Antibodies

The list and specifications of the primary and secondary antibodies used can be found in Supp. Table 1-3. The specificities of the primary antibodies were extensively tested, using knock-out mice if possible. Secondary antibodies were extensively tested for possible cross-reactivity with the other antibodies used, and possible tissue labeling without primary antibodies was also tested to exclude auto-fluorescence or specific background labeling. No specific-like staining was observed under these control conditions. Combinations of the used primary and secondary antibodies in the different experiments are listed in Supp. Table 4-5.

Perfusions

Mice used in 2P imaging experiments were deeply anaesthetized with 2% isoflurane. Mice used in all other experiments were anesthetized with 2% isoflurane followed by an intraperitoneal injection of an anesthetic mixture (containing 8.3 mg/ml ketamine, 1.7 mg/ml xylazine-hydrochloride, 0.8 mg/ml promethazinium-chloride) to achieve deep anesthesia. The mice were then perfused transcardially (protocol A) with 0.1M phosphate-buffered saline (PBS, pH 7.4) solution for 2 min followed by 30 ml of 4% freshly depolymerized paraformaldehyde (PFA) solution; (protocol B) with PBS for 2 min, followed by PFA for 40 min, followed by PBS for 10 min; (protocol C) with artificial cerebrospinal fluid (ACSF) for 2 min containing the following reagents (in mM): 125.0 NaCl, 2.5 KCl, 25.0 glucose, 1.25 NaH_2PO_4, 2.5 $CaCl_2$-$2H_2O$, 2 $MgCl_2$-$6H_2O$ and 26 $NaHCO_3$. All salts were obtained from Sigma-Aldrich. After perfusion, brains were removed from the skull, and brains perfused using protocols A and B were immersion-fixed in 4% PFA with or without 0.2% glutaraldehyde (GA) for 2 h. Brains were cut into 50 or 60 μm sections using a vibrating microtome (Leica VT1200S or Vibratome 3000).

Fluorescent immunohistochemistry and laser-scanning confocal microscopy

Perfusion-fixed sections were washed in 0.1 M phosphate buffer (PB, pH 7.4), and incubated in 30% sucrose overnight for cryoprotection. Sections were then freeze-thawed over liquid nitrogen three times for antigen retrieval. Sections were subsequently washed in PB and Tris-buffered saline (TBS, pH 7.4) and blocked in 1% human serum albumin in TBS (HSA; Sigma-Aldrich) and then incubated in a mixture of primary antibodies for 48-72 h. This was followed by extensive washes in TBS, and incubation in the mixture of appropriate secondary antibodies overnight. For visualizing cell layers in the

hippocampus, nuclear counterstaining was done on forebrain sections using Draq5 (1:1000, Biostatus) according to the manufacturer`s protocol. Following this, sections were subsequently washed in TBS and PB, dried on slides and covered with Aquamount (BDH Chemicals Ltd) or with Fluoromount-G Mounting Medium (Invitrogen). For the viral injection and retrograde tracing experiments, each injection site was reconstructed from 50 μm sections using a Zeiss Axioplan2 microscope. For the retrograde tracing experiments, we also estimated what percentage of the injected brain area was labeled with the tracer. Every part of the injected tissue containing even low levels of tracer was considered as part of the injection site. We fitted every image of the injection sites to the corresponding outlines of the atlas (72), and determined the ratio of the volumes of the injection sites to the injected brain area, using the Fiji/ImageJ software. The brain areas measured were the following based on the atlas: in the hippocampus, the dentate gyrus and the regions CA1-3; in the MS, the medial septal area and the vertical diagonal band of Broca. Sections were evaluated using a Nikon A1R confocal laser-scanning microscope system built on a Ti-E inverted microscope with a 10× air objective or with a 0.45 NA CFI Super Plan Fluor ELWD 20XC or with a 1.4 NA CFI Plan Apo VC 60× oil objective or with a Nikon Ni-E C2+ confocal system equipped with a 0.75 NA Plan Apo VC DIC 20× objective, both operated by NIS-Elements AR 4.3 software. Regions of interests were reconstructed in z-stacks; distance between the focal planes was 0.5 μm for examined synaptic contacts and 2 μm for examined neuronal somata.

In case of the monosynaptic rabies tracing experiments, coronal sections spaced at 300 μm were prepared from the whole brain for confocal laser-scanning microscopy, and every transsynaptically labeled cell was scanned using a Nikon Ni-E C2+ confocal system equipped with a 0.13 NA Plan Fluor 4× objective operated by NIS-Elements AR 4.3 software. The cell counting was performed using the Adobe Photoshop CS6 software.

Immunogold-immunoperoxidase double labeling and electron microscopy

Perfusion-fixed sections were washed in 0.1 M phosphate buffer (PB) for 1 hour, then cryoprotected by incubation in 30% sucrose overnight and freeze-thawed three times over liquid nitrogen. For synaptic detection of gephyrin, sections were washed in 0.1 M PB and in TBS and blocked in 1% human serum albumin in TBS (HSA; Sigma-Aldrich), followed by incubation in a mixture of primary antibodies for 48-72 h. For synaptic detection of GABAA-receptor γ2 subunit, sections were pretreated with 0.2 M HCl solution containing 2 mg/ml pepsin (Dako) at 37°C for 8 min. Then sections were blocked in 1% HSA in TBS, followed by incubation in a mixture of primary antibodies. After repeated washes in TBS, sections were incubated in blocking solution (Gel-BS) containing 0.2% cold water fish skin gelatin (Aurion) and 0.5% HSA in TBS for 1 h. Sections were then incubated in mixtures of secondary antibody solutions overnight. After intensive washes in TBS, the sections were treated with 2% glutaraldehyde in 0.1 M PB for 15 min to fix the gold particles in the tissue. To develop the labeling for NI fibers, this was followed by incubation in avidin-biotinylated horseradish peroxidase complex (Elite ABC; 1:300; Vector Laboratories) diluted in TBS for 3 h. The immunoperoxidase reaction was developed using 3-3′-diaminobenzidine (DAB; Sigma-Aldrich) as chromogen. To enlarge immunogold particles, this was followed by incubation in silver enhancement solution (SE-EM; Aurion) for 40-70 min at room temperature. The sections were treated with 0.5% osmium tetroxide in 0.1 M PB on ice

and they were dehydrated in ascending alcohol series and in acetonitrile and embedded in Durcupan (ACM; Fluka). During dehydration, the sections were treated with 1% uranyl-acetate in 70% ethanol for 20 min. After this, 70-100 nm serial sections were prepared using an ultramicrotome (Leica EM UC6) and collected on single-slot copper grids. Sections were examined using a Hitachi H-7100 electron microscope and a Veleta CCD camera driven by the iTEM 5.0 software (Olympus). Randomly sampled terminals of the NI establishing synaptic contacts in the HIPP and MS were always fully reconstructed.

Silver-gold intensified and nickel-intensified immunoperoxidase double labeling (SI-DAB/DAB-Ni)

Perfusions, sectioning and incubations of sections in primary antibody solutions were performed as described. The SI-DAB reaction was followed by subsequent washes in the appropriate secondary antibody solutions for 24h in TBS. After subsequent washes in TBS and incubation in avidin-biotin-peroxidase complex for 3 h (ABC Elite 1:300, Vector Laboratories), ammonium nickel sulphate-intensified 3-3'-diaminobenzidine (DAB-Ni) was used for the development of immunoperoxidase reaction. This reaction was further intensified with silver-gold (SI/DAB) as described in detail in Dobó et al. (74). This intensification step converts the labeling from homogenous to granular by loading fine gold particles onto the DAB-Ni deposit. After washes in TBS, sections were blocked in 1% HSA for 1 h and incubated in primary antibody solutions for the second DAB-Ni reaction for 48-72 h. This step was followed by incubation with ImmPRESS secondary antibody solutions overnight. The second immunoperoxidase reaction was developed by DAB-Ni, resulting in a homogenous deposit, which was clearly distinguishable from the silver-gold intensified SI-DAB at the electron microscopic level (74). Further dehydration, contrasting and processing of the sections for electron microscopy was performed as described above.

In vitro slice preparation

In all slice studies, mice were decapitated under deep isoflurane anesthesia. The brain was removed and placed into an ice-cold cutting solution, which had been bubbled with 95% O2/5% CO2 (carbogen gas) for at least 30 min before use. The cutting solution contained the following (in mM): 205 sucrose, 2.5 KCl, 26 NaHCO3, 0.5 CaCl2, 5 MgCl2, 1.25 NaH2PO4, 10 glucose. After this, 300-450 μm horizontal slices of ventral hippocampi or 300 μm coronal brainstem slices containing the nucleus incertus were cut using a Vibratome (Leica VT1000S). After acute slice preparation, slices were placed in an interface-type holding chamber for recovery. This chamber contained standard artificial cerebrospinal fluid (ACSF) at 35°C that was gradually cooled to room temperature. The ACSF solution contained the following (in mM): 126 NaCl, 2.5 KCl, 26 NaHCO3, 2 CaCl2, 2 MgCl2, 1.25 NaH2PO4 and 10 glucose, saturated with carbogen gas. All salts and drugs were obtained from Sigma-Aldrich or Molar Chemicals LTD.

Intracellular recordings

The composition of the intracellular pipette solution was the following (in mM): 110 K-gluconate, 4 NaCl, 20 HEPES, 0.1 EGTA, 10 phosphocreatine, 2 ATP, 0.3 GTP, 3 mg/ml biocytin adjusted to pH 7.3–7.35 using KOH (285–295 mOsm/L). Whole-cell series resistance was in the range of 5–15 MΩ. Series resistance was not compensated but

was frequently monitored, and cells where the values changed more than 25% during recording were discarded from further analysis. Voltage measurements were not corrected for the liquid junction potential. To record GABAergic currents, membrane potential was clamped far (~0 mV) from GABA reversal potential. In case of intracellular recordings, fast glutamatergic transmission was blocked by adding the α-amino-3-hydroxy-5-methyl-4-isoxazolepropionic acid (AMPA)-receptor antagonist NBQX (20 μM; Hello Bio Inc.) and the N-methyl-D-aspartate (NMDA)-receptor antagonist AP-5 (50 μM; Tocris Bioscience) to the recording solution. To test GABAA-receptor dependent synaptic transmission, we administered the GABAA-receptor antagonist gabazine (5 μM; Tocris Bioscience) into the ACSF. All drugs were administered from stock solutions via pipettes into the ACSF containing superfusion system. For ChR2 illumination, we used a blue laser diode (447 nm, Roithner LaserTechnik GmbH) attached to a single optic fiber (Thorlabs) positioned above the hippocampal slice. For ArchT illumination, we used a red laser diode (640 nm, iBeam smart, Toptica Photonics) with optic fiber positioned above NI. Cells recorded in current clamp configuration were depolarized above firing threshold to test the effectivity of ArchT mediated inhibition on action potential generation.

Digital signal processing, analysis and statistics for in vitro experiments

All data were processed and analyzed off-line using self-developed programs written in Python 2.7.0 and Delphi 6.0 by A.I.G. and D.S. In every in vitro experiment, we used median and 25%-75% interquartile range to describe data groups because they did not display a Gaussian distribution.

In vivo two-photon calcium imaging

Calcium imaging in head-fixed, behaving mice was performed using a two-photon microscope equipped with an 8 kHZ resonant scanner (Bruker) and a Ti:Sapphire laser (Chameleon Ultra II, Coherent) tuned to 920 nm. For image acquisition we used a Nikon 40× NIR Apo water-immersion objective (0.8 NA, 3.5 mm WD) coupled to a piezo-electric crystal (Bruker). To adjust the angle of the imaging window to the plane of the front lens of the objective, we set the angle of the fixed-head with two goniometers (Edmond Optics). Fluorescent signals were collected by a GaAsP photomultiplier tube (Hamamatsu 7422P-40) at 1-1.5 × digital zoom covering 300 × 300 μm - 200 × 200 μm with 512 × 512 pixels per imaging plane. To minimize the loss of bouton calcium signals caused by z-motion of the brain, we imaged from 5 planes separated by 2 μm in z at 5 Hz.

Behavior for two-photon calcium imaging

For the in vivo head-fixed 2P calcium-imaging experiments, behavioral training of the mice was started three days after implantation surgery. Mice were hand habituated, water restricted (>90 percent of their pre-deprivation body weight) and trained for 5-7 days to run on a 2 m-long cue-less burlap belt on a treadmill for water rewards, while being head-fixed (gradually decreasing the number of reward zones from 15 covering the full length of the belt to randomly delivered 3 water rewards). Mice were also habituated to the 2P setup and the scanner and shutter sounds prior to the actual 2P imaging experiments. The treadmill was equipped with a lick-port for water delivery and lick

detection. Locomotion was recorded by tracking the rotation of the treadmill wheel using an optical rotary encoder (256 CPR, Bourns). Stimulus presentation and behavioral read-out were driven by microcontroller systems (Arduino), using custom made electronics. During random foraging experiments three water rewards were presented per lap in random locations, while mice were running on a cue-less burlap belt. In salience experiments, discrete stimuli were presented as described (41), with slight modifications. Air-puff (duration: 200 ms, flow rate: 4 LPM), water (duration of valve opening: 200 ms), light (duration: 200 ms, red LED) and tone (duration: 200 ms, frequency: 2500 Hz, from one speaker below the mice) were presented randomly within a 5 s stimulus time, the pre-stimulus time was 5 s, the post-stimulus time was 15 s. Stimuli were repeated 10× for each modality in a pseudorandom order during one experiment.

Two-photon calcium imaging data pre-processing

The acquired 2P imaging data were pre-processed for further analysis using the SIMA software package (76). Motion correction and extraction of dynamic GCaMP6f fluorescent signals were conducted as described (77). Regions of interest (ROIs) were drawn manually over the time-averages of motion corrected time-series to isolate the bouton calcium signals of GCaMP6f-expressing axons. Any imaging frames with residual motion artifacts were excluded from further analysis. Relative fluorescence change (ΔF/F) was calculated by first smoothing the raw fluorescence trace for each ROI with a first-order Savitzky-Golay filter (60 window) to estimate baseline fluorescence. The baseline was then subtracted from the lightly filtered raw fluorescence (1 second window), which was divided by the baseline to obtain ΔF/F.

Analysis of two-photon calcium imaging data

Bouton responses. Peri-event time histograms (PETHs) and peri-stimulus time histograms (PSTHs) were calculated by extracting each bouton's ΔF/F in a window around the onset of each event/stimulus (plotted as -5 to +10 sec around the onset). For the data presented in Fig. 3, we first averaged each ROI's responses across all iterations of the stimulus/event, and then plotted the grand mean of responses across ROIs with a 99% confidence interval via bootstrap resampling. Only boutons with significant responses to the stimulus were included in the plotted PETHs in Fig. 3E or PSTHs in Fig. 3F.

Bouton response significance. We assessed whether a bouton was significantly modulated by each stimulus/event by a bootstrap test. For each presentation of a stimulus or event for a ROI, we calculated the change in fluorescence from five seconds before presentation (Pre) to five seconds after (Post). We then calculated a bootstrapped confidence interval on the average change in fluorescence during stimulus presentation by bootstrap resampling. P-values for each stimulus/ROI pair were calculated as 1 minus the fraction of bootstrapped averages greater than zero (less than zero for the run-stop analysis). ROIs were considered to have a significant response to a stimulus/event if the bootstrapped p-value was < 0.05. This threshold is marked on the summary plots in Fig. 3H-I to denote the proportion of ROIs expected to display significance by chance. We calculated each proportion from the total population of ROIs that responded to at least 1 stimulus, to exclude the fraction of boutons in the FOVs that did not display significant dynamics.

Statistics for two-photon calcium imaging

Statistical differences in bouton fluorescence when mice were stationary and running was tested via Wilcoxon signed-rank test. PSTH significance for each ROI/event pair was determined by a bootstrap test as described. Z-tests were used to compare ROI proportions using the Bonferroni procedure to correct p-values for multiple comparisons, where appropriate.

Jaccard similarity test was carried out on data presented in Fig 3J to assess the significance of the overlap in ROI populations activated by each stimulus pair. Using a permutation test, we tested whether the overlap between the ROIs recruited by each stimulus is any less than what we would expect from random selection of ROIs from the population. We report the p-values from the procedure above for all stimulus pairs.

Optogenetics and contextual fear conditioning (CFC)

After optic fiber implantations, mice were transferred to the animal room of the behavioral unit, where they received 5 days of handling. Behavioral experiments were performed in a separate experimental room. On the 6th day, mice were placed into the first environmental context (environment "A") in a plexiglass shock chamber (25 cm × 25 cm × 40 cm) that was enriched with a specific combination of cues - olfactory (citrus scent), visual (black and white striped wall), spatial (square-shaped chamber), auditory (white noise) and tactile (metal bars on the floor). Mice were allowed to freely move in the first environment for 2 min to record baseline freezing levels. Mice were considered to display freezing behavior, if they did not make any movement other than breathing for at least 2 seconds. After this, mice received 4 foot-shocks (2 seconds, 1-2 mA intensity, 30 seconds inter-shock interval). Optogenetic stimulation (15 mW intensity at the tip of the optic fiber, 5 ms blue laser light pulses at 25 Hz for 6 seconds, at 473 nm wavelength) was precisely aligned with the shocks, starting 2 seconds before shock onset and finishing 2 seconds after shock offset. For the "ChR2-shifted" group, this laser stimulation was shifted by 15 seconds after shock onset. Foot shocks and laser pulses were driven by a custom-made TTL pulse generator (Supertech Instruments). After four successfully delivered shocks, mice were placed back into their home cages for 24 h. On the 7th day, mice were placed back into the first environment for 3 minutes to record freezing behavior. (The shock chamber was cleaned thoroughly with citrus soap between mice). This was followed by 5 days of extensive handling to achieve full fear extinction that reset freezing behavior to a normal baseline. On the 13th day, mice were placed into the second environmental context (environment "B"), composed of another set of cues - olfactory (macadamia nut scent), visual (black dotted walls with white background), spatial (bended chamber walls), auditory (no noise) and tactile (metal bars on the floor) cues. Baseline freezing levels were recorded for 3 minutes, followed by 4 shocks without optogenetic stimulation. After receiving the shocks, mice were placed back into their home cages and the shock chamber was cleaned thoroughly with macadamia nut soap. Then 24 h later, on the 14th day, freezing behavior was recorded in the second environment for 3 minutes. The behavior of the mice was recorded with a JVC GC-PX100 camcorder, and freezing behavior was analyzed manually using the Solomon Coder software. We considered freezing behavior periods as those when mice displayed only respiration-related movements for at least 2 seconds. The experimenter evaluating

freezing levels was blinded to the conditions and history of the mice. Mice showing higher than 5% baseline freezing levels in environment "A" were excluded from further analysis.

Optogenetics and delay cued fear conditioning (CuedFC)

After optic fiber implantations, mice were transferred to the animal room of the behavioral unit of the institute, where they received 5 days of handling. On the 6th day, mice were placed into the first environmental context (environment "A") in a plexiglass shocking chamber (25 cm × 25 cm × 31 cm) that was enriched with a specific combination of cues - olfactory (macadamia nut scent), visual (black dotted wall with white background), spatial (bended chamber walls), auditory (white noise) and tactile (metal bars on the floor). Mice were allowed to freely move in the first environment for 3 minutes to record baseline freezing levels. After this, mice received 3 shocks (2 seconds, 2 mA intensity, 60 seconds inter-shock interval) that were paired with an auditory cue (30s long sound at 7500 kHz). The footshocks and the auditory cues were co-terminated each time. After receiving the last shock, mice were kept in the context for another 30 seconds. During the experiment, lasting 6 minutes, mice received a continuous yellow laser light illumination (15 mW intensity at the tip of the optic fiber at 593 nm wavelength). After 3 successfully delivered shocks, mice were placed back into their home cages for 24 h. On the 7th day, mice were placed back into the first environment for 3 minutes to record freezing behavior related to the contextual fear memories. Then 24 h later, on the 8th day, mice were placed into a second environmental context (environment "B") with distinct cues - olfactory (citrus scent), visual (black and white striped wall), spatial (square shaped chamber), auditory (no noise) and tactile (plastic floor). Here, after 3 minutes mice were presented with the auditory cue for 1 minute to record freezing behavior related to the cued fear memories. The behavior of mice was recorded with a JVC GC-PX100 camcorder, and freezing behavior was analyzed manually using the Solomon Coder software. The experimenter evaluating freezing levels was blind to the conditions of the mice. Mice displaying higher than 5% baseline freezing levels in environment "A" were excluded from the further analysis.

Elevated plus maze (EPM) after optogenetic CFC

One (1) hour after freezing behavior assessment in the first environment (7th day) we placed the mice into an EPM to test their anxiety levels. The cross-shaped EPM apparatus consisted of two open arms with no walls (30 cm × 7 cm) and two closed arms (30 cm high walls) and was on a pedestal 50 cm above floor level (Fig. 6A). The behavior of the mice was recorded with a JVC GC-PX100 camcorder and evaluated using an automated system (Noldus Ethovision 10.0; Noldus Interactive Technologies). Behavior was measured as total time in the open and closed arms.

Statistics for optogenetic behavioral experiments

In every behavioral experiment, we used median and 25%-75% interquartile range to describe data groups, because they did not display a Gaussian distribution. To test for statistically significant differences in independent data populations, we used the Mann-Whitney U-test, and in dependent data populations, we used the two-sided Wilcoxon signed-rank test.

In vivo electrophysiological recordings in freely behaving mice

Electrophysiological recordings were commenced after a 7-day post-surgery recovery and habituation to 'connectorization'. The signal from the silicon probe was multiplexed by RHA2132 chip (Intan Technologies, Los Angeles, CA, USA) and transmitted through a lightweight flexible cable to the signal acquisition system (KJE-1001, Amplipex Ltd, Szeged, Hungary) at 20 kHz sampling rate. The movement of the mouse was tracked by a marker-based, high speed (120 frame/s) 4-camera motion capture system and reconstructed in 3D (Motive, OptiTrack, NaturalPoint Inc, Corvallis, OR, USA). The markers needed for tracking were attached to the headstage connected to the silicon probe and to the shielding mesh. After home cage recording, mice were placed into an open arena (40 × 60 cm) and into a linear track (100 × 9 cm). Recordings were repeated 1-7 days later. In each recording situation, blue (473 nm) light stimulation was triggered manually by the experimenter controlling the TTL pulse generator (Spike2 and micro1401mkII, CED Ltd, Cambridge, UK). Various trains of 5 ms long TTL pulses were used: constantly repeating at 5, 15 or 25 Hz frequency (50-100 pulses in total per session) or delivered in a theta burst protocol (TBS, 3 or 5 pulses at 25 or 50 Hz in bursts repeated at 5 or 10 Hz). TTL pulses were fed into the power supply of the laser (IKE-473-LN-100T with a power supply (IKE-PS-300, IkeCool Corp, Anaheim, CA, USA) coupled to a 105 μm core diameter multi-mode patch cable (Thorlabs GmbH, Dachau/Munich, Germany) terminating in a ceramic ferrule. This ferrule was connected by a ceramic mating sleeve to either the incertus-implanted or the control optical fiber, plus the mating sleeve was covered by a small black plastic tube to minimize the light leakage. The light intensity at the tip of the fiber was approximately 9-13 mW prior to recordings. Mice were recorded in 3 - 9 sessions for 2 - 5 weeks. Mice were perfused transcardially with 4%PFA after the electrophysiological recordings were completed, and the brains were processed for histological verification of the viral transduction zone and implantation. Data from mice with confirmed transduction, optical fiber position and silicon probe track colored by DiI (Molecular Probes, Cat. No.: D282) prior to the implantation were used in the analysis (n = 5).

Data analysis and statistics for in vivo experiments

The analysis was performed in MATLAB environment (MathWorks, Natick, MA, USA) by custom-written functions and scripts. Local field potential (LFP) signal was downsampled at 1 kHz. Channels from strata pyramidale, radiatum, lacunosum-moleculare, moleculare and hilus were identified by characteristic physiological markers (amplitude of ripple activity, reversal of sharp-waves, phase-shift of theta oscillation and sink-source distribution on current source density profiles) and probe track location in histological preparations. The instant speed of the mouse was calculated from the 3D-tracked position data synchronized to the LFP recordings. To reduce the velocity noise, the harmonic mean of instant speed (calculated by overlapping 11-sample sliding segments, omitting speed data when the increment of instant acceleration was more than 5-fold) smoothed by a Savitzky-Golay filter (occasional negative values in the result were replaced by the linear interpolation between surrounding positive values) was used in the analysis. The stimulation sessions were categorized by whether the mouse was running or sleeping in REM state at the illumination onset. The criteria for running episodes were:

(a) average speed of the mouse in 4 subsequent 0.5 s long time segments preceding the stimulus onset above 4 cm/s and (b) higher power in theta band (5-12 Hz) than in delta band (1-4 Hz) assessed by the Welch's power spectral density estimate (periodogram) of the pyramidal LFP in the 2 s preceding the stimulus onset. The criteria for REM sleep episodes were: (a) absence of synchronous activity in the 300-1000 Hz band of LFP across all neighboring channel pairs, (b) average speed below 4 cm/s and (c) higher power in theta band than in delta band of LFP (the last two criteria were measured by the same method as detailed above in the running definition). Running episodes were pooled together from recordings made in the open arena and linear track, REM episodes were identified in home cage recordings. LFP changes in the pyramidal layer of CA1 induced by the optical stimulations were assessed by the ratio of spectral power distribution calculated by Welch's overlapped segment averaging estimator during the illumination and the preceding 2 s. Changes in low (5-8 Hz) and high theta (8 - 12 Hz) band activity (spectral power was summed in the given frequency range) among different stimulation protocols were compared by one-way Kruskal-Wallis ANOVA followed by Tukey's honestly significant difference procedure. The effects of the stimulation protocol that evoked significantly stronger power change in the high theta band than other in protocols (i.e., 25 Hz stimulation conducted in n = 4 mice, both NI GABAergic neuron and control illumination) were detailed in further analysis steps. In addition to low and high theta band, spectral power changes of the pyramidal LFP in the range of slow gamma (here restricted to 30-45 Hz to exclude rhythms generated by the repeating light-pulse-evoked transients at 25 Hz and its harmonics such as 50 Hz) and mid gamma (60-100 Hz) were also examined. Time-frequency decomposition of pyramidal LFP with continuous wavelet transform (78) and subsequent bias correction of spectral power (79) was used to calculate instant power. Pairing of instant power and speed data during stimulation, and the preceding and following 4 s allowed us to disparately examine the changes in the low and high theta band power when mice were quiet (instant speed: 0-4 cm/s) and moving (instant speed > 4 cm/s). Current source density (CSD) maps were calculated to uncover electric responses upon stimulation in more superficial layers of CA1 such as stratum radiatum and lacunosum-moleculare and in the dentate gyrus. For CSD analysis, noisy and low impedance channels were excluded manually. Pulse-onset-triggered CSD averages were calculated in ±100 ms around the onset of light pulses during stimulation, and for the preceding 2 s, the intervals of the original pulse train were shifted with a random start time. Theta-peak-triggered CSD averages were calculated in ±250 ms around the peaks of theta cycles (the phase was computed from the Hilbert transform of 8 - 12 Hz band filtered pyramidal LFP signal) when instant power of pyramidal theta oscillation was higher than that of delta (the power ratio was computed from bias-corrected time-frequency decomposition of LFP with continuous wavelet transform). For assessment of stimulation-induced current changes, data were temporally (in ±10 ms around the maximal sink following the onset of pulses or the peaks of theta cycles) and spatially (channels in the same layer of hippocampus) averaged. For visualization purposes only, CSD maps were smoothed by a Gaussian filter after 100-times linear interpolation between each channels. For statistical comparisons of in vivo physiological data, non-parametric two-sided Wilcoxon rank sum (control vs. NI GABAergic neuron stimulation) and signed-rank tests (before vs. during stimulation or during vs. after stimulation) were used.

Data and code availability

Data generated and analysed during the current study are presented in the manuscript or in the Supplementary Materials file, while additional datasets and custom written codes for in vivo electrophysiological recordings, 2P-imaging and data analysis are available from the following links: https://figshare.com/s/9fb345fc23ac2ac94fcd and https://figshare.com/s/5b0c6be2431caf10272b

Supplementary Text for Main Figures 1-6

Supplementary Data for Main Fig. 1

Figure 1C: The vast majority of eYFP-positive fibers was positive for relaxin-3 (at least 194/210) and vGAT (at least 351/357, white arrowheads), and the majority of the relaxin-3 positive boutons also contained eYFP- (at least 388/410) and vGAT-positivity (at least 402/410), indicating that effectively all relaxin-3-containing fibers targeting the hippocampus originate from the NI.

Figure 1D: Synapses established by the NI were positive for the GABAA-receptor γ2 subunit (at least 35/48, upper row) and the scaffolding protein gephyrin (at least 55/62, lower row). The sizes of synapses established by NI neurons were measured on the immunoreactions for gephyrin, on fully reconstructed synapses from 70 nm thick serial sections. Synapse areas are given (in μm2) as follows (median [25%-75% quartiles]): CA1 (n=19): 0.22 [0.12-0.39]; hilus (n=17): 0.22 [0.19-0.25].

Figure 1I: The majority of relaxin-3 positive NI fibers establish synaptic contacts marked by gephyrin on SOM-positive interneurons in the hippocampus (at least 264/424).

Figure 1J: The in vitro recorded neurons in the stratum oriens (n=18) were post-hoc characterized morphologically (6 O-LM cells [4 of them confirmed SOM positive], 4 projection cells, 1 bistratified cell, 7 unidentified cells) and neurochemically (at least 12/18 SOM-positive cells).

Figure 1N: IPSC amplitudes (in pA) are as follows (median [25%-75% quartiles]): control (red): 32.74 [30.75-44.59], gabazine (blue): 0 [0-0], washout (yellow): 18.45 [11.91-25.25].

Supplementary Data for Main Fig. 2

Figure 2C: The majority of eYFP-positive fibers was positive for relaxin-3 (at least 154/241) and vGAT (at least 212/241), and the majority of the relaxin-3 positive boutons also contained eYFP- (at least 169/190) and vGAT-immunoreactivity (at least 187/190), indicating that effectively all relaxin-3-containing fibers targeting the hippocampus arise from the NI.

Figure 2D: NI synapses in the MS, contained the GABAA-receptor γ2 subunit (at least 28/28, upper row) or the scaffolding protein gephyrin (at least 43/44, lower row. The sizes of synapses established by NI were measured on the basis of immunoreactions for gephyrin, on fully reconstructed synapses from 70 nm serial sections. Synapse areas are given (in μm2) as follows (median [25%-75% quartiles]): MS (n=32): 0.24 [0.19-0.29].

Figure 2F: At least 148/270 relaxin-3 positive terminals established synapses with vGluT2-positive profiles. The majority of medial septal vGluT2-positive cells received at least one such contact in the examined area (at least 45/80 counted cells).

Figure 2H: At least 21/280 relaxin-3 positive terminals contacted ChAT-positive cell profiles. Medial septal ChAT-positive neurons received at least one such contact in the examined area (at least 14/38 counted cells).

Supplementary Data for Main Fig. 4

Figure 4C: Abbreviations: A24a: cingulate cortex area 24a; A24b: cingulate cortex area 24b; ATg: anterior tegmental nucleus (Gudden); DMTg; dorsomedial tegmental nucleus; DR: dorsal raphe; DTg: dorsal tegmental nucleus; Gi: gigantocellular nucleus; HDB: horizontal limb of the diagonal band of Broca; iRt: isthmic reticular formation; LDTg: laterodorsal tegmental nucleus; LH: lateral hypothalamus; LHb: lateral habenula; LPo: lateral preoptic area; MM: mammillary bodies; MRR: median raphe region; mRt: mesencephalic reticular formation; MS:medial septum; NPr: nucleus prepositus; PAG: periaqueductal grey matter; PH: posterior hypothalamus; PNO: nucleus pontis oralis; SIB: substantia innominata of the basal forebrain; SUM: supramammillary nucleus; VDB: vertical limb of the diagonal band of Broca; VTA: ventral tegmental area; ZI: zona incerta

Supplementary Data for Main Fig. 6

Figure 6A: Population data for the freezing levels (in % of total time) in the environment ”A” for n=9 ChR2 and n=10 CTRL mice that received foot-shock-aligned stimulation of NI are as follows: (median [25%-75% quartiles]): ChR2: 1.22 [0.00-2.45], CTRL: 13.63 [5.01-21.36] (**: p=0.003, Mann-Whitney U-test).

Population data for the time spent in open arms of the EPM (in seconds) for n=7 ChR2 and n=10 CTRL mice that received foot-shock-aligned stimulation of NI are as follows: (median [25%-75% quartiles]): ChR2: 34.36 [18.64-97.44], CTRL: 12.00 [0.88-23.76] (*: p=0.022, Mann-Whitney U-test).

Figure 6B: Population data for the freezing levels (in % of total time) for n=21 ChR2 mice that received foot-shock-aligned stimulation of NI fibers in the HIPP, are as follows: (median [25%-75% quartiles]): environment ”A”: 3.67 [2.22-6.34], environment ”B”: 12.01 [4.78-18.24] (**: p=0.007, Wilcoxon signed-rank test).

Population data for the freezing levels (in % of total time) for n=14 CTRL mice that received foot-shock-aligned stimulation of NI fibers in the HIPP are as follows: (median [25%-75% quartiles]): environment ”A”: 6.67 [0.00-19.02], environment ”B”: 15.63 [5.90-18.13] (n.s.: non-significant, p=0.196, Wilcoxon signed-rank test).

Figure 6C: Population data for the freezing levels (in % of total time) for n=6 ChR2-light-aligned and n=6 ChR2-light-shifted mice, are as follows: (median [25%-75% quartiles]): ChR2-aligned: 4.34 [2.22-6.56], ChR2-shifted: 20.86 [8.79-25.36] (**: p=0.008, Mann-Whitney U-test).

Figure 6D: Population data for the contextual freezing levels (in % of total time) in the environment ”A” for n=5 ArchT and n=6 CTRL mice are as follows: (median [25%-75% quartiles]): ArchT: 15.11 [13.67-17.56], CTRL: 6.11 [4.11-8.67] (*: p=0.022, Mann-Whitney U-test).

Population data for the cued freezing levels (in % of total time) in the environment ”B” for n=5 ArchT and n=6 CTRL mice are as follows: (median [25%-75% quartiles]): ArchT: 36.50 [33.33-39.67], CTRL: 40.33 [32.00-52.67] (n.s.: non-significant, p=0.784, Mann-Whitney U-test).

Fig. S1. Supplementary anatomical details of NI GABAergic neuronal projections

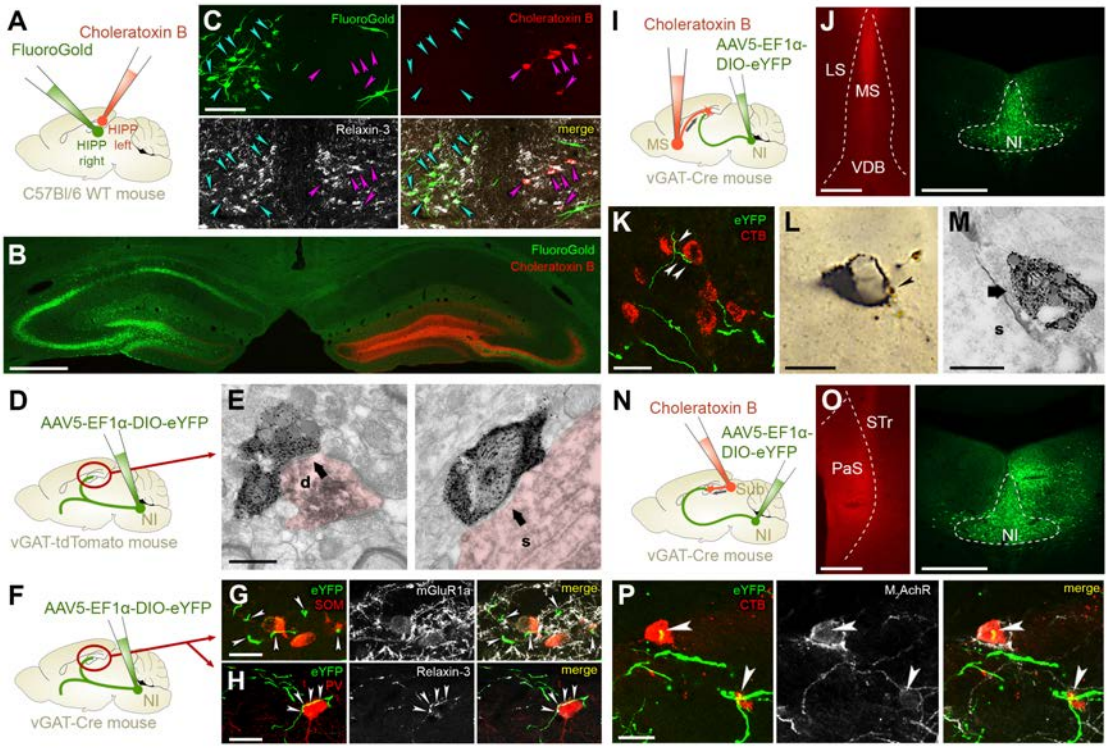

A: Double retrograde tracing in the bilateral hippocampi using FG in the right and CTB in the left hemisphere, respectively, in C57Bl/6 wild-type mice (n=2).
B: A representative injection site illustrating green FG labeling and red CTB labeling in the hippocampi of right and left hemispheres, respectively. Scale bar: 500 µm.
C: FG labeled neurons (green, cyan arrowheads) and CTB labeled neurons (red, magenta arrowheads) are mainly located in the ipsilateral NI, in the right or left hemisphere, respectively. Only a few NI neuron were positive for both retrograde tracers (18/315). The majority of the retrogradely-labeled neurons was relaxin-3 positive (white, 222/315). Scale bar: 100 µm.
D: AAV2/5-EF1α-DIO-eYFP was injected into the NI of vGAT-tdTomato reporter mice (n=2).
E: Electron microscopic images reveal SI-DAB (grainy precipitate) containing NI fibers establishing symmetrical synaptic contacts (black arrows) with DAB-Ni (dark precipitate, false-colored with faint red) containing hippocampal interneuron dendrites (d) and somata (s). The majority of NI fibers established synaptic contacts with DAB-Ni positive GABAergic profiles (total: 62/71, 55 on dendrites, 7 on somata). Scale bar: 600 nm.
F: AAV2/5-EF1α-DIO-eYFP was injected into the NI of vGAT-Cre mice (n=7).
G: NI fibers labeled with eYFP (green) establish putative contacts (white arrowheads) with SOM-positive (red) and mGluR1α-positive (white) interneurons in the stratum oriens of the dorsal CA1. Scale bar: 20 µm.

H: Many of the SOM-positive interneurons are parvalbumin (PV)-positive in stratum oriens of HIPP. NI fibers labeled with eYFP (green) and positive for relaxin-3 (white) establish putative contacts (white arrowheads) with a PV-positive interneuron (red) in the stratum oriens of the dorsal CA1. Scale bar: 20 μm.
I: AAV2/5-EF1α-DIO-eYFP was injected into the NI and CTB was injected into the MS of the same vGAT-Cre mice (n=2) to label hippocamposeptal projection neurons.
J: Representative injection sites illustrating red CTB labeling in the MS and green eYFP labeling in the NI. Abbreviations: LS: lateral septum; MS: medial septum; VDB: ventral limb of the diagonal bands of Broca. Scale bars: 500 μm.
K: eYFP-positive NI fibers in the HIPP (green) establish putative contacts (white arrowheads) with CTB-positive hippocamposeptal interneurons (red). Scale bar: 20 μm.
L: A NI fiber labeled with brown SI-DAB establishes a synaptic contact with a CTB-positive hippocamposeptal interneuron labeled with black DAB-Ni precipitate in the DG. The NI terminal reconstructed with correlated light- and electron microscopy is indicated with a black arrowhead. Scale bar: 10 μm.
M: The same terminal marked in S also has a symmetrical synaptic contact (black arrow) on the soma (s) of a hippocamposeptal interneuron. Scale bar: 600 nm.
N: AAV2/5-EF1α-DIO-eYFP was injected into the NI and CTB was injected into the subiculum of the same vGAT-Cre mice (n=2) to label hippocampo-retrohippocampal projection neurons.
O: Representative injection sites illustrating red CTB labeling in the subiculum and green eYFP labeling in the NI. Abbreviations: PaS: parasubiculum; STr: subiculum, transition area. Scale bars: 500 μm.
P: eYFP-positive NI GABAergic fibers in the HIPP (green) establish putative contacts (white arrowheads) with CTB-positive hippocampo-retrohippocampal interneurons (red), which are also positive for the type 2 muscarinic acetylcholine receptor (M2AChR, white). Scale bar: 20 μm.

Fig. S2 Projection patterns of NI and surrounding nuclei

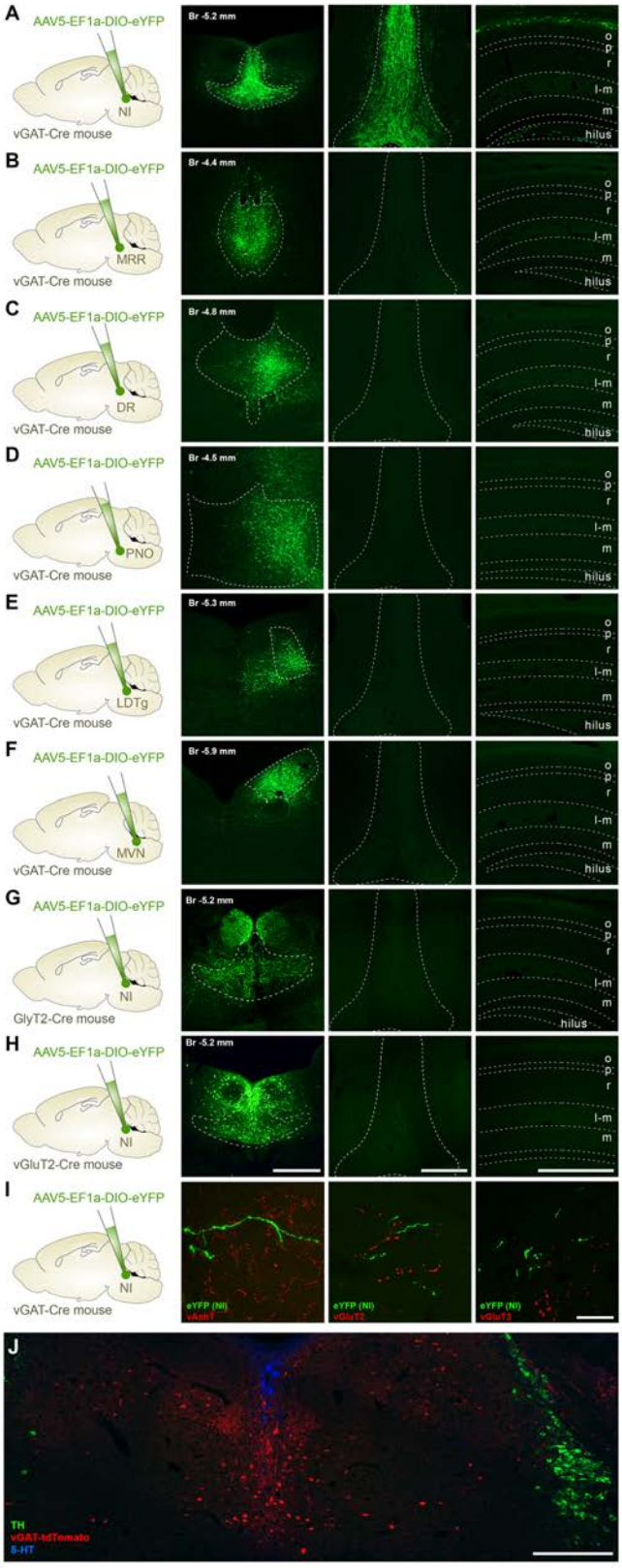

A-H: AAV2/5-EF1α-DIO-eYFP was injected into various areas in the brainstem in vGAT-Cre, vGluT2-Cre or GlyT2-Cre mice. The images illustrate representative coronal sections from the region of the different injection sites and from the hippocampus and MS, respectively. The centers of the injection sites were also identified and defined by their anteroposterior coordinates from Bregma. Note, that the characteristic vGAT-positive fiber labeling of the NI in these forebrain areas can be observed only in vGAT-Cre mice (A), and it is absent, when the AAV-eYFP was injected into the neighboring brain areas or into vGluT2-Cre or GlyT2-Cre mice. Scale bars (panel H) 500 μm for all images (columns of A-H).
A: AAV2/5-EF1α-DIO-eYFP was injected into the nucleus incertus (NI) of vGAT-Cre mice (n=7).
B: AAV2/5-EF1α-DIO-eYFP was injected into the median raphe region (MRR) of vGAT-Cre mice (n=2).
C: AAV2/5-EF1α-DIO-eYFP was injected into the dorsal raphe (DR) of vGAT-Cre mice (n=2).
D: AAV2/5-EF1α-DIO-eYFP was injected into the nucleus pontis oralis (PNO) of vGAT-Cre mice (n=2).
E: AAV2/5-EF1α-DIO-eYFP was injected into the laterodorsal tegmental nucleus (LDTg) of vGAT-Cre mice (n=2).

F: AAV2/5-EF1α-DIO-eYFP was injected into the medial vestibular nucleus (MVN) of vGAT-Cre mice (n=2).
G: AAV2/5-EF1α-DIO-eYFP was injected into the NI of GlyT2-Cre mice (n=2).
H: AAV2/5-EF1α-DIO-eYFP was injected into the NI of vGluT2-Cre mice (n=2).
I: AAV2/5-EF1α-DIO-eYFP was injected into the nucleus incertus (NI) of vGAT-Cre mice (n=2). We did not observe any meaningful co-localization of AAV-eYFP containing NI fibers and vesicular acetylcholine transporter (vAChT, only 3/320) or vGluT2 (only 3/206) or vGluT3 (0/216) in the dorsal CA1 of the hippocampus, measured in n=2 mice per reaction, respectively. The apparent labeling was likely false positives. Scale bar: 20 μm for all images per row.
J: A representative coronal section from the pons of a vGAT-tdTomato mouse (n=2 mice tested) illustrates that GABAergic neurons of the NI (red) do not co-express tyrosine-hydroxylase (TH, green) or serotonin (5-HT, blue). Scale bar: 250 μm.

Fig. S3 Supplementary data from in vitro recordings of NI GABAergic cells

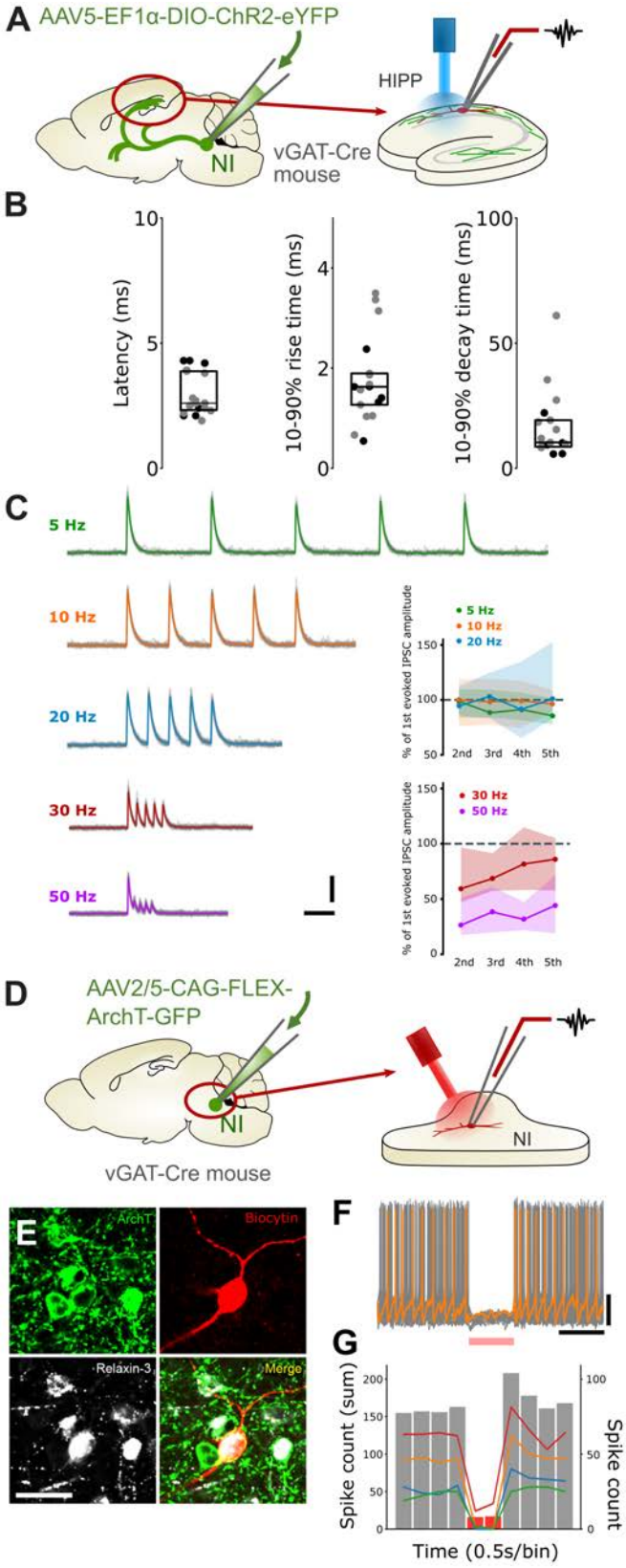

A: Experimental design of optogenetic in vitro intracellular recordings (experiment described in detail in Fig. 1J).
B: Population data (n=18 cells) for in vitro recorded IPSC latencies (defined as time between stimulus onset and 10% of IPSC amplitude), 10-90% rise times and 10-90% decay times. Data are presented (in ms) as follows (median [25%-75% quartiles]): Latency: 2.6 [2.3-3.55], 10-90% rise time: 1.63 [1.28-1.89], 10-90% decay-time: 11.11 [8.77-19.02]. Black dots represent cells that could be both reconstructed and identified as OLM cells.
C: Left panel displays averaged IPSCs from the O-LM cell in Fig. 1K. Optical stimulation was delivered at 5 Hz (green), 10 Hz (yellow), 20 Hz (blue), 30 Hz (red) and 50 Hz (purple) to test frequency-dependent short-term plasticity. At lower (5-20 Hz) frequencies, no short-term plasticity was evident. The cell displayed STD at higher (30-50 Hz) stimulation frequencies, although it is not clear whether ChR2 stimulation-failure at these higher 50 Hz frequencies may have contributed to an increased STD. Scale bars: 100 ms, 200 pA. Right panel: population data showing changes in amplitudes for 17 cells are as follows (median [25%-75% quartiles]): 5 Hz: 2nd 98.65 [83.66-109.43], 3rd 88.22 [83.95-109.43], 4th 91.17 [81.57-106.88], 5th 85.54 [77.57-101.30]; 10 Hz: 2nd 99.87[76.23-118.95], 3rd 98.25 [77.38-119.10], 4th 99.14 [74.52-117.21], 5th 96.28 [89.98-109.05];

20 Hz: 2nd 94.33 [85.83-112.23], 3rd 103.25 [83.24-124.86], 4th 91.29 [65.20-135.02], 5th 100.83 [83.11-152.76], 30 Hz: 2nd 59.40 [46.94-96.68], 3rd 68.44 [57.20-91.52], 4th 81.72 [58.09-114.66], 5th 85.98 [57.73-105.00] and 50 Hz: 2nd 26.48 [17.24-51.00], 3rd 38.37 [19.77-60.98], 4th 31.68 [21.82-47.16], 5th 44.27 [18.81-71.62].
D: Experimental design of optogenetic in vitro intracellular recordings from NI cells. AAV2/5-CAG-FLEX-ArchT-GFP was injected into the NI of a vGAT-Cre mouse (n=1). After 6 weeks of survival, 300-µm-thick horizontal slices containing NI were cut from the brainstem and transferred into a dual-superfusion chamber. NI neurons were whole-cell patch clamped in current clamp mode, and the firing activity of the neurons was measured, while the slices were illuminated with red light. The recorded neurons (n=4) were post-hoc characterized neurochemically (3 were confirmed to be relaxin-3 positive).
E: Confocal laser scanning fluorescent image illustrates a representative GABAergic NI neuron expressing ArchT (green) that was recorded and filled with Biocytin (red). The neuron was positive for relaxin-3. Scale bar: 20 µm.
F: In vitro red-light illumination effectively blocked action potential generation in the GABAergic NI neuron shown in D. Twenty (20) overlaid membrane potential traces are shown with 1 sec-long illumination periods (orange bar). A sample trace is provided (yellow). Scale bars: 1s, 20 mV.
G: Population data illustrating action potential blockade upon illumination of NI neurons expressing ArchT (80 stimulation periods from 4 cells). Cumulative spike count is represented by bars, while individual cell spike counts are represented by lines. Yellow line indicates the cell shown in D-E.

Fig. S4 Injection sites and optic fiber localizations

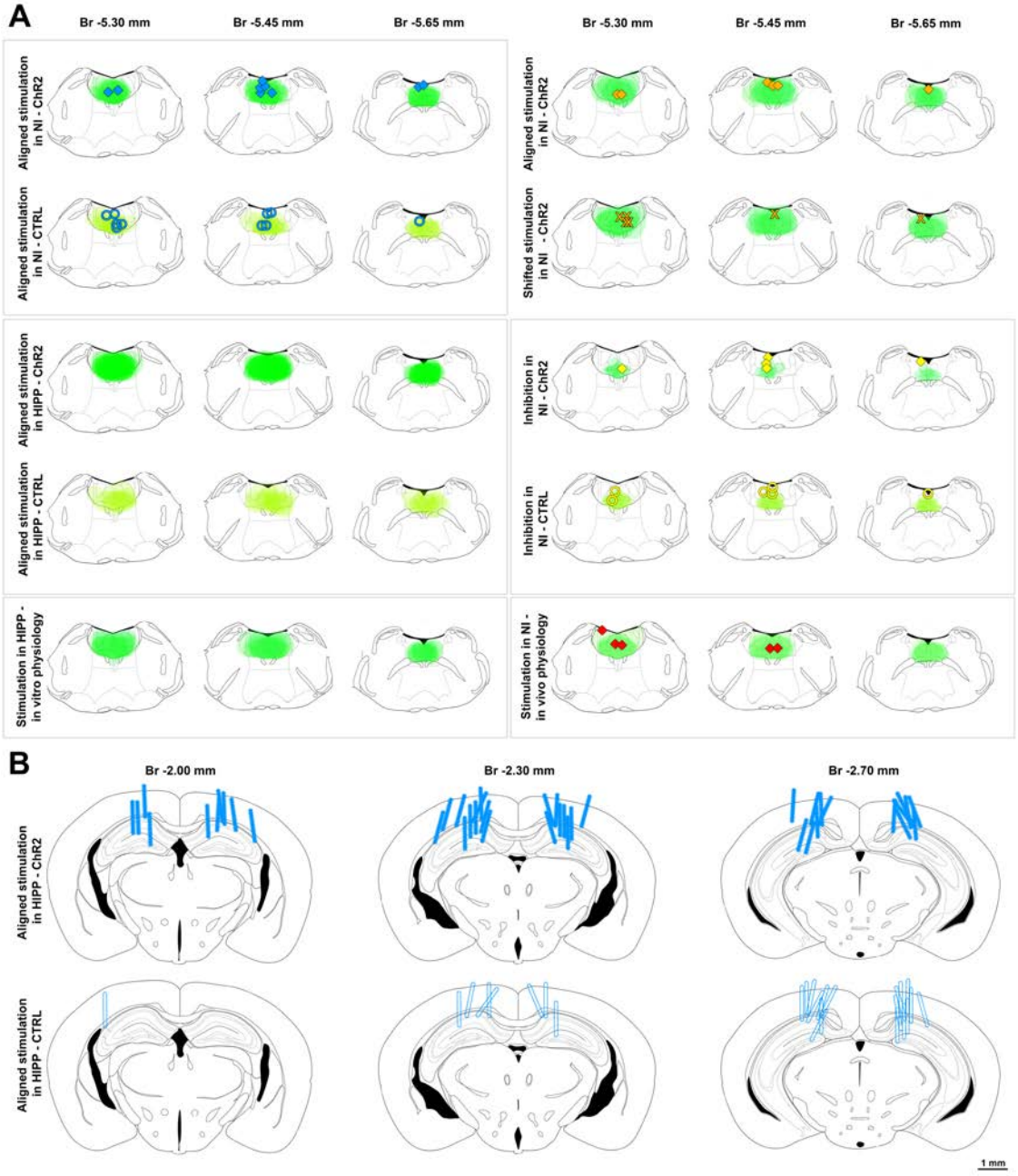

A: Summary of virus injection sites in every mouse used in the behavioral, in vivo or in vitro optogenetic experiments. The virus injection sites in the different mice participating in the different experiments were checked one-by-one and overlaid onto each other. AAV2/5-EF1a-DIO-ChR2-eYFP (ChR2) or AAV2/5-CAG-FLEX-ArchT-GFP (ArchT) expression is labeled with green, AAV2/5-EF1a-DIO-eYFP (CTRL) expression is labeled with yellow in the area of NI and adjacent structures at 3 different coronal levels (Bregma -5.30, -5.45 and -5.65 mm, respectively). The tips of the optic fibers positioned over the NI are also labeled as follows:

- Experiments comparing foot-shock-aligned ChR2 vs. CTRL stimulation in the NI (described in Fig. 6A):
Blue rhombs: optic fibers in ChR2-expressing mice, foot-shock-aligned stimulation.
Blue circles: optic fibers in CTRL-expressing mice, foot-shock-aligned stimulation.
- Experiments comparing foot-shock-aligned stimulation vs. 15 seconds-shifted stimulations in the NI (described in Fig. 6C):
Orange rhombs: optic fibers in ChR2-expressing mice, foot-shock-aligned stimulation.
Orange "X"-s: optic fibers in ChR2-expressing mice, foot-shock-shifted stimulation.
- Experiments comparing ArchT vs. CTRL inhibition (described in Fig. 6D):
Yellow rhombs: optic fibers in ArchT-expressing mice, inhibition.
Yellow circles: optic fibers in CTRL-expressing mice, inhibition.
- In vivo physiology experiments (described in Fig. 6 and Fig. S4):
Red rhombs: optic fibers in ChR2-expressing mice, stimulation in the in vivo physiology experiments.
B: Positions of the etched optic fibers at 3 different coronal levels (Bregma -2.00, -2.30 and -2.70, respectively) in experiments comparing foot-shock-aligned ChR2 vs. CTRL stimulation in the HIPP (described in Fig. 6B):
Blue multiple-pointed filled rods: etched optic fibers in ChR2-expressing mice, footshock-aligned stimulation.
Blue empty rods: etched optic fibers in CTRL-expressing mice, foot-shock-aligned stimulation.

Fig. S5 In vivo hippocampal recordings during optogenetic stimulation of NI GABAergic cells

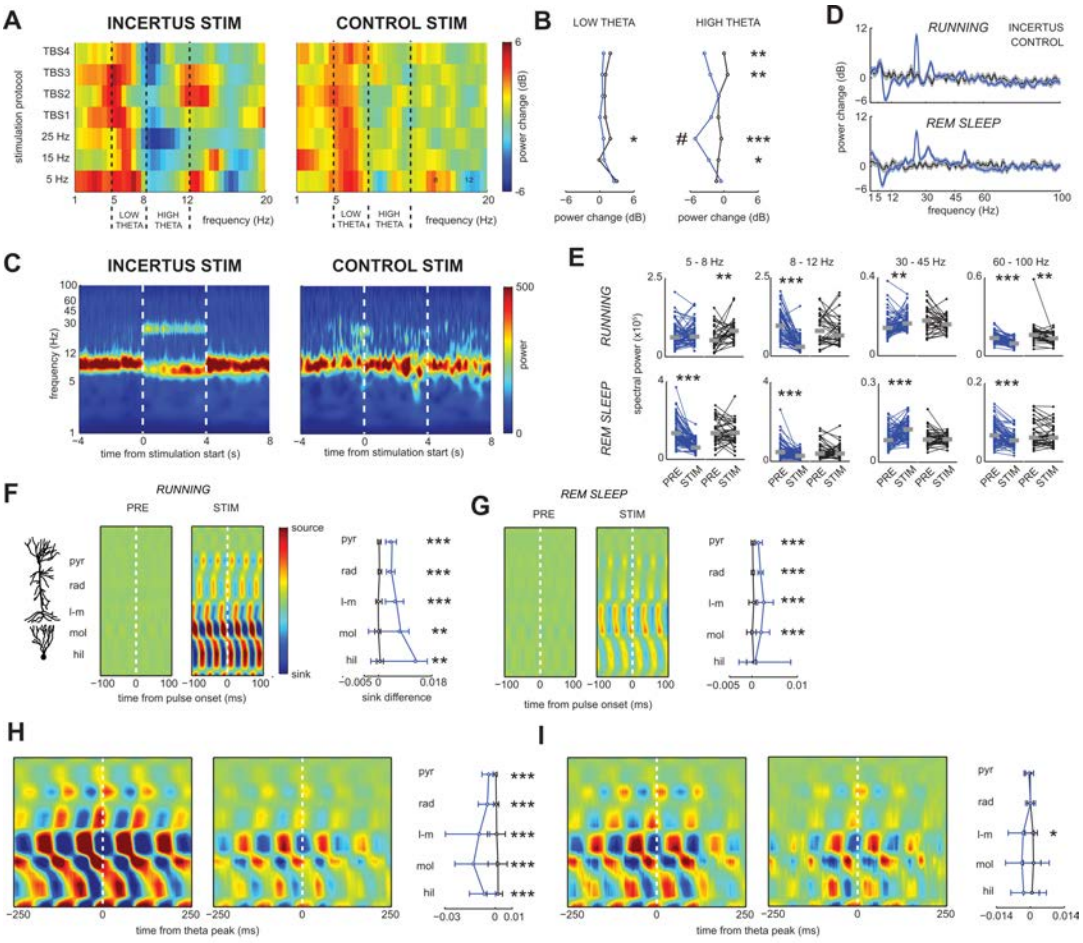

A: Average spectral power change determined as the ratio of Welch's periodograms (spectral power distribution calculated by Welch's overlapped segment averaging estimator) of pyramidal LFP to the preceding 2 seconds-long non-stimulated segment during various stimulation protocols. Running episodes were selected during NI GABAergic neuron (INCERTUS, left) and control stimulations (CONTROL, right). TBS: theta burst stimulation, TBS1: 3 pulses at 25 Hz in bursts repeated by 5 Hz, TBS2: 3 pulses at 50 Hz in bursts repeated by 5 Hz, TBS3: 5 pulses at 50 Hz in bursts repeated by 5 Hz, TBS4: 3 pulses at 50 Hz in bursts repeated by 10 Hz.
B. Changes of summed spectral power in low theta (5-8 Hz, left) and high theta (8-12 Hz, right) bands. Plots show medians of data in rows corresponding to stimulation protocols in A (blue: NI GABAergic neuron stimulation, black: control stimulation). Significant effect of various stimulation protocols on high theta band power was revealed by Kruskal-Wallis ANOVA ($\chi 2(6) = 40.9278$, $p < 0.001$ for NI GABAergic neuron stimulation and $\chi 2(6) = 3.229$, $p = 0.7796$ for control stimulation). Post-hoc test (Tukey's honestly significant difference procedure) proved that 25 Hz stimulation (marked by #) had a significantly different effect to the other protocols. In contrast, these stimulation

protocols had no statistically different effect on low theta band power (Kruskal-Wallis ANOVA, $\chi 2(6) = 3.7744$, $p = 0.7072$ for NI GABAergic neuron stimulation and $\chi 2(6) = 4.0376$, $p = 0.6716$ for control stimulation). On the right side of the plots, significant differences between NI GABAergic neuron and control stimulations are indicated (*: $p < 0.05$, **: $p < 0.01$, ***: $p < 0.001$ two-sided Wilcoxon rank sum test).
C. Time-resolved spectral changes during 25 Hz stimulation demonstrated by the continuous wavelet transform of the pyramidal layer LFP. Here, the same data are illustrated as in Fig. 6B, but the frequency scale is expanded to 100 Hz. Notably, besides theta suppression, the power of the 25-30 Hz band was increased by NI GABAergic neuron stimulation. However, this effect might have resulted from the interaction of incertus-triggered oscillations and rhythms accompanying the stimulation-induced brain state change (e.g. slow gamma).
D. Ratio of Welch's periodograms of pyramidal layer LFP during 25 Hz NI GABAergic cell (blue) and control stimulation (black) to the preceding 2 seconds-long non-stimulated segment (expressed in dB). Mean ± SEM for all stimulations when mice ($n = 4$) were running (top) or sleeping in REM state (bottom) are shown. Reduction in theta power can be detected by wavelet-based decomposition. Additional two peaks of increased activity at 25 and around 30 Hz can also be distinguished, the latter might reflect elevated slow gamma activity.
E. Pyramidal spectral band power (frequency range indicated above the graphs) computed by Welch's method during 25 Hz stimulation (STIM) and preceding 2 seconds-long non-stimulated segment (PRE). Data of all individual stimulation sessions when mice were running (top) or sleeping in REM state (bottom) are plotted (blue: NI GABAergic neuron stimulation, black: control stimulation). Grey lines indicate group medians, significant differences between data groups are indicated (**: $p < 0.01$, ***: $p < 0.001$, two-sided Wilcoxon signed-rank test). Suppression of higher theta band (8-12 Hz) activity, also shown in Fig. 6C by wavelet-based decomposition, is confirmed, and additionally, oscillation around 30 Hz distinct from the evoked activity at 25 Hz was significantly stronger during stimulation than in preceding period (power in 30 - 45 Hz band).
F-I. Depth profile of hippocampal electrical activity. On the left side of every image, current source density maps of averaged LFP from a mouse during NI GABAergic neuron stimulation (STIM) and preceding 2 seconds-long non-stimulated segment (PRE) are shown. Schematic principal neurons of CA1 and dentate gyrus were arranged to the corresponding recording sites of the silicon probe. On the right side of every image, averaged difference of maximal sinks (STIM-PRE) during all 25 Hz NI GABAergic neuron (blue) and control (black) stimulations in $n = 4$ mice are displayed as group medians and 25th - 75th percentile range. Significant difference between NI GABAergic neuron and control stimulations are indicated (*: $p < 0.05$, **: $p < 0.01$, ***: $p < 0.001$, two-sided Wilcoxon rank sum test). Current source density maps are averaged by the individual stimulation pulses repeated at 25 Hz (F, G), or by the peaks of pyramidal layer theta cycles (H, I) in running (F, H) or REM sleep episodes (G, I). White dashed lines on the maps indicate the pulse onset (F,G), or the peak of the theta cycle (H,I).
Abbreviations: pyr: stratum pyramidale; rad: stratum radiatum; l-m: stratum lacunosum-moleculare; mol: stratum moleculare; hil: hilus.

Fig. S6 Supplementary control data for contextual fear conditioning experiments

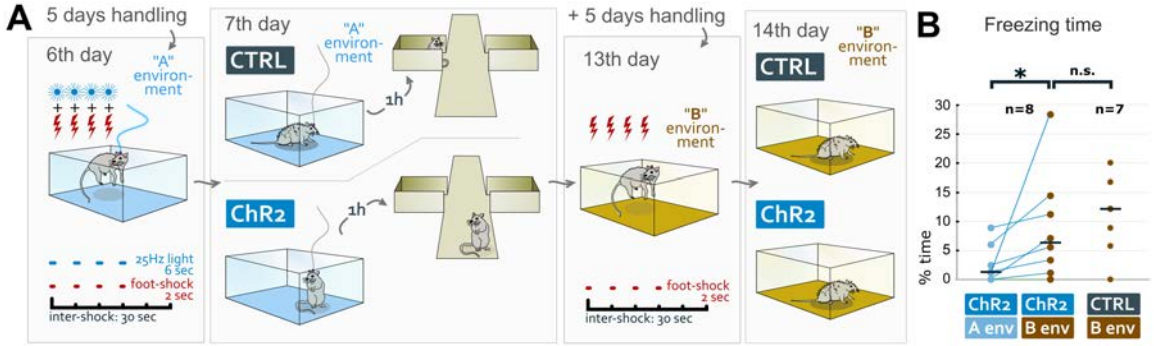

A: Illustration of the experimental design that was used as an additional control for experiments described in Fig. 6A. ChR2- or CTRL-mice were placed into a multisensory context (environment ”A”) to receive foot-shocks and foot-shock-aligned optogenetic stimulation of NI. On the 6th day, freezing behavior in environment ”A” was analyzed, followed by assessment of anxiety levels in the elevated plus maze, 1 hour later. After 5 days of extensive handling, on the 13th day, mice were placed into a completely new context (environment ”B”). Here, they displayed normal exploratory behavior without freezing, indicating that their previously established fear memories were specific for environment ”A”. In environment ”B” they received 4 foot-shocks (2 mA, 2 s) with a 30 second inter-shock interval without laser stimulation. On day 14, mice were placed back to environment ”B” to analyze their freezing behavior.
B: ChR2 mice spent significantly more time freezing in environment ”B” than in environment ”A”, indicating that NI successfully inhibited contextual fear memory formation in environment ”A”. Population data for freezing (in % of total time) are as follows (median [25%-75% quartiles]): ChR2 in environment ”A”: 1.22 [0.00-2.45], ChR2 in environment ”B”: 6.34 [2.22-12.85] (*: p=0.018, Wilcoxon signed-rank test). Freezing levels of ChR2 and CTRL mice were not different in environment ”B”, indicating that both groups of mice were capable of forming contextual fear memories. Population data for freezing (in % of total time) are as follows (median [25%-75% quartiles]): ChR2 in environment ”B”: 6.34 [2.22-12.85], CTRL in environment ”B”: 12.12 [5.78-16.80] (n.s: non-significant, p=0.417, Mann-Whitney U-test). Graph shows individual data (dots) and medians (lines).

Table S1. Primary antibodies and retrograde tracers

Antigen	Host	Dilution	Source	Catalog number
Calbindin	Rabbit	1:2000	Kind gift from K. Baimbridge	-
choline acetyltransferase (ChAT)	Mouse	1:1000	Kind gift from C. Cozzari	-
Choleratoxin B subunit	Goat	1:20000	List Biologicals	#703
Choleratoxin B subunit	Mouse	1:2000	Abcam	ab1003
eGFP	Chicken	1:1000	Abcam	ab13970
eGFP	Chicken	1:2000	ThermoFisher Scientific	A10262
eGFP	Rabbit	1:1000	ThermoFisher Scientific	A11122
FluoroGold	Rabbit	1:500	Chemicon	AB153-i
GABA-A-g2	Rabbit	1:1000	Synaptic Systems	224 003
Gephyrin	Mouse	1:100	Synaptic Systems	147 021
Gephyrin	Rabbit	1:300-1:2000	Synaptic Systems	147 008
M2	Rat	1:500	Chemicon	MAB367
mCherry	Rabbit	1:5000	BioVision	5993-100
mGluR1a	Rabbit	1:2000	ImmunoStar	24426
Parvalbumin	Guinea pig	1:10000	Synaptic Systems	195 004
Parvalbumin	Rabbit	1:2000	Kind gift from K. Baimbridge	-
Relaxin-3	Mouse	1:20-1:1000	Provided by A.L. Gundlach	-
RFP	Rat	1:2000-1:5000	Chromotek	5F8
Serotonin	Rabbit	1:10000	ImmunoStar	20080
Somatostatin	Rabbit	1:1000	Acris/OriGene	AP33464SU-N
Somatostatin	Rat	1:300-1:1000	Chemicon	MAB354
tyrosine hydroxylase (TH)	Mouse	1:2000	ImmunoStar	22941
vesic. acetylcholine transporter (vAchT)	Goat	1:10000	ImmunoStar	24286
vesicular GABA transporter (vGAT)	Guinea pig	1:2000	Synaptic Systems	131 004
vesicular glutamate transporter type 2 (vGluT2)	Guinea pig	1:2000	Synaptic Systems	135 404
(vGluT3)	Rabbit	1:500	Synaptic Systems	135 203
Choleratoxin B subunit		0,5%	List Biologicals	#104
FluoroGold		2%	FluoroChrome Inc.	-

Table S2. Characterization of the primary antibodies and retrograde tracers used.

Antigen	Host	Specificity	Characterized in
Calbindin	Rabbit	The antibody recognizes one major broad band of the expected molecular weight (28 kDa) on western blots from rat cerebellum samples and immunostaining was abolished by preadsorption with the immunogen.	[1]
choline acetyltransferase (ChAT)	Mouse	Staining is typical for cholinergic cells; complete overlap of staining with eYFP-positive cells in ChAT-iRES-Cre mice injected with AAV-EF1a-DIO-eYFP.	[2,3]
Choleratoxin B subunit	Goat	No staining in non-injected mice.	[4]
Choleratoxin B subunit	Mouse	No staining in non-injected mice.	[5]
eGFP (Abcam)	Chicken	No staining in mice not injected with eGFP-expressing virus.	Information of the distributor
eGFP (Thermo Fisher Sci.)	Chicken	No staining in mice not injected with eGFP-expressing virus.	Information of the distributor
eGFP	Rabbit	No staining in mice not injected with eGFP-expressing virus.	Information of the distributor
FluoroGold	Rabbit	No staining in non-injected mice.	[6]
GABA-A-γ2	Rabbit	No staining in GABA-A-γ2 floxed mice in areas injected with AAV-Cre (conditional knockout); extracellular epitope.	[7]
Gephyrin	Mouse	KO verified.	Information of the distributor
Gephyrin	Rabbit	KO verified.	Information of the distributor
M2	Rat	KO verified.	[8]
mCherry	Rabbit	No staining in mice not injected with mCherry-expressing virus.	Information of the distributor
mGluR1a	Rabbit	Several antibodies for different epitopes gave the same labeling pattern.	[9]
Parvalbumin	Guinea pig	Labels the same cell populations in the brain as other antibodies to parvalbumin.	Information of the distributor, [10]
Parvalbumin	Rabbit	Labels the same cell populations in the brain as other antibodies to parvalbumin.	[11,12]
Relaxin-3	Mouse	KO verified.	[13]
RFP	Rat	No staining in mice not injected with mCherry-expressing virus.	Information of the distributor
Serotonin	Rabbit	Staining is typical for serotonergic neurons, complete overlap with TpH-staining.	[14,15]
Somatostatin	Rabbit	Labels the same neuron populations in the brain as other antibodies to somatostatin.	[16]

Somatostatin	Rat	Labels the same neuron populations in the brain as other antibodies to somatostatin.	[17]
TH	Mouse	Staining is typical for TH-positive neurons.	[18]
vesicular acetylcholine transporter (vAchT)	Goat	Complete overlap with ChAT staining.	[3]
vesicular GABA transporter (vGAT)	Guinea pig	KO verified.	Information of the distributor
vesicular glutamate transporter type 2 (vGluT2)	Guinea pig	The antibody recognizes one major broad band of the expected molecular weight (65 kDa) on western blots of a synaptic vesicle fraction of rat brain and immunostaining was abolished by preadsorption with the immunogen.	Information of the distributor, [19]
vesicular glutamate transporter type 3 (vGluT3)	Rabbit	KO verified.	Information of the distributor
Choleratoxin B subunit		Retrograde tracer.	[20]
FluoroGold		Retrograde tracer.	[20]

Footnote: [1] A.M.J. Buchan, K.G. Baimbridge, Peptides 9 (1988) 333–338. [2] A. Chédotal et al. Brain Res. 646 (1994) 181–193. [3] V.T. Takács et al., Nat. Commun. 9 (2018). [4] P.J.W.C. Dederen et al., Histochem. J. 26 (1994) 856–862. [5] K.T. Hamorsky et al. PLoS Negl. Trop. Dis. 7 (2013). [6] C. Varga et al. J. Neurosci. 22 (2002) 6186–6194. [7] Z. Rovo et al. J. Neurosci. 34 (2014) 7137–7147. [8] K.A. Kohlmeier et al. J. Neurophysiol. 108 (2012) 2751–2766. [9] R.G.E. Notenboom et al., Brain 129 (2006) 96–107. [10] L. Massi et al., J. Neurosci. 32 (2012) 16496–16502. [11] F. Condé et al. J. Comp. Neurol. 341 (1994) 95–116. [12] F. Mascagni et al. Neuroscience 158 (2009) 1541–1550. [13] S. Ma et al. J. Physiol. 591 (2013) 3981–4001. [14] S.R. Fox, E.S. Deneris, J. Neurosci. 32 (2012) 7832–42. [15] S. KE et al., Brain Struct. Funct. 222 (2016) 287–299. [16] F. Antonucci et al. J. Neurosci. 32 (2012) 1989–2001. [17] Y. Kubota et al. Cereb. Cortex 21 (2011) 1803–1817. [18] M. Chermenina et al. Parkinsons. Dis. 1 (2015). [19] J. Broms et al. J Comp Neurol 523 (2016) 359–380. [20] J.L. Lanciego et al. J. Chem. Neuroanat. 42 (2011) 157–183.

Table S3. Secondary antibodies.

Raised in (species)	Raised against (species)	Conjugated with	Dilution	Source	Catalog number
Chicken	Rat	Alexa 647	1:500	ThermoFisher Scientific	A21472
Donkey	Rabbit	Alexa 647	1:500	Jackson Immunoresearch	711-605-152
Donkey	Mouse	Alexa 647	1:500	Jackson Immunoresearch	715-605-151
Donkey	Guinea pig	Alexa 647	1:500	Jackson Immunoresearch	706-605-148
Goat	Chicken	Alexa 488	1:1000	ThermoFisher Scientific	A11039
Donkey	Chicken	Alexa 488	1:300	Jackson Immunoresearch	703-545-155
Donkey	Goat	Alexa 488	1:500	ThermoFisher Scientific	A11055
Donkey	Rabbit	Alexa 488	1:1000	ThermoFisher Scientific	A21206
Donkey	Mouse	Alexa 488	1:500	ThermoFisher Scientific	A21202
Goat	Guinea pig	Alexa 488	1:500	ThermoFisher Scientific	A11073
Donkey	Goat	Alexa 594	1:500	ThermoFisher Scientific	A11058
Donkey	Guinea pig	Cy3	1:500	Jackson Immunoresearch	706-166-148
Donkey	Rabbit	Alexa 594	1:500	ThermoFisher Scientific	A21207
Donkey	Rat	Alexa 594	1:500	ThermoFisher Scientific	A21209
Donkey	Guinea pig	Alexa 594	1:500	Jackson Immunoresearch	706-585-148
Donkey	Mouse	Alexa 594	1:500	ThermoFisher Scientific	A21203
Goat	Chicken	biotinylated	1:200	Vector Laboratories	BA-9010
Goat	Rat	biotinylated	1:1000	Jackson Immunoresearch	112-066-062
Donkey	Mouse	biotinylated	1:1000	Jackson Immunoresearch	715-066-151
Donkey	Rabbit	biotinylated	1:1000	Jackson Immunoresearch	711-065-152
Goat	Rat	Horseradish peroxidase (ImmPress)	1:3	Vector Laboratories	MP-7444
Horse	Mouse	Horseradish peroxidase (ImmPress)	1:3	Vector Laboratories	MP-7402
Goat	Mouse	0.8 nm gold	1:50	Aurion	800 022
Goat	Rabbit	1.4 nm gold	1:100	Nanoprobes	#2004
	streptavidin	Alexa 594	1:500	ThermoFisher Scientific	S11227

Table S4. Primary and secondary antibody combinations used in immunofluorescence experiments.

Mouse strain	Primary antibodies used	Secondary antibodies used
C57Bl/6 WT	rabbit-anti-FluoroGold goat-anti-Choleratoxin B	Alexa 488-conjugated donkey-anti-rabbit Alexa 594-conjugated donkey-anti-goat
C57Bl/6 WT	rabbit-anti-FluoroGold goat-anti-Choleratoxin B mouse-anti-Relaxin-3	Alexa 488-conjugated donkey-anti-rabbit Alexa 594-conjugated donkey-anti-goat Alexa 647-conjugated donkey-anti-mouse
C57Bl/6 WT	guinea pig-anti-Parvalbumin mouse-anti-Relaxin-3 rabbit-anti-Gephyrin	Alexa 488-conjugated goat-anti-guinea pig Alexa 594-conjugated donkey-anti-mouse Alexa 647-conjugated donkey-anti-rabbit
ChAT-iRES-Cre; vGluT2-iRES-Cre	chicken-anti-eGFP (ThermoFisher) mouse-anti-Relaxin-3 rabbit-anti-Gephyrin	Alexa 488-conjugated goat-anti-chicken Alexa 594-conjugated donkey-anti-mouse Alexa 647-conjugated donkey-anti-rabbit
SOM-iRES-Cre	chicken-anti-eGFP (ThermoFisher) mouse-anti-Relaxin-3 rabbit-anti-Gephyrin	Alexa 488-conjugated goat-anti-chicken Alexa 594-conjugated donkey-anti-mouse Alexa 647-conjugated donkey-anti-rabbit
vGAT-Cre	chicken-anti-eGFP (ThermoFisher) rat-anti-somatostatin rabbit-anti-mGluR1alpha	Alexa 488-conjugated goat-anti-chicken Alexa 594-conjugated donkey-anti-rat Alexa 647-conjugated donkey-anti-rabbit
vGAT-Cre	chicken-anti-eGFP (ThermoFisher) mouse-anti-Relaxin-3 rabbit-anti-parvalbumin	Alexa 488-conjugated goat-anti-chicken Alexa 594-conjugated donkey-anti-mouse Alexa 647-conjugated donkey-anti-rabbit
vGAT-iRES-Cre, GlyT2-iRES-Cre, vGluT2-iRES-Cre	chicken-anti-eGFP (ThermoFisher)	Alexa 488-conjugated goat-anti-chicken
vGAT-tdTomato	mouse-anti-tyrosine hydroxylase rabbit-anti-serotonin	Alexa 488-conjugated donkey-anti-mouse Alexa 647-conjugated donkey-anti-rabbit
vGAT-Cre	rabbit-anti-eGFP	Alexa 488-conjugated donkey-anti-rabbit
vGAT-Cre	chicken-anti-eGFP (Abcam)	Alexa 488-conjugated donkey-anti-chicken
vGAT-Cre	rat-anti-RFP	Alexa 594-conjugated donkey-anti-rat
vGAT-Cre	chicken-anti-eGFP (ThermoFisher) rat-anti-RFP	Alexa 488-conjugated goat-anti-chicken Alexa 594-conjugated donkey-anti-rat
vGAT-Cre	mouse-anti-ChAT rabbit-anti-mCherry	Alexa 488-conjugated donkey-anti-mouse Alexa 594-conjugated donkey-anti-rabbit
vGAT-Cre	guinea pig-anti-Parvalbumin rat-anti-RFP rabbit-anti-Calbindin	Alexa 488-conjugated goat-anti-guinea pig Alexa 594-conjugated donkey-anti-rat Alexa 647-conjugated donkey-anti-rabbit

vGAT-Cre	rat-anti-RFP guinea pig-anti-vGluT2	Alexa 594-conjugated donkey-anti-rat Alexa 647-conjugated donkey-anti-guinea pig
vGAT-Cre	goat-anti-vAchT rat-anti-RFP	Alexa 488-conjugated donkey-anti-goat Alexa 594-conjugated donkey-anti-rat
vGAT-Cre	rat-anti-RFP rabbit-anti-vGluT3	Alexa 594-conjugated donkey-anti-rat Alexa 647-conjugated donkey-anti-rabbit
vGAT-Cre	chicken-anti-eGFP (ThermoFisher) mouse-anti-Relaxin-3 guinea pig-anti-vGAT	Alexa 488-conjugated goat-anti-chicken Alexa 594-conjugated donkey-anti-mouse Alexa 647-conjugated donkey-anti-guinea pig
vGAT-Cre	chicken-anti-eGFP (ThermoFisher) guinea pig-anti-vGAT mouse-anti-Relaxin-3	Alexa 488-conjugated goat-anti-chicken Cy3-conjugated donkey-anti-guinea pig Alexa 647-conjugated donkey-anti-mouse
vGAT-Cre	rabbit-anti-eGFP goat-anti-Choleratoxin B	Alexa 488-conjugated donkey-anti-rabbit Alexa 594-conjugated donkey-anti-goat
vGAT-Cre	rabbit-anti-eGFP goat-anti-Choleratoxin B rat-anti-M2 receptor	Alexa 488-conjugated donkey-anti-rabbit Alexa 594-conjugated donkey-anti-goat Alexa 647-conjugated chicken-anti-rat
vGAT-Cre	chicken-anti-eGFP (ThermoFisher) Alexa 594-conjugated Streptavidin rat-anti-somatostatin	Alexa 488-conjugated donkey-anti-rabbit Alexa 594-conjugated Streptavidin Alexa 647-conjugated donkey-anti-rat
vGAT-Cre	chicken-anti-eGFP (ThermoFisher) Alexa 594-conjugated Streptavidin rabbit-anti-somatostatin	Alexa 488-conjugated donkey-anti-rabbit Alexa 594-conjugated Streptavidin Alexa 647-conjugated donkey-anti-rabbit

Table S5. Primary and secondary antibody combinations used in the double immunogold-immunoperoxidase and in the double immunoperoxidase experiments.

C57Bl/6 WT	mouse-anti-Relaxin-3 rabbit-anti-Gephyrin	biotinylated donkey-anti-mouse 1.4 nm gold-conjugated goat-anti-rabbit
C57Bl/6 WT	mouse-anti-Relaxin-3 rabbit-anti-GABA-A-g2	biotinylated donkey-anti-mouse 1.4 nm gold-conjugated goat-anti-rabbit
vGAT-Cre	rabbit-anti-mCherry mouse-anti-Gephyrin	biotinylated donkey-anti-rabbit 0.8 nm gold-conjugated goat-anti-mouse
vGAT-Cre	rat-anti-RFP rabbit-anti-GABA-A-g2	biotinylated goat-anti-rat 1.4 nm gold-conjugated goat-anti-rabbit
vGAT-tdTomato	chicken-anti-eGFP (ThermoFisher) rat-anti-RFP	biotinylated goat-anti-chicken ImmPress goat-anti-rat
vGAT-Cre	chicken-anti-eGFP (ThermoFisher) rat-anti-somatostatin	biotinylated goat-anti-chicken ImmPress goat-anti-rat
vGAT-Cre	chicken-anti-eGFP (ThermoFisher) mouse-anti-Choleratoxin B	biotinylated goat-anti-chicken ImmPress horse-anti-mouse

Table S6. Quantification of monosynaptically-labeled neurons with rabies virus in the different brain areas projecting to GABAergic NI neurons.

Brain Area/Nucleus	Median %	Estimation of cell numbers per brain area			Behavioral relevance	References for behavioral relevance
		Mouse 1	Mouse 2	Mouse 3		
Prefrontal cortex	2,6%	174	654	138	fear behavior, reward, aversion	[1,2]
Cingulate cortex	1,4%	210	156	72	negative outcome of choice, aversion	[3]
Secondary motor cortex	1,3%	102	198	72	adaptive choice behavior, linking sensory cues to motor actions	[4]
Medial septum + Ventral limb of the diagonal band of Broca	1,3%	150	192	102	theta generation, episodic memory, sleep-wake cycles, motor control	[5–7]
Horizontal limb of the diagonal band of Broca + Substantia Innominata + nucleus basalis	1,3%	156	138	102	unexpected events with emotional valence	[8]
Lateral preoptic area	1,2%	54	186	162	aversion, reward system, CRH input into NI	[9]
Lateral habenula	4,1%	162	636	342	aversion, reward system	[9–11]
Zona incerta	2,3%	198	354	132	fear, freezing, attention, motor control	[12–14]
Lateral hypothalamus	4,3%	228	678	234	feeding-related reward behavior	[15–17]
Posterior hypothalamus	2,3%	276	276	138	theta rhythm, spatial memory	[18,19]
Mammillary body/ supramammillary	5,0%	600	960	60	motor control (head direction), memory formation, REM sleep	[19–22]
Periaqueductal grey	3,8%	696	390	198	freezing behavior	[23]
Ventral tegmental area	1,7%	204	66	96	reward processing, aversion	[2]
Mesencephalic reticular formation	1,5%	306	240	6	movement initiation	[24]
Dorsal raphe	3,8%	516	276	198	reward-related behavior, sleep-wake cycles	[25,26]
Median raphe	20,2%	2022	3156	1224	fear memory consolidation, anxiety and fear	[27,28]
Nucleus pontis oralis	6,3%	414	984	600	REM sleep, theta generation	[29,30]
Isthmic reticular formation	1,3%	42	210	108	movement initiation	[24]
Anterior/ventral tegmental nucleus (Gudden)	2,3%	300	102	120	REM sleep, theta generation, memory, motor control (head direction)	[31–34]
Laterodorsal tegmental nucleus	8,0%	954	N/A	N/A	reward processing (cocaine addiction)	[2,35]
Dorsomedial tegmental area	1,7%	444	258	78	REM sleep	[36]
Nucleus pontis caudalis	3,9%	462	636	114	motor control (movement initiation, acoustic startle, eye movement), REM sleep	[29,37,38]
Medial parabrachial nucleus	1,4%	168	42	84	taste perception (flavor avoidance), REM-NREM sleep-stage transitions	[39,40]
Nucleus prepositus	1,1%	312	168	12	motor control (head direction)	[41,42]
Gigantocellular nucleus	4,2%	504	678	102	sleep-wake cycles, motor control (REM atonia, emotional movement)	[40,43,44]
TOTAL	88,3%	11982	15630	5238		

Footnote: [1] R.R. Rozeske et al., Brain Behav. 14 (2015) 22–36. [2] S. Lammel et al., Nature 491 (2012) 212–217. [3] T. Kawai et al., Neuron 88 (2015) 792–804. [4] F. Barthas, A.C. Kwan, Trends Neurosci. 40 (2017) 181–193. [5] M. Vandecasteele et al., Proc. Natl. Acad. Sci. 111 (2014) 13535–13540. [6] R. Boyce et al., Science (80-.). 352 (2016) 812. [7] F. Fuhrmann et al., Neuron 86 (2015) 1253–1264. [8] B. Hangya et al., Cell 162 (2015) 1155–1168. [9] D.J. Barker et al., Cell Rep. 21 (2017) 1757–1769. [10] A.M. Stamatakis, G.D. Stuber, Nat. Neurosci. 15 (2012) 1105–1107. [11] T.C. Jhou et al., Neuron 61 (2009) 786–800. [12] X.L. Chou et al., Nat. Commun. 9 (2018) 1–12. [13] S. Chometton et al., Brain Struct. Funct. 222 (2017) 2507–2525. [14] G.D.R. Watson et al., J. Neurosci. 35 (2015) 9463–9476. [15] J.-J. Liu et al., J. Neurosci. 37 (2017) 11854–11866. [16] M. Fattahi et al., Addict. Biol. (2018). [17] A.G. Choudhary et al., Brain Struct. Funct. 223 (2018) 1313–1328. [18] R. Bocian et al., Hippocampus 26 (2016) 1354–1369. [19] B.E. Gutiérrez-Guzmán et al., Eur. J. Pharmacol. 682 (2012) 99–109. [20] C.M. Dillingham et al., Neurosci. Biobehav. Rev. 54 (2015) 108–119. [21] S.D. Vann, J.P. Aggleton, Nat. Rev. Neurosci. 5 (2004) 35–44. [22] P.H. Luppi et al., Curr. Opin. Neurobiol. 44 (2017) 59–64. [23] P. Tovote et al., Nature, Press 534 (2016) 206–212. [24] T.K. Roseberry et al., Cell 164 (2016) 526–537. [25] M. Luo et al., Learn Mem 22 (2015) 452–460. [26] J.M. Monti, Sleep Med. Rev. 15 (2011) 269–281. [27] D. V Wang et al., Nat. Neurosci. 18 (2015) 728–35. [28] T.G. Andrade et al., J. Psychopharmacol. 27 (2013) 1107–15. [29] L.D. Sanford et al., J. Neurophysiol. 90 (2003) 938–945. [30] R.P. Vertes, B. Kocsis, Neuroscience 81 (1997) 893–926. [31] P. Torterolo et al., Brain Res. 944 (2002) 184–189. [32] M.H. Bassant et al., Hippocampus 11 (2001) 809–813. [33] P.E. Sharp et al., Behav. Neurosci. 115 (2001) 571–588. [34] S.D. Vann, Brain 132 (2009) 2372–2384.

[35] K. Kaneda, Eur. J. Neurosci. (2018) 0–1. [36] S. Valencia Garcia et al., Brain Struct. Funct. 223 (2018) 2733–2751. [38] J. Márquez-Ruiz, M. Escudero, Sleep 33 (2010) 1517–1527. [39] M.L. De La Torre, Á. Agüero, Exp. Brain Res. 194 (2009) 207–218. [40] Y. Hayashi et al., Science (80). 350 (2015) 957–962. [41] W.N. Butler et al., Curr. Biol. 27 (2017) 1259–1267. [42] W.N. Butler, J.S. Taube, J. Neurosci. 35 (2015) 2547–2558. [43] E.M. Martin et al., J. Comp. Neurol. 519 (2011) 2574–2593. [44] Y.-Y. Lai et al., J. Neurophysiol. 104 (2010) 2024–2033.

Table S7. Immunochemical characterization of basal forebrain neurons (medial septum, vertical and horizontal limbs of the diagonal bands of Broca and substantia innominata pooled) monosynaptically projecting onto GABAergic NI neurons.

	Number	Percentage to total number of cells labeled
Total counted basal forebrain neurons for analyzing ChAT-positivity	35	2,86%
ChAT-positive neurons (n=1 mouse)	1	
Total counted basal forebrain neurons for analyzing PV-positivity	97	18,56%
PV-positive neurons (n=3 mice)	18	
Total counted basal forebrain neurons for analyzing CB-positivity	97	5,15%
CB-positive neurons (n=3 mice)	5	